# METHANE: A BIORESOURCE FOR FUEL AND BIOMOLECULES

EDITED BY: Obulisamy Parthiba Karthikeyan, Deepak Kumaresan, Marina G. Kalyuzhanaya, Kirsten Heimann, Chettiyappan Visvanathan and Nidia S. Caetano

PUBLISHED IN: Frontiers in Microbiology and Frontiers in Environmental Science

frontiers Research Topics

# frontiers



ISSN 1664-8714
ISBN 978-2-88963-562-7
DOI 10.3389/978-2-88963-562-7

## About Frontiers

Frontiers is more than just an open-access publisher of scholarly articles: it is a pioneering approach to the world of academia, radically improving the way scholarly research is managed. The grand vision of Frontiers is a world where all people have an equal opportunity to seek, share and generate knowledge. Frontiers provides immediate and permanent online open access to all its publications, but this alone is not enough to realize our grand goals.

## Frontiers Journal Series

The Frontiers Journal Series is a multi-tier and interdisciplinary set of open-access, online journals, promising a paradigm shift from the current review, selection and dissemination processes in academic publishing. All Frontiers journals are driven by researchers for researchers; therefore, they constitute a service to the scholarly community. At the same time, the Frontiers Journal Series operates on a revolutionary invention, the tiered publishing system, initially addressing specific communities of scholars, and gradually climbing up to broader public understanding, thus serving the interests of the lay society, too.

## Dedication to Quality

Each Frontiers article is a landmark of the highest quality, thanks to genuinely collaborative interactions between authors and review editors, who include some of the world's best academicians. Research must be certified by peers before entering a stream of knowledge that may eventually reach the public - and shape society; therefore, Frontiers only applies the most rigorous and unbiased reviews.
Frontiers revolutionizes research publishing by freely delivering the most outstanding research, evaluated with no bias from both the academic and social point of view. By applying the most advanced information technologies, Frontiers is catapulting scholarly publishing into a new generation.

## What are Frontiers Research Topics?

Frontiers Research Topics are very popular trademarks of the Frontiers Journals Series: they are collections of at least ten articles, all centered on a particular subject. With their unique mix of varied contributions from Original Research to Review Articles, Frontiers Research Topics unify the most influential researchers, the latest key findings and historical advances in a hot research area! Find out more on how to host your own Frontiers Research Topic or contribute to one as an author by contacting the Frontiers Editorial Office: researchtopics@frontiersin.org

# METHANE: A BIORESOURCE FOR FUEL AND BIOMOLECULES

Topic Editors:
**Obulisamy Parthiba Karthikeyan,** University of Houston, United States
**Deepak Kumaresan,** Queen's University Belfast, United Kingdom
**Marina G. Kalyuzhanaya,** San Diego State University, United States
**Kirsten Heimann,** Flinders University, Australia
**Chettiyappan Visvanathan,** Asian Institute of Technology, Thailand
**Nidia S. Caetano,** Instituto Superior de Engenharia do Porto (ISEP), Portugal

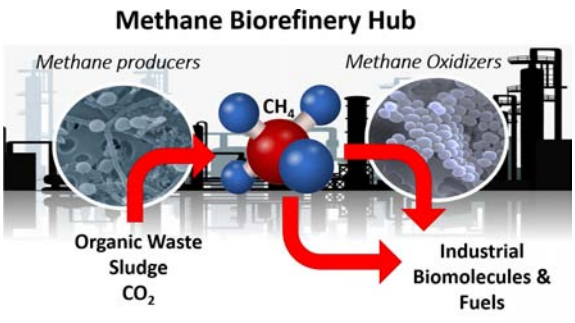


SEM images, Copyright Dennis Kunkel Microscopy, Inc.

**Citation:** Karthikeyan, O. P., Kumaresan, D., Kalyuzhanaya, M. G., Heimann, K., Visvanathan, C., Caetano, N. S., eds. (2020). Methane: A Bioresource for Fuel and Biomolecules. Lausanne: Frontiers Media SA. doi: 10.3389/978-2-88963-562-7

# Table of Contents

frontiers in Environmental Science

EDITORIAL
published: 05 February 2020
doi: 10.3389/fenvs.2020.00009

# Editorial: Methane: A Bioresource for Fuel and Biomolecules

*Marina G. Kalyuzhnaya*[1], *Deepak Kumaresan*[2], *Kirsten Heimann*[3], *Nidia S. Caetano*[4], *Chettiyappan Visvanathan*[5] *and Obulisamy Parthiba Karthikeyan*[6,7]*

[1] Department of Biology, San Diego State University, San Diego, CA, United States, [2] School of Biological Sciences, Queen's University of Belfast, Belfast, United Kingdom, [3] Centre for Marine Bioproducts Development, College of Medicine and Public Health, Flinders University, Adelaide, SA, Australia, [4] Department of Chemical Engineering, Instituto Superior de Engenharia Do Porto, Porto, Portugal, [5] Department of Energy, Environment, and Climate, School of Environment, Resources and Development, Asian Institute of Technology, Pathumthani, Thailand, [6] Department of Civil and Environmental Engineering, University of Michigan, Ann Arbor, MI, United States, [7] Department of Engineering Technology, College of Technology, University of Houston, Houston, TX, United States

**Keywords: methane, methanotrophs, electron transfer, bioreactor, value addition and sustainability**

OPEN ACCESS

***Edited by:***
*Hyung-Sool Lee,*
*University of Waterloo, Canada*

***Reviewed by:***
*Seung Gu Shin,*
*Pohang University of Science and Technology, South Korea*
*Wei-Min Wu,*
*Stanford University, United States*

****Correspondence:***
*Obulisamy Parthiba Karthikeyan*
*opkens@gmail.com;*
*pobulisa@umich.edu*

***Specialty section:***
*This article was submitted to Microbiotechnology, Ecotoxicology and Bioremediation, a section of the journal Frontiers in Environmental Science*

***Received:*** *18 October 2019*
***Accepted:*** *13 January 2020*
***Published:*** *05 February 2020*

***Citation:***
*Kalyuzhnaya MG, Kumaresan D, Heimann K, Caetano NS, Visvanathan C and Parthiba Karthikeyan O (2020) Editorial: Methane: A Bioresource for Fuel and Biomolecules. Front. Environ. Sci. 8:9. doi: 10.3389/fenvs.2020.00009*

## Editorial on the Research Topic

## Methane: A Bioresource for Fuel and Biomolecules

Methane ($CH_4$), a highly reduced C1 compound, is one of the long-lived atmospheric gases with high global warming potential i.e., 28–36 times that of $CO_2$ over 100 years. The atmospheric levels of $CH_4$ reached ∼1863 part per billions (ppb) in 2014, and annual increase of atmospheric $CH_4$ level thereafter measured as ∼10 ppb. The $CH_4$ is projected to drive the rise in global temperature of ∼4–6°C by 2050, and thus it is currently considered as the main target for global climate stabilization and mitigation (COP-21, 2015). Capturing anthropogenic $CH_4$ to produce value products is highly feasible, but the great challenge is that to tap, concentrate, purify, store, transport, and utilize the $CH_4$ from different point emission sources is presently not economically viable.

In this special issue, a conceptual model of "Methane-Biorefinery Hub" is proposed as a sustainable development to mitigate the $CH_4$ emissions from the most significant anthropogenic sources. The idea of "Methane-Biorefinery Hub" is deeply rooted in natural $CH_4$ production and consumption processes (**Figure 1**). While in general, with a few exceptions, the natural $CH_4$ cycle is balanced, the anthropogenic disturbances have typically led to increase the $CH_4$ emissions. Thus, better understanding of mechanisms that control $CH_4$ cycle in nature can be used to engineer better systems in human-built environments. For example, Holmes et al.. established that the bacteria (donors) and archaea (acceptors) communicate through nano-wires or electron transfer molecules i.e., the electrons transfer through e-pili (i.e., direct interspecies electron transfer), while protons diffusion (direct interspecies hydrogen transfer) is regulated by the partial pressure of the bioreactor system. Mimicking natural processes in laboratory/pilot-scale bioreactors that are designed to optimize specific operational conditions to regulate such communication may lead to successful implementation of technology to effectively utilize the waste materials e.g., municipal solid waste, food waste, industrial organics and wastewaters, or low-grade coals with/without the aid of external carbon/electron sources to produce $CH_4$ as bio-energy, as shown by Yang et al. As pointed out by Wojcieszak et al., well-balanced microbial consortium are crucial for efficient biogas production, and inoculum sampled from typical methanogenic environments can be gradually adapted to industrial installations to allow effective biogas production. Addition of microbial supplements, metals/nutrients, organic sources (Zaldívar Carrillo et al.), electron

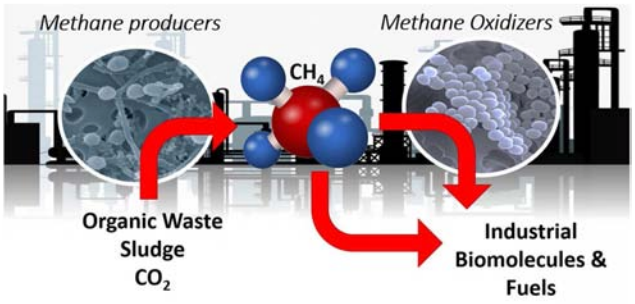


**FIGURE 1 |** Methane biorefinery for value chemical and biofuels. Microbial images (SEM) courtesy of Dr. Dennis Kunkel.

conductive materials or electrodes, and altering the head-space gas composition (and partial pressure) are proposed as options for facilitating electron transfer and microbial interactions, while it may also change the equilibrium between dissolved vs. gas phase $CH_4$ concentrations within the system.

Another unique approach for recovering dissolved $CH_4$ using degassing membrane contactors was proposed by Velasco et al.. While still at the stage of infancy, this unique technology highlights limitless opportunities for innovative approaches in $CH_4$ capturing. If not recovered effectively, the dissolved $CH_4$ and manipulating conditions may be expected to fuel the anaerobic methane oxidizers (ANME), and also sulfate reducing bacteria (SRB), to thrive and compete with methanogens for electrons/protons that may lead to low $CH_4$ yield. The ANME possess a reverse methanogenesis process, i.e., utilizing $CH_4$ (and $CO_2$) as carbon sources to produce acetate or other products. On the other hand SRB compete with methanogens for similar substrates or electron donors. So, there may not be a competition between SRB and ANME for substrate, but it required investigation. On the other hand, the industrial applications of ANME are challenging, and still limited by the number of unresolved biochemical questions. However, an example of how a solid understanding of enzyme kinetics and energy transfer between the microbial communities can be used to manipulate the operating conditions to either facilitate or eliminate methane production was presented by Grisewood et al.. Alternatively, establishment of co-cultures of methanogens and ANME to produce value chemicals from anaerobic digestion processes was proposed and validated using a newly developed mathematical model by Nazem-Bokaee and Maranas, which, however, still relies on the electron coupling theory. Once fully understood, the ANME-based approach could be a viable option for reducing $CH_4$ emissions from natural settings, while aerobic oxidation is recommended for industrial-scale organic digestion facilities.

The aerobic $CH_4$ oxidization process is easily coupled with digesters, while the process can yield a number of value products such as polymers, organic acids, single cell protein (SCP), compatible solutes, short/long chain fatty acids, omega fatty acids, vitamins, methanol, formate, etc. Methanotrophs are classified into Group I and Group II based on their physiology. Group I methanotroph e.g., *Methylococcus capsulatus* (Bath) is reported to produce SCP, while Group-II methanotrophs (e.g., *Methylosinus trichosporium* OB3b) are capable of accumulating biopolymers/SFA/LFA from $CH_4$. An example of coupled production is highlighted by the work of Henard et al.. Metabolic modeling can further impower application of natural $CH_4$ consuming bacteria, as exemplified by Lieven et al.. While it is widely acknowledged that the natural capacities of microbial systems (as axenic or mixed cultures) in $CH_4$-consumption and accumulation of value products are governed by a number of factors e.g., carbon, nutrients, and metals, we are only now applying the knowledge for improving their industrial potential. Further, an example of how nitrogen starvation activates polyhydroxyalkanoate accumulation and alters the fatty acid compositions in biomass is provided by Tays et al.. The metal-switch impacts on the key enzyme activities, kinetics, the internal electron pool, and the carbon flux e.g., are described in the work by Akberdin et al..

Nevertheless, the industrial applications and innovations remain to be challenged by long-standing fundamental questions regarding $CH_4$ biocatalysts; including: (a) source of electron donors for $CH_4$ activation as well as electron acceptors for process intensification; (b) regulation of contaminations or development of efficient strategies for controlling natural communities or synthetic co-cultures; (c) improved genetic traceability of methanotrophs in a mixed consortium and (d) coupling of $CH_4$-conversion potential with efficient nitrogen fixation and denitrification. We would like to acknowledge significant progress in developing systems biology toolbox for manipulating methanotrophic bacteria, as well as new advances in overcoming technological bottlenecks related to $CH_4$ mass-transfer limitation. Yet, some challenges still remain. New developments highlight additional need for further research, specifically in areas of $O_2$-capturing, cell immobilization, $CH_4$ and $CO_2$ conversion by coculture of methanotrophs and algae/methylotrophs, coupling $CH_4$ conversion and electrocatalysis. Algae and methanotrophs exchange nutrients during co-culturing are beneficial, while methylotrophs helps to alleviate any methanol toxicity.

The papers published in this special issue confirm that $CH_4$ emission/production is related to the microbiomes of the system, which are easy to be manipulated through biological/chemical augmentation methods. By coupling $CH_4$ production with either ANME or methanotrophs, emissions could be significantly reduced and high-value products could be recovered through an integrated "Methane-Biorefinery" approach. Interestingly, in the work by Burton et al. it was concluded that the aerobic methanotrophs, methylotrophs and methanogenic archaea found to have common lineage i.e., use tetrahydromethanopterin ($H_4$MPT) and/or tetrahydrofolate ($H_4$F) as coenzymes in one-carbon (C1) transfer pathways that have been overlooked in the past and the relationships need to be well-studied for harnessing the benefits under "Microbiome" theory.

## AUTHOR CONTRIBUTIONS

OP and MK written this editorial. NC, KH, CV, and DK edited the final text. All authors approved the final version.

**Conflict of Interest:** The authors declare that the research was conducted in the absence of any commercial or financial relationships that could be construed as a potential conflict of interest.

frontiers in Microbiology

ORIGINAL RESEARCH
published: 25 September 2018
doi: 10.3389/fmicb.2018.02239

# Combined Effects of Carbon and Nitrogen Source to Optimize Growth of Proteobacterial Methanotrophs

*Catherine Tays[1,2], Michael T. Guarnieri[3], Dominic Sauvageau[2] and Lisa Y. Stein[1]**

*[1] Department of Biological Sciences, University of Alberta, Edmonton, AB, Canada, [2] Department of Chemical and Materials Engineering, University of Alberta, Edmonton, AB, Canada, [3] National Renewable Energy Laboratory, Golden, CO, United States*

Methane, a potent greenhouse gas, and methanol, commonly called wood alcohol, are common by-products of modern industrial processes. They can, however, be consumed as a feedstock by bacteria known as methanotrophs, which can serve as useful vectors for biotransformation and bioproduction. Successful implementation in industrial settings relies upon efficient growth and bioconversion, and the optimization of culturing conditions for these bacteria remains an ongoing effort, complicated by the wide variety of characteristics present in the methanotroph culture collection. Here, we demonstrate the variable growth outcomes of five diverse methanotrophic strains – *Methylocystis* sp. Rockwell, *Methylocystis* sp. WRRC1, *Methylosinus trichosporium* OB3b, *Methylomicrobium album* BG8, and *Methylomonas denitrificans* FJG1 – grown on either methane or methanol, at three different concentrations, with either ammonium or nitrate provided as nitrogen source. Maximum optical density (OD), growth rate, and biomass yield were assessed for each condition. Further metabolite and fatty acid methyl ester (FAME) analyses were completed for *Methylocystis* sp. Rockwell and *M. album* BG8. The results indicate differential response to these growth conditions, with a general preference for ammonium-based growth over nitrate, except for *M. denitrificans* FJG1. Methane is also preferred by most strains, with methanol resulting in unreliable or inhibited growth in all but *M. album* BG8. Metabolite analysis points to monitoring of excreted formic acid as a potential indicator of adverse growth conditions, while the magnitude of FAME variation between conditions may point to strains with broader substrate tolerance. These findings suggest that methanotroph strains must be carefully evaluated before use in industry, both to identify optimal conditions and to ensure the strain selected is appropriate for the process of interest. Much work remains in addressing the optimization of growth strategies for these promising microorganisms since disregarding these important steps in process development could ultimately lead to inefficient or failed bioprocesses.

**Keywords: methanotrophic bacteria, methane, methanol, ammonium, nitrate, FAME**

OPEN ACCESS

***Edited by:***
*Obulisamy Parthiba Karthikeyan, University of Michigan, United States*

***Reviewed by:***
*Mariusz Cycoń, Medical University of Silesia, Poland*
*Muhammad Farhan Ul Haque, University of East Anglia, United Kingdom*

***Correspondence:**
*Lisa Y. Stein*
*lisa.stein@ualberta.ca*

***Specialty section:***
*This article was submitted to Microbiotechnology, Ecotoxicology and Bioremediation, a section of the journal Frontiers in Microbiology*

***Received:*** *25 April 2018*
***Accepted:*** *03 September 2018*
***Published:*** *25 September 2018*

***Citation:***
*Tays C, Guarnieri MT, Sauvageau D and Stein LY (2018) Combined Effects of Carbon and Nitrogen Source to Optimize Growth of Proteobacterial Methanotrophs. Front. Microbiol. 9:2239. doi: 10.3389/fmicb.2018.02239*

## INTRODUCTION

Methane-oxidizing bacteria (MOB), or methanotrophs, oxidize single-carbon molecules, specifically methane, to be used as their sole carbon and energy source. Methanotrophs are widely distributed in the environment, from rice paddies to upland soils to marine environments, among others (Bender and Conrad, 1994). Methanotrophic bacteria are taxonomically diverse and are found in the phyla Verrucomicrobiae (Dunfield et al., 2007), NC10 (Ettwig et al., 2009), and Proteobacteria (Bowman, 2006; Kelly et al., 2014; Webb et al., 2014). Within the Proteobacteria, which encompass the majority of currently cultured methanotrophs, MOB can be further classified as Alphaproteobacteria (Alpha-MOB and Type II) or Gammaproteobacteria (Gamma-MOB, Type I, or Type X), with each group having distinct physiological traits. Differentiating traits include their primary central carbon pathways (serine pathway in Alpha-MOB and ribulose monophosphate pathway in Gamma-MOB), orientation and distribution of intracytoplasmic membranes (ICMs), and composition of lipids in terms of fatty acid proportions (Hanson and Hanson, 1996).

Methane is the natural energy and carbon substrate of methanotrophs, the first molecule that is activated in their central oxidation pathway through the enzyme methane monooxygenase (MMO). MMO oxidizes methane to methanol, which is sequentially oxidized to carbon dioxide *via* formaldehyde and formate or incorporated at the level of formaldehyde into cell biomass (Hanson and Hanson, 1996). Though the pathway of methane oxidation to carbon dioxide is overall energy generating, the MMO enzyme requires energy in the form of two reducing equivalents (Hanson and Hanson, 1996). Methanotrophs can also grow exclusively on methanol and it has thus been investigated as an alternate carbon source for their culture. However, due to its toxicity, methanol as a sole growth substrate generally results in lower yields, despite the apparently decreased energetic and oxygen demands of methanol-grown cultures (Whittenbury et al., 1970; van Dijken and Harder, 1975; Best and Higgins, 1981). An exception to poor growth on methanol is the Gamma-MOB strain *Methylomicrobium buryatense* 5B, which was shown to grow faster and to higher yields when grown on methanol in batch culture (up to a concentration 1.75 M) than on methane (Eshinimaev et al., 2002). The related strain *M. buryatense* 5GB1 grew better on methane than on methanol in a bioreactor, but still demonstrated robust growth on methanol (Gilman et al., 2015), as did *Methylomicrobium alcaliphilum* 20Z (Akberdin et al., 2018).

Aside from carbon source, most methanotrophs utilize either ammonium or nitrate as nitrogen sources for assimilation while some have the capacity to fix $N_2$. Theoretically, use of ammonium as a nitrogen source should be bioenergetically favorable compared to nitrate, given that it can be directly assimilated into cell biomass. However, the structural similarity between ammonium and methane leads to competitive inhibition of MMO enzymes and co-oxidation of ammonia to the cytotoxic products, hydroxylamine and nitrite (Nyerges and Stein, 2009). Toxicity and inhibition of methane oxidation by ammonium, hydroxylamine and nitrite vary significantly among methanotrophic strains (Nyerges and Stein, 2009). MOB that encode and express hydroxylamine dehydrogenase enzymes (HAO) with similarity to those found in ammonia-oxidizing bacteria can more easily overcome hydroxylamine toxicity derived from the oxidation of ammonia (Campbell et al., 2011). Yet these same strains, such as *Methylocystis* sp. Rockwell, can still be sensitive to nitrite toxicity (Nyerges et al., 2010). Then again, some methanotrophs encode and express nitrite and nitric oxide reductase enzymes that can detoxify nitrite and are thus less susceptible to these cytotoxic effects (Kits et al., 2015a; Mohammadi et al., 2017; Stein and Klotz, 2011). The presence and expression of genes for overcoming toxic intermediates of nitrogen metabolism are not phylogenetically coherent among the MOB as the ability to oxidize ammonia (i.e., nitrify) and/or reduce nitrogen oxides (i.e., denitrify) are fairly randomly distributed across MOB taxa (Stein and Klotz, 2011).

Because carbon (e.g., methane or methanol) and nitrogen (e.g., ammonium, nitrate, or N-limitation) sources have different effects on the physiology and growth of individual MOB strains, the optimization of growth medium has to be empirically determined for each isolate. For instance, a study comparing growth of the Alpha-MOB, *Methylosinus trichosporium* OB3b, and the Gamma-MOB, *Methylomicrobium album* BG8, revealed that *M. album* BG8 grew better on lower methane concentrations. Moreover, the combination of methanol and methane further enhanced growth of *M. album* BG8 over *M. trichosporium* OB3b, while *M. trichosporium* OB3b fared better than *M. album* BG8 under nitrate limitation due to its ability to fix $N_2$ (Graham et al., 1993). Another study showed that the Alphas-MOB *Methylocystis* sp. Rockwell grew significantly better with ammonium, rather than nitrate, as N-source, whereas the Gamma-MOB *M. album* BG8 preferred nitrate and was uninhibited by high nitrite concentrations in the medium (Nyerges et al., 2010). A study of *Methylocystis* sp. strain SC2, showed no inhibition of growth activity with up to 30 mM ammonium, three times the standard amount in ammonium mineral salts (AMS) medium (Dam et al., 2014). Beyond growth implications, nitrogen source can also have other important implications for bioindustry. For example, nitrogen starvation serves as the most common trigger for inducing production of polyhydroxybutyrate (PHB), a carbon-based storage molecule which is a truly biodegradable polymer (Sundstrom and Criddle, 2015). Through different growth/limitation schemes, nitrogen limitation has resulted in high yields of PHB at high molecular weights; though these studies generally consider nitrogen source concentration and do not focus on nitrogen species (Khosravi-Darani et al., 2013). This is especially relevant as techno-economic analyses favor ammonium as an N-source; nitrate is a key cost driver in most bioconversion processes. As such, the growth and metabolic implications of nitrogen source are important considerations when evaluating strains for their bioindustrial potential.

The current study compares the effects of carbon source (methane or methanol) and nitrogen source (ammonium or nitrate) on growth rates and biomass yields of three Alpha-MOB and two Gamma-MOB under batch cultivation. The objectives of

this study are to: (1) compare strain-to-strain variation in their carbon/nitrogen preference, (2) find preferred carbon/nitrogen combinations for each strain, and (3) determine whether changes in carbon/nitrogen sources affect the phospholipid fatty acid (PLFA) composition and/or abundance in representative strains of Alpha- and Gamma-MOB. Previous studies of strains of *M. buryatense* grown in methanol showed a significant reduction in fatty acid methyl esters (FAME) and visible reduction of ICMs (Eshinimaev et al., 2002; Gilman et al., 2015), which is logical as MMO enzymes housed in ICMs are not necessary for growth on methanol. Whether growth on methanol results in a compositional change in PLFAs remains understudied in MOB. The results of this study are useful to demonstrate the range of strain-to-strain variation in carbon/nitrogen preference among MOB toward optimized growth of strains with industrial potential.

# MATERIALS AND METHODS

## Growth and Maintenance of Methanotrophic Bacteria

Five MOB isolates were selected to provide a wide comparative assessment of their growth characteristics on different carbon/nitrogen source combinations. Strains included three Alpha-MOB: *Methylocystis* sp. strain Rockwell (ATCC 49242), *Methylocystis* sp. strain WRRC1 (gift from Mango Materials), and *Methylosinus trichosporium* OB3b; and two Gamma-MOB: *Methylomicrobium album* BG8 (ATCC 33003) and *Methylomonas denitrificans* FJG1 (Kits et al., 2015b).

Cultures were grown using either AMS or nitrate mineral salts (NMS) medium (Whittenbury et al., 1970), containing either 10 mM ammonium chloride (AMS) or 10 mM potassium nitrate (NMS) as N-source. For all growth experiments, Wheaton media bottles (250 mL) closed with butyl-rubber septa caps and filled with 100 mL medium, were used as previously reported (Kits et al., 2015b). The copper ($CuSO_4$) concentration in the final medium was 5 μM for all media formulations. The media were buffered to pH 6.8 through addition of 1.5 mL phosphate buffer (26 g/L $KH_2PO_4$, 33 g/L $Na_2HPO_4$) and inoculated with 1 mL (1%) of previously grown cultures that had been passaged once in identical conditions to each of the experimental conditions; as such, initial biomass at inoculation varied somewhat, reflecting the growth result of the inoculum culture.

Methane was provided *via* injection through a 0.22-μm filter-fitted syringe. 0.5, 2, or 2.5 mmol of methane were provided and the pressure was maintained at 1 atm by removing the equivalent amount of gas headspace *via* syringe prior to methane addition. To delay onset of hypoxia, the 2.5 mmol methane incubations were conducted under approximately 1.05 atm. In the appropriate experiments, 0.5, 1, or 2 mmol of pure high performance liquid chromatography (HPLC) grade methanol were added and the cultures were kept at a pressure of 1 atm. All cultures were incubated at 30°C, the optimal growth temperature for all five strains, with shaking at 150 rpm. Experiments were performed with replication ($n$ = 3) for all conditions.

## Analysis of Growth

To monitor growth, 500-μL samples were extracted from cultures *via* sterile syringe at regular intervals over lag, exponential, and stationary phases. Although each growth experiment was performed multiple times to ensure consistency of growth rates and yields with each treatment, three technical replicates used for each condition to calculate standard deviations and to perform statistical analysis with even numbers of samples for each strain and condition. Growth was assessed using optical density (OD) measurements at 540 nm in a 48-well microplate (Multiskan Spectrum, Thermo Scientific). Growth rates were calculated from points on the growth curve covering an interval of logarithmic growth using the following formula (Eq. 1), where α = the growth rate constant, $N$ = number of cells (herein defined by OD measurements), and $t$ = time:

$$\alpha = \frac{\ln\left(\frac{N_T}{N_0}\right)}{(t_T - t_0)} \quad (1)$$

Growth yield was determined as the change in biomass (as measured by OD) per mole of carbon source supplied. OD was selected as a growth metric due to its widespread use in industrial bioprocess monitoring. Optimal growth conditions were chosen by weighted evaluation of both growth rate and yield, as described in Eq. 2, with the highest resultant value selected as optimal:

$$x = \left(0.25 \times \frac{\text{yield}}{\text{max yield}}\right) + \left(0.75 \times \frac{\text{growth rate}}{\text{max growth rate}}\right) \quad (2)$$

Culture purity was assured through phase contrast microscopy and plating of culture on TSA/nutrient agar plates, where lack of growth demonstrated lack of contamination. Multivariate ANOVA was done using R Studio to identify contribution of factors to outcomes, as well as any interaction effects between factors.

Methane and oxygen were measured using a gas chromatograph with TCD detector (GC-TCD, Shimadzu; outfitted with a molecular sieve 5A and Hayesep Q column, Alltech). A 250-μL gas-tight syringe (SGE Analytical Science; 100 μL/injection) was used to extract and inject headspace samples. Injection and detection temperatures were 120°C and oven temperature was 90°C with current set to 90 mA, using helium carrier gas (Ultra High Purity, Praxair) at 200 kPa. Gas concentrations were calculated using standard curves of known amounts of the respective pure gases (Praxair).

## Phospholipid Fatty Acid (PLFA) Analysis

*M. album* BG8 and *Methylocystis* sp. Rockwell were selected for PLFA analysis. Cultures were grown as detailed above, with either 2.5 mmol methane or 1 mmol methanol provided as carbon source as these conditions were most favorable for biomass accumulation. Cultures were also grown with either ammonium or nitrate as N-source for comparison. Samples for analysis were collected upon reaching maximum $OD_{540}$ but prior to the onset of stationary phase. Cells were collected by vacuum filtration onto a 0.22-μm filter, which was washed with sterile medium, at which time the cells were transferred into a microcentrifuge

tube and pelleted before being frozen at −80°C. Cell pellets ($n$ = 6 for each condition) were analyzed for PLFA content at the National Renewable Energy Laboratory (NREL) in Golden, CO, United States.

Whole biomass lipid content was measured through FAME analysis as described previously (Henard et al., 2016). Briefly, 10 mg of lyophyilized biomass (dried overnight at 40°C under vacuum) were homogenized with 0.2 mL of chloroform:methanol (2:1, v/v), and the resulting solubilized lipids were transesterified *in situ* with 0.3 mL of HCl:methanol (5%, v/v) for 1 h at 85 °C in the presence of a known amount of tridecanoic acid (C13) methyl ester as an internal standard. FAMEs were extracted with hexane (1 mL) at room temperature for 1 h and analyzed by gas chromatography: flame ionization detection (GC:FID) on a DB-WAX column (30 m × 0.25 mm i.d. and 0.25 μm film thickness).

## Metabolite Analysis

Supernatant (1 mL) from the same cultures used for PLFA analysis were collected *via* sterile syringe and passed through a 0.22-μm syringe filter to remove cells, with replicates grown for each condition ($n$ = 3). Culture supernatants ($n$ = 3), were analyzed for metabolites at the NREL in Golden, CO, United States. HPLC was used to detect lactate, formate, acetate, and methanol in culture supernatants, as described previously (Henard et al., 2016). Briefly, culture supernatant was filtered using a 0.2-μm syringe filter or 0.5 mL 10K MWCO centrifuge tube (Life Technologies) and then separated using a model 1260 HPLC (Agilent, Santa Clara, CA, United States) and a cation H HPx-87H column (Bio-Rad). A 0.1-mL injection volume was used in 0.01 N sulfuric acid with a 0.6 mL/min flow rate at 55°C. DAD detection was measured at 220nm and referenced at 360 nm, and organic acid concentrations were calculated by regression analysis compared to known standards. For analysis of comparisons between conditions, significance was determined by standard $t$-test, with $\alpha < 0.05$; all differences denoted as significant met this standard.

## RNA Extraction

Total RNA was extracted from *Methylocystis* sp. Rockwell and *M. album* BG8 cells grown in either AMS or NMS, with methanol (1 mmol) or methane (2.5 mmol) provided as carbon source, at late log phase, using the MasterPure RNA purification kit (Epicentre). Briefly, cells were inactivated with phenol-stop solution (5% phenol and 95% ethanol) and pelleted through centrifugation. Nucleic acid from *Methylocystis* sp. Rockwell and *M. album BG8* were purified according to manufacturer's instructions, with the following modifications: 1 mg total Proteinase K was added for *Methylocystis* sp. Rockwell, and 0.35 mg total Proteinase K was added for *M. album* BG8. In addition, samples of *Methylocystis* sp. Rockwell grown on methanol were processed with organic solvent extraction in place of MPC precipitation as follows: extract sequentially with equal volume of phenol (acetate-buffered, pH 4.2), equal volume of 1:1 phenol:chloroform, and equal volume of 24:1 chloroform:isoamyl alcohol, before resuming MasterPure total nucleic acid precipitation protocol at the isopropanol addition step. RNA quantity and quality were assessed using a BioAnalyzer (Agilent Technologies).

## RNA Sequencing and Assembly

RNA-Seq was performed by the Department of Energy Joint Genome Institute (DOE, JGI), using Illumina HiSeq-2000 technology. Raw reads, JGI transcriptomic analysis, and additional supporting information were made available through the JGI Genome Portal, under proposal ID 1114. Raw reads were trimmed and quality checked using CLC Genomics Workbench with quality scores (limit 0.05) and length filter (>30 bp). CLC RNASeq Assembler was then used to map reads to genome using default settings. Gene expression and differential expression were calculated using CLC Genomics Workbench, using reads per kilobase of transcript per million mapped reads (RPKM) as normalized gene expression levels. Due to its prevalence in literature, nitrate-methane was selected as the reference condition to serve as a standard of comparison, and all other expression levels were judged relative to expression under this condition. Significance in differential expression was considered at an $n$-fold change of $>|1.25|$ and false discovery rate (FDR) adjusted $p$-value of <0.05, calculated by CLC Genomics Workbench. All *Methylocystis* sp. Rockwell conditions were completed with $n$ = 3 replicates, as was *M. album* BG8 NMS/$CH_3OH$, while the remaining three samples were $n$ = 2 replicates.

# RESULTS

## Effect of Carbon and Nitrogen Sources on Growth Rates and Yields of Methanotrophs

The effects of two carbon (methane and methanol) and two nitrogen (ammonium and nitrate) sources on the growth rates and yields of three Alpha-MOB and two Gamma-MOB were compared. The range of carbon amounts added to the 100-mL cultures was chosen from a point of limitation to excess as follows. At 0.5 mmol methane, the cultures were found to be carbon limited, as demonstrated by complete depletion of methane coinciding with the onset of stationary phase (**Supplementary Figure S1**). At 2.5 mmol methane, the cultures were found to be oxygen limited as the onset of stationary phase coincided with the depletion of oxygen, while methane remained in the gas headspace (**Supplementary Figure S2**). Therefore, the comparison of growth between 0.5 and 2.5 mmol carbon were selected to include growth conditions that ranged between carbon limitation and oxygen limitation.

**Figure 1** shows the maximum $OD_{540}$ obtained for all strains and conditions tested (varying amounts of C-source, with 10 mM ammonium or nitrate in 100-mL cultures). The time points at which maximum optical densities were achieved, from the average of replicates, are given in **Supplementary Table S1**. Due to the mass transfer limitation of methane into the liquid medium, the apparent carbon availability to the culture is mediated by the surface area of the liquid–gas interface, whereas methanol is immediately available to the culture. This could

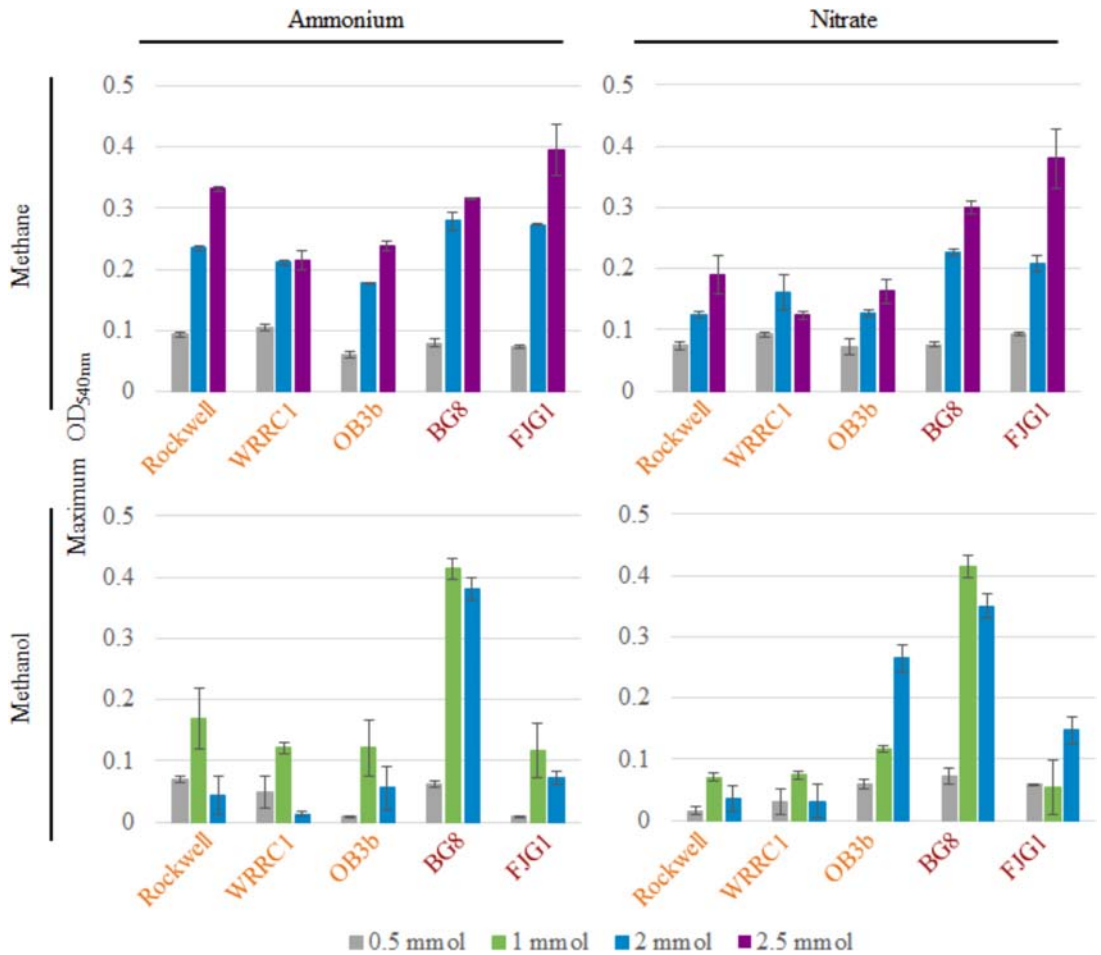


**FIGURE 1 |** Maximum $OD_{540}$ of 100-mL cultures of methanotrophic bacteria provided with 10 mM ammonium or nitrate and varying amounts of methane or methanol. Error bars represent standard deviations for $n = 3$ technical replicates per condition. Alpha-MOB strain names are indicated in orange and Gamma-MOB names are indicated in red.

lead to faster growth rates in methanol-grown cultures, as a much higher proportion of substrate is readily available for use from the time of inoculation. In some cases, the toxicity of methanol could actually result in the opposite effect, with growth inhibition occurring at higher concentrations of methanol in batch culture.

For methane-grown cultures, ammonium as the N-source resulted in overall higher biomass ($OD_{540}$) than with nitrate, particularly for the three Alpha-MOB (**Figure 1**). At the highest methane amount tested (2.5 mmol), the two Gamma-MOB showed little difference in $OD_{540}$ between ammonium and nitrate. In all strains, the 0.5 mmol methane condition showed low $OD_{540}$ in agreement with the carbon limitation that this condition imposes. With nitrate, the *Methylocystis* sp. WRRC1 achieved lower $OD_{540}$ when grown with 2.5 mmol compared to 2 mmol methane, unlike the other strains. Methanol-grown cultures generally reached a lower maximum $OD_{540}$ than methane-grown cultures, which is apparent in both the 0.5 and 2 mmol carbon amended cultures. A notable exception to this trend was with *M. album* BG8, which showed a maximum $OD_{540}$ when grown in 1 or 2 mmol methanol, in either ammonium or nitrate (**Figure 1** and **Supplementary Figure S3**).

Methane-grown cultures were generally more replicable in terms of growth yields ($OD_{540}$/mol-C source) (**Table 1**) and length of lag phase (**Supplementary Table S2**) than methanol-grown cultures. Extremely low, or even absence of growth was observed among replicate cultures grown on methanol. However, higher growth yields were still achieved with 1 versus 2 mmol methanol for all strains, suggesting toxicity for 2 mmol methanol (representing a concentration of 0.2 mM). As all of the carbon was consumed in the 0.5–1 mmol carbon-amended cultures, the calculated growth yields were highest under these conditions, and were higher with methane than with methanol except for *M. album* BG8 (**Table 1**).

Conditions in which methane was the carbon source and ammonium was the nitrogen source resulted in generally high growth rates for all strains. Methanol led to generally slower growth than methane, with the exception of *M. album* BG8 (**Table 2**). Lag phases also tended to be much longer for growth

**TABLE 1 |** Growth yields ($OD_{540nm}$/mol-C source) of methanotrophic bacteria grown in combinations of different carbon and nitrogen sources.

| Strain | Carbon (mmol) | Methane | | Methanol | |
|---|---|---|---|---|---|
| | | $NH_4^+$ | $NO_3^-$ | $NH_4^+$ | $NO_3^-$ |
| Rockwell | 0.5 | **188 (±7.98)** | 149 (±13.2) | 138 (±9.44) | 29.7 (±13.8) |
| | 1 | – | – | 169 (±50) | 70.5 (±6.75) |
| | 2 | 118 (±1.78) | 62.2 (±2.48) | 21.7 (±15.9) | 17.6 (±10.7) |
| | 2.5 | 133 (±1.88) | 75.8 (±12.7) | – | – |
| WRRC1 | 0.5 | **210 (±9.51)** | 185 (±7.5) | 98.3 (±51.8) | 60.1 (±39.6) |
| | 1 | – | – | 121 (±8.44) | 73.7 (±6.4) |
| | 2 | 106 (±1.69) | 80.4 (±14.9) | 6.17 (±1.93) | 15.6 (±13.3) |
| | 2.5 | 86.0 (±6.42) | 49.3 (±2.89) | – | – |
| OB3b | 0.5 | 123 (±10.2) | **144 (±26.8)** | 19.5 (±1.71) | 120 (±15.7) |
| | 1 | – | – | 121 (±45.9) | 116 (±5.14) |
| | 2 | 89.1 (±0.671) | 63.7 (±2.09) | 27.9 (±17.5) | 132 (±10.7) |
| | 2.5 | 95.5 (±3.12) | 65.1 (±7.68) | – | – |
| BG8 | 0.5 | 159 (±12.7) | 151 (±7.56) | 123 (±10.2) | 144 (±26.8) |
| | 1 | – | – | 414 (±17) | **415 (±17.3)** |
| | 2 | 140 (±7.59) | 113 (±2.79) | 190 (±9) | 175 (±9.67) |
| | 2.5 | 127 (±0.327) | 120 (±4.01) | – | – |
| FJG1 | 0.5 | 147 (±4.63) | **187 (±3.57)** | 19.9 (±1.15) | 117 (±2.27) |
| | 1 | – | – | 116 (±43.3) | 54.9 (±44.5) |
| | 2 | 137 (±0.283) | 104 (±6.65) | 36.2 (±5.1) | 73.5 (±11.3) |
| | 2.5 | 158 (±16.5) | 152 (±19.3) | – | – |

*Standard deviations of three technical replicates are reported in parentheses. Bold values are the maximum yields for each strain. Dashes indicate conditions that were not examined.*

**TABLE 2 |** Growth rates of methanotrophic bacteria in different combinations of carbon and nitrogen sources, reported as change in optical density (540 nm) per hour.

| Strain | Carbon (mmol) | Methane | | Methanol | |
|---|---|---|---|---|---|
| | | $NH_4^+$ | $NO_3^-$ | $NH_4^+$ | $NO_3^-$ |
| Rockwell | 0.5 | 0.112 (±0.002) | **0.116 (±0.007)** | 0.0246 (±0.002) | 0.0186 (±0.001) |
| | 1 | – | – | 0.0389 (±0.004) | 0.0144 (±0.006) |
| | 2 | 0.0995 (±0.004) | 0.0614 (±0.007) | 0.0402 (±0.006) | 0.0579 (±0.032) |
| | 2.5 | 0.113 (±0.004) | 0.0491 (±0.009) | – | – |
| WRRC1 | 0.5 | 0.111 (±0.019) | **0.128 (±0.002)** | 0.0266 (±0.01) | 0.0302 (±0.004) |
| | 1 | – | – | 0.0570 (±0.003) | 0.0263 (±0.002) |
| | 2 | 0.123 (±0.004) | 0.0763 (±0.008) | 0.0201 (±0.003) | 0.0167 (±0.001) |
| | 2.5 | 0.0640 (±0.005) | 0.0572 (±0.011) | – | – |
| OB3b | 0.5 | 0.0778 (±0.011) | 0.0594 (±0.012) | 0.0146 (±0.007) | 0.0393 (±0.01) |
| | 1 | – | – | 0.0460 (±0.005) | 0.0411 (±0.011) |
| | 2 | **0.121 (±0.009)** | 0.0685 (±0.007) | 0.0547 (±0.033) | 0.0566 (±0.006) |
| | 2.5 | 0.0811 (±0.012) | 0.0497 (±0.008) | – | – |
| BG8 | 0.5 | 0.144 (±0.011) | 0.0918 (±0.006) | 0.0340 (±0.004) | 0.0383 (±0.001) |
| | 1 | – | – | **0.144 (±0.044)** | 0.131 (±0.05) |
| | 2 | 0.130 (±0.033) | 0.0978 (±0.023) | 0.0551 (±0.016) | 0.0471 (±0.009) |
| | 2.5 | 0.119 (±0.039) | 0.101 (±0.053) | – | – |
| FJG1 | 0.5 | 0.0856 (±0.016) | 0.110 (±0.007) | 0.0224 (±0.007) | 0.0596 (±0.004) |
| | 1 | – | – | 0.127 (±0.008) | 0.107 (±0.037) |
| | 2 | 0.164 (±0.005) | 0.129 (±0.008) | 0.0590 (±0.025) | 0.0648 (±0.01) |
| | 2.5 | **0.289 (±0.07)** | 0.188 (±0.034) | – | – |

*Standard deviations of three technical replicates are reported in parentheses. Bold values are the maximum growth rates during exponential phase for each strain. Dashes indicate conditions that were not examined.*

on methanol than methane (**Supplementary Figure S3** and **Supplementary Table S2**), although the duration of lag phases for methanol-grown cultures was generally shorter for the Gamma-MOB than for the Alpha-MOB. This may be related to poorer growth in the inoculum culture or periods of adaptation to the condition and it is important to note that continuous bioprocessing operation may mitigate these impacts. Some of the strains were not able to achieve exponential growth on methanol (0.5 mmol methanol: *Methylocystis* sp. Rockwell with nitrate, *M. trichosporium* OB3b with ammonium, *M. denitrificans* FJG1 with nitrate, 2 mmol methanol: *Methylocystis* sp. WRRC1 with ammonium, *M. denitrificans* FJG1 with ammonium). Notably, an exponential phase could be measured for all strains grown in either ammonium or nitrate when provided with 1 mmol methanol, suggesting that this intermediate methanol amount (representing a concentration of 0.1 mM) was neither carbon limiting nor toxic to the cells and was the optimal concentration among the conditions tested in this study.

While clearly distinct growth outcomes can be noted, multivariate ANOVA analysis was completed to distinguish how strain type, carbon amount, carbon source, and nitrogen source alone and in combination contributed to maximum OD, growth rate, and growth yield for each strain (**Table 3**). All factors and combinations had statistically significant effects on maximum OD. Growth rate was also significantly impacted by each individual major factor, as well as by a variety of combinatorial factors. Growth yield was least affected by the analyzed factors though strain, carbon amount, and carbon type all had significant effects.

Analysis of gene expression of the central methane oxidation pathway showed no notable difference in expression of MMO genes for *Methylocystis* sp. Rockwell grown on methane with either nitrate or ammonium despite the observed differences in growth (**Figure 1** and **Supplementary Table S3**). However, significant decreases in MMO gene expression levels were observed for growth of *Methylocystis* sp. Rockwell on methanol. In addition, expression of methanol dehydrogenase and formaldehyde activating protein genes were significantly decreased in methanol-ammonium grown cells (**Supplementary Table S3**). While these decreases in gene expression may point to a potential growth bottleneck, i.e., formaldehyde toxicity, changes in expression of these same genes were not observed in methanol-nitrate grown cells. In contrast to *Methylocystis* sp. Rockwell, expression of MMO genes in *M. album* BG8 increased in the methanol-ammonium, but not the methanol-nitrate, growth condition relative to the methane-nitrate growth condition (**Supplementary Tables S3, S4**). In the methanol-nitrate growth condition, genes for formaldehyde oxidation showed increased expression levels relative to the methane-nitrate control, while cells grown on ammonium with either carbon source showed no significant differences in expression of these genes.

**TABLE 3 |** Multifactorial analysis of variance (ANOVA) on measurements of maximum optical density, growth rate, and yield for each condition tested.

| | Maximum OD | Growth rate | Yield |
|---|---|---|---|
| Strain | **$<2.00 \times 10^{-16}$** | **$<2.00 \times 10^{-16}$** | **$7.83 \times 10^{-5}$** |
| CAmt | **$<2.00 \times 10^{-16}$** | **$9.87 \times 10^{-12}$** | **$6.91 \times 10^{-13}$** |
| Carbon | **$<2.00 \times 10^{-16}$** | **$<2.00 \times 10^{-16}$** | **$8.40 \times 10^{-13}$** |
| Nitrogen | **$3.10 \times 10^{-7}$** | **$3.97 \times 10^{-5}$** | $3.02 \times 10^{-1}$ |
| Strain:CAmt | **$<2.00 \times 10^{-16}$** | **$<2.00 \times 10^{-16}$** | **$5.67 \times 10^{-3}$** |
| Strain:carbon | **$<2.00 \times 10^{-16}$** | **$2.57 \times 10^{-2}$** | $1.36 \times 10^{-1}$ |
| CAmt:carbon | **$7.47 \times 10^{-3}$** | $1.48 \times 10^{-1}$ | **$5.52 \times 10^{-6}$** |
| Strain:nitrogen | **$5.67 \times 10^{-12}$** | $9.45 \times 10^{-1}$ | $4.28 \times 10^{-1}$ |
| CAmt:nitrogen | **$9.76 \times 10^{-10}$** | **$3.17 \times 10^{-4}$** | $3.58 \times 10^{-1}$ |
| Carbon:nitrogen | **$1.36 \times 10^{-10}$** | **$7.49 \times 10^{-4}$** | $1.67 \times 10^{-1}$ |
| Strain:CAmt:carbon | **$3.84 \times 10^{-15}$** | **$3.95 \times 10^{-2}$** | $7.64 \times 10^{-1}$ |
| Strain:CAmt:nitrogen | **$2.06 \times 10^{-4}$** | **$3.01 \times 10^{-2}$** | $9.57 \times 10^{-1}$ |
| Strain:carbon:nitrogen | **$3.21 \times 10^{-5}$** | $7.55 \times 10^{-1}$ | $6.30 \times 10^{-1}$ |
| CAmt:carbon:nitrogen | **$1.27 \times 10^{-8}$** | $1.50 \times 10^{-1}$ | $7.26 \times 10^{-1}$ |
| Strain:CAmt:carbon:nitrogen | **$7.43 \times 10^{-3}$** | $4.35 \times 10^{-1}$ | $7.74 \times 10^{-1}$ |

*Values represent calculated p-values from F-tests. Bolded values represent those factors and combinations of factors (interactions) showing statistically significant, measureable effects on the outcome assessed at $\alpha = 0.05$.*

## Effect of Carbon and Nitrogen Sources on Small Metabolites

To expand the analysis of carbon and nitrogen effects on methanotrophs, two strains, the Alpha-MOB *Methylocystis* sp. Rockwell and the Gamma-MOB *M. album* BG8, were selected for analysis of excreted metabolites, representing different types of methanotrophs as well as distinct substrate-based growth effects as measured by OD. Cultures were grown with either 1 mmol methanol or 2.5 mmol methane with either ammonium or nitrate at 10 mM. For all conditions tested – either strain with all carbon–nitrogen combinations – a significant amount of glycerol was measured (**Table 4**). Lactic acid was measurable for *Methylocystis* sp. Rockwell grown in methane-ammonium and methanol-nitrate. *Methylocystis* sp. Rockwell, but not *M. album* BG8, excreted formic acid in all cultures except when grown on methane-ammonium, with more detected in the methanol-grown cultures. Interestingly, *M. album* BG8 grown in methanol and nitrate produced small amounts of xylitol. While the origins of this sugar alcohol were not further investigated, its source could potentially be X5P-derived xylulose, which could implicate a pentose-phosphate pathway or phosphoketolase (PKT) bottleneck with implications for bioindustrial potential. RNA-Seq analysis identified no change in gene expression of PKT in this condition relative to nitrate-methane in *M. album* BG8. This condition did however show significant upregulation of formaldehyde-activating protein genes and down-regulation of formate dehydrogenase genes, which is not observed in either methane-ammonium or methanol-ammonium (**Supplementary Table S4**).

## Effect of Carbon and Nitrogen Sources on PLFA Composition and Abundance

In order to determine if the combinations of carbon and nitrogen sources were significantly altering membrane structure, FAME analysis was conducted on *Methylocystis* sp. Rockwell and

*M. album* BG8. All measured fatty acids were between C10 and C18, with no measurable C8 or C20–24 (which were included in the analysis standards). Overall abundance of percent biomass was determined for each strain and growth condition (**Figure 2**), and ANOVA analysis was completed to determine whether strain type, carbon type, and nitrogen type contributed to overall measured FAMEs (**Supplementary Tables S5, S6**). Total fatty acid abundance was significantly lower in methanol-grown cultures of *Methylocystis* sp. Rockwell. Furthermore, cultures of *Methylocystis* sp. Rockwell grown with ammonium had lower abundance of fatty acids than cultures grown with nitrate. In contrast, there was no significant difference in total fatty acid abundance across conditions for *M. album* BG8. Overall, strain-type, carbon and nitrogen sources and their interactions were determined to have significant impact on abundance of FAMEs (**Supplementary Table S5**).

In all conditions tested, over 93% of the fatty acid content in *Methylocystis.* sp. Rockwell was composed of only two species: C18:1n9, accounting for approximately 70–75% of the measured FAMEs, and C18:1n7, accounting for approximately 18–25% of the total FAMEs (**Supplementary Table S7**). All other fatty acids measured individually contributed less than 1.55% of the measured FAMEs. By contrast, the profile of *M. album* BG8 showed four different fatty acids contributing a substantial portion (12% or higher) of the total FAMEs measured. In descending order of prominence, these fatty acids were: C16:1n6 (36–38%), C16:1n9 (23–27%), C16:1n7 (15–20%), and C16:0 (12–15%) (**Supplementary Table S7**).

While the general profiles held true in all cultures conditions, the relative abundance of each fatty acid varied (**Figure 3**). In *M. album* BG8, the abundance of fatty acid C16:1n6 in cells grown in methane compared to methanol was ca. 0.95:1 for both nitrogen sources. Conversely, higher proportions of the fatty acid C16:1n7 can be found in methane-fed compared to methanol-fed cultures, with differences in the abundance of this fatty acid measured at values of 1.13:1 in cells grown on ammonium and 1.33:1 in nitrate-grown cells. Both fatty acid proportions changed significantly in their response to carbon source (**Supplementary Table S6**).

Other effects of nitrogen source were noted in the C16:0 proportions, with nitrate-grown cells containing approximately 1.13 times the proportion found in ammonium-grown cells (**Supplementary Table S6**). Interestingly, the proportion of C16:1n9 was 1.12–1.15× more abundant in the methanol-nitrate condition relative to all the other conditions, though neither carbon nor nitrogen source was judged to have a significant effect.

In *Methylocystis* sp. Rockwell, a significantly lower proportion of C18:1n7 was measured as a component of total FAMEs in methanol-grown cells, with methane-grown cells possessing approximately 1.32× more C18:1n7, proportionally, regardless of nitrogen source. Carbon source likewise appeared to affect C18:1n9 composition, although conversely: methane-grown cells contained proportionally less of this fatty acid compared to methanol-grown cells, approximately 0.95:1. Both major fatty acids, C18:1n7 and C18:1n9, were significantly affected by carbon but not nitrogen source (**Supplementary Table S6**). RNA-Seq analysis of fatty acid biosynthesis pathway genes showed significantly decreased expression levels for an ACP dehydratase in *Methylocystis* sp. Rockwell grown with methanol-ammonium, and no significant change in expression under the other conditions, compared to the methane-nitrate control (**Supplementary Table S3**). In contrast, several genes in the fatty acid biosynthesis pathway in *M. album* BG8, grown only under the methanol-nitrate condition, showed both significant increase in ACP synthase gene or decreases in three genes (two ACP reductases and one ACP synthase) relative to the methane-nitrate growth condition (**Supplementary Table S4**).

# DISCUSSION

## Optimal Carbon–Nitrogen Combinations for Growth of Methanotrophic Strains

Optimization of growth is generally approached in one of two ways, either from a maximum biomass or a fastest growth rate perspective. In an industrial context, both of these parameters have value and should be accounted for in a multi-objective optimization approach. By evaluating growth yields (**Table 1**) and growth rates (**Table 2**) together, we can determine for each strain an optimal combination of carbon–nitrogen sources, and to a lesser extent, carbon amount, leading to the best growth outcomes (**Figure 4**). The biggest limitations to these analyses are as follows: (1) lag phase was not accounted for since the use of pre-cultures and continuous cultures can overcome this limitation, (2) there is incomplete methane oxidation at higher concentrations due to $O_2$ limitation (representative data in **Supplementary Figure S2**), and (3) methanol toxicity was observed at high concentrations. However, the analysis did reveal preferred combinations of carbon–nitrogen sources for each strain tested that can be further optimized to achieve the best outcomes in industrial applications.

For *Methylocystis* sp. Rockwell, methane-ammonium was the preferred carbon–nitrogen combination enabling greater yield and high growth rates, particularly for the 0.5 mmol methane amount where the carbon was completely oxidized (**Figure 4**). This condition is also most favorable for *M. trichosporium* OB3b that while achieving slightly greater yield in methane-nitrate, experienced its fastest growth rate in methane-ammonium (**Tables 1**, **2**). The optimal condition for *Methylocystis* sp. WRRC1, however, was found to be methane-nitrate at 0.5 mmol carbon source, though the weighted difference with growth rate and yield in methane-ammonium was small. In terms of industrial application, this could impact strain selection, especially when considering alternative products to biomass, fatty acids, and organic acids, as described here; previous work has found, for instance, that ammonium is a preferred nitrogen source for PHB production in *Methylocystis parvus* OBBP, but nitrate was more productive for *Methylosinus trichosporium* OB3b (Rostkowski et al., 2013). Combinatorial factors must also be considered, however, as different carbon sources may be preferred given certain nitrogen sources, or vice versa. A novel

**TABLE 4 |** Concentrations of metabolites excreted to supernatant by *Methylocystis* sp. Rockwell and *M. album* BG8 grown with different carbon and nitrogen sources reported in g/L.

| Strain | Metabolite (g/L) | Methane | | Methanol | |
|---|---|---|---|---|---|
| | | $NH_4^+$ | $NO_3^-$ | $NH_4^+$ | $NO_3^-$ |
| Rockwell | Glycerol | 0.311 (±0.027) | 0.290 (±0.026) | 0.338 (±0.053) | 0.396 (±0.048) |
| | Lactic acid | 0.039 (±0.055) | – | – | 0.019 (±0.027) |
| | Formic acid | – | 0.009 (±0.013) | 0.138 (±0.005) | 0.106 (±0.023) |
| | Xylitol | – | – | – | – |
| BG8 | Glycerol | 0.381 (±0.054) | 0.371 (±0.037) | 0.279 (±0.020) | 0.370 (±0.110) |
| | Lactic acid | – | – | – | – |
| | Formic acid | – | – | – | – |
| | Xylitol | – | – | – | 0.052 (±0.074) |

*Methane was supplied at 2.5 mmol while methanol was supplied at 1 mmol per 100 mL of culture; respective nitrogen sources were supplied at 10 mM. Standard deviations of three technical replicates are reported in parentheses. Dashes indicate metabolites that were under the limit of detection.*

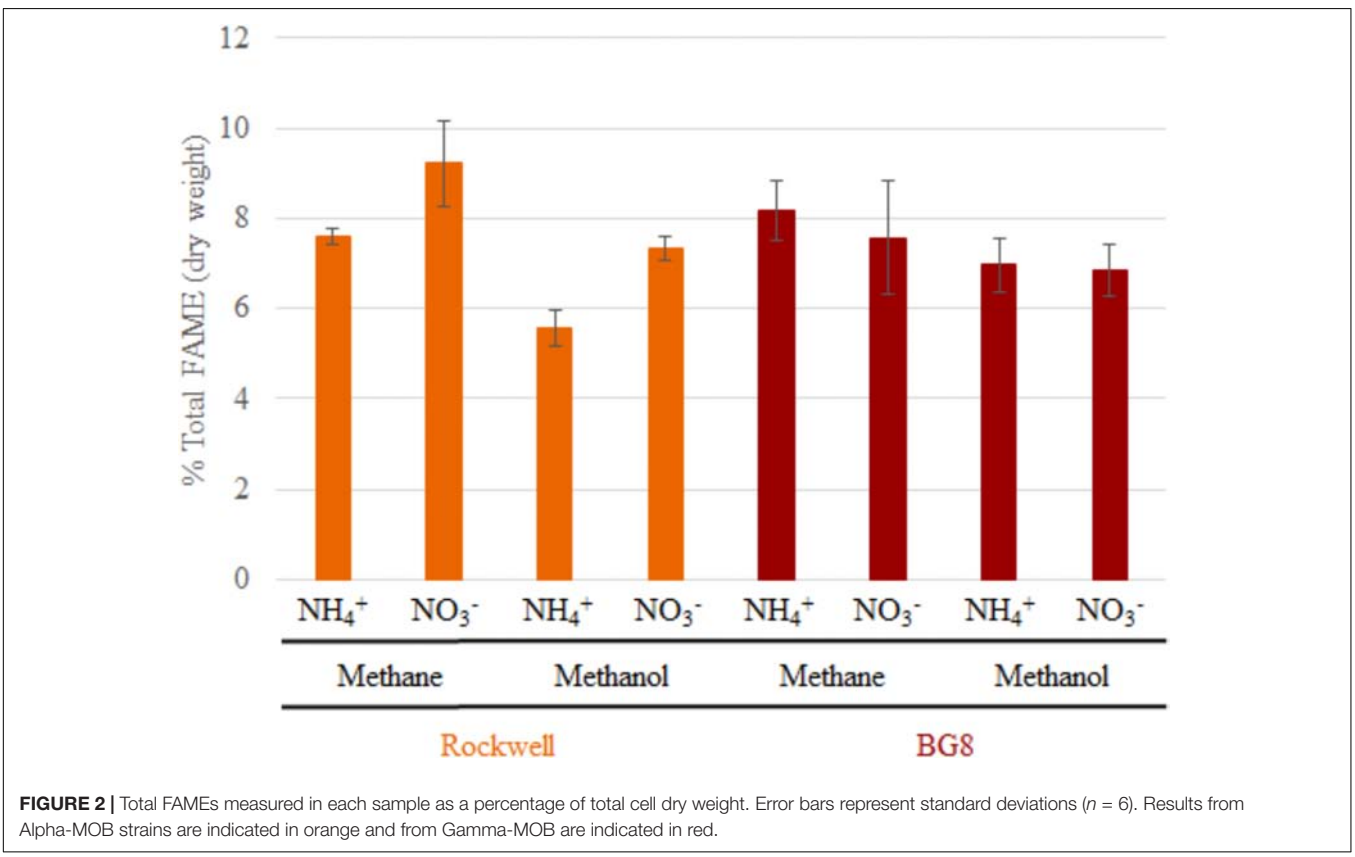


**FIGURE 2 |** Total FAMEs measured in each sample as a percentage of total cell dry weight. Error bars represent standard deviations ($n$ = 6). Results from Alpha-MOB strains are indicated in orange and from Gamma-MOB are indicated in red.

modeling-based approach has been applied to *M. trichosporium* OB3b examining such effects and demonstrates that optimal growth conditions do not match optimal PHB production conditions, and that the source of carbon, methane or methanol, changes nitrogen source preference for both metrics (Zaldívar Carrillo et al., 2018).

With these results, a balance between improved growth or product yield must be considered for *M. trichosporium* OB3b, which may not be required for *Methylocystis* sp. WRRC1 or *Methylocystis* sp. Rockwell, as PHB optimization has not yet been formally evaluated in these strains. This balance of optimization can have significant effects and must be carefully considered; use of methanol as a carbon source for production of PHB in *M. trichosporium* OB3b not only led to five times more PHB than methane but also resulted in significantly longer lag phase and delayed growth (Zaldívar Carrillo et al., 2018). Even in terms of product quality, use of methanol as a carbon source can also lead to improved molecular weight of PHB (Xin et al., 2011; Ezhov et al., 2017), but as noted in this study, may not favor optimal biomass accumulation, significantly effecting the efficiency of the overall process.

**A** C16:0

| | | Methane | | Methanol | |
|---|---|---|---|---|---|
| | | $NH_4^+$ | $NO_3^-$ | $NH_4^+$ | $NO_3^-$ |
| Methane | $NH_4^+$ | 1.00 | | | |
| | $NO_3^-$ | **1.13** | 1.00 | | |
| Methanol | $NH_4^+$ | 0.98 | **0.86** | 1.00 | |
| | $NO_3^-$ | **1.21** | 1.07 | **1.23** | 1.00 |

**B** C16:1n6

| | | Methane | | Methanol | |
|---|---|---|---|---|---|
| | | $NH_4^+$ | $NO_3^-$ | $NH_4^+$ | $NO_3^-$ |
| Methane | $NH_4^+$ | 1.00 | | | |
| | $NO_3^-$ | 0.99 | 1.00 | | |
| Methanol | $NH_4^+$ | **0.96** | 0.96 | 1.00 | |
| | $NO_3^-$ | **0.95** | **0.96** | 0.99 | 1.00 |

**C** C16:1n7

| | | Methane | | Methanol | |
|---|---|---|---|---|---|
| | | $NH_4^+$ | $NO_3^-$ | $NH_4^+$ | $NO_3^-$ |
| Methane | $NH_4^+$ | 1.00 | | | |
| | $NO_3^-$ | 0.92 | 1.00 | | |
| Methanol | $NH_4^+$ | **1.13** | **1.23** | 1.00 | |
| | $NO_3^-$ | **1.22** | **1.33** | 1.08 | 1.00 |

**D** C16:1n9

| | | Methane | | Methanol | |
|---|---|---|---|---|---|
| | | $NH_4^+$ | $NO_3^-$ | $NH_4^+$ | $NO_3^-$ |
| Methane | $NH_4^+$ | 1.00 | | | |
| | $NO_3^-$ | 1.03 | 1.00 | | |
| Methanol | $NH_4^+$ | 1.01 | 0.98 | 1.00 | |
| | $NO_3^-$ | **0.88** | **0.85** | **0.87** | 1.00 |

**E** C18:1n7

| | | Methane | | Methanol | |
|---|---|---|---|---|---|
| | | $NH_4^+$ | $NO_3^-$ | $NH_4^+$ | $NO_3^-$ |
| Methane | $NH_4^+$ | 1.00 | | | |
| | $NO_3^-$ | 0.98 | 1.00 | | |
| Methanol | $NH_4^+$ | **1.33** | **1.36** | 1.00 | |
| | $NO_3^-$ | **1.29** | **1.31** | 0.97 | 1.00 |

**F** C18:1n9

| | | Methane | | Methanol | |
|---|---|---|---|---|---|
| | | $NH_4^+$ | $NO_3^-$ | $NH_4^+$ | $NO_3^-$ |
| Methane | $NH_4^+$ | 1.00 | | | |
| | $NO_3^-$ | **1.03** | 1.00 | | |
| Methanol | $NH_4^+$ | **0.96** | 0.93 | 1.00 | |
| | $NO_3^-$ | **0.97** | **0.94** | 1.01 | 1.00 |

| | *M. album* BG8 | | | | *M.* sp. Rockwell | |
|---|---|---|---|---|---|---|
| | **C16:0** | **C16:1n6** | **C16:1n7** | **C16:1n9** | **C18:1n7** | **C18:1n9** |
| Carbon | 6.90E-01 | **2.32E-03** | **1.49E-03** | *9.59E-02* | **3.00E-07** | **5.77E-03** |
| Nitrogen | **1.06E-03** | 6.13E-01 | 7.97E-01 | 2.22E-01 | 5.20E-01 | 2.79E-01 |
| Carbon:Nitrogen | 3.61E-01 | 9.75E-01 | 1.58E-01 | *5.83E-02* | 9.31E-01 | 5.22E-01 |

**FIGURE 3 |** Relative changes in the abundances of primary FAMEs for cells grown with various combinations of carbon and nitrogen sources in *M. album* BG8 **(A–D)** and *Methylocystis* sp. strain Rockwell **(E,F)**. Bold values signify statistically different by unpaired *t*-test ($\alpha < 0.05$).

Application in a bioprocess will also necessarily consider rate and titer of the desired product, as these might dictate which substrate condition is most favorable for the particular process, including, for instance, operational mode (i.e., batch versus fed-batch, continuous etc.). Other factors than carbon and nitrogen sources must also be considered when

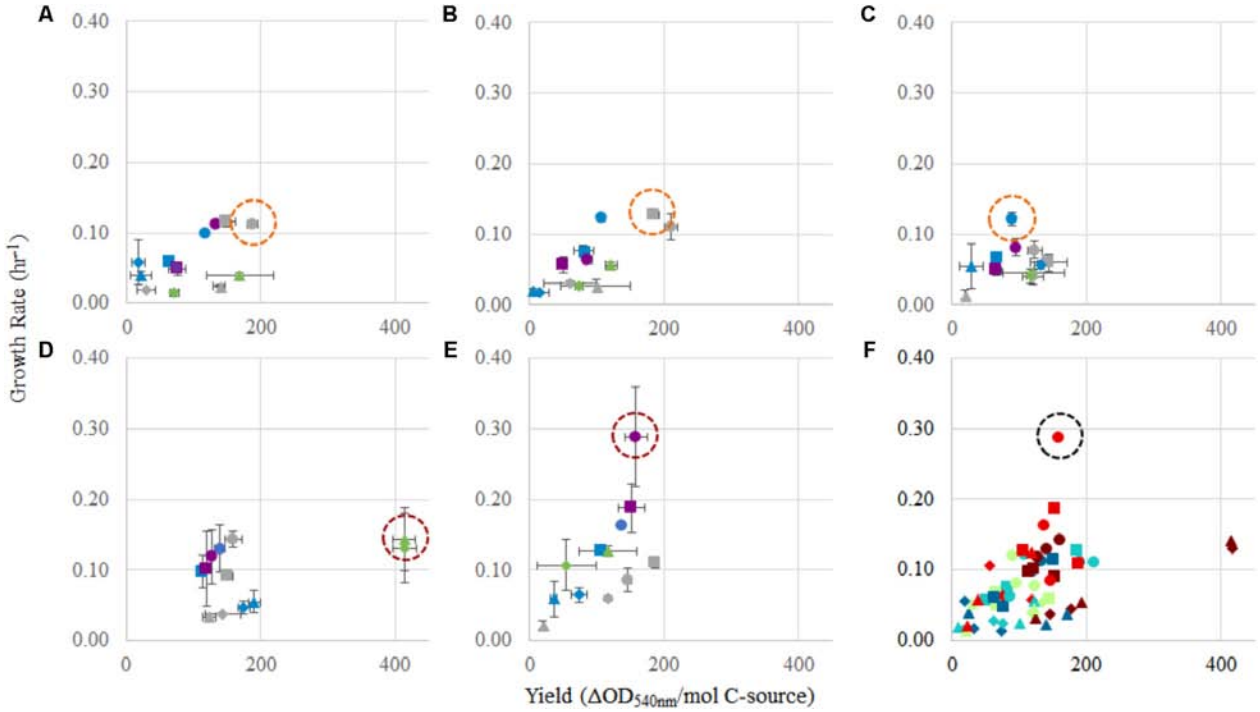


**FIGURE 4 |** Comparison of yield ($OD_{540\ nm}$/mol C) and growth rate ($h^{-1}$) for each strain, and in each condition tested. For panels **(A–E)**: **(A)** *Methylocystis* sp. Rockwell, **(B)** *Methylocystis* sp. WRRC1, **(C)** *M. trichosporium* OB3b, **(D)** *M. album* BG8, and **(E)** *M. denitrificans* FJG1. Carbon source amounts are: 0.5 mmol (gray), 1 mmol (green), 2 mmol (blue), and 2.5 mmol (purple). Carbon/nitrogen conditions are represented by: methane/$NH_4^+$ (circles), methane/$NO_3^-$ (squares), methanol/$NH_4^+$ (triangles), and methanol/$NO_3^-$ (diamonds). Panel **(F)** shows a combination of panels **(A–E)** together. Circles indicate best conditions for each strain **(A–E)**, or overall **(F)**.

developing an industrial process. Copper is well noted for its significance in controlling expression of pMMO and sMMO in methanotrophs (Semrau et al., 2010), and lanthanides have recently been implicated in regulating the expression of alternative methanol dehydrogenases (Farhan Ul Haque et al., 2015); neither of which were examined in this study. Nevertheless, beyond biomass, these findings may have widespread implications for diverse products, and specifically the optimized conditions for processes developed to generate these bioproducts.

While *M. album* BG8 grew favorably in most conditions tested, the 1 mmol methanol conditions proved most preferable for *M. album* BG8, with a slight preference for the methanol–ammonium combination over methanol-nitrate, largely due to the high yield resulting from these conditions. Of the five strains tested, *M. album* BG8 showed the least inhibition by substrate condition, with relatively high values resulting from analysis of weighted growth rates and yield in every experimental group. This outcome could lend well to potential future process development with this strain, given its inherent adaptability. Likely, the growth condition chosen for bioindustrial operation will need to reflect the product and process being developed; ultimately, incorporation of oxygen usage will be required to define key cost drivers and optimal process configurations. Regardless, a related industrially relevant strain, *Methylomicrobium buryatense* 5GB1, was previously found to grow faster in methane, not methanol (Gilman et al., 2015); so, this finding could point to a specialized use of *M. album* BG8 in certain industrial effluents, wherein higher concentrations of methanol can serve as a challenge for many methanotrophs.

By contrast, the best combined growth yield and rate for *M. denitrificans* FJG1 was observed with 2.5 mmol methane with either N-source suggesting efficient use of methane by this strain even under $O_2$ limitation. This is interesting as this strain has an active metabolism under hypoxia, allowing for continued methane oxidation even under exceedingly low $O_2$ tensions (Kits et al., 2015b), but only in nitrate, not ammonium. The growth benefit of ammonium is therefore, in this strain, unexpected. Although the lag phases for these cultures could be quite long, especially under methanol growth (**Supplementary Table S2**), the shortest lag times were observed with higher methane amounts (2.5 mmol). In an industrial process context, these data suggest that initial growth of methanotrophs could be augmented by using a higher initial methane condition before altering the carbon loading rate to achieve optimal growth yields and rates.

The excretion of particular metabolites lends clues to the efficiency of metabolism and growth of the two strains examined in more details. The accumulation of formate during growth of *Methylocystis* sp. Rockwell, particularly when grown on methanol, could imply sub-optimal conditions, and specifically

an imbalance in intracellular redox potential or assimilatory bottlenecks (**Table 3**). Excretion of excess formate suggests that the C1 assimilatory pathway is not going to completion; which could explain the noticeably poorer growth outcomes, especially when growing on methanol. Decreased expression of the MMO, methanol dehydrogenase, and formaldehyde-activating protein under methanol–ammonium growth is similar to the decreased expression of genes observed for methanol growth of *M. trichosporium* OB3b (Farhan Ul Haque et al., 2017). In stark contrast, *M. album* BG8 grew robustly on methanol and even showed increased expression of genes for MMO under methanol-ammonium growth, and formaldehyde oxidation genes under methanol-nitrate growth (**Supplementary Table S4**). *M. album* BG8 also did not excrete formate (**Table 3**). Formate has been observed as an excreted metabolite during growth of other Gamma-MOB; its concentration increased as a function of unbalanced growth under oxygen limitation (Kalyuzhnaya et al., 2013) and during growth on methanol (Gilman et al., 2015), suggesting its utility as a metabolic marker for sub-optimal conditions. Production of lactate by *Methylocystis* sp. Rockwell suggests anaerobic metabolism, although this product has not been reported for other Alpha-MOB. However, *Methylocystis parvis* has been reported to produce other fermentation products like succinate and acetate during anaerobic metabolism (Vecherskaya et al., 2009). *M. album* BG8 did not excrete measurable formate into the medium under any condition, suggesting complete oxidation of methane/methanol to $CO_2$ under all tested conditions.

## Carbon and Nitrogen Effects on Lipid Composition in Alpha- and Gamma-MOB

Analysis of PLFA compositions and abundances in *Methylocystis sp.* Rockwell confirmed prior studies of other *Methylocystis* sp. strains in which relative PLFA abundances, but not compositions, changed for cells grown in methane or methanol or in methane plus methanol (Bodelier et al., 2009). Overall, analysis of total fatty acids as a percentage of cell dry weight showed greater change in abundance with variation in carbon and nitrogen source in *Methylocystis* sp. Rockwell compared to *M. album* BG8 (**Figure 2**). However, both strains showed specific PLFA changes in response to different carbon and nitrogen sources (**Figure 3**). *Methylocystis* sp. Rockwell generally grew more robustly with ammonium, yet it produced significantly less PLFA than when growing with nitrate in either methane or methanol. Furthermore, methanol growth decreased the abundance of PLFA even further when compared to growth on methane. This is in agreement with previous work on *M. buryatense* 5GB1, which similarly showed a decrease in total FAMEs when grown in methanol compared to methane (Gilman et al., 2015). Overall, the FAMEs profile of *Methylocystis* sp. Rockwell, 93% composed of only two separate fatty acid types and over 75% C18:1n9, may point to suitability for use in biodiesel production, as high abundance, heavily synthesized fatty acid. The relationship between PLFA abundance and growth characteristics remains to be defined and points to an interesting area for future investigation. The PLFA abundance changes in response to carbon and nitrogen sources by *Methylocystis* sp. Rockwell is in stark contrast with the relative lack of change in *M. album* BG8.

Significant changes in gene expression of four fatty acid biosynthesis genes in *M. album* BG8 versus one in *Methylocystis* sp. Rockwell (**Supplementary Tables S3, S4**), suggests that regulation of these pathways differs dramatically between these two organisms. Expression of four fatty acid biosynthesis genes significantly changed in *M. album* BG8 when grown with methanol-nitrate even though overall abundance of fatty acids remained unchanged, suggesting a discrepancy between transcription and enzymatic activity levels. Thus, while transcriptomic analysis remains a powerful and versatile tool for informing process and culturing decisions, it also must be paired with other strategies to achieve concrete insights into pathway regulation and control.

# CONCLUSION

The results of this study clearly show that nutrient combinations greatly impact growth yields and rates in Alpha- and Gamma-MOB, and must be carefully considered on a strain-by-strain basis when developing bioprocessing strategies. In all cases, a multi-objective optimization approach, even rudimentary, should be considered to assess advantageous conditions for both growth yields and rates.

While a single medium may support growth of most methanotrophs (i.e., NMS and AMS), some formulations are obviously better suited to some strains rather than others. Though pathways and enzymes in these organisms may be well understood, we do not yet possess the ability to necessarily predict these optimal conditions based purely on theoretical understanding (i.e., which is calculated to be most efficient). Further work will need to be completed to address this aspect of the work, if bioindustrial optimization is to be streamlined.

These results also highlight the benefit of using certain key metabolites to evaluate nutrient effects on growth, as accumulation may point to unbalanced growth or challenging growth conditions. This has implications in understanding carbon flux, an important consideration in optimizing bioindustrial processes. These growth conditions also lead to variable FAME synthesis, helpful if the industrial process could benefit from a higher accumulation of lipids in the cell. Overall, notable differences in FAMEs response across strains are expected, which further points to strain-specific optimization (although preliminary evidence suggest that total PLFA abundance in Alpha-MOB may not be as sensitive to C- and N-sources).

While this work provides a survey of different strains growing on various combinations of carbon and nitrogen sources, many other aspects of culture optimization – including copper concentrations, phosphorous and other trace elements, and lanthanides – should also be addressed in a similar fashion. The application of these optimized conditions to common bioindustrial processes, e.g., bioreactors operating in continuous or semi-continuous modes, would also provide an interesting

avenue of further study, examining efficiency through scale up and industrial applications.

## AUTHOR CONTRIBUTIONS

CT, DS, and LS conceived the idea. CT carried out the experiments and created the figures and tables. MG supervised the FAME analysis and provided the corresponding analysis. CT, MG, DS, and LS wrote the manuscript. DS and LS supervised the work. All authors have given consent to the final version of the manuscript.

## FUNDING

This work was supported by grants to LS and DS from Alberta Innovates Bio Solutions and the Biorefining Conversions Network, and from Canada First Research Excellence Fund/Future Energy Systems.

## ACKNOWLEDGMENTS

The authors thank Stefanie Van Wychen and Holly Smith (NREL) for contributions to FAME and metabolite analyses, respectively. Mango Materials Inc. generously provided the bacterium *Methylocystis* sp. WRRC1.

## SUPPLEMENTARY MATERIAL

The Supplementary Material for this article can be found online at: https://www.frontiersin.org/articles/10.3389/fmicb.2018.02239/full#supplementary-material

## REFERENCES

Akberdin, I. R., Thompson, M., Hamilton, R., Desai, N., Alexander, D., Henard, C. A., et al. (2018). Methane utilization in *Methylomicrobium alcaliphilum* 20ZR: a systems approach. *Sci. Rep.* 8:2512. doi: 10.1038/s41598-018-20574-z

Bender, M., and Conrad, R. (1994). Methane oxidation activity in various soils and fresh-water sediments: occurrence, characteristics, vertical profiles, and distribution on grain-size fractions. *J. Geophys. Res. Atmos.* 99, 16531–16540. doi: 10.1029/94JD00266

Best, D. J., and Higgins, I. J. (1981). Methane-oxidizing activity and membrane morphology in a methanol-grown obligate methanotroph, *Methylosinus trichosporium* OB3b. *J. Gen. Microbiol.* 125, 73–84.

Bodelier, P. L., Gillisen, M. J., Hordijk, K., Damste, J. S., Rijpstra, W. I., Geenevasen, J. A., et al. (2009). A reanalysis of phospholipid fatty acids as ecological biomarkers for methanotrophic bacteria. *ISME J.* 3, 606–617. doi: 10.1038/ismej.2009.6

Bowman, J. (2006). "The methanotrophs - the families Methylococcaceae and Methylocystaceae," in *The Prokaryotes*, Vol. 5, ed. M. Dworkin (New York, NY: Springer), 266–289.

Campbell, M. A., Nyerges, G., Kozlowski, J. A., Poret-Peterson, A. T., Stein, L. Y., and Klotz, M. G. (2011). Model of the molecular basis for hydroxylamine oxidation and nitrous oxide production in methanotrophic bacteria. *FEMS Microbiol. Lett.* 322, 82–89. doi: 10.1111/j.1574-6968.2011.02340.x

Dam, B., Dam, S., Kim, Y., and Liesack, W. (2014). Ammonium induces differential expression of methane and nitrogen metabolism-related genes in *Methylocystis* sp. strain SC2. *Environ. Microbiol.* 16, 3115–3127. doi: 10.1111/1462-2920.12367

Dunfield, P. F., Yuryev, A., Senin, P., Smirnova, A. V., Stott, M. B., Hou, S., et al. (2007). Methane oxidation by an extremely acidophilic bacterium of the phylum Verrucomicrobia. *Nature* 450, 879–882. doi: 10.1038/nature06411

Eshinimaev, B. T., Khmelenina, V. N., Sakharovskii, V. G., Suzina, N. E., and Trotsenko, Y. A. (2002). Physiological, biochemical, and cytological characteristics of a haloalkalitolerant methanotroph grown on methanol. *Microbiology* 71, 512–518. doi: 1020594300166

Ettwig, K. F., van Alen, T., van de Pas-Schoonen, K. T., Jetten, M. S. M., and Strous, M. (2009). Enrichment and molecular detection of denitrifying methanotrophic bacteria of the NC10 phylum. *Appl. Environ. Microbiol.* 75, 3656–3662. doi: 10.1128/Aem.00067-09

Ezhov, V. A., Doronina, N. V., Shmareva, M. N., and Trotsenko, Y. A. (2017). Synthesis of high-molecular-mass polyhydroxybutyrate from methanol in *Methyloligella halotolerans* C2. *Appl. Biochem. Microbiol.* 53, 47–51. doi: 10.1134/S0003683817010112

Farhan Ul Haque, M., Gu, W., Baral, B. S., DiSpirito, A. A., and Semrau, J. D. (2017) Carbon Source Regulation Of Gene Expression In *Methylosinus trichosporium* Ob3b. *Appl. Microbiol. Biotechnol.* 101, 3871–3879. doi: 10.1007/S00253-017-8121-Z

Farhan Ul Haque, M., Kalidass, B., Bandow, N., Turpin, E. A., DiSpirito, A. A., and Semrau, J. D. (2015). Cerium regulates expression of alternative methanol dehydrogenases in *Methylosinus trichosporium* OB3b. *Appl. Environ. Microbiol.* 81, 7546–7552. doi: 10.1128/aem.02542-15

Gilman, A., Laurens, L. M., Puri, A. W., Chu, F., Pienkos, P. T., and Lidstrom, M. E. (2015). Bioreactor performance parameters for an industrially-promising methanotroph *Methylomicrobium buryatense* 5GB1. *Microb. Cell Fact.* 14:182. doi: 10.1186/s12934-015-0372-8

Graham, D. W., Chaudhary, J. A., Hanson, R. S., and Arnold, R. G. (1993). Factors affecting competition between type-I and type-II methanotrophs in 2-organism, continuous-flow reactors. *Microb. Ecol.* 25, 1–17.

Hanson, R. S., and Hanson, T. E. (1996). Methanotrophic bacteria. *Microbiol. Rev.* 60, 439–471.

Henard, C. A., Smith, H., Dowe, N., Kalyuzhnaya, M. G., Pienkos, P. T., and Guarnieri, M. T. (2016). Bioconversion of methane to lactate by an obligate methanotrophic bacterium. *Sci. Rep.* 6:21585. doi: 10.1038/srep21585

Kalyuzhnaya, M. G., Yang, S., Rozova, O. N., Smalley, N. E., Clubb, J., Lamb, A., et al. (2013). Highly efficient methane biocatalysis revealed in a methanotrophic bacterium. *Nat. Commun.* 4:2785. doi: 10.1038/ncomms3785

Kelly, D. P., McDonald, I. R., and Wood, A. P. (2014). "The family methylobacteriaceae," in *The Prokaryotes: Alphaproteobacteria and Betaproteobacteria.* eds E. Rosenberg, E. F. DeLong, S. Lory, E. Stackebrandt, and F. Thompson (Berlin: Springer), 313–340.

Khosravi-Darani, K., Mokhtari, Z.-B., Amai, T., and Tanaka, K. (2013). Microbial production of poly(hydroxybutyrate) from C-1 carbon sources. *Appl. Microbiol. Biotechnol.* 97, 1407–1424. doi: 10.1007/s00253-012-4649-0

Kits, K. D., Campbell, D. J., Rosana, A. R., and Stein, L. Y. (2015a). Diverse electron sources support denitrification under hypoxia in the obligate methanotroph *Methylomicrobium album* strain BG8. *Front. Microbiol.* 6:1072. doi: 10.3389/fmicb.2015.01072

Kits, K. D., Klotz, M. G., and Stein, L. Y. (2015b). Methane oxidation coupled to nitrate reduction under hypoxia by the Gammaproteobacterium *Methylomonas denitrificans*, sp. nov. type strain FJG1. *Environ. Microbiol.* 17, 3219–3232. doi: 10.1111/1462-2920.12772

Mohammadi, S. S., Pol, A., van Alen, T., Jetten, M. S. M., and Op den Camp, H. J. M (2017). Ammonia oxidation and nitrite reduction in the verrucomicrobial methanotroph *Methylacidiphilum fumariolicum* SoIV. *Front. Microbiol.* 8:1901. doi: 10.3389/fmicb.2017.01901

Nyerges, G., Han, S. K., and Stein, L. Y. (2010). Effects of ammonium and nitrite on growth and competitive fitness of cultivated methanotrophic bacteria. *Appl. Environ. Microbiol.* 76, 5648–5651. doi: 10.1128/aem.00747-10

Nyerges, G., and Stein, L. Y. (2009). Ammonia cometabolism and product inhibition vary considerably among species of methanotrophic bacteria. *FEMS Microbiol. Lett.* 297, 131–136. doi: 10.1111/j.1574-6968.2009.01674.x

Rostkowski, K. H., Pfluger, A. R., and Criddle, C. S. (2013). Stoichiometry and kinetics of the PHB-producing type II methanotrophs *Methylosinus*

*trichosporium* OB3b and *Methylocystis parvus* OBBP. *Bioresour. Technol.* 132, 71–77. doi: 10.1016/j.biortech.2012.12.129

Semrau, J. D., DiSpirito, A. A., and Yoon, S. (2010). Methanotrophs and copper. *FEMS Microbiol. Rev.* 34, 496–531. doi: 10.1111/j.1574-6976.2010.00212.x

Stein, L. Y., and Klotz, M. G. (2011). Nitrifying and denitrifying pathways of methanotrophic bacteria. *Biochem. Soc. Trans.* 39, 1826–1831. doi: 10.1042/BST20110712

Sundstrom, E. R., and Criddle, C. S. (2015). Optimization of methanotrophic growth and production of poly(3-hydroxybutyrate) in a high-throughput microbioreactor system. *Appl. Environ. Microbiol.* 81, 4767–4773. doi: 10.1128/aem.00025-15

van Dijken, J. P., and Harder, W. (1975). Growth yields of microorganisms on methanol and methane - a theoretical study. *Biotechnol. Bioeng.* 17, 15–30. doi: 10.1002/bit.260170103

Vecherskaya, M., Dijkema, C., Ramírez-Saad, H., and Stams, A. J. M. (2009). Microaerobic and anaerobic metabolism of a *Methylocystis parvus* strain isolated from a denitrifying bioreactor. *Environ. Microbiol. Rep.* 1, 442–449. doi: 10.1111/j.1758-2229.2009.00069.x

Webb, H. K., Ng, H. J., and Ivanova, E. P. (2014). "The family methylocystaceae," in *The Prokaryotes: Alphaproteobacteria and Betaproteobacteria,* eds E. Rosenberg, E. F. DeLong, S. Lory, E. Stackebrandt, and F. Thompson (Berlin: Springer), 341–347.

Whittenbury, R., Phillips, K. C., and Wilkinson, J. F. (1970). Enrichment, isolation and some properties of methane-utilizing bacteria. *J. Gen. Microbiol.* 61, 205–218. doi: 10.1099/00221287-61-2-205

Xin, J., Zhang, Y., Dong, J., Song, H., and Xia, C. (2011). An experimental study on molecular weight of poly-3-hydroxybutyrate (PHB) accumulated in *Methylosinus trichosporium* IMV 3011. *Afr. J. Biotechnol.* 10, 7078–7087.

Zaldívar Carrillo, J. A., Stein, L. Y., and Sauvageau, D. (2018). Defining nutrient combinations for optimal growth and polyhydroxybutyrate production by *Methylosinus trichosporium* OB3b using response surface methodology. *Front. Microbiol.* 9:1513. doi: 10.3389/fmicb.2018.01513

**Conflict of Interest Statement:** The authors declare that the research was conducted in the absence of any commercial or financial relationships that could be construed as a potential conflict of interest.

frontiers in Microbiology

ORIGINAL RESEARCH
published: 04 December 2018
doi: 10.3389/fmicb.2018.02947

# A Genome-Scale Metabolic Model for *Methylococcus capsulatus* (Bath) Suggests Reduced Efficiency Electron Transfer to the Particulate Methane Monooxygenase

*Christian Lieven[1]*, Leander A. H. Petersen[2,3], Sten Bay Jørgensen[3], Krist V. Gernaey[3], Markus J. Herrgard[1] and Nikolaus Sonnenschein[1]*

[1] The Novo Nordisk Foundation Center for Biosustainability, Technical University of Denmark, Kongens Lyngby, Denmark, [2] Unibio A/S, Kongens Lyngby, Denmark, [3] Department of Chemical and Biochemical Engineering, Technical University of Denmark, Kongens Lyngby, Denmark

**Background:** Genome-scale metabolic models allow researchers to calculate yields, to predict consumption and production rates, and to study the effect of genetic modifications *in silico*, without running resource-intensive experiments. While these models have become an invaluable tool for optimizing industrial production hosts like *Escherichia coli* and *S. cerevisiae*, few such models exist for one-carbon (C1) metabolizers.

**Results:** Here, we present a genome-scale metabolic model for *Methylococcus capsulatus* (Bath), a well-studied obligate methanotroph, which has been used as a production strain of single cell protein (SCP). The model was manually curated, and spans a total of 879 metabolites connected via 913 reactions. The inclusion of 730 genes and comprehensive annotations, make this model not only a useful tool for modeling metabolic physiology, but also a centralized knowledge base for *M. capsulatus* (Bath). With it, we determined that oxidation of methane by the particulate methane monooxygenase could be driven both through direct coupling or uphill electron transfer, both operating at reduced efficiency, as either scenario matches well with experimental data and observations from literature.

**Conclusion:** The metabolic model will serve the ongoing fundamental research of C1 metabolism, and pave the way for rational strain design strategies toward improved SCP production processes in *M. capsulatus*.

**Keywords: COBRA, genome-scale metabolic reconstruction, C1 metabolism, single cell protein, methanotrophy, constraint-based reconstruction and analysis**

OPEN ACCESS

***Edited by:***
*Marina G. Kalyuzhanaya, San Diego State University, United States*

***Reviewed by:***
*Jin Wang, Auburn University, United States*
*Jeffrey Orth, Intrexon, United States*

****Correspondence:***
*Christian Lieven*
*clie@biosustain.dtu.dk*

***Specialty section:***
*This article was submitted to Microbiotechnology, Ecotoxicology and Bioremediation, a section of the journal Frontiers in Microbiology*

***Received:*** *23 July 2018*
***Accepted:*** *16 November 2018*
***Published:*** *04 December 2018*

***Citation:***
*Lieven C, Petersen LAH, Jørgensen SB, Gernaey KV, Herrgard MJ and Sonnenschein N (2018) A Genome-Scale Metabolic Model for Methylococcus capsulatus (Bath) Suggests Reduced Efficiency Electron Transfer to the Particulate Methane Monooxygenase. Front. Microbiol. 9:2947. doi: 10.3389/fmicb.2018.02947*

## INTRODUCTION

The Gram-negative, obligate-aerobe *Methylococcus capsulatus* (Bath) is a methane oxidizing, gamma-proteobacterium. Since its initial isolation by Foster and Davis (1966), the organism has been subject to a wide array of studies. The global role of *M. capsulatus* as a participant in the carbon cycle has been elucidated (Hanson and Hanson, 1996; Jiang et al., 2010) as well as its effects on

human (Indrelid et al., 2017) and animal health and disease (Kleiveland et al., 2013). Specifically the latter studies have been triggered by a considerable commercial interest in *M. capsulatus* (Bath) as the primary microbe used for the production of Single Cell Protein (SCP) as animal feed starting in the 70 s (Øverland et al., 2010). Now that hydraulic fracturing has made natural gas a cheap and abundant feedstock (Ritala et al., 2017), the application of *M. capsulatus* (Bath) for this purpose is being explored again (Nunes et al., 2016; Petersen et al., 2017). Another portion of studies, however, has focused on uncovering the biochemical and genetic basis of the organism's unique metabolism (Anthony, 1983). Yet, the greatest interest has been the role and function of the initial enzyme in methanotrophy, methane monooxygenase (Ross and Rosenzweig, 2017), responsible for oxidation of methane to methanol.

*Methylococcus capsulatus* (Bath) is able to express two distinct types of methane monooxygenases: a soluble form of methane monooxygenase (sMMO) and a particulate, or membrane-bound form (pMMO). The expression of these enzymes is strongly influenced by the extracellular concentration of copper; when *M. capsulatus* (Bath) is grown in the presence of low levels of copper the sMMO is active, while the pMMO is predominantly active at high levels. Both enzymes require an external electron donor to break a C-H bond in methane. While the electron donor for the sMMO is NADH (Colby and Dalton, 1978, 1979; Lund et al., 1985; Blazyk and Lippard, 2002), the native reductant to the pMMO has not yet been elucidated due to difficulties to purify the enzyme and assay its activity *in vitro* (Ross and Rosenzweig, 2017). Three hypotheses regarding the mode of electron transfer to the pMMO have been suggested previously:

(1) In the *redox-arm* mode (Dawson and Jones, 1981), the methanol dehydrogenase (MDH) passes electrons via cytochrome c555 (cL) (Anthony, 1992) and cytochrome c553 (cH) (DiSpirito et al., 2004) to either a CBD- or AA3-type terminal oxidase (Larsen and Karlsen, 2016) and thus contributes to building up a proton motive force (PMF) and the synthesis of ATP (**Figure 1**). The electrons required for the oxidation of methane are provided through ubiquinone (Q8H2). Reactions downstream of MDH responsible for oxidizing formaldehyde to $CO_2$ feed electrons into the Q8 pool. This includes dye-linked formaldehyde dehydrogenase (DL-FALDH), formate dehydrogenase (FDH) and any NAD reducing reactions which ultimately contribute electrons through the NADH dehydrogenases (NDH-1, NDH-2, NQR). See **Figure 1**. Although no binding site has been identified, there is support for pMMO reduction by endogenous quinols (Shiemke et al., 2004).

(2) With the *direct coupling* mode, the MDH is able to directly pass electrons to the pMMO (Wolfe and Higgins, 1979; Leak and Dalton, 1983; Culpepper and Rosenzweig, 2014). Here, cytochrome c555 is the electron donor to the pMMO instead of ubiquinol. This mode is supported by results from cryoelectron microscopy which indicates that the pMMO and the MDH form a structural enzyme complex (Myronova et al., 2006).

(3) The *uphill electron transfer* mode supposes that the electrons from cytochrome c553 can reach the ubiquinol-pool facilitated by the PMF at the level of the ubiquinol-cytochrome-c reductase. This mode was proposed by Leak and Dalton (1986b) as it could explain the observed reduced efficiency.

A genome-scale metabolic model (GEM) not only represents a knowledge base that combines the available physiological, genetic and biochemical information of a single organism (Thiele and Palsson, 2010), but also provides a testbed for rapid prototyping of a given hypothesis (Benedict et al., 2012). Hence, we present the first manually curated GEM for *M. capsulatus* Bath, with the intent of supplying the basis for hypothesis-driven metabolic discovery and clearing the way for future efforts in metabolic engineering (Kim et al., 2015). Using the GEM, we investigate the nature of electron transfer in *M. capsulatus* (Bath) by comparing the model's predictions against experimental data from Leak and Dalton (1986a). Furthermore, we compare its predictions to those of the model of *Methylomicrobium buryatense* 5G(B1) (de la Torre et al., 2015) and explain notable differences by considering the proposed electron transfer modes.

# RESULTS AND DISCUSSION

## Reconstruction

The presented genome-scale metabolic reconstruction of *M. capsulatus* (Bath) termed iMcBath is based on BMID000000141026, an automatic draft published as part of the Path2Models project (Büchel et al., 2013). The whole genome sequence of *M. capsulatus* (Bath) (GenBank AE017282.2; Ward et al., 2004) was used to aid the curation process and to supply annotations (see section "Materials and Methods"). This metabolic reconstruction consists of 843 enzymatic reactions that interconvert and transport 759 unique metabolites. The total number of reactions, including exchange, demand and the biomass reactions, is 913. The model attributes reactions and metabolites to four distinct compartments: The cytosol, the periplasm, an intramembranous compartment and the medium, which is referred to as extracellular in the model. Gene-Protein-Reaction rules (GPR) associated with 730 unique genes support 86.97% of the included reactions with, leaving 119 reactions without a GPR. The GPRs include representation of 43 enzyme complexes.

The model and all scripts used during reconstruction are made available publicly on Github at https://github.com/ChristianLieven/memote-m-capsulatus. The model is available in the community-standard SMBL format (Level 3 Version 2 with FBC; Olivier and Bergmann, 2015) and a JSON format that is native to cobrapy (Ebrahim et al., 2013).

## Biomass Reaction

In stoichiometric models biological growth is represented as the flux through a special demand reaction. The so-called biomass reaction functions as a drain of metabolites, which are either highly reduced non-polymeric macromolecules such as lipids and steroids or precursors to typical biopolymers such as nucleic acids, proteins or long-chain carbohydrates. The stoichiometry of an individual precursor was calculated from the principal composition of *M. capsulatus* (Bath) as reported

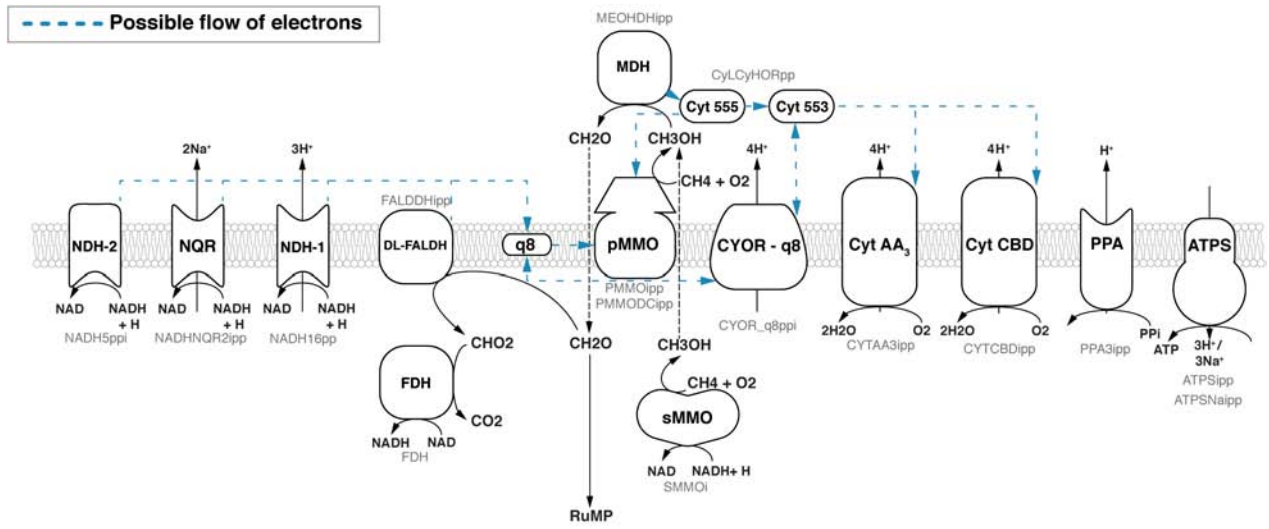


**FIGURE 1 |** Overview of the respiratory chain in *Methylococcus capsulatus* Bath as implemented in iMcBath. Black text in the center of the symbols denotes the common abbreviation, while the faint gray text below denotes the corresponding reaction ID in the metabolic model. Blue dotted arrows indicate possible flow of electrons between respiratory components. The individual electron transfer modes to the pMMO are outlined in greater detail in **Figure 2**.

by Unibio (2018). The monomer composition of individual macromolecules was calculated from different sources. A detailed account of the resources is provided in the methods section and an overview of the biomass reaction is given in **Supplementary Table 1**.

The growth-associated maintenance (GAM) and the non-growth associated maintenance (NGAM) requirements for *M. capsulatus* are yet to be determined experimentally. Therefore, a GAM value of 23.087 mmol ATP $gDW^{-1}$ $h^{-1}$ was estimated according to Thiele and Palsson (2010) based on the data for *Escherichia coli* published by Neidhardt et al. (1990). The value for GAM is expected to increase with the growth rate of the cells (Varma et al., 1993). Like de la Torre et al. (2015) had done for *M. buryatense* 5G(B1), we assumed the NGAM of *M. capsulatus* (Bath) to be similar to that of *E. coli* thus setting it to 8.39 mmol ATP $gDW^{-1}$ $h^{-1}$ (Feist et al., 2010).

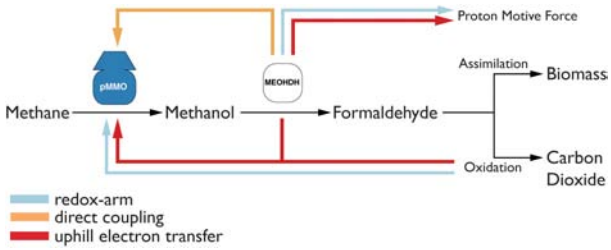


**FIGURE 2 |** The three possible modes of electron transfer to the pMMO. (1) *Redox-arm*: The methanol dehydrogenase transfers electrons to the terminal oxidase which contributes to increasing the proton motive force (PMF), while the pMMO draws electrons from the quinone pool. (2) *Direct coupling*: Electrons from the oxidation of methanol are transferred directly to the pMMO. (3) *Uphill electron transfer*: Electrons from the methanol dehydrogenase feed back into the ubiquinol-pool.

## Metabolism

To study which of the three modes of electron transfer is active in *M. capsulatus* (Bath), they were each implemented in the model. The implementation is illustrated in **Figure 2**. To include the *redox-arm* we implemented the reaction representing the particulate methane monooxygenase, in the model termed as PMMOipp, utilizing Q8H2 as a cofactor. Accordingly, a variant of the pMMO reaction was added to account for a possible direct coupling to the MDH. In this variant reaction, termed PMMODCipp, the cofactor is cytochrome c555, represented as the metabolite focytcc555_p in the model. To enable an *uphill electron transfer*, the reaction representing the ubiquinol-cytochrome-c reductase (CYOR_q8ppi in the model), was constrained to be reversible while keeping PMMOipp active.

Following the path of carbon through metabolism downstream from the MDH, the model includes both the reaction for a ubiquinone-dependent formaldehyde dehydrogenase (Zahn et al., 2001), termed FALDDHipp, and an NAD-dependent version, termed ALDD1 (**Figure 3**). Despite of the initial evidence for the latter reaction (Tate and Dalton, 1999) having been dispelled by Adeosun et al. (2004), it was added to allow further investigation into the presence of a putative enzyme of that function. An additional pathway for formaldehyde oxidation represented in both genome and model is the tetrahydromethanopterin(THMPT)-linked pathway (Vorholt, 2002).

Formaldehyde assimilation in *M. capsulatus* (Bath) occurs primarily through the ribulose monophosphate (RuMP)-pathway. As outlined by Anthony (1983), the RuMP-pathway has four hypothetical variants. Based on the annotated genome published by Ward et al. (2004), we identified

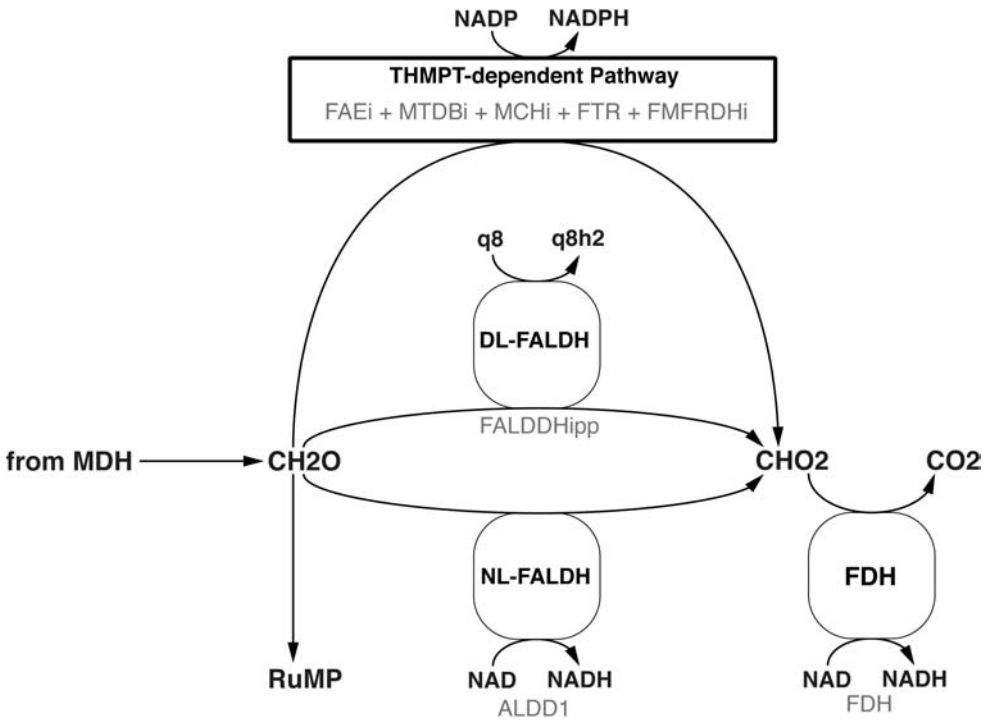


**FIGURE 3 |** Three different formaldehyde oxidation pathways are represented in the model. Black text denotes the common name, while faint gray text denotes the reaction ID in the metabolic model.

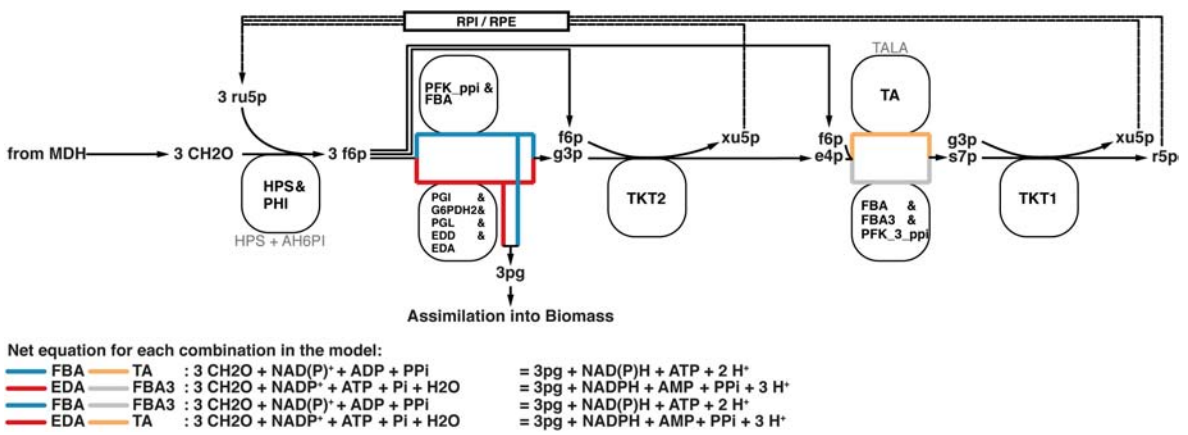


**FIGURE 4 |** All four variants of the RuMP pathway are represented in the metabolic model. If there is a common enzyme name the black text denotes the common name, while faint gray text denotes the reaction ID in the metabolic model. Otherwise the black text is also the reaction ID in the model.

not only both C6 cleavage pathways depending either on the 2-keto, 3-deoxy, 6-phosphogluconate (KDPG) aldolase (EDA) or the fructose bisphosphate aldolase (FBA), but also the transaldolase (TA) involved in the rearrangement phase that regenerates ribulose 5-phosphate. The alternative to a transaldolase-driven rearrangement step is the use of a sedoheptulose bisphosphatase, which was not included in the initial annotation. Strøm et al. (1974) could not detect specific activity using cell-free preparations. Yet, we decided to add a corresponding reaction for two reasons. First, the FBA has been characterized to reversibly catalyze sedoheptulose bisphosphate cleavage (Rozova et al., 2010), which is reflected by the reaction FBA3 in the model. Second, the pyrophosphate-dependent 6-phosphofructokinase (PFK_3_ppi) was reported to have higher affinity and activity to the reversible phosphorylation of seduheptulose phosphate than compared to fructose 6-phosphate (Reshetnikov et al., 2008). Thus, all of the resulting four combinations that make up the RuMP-pathway are represented in this metabolic model (**Figure 4**).

The genome of *M. capsulatus* (Bath) encodes genes for a complete Calvin Benson Bassham (CBB) cycle (Taylor, 1977; Taylor et al., 1980; Baxter et al., 2002) and a partial Serine pathway for formaldehyde assimilation (Ward et al., 2004). It was argued by Taylor et al. (1981) that *M. capsulatus* (Bath) can metabolize glycolate [a product of the oxygenase activity of the ribulose bisphosphate carboxylase (RBPC)] via this pathway. Both Taylor and Ward, further suggested the presence of unique key enzymes to complete the Serine pathway, such as hydroxymethyl transferase, hydroxypyruvate reductase and malate-CoA lyase. However, since the gene annotation did not reflect this and the RuMP pathway is reportedly the main pathway for formaldehyde assimilation (Kelly et al., 2005), these putative reactions were not included.

All genes of the TCA cycle were identified in the genome sequence and all associated reactions were included accordingly (Ward et al., 2004). Because no activity of the 2-oxoglutarate dehydrogenase has so far been measured *in vivo* (Wood et al., 2004; Kelly et al., 2005), the associated reactions have been constrained to be blocked (both lower and upper bounds were set to zero). This way they can easily be activated if needed. For instance, if a growth condition is discovered where activity for this enzyme can be detected.

Based on reactions already present in BMID000000141026, the information in the genome annotation, and the measured biomass composition, we curated the biosynthetic pathways of all proteinogenic amino acids, nucleotides, fatty acids, phospholipids, panthothenate, coenzyme A, NAD, FAD, FMN, riboflavin, thiamine, myo-inositol, heme, folate, cobalamine, glutathione, squalene, lanosterol, peptidoglycan. Since no corresponding genes could be identified, reactions catalyzing the biosynthesis of lipopolysaccharide (LPS) were adopted from iJO1366 (Orth et al., 2011) under the assumption that the biosynthesis steps among gram-negative bacteria require amounts of ATP comparable to *E. coli*.

*Methylococcus capsulatus* (Bath) is able to metabolize the nitrogen sources ammonium ($NH_4$) and nitrate ($NO_3$) in a variety of ways. When the extracellular concentration of $NH_4$ is high (>1 mM), alanine dehydrogenase (ADH) is the primary pathway for nitrogen assimilation into biomass, when it is low (<1 mM) assimilation is carried out via the glutamine synthetase/glutamine synthase (GS/GOGAT) pathway (Murrell and Dalton, 1983). In addition to assimilation, the two monooxygenases are able to oxidize ammonium to hydroxylamine (Colby and Dalton, 1978; Bédard and Knowles, 1989), which is then further oxidized by specific enzymes first to nitrite (Bergmann et al., 1998; **Figure 5**), and even to dinitrogen oxide (Campbell et al., 2011). $NO_3$ is reduced to $NH_4$ via nitrite and ultimately assimilated via GS/GOGAT. Furthermore, it has been shown that *M. capsulatus* (Bath) is able to fix atmospheric nitrogen ($N_2$) (Murrell et al., 1983). The nitrogenase gene cluster has been identified (Oakley and Murrell, 1991) and annotated accordingly (Ward et al., 2004), and the corresponding reactions have been included in the model. As the enzyme has not yet been specifically characterized, the nitrogenase reaction was adapted from iAF987 (Feist et al., 2014). A schema showing these reactions side-by-side is displayed in **Figure 6**.

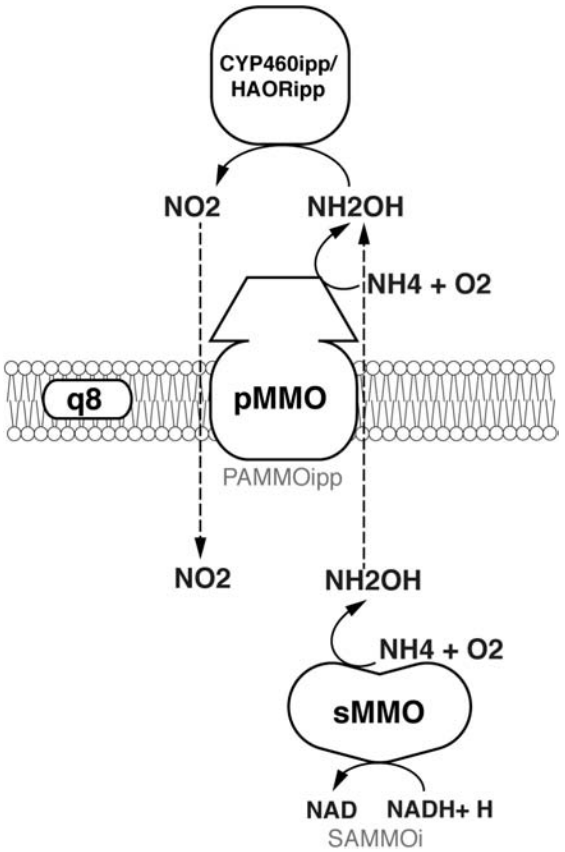


**FIGURE 5 |** Oxidation of ammonia to nitrite.

A metabolic map of all the reactions in the model was built using Escher (King et al., 2015) and is available as **Supplementary Figure 1**.

## Prediction of Transport Reactions

As a last step we added transport reactions that were not in the draft reconstruction. Inferring membrane transport reactions from the genome sequence is difficult, as usually the precise 3D structure of transport proteins dictates which metabolite classes can be transported (Mishra et al., 2014). Even if the substrates are known, the energy requirements of transport are often undefined. Working on protein sequence matches using PsortB 3.0 (Yu et al., 2010), combined with BLAST (Altschul et al., 1990) matches against TransportDB (Elbourne et al., 2017) and the Transporter Classification Database (TCDB) (Saier et al., 2006), we were able to identify 56 additional transport reactions. We have limited the number of transporters to be added, focusing specifically on transporters with known mechanisms and transport of metabolites already included in the model. A list of putative transport-associated genes that we did not consider is available at https://github.com/ChristianLieven/memote-m-capsulatus. Ward et al. (2004) hypothesized that some of these genes may facilitate the uptake of sugars for growth. Kelly et al. (2005) argue that these genes instead may allow a

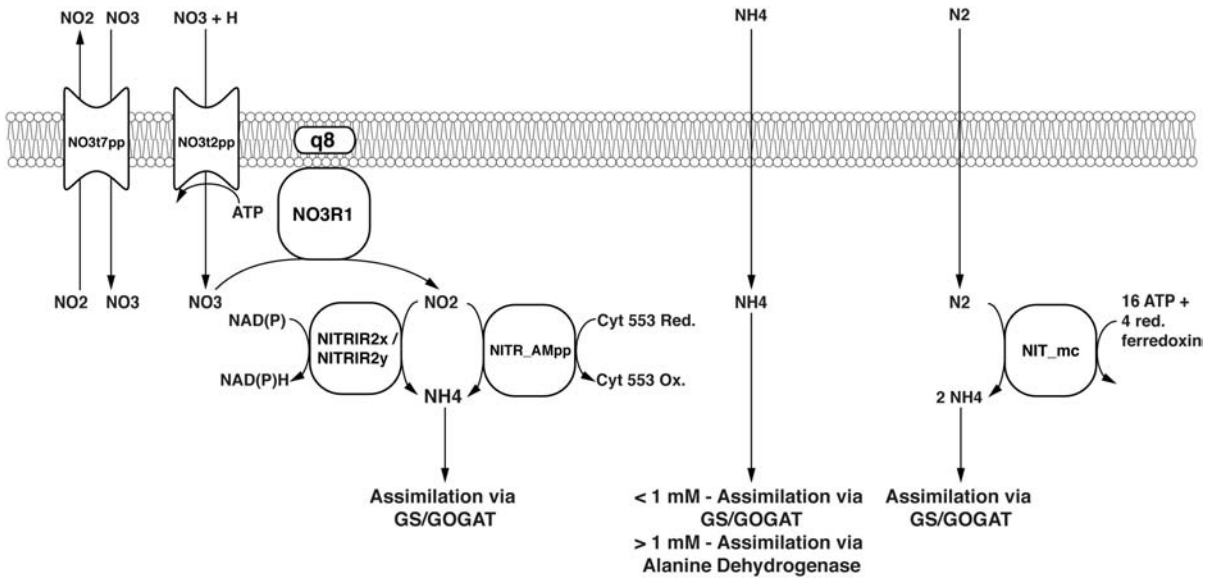


**FIGURE 6 |** Nitrogen assimilation and fixation pathways represented in the model. Black text in the center of the symbols denotes reaction IDs. Common names are used for metabolites.

function similar to *Nitrosomas europaea*, which is able grow on fructose as a carbon-source with energy from ammonia oxidation (Hommes et al., 2003; Kelly et al., 2005). Thus, this list is a good starting point to study potential alternate carbon source use by *M. capsulatus* (Bath).

## Parameter Fitting to Determine the Mode of Electron Transfer

To determine which combination of the three aforementioned electron transfer modes is active in *M. capsulatus* (Bath), we constrained the model based on experiments conducted by Leak and Dalton (1986a). Since the three modes relate to how the pMMO receives electrons, we focused on the data generated by growing *M. capsulatus* (Bath) in high-copper medium, which is the condition in which pMMO is predominantly active. We used the average of carbon and oxygen-limited measurements as a reference. Having constrained the model, we compared the Leak and Dalton's measurements for the ratio of oxygen consumption to methane consumption ($O_2/CH_4$) to the predictions of the model (**Figure 7**). We considered the $O_2/CH_4$ ratio to be a key metric for the respiratory chain in *M. capsulatus* (Bath), as it is a function of the mode of electron transfer to the pMMO. The central carbon metabolism was left unconstrained.

Under the assumption that the mode of electron transfer to pMMO would be independent of the source of nitrogen, we compared the $O_2/CH_4$ ratios of the model constrained to employ one of the three modes of electron transfer exclusively to the corresponding reference values of *M. capsulatus* (Bath) grown on either $NO_3$ or $NH_4$. However, neither of the modes adequately represented the measured $O_2/CH_4$ ratios of about 1.43 and 1.6, respectively. Although Leak and Dalton had proposed that the *reverse* or *uphill electron transfer* is the most probable mode (Leak and Dalton, 1986b), the model predictions allowing for an unbounded *uphill transfer* did not support this (**Figure 7E**), as the efficiency was almost comparable to predictions using *direct coupling*.

We altered the efficiency of the three modes to determine whether the fit could be improved. For the *redox arm*, we gradually decreased the mol protons required for the synthesis of 1 mol ATP, thereby improving the efficiency. This did not change the $O_2/CH_4$ ratio (see **Figure 7A**). de la Torre et al. (2015) constructed a GEM for *M. buryatense* 5G(B1) to investigate growth yields and energy requirements in different conditions. Similar to the results presented herein, they found that the *redox-arm* mode correlated least with their experimental data for *M. buryatense*.

We decreased the efficiency of the *direct coupling* mode (PMMODCipp) by forcing a portion of the flux through the regular pMMO reaction (PMMOipp) using ratio constraints (**Figure 7B**). To achieve a ratio representing the measured value of 1.43 required a large decrease in efficiency with almost 85% of the incoming carbon routed through the regular pMMO reaction (see **Supplementary Table 2**). Lastly, we iteratively constrained the lower bound of the reaction associated with the ubiquinol-cytochrome-c reductase (CYOR_q8ppi), to reduce the efficiency of the *uphill-electron transfer* (**Figure 7C**).

Leak and Dalton (1986b) developed mathematical models for each mode based on previous calculations (Harder and Van Dijken, 1976; Anthony, 1978). Their models lead them to conclude that both *direct coupling* and *uphill electron transfer* operating at reduced efficiency may account for the observed high ratios of $O_2/CH_4$, which agrees with our predictions. Since experimental

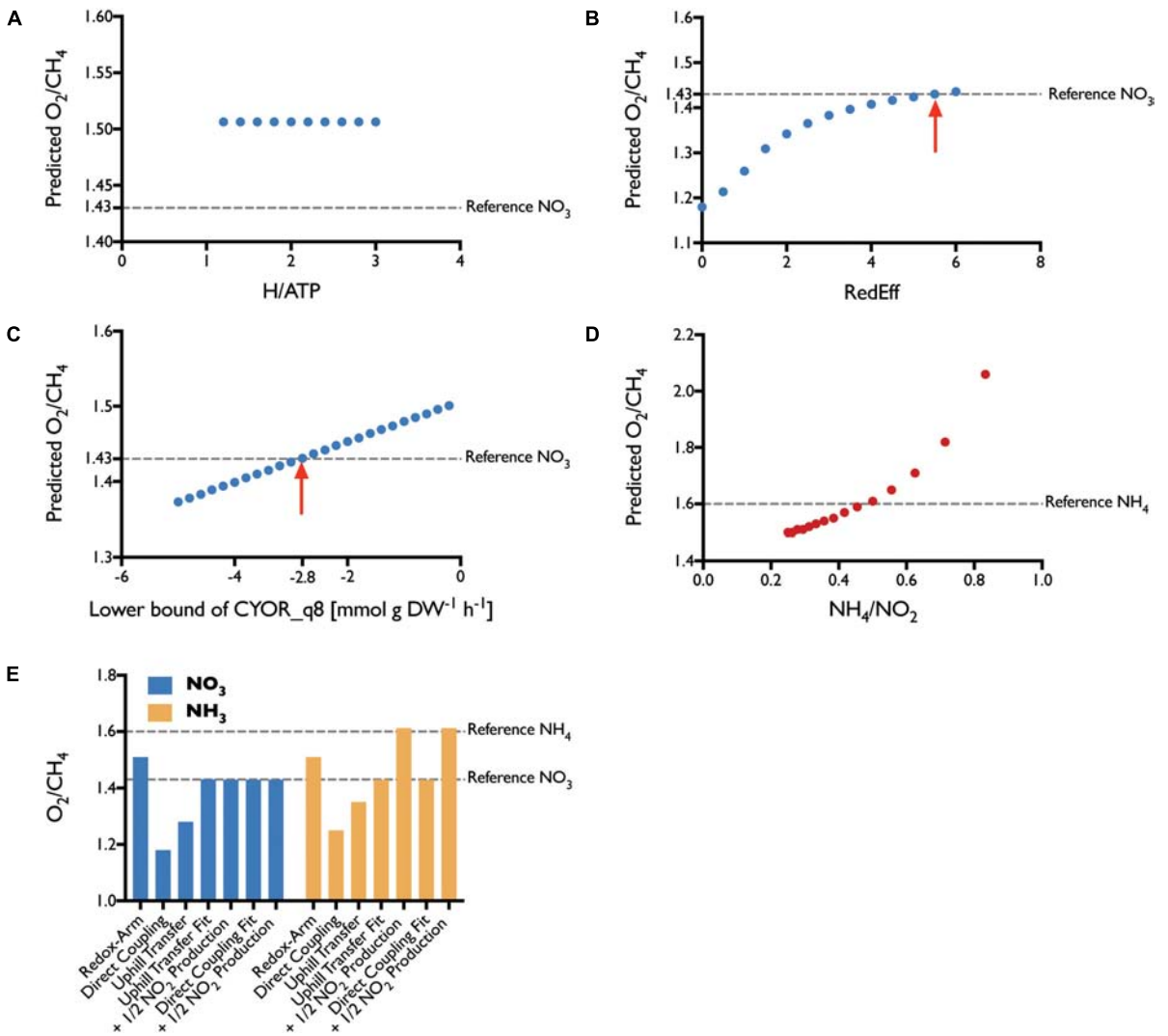


**FIGURE 7 |** Parameter Fit. The efficiency of each transfer mode was varied iteratively to determine the best fit. **(A)** For the *redox-arm* mode we varied the ratio of protons required per synthesis of 1 mol ATP, with no effect. **(B)** Fitting the *direct-coupling* mode, we forced a portion of the flux through the PMMOipp reaction. The red arrow marks the best fit with 5.5 times more carbon flux through PMMOipp than PMMODCipp. **(C)** The *Uphill-electron transfer* was fit by allowing reverse flux through the ubiquinol-cytochrome c reductase (CYOR_q8) reaction. The red arrow marks the best fit at a lower bound of **–**2.8 mmol g $DW^{-1}$ $h^{-1}$. **(D)** To account for energy loss through $NH_3$ oxidation, several ratios of $NH_4$ uptake to $NO_2$ production were considered. The closest fit was achieved with a ratio of around 0.5. **(E)** Without reducing electron transfer efficiency none of the modes could fit the reference value for $NO_3$. For $NH_3$, the reference was met after accounting for the effect of $NH_3$ oxidation to $NO_2$. Reduced efficiency *uphill electron transfer* and *direct coupling* both allow prediction of $O_2/CH_4$ ratios that agree well with the literature reference.

results on the nature of protein–protein interactions between pMMO and MDH seem to be inconclusive (Myronova et al., 2006; Culpepper and Rosenzweig, 2014; Ross and Rosenzweig, 2017), neither of the modes can be ruled out entirely.

## Parameter Fitting to Determine the Impact of $NH_4$ Oxidation

Leak and Dalton pointed out, that the unexpectedly high $O_2/CH_4$ ratio of 1.6 was the product of latent $NH_4$ oxidation rather than assimilation leading to elevated levels of $NO_2$ which detected at medium concentrations of around 200 μM (Leak and Dalton, 1986a). They were uncertain whether this increase in the ratio of $O_2/CH_4$ could be attributed to the energetic burden of oxidizing $NH_4$ or an uncoupling effect of $NO_2$.

To investigate this effect, we introduced a ratio constraint (see Methods) coupling the uptake of $NH_4$ to the excretion of $NO_2$ and explored a number of values for this ratio (**Figure 7C**). According to the simulations, the energy spent oxidizing about 50% of incoming $NH_4$ to $NO_2$ is sufficient to account for the observed, high $O_2/CH_4$ ratio of 1.6. Although this shows that the loss of energy could be significant enough to account for the increased ratio, this does not exclude a potential combined effect because of energy decoupling.

Regardless it shows that calculations using the metabolic model can accurately reflect the *in vivo* behavior of *M. capsulatus* (Bath).

## Validation of the Model

Specific growth rates of 0.25 and 0.37 $h^{-1}$ were measured by Joergensen and Degn (1987) for *M. capsulatus* (Bath) on copper-free and copper-rich $NO_3$ mineral salt medium, respectively. Simulations of iMcBath with an active sMMO reaction yielded 0.19 $h^{-1}$ on $NO_3$ and 0.26 $h^{-1}$ on $NH_4$ as the nitrogen source, as well as 0.20 $h^{-1}$ for growth driven by the pMMO on $NO_3$ and 0.30 $h^{-1}$ on $NH_4$. The predicted growth rates scale together with the uptake rates for methane and the respective nitrogen sources. The uptake rate for methane in iMcBath was constrained to 18.46 mmol $g_{DW}{}^{-1}$ $h^{-1}$, a value adopted from de la Torre et al. (2015) due to the lack of a specific measurement for *M. capsulatus* (Bath). Uptake rates for $NO_3$ and $NH_4$ have been left unconstrained for the same reasons. An adjustment of the scale will be possible as soon as these data become available.

The model qualitatively agrees with a report from Patel and Hoare (1971), who determined that *M. capsulatus* (Bath) is capable of using certain amino acids as sources for nitrogen (**Table 1**). Although the transport reactions for these amino acids could not be inferred, the addition of corresponding boundary reactions sufficed to predict growth using FBA. However, the predicted growth rates are not comparable as it seems that in the model some of the carbon is assimilated as the amino acids are ultimately converted into pyruvate. On L-glutamate and L-glutamine as N-sources the model further predicts the production of alpha-ketoglutarate, and on L-valine that of alpha-ketoisovalerate. This is in accordance with findings by Patel and Hoare (1971).

**TABLE 1 |** Model validation against experimental conditions from literature.

| Growth condition | Predicted growth rate [$h^{-1}$] | Measured growth rate [$h^{-1}$] |
|---|---|---|
| sMMO – $NO_3$ | 0.18 | 0.12[1] |
| sMMO – $NH_4$ | 0.23 | 0.09[1] |
| sMMO – L-Alanine | 1.0 | 0.08[1] |
| sMMO – L-Aspartate | 1.0 | 0.11[1] |
| sMMO – L-Asparagine | 1.0 | 0.11[1] |
| sMMO – L-Cysteine | 1.0 | 0.09[1] |
| sMMO – L-Glutamate | 0.47 | 0.11[1] |
| sMMO – L-Glutamine | 0.47 | 0.11[1] |
| sMMO – L-Valine | 0.46 | 0.07[1] |
| **Growth condition** | **Predicted growth rate [$h^{-1}$]** | **Experimental observation** |
| $CO_2 + H_2 - NO_3$ | 0.05 | Growth observed[2] |
| $CO_2 - NO_3$ | Infeasible | No growth[2] |
| $H_2 - NO_3$ | 0 | No growth[2] |
| $CO_2$ + Formate $- NO_3$ | 0.06 | Growth observed[2] |
| Formate $- NO_3$ | 0.06 | No growth[2] |

[1]*Patel and Hoare (1971) converted from Doubling Time [h-1],* [2]*Baxter et al. (2002).*

To further validate iMcBath, we simulated autotrophic growth on carbon dioxide and molecular hydrogen ($H_2$) as observed previously by Baxter et al. (2002). Indeed, growth was possible using carbon dioxide as the C-source and $H_2$ as the source of energy (**Table 1**). Replacement of $H_2$ with formate also allowed the production of biomass, although formate is both assimilated and oxidized. This is because the model allows for the consumption of cytosolic carbon dioxide created as the end-product of formate oxidation. In addition to the ribulose-bisphosphate carboxylase converting $CO_2$ to 3-phosphoglycerate, this mode of operation relies on the pyrophosphate-dependent 6-phosphofructokinase (PFK_3_ppi) to reversibly convert sedoheptulose-1,7-bisphosphate to sedoheptulose-7-phosphate and fructose bisphosphate to fructose-6-phosphate thus providing these intermediates to the RuMP cycle (Reshetnikov et al., 2008). Growth just on carbon dioxide or molecular hydrogen exclusively could not be simulated as reported by the authors.

Flux balance analysis confirms the results from Stanley and Dalton (1982) predicting latent $CO_2$ fixation even during growth on methane.

## Comparison With Other Models

We compared iMcBath, the preceding automated draft reconstruction BMID000000141026, and a GEM of the gram-negative, gamma-proteobacterium *M. buryatense* strain 5G(B1) (de la Torre et al., 2015) to illustrate how much the model has progressed from the draft through manual curation and how the mode of electron transfer affects growth parameters within the group of gamma-proteobacteria (see **Table 2**).

Unsurprisingly, the automated draft generally performs quite poorly in comparison with the curated models. It's not possible to produce biomass from methane, even in rich media conditions, which is indicative of gaps in the pathways leading toward individual biomass components. Moreover, ATP can be produced without the consumption of substrate, which in turn means that key energy reactions are not constrained thermodynamically to have the correct reversibility. In the draft, 51% of the reactions are not supported by Gene-Protein-Reaction rules (GPR), while in iMb5G(B1) this percentage is only 32% and in iMcBath the percentage of these reactions is under 20%. GPRs allow modelers to distinguish between isozymes and enzyme complexes by connecting gene IDs either through boolean "OR" or "AND" rules. In iMcBath, 25 complexes in total were curated and formulated as GPR. Neither the draft model nor iMb5G(B1) make this distinction.

In the automated draft, the oxidation of methane was only possible through a reaction representing the sMMO (MNXR6057). In iMcBath, this was corrected by also implementing reactions that represent the pMMO, one with ubiquinone as the electron donor (PMMOipp), and another that receives electrons from the MDH (PMMODCipp). *M. capsulatus* (Bath), like *M. buryatense 5G*(B1), expresses both the soluble and the particulate monooxygenase depending on the availability of copper in the medium. In iMb5G(B1), however, only the particulate monooxygenase is represented by the reaction "pMMO." The ability of *M. capsulatus* (Bath) to

**TABLE 2 |** Model Comparison.

| | iMcBath | BMID000000141026 | iMb5G(B1) |
|---|---|---|---|
| **Structure** | | | |
| Methane oxidation | SMMOi, PMMOipp, PMMODCipp | MNXR6057 | pMMO |
| Growth on N-sources | Urea, $NO_2$, $NO_3$, $NH_4$, $N_2$, Ala, Asn, Asp, Cys, Gln, Glt, Val | No Growth | $NO_3$ |
| **Performance** | | | |
| ATP Production closed exchanges | False | True | False |
| ATP Production rate – $NH_4$ | 0.775 | 1000 | 1 |
| ATP Production rate – $NO_3$ | 0.365 | 1000 | 0.519 |
| Growth rate – pMMO – $NH_4$ | 0.300 | No growth | 0.34 |
| Growth rate – pMMO – $NO_3$ | 0.205 | No growth | 0.27 |
| $O_2/CH_4$ Ratio – pMMO – $NH_4$ | 1.434 | No growth | 1.156 |
| $O_2/CH_4$ Ratio – pMMO – $NO_3$ | 1.430 | No growth | 1.116 |
| **Specifications** | | | |
| Reactions without GPR | 119 | 950 | 129 |
| Enzyme complexes | 43 | 0 | 0 |
| Total # genes | 730 | 589 | 313 |
| Total # metabolites | 879 | 935 | 403 |
| Total # reactions | 913 | 1858 | 402 |

*The presented reconstruction iMcBath, the automated draft BMID000000141026 and iMb5G(B1), a genome-scale reconstruction of Methylomicrobium buryatense strain 5G(B1).*

grow on ammonia, nitrate and nitrogen has been characterized experimentally (Murrell and Dalton, 1983). In addition to that, however, iMcBath also predicts growth on nitrite and urea. Nitrite is an intermediate in the assimilation of nitrate, yet also reported to elicit toxic effects (Leak and Dalton, 1986a; Nyerges and Stein, 2009), hence *in vivo* growth may only be possible on low concentrations. Growth on urea is possible in the model since we identified *MCA1662* as an ATP-driven urea transporter and gap-filled a urease reaction when curating the cobalamine biosynthesis pathway. As a consequence of this, urea can be taken up into the cytosol and broken down into ammonia and carbon dioxide, the former of which is then assimilated. Further experimental work is necessary to verify this *in vivo*. *M. buryatense* 5G(B1) is reported to grow on nitrate, ammonia and urea, yet without adding the respective transport reactions iMb5G(B1) only grows on nitrate. While the draft model for *M. capsulatus* (Bath) contains exchange reactions for all the tested nitrogen sources except for urea, it couldn't grow at all, which again is likely because of gaps in the pathways leading to biomass precursor metabolites.

The difference between *M. capsulatus* (Bath) and *M. buryatense* 5G(B1) becomes apparent when comparing the growth energetics of iMcBath and iMb5G(B1). iMb5G(B1) produces more mmol $gDW^{-1}$ $h^{-1}$ ATP than iMcBath. Because of this the hypothetical growth-rates predicted by iMb5G(B1) are higher than those of iMcBath regardless of the respective nitrogen source. This difference is likely a direct consequence of the mode of electron transfer to the monooxygenase and thus the efficiency of the methane oxidation reaction in total. When comparing the ratio of the uptake rate of oxygen and the uptake rate of methane for the two models, we can see that the resulting values in iMb5G(B1) are lower than in iMcBath. It was recently reported, that instead of the reverse-electron transfer and redox-arm mode active in *M. capsulatus* (Bath), a mixture of *direct coupling* from pMMO to MDH and *reverse electron transfer* seems to be the most likely mode in *M. buryatense* 5G(B1) (de la Torre et al., 2015).

## CONCLUSION

iMcBath is the first, manually curated, GEM for *M. capsulatus* (Bath). With iMcBath, we combine biochemical knowledge of half a century of research on *M. capsulatus* (Bath) into a single powerful resource, providing the basis for targeted metabolic engineering, process design and optimization, omic-data contextualization and comparative analyses. We applied the metabolic model to study the complex electron transfer chain of *M. capsulatus*, by analyzing the three modes of electron transfer that had been proposed previously (Leak and Dalton, 1986b). We did so by corresponding each mode with the flux through a reaction in the model, and consequently comparing the predicted $O_2/CH_4$ ratios to experimentally measured values by Leak and Dalton (1986a). Simulation and experiment agreed either when the model was constrained to employ the *uphill electron transfer* at reduced efficiency or *direct coupling* at strongly reduced efficiency for *M. capsulatus* (Bath) grown *in silico* on $NO_3$ as the source of nitrogen. Further experimental validation is required as neither mode can be ruled out exclusively. The experimentally observed effect of $NH_4$ oxidation to $NO_2$ could be replicated by considering the energy burden alone.

Future applications of the metabolic model could include hypothesis testing of the regulation of the MMO in other growth conditions (Kelly et al., 2005), studying the effects of the predicted hydrogenases on the energy metabolism of *M. capsulatus* (Bath) (Ward et al., 2004), and exploring venues of metabolic engineering for an improved production of metabolites (Kalyuzhnaya, 2016). Improved validation of the model requires more experimental data, which is surprisingly sparse. Specific uptake and growth rates in various conditions, as well as gene deletion studies are paramount to improving iMcBath. The authors would like to reach out to any experts on *M. capsulatus* to get involved in maintaining and improving iMcBath. The model and additional data is hosted publicly on Github[1]. Any

[1]https://github.com/ChristianLieven/memote-m-capsulatus

contributions are welcome regardless of whether they come in the form of pull requests, issues, comments, or suggestions.

# MATERIALS AND METHODS

## Model Curation

Starting reconstruction on the basis of an automated draft required additional effort to be able to use it for calculations. The automated draft used two sets of ID namespaces, BiGG (King et al., 2016) and MetaNetX (MNX) (Ganter et al., 2013). Hence, the first step in the curation efforts consisted of unifying the namespace by mapping all metabolite and reaction identifiers from MNX into the human-readable BiGG namespace. Individual metabolites and reactions with unmappable IDs, that could not be identified in the BiGG database and for which there was little evidence in the form of GPR rules, were removed from the model. Several metabolite formulas contained polymer units, and many reactions lacked EC numbers. Using the MNX spreadsheet exports "chem_prop.tsv" and "reac_prop.tsv" from version 1.0 (Bernard et al., 2014) and 2.0 (Moretti et al., 2016) most of these issues were resolved. Due to said malformed and missing metabolite formulae, many reactions were not mass-charge-balanced. We used the "check_mass_balance" function in cobrapy (Ebrahim et al., 2013) to identify and balance 99.4% of the reactions in the model. The remaining five reactions, belonging to fatty acid biosynthesis, involve a lumped metabolite that represents the average fatty acid content of *M. capsulatus* (Bath).

After mapping the reaction and metabolite identifiers from the MetaNetX namespace to the BiGG namespace, we proceeded with the curation efforts as follows: First, we chose a subsystem of interest, then we picked a pathway and using information from either the genome sequence, published articles, the metacyc or uniprot databases, and lastly, we enriched each enzymatic step in said pathway with as much information as possible. Information that was added included for instance: GPR, reaction localization, EC numbers, a confidence score, possible cofactors and inhibitors and cross references to other databases such as KEGG, BIGG and MetaNetX. For each metabolite involved in these reactions, we defined the stoichiometry, charge and elemental formula, either based on the corresponding entries in the BiGG database or on clues from literature.

If reactions from a pathway were present in the draft, we checked their constraints and directionality, consulting the corresponding reactions in MetaCyc (Caspi et al., 2014). This was necessary as many of the irreversible reactions in the draft reconstruction seemed to have been "inverted" when compared to the corresponding reactions in the reference databases, which made flux through them impossible in normal growth conditions.

The energy metabolism and methane oxidation were curated first. Except for the reaction representing the sMMO, all reactions were newly constructed, as they were absent in the draft. Then, in order to achieve sensible FBA solutions for growth on methane, the central carbon metabolism, amino acid and nucleotide biosynthesis pathways were manually curated. Simultaneous to the manual curation a metabolic pathway map was created in Escher, which helped us to maintain a visual checklist of curated pathways.

The automated draft contained a rudimentary, generic biomass reaction, which only accounted for the production of proteins, DNA and RNA, but not for the biosynthesis of a cell wall and cell membrane, the maintenance of a cofactor pool, the turnover of trace elements or the energetic costs associated with growth. After calculating a more specific biomass composition for *M. capsulatus* (Bath), further pathway curation was necessary to achieve growth *in silico*. This included the biosynthesis pathways of fatty acids (even, odd and cyclopropane varieties), phospholipids, coenzyme A, Ubiquinol, Lanosterol, FAD, FMN, Riboflavin, NAD and NADP, Heme, Glutathione, Cobalamin, Thiamine, Myo-Inositol, and Lipopolysaccharides. The corresponding biosynthetic pathways were gap-filled and manually curated. To identify the appropriate pathways, MetaCyc pathway maps from the *M. capsulatus* (Bath) specific database were used to compare the reactions that were present in the draft reconstruction[2].

To account for the reported differences in ammonia assimilation of *M. capsulatus* (Bath) when grown in the presence of excess ammonia versus the growth on either atmospheric nitrogen or nitrate, we curated the nitrogen metabolism including the oxidation of ammonia to nitrite via hydroxylamine, the reduction of nitrate and nitrite, the glutamine synthetase/ glutamate synthase reactions and the ADH. Reversible degradation reactions producing ammonia that would potentially bypass the characterized ammonia assimilation pathways were constrained to be irreversible accordingly.

After we had enriched the annotations already in the draft with annotations from the metabolic models iJO1366 (Orth et al., 2011), iRC1080 (Chang et al., 2011), iJN678 (Nogales et al., 2012), and iHN637 (Nagarajan et al., 2013), they were converted into a MIRIAM-compliant format. As a final step, we manually added transport reactions to reflect the uptake energetics of cofactors.

Throughout the reconstruction process, we iteratively tested and validated the reconstruction. For instance, we checked the mass and charge balance of each reaction, attempting to manually balance those that weren't balanced. In the majority of cases metabolites were missing formula or charge definitions. In order to remove energy generating cycles, problematic reactions were manually constrained to be irreversible. Validation was carried out against growth data (Leak and Dalton, 1986a), which was also the point of reference for the parameter fitting.

## Biomass Composition

For the principal components of biomass, measurements were made available through the website of our collaborators Unibio (2018). This included specifically the content of RNA (6.7%), DNA (2.3%), crude fat (9.1%), and glucose (4.5%) as a percentage of the cell dry weight. We did not use the percentage values for crude protein (72.9%) and N-free extracts (7.6%) as these measurements are fairly inaccurate relying on very generalized factors. The percentage value of Ash 550 (8.6%) measurements

[2]https://biocyc.org/organism-summary?object=MCAP243233

was inconsistent with the sum of its individual components (4.6%) and was hence excluded.

On the homepage of Unibio, we were also able to find g/kg measurements of all amino acids except for glutamine and asparagine, trace elements and vitamins, which could directly be converted into mmol/g DW. However, we omitted some of data: The stoichiometries for Selenium, Cadmium, Arsenic, Lead, and Mercury were not included in the biomass reaction as their values were negligibly small. Beta-Carotene (Vitamin A) and Gama-Tocopherol (Vitamin E) were omitted because no genes were found supporting their biosynthesis, in addition to both being reportedly below the detection limit (Øverland et al., 2010).

For the lack of better measurements, and assuming that *M. buryatense* and *M. capsulatus* (Bath) are more similar than *M. capsulatus* (Bath) and *E. coli*, the stoichiometries of glutamine and asparagine, intracellular metabolites such as ribulose-5-phosphate, organic cofactors such as coenzyme A, and cell wall components such as LPS were introduced from de la Torre et al. (2015).

Using the GC content calculated from the genome sequence (Ward et al., 2004) and the percentage measurements from Unibio for RNA and DNA, we were able to calculate the stoichiometries of all individual nucleobases.

Unibio's measurements that 94% of the crude fat portion were fatty acids conflicted with previously published results, which indicated that in fact phospholipids are likely to be the main lipid component in *M. capsulatus* (Bath) (Makula, 1978; Müller et al., 2004). Thus, we assumed 94% of the crude fat to be phospholipids. This meant that 6% of the crude fat was composed of fatty acids, the distributions of which were again provided by Unibio. However, in order to calculate the stoichiometry of each fatty acid we recalculated the distribution to exclude the unidentified part. Makula had also measured the composition of the phospholipid pool itself (Makula, 1978), from which we calculated the corresponding stoichiometries for phosphatidylethanolamine, phosphatidylcholine, phosphatidylglycerol, and cardiolipin.

Bird et al. (1971) had reported the percentage of squalene and sterols of dry weight, which we converted into mmol/g DW without further corrections. Since the genes for hopanoid synthesis were identified we included diplopterol in the biomass reaction (Ward et al., 2004; Nakano et al., 2007). For a lack of more detailed measurements we estimated a similar contribution to the overall composition as squalene. We specifically used lanosterol to represent the general class of sterols in the biomass reaction, since we had only been able to reconstruct the synthesis pathway of lanosterol and since lanosterol is a key precursor metabolite in the biosynthesis of all other sterols.

The growth associated maintenance (GAM) energy requirements were calculated in accordance with protocol procedures outline in **Figure 13** of Thiele and Palsson (2010). The final value of 23.087 mmol ATP $g_{DW}{}^{-1}$ $h^{-1}$ is the sum of the amount of ATP required to synthesize the proportional content of proteins, DNA and RNA per one gram of cell dry weight (DW). For each component *i* we obtained the synthesis energy coefficient *C* [mmol ATP/ mmol component] from Thiele and Palsson (2010), who calculated them based on Tables 5 and 6 of Chapter 3 in Neidhardt et al. (1990). With $x$ denoting the amount of a specific component $\boldsymbol{i}$ per gram DW [mmol component/ $g_{DW}$], the following formula determines the GAM requirement:

$$\sum_{i=1}^{n}(x_i C_i) \tag{1}$$

Specifically, the coefficients used herein are $C_P = 4.324$, $C_D = 1.365$, $C_R = 0.406$ and $x_P = 5.312$, $x_D = 0.047$, $x_R = 0.135$.

## Transport Reactions

The identification of transport reactions involved the two databases for transport proteins, the TCDB (Saier et al., 2016) and the Transport Database (TransportDB) (Elbourne et al., 2017), and two computational tools, PSORTb v3.0 (Yu et al., 2010) and BLASTp (Altschul et al., 1990). We employed the following semi-automatic way of inferring the putative function of transport proteins in *M. capsulatus* (Bath).

Using the protein sequences in AE017282.2_protein.faa (Ward et al., 2004), we determined the subcellular location of each protein using PSORTb v3.0. We filtered the results and focused only on proteins with a final score larger than 7.5, which the authors of PSORTb consider to be meaningful. We combined this list with the *M. capsulatus* (Bath) specific entries from the TransportDB, which allowed us to use the PSORT-scores as an additional measure of confidence. At this point, 242 putative transport proteins were identified. From this list we then selected all proteins which were predicted to transport metabolites and were already included in the model, which reduced the number to 133. Since for many of the entries, the exact mechanism of transport is unknown, we combined the previously selected transporters with the results from running BLAST against the TCDB. The *e*-value and bitscore from BLAST provided yet another measure to confidently assess the correctness of the automatic TransportDB predictions, and the Transporter Classification-Numbers (TC-numbers) allowed us to gather information on the mechanism of transport. This led to a list of 97 transport proteins with high confidence, which was filtered once more as follows.

We checked the general description for a given specific TC-number, and then considered the BLAST result to read about a given transporter in more detail, especially with regards to finding the specific substrates. When we were able to identify the corresponding transport reaction in the BiGG database, we incorporated only the simplest, smallest set of reactions. In cases of conflicts between our own BLAST results and the automatic TransportDB transporter annotation, we preferentially trusted the BLAST results. Thus we ultimately added 75 transporter-encoding genes connected via GPR to 56 distinct transport reactions.

## Applied Constraints

To identify which mode of electron transfer is active in *M. capsulatus* (Bath), we fit the solutions of flux balance analysis using iMcBath to measured values (Leak and Dalton, 1986a). The authors had experimentally determined the $O_2/CH_4$ ratio and the growth yield of *M. capsulatus* (Bath) in several conditions. They varied the nitrogen source using $KNO_3$, $NH_4CL$, and both

simultaneously; the concentration of copper in the medium, which directly affects the activity of either sMMO or pMMO; and whether the culture was oxygen or carbon limited.

The baseline constraints applied to the model allowed only the uptake of $CH_4$, $O_2$, $SO_4$, $PO_4$, either $NH_4$ or $NO_3$, and an array of mineral salts which are required by the biomass equation. The methane uptake rate was limited to allow at most 18.46 mmol $g_{DW}^{-1}$ $h^{-1}$ (adopted from de la Torre et al., 2015), all remaining uptake rates were left unconstrained. We accounted for the differential expression of ADH (model reaction ID: ALAD_L) in the presence of excess $NH_4$ in the medium by blocking the GS/GOGAT (model reaction ID: GLNS). In the presence of $NO_3$ or $N_2$ we allowed flux through both reactions (Murrell and Dalton, 1983). Maximization of flux through the biomass equation was set as the objective for parsimonious flux balance analysis with which all calculations were done.

Since each electron transfer mode, respectively, is represented by the flux through one specific reaction in the model (model reaction IDs: *redox-arm* = PMMOipp, *direct coupling* = PMMODCipp, and *uphill electron transfer* = CYOR_q8ppi), we were able to investigate each simply by allowing flux through the corresponding reaction.

Several studies have shown that $NH_4$ is a co-metabolic substrate to the methane monooxygenases in *M. capsulatus* (Bath) leading to the production of hydroxylamine first and nitrite later (Hutton and Zobell, 1953; Bédard and Knowles, 1989; Nyerges and Stein, 2009). Hence, when simulating the growth on $NH_4$ we assumed that varying ratios $r$ of the nitrogen taken up would eventually be converted into nitrite (**Figure 7**).

$$v_{EX_{nh4e}} + r v_{EX_{no2e}} = 0 \tag{2}$$

The program code and data for all analyses presented in this publication are available as *Model 15 Calculations.ipynb* at https://github.com/ChristianLieven/memote-m-capsulatus.

### Stoichiometric Modeling

The reactome of an organism can be represented mathematically as a stoichiometric matrix *S*. Each row of *S* corresponds to a unique compound, while each column corresponds to a metabolic reaction. Hence the structure of the matrix for an organism with $m$ compounds and $n$ reactions equals $m \times n$. The values in each row denote the stoichiometric coefficients of that metabolite in all reactions. The coefficients are either negative for compounds that are educts, positive for those that are products, or zero for those that are not involved in a given metabolic reaction.

The vector $v$ of length $n$ contains as values the turnover rates of each reaction. These rates are commonly referred to as fluxes and are given the unit mmol $gDW^{-1}$ $h^{-1}$. Vector $v$ is also referred to as the flux vector.

## AVAILABILITY OF DATA AND MATERIALS

The metabolic model, scripts and corresponding datasets generated and/or analyzed during the current study are available in the GitHub repository.

1. Archived: https://github.com/ChristianLieven/memote-m-capsulatus
2. Most Recent: https://github.com/ChristianLieven/memote-m-capsulatus/tree/develop

The data that support the biomass equation constructed in this study are available from Unibio at

1. http://www.unibio.dk/end-product/chemical-composition-1
2. http://www.unibio.dk/end-product/chemical-composition-2

Restrictions may apply to the accessibility of these data. Data are however available from the authors upon reasonable request and with permission of Unibio.

## AUTHOR CONTRIBUTIONS

CL collected and analyzed the data, reconstructed the metabolic model, drafted and revised the manuscript. LP and SJ provided feedback on the metabolic behavior of *M. capsulatus* (Bath), discussed improvements to the model and revised the manuscript. KG, MH, and NS conceived and supervised the study and revised the manuscript critically. All authors read and approved the manuscript.

## FUNDING

This work has been funded by the Novo Nordisk Foundation and the Innovation Fund Denmark [project "Environmentally Friendly Protein Production (EFPro2)"].

## ACKNOWLEDGMENTS

The authors would like to acknowledge Budi Juliman Hidayat, Subir Kumar Nandi, and John Villadsen for sharing their experiences with *M. capsulatus* (Bath), Mitch Pesesky, David Collins, Marina Kalyuzhnaya, Ilya Akberdin, and Sergey Stolyar for insightful discussions at the GRC C1 Conference 2016, and Kristian Jensen, Joao Cardoso, and Marta Matos for their help with software problems and feedback on the implementation.

## SUPPLEMENTARY MATERIAL

The Supplementary Material for this article can be found online at: https://www.frontiersin.org/articles/10.3389/fmicb.2018.02947/full#supplementary-material

**FIGURE S1** | Genome-scale Metabolic Map. High-resolution image of the genome-scale metabolic map of iMcBath. The metabolic map was constructed using escher.

**TABLE S1** | Stoichiometry of the biomass reaction in iMcBath. Table showing the stoichiometry and references of all components in the biomass reaction.

**TABLE S2** | iMcBath performance overview. Predicted uptake rates, growth rates, growth yield and performance ratios in various conditions. The script that generated this table is available online in the corresponding GitHub repository: https://github.com/ChristianLieven/memote-m-capsulatus.

## REFERENCES


Adeosun, E. K., Smith, T. J., Hoberg, A. M., Velarde, G., Ford, R., and Dalton, H. (2004). Formaldehyde dehydrogenase preparations from *Methylococcus capsulatus* (Bath) comprise methanol dehydrogenase and methylene tetrahydromethanopterin dehydrogenase. *Microbiology* 150, 707–713. doi: 10.1099/mic.0.26707-0

Altschul, S. F., Gish, W., Miller, W., Myers, E. W., and Lipman, D. J. (1990). Basic local alignment search tool. *J. Mol. Biol.* 215, 403–410. doi: 10.1016/S0022-2836(05)80360-2

Anthony, C. (1978). The prediction of growth yields in methylotrophs. *Microbiology* 104, 91–104.

Anthony, C. (1983). *The Biochemistry of Methylotrophs*. London: Academic Press. doi: 10.1016/0300-9629(83)90116-0

Anthony, C. (1992). The c-type cytochromes of methylotrophic bacteria. *Biochim. Biophys. Acta* 1099, 1–15. doi: 10.1016/0005-2728(92)90181-Z

Baxter, N. J., Hirt, R. P., Bodrossy, L., Kovacs, K. L., Embley, T. M., Prosser, J. I., et al. (2002). The ribulose-1,5-bisphosphate carboxylase/oxygenase gene cluster of *Methylococcus capsulatus* (Bath). *Arch. Microbiol.* 177, 279–289. doi: 10.1007/s00203-001-0387-x

Bédard, C., and Knowles, R. (1989). Physiology, biochemistry, and specific inhibitors of CH4, $NH4^+$, and CO oxidation by methanotrophs and nitrifiers. *Microbiol. Rev.* 53, 68–84.

Benedict, M. N., Gonnerman, M. C., Metcalf, W. W., and Price, N. D. (2012). Genome-scale metabolic reconstruction and hypothesis testing in the methanogenic archaeon *Methanosarcina acetivorans* C2A. *J. Bacteriol.* 194, 855–865. doi: 10.1128/JB.06040-11

Bergmann, D. J., Zahn, J. A., Hooper, A. B., and DiSpirito, A. A. (1998). Cytochrome P460 genes from the methanotroph *Methylococcus capsulatus* bath. *J. Bacteriol.* 180, 6440–6445.

Bernard, T., Bridge, A., Morgat, A., Moretti, S., Xenarios, I., and Pagni, M. (2014). Reconciliation of metabolites and biochemical reactions for metabolic networks. *Brief. Bioinform.* 15, 123–135. doi: 10.1093/bib/bbs058

Bird, C. W., Lynch, J. M., Pirt, F. J., Reid, W. W., Brooks, C. J. W., and Middleditch, B. S. (1971). Steroids and Squalene in *Methylococcus capsulatus* grown on Methane. *Nature* 230, 473–474. doi: 10.1038/230473a0

Blazyk, J. L., and Lippard, S. J. (2002). Expression and characterization of ferredoxin and flavin adenine dinucleotide binding domains of the reductase component of soluble methane monooxygenase from *Methylococcus capsulatus* (Bath). *Biochemistry* 41, 15780–15794. doi: 10.1021/bi026757f

Büchel, F., Rodriguez, N., Swainston, N., Wrzodek, C., Czauderna, T., Keller, R., et al. (2013). Path2Models: large-scale generation of computational models from biochemical pathway maps. *BMC Syst. Biol.* 7:116. doi: 10.1186/1752-0509-7-116

Campbell, M. A., Nyerges, G., Kozlowski, J. A., Poret-Peterson, A. T., Stein, L. Y., and Klotz, M. G. (2011). Model of the molecular basis for hydroxylamine oxidation and nitrous oxide production in methanotrophic bacteria. *FEMS Microbiol. Lett.* 322, 82–89. doi: 10.1111/j.1574-6968.2011.02340.x

Caspi, R., Altman, T., Billington, R., Dreher, K., Foerster, H., Fulcher, C. A., et al. (2014). The MetaCyc database of metabolic pathways and enzymes and the BioCyc collection of Pathway/Genome Databases. *Nucleic Acids Res.* 42, D459–D471. doi: 10.1093/nar/gkt1103

Chang, R. L., Ghamsari, L., Manichaikul, A., Hom, E. F. Y., Balaji, S., Fu, W., et al. (2011). Metabolic network reconstruction of Chlamydomonas offers insight into light-driven algal metabolism. *Mol. Syst. Biol.* 7:518. doi: 10.1038/msb.2011.52

Colby, J., and Dalton, H. (1978). Resolution of the methane mono-oxygenase of *Methylococcus capsulatus* (Bath) into three components. Purification and properties of component C, a flavoprotein. *Biochem. J.* 171, 461–468. doi: 10.1042/bj1710461

Colby, J., and Dalton, H. (1979). Characterization of the second prosthetic group of the flavoenzyme NADH–acceptor reductase (component C) of the methane mono-oxygenase from *Methylococcus capsulatus* (Bath). *Biochem. J.* 177, 903–908. doi: 10.1042/bj1770903

Culpepper, M. A., and Rosenzweig, A. C. (2014). Structure and protein–protein interactions of methanol dehydrogenase from *Methylococcus capsulatus* (Bath). *Biochemistry* 53, 6211–6219. doi: 10.1021/bi500850j

Dawson, M. J., and Jones, C. W. (1981). Energy conservation in the terminal region of the respiratory chain of the methylotrophic bacterium *Methylophilus methylotrophus*. *Eur. J. Biochem.* 118, 113–118. doi: 10.1111/j.1432-1033.1981.tb05492.x

de la Torre, A., Metivier, A., Chu, F., Laurens, L. M., Beck, D. A., Pienkos, P. T., et al. (2015). Genome-scale metabolic reconstructions and theoretical investigation of methane conversion in *Methylomicrobium buryatense* strain 5G(B1). *Microb. Cell Fact.* 14:188. doi: 10.1186/s12934-015-0377-3

DiSpirito, A. A., Kunz, R. C., Choi, D.-W., and Zahn, J. A. (2004). "Respiration in methanotrophs," in *Respiration in archaea and bacteria*, ed. D. Zannoni (Berlin: Springer), 149–168. doi: 10.1007/978-1-4020-3163-2_7

Ebrahim, A., Lerman, J. A., Palsson, B. O., and Hyduke, D. R. (2013). COBRApy: cOnstraints-based reconstruction and analysis for python. *BMC Syst. Biol.* 7:74. doi: 10.1186/1752-0509-7-74

Elbourne, L. D. H., Tetu, S. G., Hassan, K. A., and Paulsen, I. T. (2017). TransportDB 2.0: a database for exploring membrane transporters in sequenced genomes from all domains of life. *Nucleic Acids Res.* 45, D320–D324. doi: 10.1093/nar/gkw1068

Feist, A. M., Nagarajan, H., Rotaru, A.-E. E., Tremblay, P.-L. L., Zhang, T., Nevin, K. P., et al. (2014). Constraint-based modeling of carbon fixation and the energetics of electron transfer in Geobacter metallireducens. *PLoS Comput. Biol.* 10:e1003575. doi: 10.1371/journal.pcbi.1003575

Feist, A. M., Zielinski, D. C., Orth, J. D., Schellenberger, J., Herrgard, M. J., and Palsson, B. O. (2010). Model-driven evaluation of the production potential for growth-coupled products of *Escherichia coli*. *Metab. Eng.* 12, 173–186. doi: 10.1016/j.ymben.2009.10.003

Foster, J. W., and Davis, R. H. (1966). A methane-dependent coccus, with notes on classification and nomenclature of obligate, methane-utilizing bacteria. *J. Bacteriol.* 91, 1924–1931.

Ganter, M., Bernard, T., Moretti, S., Stelling, J., and Pagni, M. (2013). MetaNetX.org: a website and repository for accessing, analysing and manipulating metabolic networks. *Bioinformatics* 29, 815–816. doi: 10.1093/bioinformatics/btt036

Hanson, R. S., and Hanson, T. E. (1996). Methanotrophic bacteria. *Microbiol. Rev.* 60, 439–471.

Harder, W., and Van Dijken, J. P. (1976). "Theoretical considerations on the relation between energy production and growth of methane-utilizing bacteria," in *Microbial Production and Utilization of Gases,* eds H. G. Schlegel, N. Pfennig and G. Gottschalk (Gottingen: Goltze Verlag), 403–418.

Hommes, N. G., Sayavedra-Soto, L. A., and Arp, D. J. (2003). Chemolithoorganotrophic growth of Nitrosomonas europaea on fructose. *J. Bacteriol.* 185, 6809–6814. doi: 10.1128/JB.185.23.6809-6814.2003

Hutton, W. E., and Zobell, C. E. (1953). Production of nitrite from ammonia by methane oxidizing bacteria. *J. Bacteriol.* 65, 216–219.

Indrelid, S., Kleiveland, C., Holst, R., Jacobsen, M., and Lea, T. (2017). The soil bacterium *Methylococcus capsulatus* bath interacts with human dendritic cells to modulate immune function. *Front. Microbiol.* 8:320. doi: 10.3389/fmicb.2017.00320

Jiang, H., Chen, Y., Jiang, P., Zhang, C., Smith, T. J., Murrell, J. C., et al. (2010). Methanotrophs: multifunctional bacteria with promising applications in environmental bioengineering. *Biochem. Eng. J.* 49, 277–288. doi: 10.1016/j.bej.2010.01.003

Joergensen, L., and Degn, H. (1987). Growth rate and methane affinity of a turbidostatic and oxystatic continuous culture of *Methylococcus Capsulatus* (BATH). *Biotechnol. Lett.* 9, 71–76. doi: 10.1007/BF01043398

Kalyuzhnaya, M. G. (2016). "Methane biocatalysis: selecting the right microbe," in *Biotechnology for Biofuel Production and Optimization*, eds C. Eckert and C. Trinh (Amsterdam: Elsevier B.V). doi: 10.1016/B978-0-444-63475-7.00013-3

Kelly, D. P., Anthony, C., and Murrel, J. C. (2005). Insights into the obligate methanotroph *Methylococcus capsulatus*. *Trends Microbiol.* 13, 195–198. doi: 10.1016/j.tim.2005.03.002

Kim, B., Kim, W. J., Kim, D. I., and Lee, S. Y. (2015). Applications of genome-scale metabolic network model in metabolic engineering. *J. Ind. Microbiol. Biotechnol.* 42, 339–348. doi: 10.1007/s10295-014-1554-9

King, Z. A., Dräger, A., Ebrahim, A., Sonnenschein, N., Lewis, N. E., and Palsson, B. O. (2015). Escher: a web application for building, sharing, and embedding data-rich visualizations of biological pathways. *PLoS Comput. Biol.* 11:e1004321. doi: 10.1371/journal.pcbi.1004321

King, Z. A., Lu, J., Dräger, A., Miller, P., Federowicz, S., Lerman, J. A., et al. (2016). BiGG Models: a platform for integrating, standardizing and sharing genome-scale models. *Nucleic Acids Res.* 44, D515–D522. doi: 10.1093/nar/gkv1049

Kleiveland, C. R., Hult, L. T. O., Spetalen, S., Kaldhusdal, M., Christofferesen, T. E., Bengtsson, O., et al. (2013). The noncommensal bacterium *Methylococcus capsulatus* (Bath) ameliorates dextran sulfate (sodium salt)-induced ulcerative colitis by influencing mechanisms essential for maintenance of the colonic barrier function. *Appl. Environ. Microbiol.* 79, 48–57. doi: 10.1128/AEM.02464-12

Larsen, Ø., and Karlsen, O. A. (2016). Transcriptomic profiling of *Methylococcus capsulatus* (Bath) during growth with two different methane monooxygenases. *Microbiologyopen* 5, 254–267. doi: 10.1002/mbo3.324

Leak, D. J., and Dalton, H. (1983). In vivo studies of primary alcohols, aldehydes and carboxylic acids as electron donors for the methane mono-oxygenase in a variety of methanotrophs. *Microbiology* 129, 3487–3497. doi: 10.1099/00221287-129-11-3487

Leak, D. J., and Dalton, H. (1986a). Growth yields of methanotrophs - 1. Effect of copper on the energetics of methane oxidation. *Appl. Microbiol. Biotechnol.* 23, 470–476. doi: 10.1007/BF02346062

Leak, D. J., and Dalton, H. (1986b). Growth yields of methanotrophs 2. A theoretical analysis. *Appl. Microbiol. Biotechnol.* 23, 477–481. doi: 10.1007/BF02346063

Lund, J., Woodland, M. P., and Dalton, H. (1985). Electron transfer reactions in the soluble methane monooxygenase of *Methylococcus capsulatus* (Bath). *Eur. J. Biochem*. 147, 297–305. doi: 10.1111/j.1432-1033.1985.tb08750.x

Makula, R. A. (1978). Phospholipid composition of methane-utilizing bacteria. *J. Bacteriol.* 134, 771–777.

Mishra, N. K., Chang, J., and Zhao, P. X. (2014). Prediction of membrane transport proteins and their substrate specificities using primary sequence information. *PLoS One* 9:e100278. doi: 10.1371/journal.pone.0100278

Moretti, S., Martin, O., Van Du Tran, T., Bridge, A., Morgat, A., and Pagni, M. (2016). MetaNetX/MNXref–reconciliation of metabolites and biochemical reactions to bring together genome-scale metabolic networks. *Nucleic Acids Res.* 44, D523–D526. doi: 10.1093/nar/gkv1117

Müller, H., Hellgren, L. I., Olsen, E., and Skrede, A. (2004). Lipids rich in phosphatidylethanolamine from natural gas-utilizing bacteria reduce plasma cholesterol and classes of phospholipids: a comparison with soybean oil. *Lipids* 39, 833–841. doi: 10.1007/s11745-004-1304-15

Murrell, J. C., and Dalton, H. (1983). Ammonia assimilation in *Methylococcus capsulatus* (Bath) and other obligate methanotrophs. *J. Gen. Microbiol.* 129, 1197–1206. doi: 10.1099/00221287-129-4-1197

Murrell, J. C., Dalton, H., Murrell, J., Colin, Dalton, H., Colin Murrell, J., Dalton, H., et al. (1983). Nitrogen fixation in obligate methanotrophs. *Microbiology* 129, 3481–3486. doi: 10.1099/00221287-129-11-3481

Myronova, N., Kitmitto, A., Collins, R. F., Miyaji, A., and Dalton, H. (2006). Three-dimensional structure determination of a protein supercomplex that oxidizes methane to formaldehyde in *Methylococcus capsulatus* (Bath). *Biochemistry* 45, 11905–11914. doi: 10.1021/bi061294p

Nagarajan, H., Sahin, M., Nogales, J., Latif, H., Lovley, D. R., Ebrahim, A., et al. (2013). Characterizing acetogenic metabolism using a genome-scale metabolic reconstruction of *Clostridium ljungdahlii*. *Microb. Cell Fact.* 12:118. doi: 10.1186/1475-2859-12-118

Nakano, C., Motegi, A., Sato, T., Onodera, M., and Hoshino, T. (2007). Sterol biosynthesis by a prokaryote: first in vitro identification of the genes encoding squalene epoxidase and lanosterol synthase from *Methylococcus capsulatus*. *Biosci. Biotechnol. Biochem.* 71, 2543–2550. doi: 10.1271/bbb.70331

Neidhardt, F. C., Ingraham, J. L., and Schaechter, M. (1990). *Physiology of the Bacterial Cell: a Molecular Approach*. Sunderland, MA: Sinauer Associates.

Nogales, J., Gudmundsson, S., Knight, E. M., Palsson, B. O., and Thiele, I. (2012). Detailing the optimality of photosynthesis in cyanobacteria through systems biology analysis. *Proc. Natl. Acad. Sci. U.S.A.* 109, 2678–2683. doi: 10.1073/pnas.1117907109

Nunes, J. J., Aufderheide, B., Ramjattan, D. M., and Dass, R. (2016). Enhanced production of single cell protein from *M. capsulatus* (Bath) growing in mixed culture. *J. Microbiol. Biotechnol. Food Sci.* 6, 894–899. doi: 10.15414/jmbfs.2016/17.6.3.894-899

Nyerges, G., and Stein, L. Y. (2009). Ammonia cometabolism and product inhibition vary considerably among species of methanotrophic bacteria. *FEMS Microbiol. Lett.* 297, 131–136. doi: 10.1111/j.1574-6968.2009.01674.x

Oakley, C. J., and Murrell, J. C. (1991). Cloning of nitrogenase structural genes from the obligate methanotroph *Methylococcus capsulatus* (Bath). *FEMS Microbiol. Lett*. 62, 121–125. doi: 10.1111/j.1574-6968.1991.tb04429.x

Olivier, B. G., and Bergmann, F. T. (2015). The systems biology markup language (SBML) level 3 package: flux balance constraints. *J. Integr. Bioinform.* 12:269. doi: 10.2390/biecoll-jib-2015-269

Orth, J. D., Conrad, T. M., Na, J., Lerman, J. A., Nam, H., Feist, A. M., et al. (2011). A comprehensive genome-scale reconstruction of *Escherichia coli* metabolism–2011. *Mol. Syst. Biol.* 7:535. doi: 10.1038/msb.2011.65

Øverland, M., Tauson, A.-H., Shearer, K., and Skrede, A. (2010). Evaluation of methane-utilising bacteria products as feed ingredients for monogastric animals. *Arch. Anim. Nutr.* 64, 171–189. doi: 10.1080/17450391003691534

Patel, R. N., and Hoare, D. S. (1971). Oxidation of C-1 compounds capsulatus physiological studies of methane and methanol- oxidizing bacteria?: oxidation of c-1 compounds by *Methylococcus capsulatus*. *J. Bacteriol.* 107, 187–192.

Petersen, L. A. H., Villadsen, J., Jørgensen, S. B., and Gernaey, K. V. (2017). Mixing and mass transfer in a pilot scale U-loop bioreactor. *Biotechnol. Bioeng.* 114, 344–354. doi: 10.1002/bit.26084

Reshetnikov, A. S., Rozova, O. N., Khmelenina, V. N., Mustakhimov, I. I., Beschastny, A. P., Murrell, J. C., et al. (2008). Characterization of the pyrophosphate-dependent 6-phosphofructokinase from *Methylococcus capsulatus* Bath. *FEMS Microbiol. Lett.* 288, 202–210. doi: 10.1111/j.1574-6968.2008.01366.x

Ritala, A., Häkkinen, S. T., Toivari, M., and Wiebe, M. G. (2017). Single cell protein—state-of-the-art, industrial landscape and patents 2001–2016. *Front. Microbiol.* 8:2009. doi: 10.3389/fmicb.2017.02009

Ross, M. O., and Rosenzweig, A. C. (2017). A tale of two methane monooxygenases. *J. Biol. Inorg. Chem.* 22, 307–319. doi: 10.1007/s00775-016-1419-y

Rozova, O. N., Khmelenina, V. N., Mustakhimov, I. I., Reshetnikov, A. S., and Trotsenko, Y. A. (2010). Characterization of recombinant fructose 1, 6 bisphosphate aldolase from *Methylococcus capsulatus* bath. *Biochemistry* 75, 892–898.

Saier, M. H. Jr., Tran, C. V., and Barabote, R. D. (2006). TCDB: the Transporter Classification Database for membrane transport protein analyses and information. *Nucleic Acids Res.* 34, D181–D186. doi: 10.1093/nar/gkj001

Saier, M. H., Reddy, V. S., Tsu, B. V., Ahmed, M. S., Li, C., and Moreno-Hagelsieb, G. (2016). The Transporter Classification Database (TCDB): recent advances. *Nucleic Acids Res.* 44, D372–D379. doi: 10.1093/nar/gkv1103

Shiemke, A. K., Arp, D. J., and Sayavedra-Soto, L. A. (2004). Inhibition of membrane-bound methane monooxygenase and ammonia monooxygenase by diphenyliodonium: implications for electron transfer. *J. Bacteriol.* 186, 928–937. doi: 10.1128/JB.186.4.928-937.2004

Stanley, S. H., and Dalton, H. (1982). Role of Ribulose-l, 5-bisphosphate Carboxylase / Oxygenase in. *J. Gen. Microbiol.* 128, 2927–2935.

Strøm, T., Ferenci, T., and Quayle, J. R. (1974). The carbon assimilation pathways of *Methylococcus capsulatus*, *Pseudomonas methanica* and *Methylosinus trichosporium* (OB3B) during growth on methane. *Biochem. J.* 144, 465–476. doi: 10.1042/bj1440465

Tate, S., and Dalton, H. (1999). A low-molecular-mass protein from *Methylococcus capsulatus* (Bath) is responsible for the regulation of formaldehyde dehydrogenase activity in vitro. *Microbiology* 145(Pt 1), 159–167. doi: 10.1099/13500872-145-1-159

Taylor, S. (1977). Evidence for the presence of ribulose 1,5-bisphosphate carboxylase and phosphoribonuclease in *Methylococcus capsulatus* (bath). *FEMS Microbiol. Lett.* 2, 305–307. doi: 10.1016/0378-1097(77)90057-x

Taylor, S., Dalton, H., and Dow, C. (1980). Purification and initial characterisation of ribulose 1,5-bisphosphate carboxylase from *Methylococcus capsulatus* (Bath). *FEMS Microbiol. Lett.* 8, 157–160. doi: 10.1016/0378-1097(80)90021-x

Taylor, S. C., Dalton, H., and Dow, C. S. (1981). Ribulose- 1,5-bisphosphate carboxylase/oxygenase and carbon assimilation in *Methylococcus capsulatus* (Bath). *Microbiology* 122, 89–94. doi: 10.1099/00221287-122-1-89

Thiele, I., and Palsson, B. Ø. (2010). A protocol for generating a high-quality genome-scale metabolic reconstruction. *Nat. Protoc.* 5, 93–121. doi: 10.1038/nprot.2009.203

Unibio (2018). *Unibio Homepage*. Available at: www.unibio.dk

Varma, A., Boesch, B. W., and Palsson, B. O. (1993). Stoichiometric interpretation of *Escherichia coli* glucose catabolism under various oxygenation rates. *Appl. Environ. Microbiol.* 59, 2465–2473.

Vorholt, J. A. (2002). Cofactor-dependent pathways of formaldehyde oxidation in methylotrophic bacteria. *Arch. Microbiol.* 178, 239–249. doi: 10.1007/s00203-002-0450-2

Ward, N., Larsen, Ø., Sakwa, J., Bruseth, L., Khouri, H., Durkin, A. S., et al. (2004). Genomic insights into methanotrophy: the complete genome sequence of *Methylococcus capsulatus* (Bath). *PLoS Biol.* 2:e303. doi: 10.1371/journal.pbio.0020303

Wolfe, R. S., and Higgins, I. J. (1979). Microbial biochemistry of methane-a study in contrasts. *Int. Rev. Biochem.* 21, 267–353.

Wood, A. P., Aurikko, J. P., and Kelly, D. P. (2004). A challenge for 21st century molecular biology and biochemistry: what are the causes of obligate autotrophy and methanotrophy? *FEMS Microbiol. Rev.* 28, 335–352. doi: 10.1016/j.femsre.2003.12.001

Yu, N. Y., Wagner, J. R., Laird, M. R., Melli, G., Rey, S., Lo, R., et al. (2010). PSORTb 3.0: improved protein subcellular localization prediction with refined localization subcategories and predictive capabilities for all prokaryotes. *Bioinformatics* 26, 1608–1615. doi: 10.1093/bioinformatics/btq249

Zahn, J. A., Bergmann, D. J., Boyd, J. M., Kunz, R. C., and DiSpirito, A. A. (2001). Membrane-associated quinoprotein formaldehyde dehydrogenase from *Methylococcus capsulatus* Bath. *J. Bacteriol.* 183, 6832–6840. doi: 10.1128/JB.183.23.6832-6840.2001

**Conflict of Interest Statement:** Unibio is a collaborator in the "Environmentally Friendly Protein Production (EFPro2)" project. CL, MH, and NS are publicly funded through the Novo Nordisk Foundation and the Innovation Fund Denmark.

The remaining authors declare that the research was conducted in the absence of any commercial or financial relationships that could be construed as a potential conflict of interest.

frontiers in Microbiology

ORIGINAL RESEARCH
published: 11 October 2018
doi: 10.3389/fmicb.2018.02439

# Substrate Specificity Analysis of Dihydrofolate/Dihydromethanopterin Reductase Homologs in Methylotrophic α-Proteobacteria

*Mark Burton, Chidinma Abanobi, Kate Tzu-Chi Wang, Yihua Ma and Madeline E. Rasche**

*Department of Chemistry and Biochemistry, Center for Applied Biotechnology Studies, California State University, Fullerton, Fullerton, CA, United States*

Methane-producing archaea and methylotrophic bacteria use tetrahydromethanopterin ($H_4$MPT) and/or tetrahydrofolate ($H_4$F) as coenzymes in one-carbon (C1) transfer pathways. The α-proteobacterium *Methylobacterium extorquens* AM1 contains a dihydromethanopterin reductase (DmrA) and two annotated dihydrofolate reductases (DfrA and DfrB). DmrA has been shown to catalyze the final step of $H_4$MPT biosynthesis; however, the functions of DfrA and DfrB have not been examined biochemically. Moreover, sequence alignment (BLAST) searches have recognized scores of proteins that share up to 99% identity with DmrA but are annotated as diacylglycerol kinases (DAGK). In this work, we used bioinformatics and enzyme assays to provide insight into the phylogeny and substrate specificity of selected Dfr and DmrA homologs. In a phylogenetic tree, DmrA and homologs annotated as DAGKs grouped together in one clade. Purified histidine-tagged versions of the annotated DAGKs from *Hyphomicrobium nitrativorans* and *M. nodulans* (respectively, sharing 69 and 84% identity with DmrA) showed only low activity in phosphorylating 1,2-dihexanoyl-*sn*-glycerol when compared with a commercial DAGK from *Escherichia coli.* However, the annotated DAGKs successfully reduced a dihydromethanopterin analog (dihydrosarcinapterin, $H_2$SPT) with kinetic values similar to those determined for *M. extorquens* AM1 DmrA. DfrA and DfrB showed little or no ability to reduce $H_2$SPT under the conditions studied; however, both catalyzed the NADPH-dependent reduction of dihydrofolate. These results provide the first evidence that DfrA and DfrB function as authentic dihydrofolate reductases, while DAGKs with greater than 69% identity to DmrA may be misannotated and are likely to function in $H_4$MPT biosynthesis.

**Keywords: methylotrophic bacteria, dihydrofolate reductase, dihydromethanopterin reductase, methanopterin, one-carbon transfer**

OPEN ACCESS

***Edited by:***
*Marina G. Kalyuzhanaya, San Diego State University, United States*

***Reviewed by:***
*Ludmila Chistoserdova, University of Washington, United States*
*Norma Cecilia Martinez-Gomez, Michigan State University, United States*

***Correspondence:**
*Madeline E. Rasche*
*merasche@fullerton.edu*

***Specialty section:***
*This article was submitted to Microbiotechnology, Ecotoxicology and Bioremediation, a section of the journal Frontiers in Microbiology*

***Received:*** *07 June 2018*
***Accepted:*** *24 September 2018*
***Published:*** *11 October 2018*

***Citation:***
*Burton M, Abanobi C, Wang KT-C, Ma Y and Rasche ME (2018) Substrate Specificity Analysis of Dihydrofolate/Dihydromethanopterin Reductase Homologs in Methylotrophic α-Proteobacteria. Front. Microbiol. 9:2439. doi: 10.3389/fmicb.2018.02439*

## INTRODUCTION

In the facultative methylotroph *Methylobacterium extorquens* AM1, growth on single-carbon ($C_1$) substrates involves the use of both tetrahydromethanopterin ($H_4$MPT) and tetrahydrofolate ($H_4$F) (Chistoserdova et al., 1998). $H_4$MPT was initially thought to be exclusive to methanogenic archaea and sulfur-dependent hyperthermophilic archaea (Achenbach-Richter et al., 1987;

DiMarco et al., 1990; Gorris et al., 1991). However, the discovery of $H_4$MPT-linked $C_1$ transfer enzymes in the Bacteria domain has provided evidence for the use of $H_4$MPT beyond a methane-generating pathway (Chistoserdova et al., 1998; Vorholt et al., 1999; Chistoserdova et al., 2004; Chistoserdova, 2016). In the aerobic α-proteobacterium *M. extorquens* AM1, methylotrophy involves the use of dephospho-$H_4$MPT in a series of oxidative steps to catabolize reduced $C_1$ compounds to $CO_2$ (Chistoserdova et al., 1998); this is in contrast to the reduction of $CO_2$ to methane in the anaerobic metabolism of methanogenic archaea (DiMarco et al., 1990). The use of methylotrophs in biotechnology has gained interest because of its application to the microbial production of useful industrial chemicals starting with $C_1$ compounds as an alternative to glucose and other conventional sugar or acid substrates (Schrader et al., 2009; Ochsner et al., 2015).

In the pathways of $H_4$MPT and $H_4$F biosynthesis, the last step requires the activity of dihydromethanopterin reductase (Dmr) or dihydrofolate reductase (Dfr). *M. extorquens* AM1 contains one dihydromethanopterin reductase (DmrA) and two putative dihydrofolate reductases, DfrA and DfrB, that, respectively, share 26% identity (41% similarity) and 34% identity (53% similarity) with DmrA. The *dmrA* gene was first discovered using transposon mutagenesis (Marx et al., 2003) and later deletion mutagenesis which produced a phenotype similar to that of mutants with deletions in $H_4$MPT biosynthesis genes (Marx et al., 2003; Rasche et al., 2004; Chistoserdova et al., 2005). Homology of DmrA to dihydrofolate reductases led to the proposal that DmrA evolved from an ancestral dihydrofolate reductase following horizontal transfer of $H_4$MPT biosynthesis genes from anaerobic archaea to aerobic bacteria (Marx et al., 2003). A driving force for the evolution of DmrA from dihydrofolate reductase may have been the lack of archaea-specific electron donors such as Factor-420 in the recipient bacteria. Absence of a corresponding archaeal electron donor could render the dihydromethanopterin reductase useless in bacteria, providing selective pressure to modify the substrate specificity of an NADPH-dependent dihydrofolate reductase to reduce dihydromethanopterin (Marx et al., 2003; Caccamo et al., 2004).

DmrA has been shown to catalyze the final step of $H_4$MPT biosynthesis in *M. extorquens* AM1 (Caccamo et al., 2004) (**Figure 1A**); however, DmrA shares no sequence homology with the FMN-containing dihydromethanopterin reductase discovered in archaea (DmrX) or related archaeal-like flavoproteins (AfpA and DmrB) from β-proteobacteria (Kalyuzhnaya et al., 2005; McNamara et al., 2014; Wang et al., 2014). The FMN prosthetic groups of DmrX and AfpA/DmrB appear to be critical for electron transfer (McNamara et al., 2014; Wang et al., 2014) and may contribute to the absence of homology with the NADPH-dependent DmrA, which lacks flavin cofactors.

In *M. extorquens*, the dihydrofolate reductase homologs DfrA and DfrB have not been examined biochemically. When originally discovered, a role for DfrA in the synthesis of $H_4$F was proposed based on its 50% sequence identity to dihydrofolate reductase from *Lactobacillus casei* (Marx et al., 2003) and the genomic location of *dfrA* near the $H_4$F synthesis genes *folC* and *folE* in *M. extorquens* (Chistoserdova et al., 2003). Furthermore, the *dfrA* gene is located directly downstream of a gene encoding a putative $H_4$F-dependent thymidylate synthase (Marx et al., 2003).

Little is known about the function of DfrB. When we conducted a BLAST search using *M. extorquens* DfrB as the sequence alignment query, only a few homologs with high sequence identity could be identified. In a phylogenetic tree, these clustered together as a single group (**Figure 2**). Among the more distantly related homologs, one clade included DfrA and numerous annotated dihydrofolate reductases (30–48% identical to DfrB). The last clade consisted of a few known DmrA sequences (34–42% identical to DfrB) and a large number of proteins annotated as diacylglycerol kinases (DAGKs) but sharing 60–99% identity with DmrA from *M. extorquens*. This is curious because DAGKs function in phosphorylation reactions rather than in the reduction of pterins, as shown in **Figure 1B**. To provide insight into possible roles of the DmrA, DfrA, and DfrB homologs, we have used bioinformatics to assess phylogenetic relationships among the homologs and enzyme assays to probe biochemical function.

# MATERIALS AND METHODS

## Bioinformatics

The DfrB nucleotide sequence (GenBank no. AY093433) (Marx et al., 2003) was used as the query in a non-redundant database BLASTx (translated nucleotide to protein) in the National Center for Biotechnology Information Database (NCBI) using default algorithm patterns with the exception of limiting to 5,000 maximum target sequences (Altschul et al., 1997). Similar results were obtained using the DfrB protein sequence in BLASTp. Sequences were aligned using the Clustal Omega program (Sievers et al., 2011; McWilliam et al., 2013; Li et al., 2015). Aligned sequences were analyzed for phylogenetic relationships and unrooted tree construction (Kumar et al., 2016). The String v10.5 database was used to assess the gene/protein-protein relationships of the neighboring genes to *dfrA* and *dmrA*

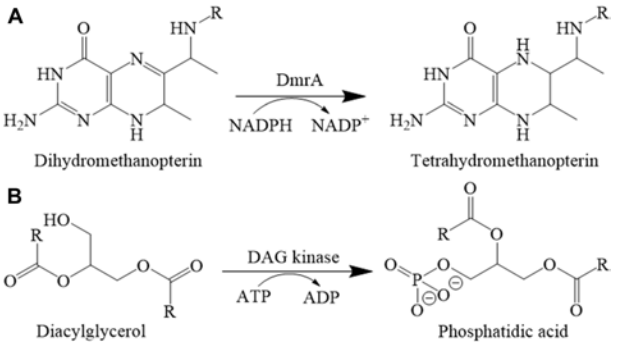


**FIGURE 1 |** Reactions catalyzed by **(A)** DmrA and **(B)** DAGK.

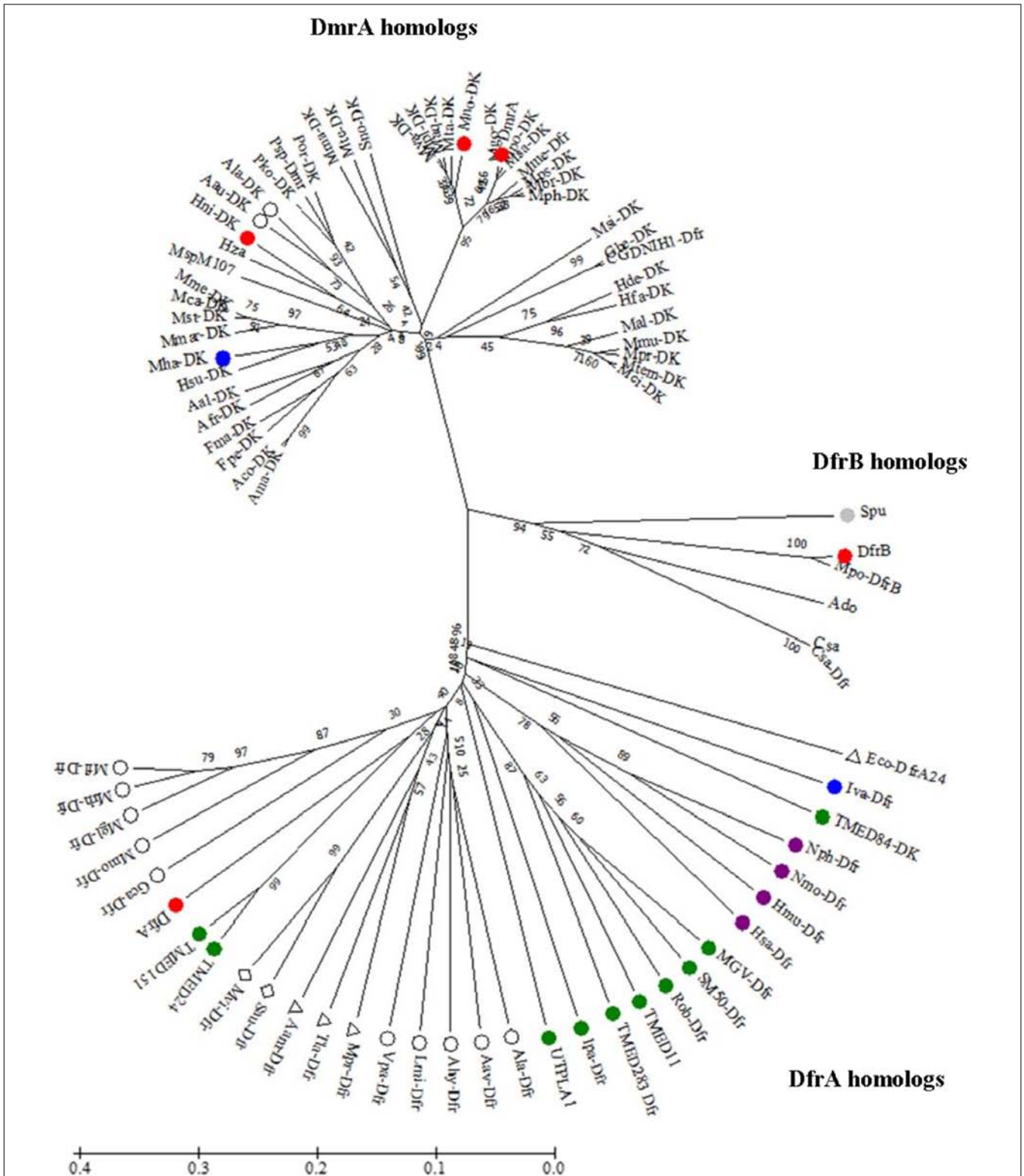


**FIGURE 2 |** Unrooted phylogenetic tree showing position of DfrB (AY093433) relative to orthologs including DfrA (AY093432) and DmrA (AY093431). Sequences were aligned using EMBL-EBI OMEGA bioinformatics tools with default parameters. Phylogenetic analysis was performed by using Maximum Likelihood method with 10,000 bootstrap replicates (Felsenstein, 1985) within MEGA7 software (Kumar et al., 2016). Abbreviation DAGK (DK). Color designations are Firmicute (blue), Actinobacteria (gray), Planctomycetes (green), Euryarchaeota (purple), β-proteobacteria (open circle), γ-proteobacteria (triangle), and δ-proteobacteria (diamond). DfrA, DfrB, DmrA, Mno-DK, and Hni-DK (red). The bar denotes 1 estimated substitution per 100 amino acid positions.

(Snel et al., 2000; von Mering et al., 2003, 2005, 2007; Jensen et al., 2009; Szklarczyk et al., 2011, 2015, 2017; Franceschini et al., 2013, 2016) and BPROM operon predictive method was applied to these genes (Li, 2011). Neighboring genes without any clear annotations in subsequent sequence alignment searches were analyzed using the Protein Homology/analogy Recognition Engine v2.0 database (Kelley et al., 2015).

## Chemicals

Luria-Bertani/Miller broth (LB) (Becton, Dickinson and Company, Franklin Lakes, NJ) was purchased from Thermo Fisher Scientific (Waltham, MA, United States). Tris(hydroxymethyl)aminomethane (Tris), 1,4-piperazinediethanesulfonic acid (PIPES), dibasic sodium phosphate ($Na_2HPO_4$), monobasic potassium phosphate ($KH_2PO_4$), D-(+)-glucose, magnesium sulfate ($MgSO_4$), β-mercaptoethanol (2-ME), kanamycin sulfate, imidazole, sodium ascorbate, magnesium acetate, and ammonium chloride ($NH_4Cl$) were also from Thermo Fisher. Isopropyl-β-D-thiogalactopyranoside (IPTG) was from Ubiquitin-Proteasome Biotechnologies (UBP-Bio, Aurora, CO). N-[Tris(hydroxyl)methyl]-2-aminoethanesulfonic acid (TES), 3-(morpholino)propanesulfonic acid (MOPS), sodium acetate, dihydrofolate ($H_2F$), NADH, NADPH, ethylenediaminetetraacetic acid (EDTA), ethylene glycol-bis(β-aminoethyl ether)-*N,N,N′,N′*-tetraacetic acid (EGTA), phosphoenolpyruvate (PEP), adenosine 5′-triphosphate (ATP), lithium chloride (LiCl), and deoxyribonuclease I (DNase I) bovine were from Sigma-Aldrich (St. Louis, MO, United States). 1,2-dihexanoyl-*sn*-glycerol was from Cayman Chemical (Ann Arbor, MI, United States). Gasses were from Airgas (Placentia, CA, United States). Unless otherwise noted, all other chemicals were purchased from Thermo Fisher Scientific.

## Gene Synthesis and Transformation

The *dfrA* and *dfrB* genes were subcloned with an N-terminal six-histidine ($H_6$) tag into the NdeI and BamHI sites of the pET-41a(+) expression vector (Novagen, Madison, WI, United States) by GenScript (Piscataway, NJ, United States). For production of $H_6$-DfrA or $H_6$-DfrB, the corresponding plasmid was transformed into chemically competent BL21(DE3) cells (Stratagene, La Jolla, CA, United States). Similarly, cell lines were created to produce DmrA (BL21 + pET41a: $H_6$-DmrA or pET41a:DmrA-$H_4$) and the annotated DAGKs from *Hyphomicrobium nitrativorans* and *M. nodulans* (BL21 + pET41a: Hni-DAGK-$H_6$) or BL21 + pET41a:Mno-DAGK-$H_6$). The estimated molecular masses of the corresponding histidine-tagged proteins are 19.3 kDa for $H_6$-DfrA, 19.4 kDa for $H_6$-DfrB, 15.8 kDa for DmrA-$H_4$, and 16.2 kDa for both Hni-DAGK-$H_6$ and Mno-DAGK-$H_6$.

## Cell Growth and Gene Induction

For the production of $H_6$-DmrA and DmrA-$H_4$, an overnight culture of BL21 cells with pET41a: $H_6$-DmrA or pET41a: DmrA-$H_4$ was used to inoculate 1 liter of a modified M9 minimal medium (Sambrook and Russell, 2001) containing 48 mM $Na_2HPO_4$, 22 mM $KH_2PO_4$, 19 mM $NH_4Cl$, and 17 mM NaCl [pH 7.4], supplemented with 0.4% (w/v) D-(+)-glucose, 2 mM $MgSO_4$, and kanamycin (50 μg/ml). Cells were grown at 37°C with shaking (180 rpm). When the optical density at 600 nm reached approximately 0.4, the cells were transferred to another platform shaker previously equilibrated to 15°C (180 rpm) for approximately 45 min. When the optical density at 600 nm reached 0.55–0.60, gene expression was induced with IPTG to 1 mM. The cells were grown at 15°C for 16 h, and then the cell suspension was centrifuged (5,000 × *g*, 15 min, 4°C). The cell pellet was washed in 30 ml of 50 mM TES [pH 8.0], collected by centrifugation (7,000 × *g*, 15 min, 4°C), and stored at −20°C.

To produce tagged DfrA, DfrB, *M. nodulans* DAGK, and *H. nitrativorans* DAGK proteins ($H_6$-DfrA, $H_6$-DfrB, Mno-DAGK-$H_6$, and Hni-DAGK-$H_6$), overnight cultures of BL21 cells with the appropriate plasmid were used to inoculate 1 L of LB medium (Bertani, 1951) containing kanamycin (50 μg/ml). Cells were grown at 37°C with shaking (180 rpm). For $H_6$-DfrA, $H_6$-DfrB, and Hni-DAGK-$H_6$, when the optical density at 600 nm reached approximately 0.6, gene expression was induced with IPTG to 1 mM. The culture was transferred to a platform shaker at 20°C, and cells were grown for 16 h with shaking (180 rpm). For Mno-DAGK-$H_6$, after induction, the culture was grown at 30°C for 6 h with shaking (180 rpm). All cells were collected by centrifugation (5,000 × *g*, 15 min, 4°C), washed with 30 ml of 50 mM TES, pH 8, centrifuged (7,000 × *g*, 15 min, 4°C), and stored at −20°C.

## Cell Lysis and Protein Purification

All cells were lysed at 20,000 lb/in$^2$ by one pass through a cold French Press cell (Thermo Fisher Corporation, Waltham, MA, United States) at 4°C in 50 mM Tris, 200 mM NaCl, 20 mM imidazole, 15 mM 2-ME [pH 8.0], and 2 μL of DNase I. Lysed cells were centrifuged for 1 h at 4°C (32,000 × *g*). The supernatant (cell-free extract, CFE) was removed and centrifuged for an additional 15 min. The CFE was incubated with 1-part Nickel Nitrilotriacetic acid resin (NiNTA, Qiagen, Germantown, MD, United States) to 4 parts CFE for 2 h with DmrA-$H_4$ or 1 h with $H_6$-DfrA, $H_6$-DfrB, Hni-DAGK-$H_6$, and Mno-DAGK-$H_6$. The CFE-NiNTA slurry was poured into a 10-ml polypropylene column (Bio-Rad Laboratories, Inc., Hercules, CA, United States) and washed three times with 5 ml of 50 mM Tris pH 8, 200 mM NaCl, 30 mM imidazole, 15 mM 2-mercaptoethanol (2-ME). Elution buffers consisted of 50 mM Tris pH 8, 200 mM NaCl, 15 mM 2-ME with 100 mM imidazole or 250 mM imidazole. Buffers were added to the column at room temperature (approximately 23°C) to minimize fluctuations in pH within the column.

Protein concentrations were determined by the Bradford procedure (Bradford, 1976) using bovine serum albumin (Pierce Biotechnology, Rockford, IL, United States) as the standard. The efficiency of protein purification and protein purity were analyzed using sodium dodecyl sulfate-polyacrylamide gel electrophoresis (SDS-PAGE) stained with Coomassie brilliant blue G-250 (Bio-Rad, Hercules, CA, United States) (Garfin, 1990). All

histidine-tagged proteins were shown to be greater than 95% pure.

## Preparation of Dihydrosarcinapterin ($H_2$SPT) From Methanogen Cell Extract

The $H_4$MPT analog tetrahydrosarcinapterin ($H_4$SPT) was obtained from the methanogen *Methanosarcina thermophila* TM-1 grown on acetate (Scott and Rasche, 2002) and purified by a previously developed method (Caccamo et al., 2004). Approximately 5 g of cells were removed from liquid nitrogen and sealed in a 37-ml amber anaerobic vial. Cells were purged with hydrogen gas for 10 min and transferred to an anaerobic chamber (Coy Products, Inc., Grass Lake, MI, United States) in 97% nitrogen and 3% hydrogen (Praxair, Inc., Danbury, CT, United States). An anoxic solution (10 ml) of 30 mM sodium acetate pH 4.3 and 200 mM 2-ME was added to re-suspend the cells. The vial containing the cells was sealed with a rubber stopper and aluminum crimp seal, boiled for 15 min (Precision Scientific, Chicago, MI, United States), allowed to cool, and then transferred into the anaerobic chamber. The boiled cell lysate was transferred in aliquots (1 mL) into 2-ml microcentrifuge tubes and centrifuged for 20 min at 13,000 × *g* (Eppendorf Minispin plus, Hauppauge, NY, United States). During centrifugation, a 2-ml column of Sephadex A-25 diethylaminoethane (DEAE) was prepared in a 10-ml polypropylene column (Bio-Rad Laboratories, Inc., Hercules, CA, United States) and equilibrated with two column volumes of 50 mM MOPS, 1 M NaCl, 150 mM 2-ME [pH 6.8], followed by two column volumes of 50 mM MOPS, 150 mM 2-ME [pH 6.8]. The column was wrapped in aluminum foil to limit light exposure within the column. An aliquot of boiled CFE (200 μL) was removed for use in methylene-$H_4$MPT reductase (MtdB) assays. The remaining boiled CFE was mixed with one volume of 50 mM MOPS, pH 6.8, 150 mM 2-ME. This mixture was added to the DEAE column. Fractions were collected from a step gradient of 50 mM MOPS, pH 6.8, 150 mM 2-ME with 0–1.0 M NaCl. Two 2-ml aliquots per NaCl step (0, 200, 400, 500, 600, and 1,000 mM) were collected. The highest concentration of $H_4$SPT was found in the first 500 mM fraction of NaCl, as determined by the MtdB enzymatic assay (Rasche et al., 2004). Fractions were sealed in 10-ml anaerobic vials wrapped in foil and stored at −80°C.

To partially oxidize the $H_4$SPT to $H_2$SPT, the first 500 mM NaCl DEAE fraction or second 400 mM NaCl DEAE fraction was exposed to air for 100 s, by gently swirling for 80 s (approximately 2 swirls/s) at 30-s intervals. Oxidation of $H_4$SPT was followed monitoring the increase in absorbance at 280 and 342 nm ($\epsilon 342_{[Methanopterin]}$ = 7.4 $mM^{-1}$ $cm^{-1}$) (van Beelen et al., 1984) and the decrease in absorbance at 302 nm ($\epsilon 302_{[H4MPT]}$ = 15.2 $mM^{-1}$ $cm^{-1}$) (Escalante-Semerena et al., 1984). Enzymatic assays were used to monitor levels of $H_4$SPT (Rasche et al., 2004) and $H_2$SPT (Caccamo et al., 2004) in addition to the wavelengths mentioned above. The oxidized 500 $mM^{-1}$ fraction was transferred into an anaerobic chamber and aliquoted (100 μL) into 0.5-ml microcentrifuge tubes and sealed in a 10-ml anaerobic vial wrapped in aluminum foil. Aliquots were stored at −80°C.

## Dfr Assay

Reactions were prepared in an anaerobic chamber (97% $N_2$ and 3% $H_2$) in sealed 2-ml quartz masked cuvettes (Starna, Atascadero, CA, United States). The initial reaction mixtures (1 ml) consisted of about 3.6 μg of protein in an anoxic solution of 500 mM Tris (pH 7.5), 20 mM sodium ascorbate, 15 mM 2-ME, 50 μM $H_2$F, and 0.1 mM NADPH. The reaction was initiated with the injection of protein using a 25-μL gas-tight syringe (Hamilton, Reno, NV, United States) that was purged with anoxic double-deionized water containing 20 mM 2-ME. The cuvette was gently inverted and placed back into the spectrophotometer. The oxidation of NADPH was monitored at 340 nm on a DU-800 spectrophotometer (Beckman Coulter, Brea, CA, United States) using a combined extinction coefficient for NADPH and $H_4$F ($\epsilon 340_{[NADPH\ +\ H4F]}$ of 12.3 $mM^{-1}$ $cm^{-1}$. The effect of pH was analyzed as described above in 200 mM sodium phosphate for pH levels 5.8–8.0 and 200 mM sodium acetate buffer for pH 5.3. The effect of temperatures were tested over the range from 15 to 37°C. The cuvettes were covered and equilibrated in a water bath for 10 min at varying temperatures prior to addition of protein.

## DmrA Assay

The DmrA assay of Caccamo et al. (2004) was used based on modifications to a Dfr assay. Reactions were prepared in an anaerobic chamber in sealed 2-ml quartz masked cuvettes. The reaction mixture (250 μL or 1 ml) consisted of about 3.6 μg of enzyme in an anoxic solution containing 500 mM sodium acetate (pH 5.3), 20 mM sodium ascorbate, 1 mM EDTA, 15 mM 2-ME, 80 μM $H_2$SPT, and 0.1 mM NADPH. The reaction was initiated with the injection of protein with a 25-μL gas-tight syringe, purged with anoxic double-deionized water containing 20 mM 2-ME. The cuvette was gently inverted and placed back into the spectrophotometer. The oxidation of NADPH was monitored at 340 nm ($\epsilon 340_{[NADPH]}$ = 6.22 $mM^{-1}$ $cm^{-1}$) (Dawson, 1986) on a DU-800 spectrophotometer.

## Specific Activity for Dfr, DmrA, and DAGK Assays and Kinetics Analysis for DmrA Assays

Rate calculations using the molar extinction coefficient for NAD(P)H were used to measure specific activity, where 1 unit is defined as 1 μmol of NAD(P)H oxidized per min per mg of protein for all assays. Enzyme kinetic constants ($K_m$ and $V_{max}$ values) were determined with a non-linear regression model fit to the Michaelis-Menten equation using GraphPad Prism v7.03 for Windows (GraphPad Software, La Jolla, CA, United States[1])

## DAGK Assay

Diacylglycerol kinases activity was assayed by coupling the oxidation of NADH to the production of phosphatidic acid (Badola and Sanders, 1997) (**Figure 1B**). The headspace of the DAG analog substrate (1,2-dihexanoyl-*sn*-glycerol in 50% ethanol) was purged under a gentle stream of nitrogen to evaporate the ethanol solvent until an oil residue remained. The

[1]www.Graphpad.com

sealed residue was transferred to an anaerobic chamber and reconstituted in an anoxic solution of 60 mM PIPES, 50 mM LiCl, 0.1 mM EDTA, 0.1 mM EGTA [pH 6.8] (150-μL) to a final concentration of 50 mg/ml (the approximate solubility of 1,2-dihexanoyl-*sn*-glycerol in phosphate buffered saline (PBS), pH 7.2.) Lactate dehydrogenase (LDH) (Roche, Mannheim, Germany), pyruvate kinase (PK) (Sigma-Aldrich, St. Louis, MO, United States), DAGK from *Escherichia coli* (Enzo Life Sciences, Farmingdale, NY, United States), and annotated DAGK from *M. nodulans* and *H. nitrativorans* were prepared by transferring 100 μL of each enzyme to 3-ml anaerobic vials and purging the headspace with a gentle stream of nitrogen for approximately 5 min on ice. The reaction was initiated with approximately 3.6 μg of protein in an anoxic reaction mixture (60 mM PIPES, pH 6.8, 50 mM LiCl, 0.1 mM EDTA, 0.1 mM EGTA), 1 mM phosphoenolpyruvate, 3 mM ATP, 2.6 mM 1,2-dihexanoyl-*sn*-glycerol, 20 mM magnesium acetate, 0.1 mM NADH, and 20 units each of LDH and PK. The oxidation of NADH was monitored using the molar absorption coefficient at 340 nm on a DU-800 spectrophotometer.

## Protein Computational Modeling

Conformational modeling of DmrA and DfrB was performed by Andrew Orry (Molsoft, San Diego, CA, United States) using the ICM package. The modeling template was the crystal structure of *Mycobacterium avium* dihydrofolate reductase co-crystallized with NADPH and trimethoprim (pdb 2w3v). The modeling method is based on the Internal Coordinates (IC) representation of molecular objects, which naturally reflects covalent bond geometry of molecule (Abagyan and Totrov, 1994; Abagyan et al., 1994). After initial placement of the aligned polypeptide chain onto the template structure, the side-chain torsion angles were predicted by simultaneous global optimization of the energy for all non-identical residues. Conformational modeling of protein side chains and loops involved internal coordinate definition of the molecular object combined with computationally efficient ICM Biased Probability Monte Carlo (BPMC) optimization. Optimization of the structures were done in an extended force field (Arnautova et al., 2011), which includes surface terms, electrostatics, and side chain entropy terms. The quality of the 3D model was assessed by an ICM procedure called Protein Health.

# RESULTS

In *M. extorquens* AM1, three genes sharing similarity to dihydrofolate reductase (*dfrA, dfrB,* and *dmrA*) have been previously identified (Marx et al., 2003). Prior to the current work, only the protein encoded by the (*dmrA*) gene had been characterized biochemically (Caccamo et al., 2004; Rasche et al., 2004). In the current study, we used a bioinformatics approach to assess phylogenetic relationships among *M. extorquens* DfrA, DfrB, and DmrA, and homologs from other organisms. We also employed enzyme assays to assess the biochemical activities of DfrA, DfrB, DmrA, and two DmrA orthologs currently annotated as DAGKs.

## Sequence Alignment Searches of DfrB Orthologs Resulted in Three Distinct Clades

DfrB orthologs obtained in a BLASTx search from a non-redundant database in NCBI were used to construct an unrooted phylogenetic tree using a maximum-likelihood method with bootstrap analyses (Dawson, 1986; Kumar et al., 2016) (**Figure 2**). The resulting tree yielded three clades. Each clade contained either DfrA, DfrB, or DmrA from *M. extorquens* AM1. The sequences surrounding DfrA were from either Euryarchaeota, Plantomycete, Proteobacteria, or a Firmicute. The small clade containing DfrB revealed sequences from Proteobacteria and Actinobacteria. The largest clade (DmrA) contained homologs from Proteobacteria and a Firmicute.

## DfrA Is Closely Related to Annotated Dfr Orthologs From Bacteria

In the phylogenetic tree, the *M. extorquens* DfrA sequence was located among orthologs from planctomycetes and β-, γ-, and δ-proteobacteria (**Figure 2**). Two of the proteins in the DfrA clade have been previously crystallized as dihydrofolate reductases: a DfrA homolog from *Moritella profunda* (Mpr-Dfr) (Hay et al., 2009), and a trimethoprim-resistant ortholog from *E. coli* (Eco-DfrA24). This observation provides support for the hypothesis that *M. extorquens* DfrA may function as a standard dihydrofolate reductase All planctomycete homologs in the phylogenetic tree grouped with DfrA. Interestingly, one planctomycete sequence was annotated as a DAGK (TMED84-DK, **Figure 2**) in the DfrA clade. However, this ortholog was found to be only 14% identical to a known DAGK from *E. coli* using a percent identity matrix generated in Clustal Omega (Sievers et al., 2011; McWilliam et al., 2013; Li et al., 2015).

To further investigate connections to folate metabolism, genes in the neighborhood of *dfrA* were analyzed using the STRING v10.5 database, and a gene/protein interaction network module was constructed with *dfrA* biosynthesis (data not shown). In various genomes, genes with connection to *dfrA* included *thyA, folC, fhs, gcvT, glyA, metH, purH, purN, fmt,* and MexAM1_META1p0830 (*fmt*-like), many of which are associated with folate-requiring pathways of coenzyme, amino acid synthesis, and purine.

## One Clade Contained a Small Group of Orthologs Sharing 45–95% Identity With DfrB

Out of the vast number of DfrB orthologs identified by the BLAST search, only five sequences grouped tightly with and are closely related to *M. extorquens* DfrB in the phylogenetic tree (**Figure 2**). One ortholog was from an actinobacterium (*Streptomyces purpurogeneiscleroticus*) and the remaining were from α-proteobacteria. Of these five, two orthologs were annotated as Dfr and the remaining three were labeled as hypothetical proteins. The highest identity to DfrB (95%) was an ortholog annotated as Dfr from *M. populi* (Mpo-DfrB, **Figure 2**).

This organism has been renamed as *M. extorquens* strain BJ001 (Marx et al., 2012).

Of the orthologs in the DfrB clade, only DfrB was located on a plasmid. Two genes located upstream of DfrB were a putative transposase and a protein of unknown function. The highest confidence for a homology match in the Phyre2 database for the protein of unknown function resulted in a riboflavin synthase domain-like superfamily (ferredoxin reductase FAD-binding domain-like family), with a reductase/isomerase/elongation factor common domain (30% identity, coverage).

## The DmrA Clade Included Annotated DAGKs From Various Bacteria

Homologs in the DmrA clade had identities ranging from 60 to 99% when compared to DmrA from *M. extorquens* AM1. The DmrA clade contained three homologs from α-proteobacteria annotated as dihydrofolate reductases (Dfr) (*M. mesophililcum, Granulibacter bethesdensis* CGDNIH1, and *M. populi*), and a large number of homologs annotated as DAGKs. Many of the annotated DAGKs contained amino acid regions predicted in NCBI to reduce dihydrofolate to $H_4F$ using NADPH as a cofactor. Thus, we tested whether some of these annotated DAGKs might function as dihydrofolate reductases or DmrA enzymes.

Most of the putative dihydromethanopterin reductases were from α-proteobacteria. The exceptions were two sequences from the β-proteobacteria *Azohydromonas australica* and *A. lata*) (respectively, 67 and 65% identity to *M. extorquens* DmrA). This is interesting because it is the first evidence of DmrA homologs in β-proteobacteria. In other β-proteobacteria, the proposed dihydromethanopterin reductases are not homologous to DmrA but instead resemble an archaeoflavoprotein (AfpA) found to restore a $C_1$ growth phenotype in *M. extorquens* following *dmrA* knockout and complementation (Kalyuzhnaya et al., 2005). The AfpA group in β-proteobacteria has been renamed as dihydromethanopterin reductase B (DmrB). The crystal structure of DmrB points to the role of FMN cofactors in electron or hydride transfer to $H_2$MPT (McNamara et al., 2014). It is intriguing that *A. australica* and *A. lata* contain homologs of both DmrA (**Figure 2**) and DmrB (with identities of 69 and 68%, respectively, to *Burkholderia xenovorans* DmrB). This raises the evolutionary question of why both forms of dihydromethanopterin reductase (DmrA and DmrB) might coexist in these organisms.

## *M. extorquens* DfrA and DfrB Enzyme Activities

To test the hypotheses that DfrA and DfrB function as dihydrofolate reductases, the enzymes were initially assayed in the presence of 50 μM $H_2F$. Under these initial conditions, $H_6$-DfrA and $H_6$-DfrB reduced $H_2F$ with specific activities of 18.5 and 3.13 U/mg, respectively (**Figure 3** and **Table 1**). These values were within 2.5-fold of the rate obtained using a known dihydrofolate reductase from *E. coli* (7.3 U/mg) (**Figure 3** and **Table 1**). When DfrA and DfrB were tested for dihydromethanopterin reductase activity, only a trace of $H_2$SPT reduction activity was observed for both enzymes (**Figure 4**, diamond and triangle; **Table 1**, column 3). This activity was only about 1% of the $H_2$SPT reduction activity of DmrA-$H_4$ measured at pH 5.3 (**Table 1**). Some caution should be taken in interpreting these data due to the histidine tags, which lacked a protease cut site and could not be removed. However, since the activities of $H_6$-DfrA and $H_6$-DfrB resembled that of untagged DfrB from *E. coli,* these data provide biochemical support that DfrA and DfrB are likely to function in converting dihydrofolate to $H_4F$ in *M. extorquens* cells.

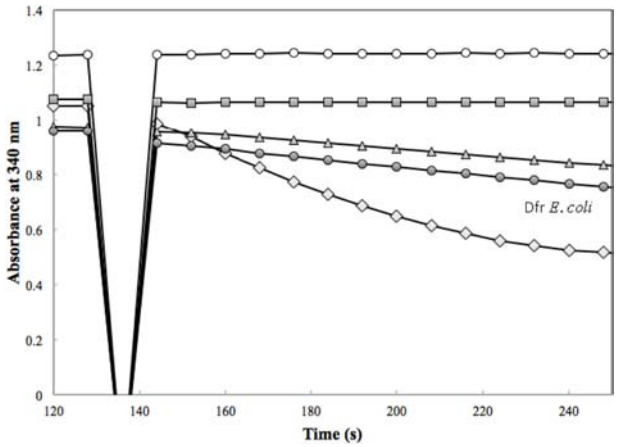


**FIGURE 3 |** Dfr activity was assessed in the presence of 50 μM $H_2F$ with 1.7 μg of $H_6$-DfrA (open diamond), 1.9 μg of $H_6$-DfrB (triangle), 3.6 μg of Mno-DAGK-$H_6$ (open circle), 3.6 μg of Hni-DAGK-$H_6$ (square), and 1.0 μg of Dfr from *Escherichia coli* (closed circle).

The effect of pH, temperature, and enzyme concentration were studied for $H_6$-DfrA and $H_6$-DfrB in preparation for kinetics studies. Over the pH range tested (5.3–8.0), the highest reaction rates for both enzymes were obtained from pH 6.8 to 7.0 (data not shown). For the temperatures tested (15–37°C or 40°C), $H_6$-DfrA showed a broad temperature optimum from about 23–40°C, while $H_6$-DfrB showed near constant reaction rates between 15 and 37°C. Thus, pH 6.8 and room temperature were used for kinetics measurements. DfrA activity showed a linear

**TABLE 1 |** Initial tests of enzyme activity in the presence of pterin and DAG substrates.

| Protein | Specific activity $H_2F$ (U/mg) | Specific activity $H_2$SPT (U/mg) | Specific activity DAG (U/mg) |
|---|---|---|---|
| Eco-Dfr | $7.7 \pm 0.52^4$ | —[a] | —[a] |
| $H_6$-DfrA | $18.5 \pm 0.52^3$ | 0.041 | —[a] |
| $H_6$-DfrB | $3.13 \pm 0.60^3$ | 0.011 | —[a] |
| DmrA-$H_4$ | —[a] | $2.24 \pm 0.26^3$ | —[a] |
| Mno-DAGK-$H_6$ | None detected | $0.63 \pm 0.34^3$ | 0.43 |
| Hni-DAGK-$H_6$ | None detected | $2.82 \pm 0.28^6$ | 0.55 |
| Eco-DAGK | —[a] | —[a] | 22.4 |

[a]*Not determined. Superscripts 3–6 denote number of replicates. For "no activity detected," the limit of detection was 0.25 mg/ml.*

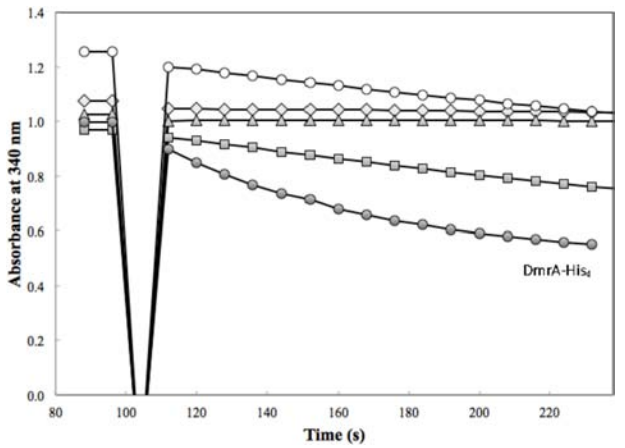


**FIGURE 4 |** DmrA activity was assessed in the presence of 83 μM $H_2$SPT with 3.4 μg of $H_6$-DfrA (open diamond), 4.1 μg of $H_6$-DfrB (triangle), 3.6 μg of Mno-DAGK-$H_6$ (open circle), 0.72 μg of Hni-DAGK-$H_6$ (square), and 4.3 μg of DmrA-$H_4$ (closed circle).

response to increasing enzyme concentration up to 1.8 μg per assay (0.093 μM $H_6$-DfrA), while DfrB activity was linear up to 3.6 μg per assay (0.18 μM $H_6$-DfrB).

To estimate kinetic values, the concentration of dihydrofolate was tested over the range from 0 to 150 μM (**Figure 5**). When fit to the Michaelis-Menten equation for a hyperbola, the estimated $K_M$ values were similar (14 ± 3.0 μM dihydrofolate for DfrA and 18 ± 8.9 μM for DfrB). The estimated $V_{max}$ for DfrA was 52 ± 2.8 U/mg, corresponding to a $k_{cat}$ of 17/s. The $V_{max}$ for DfrB was about 2.5 times lower (22.5 ± 4.2 U/mg, $k_{cat}$ of 7.2/s).

## Enzyme Activity Assays for Orthologs Within the DmrA Clade

The activity of *M. extorquens* DmrA-$H_4$ was compared with two annotated DAGKs sharing different degrees of identity with *M. extorquens* DmrA. The *M. nodulans* homolog (Mno-DAGK- $H_6$) was 84% identical to DmrA, and the *H. nitrativorans* homolog (Hni-DAGK-$H_6$) was 69% identical to DmrA. We first tested whether these enzymes showed NADPH-dependent dihydrofolate reductase activity, but no activity was detected with the addition of either the Mno or Hni enzyme (**Figure 3** and **Table 1**).

Annotated DAGKs from *M. nodulans* and *H. nitrativorans* were both capable of reducing $H_2$SPT (**Figure 4**). Under the initial screening conditions, the specific activity of the Hni-DAGK-$H_6$ was about the same as that of DmrA-$H_4$, while the rate for Mno-DAGK-$H_6$ was 3–4 times lower (**Table 1**). The lower activity of Mno-DAGK-$H_6$ in the initial screening studies may be explained by the higher $K_M$ values obtained later in the kinetics studies (**Table 2**). The Mno-DAGK-$H_6$ appeared to have lower affinity for $H_2$SPT (apparent $K_M$ of 695 μM $H_2$SPT) compared to the apparent $K_M$ values for *M. extorquens* DmrA-$H_4$ and Hni-DAGK-$H_6$ (193 and 102 μM $H_2$SPT, respectively). Despite the differences in $K_M$ values, the $V_{max}$ estimates for the three enzymes were similar, differing only by a factor of two (**Table 2**).

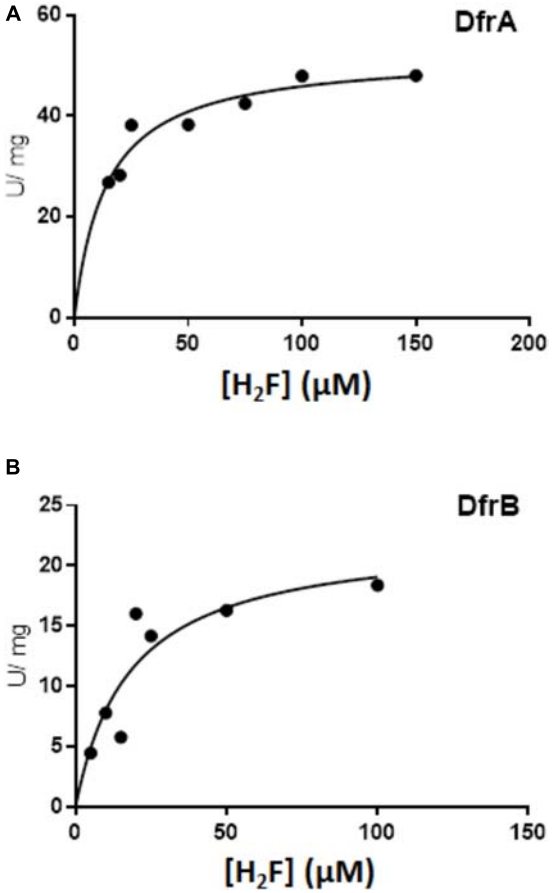


**FIGURE 5 |** Kinetics of DfrA and DfrB with dihydrofolate as the substrate. Dihydrofolate reductase activity was measured as described in Section "Materials and Methods" in the presence of 100 μM NADPH and either DfrA **(A)** or DfrB **(B)**. Data were fit to the equation for a hyperbola using non-linear least-squares fit with GraphPad Prism 7.04 Software. The estimated $K_M$ and $V_{max}$ values are presented in the Section "Results."

## DAGK Assays for Homologs Within the DmrA Clade

To test the alternative hypothesis that the DmrA homologs might contain the annotated DAGK activity, a modified DAGK assay was performed (**Figure 6A**). In these studies, the DAG analog, 1,2-dihexanoyl-*sn*-glycerol was used, but β-octyl glucoside (OG) and dimyristoyl phosphatidylcholine (DMPC) were excluded. To show that the modified assay was functioning properly in our lab,

**TABLE 2 |** Kinetic values (apparent $K_M$, $V_{max}$, and $k_{cat}$) for DmrA and DmrA orthologs.

| Protein | $K_{M(app)}$ | $V_{max}$ (U/mg) | $k_{cat}$($s^{-1}$) |
|---|---|---|---|
| *M. extorquens* AM1 DmrA-$H_4$ | 193 ± 71[4] | 5.72 ± 1.2[4] | 1.5 |
| Mno-DAGK-$H_6$ | 695 ± 176[3] | 5.94 ± 2.6[3] | 1.6 |
| Hni-DAGK-$H_6$ | 102 ± 73[2] | 10.9 ± 1.8[2] | 2.9 |

*Superscripts 2–4 denote number of replicates.*

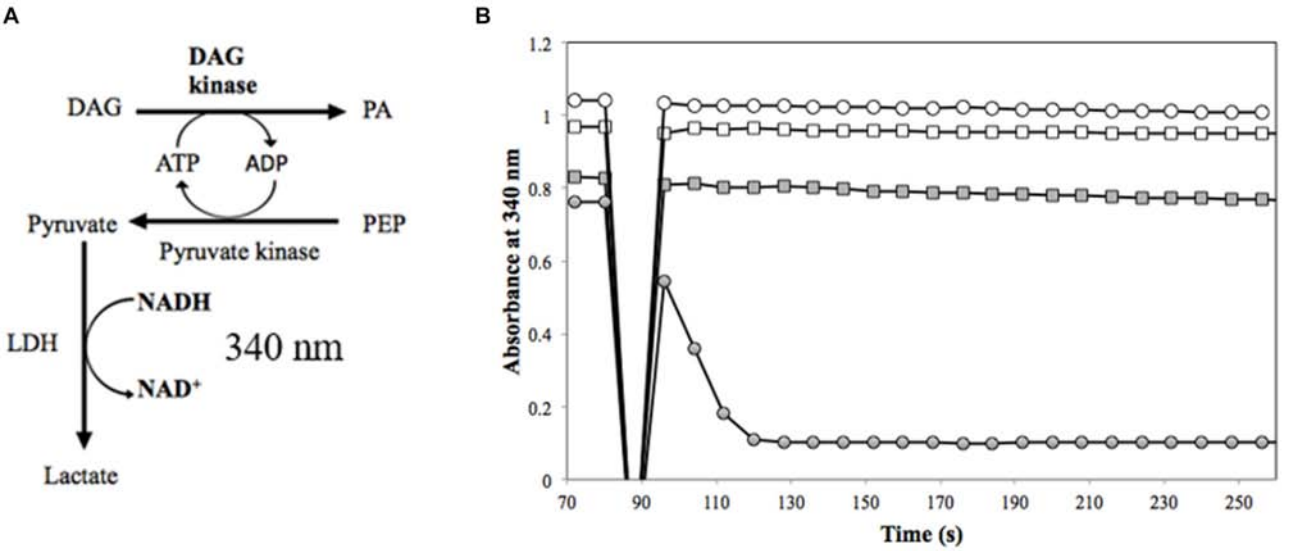


**FIGURE 6 |** Measurement of DAGK activity. **(A)** In the DAGK assay (Badola and Sanders, 1997), the conversion of DAG to phosphatidic acid (PA) produces ADP, which is used in the pyruvate kinase reaction to convert phosphoenolpyruvate (PEP) to pyruvate. This reaction is coupled to the reduction of pyruvate to lactate by lactate dehydrogenase (LDH). The oxidation of NADH is monitored as a loss in absorbance at 340 nm for DAGK activity. There is a 1:1 ratio of one mole of PA produced to one mole NADH oxidized. **(B)** DAGK activity of 3.5 μg of Mno-DAGK-$H_6$ (open circle), 3.6 μg of Hni-DAGK-$H_6$ (square), boiled Hni-DAGK-$H_6$ (closed square) compared to DAGK control from *E. coli* (closed circle).

DAGK from *E. coli* was tested as a control (**Figure 6B**). Under the conditions used, the specific activity of the *E. coli* enzyme (1 μg of protein) was 24.2 U/mg (**Table 1**), which is comparable to the published value of 22.0 U/mg (Badola and Sanders, 1997).

In the DAGK assay, the addition of 3.5 μg of Mno-DAGK-$H_6$ or Hni-DAGK-$H_6$ produced specific activities of 0.43 and 0.55 U/mg, respectively (**Figure 6B** and **Table 1**). This rate was only 1–2% of the activity of commercially purchased Eco-DAGK when comparable amounts of enzyme were used. The slow rate of Hni-DAGK-$H_6$ activity proceeded constantly over a course of 5 min, in contrast with that of the boiled enzyme control, which yielded no activity (**Figure 6B**).

## DISCUSSION

The results of the current study may be interpreted in the context of the previously published model predicting that the *M. extorquens* DmrA protein evolved from an ancestral dihydrofolate reductase (Dfr) following transfer of $H_4$MPT biosynthesis genes from archaea to bacteria (Marx et al., 2003). This hypothesis is based on the sequence similarity of DmrA to known dihydrofolate reductase sequences, combined with the observation that disruption of the *M. extorquens dmrA* gene produces a phenotype similar to that of deletion mutants in $H_4$MPT biosynthesis genes (Marx et al., 2003; Rasche et al., 2004; Chistoserdova et al., 2005). Due to the absence of archaeal redox cofactors in bacteria, archaeal oxidoreductases like dihydromethanopterin reductases may have been non-functional in bacteria. To resolve this issue, two separate lineages of bacterial dihydromethanopterin reductases appear to have evolved: one of bacterial origin (DmrA) found almost exclusively in α-proteobacteria, and a second lineage (AfpA/DmrB) derived from an archaeal flavoprotein called DmrX.

The results of the current study are consistent with a bacterial origin for DmrA in α-proteobacteria. The phylogenetic tree in **Figure 2** places *M. extorquens* DfrA, DfrB, and DmrA in separate clades. Duplication of a *dfr* gene followed by mutations that changed specificity for the pterin substrate would account for the presence of both dihydrofolate reductase and dihydromethanopterin reductase activities in extant α-proteobacteria (**Table 1**).

*Methylobacterium extorquens* DfrA has been proposed to function as a standard dihydrofolate reductase based on co-localization of *dfrA* with genes encoding $H_4$F biosynthesis and $H_4$F-dependent enzymes and additional gene neighborhood analysis of multiple genomes (Chistoserdova et al., 2003; Marx et al., 2003; this study). Prokaryotic genes of related functions often occur together in operons or gene clusters, as demonstrated by the large cluster of proteobacterial genes related to $H_4$MPT-dependent metabolism (Chistoserdova et al., 1998; Kalyuzhnaya et al., 2005). In the current study, the dihydrofolate reductase activities of DfrA and DfrB were demonstrated biochemically for the first time and were comparable to the activity of a known Dfr from *E. coli* (**Table 1** and **Figure 5**). The evolutionary potential for altering substrate specificity from dihydrofolate to dihydromethanopterin is also supported to some extent by enzymatic assays in which traces of $H_2$SPT reduction activity were detected (**Table 1**). Conversely, *M. extorquens* DmrA has been shown to reduce $H_2$SPT at relatively high rates and dihydrofolate at low rates (Caccamo et al., 2004), possibly

representing a vestige of an ancestral dihydrofolate reductase activity.

Protein computational modeling also demonstrates the potential for changing the specificity of dihydrofolate reductase toward affinity for dihydromethanopterin. Molecular models of *M. extorquens* DmrA and DfrB were constructed by Andrew Orry (Molsoft L.L.C., San Diego, CA, United States) (**Figure 7**) and predict that DmrA (**Figure 7**, yellow ribbon structure) and DfrB (green ribbon structure) share a similar overall protein fold consisting of primarily parallel β-sheets connected by α-helices. In particular, secondary structural features are conserved in the NADPH binding domain, which includes DmrA residues 59 to 85. This would account for the conserved use of NADPH as an electron donor by both DmrA and DfrA. Unique structural features of DmrA occur in the active site region distant from the NADPH binding domain, where the pterin substrate is presumed to bind. The DmrA model shows an insertion of 7 amino acids (residues 25–31) forming a loop that is absent in the models of DfrB and *Mycobacterium* dihydrofolate reductase (**Figure 7**). Another difference is that DmrA also lacks two of the C-terminal β-strands found in the dihydrofolate reductase structures. Although the DmrA model could not predict the details of the DmrA pterin binding site with confidence, the insertion of a DmrA loop and the loss of two β-strands over evolutionary time might have served to accommodate the structural differences between dihydromethanopterin and dihydrofolate. A crystal structure of DmrA would be needed to create a detailed model of the dihydromethanopterin binding site.

The function of the second dihydrofolate reductase in *M. extorquens* (DfrB) remains a mystery. The estimated $K_M$ values for DfrA and DfrB were similar, while the $V_{max}$ for DfrB appeared lower than that of DfrA (**Figure 5**). The presence of a second Dfr is not uncommon in bacteria. Multiple copies of dihydrofolate reductase can provide varying sensitivities to folate competitors such as trimethoprim (Huovinen, 1987). The *M. extorquens dfrB* gene is located on a megaplasmid, and the protein has 47% similarity to a trimethoprim-resistant dihydrofolate reductase encoded on *E. coli* plasmid *pCJ001*, leading to a hypothesis for a role of DfrB in antimicrobial resistance (Jansson and Skold, 1991; Marx et al., 2003). Another proposed role for *M. extorquens* DfrB as an intermediate in the evolution of DmrA may be inferred from the closer sequence identity between DfrB and DmrA (34% identical) compared that of DfrA (26% identical to DmrA) (Marx et al., 2003) and the phylogenetic position of the DfrB clade between DfrA and DmrA (**Figure 2**). While this might be possible, the similar low rates of $H_2$SPT reduction by DfrA and DfrB (**Table 1**) do not seem to favor DfrB as a preferred intermediate in the evolution toward DmrA.

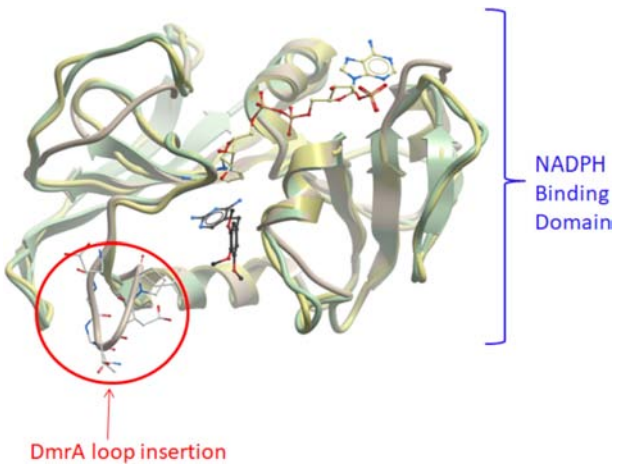


**FIGURE 7 |** Computational models of DmrA and DfrB. 3D models of DmrA and DfrB were constructed at described in Section "Materials and Methods" using ICM-Pro (Molsoft, San Diego, CA, United States) with *Mycobacterium avium* dihydrofolate reductase as the template (pdb 2w3v). The NADPH binding sites appeared conserved between the two protein models (blue label) with the position of NADPH predicted by analogy to the template structure. An insertion of 7 amino acids in DmrA (residues 25–31) formed a unique loop (circled in red). The DmrA model also predicted the deletion of two C-terminal β-strands found in both DfrB and the template.

For the DmrA clade, the current annotation of many orthologs as DAGKs was surprising based on sequence alignments. For example, while the annotated DAGKs from *M. nodulans* and *H. nitrativorans* are 84 and 69% identical to *M. extorquens* DmrA, they share only 15 and 12% identity, respectively, with a known DAGK from *E. coli*. Dihydromethanopterin reductase activity measured at pH 5.3 was observed for Mno-DAGK-$H_6$ and Hni-DAG-kinase-$H_6$ (**Figure 4** and **Tables 1**, 2), while dihydrofolate reductase activity was not detectable for either enzyme under the conditions studied (**Table 1** and **Figure 3**). The DAGK activities of the two enzymes were also very low compared to the activity of a known *E. coli* DAGK under the same conditions (1–2%) (**Table 1** and **Figure 6**). At this time, we cannot rule out the possibility that the annotated DAGKs in this study may be bifunctional enzymes with both DmrA and DAGK activities playing a role in methylotroph cells. However, given the low sequence identity to characterized DAGKs, the low DAGK activities (**Figure 6**), and kinetics values similar to those of DmrA (**Table 2**), we propose that DAGKs sharing at least 69% identity with *M. extorquens* AM1 DmrA should be renamed as dihydromethanopterin reductases.

An explanation for the large apparent $K_M$ difference between Mno-DAGK-$H_6$ and DmrA-$H_4$ might be attributed to either the protein structural health following purification through nickel affinity chromatography or the physical and chemical environment in which *M. nodulans* is found in nature. *M. nodulans* exhibits both nitrogen-fixation and specific nodulation of *Crotalaria* species. These features have not been observed in the *Methylobacterium* species that have been tested thus far (Sy et al., 2001). In the nodule environment, high amounts of methanol and methylotrophic activity have been observed (Jourand et al., 2005). A high apparent $K_M$ for $H_2$MPT may enable *M. nodulans* to regulate dihydromethanopterin reductase activity to accommodate large influxes of methanol.

Another point of interest is the finding of a DmrA homolog in *A. lata* and *A. australica*. These two species of β-proteobacteria also contain an archaea-like dihydromethanopterin reductase with a redox-active FMN cofactor (AfpA/DmrB)

(Ding and Ferry, 2004; Kalyuzhnaya et al., 2005). The presence of two phylogenetically diverse forms of dihydromethanopterin reductase (DmrA and DmrB) in a single organism invites additional studies of the evolutionary history and differential roles of the two enzymes in the $C_1$ metabolism of these cells.

Methylotrophic microorganisms are valuable in biotechnology processes that use methanol as an alternative to sugars as a carbon substrate for the biosynthesis of industrial products such as biofuels and biopolymers (Schrader et al., 2009). Additional benefits include the potential to synthesize polyhydroxybutyrates and uncommon dicarboxylic acids or polyketides using the ethylmalonyl-CoA pathway of *Methylobacterium* species. The ability to grow on minimal media might also simplify product recovery compared to the separations required with rich media, such as Luria broth (Ochsner et al., 2015). Using a natural methylotroph, as opposed to bioengineering *E. coli*, could eliminate the need to engineer methods to alleviate a potential buildup of formaldehyde as a toxic intermediate during methanol oxidation. The relatively high $K_M$ for DmrA (DAGK) from *M. nodulans* might allow responsiveness at higher concentrations of $H_2$SPT to help accommodate increases in methanol concentration. The ability of methylotrophs to process large extracellular concentrations of methanol, combined with the metabolic machinery to transform chemicals while avoiding formaldehyde bioaccumulation, could provide advantages for methanol-based biotechnology in the future.

## DATASET STATEMENT

All relevant data is either contained within the manuscript or will be made available by the authors, without undue reservation, to any qualified researcher.

## AUTHOR CONTRIBUTIONS

MB designed the principle experiments based on an original research idea by CA. MB, CA, KW, and YM executed the experiments and interpreted the data. MB, YM, and MR prepared the manuscript.

## FUNDING

This research was supported by National Science Foundation grant CHE-1508801 and a 2014 Development Grant from the California State University Program for Education and Research in Biotechnology (CSUPERB).

## ACKNOWLEDGMENTS

The authors are grateful to Dr. Andrew Orry (Molsoft, San Diego, CA, United States) for creating the computational models of DmrA and DfrB.

## REFERENCES

Abagyan, R., and Totrov, M. (1994). Biased probability Monte Carlo conformational searches and electrostatic calculations for peptides and proteins. *J. Mol. Biol.* 235, 983–1002. doi: 10.1006/jmbi.1994.1052

Abagyan, R., Totrov, M., and Kuznetsov, D. (1994). ICM—A new method for protein modeling and design: applications to docking and structure prediction from the distorted native conformation. *J. Comput. Chem.* 15, 488–506. doi: 10.1002/jcc.540150503

Achenbach-Richter, L., Stetter, K. O., and Woese, C. R. (1987). A possible biochemical missing link among archaebacteria. *Nature* 327, 348–349. doi: 10.1038/327348a0

Altschul, S. F., Madden, T. L., Schaffer, A. A., Zhang, J., Zhang, Z., Miller, W., et al. (1997). Gapped BLAST and PSI-BLAST: a new generation of protein database search programs. *Nucleic Acids Res.* 25, 3389–3402. doi: 10.1093/nar/25.17.3389

Arnautova, Y. A., Abagyan, R. A., and Totrov, M. (2011). Development of a new physics-based internal coordinate mechanics force field and its application to protein loop modeling. *Proteins* 79, 477–498. doi: 10.1002/prot.22896

Badola, P., and Sanders, C. R. (1997). *Escherichia coli* diacylglycerol kinase is an evolutionarily optimized membrane enzyme and catalyzes direct phosphoryl transfer. *J. Biol. Chem.* 272, 24176–24182. doi: 10.1074/jbc.272.39.24176

Bertani, G. (1951). Studies on lysogenesis. I. The mode of phage liberation by lysogenic *Escherichia coli*. *J. Bacteriol.* 62, 293–300.

Bradford, M. M. (1976). A rapid and sensitive method for the quantitation of microgram quantities of protein utilizing the principle of protein-dye binding. *Anal. Biochem.* 72, 248–254. doi: 10.1016/0003-2697(76)90527-3

Caccamo, M. A., Malone, C. S., and Rasche, M. E. (2004). Biochemical characterization of a dihydromethanopterin reductase involved in tetrahydromethanopterin biosynthesis in *Methylobacterium extorquens* AM1. *J. Bacteriol.* 186, 2068–2073. doi: 10.1128/JB.186.7.2068-2073.2004

Chistoserdova, L. (2016). Wide distribution of genes for tetrahydromethanopterin /methanofuran-linked C1 transfer reactions argues for their presence in the common ancestor of bacteria and archaea. *Front. Microbiol.* 7:1425. doi: 10.3389/fmicb.2016.01425

Chistoserdova, L., Chen, S. W., Lapidus, A., and Lidstrom, M. E. (2003). Methylotrophy in *Methylobacterium extorquens* AM1 from a genomic point of view. *J. Bacteriol.* 185, 2980–2987. doi: 10.1128/JB.185.10.2980-2987.2003

Chistoserdova, L., Jenkins, C., Kalyuzhnaya, M. G., Marx, C. J., Lapidus, A., Vorholt, J. A., et al. (2004). The enigmatic planctomycetes may hold a key to the origins of methanogenesis and methylotrophy. *Mol. Biol. Evol.* 21, 1234–1241. doi: 10.1093/molbev/msh113

Chistoserdova, L., Rasche, M. E., and Lidstrom, M. E. (2005). Novel Dephosphotetrahydromethanopterin biosynthesis genes discovered via mutagenesis in *Methylobacterium extorquens* AM1. *J. Bacteriol.* 187, 2508–2512. doi: 10.1128/JB.187.7.2508-2512.2005

Chistoserdova, L., Vorholt, J. A., Thauer, R. K., and Lidstrom, M. E. (1998). C1 transfer enzymes and coenzymes linking methylotrophic bacteria and methanogenic Archaea. *Science* 281, 99–102. doi: 10.1126/science.281.5373.99

Dawson, R. M. C. (1986). *Data for Biochemical Research*. Oxford: Clarendon Press.

DiMarco, A. A., Bobik, T. A., and Wolfe, R. S. (1990). Unusual coenzymes of methanogenesis. *Annu. Rev. Biochem.* 59, 355–394. doi: 10.1146/annurev.bi.59.070190.002035

Ding, Y. H., and Ferry, J. G. (2004). Flavin mononucleotide-binding flavoprotein family in the domain Archaea. *J. Bacteriol.* 186, 90–97. doi: 10.1128/JB.186.1.90-97.2004

Escalante-Semerena, J. C., Rinehart, K. L. Jr., and Wolfe, R. S. (1984). Tetrahydromethanopterin, a carbon carrier in methanogenesis. *J. Biol. Chem.* 259, 9447–9455.

Felsenstein, J. (1985). Confidence limits on phylogenies: an approach using the bootstrap. *Evolution* 39, 783–791. doi: 10.1111/j.1558-5646.1985.tb00420.x

Franceschini, A., Lin, J., von Mering, C., and Jensen, L. J. (2016). SVD-phy: improved prediction of protein functional associations through singular value decomposition of phylogenetic profiles. *Bioinformatics* 32, 1085–1087. doi: 10.1093/bioinformatics/btv696

Franceschini, A., Szklarczyk, D., Frankild, S., Kuhn, M., Simonovic, M., Roth, A., et al. (2013). STRING v9.1: protein-protein interaction networks, with increased coverage and integration. *Nucleic Acids Res.* 41, D808–D815. doi: 10.1093/nar/gks1094

Garfin, D. E. (1990). One-dimensional gel electrophoresis. *Methods Enzymol.* 182, 425–441. doi: 10.1016/0076-6879(90)82035-Z

Gorris, L. G., Voet, A. C., and van der Drift, C. (1991). Structural characteristics of methanogenic cofactors in the non-methanogenic archaebacterium *Archaeoglobus fulgidus*. *Biofactors* 3, 29–35.

Hay, S., Evans, R. M., Levy, C., Loveridge, E. J., Wang, X., Leys, D., et al. (2009). Are the catalytic properties of enzymes from piezophilic organisms pressure adapted? *Chembiochem* 10, 2348–2353. doi: 10.1002/cbic.200900367

Huovinen, P. (1987). Trimethoprim resistance. *Antimicrob. Agents Chemother.* 31, 1451–1456. doi: 10.1128/AAC.31.10.1451

Jansson, C., and Skold, O. (1991). Appearance of a new trimethoprim resistance gene, dhfrIX, in *Escherichia coli* from swine. *Antimicrob. Agents Chemother.* 35, 1891–1899. doi: 10.1128/AAC.35.9.1891

Jensen, L. J., Kuhn, M., Stark, M., Chaffron, S., Creevey, C., Muller, J., et al. (2009). STRING 8–a global view on proteins and their functional interactions in 630 organisms. *Nucleic Acids Res.* 37, D412–D416. doi: 10.1093/nar/gkn760

Jourand, P., Renier, A., Rapior, S., Miana de Faria, S., Prin, Y., Galiana, A., et al. (2005). Role of methylotrophy during symbiosis between *Methylobacterium nodulans* and *Crotalaria podocarpa*. *Mol. Plant Microbe Interact.* 18, 1061–1068. doi: 10.1094/MPMI-18-1061

Kalyuzhnaya, M. G., Korotkova, N., Crowther, G., Marx, C. J., Lidstrom, M. E., and Chistoserdova, L. (2005). Analysis of gene islands involved in methanopterin-linked C1 transfer reactions reveals new functions and provides evolutionary insights. *J. Bacteriol.* 187, 4607–4614. doi: 10.1128/JB.187.13.4607-4614.2005

Kelley, L. A., Mezulis, S., Yates, C. M., Wass, M. N., and Sternberg, M. J. (2015). The Phyre2 web portal for protein modeling, prediction and analysis. *Nat. Protoc.* 10, 845–858. doi: 10.1038/nprot.2015.053

Kumar, S., Stecher, G., and Tamura, K. (2016). MEGA7: molecular evolutionary genetics analysis version 7.0 for bigger datasets. *Mol. Biol. Evol.* 33, 1870–1874. doi: 10.1093/molbev/msw054

Li, R. W. (2011). *Metagenomics and its Applications in Agriculture, Biomedicine, and Environmental Studies*. Hauppauge, NY: Nova Science Publishers.

Li, W., Cowley, A., Uludag, M., Gur, T., McWilliam, H., Squizzato, S., et al. (2015). The EMBL-EBI bioinformatics web and programmatic tools framework. *Nucleic Acids Res.* 43, W580–W584. doi: 10.1093/nar/gkv279

Marx, C. J., Bringel, F., Chistoserdova, L., Moulin, L., Farhan Ul Haque, M., Fleischman, D. E., et al. (2012). Complete genome sequences of six strains of the genus *Methylobacterium*. *J. Bacteriol.* 194, 4746–4748. doi: 10.1128/JB.01009-12

Marx, C. J., O'Brien, B. N., Breezee, J., and Lidstrom, M. E. (2003). Novel methylotrophy genes of *Methylobacterium extorquens* AM1 identified by using transposon mutagenesis including a putative dihydromethanopterin reductase. *J. Bacteriol.* 185, 669–673. doi: 10.1128/JB.185.2.669-673.2003

McNamara, D. E., Cascio, D., Jorda, J., Bustos, C., Wang, T. C., Rasche, M. E., et al. (2014). Structure of dihydromethanopterin reductase, a cubic protein cage for redox transfer. *J. Biol. Chem* 289, 8852–8864. doi: 10.1074/jbc.M113.522342

McWilliam, H., Li, W., Uludag, M., Squizzato, S., Park, Y. M., Buso, N., et al. (2013). Analysis tool web services from the EMBL-EBI. *Nucleic Acids Res.* 41, W597–W600. doi: 10.1093/nar/gkt376

Ochsner, A. M., Sonntag, F., Buchhaupt, M., Schrader, J., and Vorholt, J. A. (2015). *Methylobacterium extorquens*: methylotrophy and biotechnological applications. *Appl Microbiol. Biotechnol.* 99, 517–534. doi: 10.1007/s00253-014-6240-3

Rasche, M. E., Havemann, S. A., and Rosenzvaig, M. (2004). Characterization of two methanopterin biosynthesis mutants of *Methylobacterium extorquens* AM1 by use of a tetrahydromethanopterin bioassay. *J. Bacteriol.* 186, 1565–1570. doi: 10.1128/JB.186.5.1565-1570.2004

Sambrook, J., and Russell, D. W. (2001). *Molecular Cloning: a Laboratory Manual*. Cold Spring Harbor, NY: Cold Spring Harbor Laboratory Press.

Schrader, J., Schilling, M., Holtmann, D., Sell, D., Filho, M. V., Marx, A., et al. (2009). Methanol-based industrial biotechnology: current status and future perspectives of methylotrophic bacteria. *Trends Biotechnol.* 27, 107–115. doi: 10.1016/j.tibtech.2008.10.009

Scott, J. W., and Rasche, M. E. (2002). Purification, overproduction, and partial characterization of beta-RFAP synthase, a key enzyme in the methanopterin biosynthesis pathway. *J. Bacteriol.* 184, 4442–4448. doi: 10.1128/JB.184.16.4442-4448.2002

Sievers, F., Wilm, A., Dineen, D., Gibson, T. J., Karplus, K., Li, W., et al. (2011). Fast, scalable generation of high-quality protein multiple sequence alignments using Clustal Omega. *Mol. Syst. Biol.* 7:539. doi: 10.1038/msb.2011.75

Snel, B., Lehmann, G., Bork, P., and Huynen, M. A. (2000). STRING: a web-server to retrieve and display the repeatedly occurring neighbourhood of a gene. *Nucleic Acids Res.* 28, 3442–3444. doi: 10.1093/nar/28.18.3442

Sy, A., Giraud, E., Samba, R., de Lajudie, P., Gillis, M., and Dreyfus, B. (2001). Nodulation of certain legumes of the genus *Crotalaria* by the new species *Methylobacterium*. *Can. J. Microbiol.* 47, 503–508. doi: 10.1139/w01-044

Szklarczyk, D., Franceschini, A., Kuhn, M., Simonovic, M., Roth, A., Minguez, P., et al. (2011). The STRING database in 2011: functional interaction networks of proteins, globally integrated and scored. *Nucleic Acids Res.* 39, D561–D568. doi: 10.1093/nar/gkq973

Szklarczyk, D., Franceschini, A., Wyder, S., Forslund, K., Heller, D., Huerta-Cepas, J., et al. (2015). STRING v10: protein-protein interaction networks, integrated over the tree of life. *Nucleic Acids Res.* 43, D447–D452. doi: 10.1093/nar/gku1003

Szklarczyk, D., Morris, J. H., Cook, H., Kuhn, M., Wyder, S., Simonovic, M., et al. (2017). The string database in 2017: quality-controlled protein-protein association networks, made broadly accessible. *Nucleic Acids Res.* 45, D362–D368. doi: 10.1093/nar/gkw937

van Beelen, P., Stassen, A. P., Bosch, J. W., Vogels, G. D., Guijt, W., and Haasnoot, C. A. (1984). Elucidation of the structure of methanopterin, a coenzyme from Methanobacterium thermoautotrophicum, using two-dimensional nuclear-magnetic-resonance techniques. *Eur. J. Biochem.* 138, 563–571. doi: 10.1111/j.1432-1033.1984.tb07951.x

von Mering, C., Huynen, M., Jaeggi, D., Schmidt, S., Bork, P., and Snel, B. (2003). STRING: a database of predicted functional associations between proteins. *Nucleic Acids Res.* 31, 258–261. doi: 10.1093/nar/gkg034

von Mering, C., Jensen, L. J., Kuhn, M., Chaffron, S., Doerks, T., Kruger, B., et al. (2007). STRING 7–recent developments in the integration and prediction of protein interactions. *Nucleic Acids Res.* 35, D358–D362. doi: 10.1093/nar/gkl825

von Mering, C., Jensen, L. J., Snel, B., Hooper, S. D., Krupp, M., Foglierini, M., et al. (2005). STRING: known and predicted protein-protein associations, integrated and transferred across organisms. *Nucleic Acids Res.* 33, D433–D437. doi: 10.1093/nar/gki005

Vorholt, J. A., Chistoserdova, L., Stolyar, S. M., Thauer, R. K., and Lidstrom, M. E. (1999). Distribution of tetrahydromethanopterin-dependent enzymes in methylotrophic bacteria and phylogeny of methenyl tetrahydromethanopterin cyclohydrolases. *J. Bacteriol.* 181, 5750–5757.

Wang, S., Tiongson, J., and Rasche, M. E. (2014). Discovery and characterization of the first archaeal dihydromethanopterin reductase, an iron-sulfur flavoprotein from *Methanosarcina mazei*. *J. Bacteriol.* 196, 203–209. doi: 10.1128/JB.00457-13

**Conflict of Interest Statement:** The authors declare that the research was conducted in the absence of any commercial or financial relationships that could be construed as a potential conflict of interest.

frontiers in Microbiology

ORIGINAL RESEARCH
published: 31 October 2018
doi: 10.3389/fmicb.2018.02610

# Biogas Biocatalysis: Methanotrophic Bacterial Cultivation, Metabolite Profiling, and Bioconversion to Lactic Acid

*Calvin A. Henard[1], Tyler G. Franklin[1], Batool Youhenna[2], Sergey But[3], Danny Alexander[4], Marina G. Kalyuzhnaya[2] and Michael T. Guarnieri[1]**

[1] National Renewable Energy Laboratory, National Bioenergy Center, Golden, CO, United States, [2] Biology Department, San Diego State University, San Diego, CA, United States, [3] Skryabin Institute of Biochemistry and Physiology of Microorganisms, Moscow, Russia, [4] Metabolon, Inc., Durham, NC, United States

Anaerobic digestion (AD) of waste substrates, and renewable biomass and crop residues offers a means to generate energy-rich biogas. However, at present, AD-derived biogas is primarily flared or used for combined heat and power (CHP), in part due to inefficient gas-to-liquid conversion technologies. Methanotrophic bacteria are capable of utilizing methane as a sole carbon and energy source, offering promising potential for biological gas-to-liquid conversion of AD-derived biogas. Here, we report cultivation of three phylogenetically diverse methanotrophic bacteria on biogas streams derived from AD of a series of energy crop residues. Strains maintained comparable central metabolic activity and displayed minimal growth inhibition when cultivated under batch configuration on AD biogas streams relative to pure methane, although metabolite analysis suggested biogas streams increase cellular oxidative stress. In contrast to batch cultivation, growth arrest was observed under continuous cultivation configuration, concurrent with increased biosynthesis and excretion of lactate. We examined the potential for enhanced lactate production via the employ of a pyruvate dehydrogenase mutant strain, ultimately achieving 0.027 g lactate/g DCW/h, the highest reported lactate specific productivity from biogas to date.

**Keywords: methane, methanotroph, biogas, anaerobic digestion, lactic acid, methane biocatalysis, biogas upgrading**

OPEN ACCESS

***Edited by:***
*Rajesh K. Sani,*
*South Dakota School of Mines and Technology, United States*

***Reviewed by:***
*Jeremy Semrau,*
*University of Michigan, United States*
*Sachin Kumar,*
*Sardar Swaran Singh National Institute of Renewable Energy, India*

****Correspondence:***
*Michael T. Guarnieri*
*michael.guarnieri@nrel.gov*

***Specialty section:***
*This article was submitted to Microbiotechnology, Ecotoxicology and Bioremediation, a section of the journal Frontiers in Microbiology*

***Received:*** *31 May 2018*
***Accepted:*** *12 October 2018*
***Published:*** *31 October 2018*

***Citation:***
*Henard CA, Franklin TG, Youhenna B, But S, Alexander D, Kalyuzhnaya MG and Guarnieri MT (2018) Biogas Biocatalysis: Methanotrophic Bacterial Cultivation, Metabolite Profiling, and Bioconversion to Lactic Acid. Front. Microbiol. 9:2610. doi: 10.3389/fmicb.2018.02610*

## INTRODUCTION

Methanotrophic bacteria can use methane ($CH_4$), the primary component of natural gas and anaerobic digestion (AD)-derived biogas, as a sole carbon and energy source, presenting a promising biological route for atmospheric $CH_4$ sequestration, bioremediation, and gas-to-liquid conversion for industrial applications (Kalyuzhnaya et al., 2015; Strong et al., 2015, 2016; Pieja et al., 2017). To this latter end, we have recently reported a biocatalytic route for methane conversion to lipid fuel intermediates and platform chemicals, as well as metabolic engineering strategies to enhance carbon conversion efficiency of biological gas-to-liquid conversion processes (Henard et al., 2016, 2017). Additional recent reports have demonstrated methane bioconversion to diverse product suites, including single cell protein, methanol, carboxylic acids, polyhydroxybutyrate, and

2,3-butanediol (Bothe et al., 2002; Hwang et al., 2014; Cal et al., 2016; Myung et al., 2016; Garg et al., 2018; Nguyen et al., 2018), further underscoring the potential power of methanotrophic bioconversion strategies.

Aerobic methanotrophs are ubiquitous in nature and serve as a primary environmental $CH_4$ sink, significantly contributing to the global biogeochemical carbon cycle (Anthony, 1982). An array of methanotrophic bacteria have been isolated in pure culture and primarily belong to the diverse classes of gamma- and alphaproteobacterial (Hanson and Hanson, 1996). The gammaproteobacteria *Methylococcus capsulatus* Bath and alphaproteobacteria *Methylosinus trichosporium* OB3b have served as models for understanding the fundamentals of methanotrophy and have defined two primary pathways for $CH_4$ assimilation in these organisms, the ribulose monophosphate pathway (RuMP) and the serine cycle, respectively. With a resurgent interest in applied methanotrophy (Conrado and Gonzalez, 2014; Haynes and Gonzalez, 2014; Strong et al., 2015; Clomburg et al., 2017), several novel methanotrophs have recently been isolated and their genomes sequenced, providing further insight into $CH_4$ metabolism and the development of genome scale models (Boden et al., 2011; Khmelenina et al., 2013; Kits et al., 2013; Hamilton et al., 2015; Flynn et al., 2016; Akberdin et al., 2018).

Among the most promising of these recently isolated methanotrophs are the gammaproteobacterial, haloalkaliphilic members of the genus *Methylomicrobium*, including *Methylomicrobium alcaliphilum* $20Z^R$ and *Methylomicrobium buryatense* 5G(B1), which have established genetic tools and genome scale models (Ojala et al., 2011; Gilman et al., 2015; la Torre et al., 2015; Puri et al., 2015; Henard et al., 2016; Yan et al., 2016; Akberdin et al., 2018). Several methanotrophic strains possess unique characteristics for biotechnological deployment, including differential growth rates, cultivation parameters, flux to metabolic intermediates, and end-product tolerance. However, strain selection for industrial applications is not always obvious; while some basic considerations can be applied to all biological $CH_4$ oxidation processes, the selection of a microbial catalyst is influenced by the type of application to be developed, including substrate source, product selection, and ultimately, the overall process economics of the technology (Kalyuzhnaya, 2016). Additionally, though bioconversion parameters are well-defined for pure $CH_4$ in the above-described strains, the potential for methanotrophic cultivation and bioproduction on renewable, AD-derived biogas remains to be fully evaluated, limiting adoption, and impact as a core gas-to-liquid technology.

Biogas derived from AD of waste stream sources such as municipal solid waste operations, biorefineries, and agricultural operations, offers a versatile renewable energy source. At present, biogas is primarily used to produce combined heat and power (CHP). Alternatively, AD biogas can be scrubbed for conversion to biomethane that can, in turn, be utilized as a renewable option in natural gas applications. Total domestic methane potential from landfill material, animal manure, wastewater, and organic waste (food waste) is estimated to be >400 TBtu (Department of Energy, 2017). Additionally, biogas generated from AD of lignocellulosic biomass resources is estimated to offer >4 quadrillion Btu potential energy (Department of Energy, 2017). This energy potential could displace nearly half of current domestic natural gas consumption in the electric power sector and all current natural gas consumption in the transportation sector (Department of Energy, 2017). Despite the promise of biogas as a high-volume, renewable energy source and natural gas replacement, its gaseous state prevents facile integration with extant transportation and industrial infrastructure. Additionally, biogas composition varies significantly depending upon input feedstock, but it is typically comprised of 40–65% $CH_4$, 30–40% carbon dioxide ($CO_2$), and gaseous impurities, including hydrogen sulfide ($H_2S$), ammonia, and siloxanes (Hosseini and Wahid, 2014).

In this study we explored the applicability of phylogenetically diverse methanotrophic bacteria for AD biogas utilization and conversion. We tested six variable sources of biogas derived from AD of energy crops and derivatives thereof, conducting comparative growth analyses of three representative methanotrophic cultures, *M. capsulatus* Bath, *M. trichosporium* OB3b, and *M. alcaliphilum* $20Z^R$. The impact of the various biogas streams on cellular metabolism was further investigated in *M. alcaliphilum* $20Z^R$ using global metabolomics analysis. Lastly, we demonstrated biogas conversion to lactate at the highest reported specific productivity to date by a rationally engineered *M. alcaliphilum* $20Z^R$ pyruvate dehydrogenase mutant.

# MATERIALS AND METHODS

## Bacterial Strains and Cultivation

*Methylomicrobium alcaliphilum* $20Z^R$ (Akberdin et al., 2018), *Methylosinus trichosporium* OB3b, and *Methylococcus capsulatus* Bath were cultivated in either nitrate mineral salts (NMS) medium (Bath and OB3b) or NMS medium supplemented with 3% NaCl and carbonate buffer as previously described (Whittenbury et al., 1970; Akberdin et al., 2018). To determine optimal biogas concentration and biogas effects on growth, cultures were grown in 250 ml vials containing 50 ml of growth medium. After inoculation at a starting density of $OD_{600}$ = 0.10, the vials were crimped with butyl (gray or red) stoppers to create gas-tight seals. Increasing concentrations of mock biogas (∼60% $CH_4$/40% $CO_2$) or pure $CH_4$ was added to the headspace to determine the optimal biogas concentration for growth. Biogas samples BG1-6 were added to the headspace [33% biogas (∼20% $CH_4$) in air] of serum vials to evaluate their effects on methanotrophic growth. Cultures containing pure $CH_4$ were supplemented with nitrogen to equilibrate the volume of gas added to the corresponding biogas serum vial. Cultures were incubated at 30°C ($20Z^R$ and OB3b) or 37°C (Bath) with orbital shaking at 200 rpm, and bacterial growth was measured spectrophotometrically. A second series of parallel cultures were set up for headspace composition ($CH_4$, $N_2$, $O_2$, $CO_2$, and CO) analyses and biomass yield. At each timepoint, samples of the headspace (1 ml) were injected into an SRI GC system for gas chromatography analyses. Gas consumption data were collected at the beginning and completion of each experiment. The concentrations were estimated using standard gas mixtures (Scotty Analyzed gases, Supelco Analytical, Sigma-Aldrich). Dry

Cell Weight (DCW) was either measured directly after freeze-drying or estimated from the final OD of the cell culture using the following equation: DCW = OD * (0.35 ± 0.04 g/L) (Akberdin et al., 2018). Biomass yield data ($Y_{CH4}$) were calculated using dry cell weight and consumed substrate data and represented as g biomass produced per g $CH_4$ consumed.

## Anaerobic Digestion and Biogas Generation

Various feedstock substrates were received from Idaho National Laboratory, the Ohio Soybean Council, Aemetis, and University of Illinois, Urbana-Champaign. Continuous digestions were performed in six lab-scale digesters operating at 14-L net volume per digester, which were inoculated with digester content obtained from East Bay Municipal Utility District and a local dairy (Straus, CA). Reactors were stabilized to yield equal base load gas production and began continuous operation at a loading rate ramped up to 2 kg organic dry matter per cubic meter reactor volume per day with a target hydraulic retention (HRT) of 21–28 days and run time of 2.5 HRT, monitoring for gas flow, pH and gas composition. We characterized the material composition, the theoretical biogas and $CH_4$ yield per the models of Buswell and Baserga (Achinas and Euverink, 2016), as well as the batch yield per VDI 4630 for soybean residues, corn stover, miscanthus, switchgrass, sorghum, bagasse, and two different ethanol stillage streams. In the continuous operation, we measured and quantified gas composition using gas chromatography compared to known standards.

## Metabolite Profiling

Intracellular metabolites were analyzed by Metabolon, Inc. (Durham, NC) from *M. alcaliphilum* $20Z^R$ cultured in serum vials with the headspace supplemented with 33% biogas (∼20% $CH_4$) in air as described above. Cells were collected by centrifugation when cultures reached $OD_{600}$ = 0.6–0.7 and frozen in liquid nitrogen and stored at −80°C prior to shipping to Metabolon. Metabolomic profiles were collected and processed as previously described (Henard et al., 2017; Akberdin et al., 2018). Changes in cell samples grown on biogas were compared to cell cultures grown on equivalent concentrations of $CH_4$. Welch's two-sample *t*-tests and Principal Component Analysis (PCA) were used to analyze the data. For all analyses, following normalization to protein measured by Bradford, missing values, if any, were imputed with the observed minimum for that particular compound. The statistical analyses were performed on natural log-transformed data and were considered significant if $p < 0.05$.

## Mutant Construction

Strains, plasmids, and primers used for amplification of upstream and downstream regions for construction of the pyruvate dehydrogenase (*pdh*) knockout are shown in **Table S1**. Genomic fragments, ∼600-bp of sequences flanking the dihydrolipoamide acetyltransferase subunit of the pyruvate dehydrogenase complex (MALCv4_1358) gene, were amplified by PCR, and cloned into pCM184::$Gm^R$ plasmid at AatII/NcoI (upstream region) and SacI/SacII (downstream region) sites. The resulting plasmid was introduced to the $20Z^R$ strain by biparental conjugation as described previously (Puri et al., 2015). After mating, gentamycin-resistant clones were selected on medium supplemented with acetate (5 mM), rifampicin (50 μg/mL), and gentamycin (30 μg/mL) to counter-select against *E. coli*. Then, the resulting colonies were PCR-genotyped for the absence of MALCv4_1358 gene followed by sequence verification.

**TABLE 1 |** Composition of tested biogas samples.

| Gas sample ID | Substrate | $CH_4$ (%) | $CO_2$ (%) | $H_2S$ (ppm) | Trace (<250 ppm) |
|---|---|---|---|---|---|
| BG1 | Sorghum | 49 | 50 | 2,100 | CO |
| BG2 | Corn stover | 51 | 49 | 350 | CO, Carbonyl sulfide (COS) |
| BG3 | PEI syrup | 67 | 33 | 14,000 | Hexane, CO, COS |
| BG4 | Bagasse | 48 | 52 | 200 | CO, COS |
| BG5 | Corn distiller's solids syrup | 63 | 37 | 13,000 | CO, COS, C-5, C-6 |
| BG6 | Miscanthus | 52 | 49 | 80 | CO |

## Continuous Gas Fermentation

Fifty milliliter cultures of wild-type and Δ*pdh*::$Gm^R$ *M. alcaliphilum* $20Z^R$ were grown in 150 mL bubble columns with a continuous gas flow (20% $CH_4$ or 33% mock biogas in air, 1 vvm). At indicated intervals, pH was determined, growth was measured spectrophotometrically, and a 1 mL sample was taken for HPLC analysis. After 96 h, bacteria were pelleted and freeze-dried to determine dry cell weight. HPLC was used to detect lactate in the culture supernatants. The culture supernatant was filtered using a 0.2 μm syringe filter and then a 0.1 mL injection was separated using a model 1260 HPLC (Agilent, Santa Clara, CA) and a cation H HPx-87H column (Bio-Rad). A 0.6 mL/min flow rate at 55°C with 0.01 N sulfuric acid as the mobile phase was used. DAD detection was measured at 220 nm and referenced at 360 nm, and metabolite concentrations were calculated by regression analysis compared to known standards. The identity of lactate was also confirmed by NMR analysis.

# RESULTS AND DISCUSSION

## Anaerobic Digestion of Crop Residues

AD substrates were loaded into six 14-L lab scale continuously operating digesters. Steady state off-gas analyses, including $H_2S$ and other contaminants, are shown in **Table 1**. The $CH_4$ and $CO_2$ content were found to be consistently between 48–67% and 33–52%, respectively. The trace gases ethane, propane, n-butane, and n-propane were detected at <250 ppm in all biogas streams. $H_2S$ content varied significantly between 80 and 14,000 ppm, with the highest $H_2S$ content found in the BG3 derived from a feedstock that is much higher in protein content compared to the other AD substrates, which increases gaseous sulfur components but also increases the $CH_4$ content of the gas stream (Achinas and Euverink, 2016).

**TABLE 2 |** Microbial cultures parameters on varied biogas streams.

| Carbon source | *M. alcaliphilum* 20Z$^R$ | | *M. capsulatus* Bath | | *M. trichosporium* OB3b | |
|---|---|---|---|---|---|---|
| | $Y_B$ | $T_d$ | $Y_B$ | $T_d$ | $Y_B$ | $T_d$ |
| $CH_4$ | 1.03 | 5.84 | 0.85 | 6.72 | 0.78 | 10.9 |
| BG1 | 0.95 | 7.38 | 0.81 | 13.0 | 0.69 | 14.9 |
| BG2 | 0.93 | 7.53 | 0.86 | 7.74 | 0.68 | 12.7 |
| BG3 | 0.96 | 6.03 | 0.87 | 6.95 | 0.73 | 8.63 |
| BG4 | 0.95 | 7.49 | 0.94 | 7.98 | 0.73 | 13.0 |
| BG5 | 0.96 | 6.46 | 0.93 | 7.00 | 0.70 | 9.50 |
| BG6 | 0.60 | 11.0 | 0.40 | 12.1 | 0.71 | 12.7 |

*$Y_B$, biomass yield (g DCW/g $CH_4$); $T_d$, doubling time (h). The data represent the mean 2–3 independent observations.*

## Methanotroph Culture Parameters on AD-Derived Biogas

Methanotrophic bacteria require oxygen to activate $CH_4$. Thus, AD-derived biogas will require mixing with air or pure oxygen before delivery to a methanotrophic biocatalyst. Further, $CO_2$, $H_2S$, and other biogas components have the potential to negatively affect bacterial growth. To determine the optimal biogas:air ratio we compared the growth of three diverse methanotrophs with mock biogas (60% $CH_4$, 40% $CO_2$, 0.01% $H_2S$) or pure $CH_4$ at varying concentrations ranging from 3.5% to 30% $CH_4$. The growth of all strains positively correlated to $CH_4$ concentration in the headspace, presumably due to increased gas availability in the medium, with strains cultivated on 15–30% $CH_4$ displaying optimal growth (**Figure 1**). Further, we observed no difference in growth between cultures supplied with biogas or pure $CH_4$, suggesting that high $CO_2$ levels (20% v/v) does not negatively affect these organisms under these growth conditions (**Figure 1**). Interestingly, cultures exhibited optimal growth with a much higher $CH_4$:$O_2$ ratio (3:1) than is conventionally used for methanotroph cultivation (1.25:1), indicating that methanotrophic growth is not oxygen limited under our experimental conditions.

We next evaluated methanotrophic growth on the six AD-derived biogas streams (**Table 2**). The growth of *M. alcaliphilum* 20Z$^R$ was inhibited by biogas originating from miscanthus silages (BG6); however, the strain grew comparable to pure $CH_4$ on all other biogases. *M. capsulatus* Bath growth was inhibited by both sorghum (BG1)-and miscanthus (BG6)-derived biogases, while *M. trichosporium* OB3b was only slightly inhibited by sorghum (BG1)-derived biogas. Interestingly, OB3b displayed increased growth kinetics in PEI syrup (BG3)- and CDS syrup (BG5)-derived biogas streams. Collectively, all three cultures displayed growth capacity on biogas with only minor alterations in biomass yield from $CH_4$. However, some differences in biomass yield and doubling time were observed between biogas streams, underscoring that biogas composition can dictate the methanotrophic biocatalyst most appropriate for its conversion.

## Biogas-Induced Metabolic Alterations

In order to better understand the impacts of raw biogas feedstock on the growth of methanotrophic bacteria, a series of metabolomic experiments were carried out. Since *M. alcaliphilum* 20Z$^R$ was superior to the other cultures with respect to growth and efficiency of biogas conversion, this strain was further evaluated for biochemical profiling. A summary of metabolites significantly altered during cultivation on biogas is shown in **Table S2**. As expected from the growth inhibition data, biogas derived from miscanthus (BG6) led to the most significant metabolite alterations. A PCA plot revealed that the treatment-related variation between groups was only slightly greater than the biological noise within groups (**Figure S1**). This suggests that the treatments did not cause profound perturbations in metabolism relative to the control condition. Indeed, metabolites of core metabolic pathways, including glycolytic, tricarboxylic acid, and pentose phosphate/ribulose 5 phosphate pathway metabolites were similar between $CH_4$ and the six AD-derived biogas samples (**Table S2**).

When compared to the pure $CH_4$-grown controls, several metabolite alterations pointed to a general effect on redox state related to biogas feeding. The most significant difference in metabolites of biogas-grown samples were in the glutathione biosynthetic pathway (**Figure 2**). In five of the six treatments, the levels of oxidized glutathione (GSSG) were higher while reduced glutathione (GSH) was generally lower. The oxidation product of glutathione and cysteine, cysteine-glutathione disulfide, was also higher in all biogas-grown cells. The data indicate that the pure $CH_4$-fed cells contained more favorable levels of reduced glutathione, as well as a greater capacity to produce the compound. Consistent with this, several *gamma*-glutamyl amino acids, which are co-products of glutathione recycling, were also lower in all the treatment groups. The main biosynthetic enzymes for GSH production, *gamma*-glutamylcysteine synthetase (GCS) and glutathione synthetase (GS), can also generate a side product, ophthalmate, when GCS incorporates 2-aminobutyrate instead of cysteine and then GS adds the glycine to this non-specific intermediate. We observed a conserved decrease in ophthalmate in all biogas-cultivated samples. Interestingly, ophthalmate has previously only been found in mammals and the cyanobacteria *Synechocystis* (Soga et al., 2006; Narainsamy et al., 2016). It is unknown whether ergothioneine and/or ophthalmate function as effective antioxidants in *M. alcaliphilum* 20Z$^R$, but our data suggest they are, along with GSH, associated with a general antioxidant response. However, there are very few reports detailing antioxidant responses or glutathione-mediated reactions in methanotrophic bacteria. Thus, the linked pathways could be targeted for further investigation for improving biogas utilization.

Compounds in other pathways also supported that biogas-treated cells were more oxidized or experiencing higher relative oxidative stress. Elevation of sulfate and the histidine derivative ergothioneine was observed in all the biogas cultures (**Table S2**). Ergothioneine levels were roughly correlated with sulfate levels across the different biogas treatments. Also, various one-carbon derivatives of organic acids and amino acids (methylmalonate, methylsuccinate, *N*-formylmethionine,

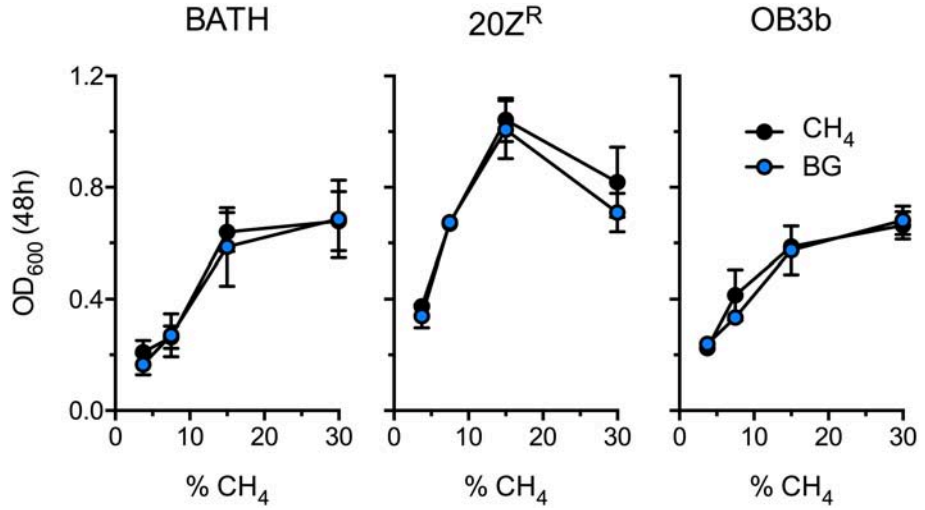


**FIGURE 1 |** Determination of the optimal biogas dilution for methanotroph cultivation. *M. capsulatus* Bath (BATH), *M. alciliphilum* $20Z^R$ ($20Z^R$), and *M. trichosporium* OB3b (OB3b) were cultivated in 250 mL serum vials with increasing concentrations of pure $CH_4$ (black) or biogas (blue) added to the headspace. The data represent the average $OD_{600}$ ± S.D. from four independent observations.

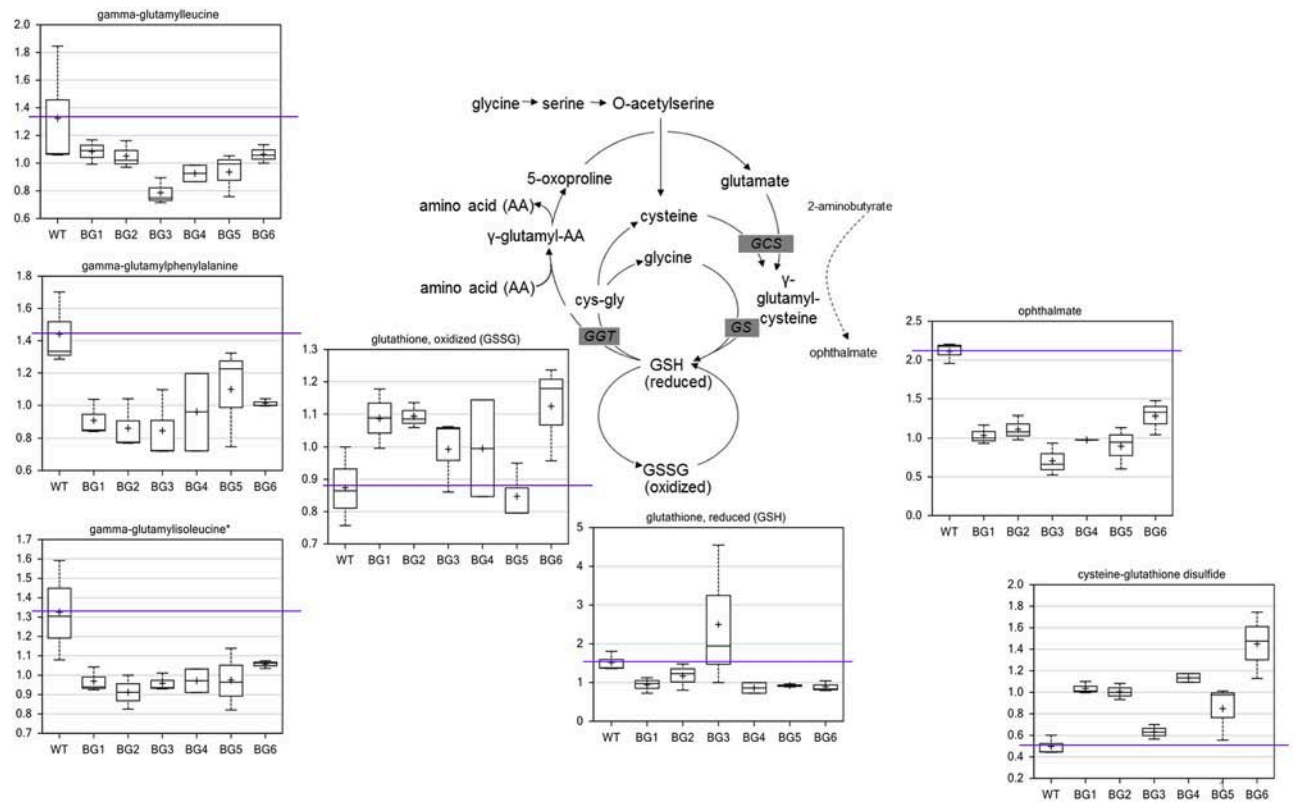


**FIGURE 2 |** Biogas-induced alterations in the redox state of glutathione and biosynthetic pathway intermediates. Metabolomic analysis of compounds associated with glutathione metabolism significantly altered during cultivation on variable biogas streams. The data represent the average ± S.D. of three independent biological samples.

2-methyserine) were higher in all the biogas treatments relative to the $CH_4$ control. The metabolite measured as the most significantly altered during biogas cultivation was ribonate, the oxidation product of ribose (**Table S2**). This compound ranged from 10- to 20-fold higher than $CH_4$-grown controls in all biogas cultivated samples. The enzyme ribose-1 dehydrogenase is NADP+ dependent (in some organisms) and can serve to provide NADPH-reducing equivalents to the system. Other compounds, such as UDP-glucuronate and pyridoxate, which are more highly oxidized versions of common metabolites, were also higher in all the biogas-grown cells. The oxidation of UDP-glucose to UDP-glucuronate by UDP-glucose dehydrogenase also produces reducing equivalents in the form of NADH. Taken together with the increased oxidized glutathione levels, these data support that components in biogas, $CO_2$, and/or contaminants, alter the intracellular redox state of the methanotroph.

## Bioconversion of Biogas to Lactate in a Continuous Gas Flow Bioreactor

Industrial processes employing methanotrophic bacteria currently operate using a continuous natural gas supply, and future industrial bioconversion of AD-derived biogas will likely require a continuous gas fermentation mode. Thus, we evaluated *M. alcaliphilum* $20Z^R$ growth in a mid-throughput gas fermentation reactor supplied with 33% biogas in air (20% $CH_4$, 13% $CO_2$) at 1 volume of gas per volume of liquid per minute. Surprisingly, we observed no bacterial growth under continuous biogas supply, potentially due to carbonic acid production as indicated by a significant drop in the pH of the culture medium (**Figure 3A** and **Figure S2**). Bacterial growth was restored by the addition of KOH that raised the pH of the medium to pH 9.5 (**Figure 3A**), suggesting that $H_2S$ or other biogas components not affecting culture pH did not affect bacterial growth. HPLC analysis of the culture medium showed that lactate was the primary organic acid secreted during cultivation under continuous gas supply, with equivalent lactate (between 80 and 120 mg/L) detected from cultures grown with pure $CH_4$ or biogas buffered with KOH after 72 h of cultivation (**Figure 3B**). Interestingly, we detected increased lactate production (between 220 and 280 mg/L) from cultures with biogas-inhibited growth during the same cultivation timeframe (**Figure 3B**). Lactate is predicted to be synthesized by *M. alcaliphilum* $20Z^R$ via the conversion of pyruvate to lactate by a lactate dehydrogenase (LDH, MALCv4_0534). We hypothesized that flux to lactate could be improved by removing pyruvate conversion to acetyl-CoA, the primary carbon flux during active growth of gammaproteobacterial methanotrophs mediated by the pyruvate dehydrogenase (Kalyuzhnaya et al., 2013; Akberdin et al., 2018). Indeed, we observed a significant increase in both lactate titer (2-3 fold) and specific productivity (four-fold) in a pyruvate dehydrogenase mutant compared to wild-type *M. alcaliphilum* $20Z^R$ when cultured with continuous $CH_4$ or biogas feed (**Figure 4**). These data suggest that this promising biocatalyst increases lactate biosynthesis and excretion in response to the low pH induced by biogas-derived carbonic acid, representing a promising fermentation configuration for organic acid production. Further, this represents the highest reported lactate specific productivity (0.027 g lactate/gDWC/h) in a methanotroph expressing its native LDH, significantly improved compared to our previous demonstrations of $CH_4$ bioconversion to lactate (Henard et al., 2016). In addition to the deletion of the pyruvate dehydrogenase, overexpression of the native *M. alcaliphilum* $20Z^R$ LDH or a heterologous LDH with known minimal negative feedback regulation like the *Lactobacillus helveticus* LDH, is a rational metabolic engineering target for increased pyruvate conversion to lactate (Henard et al., 2016; Garg et al., 2018).

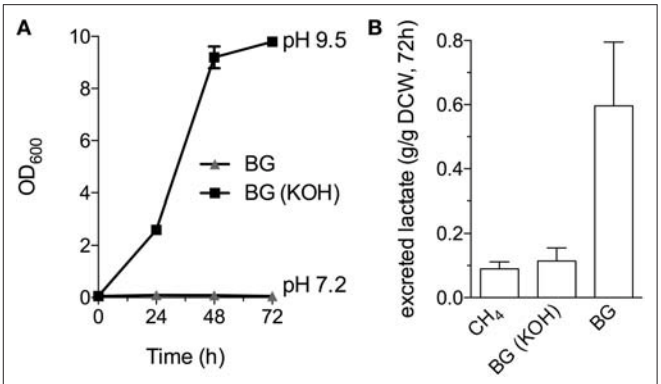


**FIGURE 3 |** *M. alcaliphilum* $20Z^R$ cultivation on a continuous biogas stream. **(A)** Bacterial growth with continuous supply of 33% biogas in air (20% $CH_4$, 13% $CO_2$, 1 vvm) with (black square) or without (gray triangle) the addition of 0.4N potassium hydroxide (KOH). **(B)** Lactate excreted into the culture medium by *M. alciliphilum* supplied with $CH_4$ or biogas (with or without KOH in the medium) detected by HPLC and normalized to dry cell weight (DCW).The data represent the average ± S.D. from three independent observations.

## CONCLUSION

Methanotrophic bacteria have recently gained intensified biotechnological interest due to their capacity to use methane as a sole carbon and energy source, in turn presenting a promising gas-to-liquid bioconversion pathway. Though numerous technology-to-market hurdles remain, these efforts serve as proof-of-concept for microbial conversion of AD-derived biogas, notably presenting a modular, up-, and down-scalable, and highly selective route to fuel and chemical intermediates.

Our data indicate that cultivation of diverse methanotrophic bacteria is feasible on biogas derived from energy crops and residues, despite containing high levels of toxic contaminants. Metabolite profiling of *M. alcaliphilum* $20Z^R$ supports that biogas components alter the intracellular redox state of this organism, which can be leveraged to guide future metabolic engineering efforts in development of efficient biogas biocatalysts. Importantly, we demonstrated bioconversion of biogas to lactate by *M. alcaliphilum* $20Z^R$, and improved lactate specific productivity via rational strain engineering in this methanotroph. Lactate is a promising chemical precursor for the production of bioplastics (Abdel-Rahman et al., 2013; Eiteman and Ramalingam, 2015), and can also be used to generate an array

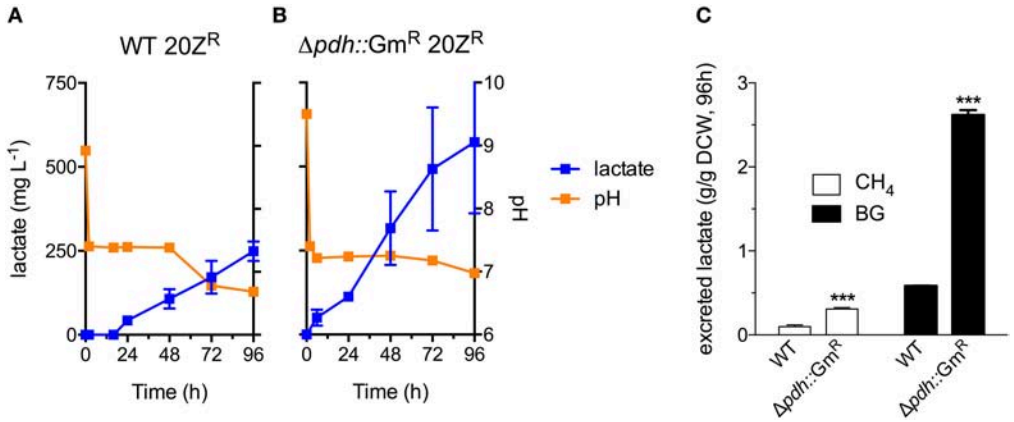


**FIGURE 4 |** A *M. alcaliphilum* 20Z$^R$ pyruvate dehydrogenase mutant exhibits increased flux to lactate. Excreted lactate (blue square), and culture pH (orange square) of wild-type (WT, **A**) and pyruvate dehydrogenase mutant (Δ*pdh*::Gm$^R$, **B**) *M. alcaliphilum* 20Z$^R$ during cultivation with continuous supply of 33% biogas in air (20% $CH_4$, 13% $CO_2$, 1 vvm) **(C)** Lactate flux from pure $CH_4$ (white bars) or biogas (black bars) in WT and Δ*pdh*::Gm$^R$ *M. alcaliphilum* 20Z$^R$ based on dry cell weight (DCW). The data represent the average ± S.D. from 2 to 4 independent observations. ***$p < 0.001$ compared to wild-type controls.

of additional chemical building blocks, including acrylic acid, propylene glycol, and pentanol. These chemical intermediates, along with polymers and fuels that could be generated from biogas, offer a viable, renewable alternative to those generated from conventional carbohydrate feedstocks, which compete with food production. Biocatalysis of conventionally flared AD biogas has the added benefit of GHG reduction while also offering a means to concurrently liquefy and upgrade $CH_4$, enabling its utilization in conventional transportation and industrial manufacturing infrastructure. Future integration of biogas biocatalysis into conventional AD and biorefinery infrastructure will provide insight into other opportunities for recycling and cost reductions, advancing a viable route to a greener bioeconomy.

## AUTHOR CONTRIBUTIONS

CH, MG, and MK designed experiments and analyzed the data. CH, TF, BY, SB, and DA performed experiments. CH, MK, DA, and MG wrote the manuscript. All authors approved the final version of the manuscript.

## FUNDING

This work was authored in part by Alliance for Sustainable Energy, LLC, the manager and operator of the National Renewable Energy Laboratory for the U.S. Department of Energy under Contract No. DE-AC36-08GO28308. Funding provided by the U.S. Department of Energy Office of Energy Efficiency and Renewable Energy Bioenergy Technologies Office DE-FOA-0001085. The views expressed in the article do not necessarily represent the views of the DOE or the U.S. Government. The U.S. Government retains and the publisher, by accepting the article for publication, acknowledges that the U.S. Government retains a non-exclusive, paid-up, irrevocable, worldwide license to publish or reproduce the published form of this work, or allow others to do so, for U.S. Government purposes.

## ACKNOWLEDGMENTS

We would like to thank Drs. Lisa Stein and Mary Lidstrom for providing the *Methylosinus trichosporium* OB3b and *Methylococcus capsulatus* Bath strains, respectively. We also thank Renee Happs and Holly Rohrer of NREL for assistance with NMR and HPLC analyses, respectively. We thank Michael Schuppenhauer of Silver Hill Partners for generating biogas samples.

## SUPPLEMENTARY MATERIAL

The Supplementary Material for this article can be found online at: https://www.frontiersin.org/articles/10.3389/fmicb.2018.02610/full#supplementary-material

## REFERENCES

Abdel-Rahman, M. A., Tashiro, Y., and Sonomoto, K. (2013). Recent advances in lactic acid production by microbial fermentation processes. *Biotechnol. Adv.* 31, 877–902. doi: 10.1016/j.biotechadv.2013.04.002

Achinas, S., and Euverink, G. J. W. (2016). Theoretical analysis of biogas potential prediction from agricultural waste. *Resour. Efficient Technol.* 2, 143–147. doi: 10.1016/j.reffit.2016.08.001

Akberdin, I. R., Thompson, M., Hamilton, R., Desai, N., Alexander, D., Henard, C. A., et al. (2018). Methane utilization in *Methylomicrobium alcaliphilum* 20ZR: a systems approach. *Sci. Rep.* 8, 1–13. doi: 10.1038/s41598-018-20574-z

Anthony, C. (1982). *The Biochemistry of Methylotrophs*. London; New York, NY: Academic Press.

Boden, R., Cunliffe, M., Scanlan, J., Moussard, H., Kits, K. D., Klotz, M. G., et al. (2011). Complete genome sequence of the aerobic marine methanotroph *Methylomonas methanica* MC09. *J. Bacteriol.* 193, 7001–7002. doi: 10.1128/JB.06267-11

Bothe, H., Møller Jensen, K., Mergel, A., Larsen, J., Jørgensen, C., Bothe, H., et al. (2002). Heterotrophic bacteria growing in association with *Methylococcus capsulatus* (Bath) in a single cell protein production process. *Appl. Microbiol. Biotechnol.* 59, 33–39. doi: 10.1007/s00253-002-0964-1

Cal, A. J., Sikkema, W. D., Ponce, M. I., Franqui-Villanueva, D., Riiff, T. J., Orts, W. J., et al. (2016). Methanotrophic production of polyhydroxybutyrate-co-hydroxyvalerate with high hydroxyvalerate content. *Int. J. Biol. Macromol.* 87, 302–307. doi: 10.1016/j.ijbiomac.2016.02.056

Clomburg, J. M., Crumbley, A. M., and Gonzalez, R. (2017). Industrial biomanufacturing: the future of chemical production. *Science* 355:aag0804. doi: 10.1126/science.aag0804

Conrado, R. J., and Gonzalez, R. (2014). Chemistry. envisioning the bioconversion of methane to liquid fuels. *Science* 343, 621–623. doi: 10.1126/science.1246929

Department of Energy (2017). *Biofuels and Bioproducts from Wet and Gaseous Waste Streams: Challenges and Opportunities*. Bioenergy Technologies Office. Available online at: https://www.energy.gov/sites/prod/files/2017/01/f34/biofuels_and_bioproducts_from_wet_and_gaseous_waste_streams_full_report_2.pdf

Eiteman, M. A., and Ramalingam, S. (2015). Microbial production of lactic acid. *Biotechnol. Lett.* 37:5. doi: 10.1007/s10529-015-1769-5

Flynn, J. D., Hirayama, H., Sakai, Y., Dunfield, P. F., Klotz, M. G., Knief, C., et al. (2016). Draft genome sequences of gammaproteobacterial methanotrophs isolated from marine ecosystems. *Genome Announc* 4:e01629-15. doi: 10.1128/genomeA.01629-15

Garg, S., Clomburg, J. M., and Gonzalez, R. (2018). A modular approach for high-flux lactic acid production from methane in an industrial medium using engineered *Methylomicrobium buryatense* 5GB1. *J. Ind. Microbiol. Biotechnol.* 45, 379–391. doi: 10.1007/s10295-018-2035-3

Gilman, A., Laurens, L. M., Puri, A. W., Chu, F., Pienkos, P. T., and Lidstrom, M. E. (2015). Bioreactor performance parameters for an industrially-promising methanotroph *Methylomicrobium buryatense* 5GB1. *Microb. Cell Fact.* 14, 1–8. doi: 10.1186/s12934-015-0372-8

Hamilton, R., Kits, K. D., Ramonovskaya, V. A., Rozova, O. N., Yurimoto, H., Iguchi, H., et al. (2015). Draft genomes of gammaproteobacterial methanotrophs isolated from terrestrial ecosystems. *Genome Announc.* 3:e00515. doi: 10.1128/genomeA.00515-15

Hanson, R. S., and Hanson, T. E. (1996). Methanotrophic bacteria. *Microbiol. Rev.* 60, 439–471.

Haynes, C. A., and Gonzalez, R. (2014). Rethinking biological activation of methane and conversion to liquid fuels. *Nat. Chem. Biol.* 10, 331–339. doi: 10.1038/nchembio.1509

Henard, C. A., Smith, H., Dowe, N., Kalyuzhnaya, M. G., Pienkos, P. T., and Guarnieri, M. T. (2016). Bioconversion of methane to lactate by an obligate methanotrophic bacterium. *Sci Rep* 6, 1–9. doi: 10.1038/srep21585

Henard, C. A., Smith, H. K., and Guarnieri, M. T. (2017). Phosphoketolase overexpression increases biomass and lipid yield from methane in an obligate methanotrophic biocatalyst. *Metabol. Eng.* 41, 152–158. doi: 10.1016/j.ymben.2017.03.007

Hosseini, S. E., and Wahid, M. A. (2014). Development of biogas combustion in combined heat and power generation. *Renew. Sustain. Energy Rev.* 40, 868–875. doi: 10.1016/j.rser.2014.07.204

Hwang, I. Y., Lee, S. H., Choi, Y. S., Park, S. J., Na, J. G., Chang, I. S., et al. (2014). Biocatalytic conversion of methane to methanol as a key step for development of methane-based biorefineries. *J. Microbiol. Biotechnol.* 24, 1597–1605. doi: 10.4014/jmb.1407.07070

Kalyuzhnaya, M. G. (2016). "Chapter 13 methane biocatalysis selecting the right microbe," in *Biotechnology for Biofuel Production and Optimization*, eds C. Eckert, and C. T. Trinh (Amsterdam: Elsevier), 353–383.

Kalyuzhnaya, M. G., Puri, A. W., and Lidstrom, M. E. (2015). Metabolic engineering in methanotrophic bacteria. *Metabol. Eng.* 29, 142–152. doi: 10.1016/j.ymben.2015.03.010

Kalyuzhnaya, M. G., Yang, S., Rozova, O. N., Smalley, N. E., Clubb, J., Lamb, A., et al. (2013). Highly efficient methane biocatalysis revealed in a methanotrophic bacterium. *Nat. Commun.* 4:3785. doi: 10.1038/ncomms3785

Khmelenina, V. N., Beck, D. A. C., Munk, C., Davenport, K., Daligault, H., Erkkila, T., et al. (2013). Draft genome sequence of *Methylomicrobium buryatense* strain 5G, a haloalkaline-tolerant methanotrophic bacterium. *Genome Announc* 1:13. doi: 10.1128/genomeA.00053-13

Kits, K. D., Kalyuzhnaya, M. G., Klotz, M. G., Jetten, M. S. M., Op den Camp, H. J. M., Vuilleumier, S., et al. (2013). Genome sequence of the obligate gammaproteobacterial *Methanotroph methylomicrobium* album strain BG8. *Genome Announc.* 1:e0017013. doi: 10.1128/genomeA.00170-13

la Torre, de, A., Metivier, A., Chu, F., Laurens, L. M. L., and Beck, D. A. C., Pienkos, P. T., et al. (2015). Genome-scale metabolic reconstructions and theoretical investigation of methane conversion in *Methylomicrobium buryatense* strain 5G(B1). *Microb. Cell Fact.* 14:188. doi: 10.1186/s12934-015-0377-3

Myung, J., Flanagan, J. C. A., Waymouth, R. M., and Criddle, C. S. (2016). Methane or methanol-oxidation dependent synthesis of poly(3-hydroxybutyrate-co-3-hydroxyvalerate) by obligate type II methanotrophs. *Process Biochem.* 51, 561–567. doi: 10.1016/j.procbio.2016.02.005

Narainsamy, K., Farci, S., Braun, E., Junot, C., Cassier-Chauvat, C., and Chauvat, F. (2016). Oxidative-stress detoxification and signalling in cyanobacteria: the crucial glutathione synthesis pathway supports the production of ergothioneine and ophthalmate. *Mol. Microbiol.* 100, 15–24. doi: 10.1111/mmi.13296

Nguyen, A. D., Hwang, I. Y., Lee, O. K., Kim, D., Kalyuzhnaya, M. G., Mariyana, R., et al. (2018). Systematic metabolic engineering of *Methylomicrobium alcaliphilum* 20Z for 2,3-butanediol production from methane. *Metabol. Eng.* 47, 323–333. doi: 10.1016/j.ymben.2018.04.010

Ojala, D. S., Beck, D. A. C., and Kalyuzhnaya, M. G. (2011). Genetic systems for moderately halo(alkali)philic bacteria of the genus Methylomicrobium. *Meth. Enzymol.* 495, 99–118. doi: 10.1016/B978-0-12-386905-0.00007-3

Pieja, A. J., Morse, M. C., and Cal, A. J. (2017). Sciencedirect methane to bioproducts: the future of the bioeconomy? *Curr. Opin. Chem. Biol.* 41, 123–131. doi: 10.1016/j.cbpa.2017.10.024

Puri, A. W., Owen, S., Chu, F., Chavkin, T., Beck, D. A. C., Kalyuzhnaya, M. G., et al. (2015). Genetic tools for the industrially promising methanotroph methylomicrobium buryatense. *Appl. Environ. Microbiol.* 81, 1775–1781. doi: 10.1128/AEM.03795-14

Soga, T., Baran, R., Suematsu, M., Ueno, Y., Ikeda, S., Sakurakawa, T., et al. (2006). Differential metabolomics reveals ophthalmic acid as an oxidative stress biomarker indicating hepatic glutathione consumption. *J. Biol. Chem.* 281, 16768–16776. doi: 10.1074/jbc.M601876200

Strong, P. J., Kalyuzhnaya, M., Silverman, J., and Clarke, W. P. (2016). A methanotroph-based biorefinery: potential scenarios for generating multiple products from a single fermentation. *Bioresour. Technol.* 215, 314–323. doi: 10.1016/j.biortech.2016.04.099

Strong, P. J., Xie, S., and Clarke, W. P. (2015). Methane as a resource: can the methanotrophs add value? *Environ. Sci. Technol.* 49, 4001–4018. doi: 10.1021/es504242n

Whittenbury, R., Phillips, K. C., and Wilkinson, J. F. (1970). Enrichment, isolation and some properties of methane-utilizing bacteria. *J. Gen. Microbiol.* 61, 205–218. doi: 10.1099/00221287-61-2-205

Yan, X., Chu, F., Puri, A. W., Fu, Y., and Lidstrom, M. E. (2016). Electroporation-based genetic manipulation in type I methanotrophs. *Appl. Environ. Microbiol.* 82, 2062–2069. doi: 10.1128/AEM.03724-15

**Conflict of Interest Statement:** The authors declare that the research was conducted in the absence of any commercial or financial relationships that could be construed as a potential conflict of interest.

frontiers in Microbiology

ORIGINAL RESEARCH
published: 18 July 2018
doi: 10.3389/fmicb.2018.01513

# Defining Nutrient Combinations for Optimal Growth and Polyhydroxybutyrate Production by *Methylosinus trichosporium* OB3b Using Response Surface Methodology

*Jorge A. Zaldívar Carrillo[1], Lisa Y. Stein[2] and Dominic Sauvageau[1]**

[1] Department of Chemical and Materials Engineering, University of Alberta, Edmonton, AB, Canada, [2] Department of Biological Sciences, University of Alberta, Edmonton, AB, Canada

OPEN ACCESS

**Edited by:**
*Obulisamy Parthiba Karthikeyan, Prolog Biologicals Pvt. Ltd., India*

**Reviewed by:**
*Ganesan Sathiyanarayanan, CEA Cadarache, France*
*Shashi Kant Bhatia, Konkuk University, South Korea*

***Correspondence:**
*Dominic Sauvageau*
*dominic.sauvageau@ualberta.ca*

**Specialty section:**
*This article was submitted to Microbiotechnology, Ecotoxicology and Bioremediation, a section of the journal Frontiers in Microbiology*

**Received:** *04 April 2018*
**Accepted:** *18 June 2018*
**Published:** *18 July 2018*

**Citation:**
*Zaldívar Carrillo JA, Stein LY and Sauvageau D (2018) Defining Nutrient Combinations for Optimal Growth and Polyhydroxybutyrate Production by Methylosinus trichosporium OB3b Using Response Surface Methodology. Front. Microbiol. 9:1513. doi: 10.3389/fmicb.2018.01513*

Methane and methanol are common industrial by-products that can be used as feedstocks for the production of value-added products by methylotrophic bacteria. Alphaproteobacterial methanotrophs are known to produce and accumulate the biopolymer polyhydroxybutyrate (PHB) under conditions of nutrient starvation. The present study determined optimal production of biomass and PHB by *Methylosinus trichosporium* OB3b as a function of carbon source (methane or methanol), nitrogen source (ammonium or nitrate), and nitrogen-to-carbon ratio during growth. Statistical regression analysis with interactions was performed to assess the importance of each factor, and their respective interactions, on biomass and PHB production. Higher biomass concentrations were obtained with methane as carbon source and with ammonium as nitrogen source. The nitrogen source that favored PHB production was ammonium for methane-grown cells and nitrate for methanol-grown cells. Response surface methodology (RSM) was used to determine conditions leading to optimal biomass and PHB production. As an example, the optimal PHB concentration was predicted to occur when a mixture of 30% methane and 70% methanol (molar basis) was used as carbon source with nitrate as nitrogen source and a nitrogen-to-carbon molar ratio of 0.017. This was confirmed experimentally, with a PHB concentration of 48.7 ± 8.3 mg/L culture, corresponding to a cell content of 52.5 ± 6.3% (cell dry weight basis). Using RSM to simultaneously interrogate multiple variables toward optimized growth and production of biopolymer serves as a guide for establishing more efficient industrial conditions to convert single-carbon feedstocks into value-added products.

**Keywords: methanotroph growth, *Methylosinus trichosporium*, polyhydroxybutyrate (PHB), optimization of biopolymer production, response surface methodology**

## INTRODUCTION

The impact of plastic pollution has motivated interest in economically viable biodegradable polymers. One such class of biopolymers is polyhydroxyalkanoates (PHAs), of which polyhydroxybutyrate (PHB) is the most widely studied representative. Current industrial production relies on using sugars as feedstock, which translates into high production costs and competition with food production. A promising alternative involves using methanotrophic bacteria that convert single-carbon compounds into PHB (Chidambarampadmavathy et al., 2017). The use of residual methane and methanol, both low value common industrial by-products, reduces both the costs of production of biomolecules, such as PHB, compared to sugar-based feedstocks (Fei et al., 2014; Strong et al., 2015) and carbon emissions from the source industry.

PHB production by methanotrophic bacteria generally requires a starvation signal that is usually accomplished by providing excess carbon while limiting the nitrogen source (Lee, 1996; Pieja et al., 2011; Zhang et al., 2017). Alphaproteobacterial methanotrophs utilize the serine cycle for formaldehyde assimilation and feed acetyl-CoA from this cycle into PHB biosynthesis (Pieja et al., 2011). Although central carbon metabolism is essentially identical among the alphaproteobacterial methanotrophs, there is substantial strain-to-strain variability in terms of preferred N-source and engagement of PHB production during N-starvation. For instance, *Methylosinus trichosporium* OB3b cultivated in medium with nitrate produced more PHB upon N-limitation than cultures grown with ammonium, whereas the opposite result was observed with *Methylocystis parvus* OBBP (Rostkowski et al., 2013; Zhang et al., 2017). The physiological influence of N-source on PHB production in methanotrophs has not yet been resolved, let alone the impact of using a combination of N-sources, nor has strain-to-strain preference for one N-source over another. In addition, the production of PHB using methanol as a sole carbon and energy source, or a mixture of methane and methanol, instead of methane alone, has not been extensively investigated for methanotrophs.

The present study aims to optimize the production of biomass and PHB in *M. trichosporium* OB3b in relation to carbon source (methane or methanol), nitrogen source (nitrate or ammonium), and the carbon to nitrogen ratio using statistical regression analysis combined with response surface methodology (RSM). RSM is a collection of statistical tools that avoids the time consuming and expensive optimization of individual parameters required in full-factorial methodology to achieve a desired response. Instead, statistical regression analysis and RSM help determine the effects of multiple variables simultaneously (i.e., independent, or process, variables) toward the response of interest (i.e., response variable) and also measure the significance of each independent variable on the response (Myers et al., 2016). This analysis enabled us to determine optimal carbon and nitrogen combinations toward the highest yield of either biomass or PHB per liter of culture of *M. trichosporium* OB3b. This study also highlights the potential of RSM to optimize methanotrophic growth medium toward production of a valuable biopolymer despite the complex interacting effects of carbon and nitrogen sources on metabolism.

## MATERIALS AND METHODS

### Cultivation

*Methylosinus trichosporium* OB3b is maintained in the Stein lab and was originally acquired as a gift from Dr. Alan DiSpirito, Iowa State University. Nitrate mineral salts (NMS) and ammonium mineral salts (AMS) media (Whittenbury et al., 1970) were used in this study. These media normally contain 10 g/L $KNO_3$ or 5 g/L $NH_4Cl$, respectively, but these concentrations were varied as required using 99 mM stock solutions of $KNO_3$ or $NH_4Cl$ to achieve the desired nitrogen to carbon ratios tested in this study.

Cultures (100 mL) were grown in serum-capped Wheaton bottles (311 mL). Prior to inoculation, filter-sterilized (0.22 μm; Corning United States) methanol (Fisher Scientific) at 10 or 20 mM, filter-sterilized methane (95 + 5% $CO_2$; Praxair, Canada) at 20 mmol/L of medium, or a mixture of the two carbon sources totaling 20 mmol carbon per liter of liquid was added as carbon source. Prior to the addition of methane, an equivalent amount of air was removed from the bottles to maintain the same headspace pressure as the methanol-amended cultures. Cultures were inoculated with 1–4% v/v of 2–5 day old stationary phase culture by injection through the septum. Cultures were incubated at 30°C and 150 rpm until analysis.

Cell dry weight was measured by extracting 20 to 30 mL culture and centrifuging at 10,000 × *g* at 4°C for 10 min (Sorvall RC 6 Plus, SS-34 rotor; Thermo Scientific). The supernatant was discarded and the pellet was resuspended in 10 mL deionized water and transferred to a tared weigh dish. The dish was placed in an oven at 60°C for drying to constant weight. Optical density of cultures was measured at a wavelength of 540 nm using a spectrophotometer (Ultrospec 50, Biochrom). A calibration curve was prepared to convert OD measurements to unit cell dry weight.

### PHB Measurement

The quantification of PHB was performed via gas chromatography using a modified methodology (Braunegg et al., 1978; Oehmen et al., 2005). A 7–10 mL sample of culture was centrifuged at 2,988 × *g* for 30 min. The supernatant was discarded and the pellet resuspended in a solution containing 2 mL chloroform and 2 mL of benzoic acid solution (40 mg/L) dissolved in methanol and acidified with 3% concentrated sulfuric acid. The sample was digested for 5 h – to depolymerize the polymer to its monomer and esterify it with methanol – in a capped glass vial in a boiling water bath. After cooling, 1 mL deionized water was added and the sample was vortexed and left to stand for phase separation. The organic phase was analyzed for methyl 3-hydroxybutyrate, the methylated form of the PHB monomer, using a gas chromatograph (7890A, Agilent Technologies) equipped with an autosampler (G4513A, Agilent Technologies) and fitted with a 30 m × 250 μm DB-5ms column (Agilent Technologies). The injector temperature was

held at 250°C, and the oven temperature was held at 80°C for 1 min, raised to 120°C at a rate of 10°C/min, and then to 270°C at 30°C/min, before being held at that temperature for 3 min. 3-samples were injected at a split ratio of 1:10. A flame ionization detector (FID) at 300°C was used. Helium was used as the carrier gas at a flow of 1.5 mL/min. The peak of methyl 3-hydroxybutyrate was resolved at 2.8 min; an internal standard of methyl benzoate was resolved at 5.4 min (Supplementary Figure S7).

## Statistical Analysis

Analysis of variance (ANOVA) was used to determine significant effects of each variable and the combinations of variables on bacterial growth. Clustered Plot Analysis was used to visualize the ANOVA results and summarize the mean, median, standard deviation, and outliers for each group of compared data. Visualization used the Matlab script[1] "notBoxPlot.m."

The impacts of C-source, N-source, N:C ratio and history of the inoculum on growth was first investigated through statistical regression analysis with interactions. To do so, a $2^4$ full factorial experimental design was performed in which each of these four factors had two levels (**Table 1**). A total of 100-mL cultures in 250-mL Wheaton bottles were performed in triplicate and analyzed for each condition. Nitrogen concentrations of 10 or 1 mM were used to achieve the high and low nitrogen-to-carbon ratio, respectively. In addition, fresh (4–8 weeks) and aged (5.5–6.3 months) inocula were used, grown initially from either methane or methanol, with ammonium or nitrate as N-source, accordingly. A separate block of experiments was conducted in duplicate with methanol grown cultures with ammonium only, initiated from 2.1 to 2.3 week and 3.1–3.3 week old inocula. These additional experiments were included due to the extensive lag periods observed in experiments performed with methanol using the older inocula; they were treated separately in the analysis and modeling exercise.

The RSM used a face-centered central composite design to depict the interactions among the variables in a cuboidal experimental space. The three variables included were C-source, N-source, and nitrogen-to-carbon ratio, each one at three levels, as required by the design (**Table 2**). The same design and cultures were used to gather data to fit response surfaces for cell dry weight, PHB concentration and PHB content (as % cell dry weight). A description of the design space and parameter coding can be found in the Supplementary Materials (Supplementary Figure S4).

**TABLE 1 |** Factors and levels used in the second-order statistical regression analysis.

| Factors investigated | Design levels | |
|---|---|---|
| Carbon source | Methane ($CH_4$) | +1 |
| | Methanol ($CH_3OH$) | −1 |
| Nitrogen source | Ammonium ($NH_4^+$) | +1 |
| | Nitrate ($NO_3^-$) | −1 |
| Nitrogen-to-Carbon ratio (N:C) | Low[1] | +1 |
| | High[2] | −1 |
| Inoculum history[3] | Fresh methane-grown | +1 |
| | Aged methane-grown | −1 |
| | Fresh methanol-grown | +1 |
| | Aged methanol-grown | −1 |

*[1]Low level of N:C was 0.046 for methane and 0.1 for methanol.*
*[2]High level of N:C was 0.46 for methane and 1.0 for methanol.*
*[3]Inocula previously grown on methane with ammonium or nitrate were used to start both methane and methanol cultures; inocula grown on methanol with ammonium were used to start only methanol cultures.*

**TABLE 2 |** Factors and levels used in the response surface methodology experiments.

| Factors investigated | Design levels |
|---|---|
| Carbon source (molar basis) | 100% methane |
| | 50% methane, 50% methanol |
| | 100% methanol |
| Nitrogen source (molar basis) | 100% ammonium |
| | 50% ammonium, 50% nitrate |
| | 100% nitrate |
| Nitrogen-to-Carbon ratio (molar basis) | 0.005 |
| | 0.025 |
| | 0.045 |

# RESULTS

## Effect of Carbon and Nitrogen Source and Inoculum History on Growth of *M. trichosporium* OB3b

Four factors were selected to investigate their impact on the growth of *M. trichosporium* OB3b: carbon source (methane or methanol), nitrogen source (ammonium or nitrate), nitrogen-to-carbon ratio (low and high), and inoculum history (fresh or aged, from methane-grown or methanol-grown cultures with either N-source). Growth curves obtained for all 64 cultures and 24 treatments are shown in Supplementary Figures S1–S3. The final $OD_{540}$ values and duration of lag phases from all experiments are reported in **Tables 3**, **4**, respectively.

The effects of each of the four factors on biomass yield were determined by ANOVA (Supplementary Table S1). Carbon source was the most significant factor, followed by nitrogen source (**Figure 1**). Overall, the average $OD_{540}$ for methane- versus methanol-grown cells was 0.31 and 0.19, respectively, and higher yields were generally achieved using ammonium over nitrate, particularly in methane-grown cells. Except for methane-grown cells with nitrate, a low N:C ratio resulted in slight, but significant, increases in biomass. There was no significant effect of inoculum age on biomass yield except for the independent experiment using younger inocula for methanol-grown cells, in which the freshest inoculum resulted in a significantly higher biomass yield (an increase of 0.039 units).

Because the absolute carbon loads were not equivalent between the methane- and methanol-grown cultures, the $OD_{540}$ values were normalized by dividing by the moles of carbon,

[1]https://www.mathworks.com/matlabcentral/fileexchange/26508-notboxplot?requestedDomain=true

**TABLE 3 |** Final $OD_{540}$ for *Methylosinus trichosporium* OB3b growth experiments.

| C-source | N-source | N:C ratio | $CH_4$-grown inoculum | | $CH_3OH$-grown inoculum | |
|---|---|---|---|---|---|---|
| | | | Fresh | Aged | Fresh | Aged |
| $CH_4$ | $NH_4^+$ | Low | 0.346 ± 0.009 | 0.354 ± 0.006 | – | – |
| $CH_4$ | $NH_4^+$ | High | 0.336 ± 0.013 | 0.331 ± 0.020 | – | – |
| $CH_4$ | $NO_3^-$ | Low | 0.270 ± 0.030 | 0.291 ± 0.007 | – | – |
| $CH_4$ | $NO_3^-$ | High | 0.275 ± 0.018 | 0.291 ± 0.008 | – | – |
| $CH_3OH$ | $NH_4^+$ | Low | 0.225 ± 0.012 | 0.193 ± 0.007 | 0.240 ± 0.016 | 0.190 ± 0.014 |
| $CH_3OH$ | $NH_4^+$ | High | 0.183 ± 0.010 | 0.193 ± 0.014 | 0.223 ± 0.009 | 0.174 ± 0.015 |
| $CH_3OH$ | $NO_3^-$ | Low | 0.197 ± 0.017 | 0.173 ± 0.016 | 0.208 ± 0.000 | 0.170 ± 0.005 |
| $CH_3OH$ | $NO_3^-$ | High | 0.156 ± 0.021 | 0.160 ± 0.007 | 0.182 ± 0.014 | 0.163 ± 0.007 |

**TABLE 4 |** Lag phase (days) for *M. trichosporium* OB3b growth experiments.

| C-source | N-source | N:C ratio | $CH_4$-grown inoculum | | $CH_3OH$-grown inoculum | |
|---|---|---|---|---|---|---|
| | | | Fresh | Aged | Fresh | Aged |
| $CH_4$ | $NH_4^+$ | Low | 1 | 2.5 | – | – |
| $CH_4$ | $NH_4^+$ | High | 1.5 | 2.5 | – | – |
| $CH_4$ | $NO_3^-$ | Low | 1.5 | 2.5 | – | – |
| $CH_4$ | $NO_3^-$ | High | 1.5 | 2.5 | – | – |
| $CH_3OH$ | $NH_4^+$ | Low | 12–14 | 9 | 5–5.5 | 9.5–10.5 |
| $CH_3OH$ | $NH_4^+$ | High | 10–13 | 12–13 | 5.5 | 9–11 |
| $CH_3OH$ | $NO_3^-$ | Low | 12–14 | 10.5 | 4.5–5 | 9–11.5 |
| $CH_3OH$ | $NO_3^-$ | High | 10.5–11 | 9 | 4.5 | 8.5 |

and the ANOVA was repeated (Supplementary Table S2). In this analysis methanol becomes the preferred C-source, ammonium remains the preferred N-source, a low N:C ratio remains favorable, and fresh inoculum was more favorable than aged inoculum (**Figure 2**).

## PHB Production as a Function of N:C Ratio

Our next objective was to determine optimized conditions for production of PHB by *M. trichosporium* OB3b. Cultures were grown with either methane or methanol and with ammonium or nitrate in a smaller liquid volume (50 mL) and in either 250-mL or 1-L bottles, corresponding to O:C ratios of 2.2:1 and 9.7:1, respectively, to avoid oxygen limitation. Although growth on methane was equivalent for cultures in both the 250-mL and 1-L bottles, PHB production increased 10-fold for cultures in 1-L bottles, suggesting that PHB production requires a high O:C ratio (**Figure 3**). PHB content was subsequently determined as a function of the N:C ratio and cell dry weight. Nitrate resulted in higher yields of PHB in methane-grown cells, whereas ammonium was the superior N-source for PHB production in methanol-grown cells (data not shown). For both carbon sources, the optimal N:C ratio was 0.025 for maximum %PHB of total cell dry weight, although the N:C ratio of 0.01 was equally effective for PHB production in methanol-grown cells (**Figure 4**). Furthermore, PHB production was five times higher in methanol- than methane-grown cells, indicating a preference for methanol for PHB production.

## Growth Response Surface Analysis

Based on the results obtained in the statistical regression analysis, a face-centered central composite design with three factors: carbon source, nitrogen source, and nitrogen-to-carbon ratio, at three levels each, was selected for the RSM analysis, for a total of 15 treatments. Cultures were grown under oxygen-rich conditions (O:C ratio of 9.7). **Figure 5** shows the response surfaces for final cell dry weight when methane (**Figure 5A**), an equimolar mixture of methane and methanol (**Figure 5B**), or methanol (**Figure 5C**) were used as carbon source and N-sources were either combined or pure. First, it is interesting to note the conditions where the maxima occur: (a) for methane, the N-source is mixed and the N:C ratio = 0.028, (b) for methane plus methanol, the N-source is nitrate and the N:C ratio = 0.026, and (c) for methanol, the N-source is nitrate and the N:C ratio = 0.026. It is also important to note the different shapes of the response surfaces, denoting different susceptibilities to the factors tested depending on the carbon source used. For example, the N-source had a much stronger impact on biomass accumulation in methanol-grown cultures compared to cultures grown on a methane alone or in a mixture of methane and methanol.

The complete array of response surfaces obtained for growth (constant C-sources, constant N-sources, and constant N:C ratios) can be found in Supplementary Figure S5. An interesting finding from these results is the strong dependence of cell dry weight on the provided C-source when ammonium is the N-source (Supplementary Figure S5d) compared to a

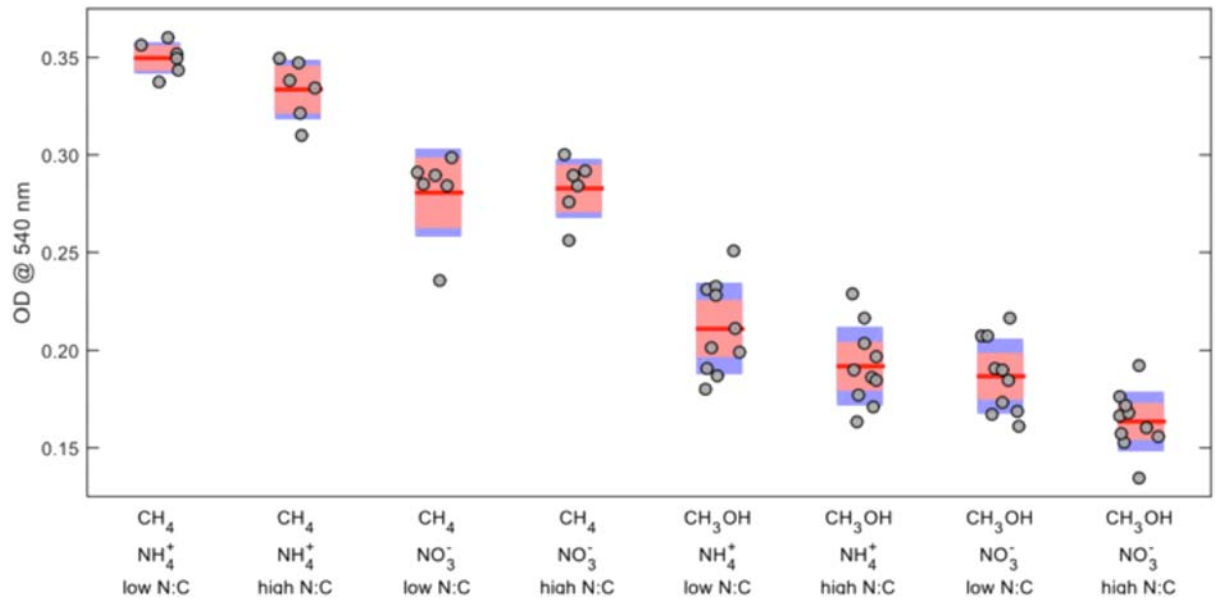


**FIGURE 1 |** Effects of combined carbon source, nitrogen source, and nitrogen-to-carbon ratio on final $OD_{540}$ of *Methylosinus trichosporium* OB3b. The *red lines* represent the mean values, the *red areas* represent the mean ± 1.96 × standard error, and the *blue areas* represent the mean ± one standard deviation.

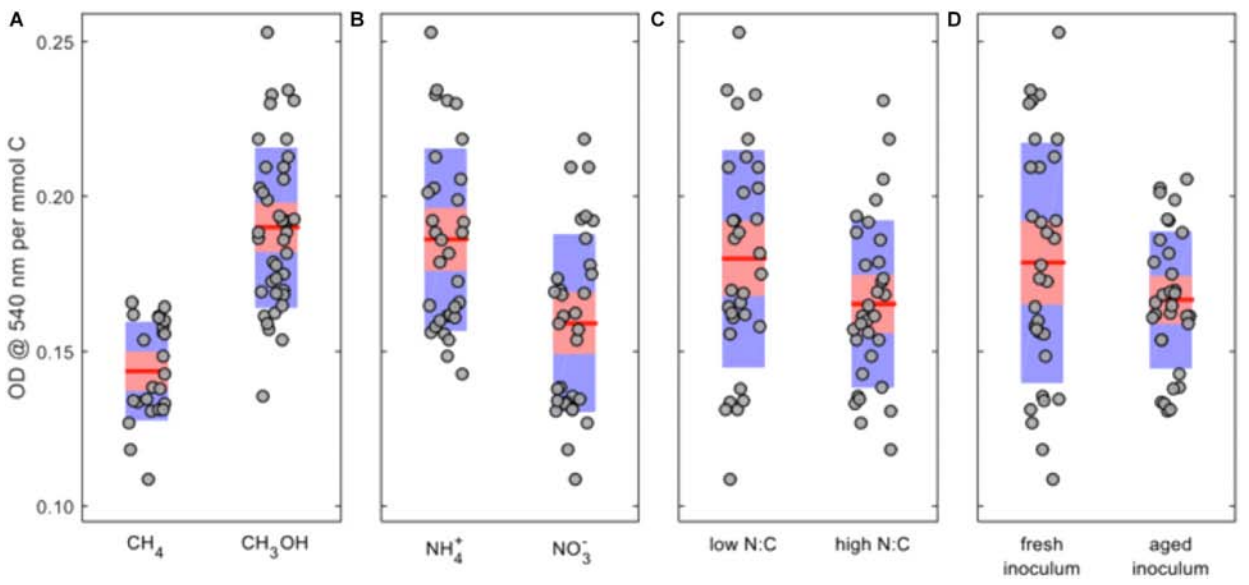


**FIGURE 2 |** Main-factor effects on normalized $OD_{540}$ for *Methylosinus trichosporium* OB3b cultures. **(A)** C-source; **(B)** N-source; **(C)** N:C ratio; and **(D)** inoculum history. The *red lines* represent the mean values, the *red areas* represent the mean ± 1.96 × standard error, and the *blue areas* represent the mean ± one standard deviation.

relative independence on C-source when nitrate is the N-source (Supplementary Figure S5f).

## PHB Concentration Response Surface Analysis

The same treatments were used to investigate the resulting PHB concentration in *M. trichosporium* OB3b as a function of C-source, N-source, and N:C ratios. Samples for PHB quantification were analyzed as soon as the optical density of the cultures reached or exceeded 0.25 and following at least 24 h of cultivation. **Figure 6** shows the response surface for the PHB concentration obtained from cultures growing on methane (**Figure 6A**), an equimolar mixture of methane and methanol (**Figure 6B**), or methanol (**Figure 6C**) with ammonium or nitrate as N-source. For methane-grown cells, the maximum PHB concentration (34 mg/L) occurred at the boundary of

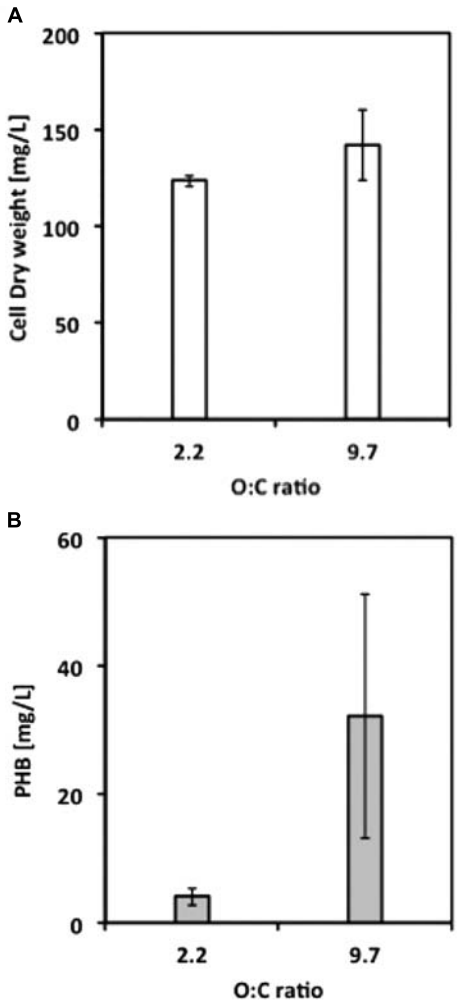


**FIGURE 3 | (A)** Final cell dry weight and **(B)** PHB concentration from *M. trichosporium* OB3b cultures grown under different O:C ratios. Error bars indicate standard deviation ($n$ = 3).

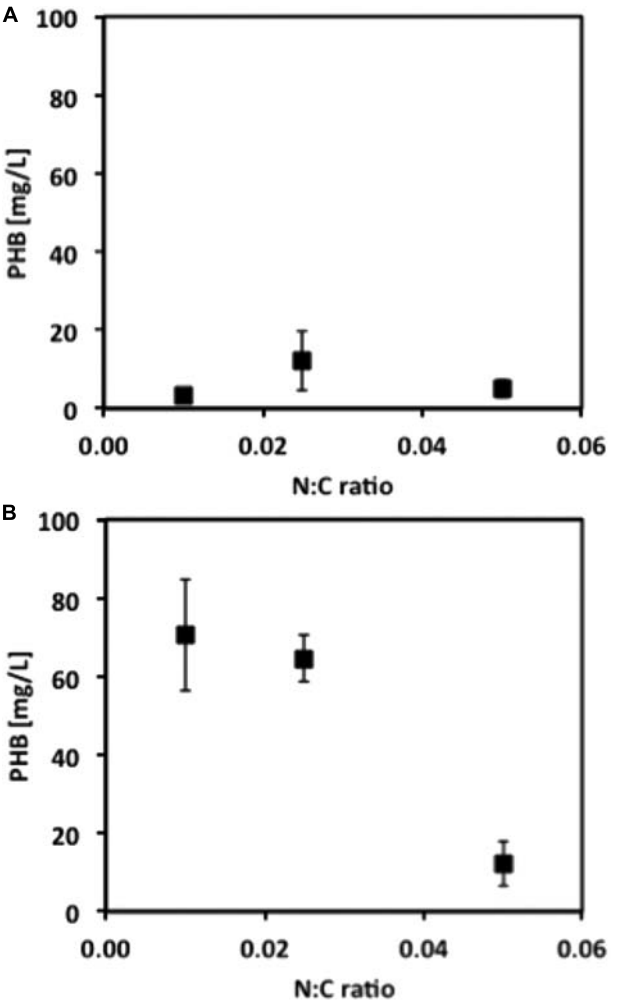


**FIGURE 4 |** PHB concentration from *M. trichosporium* OB3b cultures grown under different N:C ratios when **(A)** methane or **(B)** methanol is used as C-source. Error bars indicate standard deviation ($n$ = 3).

the experimental region representing ammonium as the sole nitrogen source (**Figure 6A**). When changing the carbon source to methanol (**Figure 6C**), the position of the maximum (37 mg/L) moved to the nitrate boundary of the experimental region. The use of mixtures of methane and methanol as carbon source had synergistic effects and higher amounts of PHB were produced than when either carbon source was used alone; the maximum PHB concentration was 39 mg/L with nitrate as the sole N-source (**Figure 6B**). In every case, the maximum value occurred at a low nitrogen-to-carbon ratio of 0.017. The complete set of response surfaces for the PHB concentration can be found in Supplementary Figure S6. As before, the shape and ranges of the surfaces help assess the dependence of PHB concentration on the various factors and conditions tested.

Based on the data, maximum PHB production was predicted to occur when the carbon source was composed of 30% methane and 70% methanol, using nitrate as the sole nitrogen source, and at a nitrogen-to-carbon ratio of 0.017 (**Figure 6D**). The predictions from the model were verified experimentally by quintuplicate cultures in two blocks at conditions close to the predicted maximum. The observed value of the PHB concentration (48.7 $\pm$ 8.3 mg/L) fell within the 95% confidence limit of the model prediction. This corresponded to a PHB cell content of 52.5 $\pm$ 6.3% on a cell dry weight basis.

## DISCUSSION

Although previous studies have been performed to optimize cultivation conditions for PHB production in *M. trichosporium* OB3b (Rostkowski et al., 2013; Zhang et al., 2017), the present work is novel in (1) presenting interactions across multiple variables using statistical regression analysis and RSM models, and (2) showing that, under appropriate conditions, significant PHB production can take place during growth.

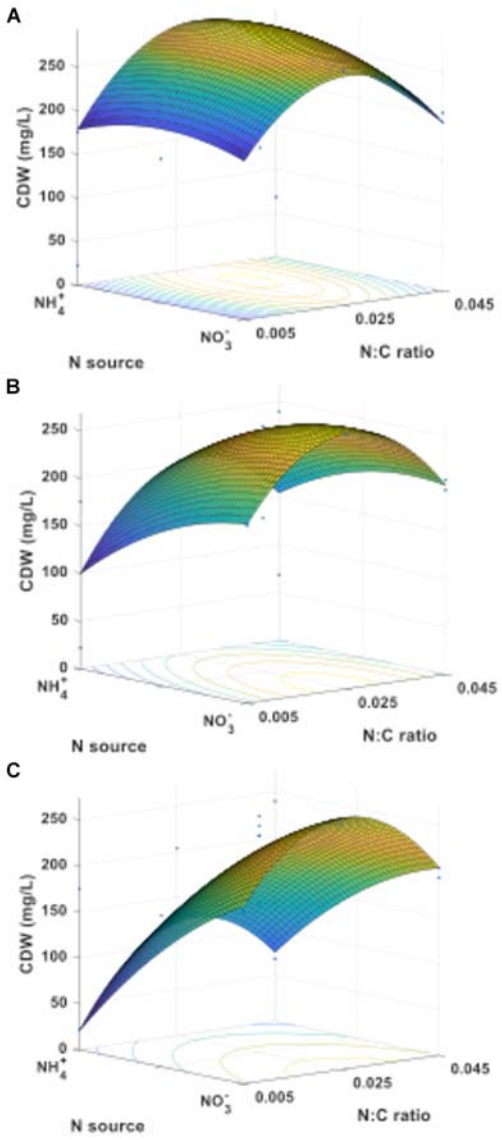


**FIGURE 5 |** Cell dry weight response surfaces for *M. trichosporium* OB3b growing on **(A)** methane, **(B)** an equimolar mixture of methane and methanol, or **(C)** methanol as C-source.

We initially examined the growth and production of PHB by *M. trichosporium* OB3b when varying the carbon source, nitrogen source, nitrogen-to-carbon ratio, and inoculum history. These experiments were used to determine the significance of each variable and of their respective interactions, based on regression analyses ($p$-value $< 0.05$; Supplementary Tables S1, S2). Although most of the parameters significantly affecting growth and growth normalized by the moles of supplied carbon are the same, the history of the inoculum and the interaction between the carbon source and N:C ratio have more significance when looking at the latter. From these analyses we can deduce models (Supplementary Equations S1, S2) that help predict the levels of biomass expected under a given set of growth conditions. It is important to note that these models provide useful information within the experimental space tested and should not be used for extrapolated conditions. It is also important to note that because the C-sources and N-sources tested lead to different physiologies and metabolic responses, within the context of these models, these factors can only be used in a discrete context (either methane or methanol; either ammonium or nitrate). Being conscious of these constraints, valuable information can be extracted from the models.

Among the variables tested, the greatest biomass was achieved when using methane over methanol as carbon source and ammonium over nitrate as nitrogen source. Methanol was modeled as a more productive carbon source when biomass accumulation (as measured by $OD_{540}$; **Table 3**) was corrected for total moles available carbon due to the low mass-transfer of methane to the medium. Inoculum age was not a significant factor in biomass accumulation, but older inocula resulted in significantly longer lag phases when methane was used as C-source (**Table 4**).

Oxygen has been established as an important factor affecting the production of PHB. Rostkowski et al. (2013) used substrate partitioning parameters (between biomass and PHB) for nitrate and ammonium which establishes the oxygen-to-carbon stoichiometric ratio necessary for PHB production at approximately 1.50. In fact, the O:C ratio was indeed a critical factor at least for methane-grown cells, suggesting that $O_2$ limitation is disadvantageous for PHB accumulation by *M. trichosporium* OB3b. However, although PHB production was observed at an O:C ratio of 2.2, the production was significantly improved when the ratio was raised to 9.7 (**Figure 3**). It is important to note that (1) the difference in O:C ratio did not affect the level of biomass produced, and that, (2) in this study, the PHB production took place during growth and was assessed at the onset of stationary phase (and not under starvation conditions as performed in most studies), which may explain the difference in optimal O:C ratio.

This information, along with the effective range of N:C ratio leading to PHB production without negatively impacting growth (**Figure 4**), was used to determine the conditions and define the experimental space for RSM. The analysis of the response surfaces obtained for biomass allow us to better understand the interactions between the factors tested (C-source, N-source, and N:C ratio), determine how they impact the responses investigated (biomass and PHB yields) and establish the extent of the variations as the parameters are changed. The models resulting from these analyses can also be used to determine the conditions leading to the optimal response within the experimental space. For example, from the RSM model, the maximum biomass yield was predicted when *M. trichosporium* OB3b was grown on methane and a mixture of 64% ammonium and 36% nitrate with a N:C ratio of approximately 0.028 (Supplementary Figure S5a). However, a more stable surface with high biomass yield was observed for a large set of conditions when the N:C ratio was kept at 0.025 and the N-source was composed mostly of nitrate, regardless of the C-source used (Supplementary Figures S5f,h).

When looking at PHB production as the response of interest, methane-grown cells accumulated more PHB with ammonium

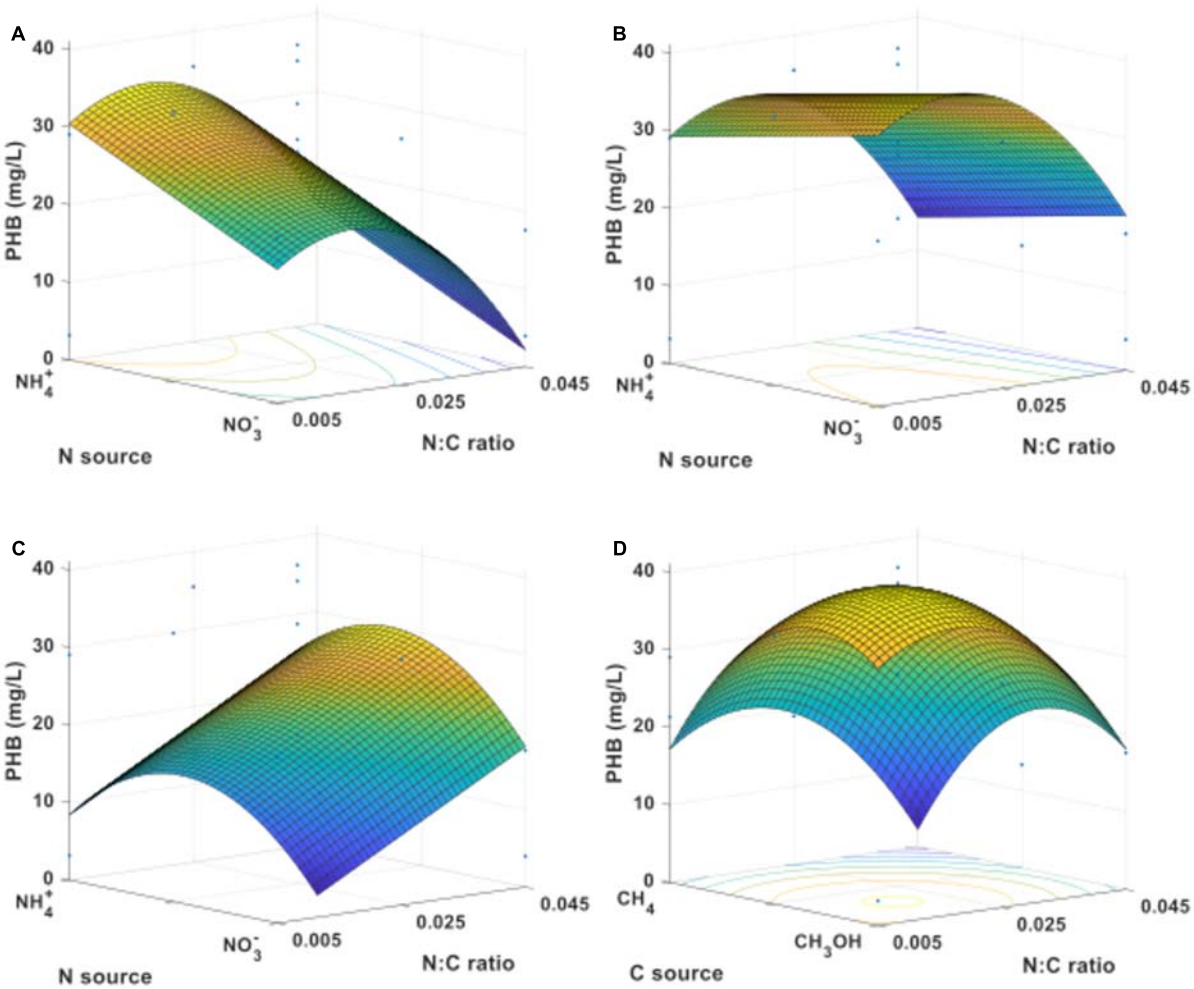


**FIGURE 6 |** PHB concentration response surfaces for *M. trichosporium* OB3b growing on **(A)** methane, **(B)** an equimolar mixture of methane and methanol, or **(C)** methanol as C-source. **(D)** Response surface leading to optimal concentration (nitrate as N-source).

as the nitrogen source (**Figure 6A**), whereas nitrate was preferred for PHB accumulation in methanol-grown cultures (**Figure 6C**). Interestingly, a greater amount of PHB accumulated when using a mixture of methane and methanol than when using either carbon source alone (**Figure 6B**), indicating a synergistic effect between the two carbon sources. In these cultures, nitrate was the preferred N-source for PHB accumulation. The maximum accumulation of PHB was predicted and confirmed experimentally from a mixture of 30% mol methane and 70% mol methanol as C-source, nitrate as the sole N-source, and a N:C ratio of 0.017. Many important observations can be made from these results. (1) The optimal N:C ratio for PHB production (0.017) is lower than the optimum ratio for biomass accumulation (0.025–0.028), highlighting how different conditions are required to optimize growth and PHB production during growth. (2) The maximum in PHB production (48.7 ± 8.3 mg/L) was obtained in simple batch operation and could be further improved through fed-batch operation. (3) The resulting PHB cell content of 52.5 ± 6.3% on a cell dry weight basis is significantly higher than that obtained in typical batch cultures without any period of nitrogen limitation. In fact, unlike prior studies on optimizing PHB accumulation in *M. trichosporium* OB3b, the results were obtained without relying on extended periods of nutrient limitation (Asenjo and Suk, 1986; Doronina et al., 2008; Rostkowski et al., 2013; Zhang et al., 2017). This suggests that PHB production occurs when the bacterial population is actively growing, albeit while maintaining a low N:C ratio and a high O:C ratio in the cultures.

In addition to finding optimal conditions for growth and PHB production, the investigation of response surfaces enabled determination of conditions for which output (cells or PHB) was less affected by varying conditions. For example, the PHB concentration showed less overall dependence on N-source when cells were grown on equimolar mixtures of methane and methanol than with single carbon sources.

Taking these results together, this study highlights how PHB production by *M. trichosporium* OB3b can be maximized by growth on a methane–methanol mixture as the C-source, nitrate

for the N-source, and a two-phase N:C ratio, in which a higher N:C ratio would favor biomass accumulation and a lower N:C ratio would benefit PHB accumulation. Proper aeration and a high O:C ratio is a critical factor for PHB production in *M. trichosporium* OB3b.

By determining the impact of multiple factors, this study serves as a guideline for establishing optimized industrial conditions for PHB production by methanotrophic bacteria using different C1 compounds and combinations as feedstock. In addition, this modeling exercise helped define specific conditions to maximize either biomass or PHB production and reveal the most critical conditions to control biological processes. As more commercially relevant products resulting from the bioconversion of methane are being identified or developed through genetic engineering, and as more methanotrophic bacterial strains undergo industrialization, it becomes important to develop rapid and efficient strategies facilitating and optimizing bioprocessing. The present study demonstrates how RSM can help rapidly identify optimal conditions for production, even in well-known systems.

## AUTHOR CONTRIBUTIONS

JZC, LS, and DS conceived the idea and wrote the manuscript. JZC carried out the experiments. JZC and DS created the images and plots. LS and DS supervised the work. All authors have given consent to the final version of the manuscript.

## FUNDING

This work was supported by a grant to LS and DS from Alberta Innovates Bio Solutions and the Biorefining Conversions Network. JZC was supported by CONACyT, SEP, and the Government of Mexico graduate studies scholarships.

## SUPPLEMENTARY MATERIAL

The Supplementary Material for this article can be found online at: https://www.frontiersin.org/articles/10.3389/fmicb.2018.01513/full#supplementary-material

## REFERENCES

Asenjo, J. A., and Suk, J. S. (1986). Microbial conversion of methane into poly-β-hydroxybutyrate (PHB): growth and intracellular product accumulation in a type-II methanotroph. *J. Ferment. Technol.* 64, 271–278. doi: 10.1016/0385-6380(86)90118-4

Braunegg, G., Sonnleitner, B., and Lafferty, R. M. (1978). Rapid gas-chromatographic method for determination of poly-beta-hydroxybutyric acid in microbial biomass. *Eur. J. Appl. Microbiol. Biotechnol.* 6, 29–37. doi: 10.1007/BF00500854

Chidambarampadmavathy, K., Karthikeyan, O. P., and Heimann, K. (2017). Sustainable bio-plastic production through landfill methane recycling. *Renew. Sustain. Energy Rev.* 71, 555–562. doi: 10.1016/j.rser.2016.12.083

Doronina, N. V., Ezhov, V. A., and Trotsenko, Iu. A. (2008). Growth of *Methylosinus trichosporium* OB3b on methane and poly-(-hydroxybutyrate biosynthesis. *Appl. Biochem. Microbiol.* 44, 182–185. doi: 10.1134/S0003683808020099

Fei, Q., Guarnieri, M. T., Tao, L., Laurens, L. M. L., Dowe, N., and Pienkos, P. T. (2014). Bioconversion of natural gas to liquid fuek: opportunities and challenges. *Biotechnol. Adv.* 32, 596–614. doi: 10.1016/j.biotechadv.2014.03.011

Lee, S. Y. (1996). Bacterial polyhydroxyalkanoates. *Biotechnol. Bioeng.* 49, 1–14. doi: 10.1002/(SICI)1097-0290(19960105)49:1<1::AID-BIT1>3.0.CO;2-P

Myers, R. H., Montgomery, D. C., and Anderson-Cook, C. M. (2016). *Response Surface Methodology: Process and Product Optimization Using Designed Experiments*. Hoboken, NJ: Wiley.

Oehmen, A., Keller-Lehmann, B., Zeng, R. J., Yuan, Z. G., and Keller, E. (2005). Optimisation of poly-beta-hydroxyalkanoate analysis using gas chromatography for enhanced biological phosphorus removal systems. *J. Chromatogr. A* 1070, 131–136. doi: 10.1016/j.chroma.2005.02.020

Pieja, A. J., Sundstrom, E. R., and Criddle, C. S. (2011). Poly-3-hydroxybutyrate metabolism in the type II methanotroph *Methylocystis parvus* OBBP. *Appl. Environ. Microbiol.* 77, 6012–6019. doi: 10.1128/AEM.00509-11

Rostkowski, K. H., Pfluger, A. R., and Criddle, C. S. (2013). Stoichiometry and kinetics of the PHB-producing Type II methanotrophs *Methylosinus trichosporium* OB3b and *Methylocystis parvus* OBBP. *Bioresour. Technol.* 132, 71–77. doi: 10.1016/j.biortech.2012.12.129

Strong, P. J., Xie, S., and Clarke, W. P. (2015). Methane as a resource: can the methanotrophs add value. *Environ. Sci. Technol.* 49, 4001–4018. doi: 10.1021/es504242n

Whittenbury, R., Phillips, K. C., and Wilkinson, J. F. (1970). Enrichment, isolation and some properties of methane-utilizing bacteria. *J. Gen. Microbiol.* 61, 205–218. doi: 10.1099/00221287-61-2-205

Zhang, T. T., Zhou, J. T., Wang, X. W., and Zhang, Y. (2017). Coupled effects of methane monooxygenase and nitrogen source on growth and poly-beta-hydroxybutyrate (PHB) production of *Methylosinus trichosporium* OB3b. *J. Environ. Sci.* 52, 49–57. doi: 10.1016/j.jes.2016.03.001

**Conflict of Interest Statement:** The authors declare that the research was conducted in the absence of any commercial or financial relationships that could be construed as a potential conflict of interest.

frontiers in Microbiology

ORIGINAL RESEARCH
published: 27 November 2018
doi: 10.3389/fmicb.2018.02735

# Rare Earth Elements Alter Redox Balance in *Methylomicrobium alcaliphilum* 20Z$^R$

*Ilya R. Akberdin[1,2,3†], David A. Collins[1], Richard Hamilton[1], Dmitry Y. Oshchepkov[2], Anil K. Shukla[4], Carrie D. Nicora[4], Ernesto S. Nakayasu[4], Joshua N. Adkins[4] and Marina G. Kalyuzhnaya[1*]*

[1] Biology Department, Viral Information Institute, San Diego State University, San Diego, CA, United States, [2] Institute of Cytology and Genetics SB RAS, Novosibirsk, Russia, [3] Novosibirsk State University, Novosibirsk, Russia, [4] Biological Sciences Division, Pacific Northwest National Laboratory, Richland, WA, United States

OPEN ACCESS

**Edited by:**
Martin G. Klotz,
Washington State University,
United States

**Reviewed by:**
Lisa Y. Stein,
University of Alberta, Canada
Huub J.M. Op den Camp,
Radboud University, Netherlands

***Correspondence:**
Marina G. Kalyuzhnaya
mkalyuzhnaya@sdsu.edu

**†Present address:**
Ilya R. Akberdin,
Novosibirsk State University,
Novosibirsk, Russia;
Institute of Cytology and Genetics SB
RAS, Novosibirsk, Russia

**Specialty section:**
This article was submitted to
Microbiological Chemistry
and Geomicrobiology,
a section of the journal
Frontiers in Microbiology

**Received:** 10 July 2018
**Accepted:** 25 October 2018
**Published:** 27 November 2018

**Citation:**
Akberdin IR, Collins DA,
Hamilton R, Oshchepkov DY,
Shukla AK, Nicora CD, Nakayasu ES,
Adkins JN and Kalyuzhnaya MG
(2018) Rare Earth Elements Alter
Redox Balance in Methylomicrobium
alcaliphilum 20Z$^R$.
Front. Microbiol. 9:2735.
doi: 10.3389/fmicb.2018.02735

**Background:** Rare Earth Elements (REEs) control methanol utilization in both methane- and methanol-utilizing microbes. It has been established that the addition of REEs leads to the transcriptional repression of MxaFI-MeDH [a two-subunit methanol dehydrogenase (MeDH), calcium-dependent] and the activation of XoxF-MeDH (a one-subunit MeDH, lanthanum-dependent). Both enzymes are pyrroquinoline quinone-dependent alcohol dehydrogenases and show significant homology; however, they display different kinetic properties and substrate specificities. This study investigates the impact of the MxaFI to XoxF switch on the behavior of metabolic networks at a global scale.

**Results:** In this study we investigated the steady-state growth of *Methylomicrobium alcaliphilum* 20Z$^R$ in media containing calcium (Ca) or lanthanum (La, a REE element). We found that cells supplemented with La show a higher growth rate compared to Ca-cultures; however, the efficiency of carbon conversion, estimated as biomass yield, is higher in cells grown with Ca. Three complementary global-omics approaches–RNA-seq transcriptomics, proteomics, and metabolomics–were applied to investigate the mechanisms of improved growth vs. carbon conversion. Cells grown with La showed the transcriptional activation of the *xoxF* gene, a homolog of the formaldehyde-activating enzyme (*fae2*), a putative transporter, genes for hemin-transport proteins, and nitrate reductase. In contrast, genes for *mxaFI* and associated cytochrome (*mxaG*) expression were downregulated. Proteomic profiling suggested additional adjustments of the metabolic network at the protein level, including carbon assimilation pathways, electron transport systems, and the tricarboxylic acid (TCA) cycle. Discord between gene expression and protein abundance changes points toward the possibility of post-transcriptional control of the related systems including key enzymes of the TCA cycle and a set of electron-transport carriers. Metabolomic data followed proteomics and showed the reduction of the ribulose-monophosphate (RuMP) pathway intermediates and the increase of the TCA cycle metabolites.

**Conclusion:** Cells exposed to REEs display higher rates of growth but have lower carbon conversion efficiency compared to cells supplemented with Ca. The most plausible explanation for these physiological changes is an increased conversion of methanol into formate by XoxF-MeDH, which further stimulates methane oxidation but limits both the supply of reducing power and flux of formaldehyde into the RuMP pathway.

**Keywords: *Methylomicrobium alcaliphilum* 20Z$^R$ strain, methanol dehydrogenase, MxaFI, XoxF, transcriptomics, proteomics, metabolomics**

## INTRODUCTION

Methanotrophs are promising systems for mitigating greenhouse gas emissions, enhancing bioremediation, and producing feed, fuel, and chemicals (Kirschke et al., 2013; Strong et al., 2016; Handler and Shonnard, 2018). This growing interest in environmental or commercial applications has directed research toward a system-level understanding of biological methane utilization (Karlsen et al., 2011; Matsen et al., 2013; Yang et al., 2013; de la Torre et al., 2015; Akberdin et al., 2018).

The metabolic network of methane oxidation is surprisingly redundant. To consume methane, a methanotroph must have at least one of the two monooxygenases (MMO) for methane oxidation: a particulate or membrane bound form of MMO (pMMO) and/or a soluble MMO (sMMO) which is compartmentalized into cytoplasm. Both enzymes require oxygen and an additional source of reducing power for methane activation, and both convert methane to methanol and water. The second metabolic reaction is catalyzed by a pyrroquinoline quinone (PQQ)-linked methanol dehydrogenase (MeDH) (Myronova et al., 2006; de la Torre et al., 2015; Semrau et al., 2018). At least two forms of MeDH have been described: a calcium-containing two-subunit MeDH, MxaFI-MeDH, and, an alternative single-subunit enzyme, XoxF-MeDH (Fitriyanto et al., 2011; Hibi et al., 2011; Nakagawa et al., 2012; Pol et al., 2014; Haque et al., 2015). Several metabolic routes can contribute to formaldehyde oxidation (Chistoserdova, 2011), and up to four formate dehydrogenases can contribute to the final step of methane oxidation (Chistoserdova et al., 2004; Chistoserdova and Kalyuzhnaya, 2018).

Numerous microelements have been established or are newly emerging as control points for primary methane oxidation (Glass and Orphan, 2012; Chidambarampadmavathy et al., 2015; Semrau et al., 2018). Three key metabolic switches have been described: (1) a copper-switch, which controls the expression and activity of primary methane oxidation (Stanley et al., 1983; Semrau et al., 2018); (2) a tungsten-molybdenum (W/Mo) switch for formate oxidation (Laukel et al., 2003; Chistoserdova et al., 2004; Akberdin et al., 2018); and (3) a La-switch, which negatively regulates the expression of MxaFI-MeDH and activates XoxF-MeDH (Haque et al., 2015; Chu and Lidstrom, 2016; Chu et al., 2016; Gu and Semrau, 2017; Semrau et al., 2018). Initial evidence with microbial systems that have all three types of these metabolic switches highlights the complexity of metabolic responses and suggests crosstalk between copper and REE pathways (Gu and Semrau, 2017; Semrau et al., 2018). Furthermore, substitutions at the level of a single metabolic step are not always metabolically neutral and can impact the overall cellular network. For example, a lack of copper is linked to a change from pMMO to sMMO, which leads to a significant drop in carbon conversion efficiencies and growth rates (Leak and Dalton, 1986; DiSpirito et al., 2016; Kenney and Rosenzweig, 2018). This change could be linked to the specific requirement of sMMO for NADH, which contributes to the redox limitation upon copper starvation (Leak and Dalton, 1986). Differences in growth rate and/or biomass yield have also been noted for a switch from Ca to REEs for some methylotrophic bacteria (Vu et al., 2016; Good et al., 2018; Masuda et al., 2018). It has been demonstrated that the expression of MxaFI-MeDH only occurs in the absence of La, making XoxF-MeDH a more preferable system for carbon utilization in microbes using the serine cycle pathway for carbon utilization (Good et al., 2018). However, it still remains unclear why the substitution of one PQQ-dependent dehydrogenase with another functionally similar PQQ-dependent dehydrogenase impacts overall carbon utilization. Both enzymes can convert methanol to formaldehyde and formaldehyde to formate *in vitro* (Anthony and Williams, 2003; Schmidt et al., 2010; Keltjens et al., 2014; Huang et al., 2018), but whether this is true *in vivo* remains controversial. The activity of MxaFI-MeDH could be modulated, making formaldehyde the main product (97%) *in vivo* (Page and Anthony, 1986). The enzyme couples methanol oxidation with the reduction of cytochrome $c_L$, which passes electrons to cythocrome $c_H$, and then to a cytochrome oxidase (Anthony and Williams, 2003). The overall balance of the reaction could be presented as following:

$$CH_3OH + {}^1/_2O_2 + 0.5-1\,ATP + 0.5-1Pi = CH_2O + H_2O + 0.5-1\,ATP$$

Dual activity, methanol-to-formaldehyde and formaldehyde to-formate, has been proposed for the XoxF-MeDHs *in vivo* (Keltjens et al., 2014). If the dual activity indeed occurs, the overall balance could be summarized as:

$$CH_3OH + O_2 + 1-2\,ATP + 1-2\,Pi = CHOOH + H_2O + 1-2\,ATP$$

While in verrucomicrobial methanotrophs (assimilating carbon via the Rubisco pathway) as well as alphaptoteobacterial

methanotrphs (assimilating carbon from formate), the dual activity does not directly impact carbon assimilation, it could be predicted that in methanotrophs with the formaldehyde assimilation pathways the dual methanol/formaldehyde activity can lead to several metabolic challenges, including redox limitation and restriction of formaldehyde flux into $C_1$-assimilation. The global metabolic consequences of a MxaFI-MeDH to XoxF-MeDH swap in microbes possessing both systems remain to be investigated. Nevertheless, XoxF-MeDH has been described as the preferred system for methane and methanol utilization (Chu et al., 2016; Yu et al., 2017; Huang et al., 2018). Five families of XoxF-MeDH homologs have been described, and it is becoming apparent that they display different catalytic properties and might be linked to different electron transport systems (Yu et al., 2017; Huang et al., 2018; Zheng et al., 2018). Some XoxF's cluster together with cytochrome-like genes; the electron acceptors for others are not apparent. Among the latter are the XoxF5-MeDHs found in gammaproteobacterial methanotrophs. An association between XoxF5 and a cytochrome b1 homolog (*xoxG4*) has been proposed (Yu et al., 2017); however, expression of the cytochrome does not parallel *xoxF* expression in *Methylomonas* LW13 and an *xoxG4*-mutant shows a strikingly different phenotype (Huang et al., 2018), indicating that an alternative electron-transfer partner (or partners) must be coupled with XoxF5-MeDH (Huang et al., 2018).

In this study, we examine the metabolic response of *Methylomicrobium alcaliphilum* $20Z^R$ to REEs at the global scale via transcriptomic, proteomic and metabolomic studies. *M. alcaliphilum* $20Z^R$ has only one enzyme for methane oxidation (pMMO, copper dependent), two MeDHs (MxaFI-MeDH and XoxF5-MeDH), and only one tungsten-dependent formate dehydrogenase and thus it represents a good model for investigating the REE-mediated switch independently from copper or W/Mo responses.

# RESULTS

## Ca vs. La: Growth Parameters

Two continuous cultures of *M. alcaliphilum* $20Z^R$ were set up as described in Material and Methods and the main growth parameters are summarized in **Table 1** and **Supplementary Figure S1**. The steady-state growth of the Ca-supplemented culture was established as a specific growth rate of 0.05 $h^{-1}$ was observed for both, 5% $CH_4$ : 5%$O_2$ (optimal) and 2.5% $CH_4$ : 10%$O_2$ (methane-limited) gas supply. The growth rate was higher for the La-supplemented culture, reaching 0.07 $h^{-1}$ and 0.06 $h^{-1}$ at optimal and methane-limited inputs, respectively. The overall biomass yield ($Y_B$) reached 1.2 in Ca-supplemented cultures and 0.67 in cultures supplemented with La. Oxygen consumption also differed between Ca and La conditions, with cells grown with La consuming more oxygen per methane converted compared to cells grown with Ca (1.28 vs. 1.12). Reduction in the methane supply and/or an increased $O_2$ supply ratio led to a 1.8-fold reduction in the growth rate of the La-supplemented cells (**Table 1**). Samples of cells grown at optimal conditions and methane-limiting conditions were used for gene expression studies. All other *omics*-studies were done only with samples of cells grown at optimal conditions.

## Ca vs. La: Gene Expression Profiles

Samples of bioreactor cultures (two biological replicates per tested growth condition) were collected for generating gene-expression profiles using RNA-sequencing technology. Transcriptomes of replicates for both growth conditions are highly similar; the Pearson's correlation between the two replicates for both Ca-added and La-added samples was >0.98. Over 800 genes were found to have statistically significant differential expression between the two growth conditions (i.e., a Benjamini-Hochberg adjusted *p*-value < 0.05) with 150 genes having a | log2| change ≥1.5 (**Table 2** and **Supplementary Table S1**).

Twenty-four genes were identified as significantly downregulated when the $20Z^R$ culture was supplemented with La instead of Ca (**Supplementary Table S1**). The set includes 13 genes encoding the two-subunit MeDh MxaFi, its corresponding cytochrome, proteins essential for the enzyme's assembly and folding, and its response regulator, MxaB (MEALZ_3449). Among the other downregulated genes were two genes (MEALZ_3990, MEALZ_3991) which encode the MotA/TolQ/ExbB proton channel family protein. CorA (MEALZ_2831) and corB (MEALZ_2832) genes, predicted to encode a copper-repressible surface-associated protein and associated di-haem cytochrome c

**TABLE 1 |** Growth parameters and substrate consumption in continuous bioreactor cultures of *M. alcaliphilum* $20Z^R$ supplemented with Ca or La.

| Growth parameters | Ca | | La | |
|---|---|---|---|---|
| | **5%$CH_4$ : 5% $O_2$** | **2.5%$CH_4$ : 10%$O_2$** | **5%$CH_4$ : 5% $O_2$** | **2.5%$CH_4$ : 10%$O_2$** |
| Dilution rate* ($h^{-1}$) | 0.05 | 0.05 | 0.07 | 0.06 |
| Biomass* (g DCW $L^{-1}$) | 0.64 ± 0.01 | 0.67 ± 0.02 | 0.75 ± 0.05 | 0.45 ± 0.02 |
| Biomass yield (g biomass $g^{-1}$ $CH_4$ consumed) | 1.2 ± 0.1 | 0.98 ± 0.04 | 0.64 ± 0.01 | 0.67 ± 0.03 |
| $O_2$:$CH_4$ consumption ratio | 1.12 ± 0.09 | NT | 1.28 ± 0.01 | NT |
| $CH_4$ consumption (mmol $g^{-1}$ DCW $h^1$) | 2.59 ± 0.26 | 3.11 ± 0.11 | 6.75 ± 0.09 | 5.55 ± 0.2 |
| Biomass produced (mg DCW $h^{-1}$) | 31.8 ± 0.5 | 33.7 ± 1.02 | 53.1 ± 0.7 | 28.7 ± 1.1 |

*NT: not tested; *dilution rate or cell concentration at steady-state.*

**TABLE 2 |** Heatmap comparing the differentially expressed genes between Ca -and La-cultures.

| Enzyme/ Pathway | Function | Gene ID | Protein ID | La-opt vs Ca-opt (log2FC) | padj | Genes (Ca) | Genes Low CH4 (Ca) | Genes (La) | Genes Low CH4 (La) | Proteins (Ca) | Proteins (La) |
|---|---|---|---|---|---|---|---|---|---|---|---|
| **methane oxidation pMMO** | methane monooxygenase subunit C | MEALZ_0514 | CCE22212 | **-0.28** | 0.08 | **65473.29** | **97740.42** | **64428.13** | **95073.12** | 25.00 | 44.00 |
| | methane monooxygenase subunit A | MEALZ_0515 | CCE22213 | **-0.44** | 0.01 | **57201.14** | **93211.90** | **50262.84** | **90700.49** | 21.50 | 22.00 |
| | methane monooxygenase subunit B | MEALZ_0516 | CCE22214 | **-0.54** | 0.00 | **53103.79** | **90712.04** | **43556.32** | **88220.61** | 446.50 | 569.50 |
| **methanol oxidation MxaFI-MeDH** | MxaL protein | MEALZ_3438 | CCE25101 | **-4.18** | 0.00 | 689.02 | 768.44 | 46.27 | 10.21 | 5.50 | ND |
| | MxaK protein | MEALZ_3439 | CCE25102 | **-4.95** | 0.00 | 659.90 | 573.90 | 26.59 | 5.76 | 3.50 | ND |
| | MxaC protein | MEALZ_3440 | CCE25103 | **-5.62** | 0.00 | 631.24 | 698.39 | 15.71 | 6.80 | 3.00 | ND |
| | MxaA protein | MEALZ_3441 | CCE25104 | **-3.99** | 0.00 | 804.54 | 642.90 | 61.33 | 5.85 | ND | ND |
| | MxaS protein | MEALZ_3442 | CCE25105 | **-6.27** | 0.00 | 843.14 | 780.22 | 13.75 | 4.87 | 4.50 | ND |
| | MxaP protein | MEALZ_3443 | CCE25106 | **-5.65** | 0.00 | 1030.53 | 884.70 | 25.34 | 4.47 | ND | ND |
| | cytochrome cL (mxaG) | MEALZ_3446 | CCE25109 | **-8.81** | 0.00 | 10717.47 | 8588.22 | 28.82 | 13.13 | 11.00 | ND |
| | methanol dehydrogenase, small subunit | MEALZ_3445 | CCE25108 | **-8.27** | 0.00 | 12616.14 | 10996.95 | 48.55 | 26.21 | 8.00 | ND |
| | methanol dehydrogenase, large subunit | MEALZ_3448 | CCE25111 | **-9.91** | 0.00 | 13570.19 | 12905.47 | 17.09 | 8.73 | 91.00 | 2.00 |
| | DNA binding response regulator | MEALZ_3449 | CCE25112 | **-4.99** | 0.00 | 514.54 | 433.88 | 20.30 | 6.16 | ND | ND |
| **XoxF-MeDH** | dehydrogenase xoxF | MEALZ_3497 | CCE25159 | **3.78** | 0.00 | 269.28 | 259.39 | 4423.36 | 4875.86 | 61.50 | 133.00 |
| | MxaJ-like protein | MEALZ_3498 | CCE25160 | **-0.20** | 0.36 | 211.51 | 172.51 | 219.11 | 166.15 | 8.50 | 7.00 |
| | cytochrome X (putative xoxG4) | MEALZ_2642 | CCE24317 | **-0.45** | 0.00 | 3210.01 | 5758.24 | 2808.10 | 6285.63 | 5.50 | 4.50 |
| **formaldehyde oxidation** | formaldehyde-activating enzyme | MEALZ_2428 | CCE24109 | **-0.34** | 0.02 | 5246.70 | 5445.82 | 4946.04 | 6451.78 | 153.50 | 158.50 |
| | formaldehyde-activating enzyme 4 | MEALZ_1456 | CCE23144 | **-0.47** | 0.01 | 1244.41 | 1027.31 | 1077.22 | 1163.18 | 13.50 | 12.00 |
| | formaldehyde-activating enzyme 2 | MEALZ_0850 | CCE22544 | **4.25** | 0.00 | 515.74 | 446.55 | 11743.57 | 5776.55 | 2.50 | 5.50 |
| | sulfide:quinone oxidoreductase// aldehyde dehydrogeanse | MEALZ_0272 | CCE21972 | **0.26** | 0.37 | 40.01 | 39.33 | 57.55 | 43.18 | 1.50 | 1.00 |
| **formate oxidation** | Tungsten-containing formate dehydrogenase, beta subunit | MEALZ_1883 | CCE23569 | **-0.15** | 0.41 | 579.98 | 436.55 | 623.33 | 480.87 | 15.00 | 14.50 |
| | Tungsten-containing formate dehydrogenase, alpha subunit | MEALZ_1882 | CCE23568 | **-0.17** | 0.33 | 499.65 | 408.24 | 530.70 | 449.79 | 30.50 | 36.00 |
| | Molybdenum containing formate dehydrogenase, delta | MEALZ_0215 | CCE21915 | **0.16** | 0.73 | 80.46 | 60.76 | 107.16 | 69.04 | ND | ND |
| | Molybdenum containing formate dehydrogenase, accessory | MEALZ_0216 | CCE21916 | **1.81** | 0.01 | 2.42 | 1.92 | 10.52 | 1.99 | ND | ND |
| | Molybdenum containing formate dehydrogenase, alpha | MEALZ_0217 | CCE21917 | **2.02** | 0.00 | 1.53 | 1.11 | 7.51 | 1.61 | ND | ND |
| **ETS Complex I** | Na(+)-translocating NADH-quinone reductase subunit F | MEALZ_2228 | CCE23914 | **-0.34** | 0.03 | 948.88 | 974.60 | 898.24 | 975.82 | 19.00 | 21.50 |
| | Na(+)-translocating NADH-quinone reductase subunit E | MEALZ_2229 | CCE23915 | **-0.54** | 0.00 | 786.28 | 842.31 | 647.84 | 841.11 | ND | ND |
| | Na(+)-translocating NADH-quinone reductase subunit D | MEALZ_2230 | CCE23916 | **-0.37** | 0.02 | 858.43 | 887.83 | 793.40 | 901.67 | 4.00 | 4.00 |
| | Na(+)-translocating NADH-quinone reductase subunit C | MEALZ_2231 | CCE23917 | **-0.23** | 0.16 | 1149.23 | 1023.87 | 1170.65 | 1045.60 | 24.00 | 27.00 |
| | Na(+)-translocating NADH-quinone reductase subunit B | MEALZ_2232 | CCE23918 | **-0.55** | 0.00 | 750.09 | 797.14 | 611.54 | 773.52 | 7.00 | 9.00 |
| | Na(+)-translocating NADH-quinone reductase subunit A | MEALZ_2233 | CCE23919 | **-0.42** | 0.00 | 882.95 | 828.70 | 789.60 | 897.33 | 23.00 | 30.50 |
| | quinolinate synthase A | MEALZ_2234 | CCE23920 | **-0.49** | 0.00 | 434.11 | 440.83 | 370.43 | 455.20 | 4.50 | 5.00 |
| | NAD-reducing hydrogenase hoxS subunit beta | MEALZ_1304 | CCE22993 | **0.08** | 0.71 | 229.65 | 145.18 | 290.34 | 164.56 | 28.50 | 33.00 |
| | NAD-reducing hydrogenase hoxS subunit delta | MEALZ_1305 | CCE22994 | **-0.06** | 0.84 | 167.49 | 135.80 | 193.26 | 140.58 | ND | ND |
| | NADH:ubiquinone oxidoreductase, subunit gamma | MEALZ_1306 | CCE22995 | **0.18** | 0.39 | 266.03 | 157.46 | 359.47 | 181.41 | 10.00 | 10.50 |
| | NAD-reducing hydrogenase hoxS subunit alpha | MEALZ_1307 | CCE22996 | **0.04** | 0.85 | 197.84 | 137.63 | 244.08 | 146.55 | 10.00 | 11.00 |
| | NADH dehydrogenase | MEALZ_1287 | CCE22976 | **-0.21** | 0.34 | 160.26 | 126.49 | 165.34 | 142.30 | 2.00 | 4.00 |
| | NADH ubiquinone oxidoreductase 2 | MEALZ_3726 | CCE25382 | **0.21** | 0.58 | 31.78 | 36.16 | 44.25 | 42.50 | 1.00 | ND |
| **ETS Complex II** | sdhX, hypothetical protein | MEALZ_2678 | CCE24353 | **-0.07** | 0.85 | 212.40 | 214.25 | 243.02 | 282.00 | ND | ND |
| | sdhB, succinate dehydrogenase | MEALZ_2679 | CCE24354 | **0.15** | 0.52 | 197.39 | 179.65 | 263.72 | 221.97 | 1.00 | 2.50 |
| | sdhA, succinate dehydrogenase | MEALZ_2680 | CCE24355 | **0.09** | 0.73 | 207.64 | 205.73 | 264.67 | 249.54 | 10.50 | 9.50 |
| | sdhE, succinate dehydrogenase, hydrophobic membrane | MEALZ_2681 | CCE24356 | **-0.04** | 0.90 | 165.45 | 184.94 | 194.39 | 209.19 | ND | ND |
| | succinate dehydrogenase cytochrome b556 subunit | MEALZ_2682 | CCE24357 | **0.27** | 0.25 | 203.43 | 155.44 | 292.92 | 214.66 | ND | ND |
| **ETS Complex III** | cytochrome c1 | MEALZ_0632 | CCE22327 | **-0.16** | 0.48 | 358.64 | 398.98 | 386.35 | 399.76 | 16.50 | 16.00 |
| | cytochrome b | MEALZ_0633 | CCE22328 | **-0.33** | 0.04 | 467.63 | 464.02 | 443.99 | 469.18 | 7.00 | 9.50 |
| | Ubiquinol-cytochrome c reductase | MEALZ_0634 | CCE22329 | **-0.24** | 0.19 | 667.87 | 562.54 | 674.46 | 577.49 | 12.50 | 17.00 |
| **Cytochromes** | cytochrome B557.5 | MEALZ_1724 | CCE23411 | **0.47** | 0.01 | 1785.56 | 192.21 | 2954.21 | 314.64 | ND | ND |
| | bacterioferritin-associated ferredoxin Bfd | MEALZ_1725 | CCE23412 | **-0.10** | 0.70 | 1361.35 | 60.92 | 1509.01 | 159.81 | ND | ND |
| | cytochrome c6 | MEALZ_0938 | CCE22632 | **-0.67** | 0.00 | 479.53 | 1507.70 | 360.87 | 1259.22 | 20.50 | 24.00 |
| | cytochrome c class I | MEALZ_0390 | CCE22090 | **-0.11** | 0.62 | 363.43 | 364.88 | 403.78 | 373.60 | 1.00 | ND |
| | cytochrome b561 | MEALZ_0602 | CCE22297 | **-0.09** | 0.79 | 115.42 | 118.04 | 130.25 | 123.28 | ND | ND |
| | cytochrome P460 | MEALZ_0918 | CCE22612 | **0.14** | 0.55 | 219.56 | 169.35 | 289.14 | 200.08 | 1.00 | 2.50 |
| | cytochrome c'-beta | MEALZ_0702 | CCE22397 | **0.40** | 0.03 | 391.12 | 318.93 | 617.20 | 401.66 | 4.00 | 3.50 |
| | cytochrome c class I | MEALZ_1120 | CCE22811 | **0.18** | 0.40 | 356.02 | 289.60 | 480.56 | 323.23 | ND | ND |
| | cytochrome c family protein | MEALZ_1295 | CCE22984 | **0.09** | 0.75 | 158.96 | 127.70 | 202.29 | 120.21 | 1.00 | ND |
| | cytochrome-c peroxidase | MEALZ_3827 | CCE25482 | **0.20** | 0.39 | 102.65 | 79.37 | 139.84 | 98.38 | 8.50 | 9.50 |
| **ETS Complex IV cytochrome caa3 oxidase** | cytochrome C oxidase polypeptide III | MEALZ_2312 | CCE23993 | **-0.53** | 0.00 | 877.93 | 905.31 | 728.71 | 799.40 | 1.00 | 1.00 |
| | cytochrome C oxidase assembly protein | MEALZ_2313 | CCE23994 | **-0.17** | 0.47 | 587.12 | 453.10 | 622.55 | 402.11 | 2.00 | 2.00 |
| | cytochrome aa3 oxidase subunit I | MEALZ_2314 | CCE23995 | **-0.55** | 0.00 | 1006.03 | 914.50 | 823.15 | 804.18 | 1.50 | 3.50 |
| | cytochrome C oxidase subunit II | MEALZ_2315 | CCE23996 | **-0.43** | 0.00 | 1208.03 | 1094.88 | 1071.89 | 974.78 | 21.00 | 25.00 |
| | Bacteriohemerythrin | MEALZ_2316 | CCE23997 | **0.36** | 0.26 | 72.90 | 53.74 | 110.44 | 57.30 | 40.50 | 42.00 |
| **ETS Complex IV cytochrome ba3 oxidase** | cytochrome c oxidase, CbaD subunit | MEALZ_1292 | CCE22981 | **-0.34** | 0.57 | 79.12 | 61.42 | 72.48 | 63.12 | 1.00 | ND |
| | cytochrome C oxidase subunit II | MEALZ_1293 | CCE22982 | **-0.17** | 0.50 | 188.64 | 156.40 | 201.29 | 164.12 | 1.00 | 1.00 |
| | cytochrome C oxidase subunit I | MEALZ_1294 | CCE22983 | **-0.67** | 0.00 | 138.55 | 145.87 | 104.11 | 138.90 | ND | ND |
| **ATP biosynthesis** | ATP synthase subunit beta 2 | MEALZ_3735 | CCE25391 | **-0.24** | 0.23 | 138.00 | 118.59 | 139.40 | 138.45 | 2.00 | 1.50 |
| | ATP synthase subunit b 2 | MEALZ_3741 | CCE25397 | **-0.14** | 0.57 | 195.05 | 170.96 | 212.03 | 186.63 | 3.50 | 4.00 |
| **RuMP and PPP** | 3-hexulose-6-phosphate isomerase | MEALZ_3952 | CCE25608 | **-0.69** | 0.00 | 7543.78 | 9636.93 | 5596.85 | 9470.10 | 21.00 | 27.50 |
| | 3-hexulose-6-phosphate synthase | MEALZ_3953 | CCE25609 | **-0.78** | 0.00 | 6740.80 | 8399.37 | 4683.75 | 8291.52 | 61.00 | 86.00 |
| | hexulose-6-phosphate synthase and isomerase | MEALZ_1912 | CCE23598 | **-0.21** | 0.22 | 765.17 | 912.68 | 792.46 | 1055.04 | 26.50 | 30.50 |
| | transaldolase | MEALZ_3948 | CCE25604 | **-0.21** | 0.20 | 4445.53 | 4118.09 | 4594.00 | 4485.83 | 172.50 | 213.50 |
| | transketolase | MEALZ_3951 | CCE25607 | **-0.54** | 0.00 | 6201.76 | 5916.17 | 5120.95 | 6328.24 | 181.50 | 208.50 |
| **EMP** | fructose-bisphosphate aldolase | MEALZ_3947 | CCE25603 | **-0.27** | 0.08 | 2769.21 | 2694.18 | 2756.52 | 2752.64 | 72.00 | 75.00 |
| | glyceraldehyde 3-phosphate dehydrogenase | MEALZ_3079 | CCE24745 | **0.06** | 0.79 | 2904.50 | 1779.34 | 3626.15 | 1978.75 | 33.50 | 55.50 |
| | pyruvate kinase II | MEALZ_3080 | CCE24746 | **-0.42** | 0.01 | 1641.40 | 1445.04 | 1470.73 | 1465.06 | 42.00 | 54.00 |
| | phosphoglycerate kinase | MEALZ_3549 | CCE25207 | **-0.20** | 0.26 | 366.72 | 300.46 | 381.43 | 311.65 | 30.50 | 31.50 |
| **EDD/oxPPP** | glucose-6-phosphate isomerase | MEALZ_0104 | CCE21808 | **-0.04** | 0.88 | 280.61 | 212.73 | 326.41 | 238.58 | 9.50 | 13.00 |
| | glucose 1-dehydrogenase 1 | MEALZ_1699 | CCE23386 | **0.70** | 0.00 | 52.47 | 46.41 | 103.56 | 49.97 | ND | 1.00 |
| | 2-dehydro-3-deoxyphosphooctonate aldolase | MEALZ_1362 | CCE23051 | **-0.48** | 0.00 | 324.44 | 229.63 | 277.71 | 242.30 | 4.00 | 4.50 |
| | 6-phosphogluconate dehydratase | MEALZ_1363 | CCE23052 | **-0.20** | 0.25 | 219.37 | 165.21 | 227.95 | 165.39 | 14.00 | 21.50 |
| **TCA** | aconitate hydratase,acnA | MEALZ_0310 | CCE22010 | **0.05** | 0.84 | 74.11 | 92.19 | 73.58 | 77.53 | 12 | 17 |
| | citrate synthase, gltA2 | MEALZ_1360 | CCE23049 | **-0.13** | 0.51 | 313.42 | 247.64 | 341.16 | 263.16 | 14.5 | 20 |
| | succinate-semialdehyde dehydrogenase, gabD | MEALZ_1576 | CCE23263 | **-0.21** | 0.37 | 104.52 | 104.08 | 108.89 | 95.86 | 3.5 | 6.5 |
| | dihydrolipoyl dehydrogenase, odhL | MEALZ_1578 | CCE23265 | **0.02** | 0.95 | 147.76 | 139.40 | 175.52 | 140.77 | 6.5 | 10 |
| | 2-oxoglutarate dehydrogenase E2, sucB | MEALZ_1579 | CCE23266 | **-0.02** | 0.94 | 198.16 | 179.64 | 233.75 | 188.30 | 7.50 | 12.50 |
| | 2-oxoglutarate dehydrogenase E1, sucA | MEALZ_1580 | CCE23267 | **-0.06** | 0.77 | 156.25 | 131.02 | 178.70 | 136.03 | 9.00 | 10.50 |
| | citrate synthase, gltA | MEALZ_3024 | CCE24690 | **-0.14** | 0.54 | 227.83 | 191.10 | 247.17 | 204.72 | 4.5 | 6.5 |
| | aconitate hydratase 2, acnB | MEALZ_3025 | CCE24691 | **-0.44** | 0.00 | 365.28 | 312.03 | 322.00 | 316.58 | 29.5 | 37.5 |
| | isocitrate dehydrogenase, NAD-dependent, icd | MEALZ_3026 | CCE24692 | **-0.41** | 0.01 | 556.01 | 465.29 | 501.12 | 486.27 | 6.5 | 9 |
| | succinyl-CoA ligase subunit alpha | MEALZ_3290 | CCE24955 | **-0.02** | 0.94 | 213.87 | 202.39 | 253.00 | 212.29 | 4.50 | 6.50 |
| | isocitrate dehydrogenase NADP-dependent, icdh | MEALZ_3844 | CCE25499 | **-0.05** | 0.83 | 173.29 | 132.26 | 199.73 | 145.75 | 17.5 | 19.5 |
| **serine cycle and $H_4$folate pathway** | malate thiokinase, small subunit | MEALZ_3215 | CCE24880 | **-0.51** | 0.00 | 344.87 | 313.74 | 291.11 | 316.04 | 4.00 | 6.50 |
| | malate thiokinase, large subunit | MEALZ_3216 | CCE24881 | **-0.35** | 0.03 | 341.67 | 332.40 | 322.50 | 320.08 | 12.50 | 10.00 |
| | malyl-CoA lyase | MEALZ_3217 | CCE24882 | **-0.43** | 0.01 | 433.51 | 442.83 | 385.66 | 449.89 | 15.50 | 20.00 |
| | serine-glyoxylate aminotransferase | MEALZ_3218 | CCE24883 | **-0.43** | 0.01 | 811.13 | 634.88 | 721.11 | 645.32 | 33.00 | 42.50 |
| | 2-hydroxyacid dehydrogenase NAD-binding | MEALZ_3219 | CCE24884 | **-0.20** | 0.39 | 139.69 | 105.92 | 145.40 | 118.71 | 6.00 | 7.50 |
| | malate dehydrogenase | MEALZ_3220 | CCE24885 | **-0.31** | 0.05 | 598.35 | 579.41 | 577.73 | 601.64 | 4.00 | 11.00 |
| | NADP-methylenetetrahydrofolate dehydrogenase | MEALZ_3221 | CCE24886 | **-0.41** | 0.06 | 148.86 | 127.89 | 133.27 | 131.38 | 5.50 | 6.50 |
| | glycerate 2-kinase | MEALZ_3222 | CCE24887 | **-0.27** | 0.26 | 61.50 | 56.46 | 61.25 | 56.93 | 1.00 | 1.50 |
| | serine hydroxymethyltransferase | MEALZ_3223 | CCE24888 | **-0.26** | 0.13 | 318.48 | 271.90 | 318.23 | 299.86 | 20.00 | 20.50 |
| | formate-tetrahydrofolate ligase | MEALZ_3224 | CCE24889 | **-0.57** | 0.00 | 242.79 | 246.92 | 195.80 | 258.02 | 7.50 | 8.50 |
| **fatty acid metabolism** | acyl-coenzyme A dehydrogenase | MEALZ_0452 | CCE22151 | **0.89** | 0.05 | 3.47 | 3.81 | 7.89 | 3.63 | ND | 1.00 |
| | 3-hydroxyacyl-CoA dehydrogenase | MEALZ_0453 | CCE22152 | **1.58** | 0.00 | 5.76 | 6.13 | 21.37 | 8.06 | 1.00 | 2.00 |
| | 3-ketoacyl-CoA thiolase | MEALZ_0454 | CCE22153 | **1.49** | 0.00 | 3.82 | 3.99 | 13.23 | 3.60 | 1.00 | 4.50 |
| | squalene--hopene cyclase | MEALZ_2523 | CCE24201 | **1.71** | 0.00 | 8.27 | 7.65 | 32.60 | 9.72 | ND | ND |
| | dihydroxyacetone kinase | MEALZ_3955 | CCE25611 | **-0.10** | 0.73 | 97.54 | 93.43 | 109.25 | 85.89 | 5.00 | 8.50 |
| | dihydroxyacetone phosphatase | MEALZ_3956 | CCE25612 | **1.79** | 0.00 | 316.11 | 273.59 | 1314.59 | 835.45 | 4.50 | 7.50 |

Gene expression (FPKMs): >2000, >500, >249, >100, >50, >10, 0-10

Protein abundances (PSC): >200, 100 - 200, 50 - 99, 21 - 49, >10, 0-9

*Red/purple represents normalized gene expression (Fragments Per Kilobase Million, FPKM) and number of observed peptides in La-grown cells; blue/aquamarine represents normalized gene expression (FPKMs) and number of observed peptides in Ca-grown cells. Details of annotated genes/proteins shown on the right are provided in* ***Supplementary Tables S1***, ***S2***.

peroxidase (Karlsen et al., 2010; Shchukin et al., 2011; Johnson et al., 2014) were also downregulated in the presence of La.

A larger number of genes (126, representing 98 operons) were upregulated when La was added instead of Ca to the growth medium (**Supplementary Table S1** and **Figure 1**). A significant portion of these genes are represented by hypothetical proteins. Among genes with predicted cellular functions are the alternative mono-subunit MeDH gene, *xoxF* (MEALZ_3497), whose expression increased by fourfold; a putative formaldehyde-activating enzyme (*fae2*) gene; an operon of genes encoding delta (*fds2D*), gamma (*fds2C)* and a partial alpha subunit (*fds2A)* of molybdenum-dependent formate dehydrogenase (Fds2); beta-oxidation pathways (FadAB) of fatty acids; and squalene-hopene cyclase. Among other annotated genes responding to the presence of La are two sets of genes homologous to urea ABC transporters and the sulfate transport system, respectively.

The expression of *xoxG4* (MEALZ_2642), the putative cytochrome b proposed to accept electrons from the XoxF5 enzyme (Yu et al., 2017), was reduced 1.5-fold compared to Ca-grown cells (**Supplementary Table S1**). The expression of the cytochrome could be correlated with methane limitation rather than with La-growth (**Figure 1**). From 22 cytochromes identified in the genome of *M. alcaliphilum* $20Z^R$, four,—cytochrome P460 (MEALZ_0918), cytochrome c1-type (MEALZ_1120), cytochrome c'-beta (MEALZ_0702) and cytochrome B557.5 (MEALZ_1724) with associated ferredoxin (MEALZ_1724)—responded positively to the addition of La.

## Ca vs. La: Proteomics Data

Samples of cell cultures were also used to investigate protein profiles at the same growth time points used for transcriptomics analyses. More than twenty-seven hundred proteins were identified by quantitative proteomic analysis (**Figure 1**, **Table 2**, and **Supplementary Table S2**).

In general, the proteomic data correlated well with the gene-expression profiles for cells grown with La, showing lower levels of MxaFI-MeDH and associated cytochrome and accessory proteins than Ca-grown cells (**Table 2** and **Supplementary Table S2**).

Also in agreement with transcriptomic profiles, XoxF5-MeDH, formaldehyde-activating enzyme 2 and 3-ketoacyl-CoA thiolase abundances increased in response to La. No change in XoxG4 abundance was observed.

However, several differences between transcriptomics and proteomics datasets were observed (**Figure 1**, **Table 2**, and **Supplementary Tables S1**, **S2**). Among them are enzymes/accessory proteins involved in the central pathways of $C_1$-assimilation (methenyltetrahydromethanopterin cyclohydrolase), the TCA/serine cycle (malate dehydrogenase), amino acid metabolism (chorismate synthase, tryptophan synthase subunit beta) and electron transport systems (cytochrome c oxidase subunit I, cytochrome bc1 and cytochrome P460)—all showing protein-abundance increases with La without significant changes in gene expression.

## Ca vs. La: Metabolic Switches

Non-targeted metabolic profiling was then applied to further investigate the consequences of the switch to REEs on cellular metabolism (**Supplementary Table S3**). The intermediates of the central metabolic pathways including the RuMP pathway (sedoheptulose-7 phosphate, fructose-6 phosphate, glucose-6 phosphate, phosphoenolpyruvate, 3-phosphoglycerate) and the first two steps of the TCA cycle (aconitate, citrate) dropped down significantly in La-grown cells compared to Ca-grown cells (**Figure 1B**), while concentrations of the TCA/serine cycle intermediates (fumarate, malate, and succinate) did not significantly change or slightly increased. The intracellular pools of amino acids produced from the TCA intermediates (glutamate, glutamine, asparagine, and ectoine), the key serine cycle intermediate (glycerate) also increased (**Figure 1B**).

Highly elevated levels of agmatine in cells grown on La could be linked to the upregulation of the urea ABC transporter permease because the substance is a precursor for urea biosynthesis. However, no urea was detected in supernatant samples even with targeted metabolite detection methods (see Material and Methods).

## Ca vs. La: Flux Balance (FBA) Simulations

Cell growth performance and metabolite data suggest that MxaFI-MeDH to XoxF-MeDH changes behavior of all central metabolic pathways downstream from methanol oxidation, indicating that the enzymes somehow differ in their functions. One possible explanation is that XoxF-MeDH has a higher affinity for its product (formaldehyde) and can convert formaldehyde to formate (Schmidt et al., 2010). Hence, the impact of the two-step conversion was tested *in silico*. The La-switch in *M. alcaliphilum* $20Z^R$ could be associated with a number of changes in the main physiological outputs, including the acceleration of $O_2$-consumption. The increase would indicate changes in redox balance and the acceleration of respiratory pathways. Taking into account that XoxF-MeDHs, including XoxF5, can convert both methanol and formaldehyde (Schmidt et al., 2010; Huang et al., 2018; Masuda et al., 2018) the La-switch could increase production of a reduced cytochrome instead of NADH (**Figure 1B**). To simulate the behavior of metabolic networks upon La-perturbation, we modified a previously developed computational model of methane metabolism (Akberdin et al., 2018) and incorporated a cytochrome-mediated formaldehyde oxidation reaction. *In silico* and observed $O_2/CH_4$ consumption ratios reached an agreement when 25% of formaldehyde pool is directed toward formate via a cytochrome-linked enzyme, such as XoxF-MeDH (**Table 3**).

# DISCUSSION

The growth and activity of methylotrophic bacteria possessing only XoxF-MeDHs strictly depend on REEs (Keltjens et al.,

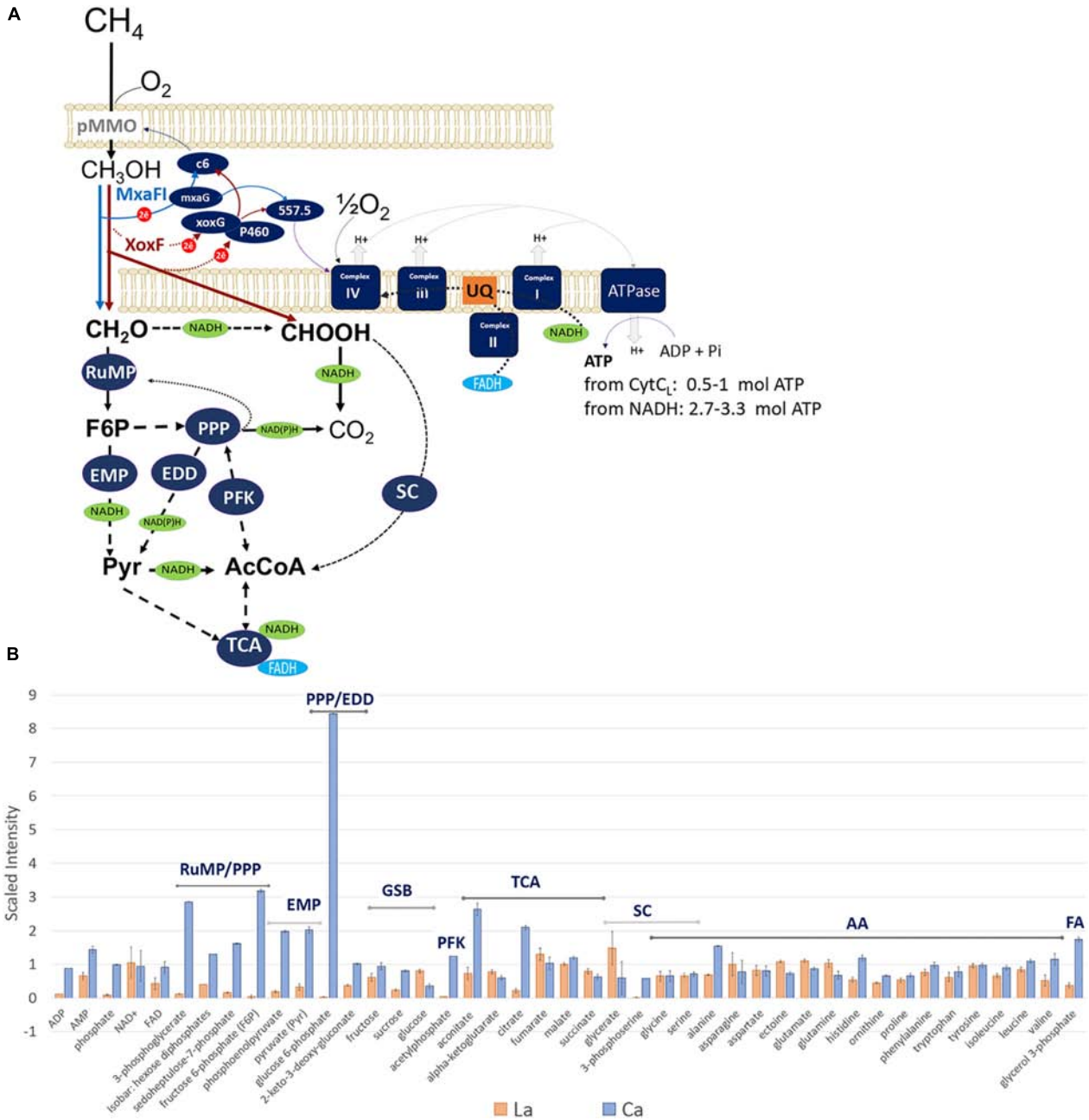


**FIGURE 1 | (A)** Central metabolic pathways of *M. alcaliphilum* 20Z$^R$. All abbreviations of metabolic pathways and enzymes are presented in the main text. **(B)** Compounds detected in cells grown with La (red) or Ca (blue).

2014; Pol et al., 2014). Methanotrophic bacteria which possess both xoxF-MeDH and mxaFI-MeDH systems tightly control expression of *mxaFI*, and switch to the xoxF enzyme when REEs are available (Chu et al., 2016; Yu et al., 2017; Huang et al., 2018; Zheng et al., 2018). Here we show that the La-supplementation affects the growth and methane consumption rates in *M.alcaliphilum* 20Z$^R$. The physiological parameter changes suggest modification of the global metabolic networks beyond a simple substitution of the one PQQ-dependent enzyme with another. To uncover the high growth rate paradox in La-supplemented cells we compiled a set of *omic*-studies, including gene expression, proteomics and metabolomics.

The whole-genome transcriptomic data did not show any significant alterations in central metabolic pathways except the switch of the primary methanol oxidation system. It should be mentioned, that while MxaFI-MeDH, and associated cytochrome $c_L$ are tremendously downregulated at both the transcript and

**TABLE 3 |** Flux balance simulations of methanotrophic growth under assumption of XoxF-MeDH driven conversion of formaldehyde to formate.

| Network | $O_2$ consumption rate (mmol g $CDW^{-1}h^{-1}$) | $O_2$:$CH_4$ consumption rates |
|---|---|---|
| Wild Type* | 13.77 | 1.18 |
| Ratio between conversion of methanol into formaldehyde ($CH_3O$) and formate (CHOOH): | | |
| 0.0 to $CH_3O$ / 1.0 to CHOOH | 19.14 | 1.64 |
| 0.25 to $CH_3O$ / 0.75 CHOOH | 17.39 | 1.49 |
| 0.5 to $CH_3O$ / 0.5 to CHOOH | 16.17 | 1.38 |
| 0.75 to $CH_3O$ / 0.25 to CHOOH | 14.95 | 1.28 |

**Flux balance analyses were carried out using modified computational model of methane metabolism (Akberdin et al., 2018). Methane uptake is set to 11.7 mmol g $CDW^{-1}h^{-1}$.*

proteins levels when $20Z^R$ cells are grown with La, XoxF-MeDH is upregulated only twofold. This implies that XoxF-MeDH might be involved in methane assimilation even under Ca-growth conditions. Taking into account the total MeDH protein counts, less XoxF-enzyme is needed to completely substitute for the MxaFI-MeDH function during La-growth. Together with increased rates of methane consumption, these observations suggest that the XoxF enzyme is more efficient than MxaFI. However, it could be speculated that the XoxF system requires higher input of methane, since the growth rate of La-supplemented cells reduced upon methane scarcity. The data indicate that XoxF operates differently than MxaFI *in vivo*.

The XoxF enzyme from $20Z^R$ is a typical XoxF5 enzyme usually found in Gammaproteobacteria. It has been proposed that the electrons from XoxF5 are transferred to a putative cytochrome cbb3-type (xoxG4, Yu et al., 2017). In this study we do not observe any correlation between XoxF and cytochrome cbb3 expression, indicating that the protein might have a different function in *M. alcaliphilum* $20Z^R$. Among all electron transfer systems, four cytochromes showed some response to La, but only one of them, cytochrome P460, was detected at the protein level. This cytochrome's activity has been associated with the second step of ammonia oxidation (Bergmann and Hooper, 1994; Cua and Stein, 2011; Caranto et al., 2016); however, its function in methanotrophic bacteria remains elusive (Zahn et al., 1994; Bergmann et al., 1998). Similarly to XoxF, the enzyme is constitutively expressed in various methanotrophs, and it might represent an alternative electron acceptor for the enzyme. To confirm this, the function must be validated via mutagenesis. Nevertheless, the observed abundance of XoxG4 or P460 could not enable the same tight coupling observed for MxaFI and MxaG. One could speculate that XoxF transfers electrons to yet unknown system and/or to pMMO via direct electron coupling or reverse electron transfer. Taking into the account that the total number of XoxF peptides never reaches the same level as MxaFI, yet methane consumption rates increase, it is possible that the direct coupling between XoxF and pMMO is more efficient than the coupling between MxaFI and pMMO. Activation of the fatty acid degradation pathways upon growth with La, as a proxy for reduction of needs for intracytoplasmic membranes for MeDH:pMMO coupling (Culpepper and Rosenzweig, 2014), provide additional support for this idea. On the other hand, La-grown cells showed higher abundances of complex III (cytochrome $bc_1$) proteins, which also opens up a possibility of more efficient reverse transfer. Overall, the abundances of cytochromes dropped slightly from 80 in Ca-grown cells to 77 in La-grown cells. Beside *mxaG* (detected only in Ca-grown cells) and *xoxG4*, two cytochromes, c6 and b557.5 were prevalent at the transcript levels in both Ca and La grown cells. The gene expression levels of the cytochromes C6 and b557.5 were contrary to each other, with cytochrome c6 being more prevalent upon methane-limiting growth (479.5 FPKM at optimal vs. 1507.7 FPKM at methane-limiting conditions), while b557.5 was highly expressed at optimal $CH_4$:$O_2$ supply (1785.6 FPKM at optimal vs. 192.2 FPKM at methane-limiting conditions). Cytochrome b557.5 might represent an equivalent of $cytc_H$, which links MeDH-associated cytochromes to complex IV (Anthony and Williams, 2003). However, it should be noted, that no peptides matching *b*557.5 were detected. Cytochrome c6 was also the most prevalent electron carrier in proteome. The cytochrome is known as a redox carrier in phototrophic organisms, which transfers electrons from cyt*bf* to photosystem I (Gupta et al., 2002). In this study, the expression of the cytochrome c6 could be connected with reduced methane supply and/or oxygenation level. However, the cytochrome was the most abundant cytochrome at protein level at all growth conditions, which makes the cytochrome the best candidate for transferring electrons to pMMO from bc1 when direct coupling is not possible (Akberdin et al., 2018). This role of the cytc6 is being validated via mutagenesis.

The gene expression profiles complemented by protein-abundance and metabolomics data highlight a set of possible post-transcriptional alterations in metabolic networks. The higher abundance of TCA/serine cycle enzymes and intermediates might be linked to increased carbon flow through those pathways. The data are consistent with the physiological data indicating that La-cells consume more methane carbon and produce more $CO_2$ per unit of biomass. Taken together, these data suggest that the substitution of Ca with La impacts the amount of NADH available for biosynthesis and/or the amount of carbon accessible for assimilation. One plausible explanation for these changes is a possible direct conversion of formaldehyde to formate by XoxF-MeDH. Both metabolomics and the flux-balance simulations further strengthen this hypothesis (**Figure 1**). The metabolomics profiles of La-grown cells could be best modeled by an assumption that 75% of the methanol is converted to formaldehyde, while 25% is converted into formate (the Spearman's index of 0.6, $p$-value = 8E–06).

La-growth is strongly associated with overexpression of two additional systems: a putative sulfate transporter (>70-fold increase) and Fae2, a formaldehyde activating enzyme (14-fold increase). A strong correlation between La-supplementation and the transporter expression suggests that the system might contribute to REE rather than sulfate acquisition. Several activities have been previously hypothesized for Fae-homologs, ranging from methyl-group sensing to reverse

conversion of methylene-tetrahydrofolate back to formaldehyde for incorporation into the RuMP pathway (Good et al., 2015). Taking into account the possibility of increased flux into formate in La-grown cells and the increase in the abundance of $H_4$folate pathway enzymes, the latter might justify the activation of an alternative Fae in *M. alcaliphilum* $20Z^R$.

Overall, our study provides a global overview of the Ca/La-switch on metabolic networks in *M. alcaliphilum* $20Z^R$ (summarized in **Figure 1**). We found that the XoxF-MeDH system provides a higher growth rate, while the MxaFI-MeDH system enables more efficient methane utilization in *M. alcaliphilum* $20Z^R$ and likely other gammaproteobacterial methanotrophs. The mechanism underlining the physiological outputs includes a number of alterations in metabolic networks, navigated by a redox swap. While La-grown cells receive a boost from more efficient coupling between pMMO and XoxF, as well as extra electron flow toward methane oxidation due to conversion of methanol to formate, they are limited in redox power. On another hand, Ca-grown cells are more balanced with respect to redox demand and their slow growth could be explained by less efficient coupling between pMMO and MxaFI. Together, these data suggest that cells possessing both enzymes would have advantages in highly dynamic and competitive environmental niches.

A number of novel proteins as well as new metabolic connections for enzymatic systems with elusive functions in methanotrophy were uncovered. The validation of the predictions arising from these global analyses awaits further investigation of factors contributing to the changes, including the identification of XoxF-MeDH electron transfer partner (including XoxF-pMMO coupling), the description of the putative La-induced transporters and the enzymatic characterization of Fae2, cytochromes bc1, P460, and c6 functions.

# MATERIALS AND METHODS

## Strain and Growth Media

*M. alcaliphilum* $20Z^R$ cells were grown using P media (g/L) (Akberdin et al., 2018): $KNO_3$, 1; $MgSO_4 \times 7H_2O$, 0.2; NaCl, 30; $CaCl_2 \times 2H_2O$, 0.02; or $LaCl_3 \times 7\ H_2O$, 0.07; and supplemented with 1 ml/L of trace element solution, 20 ml/L of phosphate solution (5.44 g $KH_2PO_4$; 5.68 g $Na_2HPO_4$) and 40 ml/L of 1 M carbonate buffer.

## Cultivation and Bioreactor Parameters

Culturing was carried out in either closed vials (batch cultures) or bioreactor cultures (fed-batch or continuous culture). Batch cultures were grown in 125 ml, 250 ml, or 1.2 L bottles with shaking at 200 r.p.m. The headspace:medium ratio was set at 4:1. Methane (99.9%, Airgas) was injected into vials to represent 20% of the headspace. Samples of batch cultures were used for metabolomics studies.

A DASbox mini bioreactor (0.5 L working volume; 250 ml culture) with two individual bioreactor units, each having automatic temperature, pH, and DO controls, a sample port for measuring OD, and a coupling to a BlueSens sensor system for simultaneous measuring off-gasses ($CH_4$, $O_2$, and $CO_2$) were used for bioreactor cultures. The bioreactor set-up is shown in **Supplementary Figure S1**. The following pre-mixed gas mixtures were used for bioreactor studies: (i) 5% $CH_4$ :5 % $O_2$, to represent optimal growth; and (ii) 2.5% $CH_4$ : 10% $O_2$ to represent methane-limiting conditions. Gas tanks were connected to a mass flow controller and the gas mixture was directly purged into the bioreactor culture at 0.2–1 sL $h^{-1}$ rates. In batch cultures, methane (99.9%, Airgas) was injected into vials to represent 20% of the headspace. The methane and oxygen consumption and $CO_2$ production rates were calculated by estimating the decline (or increase) of the corresponding compounds over time. The data were analyzed to assess yield (Y), growth rate, and $O_2$/substrate ratios. Samples of bioreactor cultures were collected for metabolomic, proteomics and transcriptomic studies.

## RNA Sequencing and Analysis

Samples (45 ml) of bioreactor cultures, La-optimum, La-CH4 limited, Ca-optimum and Ca-CH4 limited, were collected and immediately transferred into tubes containing 5 ml of the stop solution (5% water-equilibrated phenol in ethanol) (Griffiths et al., 2000). Cells were pelleted by centrifugation at 4700 rpm for 15 min, and RNA was extracted using a RNeasy kit and treated with PureLink DNaseI (ThermoFisher Scientific) according to the manufacturer's instructions. Samples were sequenced on an Illumina HiSeq2500 with ∼50 million/sample SR50 reads by IGM Genomics Center, University of California, San Diego. All experiments were performed with at least two biological replicates.

The quality of the obtained raw Fastq files was checked and analyzed with FastQC[1]. To improve the quality of the raw reads we employed the Trimmomatic tool (Bolger et al., 2014) using these procedures: removing a base from either the start or end position if the quality was low; trimming bases on a sliding window method; removing any remaining reads that are <36 bases long. The trimmed reads were aligned to the annotated *M. alcaliphilum* $20Z^R$ genome as retrieved from the NCBI database (the latest genome build ASM96853v1) on January 18, 2018 (Vuilleumier et al., 2012). Alignment was performed using TopHat2 (Kim et al., 2013). The alignments were post-processed into sorted BAM files with SAMTools version 1.4 (Li et al., 2009). Reads were attributed to open reading frames (ORFs) using the htseq-count tool from the "HTSeq" framework version 0.7.2 (Anders et al., 2015) based on gtf files with coordinates of genes from ASM96853v1 and indexed SAM file. Differential expression analysis was performed with DESeq2 1.16.1 (Love et al., 2014) using R 3.4.1. Principal component analysis of the normalized logarithmic transformed read counts was used by means of DESeq2 (Anders and Huber, 2010) in order to determine the reproducibility of analyzed replicates (**Supplementary Figure S2**). Genes were considered to be

[1]http://www.bioinformatics.babraham.ac.uk/projects/fastqc/

differentially expressed if they had an average change of greater than 1.5-fold when comparing normalized counts as well as an adjusted *p*-value of less than 0.05 to ensure statistical significance (Anders and Huber, 2010). We also applied an alternative Rockhopper 2 tool with default parameters to confirm the robustness of the results (Tjaden, 2015).

## Proteomics Study

Biomass was harvested by centrifuging 50 ml of culture for each technical replicate at 4000 rpm for 20 min. Cells pellets were frozen and stored at −80°C. SDS-lysis buffer [4% Sodium dodecyl sulfate (SDS) (w/v), 100 mM Tris–HCl pH 7.6, 100 mM dithiothreitol (DTT)] was added to the pellets, vortexed into solution and fractions (100 μl) transferred to 1.5 mL centrifuge tubes. Each sample was incubated at 95°C for 5 min to completely lyse the cells and reduce and denature the protein. The samples were cooled at 4°C for 30 min and centrifuged at 15,000 × *g* for 10 min to pellet any remaining debris. Filter Aided Sample Preparation (FASP) (Wiśniewski et al., 2009) kits were used for protein digestion (Expedeon, San Diego, CA, United States) according to the manufacturer's instructions. Briefly, 400 μl of 8 M urea (all reagents included in the kit) was added to each 500 μl 30 K molecular weight cut off (MWCO) FASP spin column and 50 μl of the sample in SDS buffer was added, centrifuged at 14,000 × *g* for 30 min to bring the sample all the way to the dead volume. The waste was removed from the bottom of the tube and another 400 μl of 8 M urea was added to the column and centrifuged again at 14,000 × *g* for 30 min and repeated once more. 400 μl of 50 mM ammonium bicarbonate (ABC) was added to each column and centrifuged for 30 min, repeated twice. The column was placed into a new fresh, clean and labeled collection tube. Digestion solution was made by dissolving 4 μg trypsin in 75 μL 50 mM ABC solution and added to the sample. Each sample was incubated for 3 h at 37°C with 800 rpm shaking on a thermomixer with a thermotop (Eppendorf, Hamburg, Germany) to reduce condensation into the cap. The resultant peptides were then centrifuged through the filter and into the collection tube at 14,000 × *g* for 15 min. The peptides in the collection tube were snap frozen in liquid $N_2$ and the column placed back into a new collection tube and digested again overnight with 150 μL of digestion solution. The following day the peptides were spun out and added to the 3 h peptide collection tube, the samples were then concentrated to ∼30 μL using a SpeedVac. Final peptide concentrations were determined using a bicinchoninic acid (BCA) assay (Thermo Scientific, Waltham, MA, United States). All of the samples were diluted to 0.2 μg/μl for MS analysis.

Peptides were resuspended in water and a total of 500 ng were analyzed by liquid chromatography-tandem mass spectrometry (LC-MS/MS) on Waters nano-Acquity M-Class dual pumping UPLC system (Milford, MA, United States) connected to a Q-Exactive HF mass spectrometer (Thermo Scientific, San Jose, CA, United States) as described in detail elsewhere (Yang et al., 2017). LC-MS/MS data was processed with DeconMSn (Mayampurath et al., 2008) and peptide identification was performed using MS-GF+ (Kim and Pevzner, 2014) using the following parameters: (1) tryptic digestion in a least one terminus of the peptide, (2) 20 ppm parent ion mass error tolerance, and (3) methionine oxidation and lysine trimethylation as variable modifications. Identifications were filtered with a probability score ≤x1e−9, resulting on a false-discovery rate ≤1% at the protein level. The number of spectra that mapped to each protein were counted that total is then reported as spectral count. The number of observed spectra were then determined using a proxy of relative abundance of proteins. The number of spectra observed were averaged across replicates and a fold-change of greater than 2 was considered significant.

## Non-Targeted Metabolite Profiling

Metabolomic analyses of cells and spent supernatant from cultures of the *M. alcaliphilum* $20Z^R$ grown on Ca or La were performed according to the published protocol (Akberdin et al., 2018).

## Flux Balance Analysis With COBRA

A recently published genome-scale model of *M. alcaliphilum* $20Z^R$ (Akberdin et al., 2018) was used to simulate the Ca-REE switch. To consider the functional activity of XoxF-MeDH, a reaction (Reaction ID: "MXALa") representing cytochrome-mediated conversion of formaldehyde into formate was included. The updated model is available on the web-site: http://sci.sdsu.edu/kalyuzhlab/.

## Urea Analysis

Cultures of *M. alcaliphilum* $20Z^R$ were grown with Ca or La (3 biological replicates per experiment) and methane as a carbon source, in closed vials (25 ml) to an OD 1 to reproduce bioreactor settings. Cells were transferred into tubes to pellet the cells by centrifugation at 4700 rpm for 15 min. The supernatant was collected and then tested for urea using a Urea kit (QuantiChrom Urea assay kit DIUR-100) following the manufacturer's procedure. The reactions were measured using a 96-well plate reader spectrophotometer synergy HT (Biotek) with two technical replicates for each specific environment. The results were compared to a standard created using the kits procedure.

# AUTHOR CONTRIBUTIONS

MK designed and coordinated the study. IA and MK analyzed the data and wrote the first draft of the manuscript. RH and DC performed cultivation experiments, and prepared samples for proteomics, RNAseq and metabolomics. DO and IA conducted RNA-seq analysis. CN, AS, EN, and JA carried out proteomics study. All authors read and approved the final manuscript.

## FUNDING

The study was financially supported by DOE under FOA DE-FOA-0001085 and by NSF-CBET award 1605031. DYO was supported by ICG SB RAS budget project (No. 0324-2018-0017).

## ACKNOWLEDGMENTS

The authors acknowledge EMSL, a national scientific user facility sponsored by the Department of Energy's Office of Biological and Environmental Research for providing the High-Performance Mass Spectrometry Facility.

## SUPPLEMENTARY MATERIAL

The Supplementary Material for this article can be found online at: https://www.frontiersin.org/articles/10.3389/fmicb.2018.02735/full#supplementary-material

**FIGURE S1 |** Schematic components of a continuous culture bioreactor. MTU-Mass Transfer Unit; MSP-Manual Sample Port; MFM-Mass Flow Meter;BS-Bluesens sensors. The protocol is adapted for working with a mini-parallel bioreactor system, such as DasBox (Eppendorf). The system is connected to a custom-built gas-distribution system, which controls the gas-mixture input. Only non-flammable mixtures of methane (5% or 2.5% $CH_4$) and oxygen (2.5–5% $O_2$) were used, and output gasses must be connected to exhaust vents. The DasBox system offers single use plastic vessels, which are handy for small-scale analyses of minerals (Cu, Fe, and La, etc.,) effects on cell growth and/or methane oxidation. Four parallel experiments have been carried in one run, providing sufficient statistical data for analysis.

**FIGURE S2 | (A)** Principal component analysis of analyzed transcriptomic datasets. Individual samples are indicated according to the next notation: light red circle – Ca-regulated growth, blue circle – La-regulated growth; **(B)** The MA-plot shows the log2 fold changes between Ca- and La-regulated growths of 20 Z over the mean of normalized counts. The *x*-axis represents the average expression of genes over samples and the *y*-axis represents the log2 fold change between the Ca-CH4 and La-CH4 growth conditions. Red circles represent differentially expressed genes with statistical significance, $p < 0.05$.

**TABLE S1 |** Complete list of differentially expressed genes.

**TABLE S2 |** Proteomics datasets.

**TABLE S3 |** Metabolomics dataset.

## REFERENCES

Akberdin, I. R., Thompson, M., Hamilton, R., Desai, N., Alexander, D., Henard, C. A., et al. (2018). Methane utilization in *Methylomicrobium alcaliphilum* 20ZR: a systems approach. *Sci. Rep.* 8:2512. doi: 10.1038/s41598-018-20574-z

Anders, S., and Huber, W. (2010). Differential expression analysis for sequence count data. *Genome Biol.* 11:R106. doi: 10.1186/gb-2010-11-10-r106

Anders, S., Pyl, P. T., and Huber, W. (2015). HTSeq—a Python framework to work with high-throughput sequencing data. *Bioinformatics* 31, 166–169. doi: 10.1093/bioinformatics/btu638

Anthony, C., and Williams, P. (2003). The structure and mechanism of methanol dehydrogenase. *Biochim. Biophys. Acta* 1647, 18–23. doi: 10.1016/S1570-9639(03)00042-6

Bergmann, D. J., and Hooper, A. B. (1994). The primary structure of cytochrome P460 of *Nitrosomonas europaea*: presence of a c-heme binding motif. *FEBS Lett.* 353, 324–326. doi: 10.1016/0014-5793(94)01072-2

Bergmann, D. J., Zahn, J. A., Hooper, A. B., and DiSpirito, A. A. (1998). Cytochrome P460 genes from the methanotroph *Methylococcus capsulatus* Bath. *J. Bacteriol.* 180, 6440–6445.

Bolger, A. M., Lohse, M., and Usadel, B. (2014). Trimmomatic: a flexible trimmer for Illumina sequence data. *Bioinformatics* 30, 2114–2120. doi: 10.1093/bioinformatics/btu170

Caranto, J. D., Vilbert, A. C., and Lancaster, K. M. (2016). Nitrosomonas europaea cytochrome P460 is a direct link between nitrification and nitrous oxide emission. *Proc. Natl. Acad. Sci. U.S.A.* 113, 14704–14709. doi: 10.1073/pnas.1611051113

Chidambarampadmavathy, K., Obulisamy, P., and Heimann, K. (2015). Role of copper and iron in methane oxidation and bacterial biopolymer accumulation. *Eng. Life Sci.* 15, 387–399. doi: 10.1002/elsc.201400127

Chistoserdova, L. (2011). Modularity of methylotrophy, revisited. *Environ. Microbiol.* 13, 2603–2622. doi: 10.1111/j.1462-2920.2011.02464.x

Chistoserdova, L., and Kalyuzhnaya, M. G. (2018). Current trends in methylotrophy. *Trends Microbiol.* 26, 703–714. doi: 10.1016/j.tim.2018.01.011

Chistoserdova, L., Laukel, M., Portais, J. C., Vorholt, J. A., and Lidstrom, M. E. (2004). Multiple formate dehydrogenase enzymes in the facultative methylotroph *Methylobacterium extorquens* AM1 are dispensable for growth on methanol. *J. Bacteriol.* 186, 22–28. doi: 10.1128/JB.186.1.22-28.2004

Chu, F., Beck, D. A., and Lidstrom, M. E. (2016). MxaY regulates the lanthanide-mediated methanol dehydrogenase switch in *Methylomicrobium buryatense*. *PeerJ* 4:e2435. doi: 10.7717/peerj.2435

Chu, F., and Lidstrom, M. E. (2016). XoxF acts as the predominant methanol dehydrogenase in the type I methanotroph *Methylomicrobium buryatense*. *J. Bacteriol.* 198, 1317–1325. doi: 10.1128/JB.00959-15

Cua, L. S., and Stein, L. Y. (2011). Effects of nitrite on ammonia-oxidizing activity and gene regulation in three ammonia-oxidizing bacteria. *FEMS Microbiol. Lett.* 319, 169–175. doi: 10.1111/j.1574-6968.2011.02277.x

Culpepper, M. A., and Rosenzweig, A. C. (2014). Structure and protein–protein interactions of methanol dehydrogenase from *Methylococcus capsulatus* (Bath). *Biochemistry* 53, 6211–6219. doi: 10.1021/bi500850j

de la Torre, A., Metivier, A., Chu, F., Laurens, L. M., Beck, D. A., Pienkos, P. T., et al. (2015). Genome-scale metabolic reconstructions and theoretical investigation of methane conversion in *Methylomicrobium buryatense* strain 5G (B1). *Microb. Cell Fact.* 14:188. doi: 10.1186/s12934-015-0377-3

DiSpirito, A. A., Semrau, J. D., Murrell, J. C., Gallagher, W. H., Dennison, C., and Vuilleumier, S. (2016). Methanobactin and the link between copper and bacterial methane oxidation. *Microbiol. Mol. Biol. Rev.* 80, 387–409. doi: 10.1128/MMBR.00058-15

Fitriyanto, N. A., Fushimi, M., Matsunaga, M., Pertiwiningrum, A., Iwama, T., and Kawai, K. (2011). Molecular structure and gene analysis of $Ce3^{+}$ -induced methanol dehydrogenase of *Bradyrhizobium* sp. MAFF211645. *J. Biosci. Bioeng.* 111, 613–617. doi: 10.1016/j.jbiosc.2011.01.015

Glass, J., and Orphan, V. J. (2012). Trace metal requirements for microbial enzymes involved in the production and consumption of methane and nitrous oxide. *Front. Microbiol.* 3:61. doi: 10.3389/fmicb.2012.00061

Good, N. M., Lamb, A., Beck, D. A. C., Martinez-Gomes, N., and Kalyuzhnaya, M. G. (2015). C1- pathways in *Methyloversatilis universalis* FAM5: genome wide gene expression and mutagenesis studies. *Microorganisms* 3, 175–197. doi: 10.3390/microorganisms3020175

Good, N. M., Walser, O. N., Moore, R. S., Suriano, C., Huff, A. F., and Martinez-Gomez, N. C. (2018). Investigation of lanthanide-dependent methylotrophy uncovers complementary roles for alcohol dehydrogenase enzymes. *bioRxiv* [Preprint]. doi: 10.1101/329011

Griffiths, R. I., Whiteley, A. S., O'Donnell, A. G., and Bailey, M. J. (2000). Rapid method for coextraction of DNA and RNA from natural environments for analysis of ribosomal DNA- and rRNA-based microbial community composition. *Appl. Environ. Microbiol.* 66, 5488–5491. doi: 10.1128/AEM.66.12.5488-5491.2000

Gu, W., and Semrau, J. D. (2017). Copper and cerium-regulated gene expression in *Methylosinus trichosporium* OB3b. *Appl. Microbiol. Biotechnol.* 101, 8499–8516. doi: 10.1007/s00253-017-8572-2

Gupta, R., He, Z., and Luan, S. (2002). Functional relationship of cytochrome c6 and plastocyanin in Arabidopsis. *Nature* 417, 567–571. doi: 10.1038/417567a

Handler, R. M., and Shonnard, D. R. (2018). "Environmental life cycle assessment of methane biocatalysis: key considerations and potential impacts," in *Methane Biocatalysis: Paving the Way to Sustainability*, eds M. G. Kalyuzhnaya and X.-H. Xing (New York City, NY: Springer Publishing), 253–270. doi: 10.1007/978-3-319-74866-5_16

Haque, M. F. U., Kalidass, B., Bandow, N., Turpin, E. A., DiSpirito, A. A., and Semrau, J. D. (2015). Cerium regulates expression of alternative methanol dehydrogenases in *Methylosinus trichosporium* OB3b. *Appl. Environ. Microbiol.* 81, 7546–7552. doi: 10.1128/AEM.02542-15

Hibi, Y., Asai, K., Arafuka, H., Hamajima, M., Iwama, T., and Kawai, K. (2011). Molecular structure of La3 + -induced methanol dehydrogenase-like protein in *Methylobacterium radiotolerans*. *J. Biosci. Bioeng.* 111, 547–549. doi: 10.1016/j.jbiosc.2010.12.017

Huang, J., Zheng, Y., and Chistoserdova, L. (2018). Lanthanide-dependent methanol dehydrogenases of XoxF4 and XoxF5 clades are differentially distributed among methylotrophic bacteria and they reveal different biochemical properties. *Front. Microbiol.* 9:1366. doi: 10.3389/fmicb.2018.01366

Johnson, K. A., Ve, T., Larsen, Ø, Pedersen, R. B., Lillehaug, J. R., Jensen, H. B., et al. (2014). CorA is a copper repressible surface-associated copper (I)-binding protein produced in Methylomicrobium album BG8. *PLoS One* 9:e87750. doi: 10.1371/journal.pone.0087750

Karlsen, O. A., Berven, F. S., and Bagstevold, J. I. (2011). "Methylococcus capsulatus (Bath): from genome to protein function, and vice versa," in *Methods in Enzymology*, Vol. 495, eds A. C. Rosenzweig and S. W. Ragsdale (Cambridge, MA: Academic Press), 63–79. doi: 10.1016/B978-0-12-386905-0.00005-X

Karlsen, O. A., Larsen, Ø, and Jensen, H. B. (2010). Identification of a bacterial di-haem cytochrome c peroxidase from *Methylomicrobium album* BG8. *Microbiology* 156(Pt 9), 2682–2690. doi: 10.1099/mic.0.037119-0

Keltjens, J. T., Pol, A., Reimann, J., and Op den Camp, H. J. (2014). PQQ-dependent methanol dehydrogenases: rare-earth elements make a difference. *Appl. Microbiol. Biotechnol.* 98, 6163–6183. doi: 10.1007/s00253-014-5766-8

Kenney, G. E., and Rosenzweig, A. C. (2018). Methanobactins: maintaining copper homeostasis in methanotrophs and beyond. *J. Biol. Chem.* 293, 4606–4615. doi: 10.1074/jbc.TM117.000185

Kim, D., Pertea, G., Trapnell, C., Pimentel, H., Kelley, R., and Salzberg, S. L. (2013). TopHat2: accurate alignment of transcriptomes in the presence of insertions, deletions and gene fusions. *Genome Biol.* 14:R36. doi: 10.1186/gb-2013-14-4-r36

Kim, S., and Pevzner, P. A. (2014). MS-GF + makes progress towards a universal database search tool for proteomics. *Nat. Commun.* 5:5277. doi: 10.1038/ncomms6277

Kirschke, S., Bousquet, P., Ciais, P., Saunois, M., Canadell, J. G., Dlugokencky, E. J., et al. (2013). Three decades of global methane sources and sinks. *Nat. Geosci.* 6, 813–823. doi: 10.1038/ngeo1955

Laukel, M., Chistoserdova, L., Lidstrom, M. E., and Vorholt, J. A. (2003). The tungsten-containing formate dehydrogenase from *Methylobacterium extorquens* AM1: purification and properties. *Eur. J. Biochem.* 270, 325–333. doi: 10.1046/j.1432-1033.2003.03391.x

Leak, D. J., and Dalton, H. (1986). Growth yields of methanotrophs. *Appl. Microbiol. Biotechnol.* 23, 470–476. doi: 10.1007/BF02346062

Li, H., Handsaker, B., Wysoker, A., Fennell, T., Ruan, J., Homer, N., et al. (2009). The sequence alignment/map format and SAMtools. *Bioinformatics* 25, 2078–2079. doi: 10.1093/bioinformatics/btp352

Love, M. I., Huber, W., and Anders, S. (2014). Moderated estimation of fold change and dispersion for RNA-seq data with DESeq2. *Genome Biol.* 15:550. doi: 10.1186/s13059-014-0550-8

Masuda, S., Suzuki, Y., Fujitani, Y., Mitsui, R., Nakagawa, T., Shintani, M., et al. (2018). Lanthanide-dependent regulation of methylotrophy in *Methylobacterium aquaticum* Strain 22A. *mSphere* 3:e00462-17. doi: 10.1128/mSphere.00462-17

Matsen, J. B., Yang, S., Stein, L. Y., Beck, D. A., and Kalyuzhanaya, M. G. (2013). Global molecular analyses of methane metabolism in methanotrophic alphaproteobacterium, *Methylosinus trichosporium* OB3b. Part I: transcriptomic study. *Front. Microbiol.* 4:40. doi: 10.3389/fmicb.2013.00040

Mayampurath, A. M., Jaitly, N., Purvine, S. O., Monroe, M. E., Auberry, K. J., Adkins, J. N., et al. (2008). DeconMSn: a software tool for accurate parent ion monoisotopic mass determination for tandem mass spectra. *Bioinformatics* 24, 1021–1023. doi: 10.1093/bioinformatics/btn063

Myronova, N., Kitmitto, A., Collins, R. F., Miyaji, A., and Dalton, H. (2006). Three-dimensional structure determination of a protein supercomplex that oxidizes methane to formaldehyde in *Methylococcus capsulatus* (Bath). *Biochemistry* 45, 11905–11914. doi: 10.1021/bi061294p

Nakagawa, T., Mitsui, R., Tani, A., Sasa, K., Tashiro, S., Iwama, T., et al. (2012). A catalytic role of XoxF1 as $La3^{+}$ -dependent methanol dehydrogenase in *Methylobacterium extorquens* Strain AM1. *PLoS One* 7:e50480. doi: 10.1371/journal.pone.0050480

Page, M. D., and Anthony, C. (1986). Regulation of formaldehyde oxidation by the methanol dehydrogenase modifier proteins of Methylophilus methylotrophus and Pseudomonas AM 1. *J. Gen. Microbiol.* 132, 1553–1563.

Pol, A., Barends, T. R., Dietl, A., Khadem, A. F., Eygensteyn, J., Jetten, M. S., et al. (2014). Rare earth metals are essential for methanotrophic life in volcanic mudpots. *Environ.Microbiol.* 16, 255–264. doi: 10.1111/1462-2920.12249

Schmidt, S., Christen, P., Kiefer, P., and Vorholt, J. A. (2010). Functional investigation of methanol dehydrogenase-like protein XoxF in *Methylobacterium extorquens* AM1. *Microbiology* 156, 2575–2586. doi: 10.1099/mic.0.038570-0

Semrau, J. D., DiSpirito, A. A., Gu, W., and Yoon, S. (2018). Metals and methanotrophy. *Appl. Environ. Microbiol.* 84:e02289-17. doi: 10.1128/AEM.02289-17

Shchukin, V. N., Khmelenina, V. N., Eshinimayev, B. T., Suzina, N. E., and Trotsenko, Y. A. (2011). Primary characterization of dominant cell surface proteins of halotolerant methanotroph *Methylomicrobium alcaliphilum* 20Z. *Microbiol.* 80:608. doi: 10.1134/S0026261711050122

Stanley, S. H., Prior, S. D., Leak, D. J., and Dalton, H. (1983). Copper stress underlies the fundamental change in intracellular location of methane mono-oxygenase in methane-oxidizing organisms: studies in batch and continuous cultures. *Biotechnol. Lett.* 5, 487–492. doi: 10.1007/BF00132233

Strong, P. J., Kalyuzhnaya, M., Silverman, J., and Clarke, W. P. (2016). A methanotroph-based biorefinery: potential scenarios for generating multiple products from a single fermentation. *Bioresour. Technol.* 215, 314–323. doi: 10.1016/j.biortech.2016.04.099

Tjaden, B. (2015). De novo assembly of bacterial transcriptomes from RNA-seq data. *Genome Biol.* 16:1. doi: 10.1186/s13059-014-0572-2

Vu, H. N., Subuyuj, G. A., Vijayakumar, S., Good, N. M., Martinez-Gomez, N. C., and Skovran, E. (2016). Lanthanide-dependent regulation of methanol oxidation systems in *Methylobacterium extorquens* AM1 and their contribution to methanol growth. *J. Bacteriol.* 198, 1250–1259. doi: 10.1128/JB.00937-15

Vuilleumier, S., Khmelenina, V. N., Bringel, F., Reshetnikov, A. S., Lajus, A., Mangenot, S., et al. (2012). Genome sequence of the haloalkaliphilic methanotrophic bacterium *Methylomicrobium alcaliphilum* 20Z. *J. Bacteriol.* 194, 551–552. doi: 10.1128/JB.06392-11

Wiśniewski, J. R., Zougman, A., Nagaraj, N., and Mann, M. (2009). Universal sample preparation method for proteome analysis. *Nat. Methods* 6, 359–362. doi: 10.1038/nmeth.1322

Yang, J., Yin, L., Lessner, F. H., Nakayasu, E. S., Payne, S. H., Fixen, K. R., et al. (2017). Genes essential for phototrophic growth by a purple alphaproteobacterium. *Environ. Microbiol.* 19, 3567–3578. doi: 10.1111/1462-2920.13852

Yang, S., Matsen, J. B., Konopka, M., Green-Saxena, A., Clubb, J., Sadilek, M., et al. (2013). Global molecular analyses of methane metabolism in methanotrophic Alphaproteobacterium, *Methylosinus trichosporium* OB3b. Part II. Metabolomics and 13C-labeling study. *Front. Microbiol.* 4:70. doi: 10.3389/fmicb.2013.00070

Yu, Z., Beck, D. A. C., and Chistoserdova, L. (2017). Natural selection in synthetic communities highlights the roles of Methylococcaceae and Methylophilaceae and suggests differential roles for alternative methanol dehydrogenases in methane consumption. *Front. Microbiol.* 8:2392. doi: 10.3389/fmicb.2017.02392

Zahn, J., Duncan, C., and DiSpirito, A. A. (1994). Oxidation of hydroxylamine by cytochrome P460 of the obligate methylotroph *Methylococcus capsulatus* Bath. *J. Bacteriol.* 176, 5879–5887. doi: 10.1128/jb.176.19.5879-5887.1994

Zheng, Y., Huang, J., Zhao, F., and Chistoserdova, L. (2018). Physiological effect of XoxG(4) on lanthanide-dependent methanotrophy. *mBio* 9:e02430-17. doi: 10.1128/mBio.02430-17

**Conflict of Interest Statement:** The authors declare that the research was conducted in the absence of any commercial or financial relationships that could be construed as a potential conflict of interest.

frontiers in Environmental Science

ORIGINAL RESEARCH
published: 27 July 2018
doi: 10.3389/fenvs.2018.00084

# Computationally Exploring and Alleviating the Kinetic Bottlenecks of Anaerobic Methane Oxidation

*Matthew J. Grisewood*[1], *James G. Ferry*[2] *and Costas D. Maranas*[1]*

[1] Department of Chemical Engineering, Pennsylvania State University, University Park, PA, United States, [2] Department of Biochemistry and Molecular Biology, Pennsylvania State University, University Park, PA, United States

The anaerobic oxidation of methane (AOM) by methanotrophic archaea offers a carbon- and electron- efficient route for the production of acetate, which can be further processed to yield liquid fuels. This acetate production pathway is initiated by methyl-coenzyme M reductase, but this enzyme can only oxidize trace amounts of methane *ex situ*. Efforts to improve the kinetics of methyl-coenzyme M reductase through enzyme engineering have been, in part, limited by low-throughput assays. Computational enzyme engineering can circumvent this limitation through the design of smaller, more focused libraries, which have a higher probability of success. By drawing from a new consensus reaction mechanism for Mcr and newly published data, the first complete kinetic characterization of the Mcr reaction mechanism is proposed. In the developed kinetic description, the rate of methyl-coenzyme M unbinding is proposed to limit Mcr overall kinetics. A revised computational method was devised to improve the rate of product release while not disrupting the reaction's activated complex. Large, hydrophobic amino acids that can assume multiple conformations were predicted to be most effective at reaching this design goal. Other rate-limiting scenarios were examined, such as (i) high-temperature (>45°C), (ii) methyltransferase-limiting, and (iii) ineffective cofactor $F_{430}$ binding. A separate library of designs is put forth for each one of these cases. These efforts mark the first computational attempt at redesigning methyl-coenzyme M reductase for reversed or improved activity, which if experimentally validated, would have a cross-cutting impact across the biotechnology and biochemistry fields by debottlenecking anaerobic methane oxidation.

**Keywords: methyl-coenzyme M reductase, Mcr, product release, anaerobic oxidation of methane, IPRO, enzyme, redesign**

OPEN ACCESS

***Edited by:***
*Nidia S. Caetano, Instituto Superior de Engenharia do Porto (ISEP), Portugal*

***Reviewed by:***
*Naresh Singhal, University of Auckland, New Zealand*
*Seung Gu Shin, Pohang University of Science and Technology, South Korea*

***Correspondence:**
*Costas D. Maranas*
*costas@psu.edu*

***Specialty section:***
*This article was submitted to Microbiotechnology, Ecotoxicology and Bioremediation, a section of the journal Frontiers in Environmental Science*

***Received:*** *30 April 2018*
***Accepted:*** *05 July 2018*
***Published:*** *27 July 2018*

***Citation:***
*Grisewood MJ, Ferry JG and Maranas CD (2018) Computationally Exploring and Alleviating the Kinetic Bottlenecks of Anaerobic Methane Oxidation. Front. Environ. Sci. 6:84. doi: 10.3389/fenvs.2018.00084*

## INTRODUCTION

Each year, marine sediments oxidize an estimated 70–300 teragrams of methane (Reeburgh, 1996; Hinrichs and Boetius, 2003) to form carbon dioxide (Knittel and Boetius, 2009), which is about 21 times less effective at trapping heat in the atmosphere (Ragsdale et al., 2017). Industrially mimicking this natural process enables the possibility of converting methane to liquid fuels in an efficient and environmentally friendly manner (Haynes and Gonzalez, 2014). Consortia of

ANaerobic MEthanotrophic archaea (ANME) and sulfate-reducing bacteria are responsible for the anaerobic oxidation of methane (AOM) in these sediments (Knittel and Boetius, 2009; Shima et al., 2012). The key enzyme for methane activation is a homolog of methyl-coenzyme M reductase (Mcr)—an enzyme that catalyzes anaerobic methanogenesis—that runs in reverse (Hoehler et al., 1994; Krüger et al., 2003; Hallam et al., 2004; Moran et al., 2005; Scheller et al., 2010; Shima et al., 2012). ANME Mcr couples the endergonic oxidation of methane to methyl-coenzyme M ($CH_3$-S-CoM) with the reduction of coenzyme M-coenzyme B heterodisulfide (CoM-S-S-CoB, HDS) to coenzyme B (HS-CoB, see Equation 1; Harmer et al., 2008; Thauer, 2011).

$$C\mathit{H}_4 + \text{CoM-S-S-CoB} \rightleftharpoons C\mathit{H}_3\text{-S-CoM} + \text{HS-CoB} \qquad \Delta G'^{\circ} = +30\ \text{kJ/mol} \quad (1)$$

The ANME in marine sediments directly donate electrons to their syntrophic sulfate-reducing bacteria partner via nanowire-like structures (McGlynn et al., 2015; Wegener et al., 2015; Scheller et al., 2016). This electron transfer yields a thermodynamically favorable net reaction (Equation 2; Thauer, 2011), but this free energy change is unlikely to support growth of both organisms (Thauer and Shima, 2008).

$$C\mathit{H}_4 + SO_4^{2-} \rightleftharpoons HCO_3^- + HS^- + \mathit{H}_2O \qquad \Delta G'^{\circ} = -21\ \text{kJ/mol} \quad (2)$$

Alternative electron acceptors [such as iron (III), manganese (IV), chromium (VI), and nitrate] are more energetically favorable than sulfate (Beal et al., 2009; Haroon et al., 2013; Mueller et al., 2015; Lu et al., 2016; Nazem-Bokaee et al., 2016; Soo et al., 2016) and can ensure thermodynamic feasibility of AOM.

Methanogenic Mcrs are $(\alpha\beta\gamma)_2$ hexamers that include two highly conserved active sites, where the nickel-containing cyclic tetrapyrrole prosthetic group known as cofactor $F_{430}$ is non-covalently bound (Ermler et al., 1997; Grabarse et al., 2000). For methanogenesis, $CH_3$-S-CoM must bind prior to HS-CoB to form a ternary complex (Wongnate and Ragsdale, 2015), and the nickel of cofactor $F_{430}$ must be present in the Ni(I) state (Goubeaud et al., 1997). The ordered binding for Mcr is facilitated through numerous important enzyme conformational changes (Grabarse et al., 2001; Cedervall et al., 2010; Ebner et al., 2010). Mcr methanogenesis is initiated through homolytic cleavage of $CH_3$-S-CoM to yield methyl radical and Ni(II)-thiolate intermediates (Chen et al., 2012; Scheller et al., 2013; Wongnate et al., 2016). This radical mechanism is also feasible for AOM, consistent with the "reverse methanogenesis" hypothesis (Krüger et al., 2003; Hallam et al., 2004; Moran et al., 2005, 2007; Nauhaus et al., 2005; Heller et al., 2008; Knittel and Boetius, 2009; Scheller et al., 2010; Chen et al., 2012; Wongnate et al., 2016). Though trace AOM in methanogens has been demonstrated (Moran et al., 2005, 2007; Scheller et al., 2010), the reported specific AOM rate of a methanogenic Mcr was 7-fold lower than that of ANME Mcr (Scheller et al., 2010). This is consistent with Mcr limiting overall AOM kinetics. By improving the activity of Mcr, the economics for the carbon- and energy-efficient bioconversion of methane to liquid fuels becomes more propitious (Haynes and Gonzalez, 2014).

Improving enzyme activity is typically attained through directed evolution approaches that mandate high-throughput screening of large variant libraries (Bloom et al., 2005; Packer and Liu, 2015). High-throughput screening is streamlined through the use of a simple assay, such as a chromogenic or fluorogenic substrate or sensor (see Xiao et al., 2015 for review). Such a simple assay for AOM by Mcr does not currently exist. AOM Mcr activity has only been monitored using limited throughput techniques that include isotopic labeling (Moran et al., 2005, 2007; Scheller et al., 2010; Soo et al., 2016) and cell growth on methane (Soo et al., 2016). The complexity of the Mcr system—exemplified by its many post-translational and cofactor modifications (Ermler et al., 1997; Grabarse et al., 2000; Shima et al., 2012; Allen et al., 2014), cofactor synthesis (Zheng et al., 2016), and oxidative inactivation (Goubeaud et al., 1997)—makes it extremely challenging to study *in vitro* and thus further limits the gamut of available assays. These limitations motivate the use of rational approaches to design small, focused libraries with a higher likelihood of success. Various rational approaches, such as site saturation mutagenesis or manual rational design, are also inapt for Mcr because of its complex chemistry and the inability to focus on one or two variable positions.

A robust approach to rationally engineer Mcr for improved catalytic activity is computational enzyme redesign. Several types of computational procedures have been successfully deployed for enzyme engineering, including *de novo* (Jiang et al., 2008; Röthlisberger et al., 2008; Faiella et al., 2009; Siegel et al., 2010; Richter et al., 2012; Garrabou et al., 2016), structure-based (Ashworth et al., 2006; Murphy et al., 2009; Grisewood et al., 2017), and sequence-based approaches (Moore and Maranas, 2004; Meyer et al., 2006; Pantazes et al., 2007) (see refs. Pantazes et al., 2011; Hilvert, 2013; Huang et al., 2016 for review). Structure-based redesign is best suited for the aim of improving AOM activity because Mcr, which has a known structure (Shima et al., 2012), naturally catalyzes this reaction (Moran et al., 2005, 2007; Scheller et al., 2010). The Iterative Protein Redesign and Optimization procedure (IPRO) is a structure-based protein redesign tool that incorporates (step 1) recursive random backbone perturbations, (step 2) deterministic rotational isomer (i.e., rotamer) optimizations, and structural refinements to improve enzyme performance toward a specific target (Saraf et al., 2006; Fazelinia et al., 2007; Grisewood et al., 2013; Pantazes et al., 2015). These structural refinements include (step 3) local ligand docking and (step 4) a force field energy minimization. Designs then have (step 5) their interaction energies with various ligands calculated, and based on these calculated energies, (step 6) the variant is accepted or rejected using the Metropolis criteria. IPRO offers key advantages over other available structure-based redesign procedures in that it can (i) handle multiple design criteria simultaneously, (ii) be easily manipulated for a problem-specific objective function, and (iii) maintain the geometry of catalytic residues using distance restraints.

In this work, we investigated the limiting steps for AOM kinetics and developed multiple case studies under which different steps may be limiting. For each of these case studies, *Methanosarcina acetivorans* serves as the host system because ANME methanotrophs have not yet been isolated (Scheller et al., 2010; Haynes and Gonzalez, 2014). *M. acetivorans* is phylogenetically closely related to ANME-2 (a specific clade of ANME; Mueller et al., 2015) archaea (Moran et al., 2007; Yan et al., 2018). The goal of improving AOM kinetics was subdivided into four separate case studies. The first case study (CS1) considered redesigning ANME-1 Mcr to accept the cofactor $F_{430}$ found in methanogenic archaea in lieu of its native cofactor (Mayr et al., 2008; Shima et al., 2012). In a second case study (CS2), we considered that Mcr may be limited by formation of the methyl radical at high temperatures (>45°C; Wongnate et al., 2016). In the third study (CS3), published Mcr binding and reaction rates were used to postulate that Mcr kinetics is limited by $CH_3$-S-CoM unbinding (Ellermann et al., 1988; Scheller et al., 2010; Chen et al., 2012; Wongnate and Ragsdale, 2015; Wongnate et al., 2016). A final investigation (CS4) examined the possibility that AOM is limited by the second step of the reverse aceticlastic pathway involving a methyl-tetrahydrosarcinapterin:coenzyme M ($CH_3$-$H_4$SPT:HS-CoM) methyltransferase (Mtr) (Benedict et al., 2012; Vepachedu and Ferry, 2012; Nazem-Bokaee et al., 2016). An overview of these case studies is provided in **Figure 1**.

## RESULTS AND DISCUSSION

For each case study, we constructed enzyme variant libraries to alleviate its particular kinetic limitation. Execution of various case studies is important for improving AOM kinetics because the precise relationship between physical conditions and the rate-limiting step is ill-defined. We describe general trends observed in the variant libraries for each case study and analyze differences between the libraries. The top results for each library are presented in each case.

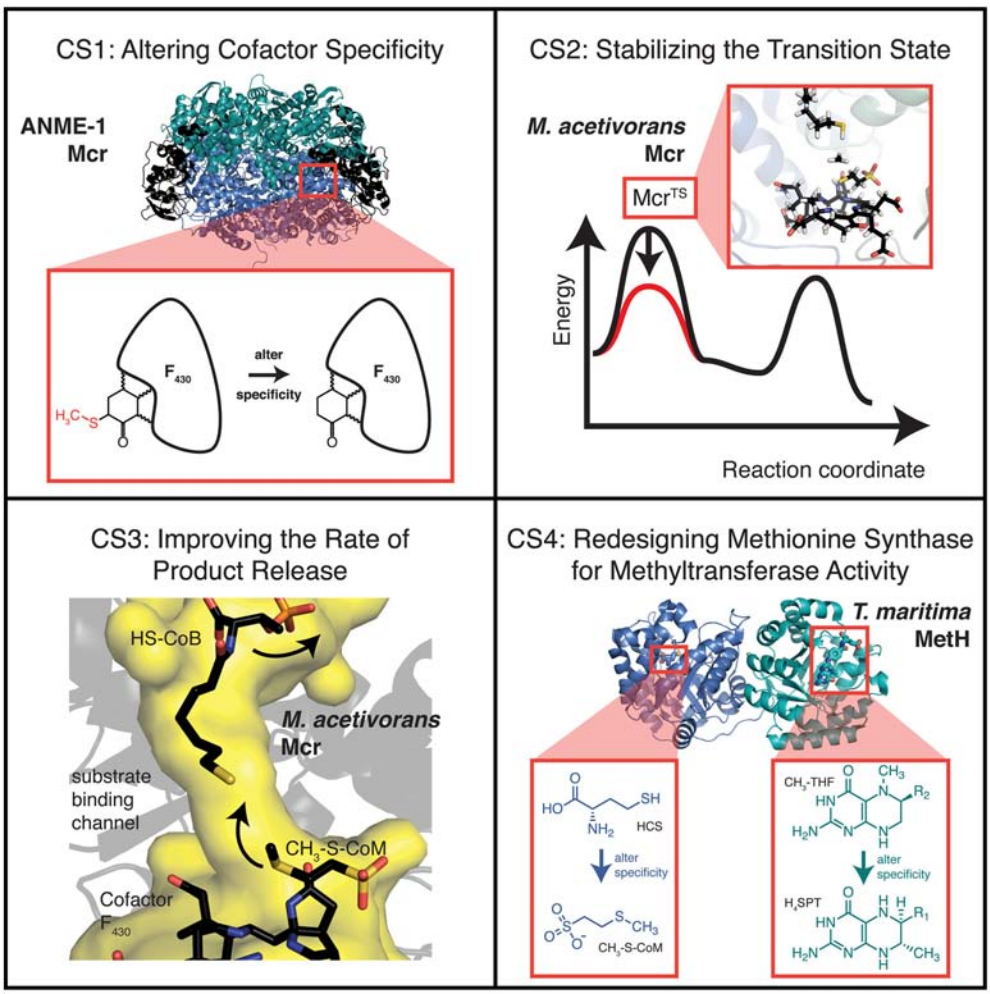


**FIGURE 1 |** Overview of the various case studies examined for improving AOM activity. Substrate, intermediate, and transition state energies for the free energy diagram shown for CS2 are taken from density functional theory calculations (Chen et al., 2012). The substrate abbreviations for CS4 are homocysteine (HCS), methyl-coenzyme M ($CH_3$-S-CoM), 5-methyltetrahydrofolate ($CH_3$-THF), and tetrahydrosarcinapterin ($H_4$SPT).

## Case Study 1: Altering Anme-1 Mcr Cofactor Specificity

The recently elucidated structure of ANME-1 Mcr (Shima et al., 2012) revealed key structural differences relative to methanogenic Mcrs. These differences included enriched regions of cysteine residues, a methylthiolation of cofactor $F_{430}$ at $C17^2$, and a distinct set of post-translationally modified amino acids (Shima et al., 2012). While the significance of each of these differences has not been fully resolved, it is reasonable to assume that they arose from evolutionary divergence or fine-tuning of the enzyme for its specific function. It has been suggested that the $17^2$-methylthiolation of cofactor $F_{430}$ is catalytically non-essential because ANME-2 Mcrs contain the unmodified cofactor (Mayr et al., 2008). Moreover, the importance of Mcr's post-translational modifications has been questioned since many of these adaptations are not conserved (Kahnt et al., 2007). In CS1, the assumption is made that these post-translational and cofactor modifications help to maintain the proper active site geometry but are non-essential for catalytic activity.

Expression of ANME-1 Mcr into the *M. acetivorans* host and subsequent AOM was recently demonstrated (Soo et al., 2016). Although ANME-1 Mcr in *M. acetivorans* was not isolated and activity validated, wild-type (WT) *M. acetivorans* is unable to perform AOM in the absence of methanogenic substrates indicating methane consumption of the engineered strain is attributable to ANME-1 Mcr and not WT Mcr (Soo et al., 2016). However, the methane consumption by ANME-1 Mcr corresponds to an AOM specific activity of only ∼20 nmol $min^{-1}$ $mg^{-1}$ (Soo et al., 2016), which is about 3-fold lower than the estimated *in vivo* activity of ANME Mcr (Scheller et al., 2010). The assumption that the $17^2$-methylthiolation of cofactor $F_{430}$ is crucial for locking the cofactor into its preferred orientation in ANME-1 Mcr implies a reduction in catalytic activity ensues if cofactor $F_{430}$ is not correctly oriented. Therefore, the reduced activity of ANME-1 Mcr expressed in *M. acetivorans* may be partially explained by the unavailability of the methylthiolated cofactor in methanogens (Mayr et al., 2008; Allen et al., 2014). Improving ANME-1 Mcr binding to the unmodified cofactor could engender increased rates for AOM when the enzyme is expressed in *M. acetivorans*.

IPRO was used to predict ANME-1 Mcr variants with improved binding to the unmodified cofactor $F_{430}$. Variable positions (i.e., design positions) were selected based on (i) proximity to $C17^2$, (ii) conservation amongst methanogens but not methanotrophs, and (iii) a review of existing literature, which suggested V419 is crucial for the $C17^2$ methylthiolation (Shima et al., 2012) (see Materials and Methods). The 10 selected design positions were Q72, L77, M78, N90, P149, I154, H157, H414, V419, and C423, which all reside within the α-subunit of ANME-1 Mcr. Five independent IPRO trajectories were simulated for 1000 iterations using ensemble structure refinements. Ensemble structure refinements are used within IPRO to sample multiple confirmations for a given protein sequence, thereby improving the accuracy of the energy calculations and quality of the results. During the five IPRO simulations, eight unique variants were identified. The top five variants are provided in **Table 1**.

In examining the top five variants presented in **Table 1**, a propensity for glycine substitutions was observed (see **Figure 2**). At first, it was thought that these substitutions were algorithmic artifacts due to unfavorable backbone conformations or to alleviate steric clashes within the active site. Despite introducing a Lennard-Jones softening term and reweighting the scoring function for the rotamer optimization step (i.e., step 2 of IPRO; Grisewood et al., 2017), this partiality for glycine persisted. Additionally, the same algorithmic architecture was employed for CS2–CS4 and for a separate enzyme system (Grisewood et al., 2017), but this glycine preference was not observed in those studies. Based on this and analyzing the top structures, it seems plausible that the glycine residues provide the required flexibility within the active site that allows other side chains to form beneficial contacts with the unmodified cofactor $F_{430}$.

The geometry of the top variants' active sites appears at an intermediate state between ANME-1 Mcr and *Methanothermobacter thermautotrophicus* (i.e., methanogenic) Mcr with their native cofactors (see **Figure 3**). It is unsurprising that the top ANME-1 variants do not bind cofactor $F_{430}$ as tightly as *M. thermautotrophicus* because the methanogenic Mcr has naturally evolved to tightly bind its cofactor. Additionally, V419 is replaced with a methylated (presumably to increase the active site hydrophobicity) glutamine in the *M. thermautotrophicus* structure. IPRO is limited in that it can only replace the valine with canonical amino acids, and in this case, hydrophobic amino acids. This restricts the gamut of possible side chain conformations within the tightly packed and highly conserved Mcr active site. Despite not achieving the same level of tight binding to cofactor $F_{430}$ relative to *M. thermautotrophicus*, the top variants demonstrate a noticeable improvement over ANME-1 Mcr in terms of the calculated interaction energies. The two closest design positions to $C17^2$ are H414 and V419, which constitute the methylthio- substituent's binding site in ANME-1 Mcr. Unlike *M. thermautotrophicus* Mcr that occupies the methylthio- binding site via a large side chain at position 419, IPRO suggests redesigns that shift the side chain of position 414 closer to $C17^2$ (see **Figure 3**). Variants that do not contain the H414G substitution (i.e., Variants 3 and 5, see **Table 1**), instead

**TABLE 1** | Top five variants of CS1, sorted by interaction energy between the enzyme and unmodified cofactor $F_{430}$.

| Variant | 1* | 2* | 3* | 4* | 5 |
|---|---|---|---|---|---|
| Q72 | – | G | – | – | – |
| L77 | – | G | G | G | – |
| M78 | – | – | – | G | – |
| N90 | G | – | – | G | – |
| H414 | G | G | L | – | L |
| V419 | – | – | G | G | – |
| C423 | G | – | G | G | – |

*No substitutions were observed for design positions P149, I154, and H157. All design positions were within the α-subunit of ANME-1 Mcr and are sorted by the interaction energy between the variant and cofactor $F_{430}$. An asterisk next to the variant number indicates a significant improvement over WT interaction energy ($p < 0.05$).*

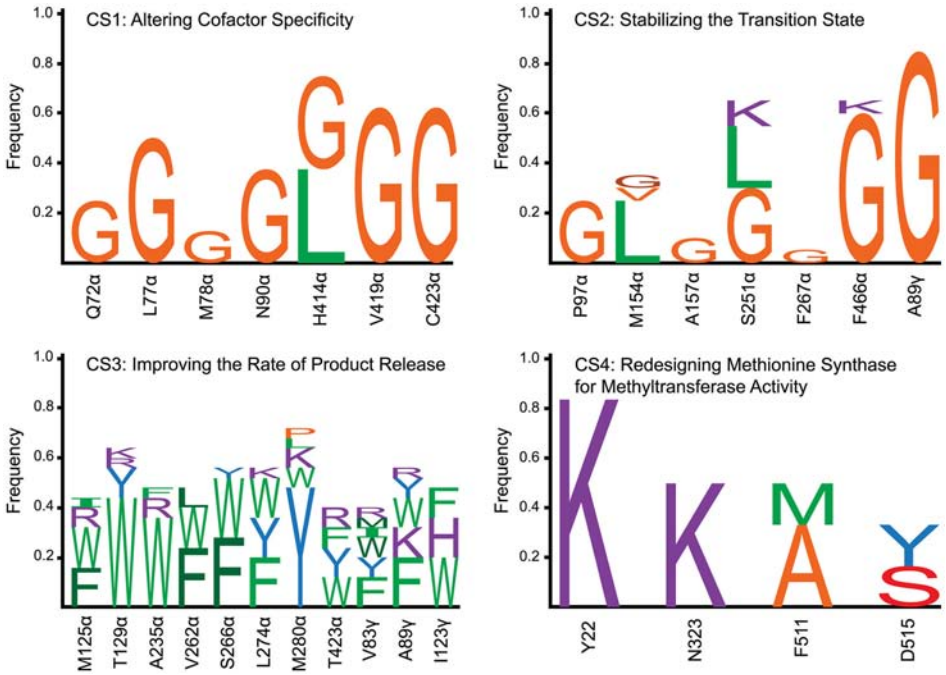


**FIGURE 2 |** Frequency of amino acid substitutions for each of the four case studies. For CS1, CS2, and CS4, all of the identified variants were incorporated into the frequency calculation. Due to the high number of variants identified in CS3, only the top 25 results were included within the plot. Wild-type amino acids are not included within the barcharts, accounting for the sum of the individual frequencies not adding to 1.0. The design positions are labeled by the wild-type one-letter amino acid code, position, and subunit (except for CS4 which only has a single subunit). Amino acid types were classified into five different categories and colored according to category. These categories were (1) large [≥162 Å$^3$ (Pommié et al., 2004)] with a non-polar side chain (green), (2) small (<162 Å$^3$) with a non-polar side chain (orange), (3) large with a polar side chain (blue), (4) small with a polar side chain (red), and charged (purple). Different shades of the same color were used to distinguish stacked one-letter codes of the same amino acid category.

force V419 closer to C17$^2$, although not to the extent of the methyl-glutamine in *M. thermautotrophicus*. The effect of the other substitutions is more subtle since these design positions are more distant from the active site.

The veracity of these results is dependent on two key assumptions. First, the ANME-1 Mcr post-translational modifications must be non-essential because the genes required to make these modifications may not exist within the host organism. Second, the 17$^2$-methylthiolation of cofactor $F_{430}$ ought to be catalytically insignificant. Since these two assumptions cannot be tested *a priori*, we considered a second case study that focused on identifying the kinetic bottleneck and redesigning the native Mcr of *M. acetivorans*, where the concerns of heterologous expression are eliminated.

## Developing a Complete Model for Mcr Kinetics

The complex chemistry undergone during Mcr catalysis has attracted numerous investigations into the enzyme's reaction mechanism, and recent findings have shown that Mcr follows a bi-bi radical-based reaction mechanism (Cedervall et al., 2010; Chen et al., 2012; Scheller et al., 2013; Wongnate and Ragsdale, 2015; Wongnate et al., 2016). This information, along with several assumptions, an existing $IC_{50}$ value for HDS during methanogenesis (Ellermann et al., 1988), and the rate of $^{13}CH_3$-S-CoM formation as a function of methane partial pressure (Scheller et al., 2010), yielded specific rate constants for each step in the mechanism. One key assumption in the development of this model is that Mcr kinetics is nearly invariant amongst various methanogenic archaea. This assumption, which is supported by very strong sequence conservation (Reeve et al., 1997) and nearly identical active site structures (Grabarse et al., 2000), enables integration of extensive data to fully characterize Mcr kinetics. These observed and estimated rate constants suggest the probable rate-limiting step of Mcr, which is the release of the produced $CH_3$-S-CoM to regenerate the free enzyme.

The full reaction mechanism of Mcr, including substrate binding and product release, is depicted in **Figure 4**. The specific rate constant for step 1 was estimated using inhibition studies (Ellermann et al., 1988) and is discussed in greater detail below. Density functional theory calculations (Chen et al., 2012) and the Eyring equation were used to estimate the specific rate constants for step 2. While the transition state for step 3 was not found, the anionic intermediate ($Mcr^{Int1}$) was only "transiently formed" and thus its kinetics must be rapid (Chen et al., 2012). The kinetics of step 4 is evaluated from fitting data to the Michaelis-Menten equation and is described in more detail below (Scheller et al., 2010). The specific rate constant for step 5 was also calculated from density functional theory calculations and the

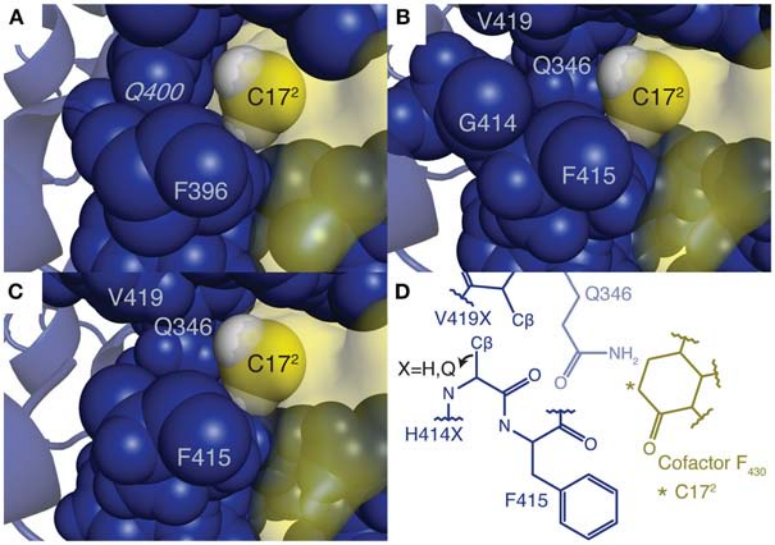


**FIGURE 3 |** Active site structures of **(A)** *M. thermautotrophicus* Mcr, **(B)** the top CS1 variant, **(C)** ANME-1 Mcr, and **(D)** an overview of all three Mcrs in complex with cofactor $F_{430}$. In subplots **(A–C)**, the unmodified cofactor $F_{430}$ is depicted as a yellow molecular surface with $C17^2$ and its two bonded hydrogen atoms (colored white) shown as spheres. Residues within six angstroms of $C17^2$ are displayed as blue spheres, while the remainder of the enzyme is represented by a blue cartoon diagram. G416 and G417 (G397 and G398 in *M. thermautotrophicus* Mcr) are not shown so that the spatial relationship between $C17^2$ and nearby amino acids is clearly visible. Residues constituting the methylthio- substituent binding site in the ANME-1 structure are labeled by their one letter amino acid abbreviation and sequence position, including the methylated glutamine (italicized). The $C17^2$ carbon is also labeled. Due to the highly conserved structures of the three Mcrs, subplot D was created, which depicts the general architecture of the active site. Residues forming the methylthio- moiety binding site are labeled using the numbering scheme of ANME-1 Mcr (Q346, H414, F415, and V419 correspond to Q332, Q395, F396, and methyl-Q400 in *M. thermautotrophicus*, respectively). Q346 is behind the other the amino acids, which is represented by its reduced opacity. The position of the Cβ is given for the second hydrogen atom in H414G (as in the top variant of CS1), but the Cβ position shifts away from $C17^2$ if a larger side chain is present.

Eyring equation (Chen et al., 2012). Step 6 does not have an energy barrier and therefore also exhibits a fast reaction rate (Chen et al., 2012). The specific rate constants for steps 7 and 8 of the mechanism are taken from electron paramagnetic resonance (EPR) and fluorescence experiments (Wongnate and Ragsdale, 2015). Calculations for steps 2 and 5 assumed a temperature of 25°C to match the EPR and fluorescence conditions (Wongnate and Ragsdale, 2015).

The kinetics of step 1 was estimated using competitive inhibition studies by HDS during methanogenesis, where an $IC_{50}$ of 0.6 mM was reported (Ellermann et al., 1988). The mechanism for HDS inhibition is depicted in **Figure 5**. $k_{12}$ in **Figure 5** is equivalent to $k_1$ (the rate constant for step 1 of methanotrophy) in **Figure 4**. Assuming Briggs-Haldane kinetics (i.e., reaction intermediate concentrations are time invariant) and that the concentration of Mcr·HDS formed via reaction 11 is negligible relative to that of reaction 12, $k_{12}$ can be expressed as a function of the $IC_{50}$ value (Equations 3, 4, see Supplementary Material).

$$k_{12} = \frac{k_{-12} + \frac{k_{-12}(k_{-10}+k_{11})}{k_{10}[HS\text{-}CoB]} + C_1 k_{-12}\left(1 + \frac{k_{13}[HS\text{-}CoB]}{k_{-13}}\right)}{IC_{50}C_1} \quad (3)$$

$$C_1 = \frac{k_{11}}{k_9\,[CH_3\text{-}S\text{-}CoM]} + \frac{k_{-9}\left(k_{-10} + k_{11}\right)}{k_9 k_{10}\,[CH_3\text{-}S\text{-}CoM]\,[HS\text{-}CoB]} \quad (4)$$

The underlying assumption that Mcr·HDS is primarily formed through reaction 12 (see **Figure 4**) is justified because methane formation (i.e., the reaction co-product) is considerably reduced in the presence of HDS (Ellermann et al., 1988), and this assumption also implies that $k_{-12} > 18\ s^{-1}$ ($k_{cat}$ for methanogenesis) (Wongnate and Ragsdale, 2015). The known HDS $IC_{50}$ value (Ellermann et al., 1988), the corresponding substrate concentrations (Ellermann et al., 1988), and known specific rate constants (Wongnate and Ragsdale, 2015) establish a lower limit for $k_{12}$ ($1.08 \times 10^6\ M^{-1}s^{-1}$). Using the $IC_{50}$ value (0.6 mM) as an approximate HDS concentration, we can estimate the specific rate constant for step 1 as $650\ s^{-1}$.

The specific rate constant for step 4 was determined using the hyperbolic dependence of reaction velocity on methane concentration ($R^2 = 0.998$), which is indicative of Michaelis-Menten kinetics (Scheller et al., 2010). Methane partial pressures (Scheller et al., 2010) were converted to concentrations using the linear relationship between concentration and pressure under moderate conditions (1–20 bar, $R^2 = 1.000$, see Supplementary Figure 1; Duan and Mao, 2006). The *in vivo* Mcr concentration (4.7 μM) was estimated from carbon monoxide-activated *Methanothermobacter marburgensis* cells (Zhou et al., 2013). Non-linear regression was used to estimate Michaelis-Menten parameters for the reaction ($k_{cat} = 0.12\ s^{-1}$, $K_M = 2.5$ mM, see Supplementary Figure 2). Established from the same experimental studies as steps 7 and 8, the lower limit for the $k_{off}$ rate is $20\ s^{-1}$ (Wongnate and Ragsdale, 2015). Using the

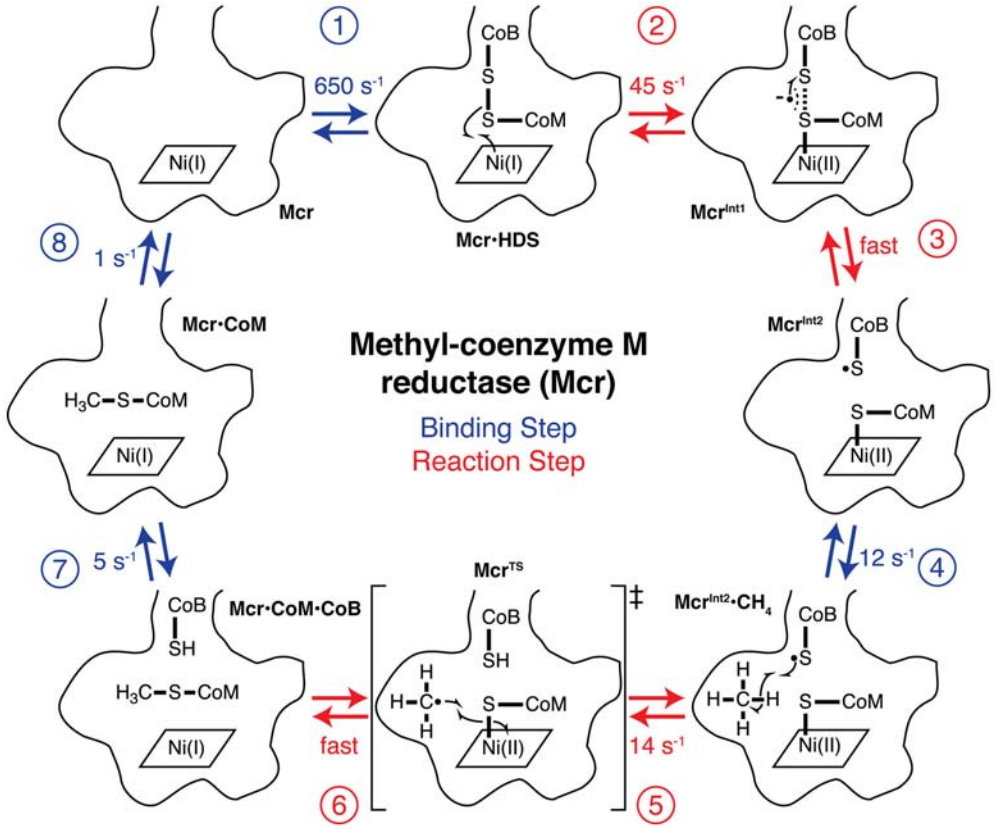


**FIGURE 4 |** The complete catalytic cycle and associated specific rate constants for AOM by Mcr. The bottom of Mcr's narrow substrate channel and cofactor $F_{430}$ binding are outlined for each step of the mechanism. Each of the reaction intermediates are numbered and labeled. The free state of Mcr first (step 1) binds HDS to form the Mcr·HDS intermediate. Ni(I) (step 2) donates an electron to HDS to form $Mcr^{Int1}$, which rapidly (step 3) interconverts to form $Mcr^{Int2}$. $Mcr^{Int2}$ (step 4) binds methane to yield $Mcr^{Int2}$·$CH_4$, which has a C-H bond homolytically (step 5) cleaved to propagate the radical reaction. The methyl radical is formed as part of the reaction's transition state ($Mcr^{TS}$). The Ni(II)-thiolate is homolytically (step 6) cleaved and donates an electron to the methyl radical, which terminates the radical mechanism. The product of step 6 is the product ternary complex (Mcr·CoM·CoB), where Mcr is bound to both $CH_3$-S-CoM and HS-CoB simultaneously. HS-CoB is (step 7) released from the active site to generate Mcr·CoM, and $CH_3$-S-CoM is subsequently (step 8) released to regenerate the free enzyme. Steps 1, 4, 7, and 8 are depicted in blue and are (un)binding steps of the reaction mechanism, while steps 2, 3, 5, and 6 are steps during the chemical reaction and are shown in red.

established $k_{off}$, $k_{cat}$, and $K_M$ values, the $k_{on}$ rate constant can be calculated ($k_{on} = 7.9\ mM^{-1}\ s^{-1}$). At 25°C and atmospheric pressure, the methane concentration is ~1.5 mM (Duan and Mao, 2006). Therefore, the lower limit of the specific rate constant for step 4 is found to be $12\ s^{-1}$.

## Case Study 2: Stabilizing the Transition State of *M. acetivorans* Mcr

While the developed model suggests product release limits Mcr AOM kinetics, it is conceivable that under a different set of physical conditions, a separate step of the mechanism could constrain the net reaction rate. This theory gains credence due to the biphasic kinetics of methyl radical formation in Mcr, which is thought to be a result of a structural transition at 30°C (Wongnate et al., 2016). Above 30°C, the entropy of activation is ~-56 J $mol^{-1}K^{-1}$ (Wongnate et al., 2016). This indicates that the energy barrier for step 5 increases (slower reaction rate) with increasing temperature beyond 30°C. Alternatively, product dissociation from enzymes (i.e., steps 7 and 8 for Mcr) are expected to have a near-zero entropy of activation (Kamerlin et al., 2008), indicating that the energy barrier is insensitive to temperature changes. Since the specific rate constant for step 5 of the reaction mechanism is only marginally larger than that of the reported rate of product release (step 8), it seems plausible that the formation of the methyl radical would constrain the net rate for AOM at higher temperatures (>45°C). In Case Study 2, Mcr variants are identified that stabilize the transition state ($Mcr^{TS}$), which corresponds to formation of the methyl radical.

*Methanosarcina acetivorans* Mcr variants were selected by IPRO with the objective function targeting an improvement in interaction energy with the transition state. Design positions were chosen on the basis of (i) proximity to the active site, and (ii) sequence diversity amongst methanogens (see Materials and Methods). The nine selected design positions were P97α, M154α, A157α, M163α, I245α, S251α, F267α, F466α, and A89γ. The transition state structure (Chen et al., 2012) was grafted into the *M. acetivorans* Mcr active site, with atoms from the resolved transition state structure fixed in place. Grafting the

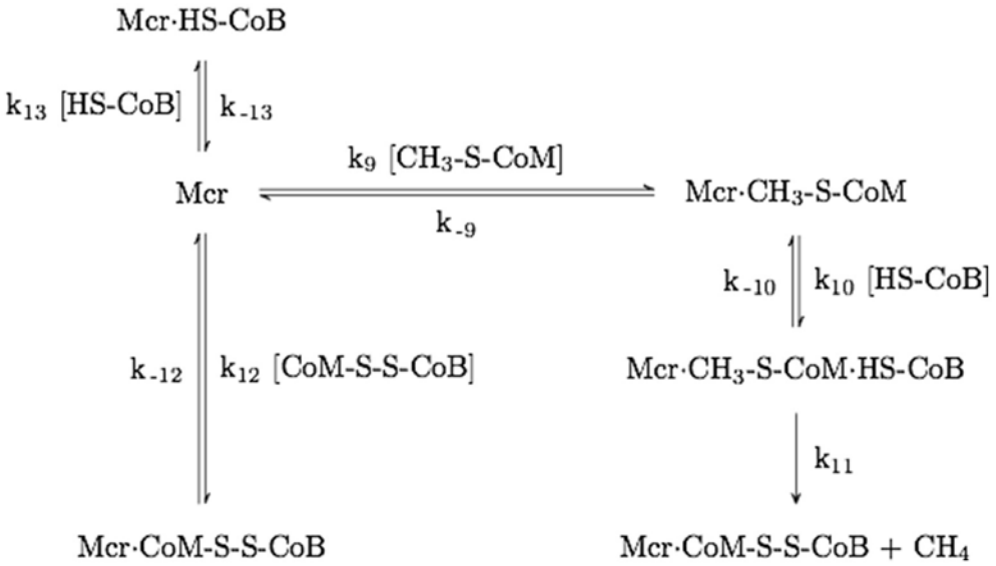


**FIGURE 5 |** Mechanism of Mcr competitive inhibition by HDS. The rate constant numbering begins with $k_9$ to avoid ambiguity with the mechanism shown in **Figure 4**.

transition state structure resulted in an unfavorable Generalized Born implicit solvation energy term (Lee et al., 2003) for the enzyme that was not readily alleviated with a force field energy minimization. Interaction energies were used in lieu of complex energies to ensure that stabilization of the transition state does not also stabilize the ground state molecules, and render the energy barrier unaltered. Ten independent IPRO trajectories were simulated for 3000 iterations each, and 20 total variants were established. The top five variants are enumerated in **Table 2**.

**Table 2** demonstrates that substitution with leucine at position M154α and a substitution with glycine at A89γ are ubiquitous. The WT Mcr structure reveals an unfavorable hydrophilic-hydrophobic contact between R152γ and A89γ (4.8 Å between the guanidino group of R152γ and Cβ of A89γ). The substitution to glycine alleviates this poor contact due to its lower hydrophobicity and longer distance to R152γ (5.2 Å). The A89γG substitution does not interact with the transition state. The other ubiquitous substitution, M154αL, indirectly removes a poor interaction with the transition state structure of cofactor $F_{430}$ (unmodified in CS2–CS4). The leucine side chain forces Q244α into an alternate conformation with respect to the WT structure. In the WT structure, two amido groups are in close proximity (one from cofactor $F_{430}$, one from Q244α), weakening nearby hydrogen bonds between Mcr and cofactor $F_{430}$. When Q244α is in its alternate conformation, caused by M154αL, these hydrogen bonds remain intact, improving the interaction energy between Mcr and the grafted transition state.

The top designs listed in **Table 2** suggest that the presence of S251αK, S251αL, and S251αG can all form beneficial interactions with the transition state. Though the nature of these side chains vary drastically, they all improve interaction energy by stabilizing a nearby loop of residues between M255α and G258α, which is immediately adjacent to cofactor $F_{430}$. S251αK stabilizes this loop by forming a hydrogen bond between the

**TABLE 2 |** Top five variants of CS2, sorted by interaction energy between the enzyme and grafted transition state.

| Variant | 1* | 2* | 3* | 4* | 5* |
|---|---|---|---|---|---|
| M154α | – | L | L | – | L |
| S251α | K | K | L | L | G |
| F466α | K | G | G | G | – |
| A89γ | G | G | G | G | G |

*Design positions are listed with their WT one-letter amino acid code, followed by sequence position and Mcr subunit. No substitutions were observed at P97α, A157α, M163α, I245α, and F267α. Variants were sorted by their interaction energy with the transition state. An asterisk is provided next to variants with significant improvements over WT ($p < 0.05$).*

S251αK ε-amino hydrogen and the unprotonated nitrogen of H145α. S251αL stabilizes the M255α-G258α loop by packing nicely within a binding site formed by M72, H73, T149, V159, and A252, all of which consitute the α-subunit. Finally, S251αG forms favorable dispersion forces with V159α, which is sandwiched between the loop and S251α. Design position F466α can accommodate substitutions to lysine or glycine in order to improve interaction energy with the grafted transition state. Similar to the S251α substitutions, both F466αK and F466αG stabilize the transition state by altering the conformation of residues lining the long, narrow substrate channel of Mcr. The residues with the most drastic changes are F463α, F464α, Q469α, N501α, and H504α, where F463α and F464α form part of the ·S-CoM binding site. Since phenylalainine is hydrophobic and ·S-CoM is largely hydrophilic, the altered conformation reduces unfavorable hydrophobic-hydrophilic interactions in the active site, thereby improving the interaction energy with the transition state. In this alternate conformation, more hydrophilic amino acids, such as Y346α, Y365β, and R121γ, can create favorable contacts with ·S-CoM in its binding pocket (see **Figure 6**).

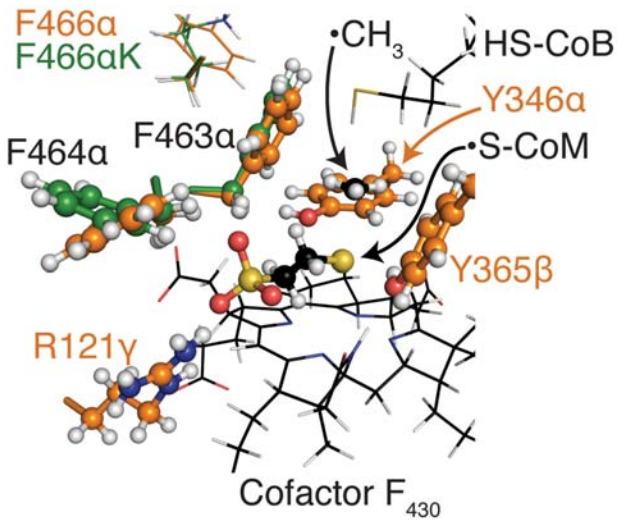


**FIGURE 6 |** Alternate positions of F463α and F464α nearby the coenzyme M binding site for top variants in CS2. The CoM moiety and residues that form its binding pocket within Mcr are shown as balls and sticks, while other key residues are shown as thin sticks. All atoms are colored by atom type (H, white; N, blue; O, red; S, yellow), while carbon atoms are colored orange for WT *M. acetivorans* Mcr, green for the top variant of CS2, and black for HS-CoB, ·CH3, S-CoM, and cofactor $F_{430}$. The conformations of F463α and F464α are largely invariant within the top CS2 variants so only the top variant is presented here.

In all, the top five CS2 designs converge to the same principles to improve interaction energy with the transition state. Substitutions at M154α (only leucine) help improve the hydrogen bonding network between Mcr and cofactor $F_{430}$. The substitutions at S251α stabilize the conformation of the loop between M255α and G258α, which directly contacts cofactor $F_{430}$. F466αK and F466αG reduce the hydrophobicity nearby the hydrophilic ·S-CoM. The substitution at position A89γ does not affect transition state binding but instead lessens an unfavorable contact formed with R152γ.

## Case Study 3: Engineering *M. acetivorans* Mcr for More Rapid Product Release

Case Study 3 was carried out to improve the rate of $CH_3$-S-CoM and HS-CoB unbinding, which are proposed to be the first and second slowest steps, respectively, of the reaction mechanism at 25°C. Though a transition state structure is unattainable for (un)binding events, the energy barrier can be lowered by raising the energy of the ground state Mcr·CoM·CoB and Mcr·CoM complexes. Destabilization of the enzyme's ground state has been demonstrated to improve catalysis for other enzyme systems (Andrews et al., 2013; Ruben et al., 2013; Phillips et al., 2016) and is particularly applicable for improving the rate of product release, where finding a transition state structure is impractical. Mcr·CoM·CoB and Mcr·CoM exhibit similar enzyme topologies and $CH_3$-S-CoM binding modes, with the key difference being increased flexibility in the Mcr substrate channel nearby the HS-CoB binding site (Cedervall et al., 2010). The low backbone root-mean-square deviation (RMSD) between Mcr·CoM·CoB and Mcr·CoM of 0.21 Å, with a ligand all-atom RMSD of 0.07 Å, supports this claim (Grabarse et al., 2001; Cedervall et al., 2010). Owing to this high structure similarity, variants that destabilize Mcr·CoM are expected to correspondingly destabilize Mcr·CoM·CoB. By destabilizing Mcr·CoM·CoB, the rates of both $CH_3$-S-CoM and HS-CoB unbinding (i.e., steps 7 and 8) are expected to increase.

The structures of $Mcr^{TS}$ and Mcr·CoM·CoB are also similar, with a ligand all-atom RMSD of 1.7 Å. Due to this similarity, it was postulated that increasing the complex energy of Mcr·CoM·CoB might also destabilize $Mcr^{TS}$. The variant structures from CS2 were used to test this hypothesis, and a strong correlation was observed between the two energies ($r = 0.73$). To account for this, IPRO's objective function was adjusted so as to minimize the difference in $Mcr^{TS}$ and Mcr·CoM·CoB complex energies. Additionally, an alternate conformation of the β-subunit between residues 364 and 370 persists in the free enzyme (Grabarse et al., 2001) near the HS-CoB binding site. A constraint was added to IPRO to prevent destabilization of the free enzyme (Mcr), while incorporating the structural differences in the β-subunit between Mcr and $Mcr^{TS}$/Mcr·CoM·CoB.

A description of the revised MILP used within the second step of an IPRO iteration is provided below:

### Sets

$i, j \in \{1, 2, \ldots, N\}$ = Set of perturbed positions in Mcr α- and/or γ- subunits

$r, s \in \{1, 2, \ldots, R_i\}$ = Set of rotamers, where $R_i$ is the number of rotamers available at position $i$

$k, l \in \{1, 2\}$ = Binding assemblies

A binding assembly is a set of ligands that has its binding affinity for the design molecule (i.e., Mcr) altered by IPRO. Each structure within the Mcr mechanism (see **Figure 4**) signifies a separate binding assembly. For CS3, there are three binding assemblies: (1) $Mcr^{TS}$, (2) Mcr·CoM·CoB, and (3) the unbound enzyme (i.e., Mcr). Only the first two binding assemblies are considered in the revised MILP. The third binding assembly is used within a subsequent MILP with its rotamers restricted to match the amino acid sequence from the first MILP's optimal solution (see Pantazes et al., 2015 for a more detailed description of the standard IPRO MILP). Thus, two MILPs are executed within a single IPRO iteration.

### Binary Variables

$$x_{irk} = \begin{cases} 1, & \textit{if rotamer r is selected at position i in binding assembly k} \\ 0, & \textit{otherwise} \end{cases}$$

### Continuous Variables

$$z_{irkjs} = \begin{cases} 1, & \textit{if rotamer r is selected at position i and rotamer s is simultaneously selected at position j in binding assembly k} \\ 0, & \textit{otherwise} \end{cases}$$

## Parameters

$E^{rc}_{irk}$ = rotamer − constant energy of rotamer $r$ at position $i$ in binding assembly $k$

$E^{rr}_{irkjs}$ = rotamer − rotamer energy between rotamer $r$ at position $i$ and rotamer $s$ at position $j$ in binding assembly $k$

$Am_{irk}$ = amino acid type of rotamer $r$ at position $i$ in binding assembly $k$

The rotamer-constant energy is the energy between a rotamer and any other non-rotamer atom within a single binding assembly (e.g., ligands and protein backbone). Using these defined sets, binary variables, continuous variables, and parameters, the MILP objective function is shown in Equation (5), subject to the constraints provided as Equations (6)–(9).

$$Minimize \sum_{i=1}^{N}\sum_{r=1}^{R_i}\left(x_{ir1}\,E^{rc}_{ir1} - x_{ir2}\,E^{rc}_{ir2}\right) - \sum_{i=1}^{N-1}\sum_{j>i}^{N}\sum_{r=1}^{R_i}\sum_{s=1}^{R_j}\left(z_{ir1js}\,E^{rr}_{ir1js} - z_{ir2js}\,E^{rr}_{ir2js}\right) \quad (5)$$

$$Am_{irk} = Am_{irl},\ \forall i,\ r,\ k,\ l \quad (6)$$

$$\sum_{r=1}^{R_i} x_{irk} = 1,\ \forall i,\ k \quad (7)$$

$$x_{irk} = \sum_{s=1}^{R_j} z_{irkjs},\ \forall i,\ r,\ k,\ j > i \quad (8)$$

$$x_{jsk} = \sum_{r=1}^{R_i} z_{irkjs},\ \forall i,\ s,\ k,\ j > i \quad (9)$$

The objective function (Equation 5) minimizes the difference in complex energy between $Mcr^{TS}$ and Mcr·CoM·CoB. Equation (6) guarantees that the same amino acid type is used at each position in both binding assemblies. Equation (7) ensures that only one rotamer is selected at each position. The continuous variable, $z_{irkjs}$, can be written as the product of the two binary variables ($x_{irk} \times x_{jsk}$) and is linearized by Equations (8) and (9).

Since the designs from CS2 did not directly interact with the substrate, we reconsidered the design positions for CS3. The design positions for CS3 were selected based on (i) proximity to the active site or the β-subunit between residues 364 and 370, where the conformation varies between Mcr and $Mcr^{TS}$/Mcr·CoM·CoB, (ii) amino acid diversity at the position, and (iii) proper orientation of the side chain toward either the multi-conformational β-subunit loop or the active site (see Materials and Methods). The 10 selected design positions for CS3 were M125α, T129α, A235α, V262α, S266α, L274α, M280α, T423α, V83γ, and A89γ. As was the case for CS2, transition state atoms for the first binding assembly were fixed in place. The third binding assembly that ensures $E(Mcr_{variant}) \leq E(Mcr_{WT})$ permitted the use of complex energies instead of interaction energies (that were used for CS2). Ten independent IPRO trajectories were executed for 100 iterations each, and 45 variants were identified. The decision to use a fewer number of iterations was made retroactively due to the large success rate and time-consuming nature of ensemble refinements (each refinement performed costs 250 additional IPRO iterations). Of the 45 identified variants, 15 showed simultaneous improvement in stabilizing $Mcr^{TS}$ and destabilizing Mcr·CoM·CoB. The top five of these 15 variants, which were sorting by ascending [$E(Mcr^{TS})$ – E(Mcr·CoM·CoB)] values, are presented as **Table 3**.

**Table 3** shows a preference for large hydrophobic amino acids (see **Figure 2**). The hydrophobic tendency is unsurprising because of the hydrophobic nature of the Mcr active site, but the large size of the substituted amino acids was unexpected due to the small accessible volume available within the active site. In analyzing the top structures presented in **Table 3**, these variants notably demonstrate alternate conformations when the rotamer in the $Mcr^{TS}$ binding assembly versus the Mcr·CoM·CoB binding assembly. In general, when the variant is in the $Mcr^{TS}$ state, the side chain does not extend toward the narrow substrate binding channel. However, when the variant is in the Mcr·CoM·CoB state, the side chain does extend toward the narrow substrate channel, partially occluding it. From a mechanistic point of view (see **Figure 4**), it is plausible that the conformational change of these residues helps to initiate product unbinding by "pushing" the products out of the active site via steric clashes. These side chains likely demonstrate a high degree of flexibility, evidenced by their different conformations in the two binding assemblies, and their overall non-specific interactions formed in both binding assemblies (see **Figure 7**). It is expected that the high flexibility of these residues drives product unbinding but similarly will likely slow the substrate binding of HDS (methane is likely small enough to still pass through the channel). Fortunately, since the predicted specific rate constant is two orders of magnitude higher for substrate binding (see **Figure 4**), these effects will likely go unnoticed since substrate binding still be unlikely to limit

**TABLE 3 |** Top five variants for simultaneously improving the rate of product release and stabilizing the transition state.

| Variant | 1* | 2* | 3* | 4* | 5* |
|---|---|---|---|---|---|
| M125α | – | – | W | – | – |
| T129α | K | Y | W | – | – |
| A235α | W | W | – | W | – |
| V262α | F | F | – | F | W |
| S266α | F | F | – | F | F |
| L274α | W | F | – | F | F |
| M280α | Y | Y | – | Y | Y |
| T423α | Y | W | – | W | – |
| V83γ | F | F | – | – | – |
| A89γ | – | – | W | – | – |
| I123γ | H | H | – | H | – |

*Design positions are listed within their one-letter amino acid abbreviation, position, and Mcr subunit. All variants are sorted by [$E(Mcr^{TS})$ – E(Mcr·CoM·CoB)] values. An asterisk next to the variant number signifies a significant improvement relative to WT ($p < 0.05$).*

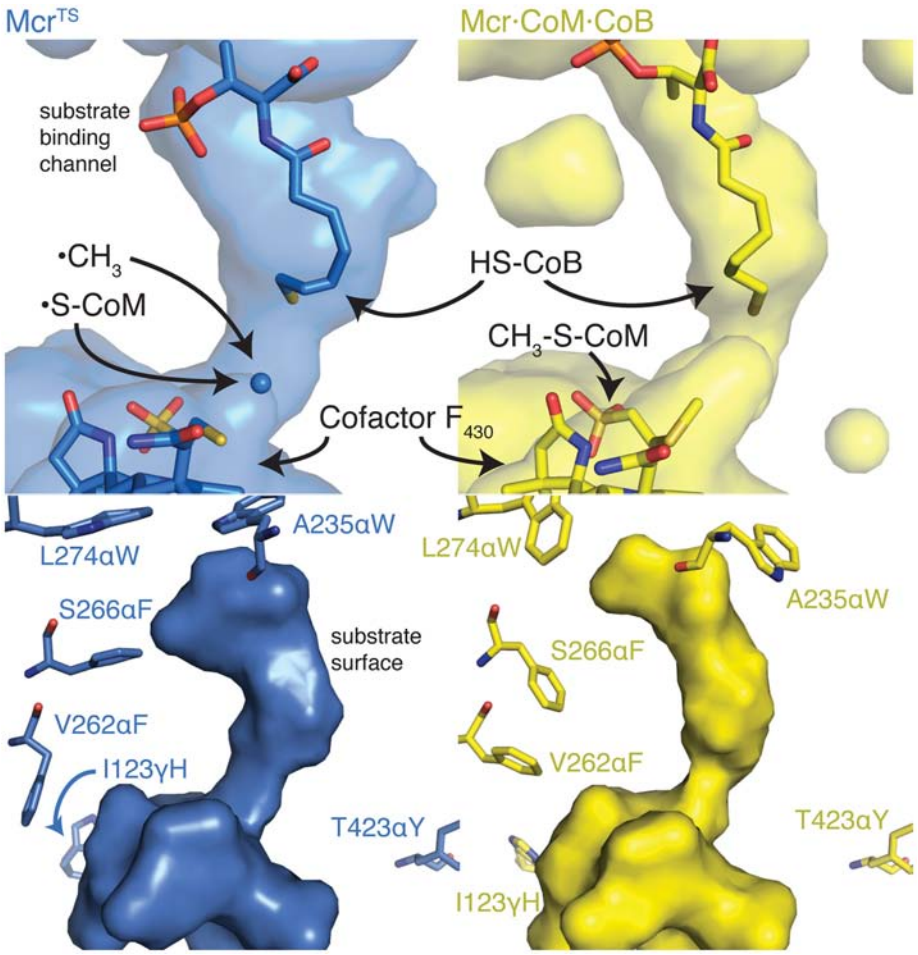


**FIGURE 7 |** The alternate conformations observed for the top CS3 variant's design positions and their effect on the substrate binding channel. The top two panels show the cavities within Mcr nearby the active site. The long thin continuous surface is the substrate binding channel. The bottom two panels illustrate the substrate surface (i.e., not the cavity) and the design positions nearby the substrates. The enzyme structures depicted in blue **(Left)** and yellow **(Right)** represent the $Mcr^{TS}$ and Mcr·CoM·CoB structures, respectively. Key residues and molecules are shown as sticks, colored by atom type, and labeled. The conformation of the yellow side chains generally extend toward the substrate(s) and thus narrow the size of the substrate channel, forcing HS-CoB to assume a more compact conformation.

the overall AOM. Another key difference between $Mcr^{TS}$ and Mcr·CoM·CoB is the more compact aliphatic chain conformation of HS-CoB in the Mcr·CoM·CoB state of the enzyme. Finally, it is noted that the WT structures, even after refinement, do not demonstrate multiple conformations in a similar manner as the variant structures.

## Case Study 4: Converting *E. coli* Methionine Synthase Into a Mtr

One final possibility that was considered is that Mcr does not limit the overall AOM kinetics, but instead, the second step of the reverse aceticlastic pathway catalyzed by Mtr may constrain the net reaction rate. Mtr, a transmembrane protein, catalyzes the transfer of a methyl group from $CH_3$-$H_4$SPT to HS-CoM and presumably catalyzes the reverse reaction for AOM. Although a soluble version of Mtr (CmtA) was discovered (Vepachedu and Ferry, 2012), this enzyme does not have a known structure and has not demonstrated reversibility, which is essential for inclusion in the AOM pathway. Moreover, homology modeling is unlikely to produce a reliable structure due to low sequence identity of available templates, where the best template covers < 60% of the CmtA sequence space and exhibits only 16% sequence overlap with CmtA (Arnold et al., 2006). Due to these problems associated with CmtA, an alternative approach is to redesign an enzyme homolog with an established structure.

One of the closest homologs to CmtA is methionine synthase (MetH), which catalyzes the transfer of a methyl group from 5-methyltetrahydrofolate to homocysteine to form tetrahydrofolate and methionine (Altschul et al., 1997). Both CmtA and MetH employ vitamin $B_{12}$ as a cofactor for the reaction. CmtA catalyzes the transfer from an aliphatic methyl thioether to a pteridine ring, yielding a thiol, and methylated pteridine ring. Similarly, MetH transfers a methyl moiety from a methylated pteridine ring to a thiol, producing a methyl thioether and pteridine ring (see **Figure 8**). Additionally, MetH has a resolved crystal structure of its N-terminal domain, where 5-methyltetrahydrofolate and

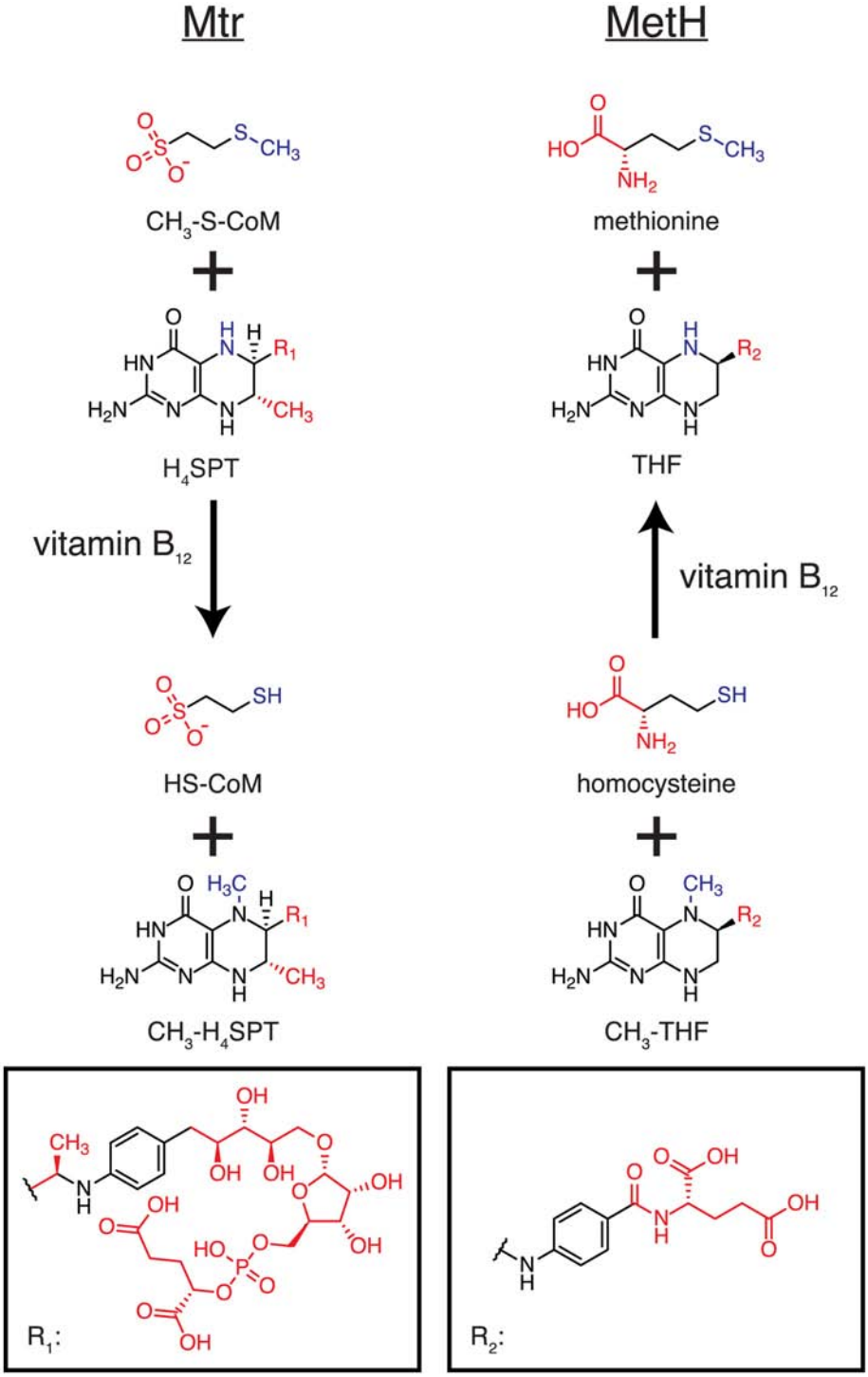


**FIGURE 8 |** Homologous reactions catalyzed by Mtr and MetH. The left column illustrates the reaction catalyzed by Mtr (and CmtA), while the right columns shows the reaction catalyzed by MetH. The reactive portions of each molecule are colored blue, and the differences between Mtr and MetH substrates/products shown in red.

homocysteine bind (PDB 1Q8J) (Evans et al., 2004), and these binding sites are distant from the enzyme's catalytic machinery (Evans et al., 2004). The specific activity of MetH is about 2-fold higher than that of CmtA (Huang et al., 2007; Vepachedu and Ferry, 2012) and is approximately equal between the forward and reverse directions (Rüdiger and Jaenicke, 1969). The similarity of the chemical reaction to that of Mtr, its known crystal structure, cytosolic localization, and high specific activity make

**TABLE 4 |** Top five variants predicted to alter MetH specificity in efforts to mimic the reaction catalyzed by Mtr.

| Variant | 1* | 2* | 3* | 4* | 5* |
|---|---|---|---|---|---|
| Y22 | K | K | K | K | K |
| N323 | – | – | K | K | – |
| F511 | M | – | A | – | A |
| D515 | – | – | Y | S | – |

*No substitutions were observed for design positions K72, D105, E320, E345, N360, N538, D541, and E542. Design position Y22 is in the $CH_3$-S-CoM binding domain, while the remaining design positions constitute part of the $H_4$SPT binding domain. All variants were sorted by their interaction energies with the Mtr substrates. An asterisk next to the variant number denotes a significant improvement in interaction energy over WT ($p < 0.05$).*

MetH a very attractive target for protein engineering. Case Study 4 aims at redesigning the MetH 5-methyltetrahydrofolate and homocysteine binding pockets to instead accommodate $H_4$SPT and $CH_3$-S-CoM, respectively.

MetH variants that demonstrate improved binding to $H_4$SPT and $CH_3$-S-CoM were found by running IPRO for 1,500 iterations over 10 independent trajectories using ensemble structure refinements. Design positions were selected on the basis of (i) distance to atoms that differ between $CH_3$-S-CoM and homocysteine or $H_4$SPT and 5-methyltetrahydrofolate, (ii) sequence diversity as determined using family sequence alignments, and (iii) unfavorable contacts formed between the WT residue at this position and the novel substrates (see Materials and Methods). Twelve design positions were selected in total. A slightly larger number of design positions were permitted due to the large distance between the binding sites. Y22, K72 and D105 were selected from the $CH_3$-S-CoM binding domain, while E320, N323, E345, N360, F511, D515, N538, D541, and E542 were selected from the $H_4$SPT binding domain. Prior to performing a production run, the WT structure was refined with the new substrates to remove as many bad contacts as possible before redesigning the enzyme. In the subsequent production run, six variants were identified with improved binding to the new substrates. The top five designs are presented in **Table 4**.

**Table 4** reveals only one substitution made within the $CH_3$-S-CoM binding domain of MetH – Y22K (see **Figure 2**). As shown in **Figure 9**, this substitution is introduced to help stabilize the negative charge of the $CH_3$-S-CoM sulfonate group. In addition to the improved electrostatics, this conformation allows for hydrogen bonds to be formed between the protein backbone and the sulfonate. These hydrogen bonds are absent from the WT structure. The positive charge of Y22K is important because there are no other positively charged residues nearby to stabilize the sulfonate.

In the $H_4$SPT-binding domain, N323K forms a salt bridge with D390. This interaction stabilizes the wall of the binding crevice and also provides additional volume in the binding site to accommodate one of the methyl substituents that exist in $H_4$SPT but not THF. Both F511M and F511A open up a cavity in the binding site, similar to the N323K substitution. In addition, both F511M and F511A push N508 toward the carbonyl group of the $H_4$SPT pteridine substituent. This movement allows a more favorable hydrogen bond to be formed between the carbonyl and N508. Both D515Y and D515S contribute to improving the stability of the binding site by creating a network of T-shaped π-π stacking interactions, including Y518 and Y519.

# MATERIALS AND METHODS

## Modeling of Enzyme and Ligand Structures

Two of the initial enzyme structures were adopted from crystallography experiments. The initial structure of ANME-1 Mcr (CS1) was taken from PDB 3SQG (Shima et al., 2012). Post-translational modifications were removed from the structure, as there is no way to ensure the presence of these modifications when heterologously expressed. The initial structure of MetH (CS4) was adopted from the N-terminal domain (residues 1–566) of *Thermotoga maritime* expressed in *Escherichia coli* [PDB 1Q8J (Evans et al., 2004)]. The WT structure of *M. acetivorans* Mcr (CS2, CS3) was generated using homology modeling (Arnold et al., 2006), with *M. barkeri* Mcr as the template structure (each subunit ≥90% sequence identity; Grabarse et al., 2000). For the alternate conformation of the β-subunit between residues 364 and 370, the amino acid sequences of the red-1 silent form (free Mcr) of *M. thermautotrophicus* Mcr and *M. acetivorans* Mcr are identical. The two flanking positions on each side of the loop were superimposed to the existing *M. acetivorans* structure, creating the model for the unbound from of Mcr used within CS3.

For CS1, the position of cofactor $F_{430}$ was determined by superimposing against the crystallized methylthiolated cofactor within ANME-1 Mcr. For CS2, the Mcr side chains that were included in transition state structure (Chen et al., 2012) were used to graft the transition state into the *M. acetivorans* Mcr structure by minimizing the RMSD between the transition state and homology modeled structure. The positions of the remaining atoms that were not included in the model of the transition state (i.e., atoms distant from the reactive portions of the molecules) were modeled using CHARMM's internal coordinate system. For CS3, the $CH_3$-S-CoM, HS-CoB, and cofactor $F_{430}$ coordinates were modeled by superimposing against the ox-1 silent version of *M. thermautotrophicus* Mcr (Grabarse et al., 2001). For CS4, the homologous portions between $CH_3$-S-CoM and homocysteine, as well as between $H_4$SPT and 5-methyltetrahydrofolate were superimposed. Docking tools were then used to further refine the initial placement of the structures.

## Design Position Selection

One of the main criteria used for design position selection for all of the case studies was a family sequence alignment. All sequence alignments were performed using Clustal-Omega (Sievers et al., 2011). The sequences to be aligned were extracted from the conserved domain database for CS2–CS4 (Marchler-Bauer et al., 2015). For CS1, differences between methanogenic and methanotrophic archaea were used and therefore manually curated (since methanogenic Mcr and methanotrophic Mcrs are still homologous). The methanogenic Mcr sequences were taken from Uniprot codes P07962, P22948, A4PJ22, D3E050, P12971, P11558, O27232, Q49605, Q58256, P11559, P07961, and

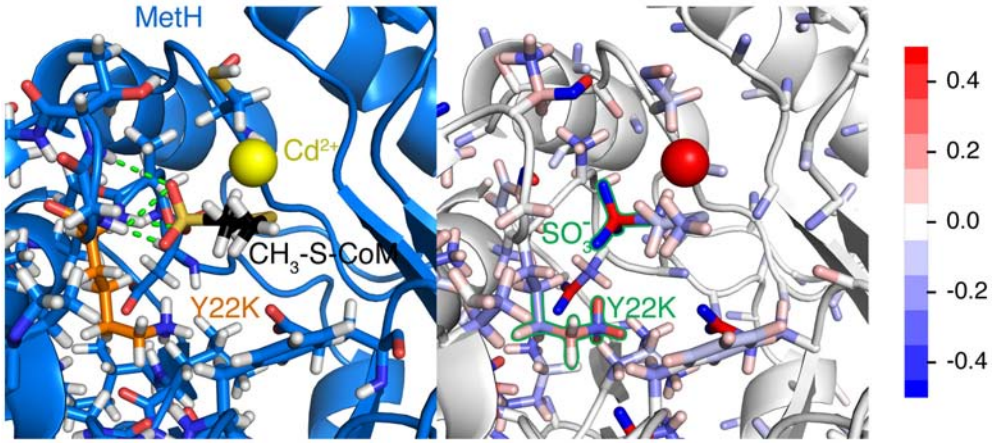


**FIGURE 9 |** Y22K substitution observed in each of the top five variants for CS4. The **(Left)** panel depicts the hydrogen bonds (green) formed between the Mcr backbone and the sulfonate group. Mcr is shown as a blue cartoon, with active site residues colored by element and represented by sticks. Y22K and $CH_3$-S-CoM are also shown as sticks with their carbon atoms colored orange and black, respectively. The cadmium ion in the active site is shown as a yellow sphere. The **(Right)** panel shows the same representation of the active site, but atoms are instead colored by partial charge. It is evident that there is a strong negative charge of the sulfonate group and a positive charge of the Y22K (keeping in mind that the positive charge is distributed amongst the H atoms). The scale for the color scheme is shown on the far right of the figure.

Q6LWZ5 (UniProt, 2015). The methanotrophic Mcr sequences were codes Q6VUA6, Q64E03, Q64EA1, Q648C5, Q64D16, D1JBK4, Q6MZD1, Q64CB7, Q64AN3, Q64EF1, Q649Z5, and Q64DN6. Only those positions that were observed in $\geq$75% of the methanotrophs and <45% of the methanogens were considered for CS1. For CS2–CS4, designs positions were considered sufficiently diverse if their sequence conservation was $\leq$70%.

Distances calculated to the active site were measured from the nickel atom of cofactor $F_{430}$, or the sulfur atoms of $CH_3$-S-CoM or HS-CoB, whichever was closest. For CS3, the Cβ atoms of the altered loop in the β- subunit were also considered in the distance calculation, and for CS2, the atoms from the transition state model were used exclusively. For CS3, the dot product was taken at each position between the Cα–Cβ vector and the vector between the Cα carbon and closest atom from the aforementioned distance screen. Positions whose dot product was <0.5 indicated that this residue was oriented away from the active site, and these positions were not permitted to serve as design positions for CS3. In CS4, unfavorable interactions associated with introducing a larger substrate into the MetH binding site were considered. The rotamer-constant energy was calculated at each position and only those with an unfavorable interaction (i.e., a positive value) remained a potential design position for CS4.

## Case Study Details

The CHARMM force field parameters were determined using the parameter files of homologs and with the aid of CGenFF (Vanommeslaeghe and MacKerell, 2012; Vanommeslaeghe et al., 2012). The Lazaridis-Karplus solvation files were created using the parameters during the model's construction (Lazaridis and Karplus, 1999). Each of the case studies incorporated multiple IPRO trajectories, an ensemble of variants to reliably estimate CHARMM energies, and on the order of ∼1,000 iterations. Fewer iterations were used for CS3 due to the high percentage of successful variants. The ensemble of structures provided distributions of energy values, which were statistically analyzed using Welch's *t*-test. Two copies of the α- subunit, one copy of the β- subunit, and one copy of the γ-subunit form an active site for Mcr. For CS1, only the α- subunits were considered because the β- and γ- subunits are not nearby the $C17^2$ atom. For CS2, all four polypeptides were incorporated as design molecules (i.e., molecules that can have their structures perturbed). For CS3, the multiple β- subunit conformations were used to take advantage of subtle active site differences between the free and bound enzymes. Therefore, the β- subunit was considered a target molecule (along with HS-CoB, $CH_3$-S-CoM, and cofactor $F_{430}$), while the two α- subunits and γ-subunit were still considered design molecules. MetH only consists of one chain and was modeled as such. CS1–CS3 incorporated IPRO's dimer constraint, which ensures that the design positions are equally perturbed and varied for each polypeptide chain. The remaining IPRO parameters were set to their default values. All IPRO parameters for each case study are provided in **Table 5**.

## CONCLUSIONS

The AOM by archaea is a complex reaction cascade that is still not fully elucidated (Thauer, 2011; Nazem-Bokaee et al., 2016). Though a consensus mechanism for AOM has been agreed upon, the role of conformational changes, post-translational modifications, the role of symbiotic partnerships, and the kinetics for the full reaction remain unknown. Adding to this complexity is the inherently challenging reaction catalyzed by Mcr, which breaks a stable C-H bond without the use of oxygen-derived

**TABLE 5 |** IPRO input parameters for CS1–CS4.

| Parameter | CS1 | CS2 | CS3 | CS4 |
|---|---|---|---|---|
| Design molecules | A. ANME-1 Mcr, α1<br>D. ANME-1 Mcr, α2 | A. *MA* Mcr, α1<br>B. *MA* Mcr, β<br>C. *MA* Mcr, γ<br>D. *MA* Mcr, α2 | A. *MA* Mcr, α1<br>C. *MA* Mcr, γ<br>D. *MA* Mcr, α2 | H. *E.coli* MetH |
| Target molecules | GS<br>B. HS-CoB<br>F. cofactor $F_{430}$<br>M. $CH_3$-S-CoM | TS<br>F. cofactor $F_{430}$<br>M. $CH_3$-S-CoM<br>O. HS-CoB | B. Bound *MA* Mcr, β<br>U. Unbound *MA* Mcr, β<br>TS<br>F. cofactor $F_{430}$<br>M. $CH_3$-S-CoM<br>O. HS-CoB<br>PS<br>P. cofactor $F_{430}$<br>Q. $CH_3$-S-CoM<br>R. HS-CoB | GS<br>C. active site $Cd^{2+}$<br>M. $CH_3$-S-CoM<br>P. $H_4$SPT<br>T. active site $H_2O$ |
| Binding assemblies | 1. Improve binding to F<br>2. Maintain binding to B and M | 1. Improve binding to F, M, and O | 1. Improve complex energy with B, F, M, and O<br>2. Worsen complex energy with B, P, Q, and R<br>3. Maintain binding to F and U | 1. Improve binding to C, M, P, and T |
| Design positions | A and D. Q72, L77, M78, N90, P149, I154, H157, H414, V419, and C423 | A and D. P97, M154, A157, M163, I245, S251, F267, and F466<br>C. A89 | A and D. M125, T129, A235, V262, S266, L274, M280, and T423<br>C. V83 and A89 | H. Y22, K72, D105, E320, N323, E345, N360, F511, D515, N538, D541, and E542 |
| Refinement used? | Yes | No | Yes | Yes |
| Independent trajectories | 5 | 10 | 10 | 10 |
| Iterations per trajectory | 1,000 | 3,000 | 100 | 1,500 |
| Force field | CHARMM | CHARMM | CHARMM | CHARMM |
| Topology file | mcr_top.rtf | mcr_top.rtf | mcr_top.rtf | meth_top.rtf |
| Parameter file | mcr_par.prm | mcr_par.prm | mcr_par.prm | meth_par.prm |
| Solvation file | mcr_sol.dat | mcr_sol.dat | mcr_sol.dat | meth_sol.dat |
| Extra constraints | 1. Dimer constraint between A and D<br>2. All atoms in B, F, and M fixed in place | 1. Dimer constraint between A and D<br>2. Fixed atoms in A (Q161), B (Y365), D (Y346), F (all), M (all), and O (all) | 1. Dimer constraint between A and D<br>2. Fixed atoms in A (Q161), B (Y365), D (Y346), F (all), M (all), and O (all) | None |
| Other | None | None | Binding assemblies 1 and 2 considered simultaneously, see section Case Study 3: Engineering *M. acetivorans* Mcr for More Rapid Product Release | None |

*There are several new abbreviations used within the table, namely Methanosarcina acetivorans (MA), ground state (GS), and product state (PS). Any parameters required to run IPRO that are not explicitly listed in the table are assumed to be their default values. These default values are prompted to the user when setting up the simulation. Molecules are listed first and are given a molecule name, followed by a description of the molecule. Target molecules are also listed beneath a header describing the molecule's state (GS, TS, or PS) The molecule's name is used when referencing it in the remainder of the table. The various input files can be found at http://www.maranasgroup.com.*

radicals (Scheller et al., 2016). In this work, we revisited existing literature to compile a more complete understanding of Mcr kinetics and which steps are likely to limit the net rate of AOM. Though the temperature ranges considered in this study are industrially relevant (>20°C), the *in vivo* conditions do not mimic the *in situ* environment. The possibility remains that a separate step may limit Mcr kinetics at even lower temperatures that more closely resemble environmental conditions (∼0°C) for AOM by ANME. The calculations and their underlying assumptions suggested that the rate of product, specifically $CH_3$-S-CoM, release limits the overall AOM kinetics. A geometric model developed by Samson and Deutch (Samson and Deutch, 1978) was used to test whether Mcr kinetics was diffusion-limited, but the derived second-order rate constant for diffusion was two orders of magnitude higher than that of methane binding (step 4 of the mechanism). Four separate case studies for improving the net AOM rate were developed, partially on the basis of these calculations.

A methanotrophic Mcr was redesigned to accept a methanogenic cofactor, assuming that the modified cofactor was exclusively important for active site rigidity. Despite the deletion of the methylthio- substituent of cofactor $F_{430}$ and its associated increase in binding cavity size, substitutions to small, hydrophobic amino acids (especially glycine) most effectively

improved binding to the methanogenic cofactor $F_{430}$. At high temperatures (>45°C), methane activation may limit the kinetics for AOM, and Mcr variants with diverse chemical properties, ranging from large and hydrophilic to small and hydrophobic, stabilize amino acids immediately adjacent to the transition state. At the low-to-mid temperature range (<45°C), large hydrophobic residues that can assume multiple conformations are favored in order to improve the rate of product release. In a final scenario, where the second step along the reverse aceticlastic pathway (i.e., Mtr) limits AOM, redesigning the substrate specificity of the more active methionine synthase homolog is achieved by introducing a positively charged residue to stabilize the negatively charged sulfonate of $CH_3$-S-CoM, and surprisingly few substitutions are required to accommodate the larger $H_4$SPT substrate. Taking these findings, later efforts can be pursued to test these variants which have the ability to not only make the conversion of methane to liquid fuels more economically viable, but also provide a deeper understanding of Mcr kinetics.

## AUTHOR CONTRIBUTIONS

MG and CM conceived the case studies. MG performed the simulations and analyzed existing kinetic data from literature. JF provided guidance during the redesign procedures. CM oversaw the simulations. MG, JF, and CM wrote and edited the manuscript. MG, JF, and CM accepted the final submitted version of the manuscript.

## FUNDING

Funding was provided by the Advanced Research Projects Agency-Energy (ARPA-E, DE-AR0000431). Additional funding was provided by The Center for Bioenergy Innovation, a U.S. Department of Energy Research Center supported by the Office of Biological and Environmental Research in the DOE Office of Science (DE-AC05-00OR22725).

## ACKNOWLEDGMENTS

We would like to thank the Penn State Institute for Cyberscience for maintaining the supercomputers that were used to generate designs. We would also like to thank the members of the ARPA-E REMOTE (Reducing Emissions using Methanotrophic Organisms for Transportation Energy) program for their useful conversations.

## SUPPLEMENTARY MATERIAL

The Supplementary Material for this article can be found online at: https://www.frontiersin.org/articles/10.3389/fenvs.2018.00084/full#supplementary-material

## REFERENCES

Allen, K. D., Wegener, G., and White, R. H. (2014). Discovery of multiple modified F(430) coenzymes in methanogens and anaerobic methanotrophic archaea suggests possible new roles for F(430) in nature. *Appl. Environ. Microbiol.* 80, 6403–6412. doi: 10.1128/AEM.02202-14

Altschul, S. F., Madden, T. L., Schaffer, A. A., Zhang, J., Zhang, Z., Miller, W., et al. (1997). Gapped BLAST and PSI-BLAST: a new generation of protein database search programs. *Nucleic Acids Res.* 25, 3389–3402. doi: 10.1093/nar/25.17.3389

Andrews, L. D., Fenn, T. D., and Herschlag, D. (2013). Ground state destabilization by anionic nucleophiles contributes to the activity of phosphoryl transfer enzymes. *PLoS Biol.* 11:e1001599. doi: 10.1371/journal.pbio.1001599

Arnold, K., Bordoli, L., Kopp, J., and Schwede, T. (2006). The SWISS-MODEL workspace: a web-based environment for protein structure homology modelling. *Bioinformatics* 22, 195–201. doi: 10.1093/bioinformatics/bti770

Ashworth, J., Havranek, J. J., Duarte, C. M., Sussman, D., Monnat, R. J. Jr., Stoddard, B. L., et al. (2006). Computational redesign of endonuclease DNA binding and cleavage specificity. *Nature* 441, 656–659. doi: 10.1038/nature04818

Beal, E. J., House, C. H., and Orphan, V. J. (2009). Manganese- and iron-dependent marine methane oxidation. *Science* 325, 184–187. doi: 10.1126/science.1169984

Benedict, M. N., Gonnerman, M. C., Metcalf, W. W., and Price, N. D. (2012). Genome-scale metabolic reconstruction and hypothesis testing in the methanogenic archaeon *Methanosarcina acetivorans* C2A. *J. Bacteriol.* 194, 855–865. doi: 10.1128/JB.06040-11

Bloom, J. D., Meyer, M. M., Meinhold, P., Otey, C. R., MacMillan, D., and Arnold, F. H. (2005). Evolving strategies for enzyme engineering. *Curr. Opin. Struct. Biol.* 15, 447–452. doi: 10.1016/j.sbi.2005.06.004

Cedervall, P. E., Dey, M., Pearson, A. R., Ragsdale, S. W., and Wilmot, C. M. (2010). Structural insight into methyl-coenzyme M reductase chemistry using coenzyme B analogues. *Biochemistry* 49, 7683–7693. doi: 10.1021/bi100458d

Chen, S.-L., Blomberg, M. R. A., and Siegbahn, P. E. M. (2012). How is methane formed and oxidized reversibly when catalyzed by ni-containing methyl-coenzyme M reductase? *Chemistry* 18, 6309–6315. doi: 10.1002/chem.201200274

Duan, Z. H., and Mao, S. D. (2006). A thermodynamic model for calculating methane solubility, density and gas phase composition of methane-bearing aqueous fluids from 273 to 523 K and from 1 to 2000 bar. *Geochim. Cosmochim. Acta* 70, 3369–3386. doi: 10.1016/j.gca.2006.03.018

Ebner, S., Jaun, B., Goenrich, M., Thauer, R. K., and Harmer, J. (2010). Binding of coenzyme B induces a major conformational change in the active site of methyl-coenzyme M reductase. *J. Am. Chem. Soc.* 132, 567–575. doi: 10.1021/ja906367h

Ellermann, J., Hedderich, R., Bocher, R., and Thauer, R. K. (1988). The final step in methane formation. Investigations with highly purified methyl-CoM reductase (component C) from Methanobacterium thermoautotrophicum (strain Marburg). *Eur. J. Biochem.* 172, 669–677. doi: 10.1111/j.1432-1033.1988.tb13941.x

Ermler, U., Grabarse, W., Shima, S., Goubeaud, M., and Thauer, R. K. (1997). Crystal structure of methyl coenzyme M reductase: the key enzyme of biological methane formation. *Science* 278, 1457–1462.

Evans, J. C., Huddler, D. P., Hilgers, M. T., Romanchuk, G., Matthews, R. G., and Ludwig, M. L. (2004). Structures of the N-terminal modules imply large domain motions during catalysis by methionine synthase. *Proc. Natl. Acad. Sci. U.S.A.* 101, 3729–3736. doi: 10.1073/pnas.0308082100

Faiella, M., Andreozzi, C., de Rosales, R. T., Pavone, V., Maglio, O., Nastri, F., et al. (2009). An artificial di-iron oxo-protein with phenol oxidase activity. *Nat. Chem. Biol.* 5, 882–884. doi: 10.1038/nchembio.257

Fazelinia, H., Cirino, P. C., and Maranas, C. D. (2007). Extending iterative protein redesign and optimization (IPRO) in protein library design for ligand specificity. *Biophys. J.* 92, 2120–2130. doi: 10.1529/biophysj.106.096016

Garrabou, X., Wicky, B. I., and Hilvert, D. (2016). Fast knoevenagel condensations catalyzed by an artificial schiff-base-forming enzyme. *J. Am. Chem. Soc.* 138, 6972–6974. doi: 10.1021/jacs.6b00816

Goubeaud, M., Schreiner, G., and Thauer, R. K. (1997). Purified methyl-coenzyme-M reductase is activated when the enzyme-bound coenzyme F430 is reduced to the Nickel(I) oxidation state by titanium(III) citrate. *Eur. J. Biochem.* 243, 110–114. doi: 10.1111/j.1432-1033.1997.00110.x

Grabarse, W., Mahlert, F., Duin, E. C., Goubeaud, M., Shima, S., Thauer, R. K., et al. (2001). On the mechanism of biological methane formation: structural evidence for conformational changes in methyl-coenzyme M reductase upon substrate binding1. *J. Mol. Biol.* 309, 315–330. doi: 10.1006/jmbi.2001.4647

Grabarse, W., Mahlert, F., Shima, S., Thauer, R. K., and Ermler, U. (2000). Comparison of three methyl-coenzyme M reductases from phylogenetically distant organisms: unusual amino acid modification, conservation and adaptation1. *J. Mol. Biol.* 303, 329–344. doi: 10.1006/jmbi.2000.4136

Grisewood, M. J., Gifford, N. P., Pantazes, R. J., Li, Y., Cirino, P. C., Janik, M. J., et al. (2013). OptZyme: computational enzyme redesign using transition state analogues. *PLoS ONE* 8:e75358. doi: 10.1371/journal.pone.0075358

Grisewood, M. J., Hernández-Lozada, N. J., Thoden, J. B., Gifford, N. P., Mendez-Perez, D., Schoenberger, H. A., et al. (2017). Computational redesign of acyl-ACP thioesterase with improved selectivity toward medium-chain-length fatty acids. *ACS Catal.* 7, 3837–3849. doi: 10.1021/acscatal.7b00408

Hallam, S. J., Putnam, N., Preston, C. M., Detter, J. C., Rokhsar, D., Richardson, P. M., et al. (2004). Reverse methanogenesis: testing the hypothesis with environmental genomics. *Science* 305, 1457-1462. doi: 10.1126/science.1100025

Harmer, J., Finazzo, C., Piskorski, R., Ebner, S., Duin, E. C., Goenrich, M., et al. (2008). A nickel hydride complex in the active site of methyl-coenzyme M reductase: implications for the catalytic cycle. *J. Am. Chem. Soc.* 130, 10907–10920. doi: 10.1021/ja710949e

Haroon, M. F., Hu, S., Shi, Y., Imelfort, M., Keller, J., Hugenholtz, P., et al. (2013). Anaerobic oxidation of methane coupled to nitrate reduction in a novel archaeal lineage. *Nature* 500, 567–570. doi: 10.1038/nature12375

Haynes, C. A., and Gonzalez, R. (2014). Rethinking biological activation of methane and conversion to liquid fuels. *Nat. Chem. Biol.* 10, 331–339. doi: 10.1038/nchembio.1509

Heller, C., Hoppert, M., and Reitner, J. (2008). Immunological localization of coenzyme M reductase in anaerobic methane-oxidizing archaea of ANME 1 and ANME 2 type. *Geomicrobiol. J.* 25, 149–156. doi: 10.1080/01490450802006884

Hilvert, D. (2013). Design of protein catalysts. *Annu. Rev. Biochem.* 82, 447–470. doi: 10.1146/annurev-biochem-072611-101825

Hinrichs, K.-U., and Boetius, A. (2003). "The anaerobic oxidation of methane: new insights in microbial ecology and biogeochemistry," in *Ocean Margin Systems,* eds G. Wefer, D. Billett, D. Hebbeln, B. B. Jørgensen, M. Schlüter, and T. C. E. van Weering (Heidelberg: Springer Berlin Heidelberg), 457–477.

Hoehler, T. M., Alperin, M. J., Albert, D. B., and Martens, C. S. (1994). Field and laboratory studies of methane oxidation in an anoxic marine sediment - evidence for a methanogen-sulfate reducer consortium. *Glob. Biogeochem. Cycles* 8, 451–463. doi: 10.1029/94GB01800

Huang, P. S., Boyken, S. E., and Baker, D. (2016). The coming of age of *de novo* protein design. *Nature* 537, 320–327. doi: 10.1038/nature19946

Huang, S., Romanchuk, G., Pattridge, K., Lesley, S. A., Wilson, I. A., Matthews, R. G., et al. (2007). Reactivation of methionine synthase from thermotoga maritima (TM0268) requires the downstream gene product TM0269. *Protein Sci.* 16, 1588–1595. doi: 10.1110/ps.072936307

Jiang, L., Althoff, E. A., Clemente, F. R., Doyle, L., Rothlisberger, D., Zanghellini, A., et al. (2008). *De novo* computational design of retro-aldol enzymes. *Science* 319, 1387–1391. doi: 10.1126/science.1152692

Kahnt, J., Buchenau, B., Mahlert, F., Kruger, M., Shima, S., and Thauer, R. K. (2007). Post-translational modifications in the active site region of methyl-coenzyme M reductase from methanogenic and methanotrophic archaea. *FEBS J.* 274, 4913–4921. doi: 10.1111/j.1742-4658.2007.06016.x

Kamerlin, S. C. L., Florian, J., and Warshel, A. (2008). Associative versus dissociative mechanisms of phosphate monoester hydrolysis: on the interpretation of activation entropies. *Chem. Phys. Chem.* 9, 1767–1773. doi: 10.1002/cphc.200800356

Knittel, K., and Boetius, A. (2009). Anaerobic oxidation of methane: progress with an unknown process. *Annu. Rev. Microbiol.* 63, 311–334. doi: 10.1146/annurev.micro.61.080706.093130

Krüger, M., Meyerdierks, A., Glockner, F. O., Amann, R., Widdel, F., Kube, M., et al. (2003). A conspicuous nickel protein in microbial mats that oxidize methane anaerobically. *Nature* 426, 878–881. doi: 10.1038/nature02207

Lazaridis, T., and Karplus, M. (1999). Effective energy function for proteins in solution. *Proteins* 35, 133–152. doi: 10.1002/(SICI)1097-0134(19990501)35:2<133::AID-PROT1>3.0.CO;2-N

Lee, M. S., Feig, M., Salsbury, F. R., and Brooks, C. L. (2003). New analytic approximation to the standard molecular volume definition and its application to generalized born calculations. *J. Comput. Chem.* 24, 1821–1821. doi: 10.1002/jcc.10367

Lu, Y.-Z., Fu, L., Ding, J., Ding, Z.-W., Li, N., and Zeng, R. J. (2016). Cr(VI) reduction coupled with anaerobic oxidation of methane in a laboratory reactor. *Water Res.* 102, 445–452. doi: 10.1016/j.watres.2016.06.065

Marchler-Bauer, A., Derbyshire, M. K., Gonzales, N. R., Lu, S. N., Chitsaz, F., Geer, L. Y., et al. (2015). Cdd: NCBI's conserved domain database. *Nucleic Acids Res.* 43, D222–D226. doi: 10.1093/nar/gku1221

Mayr, S., Latkoczy, C., Kruger, M., Gunther, D., Shima, S., Thauer, R. K., et al. (2008). Structure of an F430 variant from archaea associated with anaerobic oxidation of methane. *J. Am. Chem. Soc.* 130, 10758–10767. doi: 10.1021/ja802929z

McGlynn, S. E., Chadwick, G. L., Kempes, C. P., and Orphan, V. J. (2015). Single cell activity reveals direct electron transfer in methanotrophic consortia. *Nature* 526, 531–535. doi: 10.1038/nature15512

Meyer, M. M., Hochrein, L., and Arnold, F. H. (2006). Structure-guided SCHEMA recombination of distantly related beta-lactamases. *Protein Eng. Des.Selection* 19, 563–570. doi: 10.1093/protein/gzl045

Moore, G. L., and Maranas, C. D. (2004). Computational challenges in combinatorial library design for protein engineering. *AIChE J.* 50, 262–272. doi: 10.1002/aic.10025

Moran, J. J., House, C. H., Freeman, K. H., and Ferry, J. G. (2005). Trace methane oxidation studied in several *Euryarchaeota* under diverse conditions. *Archaea* 1, 303–309. doi: 10.1155/2005/650670

Moran, J. J., House, C. H., Thomas, B., and Freeman, K. H. (2007). Products of trace methane oxidation during nonmethyltrophic growth by Methanosarcina. *J. Geophys. Res. Biogeosci.* 112, 1–7. doi: 10.1029/2006JG000268

Mueller, T. J., Grisewood, M. J., Nazem-Bokaee, H., Gopalakrishnan, S., Ferry, J. G., Wood, T. K., et al. (2015). Methane oxidation by anaerobic archaea for conversion to liquid fuels. *J. Ind. Microbiol. Biotechnol.* 42, 391–401. doi: 10.1007/s10295-014-1548-7

Murphy, P. M., Bolduc, J. M., Gallaher, J. L., Stoddard, B. L., and Baker, D. (2009). Alteration of enzyme specificity by computational loop remodeling and design. *Proc. Natl. Acad. Sci. U.S.A.* 106, 9215–9220. doi: 10.1073/pnas.0811070106

Nauhaus, K., Treude, T., Boetius, A., and Kruger, M. (2005). Environmental regulation of the anaerobic oxidation of methane: a comparison of ANME-I and ANME-II communities. *Environ. Microbiol.* 7, 98–106. doi: 10.1111/j.1462-2920.2004.00669.x

Nazem-Bokaee, H., Gopalakrishnan, S., Ferry, J. G., Wood, T. K., and Maranas, C. D. (2016). Assessing methanotrophy and carbon fixation for biofuel production by *Methanosarcina acetivorans. Microb. Cell Fact.* 15:10. doi: 10.1186/s12934-015-0404-4

Packer, M. S., and Liu, D. R. (2015). Methods for the directed evolution of proteins. *Nat. Rev. Genet.* 16, 379–394. doi: 10.1038/nrg3927

Pantazes, R. J., Grisewood, M. J., Li, T., Gifford, N. P., and Maranas, C. D. (2015). The iterative protein redesign and optimization (IPRO) suite of programs. *J. Comput. Chem.* 36, 251–263. doi: 10.1002/jcc.23796

Pantazes, R. J., Grisewood, M. J., and Maranas, C. D. (2011). Recent advances in computational protein design. *Curr. Opin. Struct. Biol.* 21, 467–472. doi: 10.1016/j.sbi.2011.04.005

Pantazes, R. J., Saraf, M. C., and Maranas, C. D. (2007). Optimal protein library design using recombination or point mutations based on sequence-based scoring functions. *Protein Eng. Des. Sel.* 20, 361–373. doi: 10.1093/protein/gzm030

Phillips, R. S., Vita, A., Spivey, J. B., Rudloff, A. P., Driscoll, M. D., and Hay, S. (2016). Ground-State destabilization by Phe-448 and Phe-449 contributes to tyrosine phenol-lyase catalysis. *ACS Catal.* 6, 6770–6779. doi: 10.1021/acscatal.6b01495

Pommié, C., Levadoux, S., Sabatier, R., Lefranc, G., and Lefranc, M. P. (2004). IMGT standardized criteria for statistical analysis of immunoglobulin V-REGION amino acid properties. *J. Molecul. Recognit.* 17, 17–32. doi: 10.1002/jmr.647

Ragsdale, S. W., Raugei, S., Ginovska, B., and Wongnate, T. (2017). "Biochemistry of methyl-coenzyme M reductase," in *The Biological Chemistry of Nickel,* eds D. Zamble, M. Rowinska-Zyrek, and H. Kozlowski (Cambridge: The Royal Society of Chemistry), 149–169.

Reeburgh, W. S. (1996). "'Soft Spots' in the Global Methane Budget," in *Microbial Growth on $C_1$ Compounds*, eds M. E. Lidstrom and F. R. Tabita (Dordrecht: Kluwer Academic), 334–342.

Reeve, J. N., Nolling, J., Morgan, R. M., and Smith, D. R. (1997). Methanogenesis: genes, genomes, and who's on first? *J. Bacteriol.* 179, 5975–5986. doi: 10.1128/jb.179.19.5975-5986.1997

Richter, F., Blomberg, R., Khare, S. D., Kiss, G., Kuzin, A. P., Smith, A. J., et al. (2012). Computational design of catalytic dyads and oxyanion holes for ester hydrolysis. *J. Am. Chem. Soc.* 134, 16197–16206. doi: 10.1021/ja3037367

Röthlisberger, D., Khersonsky, O., Wollacott, A. M., Jiang, L., DeChancie, J., Betker, J., et al. (2008). Kemp elimination catalysts by computational enzyme design. *Nature* 453, U190–U194. doi: 10.1038/nature06879

Ruben, E. A., Schwans, J. P., Sonnett, M., Natarajan, A., Gonzalez, A., Tsai, Y., et al. (2013). Ground state destabilization from a positioned general base in the ketosteroid isomerase active site. *Biochemistry* 52, 1074–1081. doi: 10.1021/bi301348x

Rüdiger, H., and Jaenicke, L. (1969). Methionine synthesis: demonstration of the reversibility of the reaction. *FEBS Lett.* 4, 316–318. doi: 10.1016/0014-5793(69)80264-4

Samson, R., and Deutch, J. M. (1978). Diffusion-controlled reaction rate to a buried active site. *J. Chem. Phys.* 68, 285–290. doi: 10.1063/1.435494

Saraf, M. C., Moore, G. L., Goodey, N. M., Cao, V. Y., Benkovic, S. J., and Maranas, C. D. (2006). IPRO: an iterative computational protein library redesign and optimization procedure. *Biophys. J.* 90, 4167–4180. doi: 10.1529/biophysj.105.079277

Scheller, S., Goenrich, M., Boecher, R., Thauer, R. K., and Jaun, B. (2010). The key nickel enzyme of methanogenesis catalyses the anaerobic oxidation of methane. *Nature* 465, 606–608. doi: 10.1038/nature09015

Scheller, S., Goenrich, M., Thauer, R. K., and Jaun, B. (2013). Methyl-coenzyme M reductase from methanogenic archaea: isotope effects on the formation and anaerobic oxidation of methane. *J. Am. Chem. Soc.* 135, 14975–14984. doi: 10.1021/ja406485z

Scheller, S., Yu, H., Chadwick, G. L., McGlynn, S. E., and Orphan, V. J. (2016). Artificial electron acceptors decouple archaeal methane oxidation from sulfate reduction. *Science* 351, 703–707. doi: 10.1126/science.aad7154

Shima, S., Krueger, M., Weinert, T., Demmer, U., Kahnt, J., Thauer, R. K., et al. (2012). Structure of a methyl-coenzyme M reductase from black sea mats that oxidize methane anaerobically. *Nature* 481, 98–101. doi: 10.1038/nature10663

Siegel, J. B., Zanghellini, A., Lovick, H. M., Kiss, G., Lambert, A. R., St Clair, J. L., et al. (2010). Computational design of an enzyme catalyst for a stereoselective bimolecular Diels-Alder reaction. *Science* 329, 309–313. doi: 10.1126/science.1190239

Sievers, F., Wilm, A., Dineen, D., Gibson, T. J., Karplus, K., Li, W., et al. (2011). Fast, scalable generation of high-quality protein multiple sequence alignments using Clustal Omega. *Mol. Syst. Biol.* 7: 539. doi: 10.1038/msb.2011.75

Soo, V. W., McAnulty, M. J., Tripathi, A., Zhu, F., Zhang, L., Hatzakis, E., et al. (2016). Reversing methanogenesis to capture methane for liquid biofuel precursors. *Microb. Cell Fact.* 15, 11. doi: 10.1186/s12934-015-0397-z

Thauer, R. K. (2011). Anaerobic oxidation of methane with sulfate: on the reversibility of the reactions that are catalyzed by enzymes also involved in methanogenesis from $CO_2$. *Curr. Opin. Microbiol.* 14, 292–299. doi: 10.1016/j.mib.2011.03.003

Thauer, R. K., and Shima, S. (2008). Methane as fuel for anaerobic microorganisms. *Ann. N. Y. Acad. Sci.* 1125, 158–170. doi: 10.1196/annals.1419.000

UniProt, C. (2015). UniProt: a hub for protein information. *Nucleic Acids Res.* 43, D204–D212. doi: 10.1093/nar/gku989

Vanommeslaeghe, K., and MacKerell, A. D. Jr. (2012). Automation of the CHARMM General Force Field (CGenFF) I: bond perception and atom typing. *J. Chem. Inf. Model.* 52, 3144–3154. doi: 10.1021/ci300363c

Vanommeslaeghe, K., Raman, E. P., and MacKerell, A. D. Jr. (2012). Automation of the CHARMM general force field (CGenFF) II: assignment of bonded parameters and partial atomic charges. *J. Chem. Inf. Model.* 52, 3155–3168. doi: 10.1021/ci3003649

Vepachedu, V. R., and Ferry, J. G. (2012). Role of the fused corrinoid/methyl transfer protein CmtA during CO-dependent growth of *Methanosarcina acetivorans*. *J. Bacteriol.* 194, 4161–4168. doi: 10.1128/JB.00593-12

Wegener, G., Krukenberg, V., Riedel, D., Tegetmeyer, H. E., and Boetius, A. (2015). Intercellular wiring enables electron transfer between methanotrophic archaea and bacteria. *Nature* 526, 587–590. doi: 10.1038/nature15733

Wongnate, T., and Ragsdale, S. W. (2015). The reaction mechanism of methyl-coenzyme M reductase: how an enzyme enforces strict binding order. *J. Biol. Chem.* 290, 9322–9334. doi: 10.1074/jbc.M115.636761

Wongnate, T., Sliwa, D., Ginovska, B., Smith, D., Wolf, M. W., Lehnert, N., et al. (2016). The radical mechanism of biological methane synthesis by methyl-coenzyme M reductase. *Science* 352, 953–958. doi: 10.1126/science.aaf0616

Xiao, H., Bao, Z. H., and Zhao, H. M. (2015). High throughput screening and selection methods for directed enzyme evolution. *Ind. Eng. Chem. Res.* 54, 4011–4020. doi: 10.1021/ie503060a

Yan, Z., Joshi, P., Gorski, C. A., and Ferry, J. G. (2018). A biochemical framework for anaerobic oxidation of methane driven by Fe(III)-dependent respiration. *Nat. Commun.* 9:1642. doi: 10.1038/s41467-018-04097-9

Zheng, K., Ngo, P. D., Owens, V. L., Yang, X. P., and Mansoorabadi, S. O. (2016). The biosynthetic pathway of coenzyme F430 in methanogenic and *methanotrophic archaea*. *Science* 354, 339–342. doi: 10.1126/science.aag2947

Zhou, Y., Dorchak, A. E., and Ragsdale, S. W. (2013). *In vivo* activation of methyl-coenzyme M reductase by carbon monoxide. *Front. Microbiol.* 4:69. doi: 10.3389/fmicb.2013.00069

**Conflict of Interest Statement:** The authors declare that the research was conducted in the absence of any commercial or financial relationships that could be construed as a potential conflict of interest.

frontiers in Microbiology

ORIGINAL RESEARCH
published: 13 December 2018
doi: 10.3389/fmicb.2018.03109

# Electron and Proton Flux for Carbon Dioxide Reduction in *Methanosarcina barkeri* During Direct Interspecies Electron Transfer

*Dawn E. Holmes[1,2]*, Amelia-Elena Rotaru[1,3], Toshiyuki Ueki[1], Pravin M. Shrestha[1,4], James G. Ferry[5] and Derek R. Lovley[1]**

[1] Department of Microbiology, University of Massachusetts, Amherst, MA, United States, [2] Department of Physical and Biological Sciences, Western New England University, Springfield, MA, United States, [3] Department of Biology, University of Southern Denmark, Odense, Denmark, [4] Assembly Biosciences, San Francisco, CA, United States, [5] Department of Biochemistry and Molecular Biology, Pennsylvania State University, University Park, PA, United States

Direct interspecies electron transfer (DIET) is important in diverse methanogenic environments, but how methanogens participate in DIET is poorly understood. Therefore, the transcriptome of *Methanosarcina barkeri* grown via DIET in co-culture with *Geobacter metallireducens* was compared with its transcriptome when grown via $H_2$ interspecies transfer (HIT) with *Pelobacter carbinolicus*. Notably, transcripts for the $F_{420}H_2$ dehydrogenase, Fpo, and the heterodisulfide reductase, HdrABC, were more abundant during growth on DIET. A model for $CO_2$ reduction was developed from these results in which electrons delivered to methanophenazine in the cell membrane are transferred to Fpo. The external proton gradient necessary to drive the otherwise thermodynamically unfavorable reverse electron transport for Fpo-catalyzed $F_{420}$ reduction is derived from protons released from *G. metallireducens* metabolism. Reduced $F_{420}$ is a direct electron donor in the carbon dioxide reduction pathway and also serves as the electron donor for the proposed HdrABC-catalyzed electron bifurcation reaction in which reduced ferredoxin (also required for carbon dioxide reduction) is generated with simultaneous reduction of CoM-S-S-CoB. Expression of genes for putative redox-active proteins predicted to be localized on the outer cell surface was higher during growth on DIET, but further analysis will be required to identify the electron transfer route to methanophenazine. The results indicate that the pathways for electron and proton flux for $CO_2$ reduction during DIET are substantially different than for HIT and suggest that gene expression patterns may also be useful for determining whether *Methanosarcina* are directly accepting electrons from other extracellular electron donors, such as corroding metals or electrodes.

**Keywords: syntrophy, methanogenesis, $F_{420}$ dehydrogenase, heterodisulfide reductase, transcriptomics**

OPEN ACCESS

***Edited by:***
*Obulisamy Parthiba Karthikeyan, University of Michigan, United States*

***Reviewed by:***
*William Lanzilotta, University of Georgia, United States*
*Eric D. van Hullebusch, UMR7154 Institut de Physique du Globe de Paris (IPGP), France*

****Correspondence:***
*Dawn E. Holmes*
*dholmes@microbio.umass.edu*
*Derek R. Lovley*
*dlovley@microbio.umass.edu*

***Specialty section:***
*This article was submitted to Microbiological Chemistry and Geomicrobiology, a section of the journal Frontiers in Microbiology*

***Received:*** *30 July 2018*
***Accepted:*** *30 November 2018*
***Published:*** *13 December 2018*

***Citation:***
*Holmes DE, Rotaru A-E, Ueki T, Shrestha PM, Ferry JG and Lovley DR (2018) Electron and Proton Flux for Carbon Dioxide Reduction in Methanosarcina barkeri During Direct Interspecies Electron Transfer. Front. Microbiol. 9:3109. doi: 10.3389/fmicb.2018.03109*

## INTRODUCTION

The mechanisms by which methanogens conserve energy to support growth during direct interspecies electron transfer (DIET) are of interest because it is becoming increasingly apparent that DIET may be an important alternative to hydrogen interspecies transfer (HIT) for methane production in anaerobic digesters as well as methanogenic soils and sediments

(Shrestha and Rotaru, 2014; Dubé and Guiot, 2015; Cheng and Call, 2016; Lovley, 2017c). A better understanding of DIET could help with the development of molecular approaches that can be used to detect DIET in methanogenic environments (Rotaru et al., 2014b; Holmes et al., 2017) and might lead to new approaches for promoting DIET to accelerate and stabilize anaerobic digestion (Cheng and Call, 2016; Barua and Dhar, 2017; Lovley, 2017b,c; Baek et al., 2018; Park et al., 2018).

Physiological studies of DIET require defined co-cultures. *Geobacter metallireducens* is an environmentally relevant pure culture model for electron-donating partners for DIET because *Geobacter* species function as the electron-donating partner in important methanogenic environments such as anaerobic digesters (Morita et al., 2011; Rotaru et al., 2014b) and terrestrial wetlands (Holmes et al., 2017). Studies with defined co-cultures in which *G. metallireducens* was the electron-donating partner for DIET (Shrestha et al., 2013; Rotaru et al., 2014a; Ueki et al., 2018) have suggested that c-type cytochromes and electrically conductive pili [e-pili] (Lovley, 2017a) facilitate electron transport from *G. metallireducens* to the electron accepting partner.

Outer-surface *c*-type cytochromes and e-pili are also involved in electron uptake by *G. sulfurreducens* when it is the electron-accepting partner in DIET-based co-cultures with *G. metallireducens* (Summers et al., 2010; Shrestha et al., 2013; Ueki et al., 2018). However, *Methanosarcina barkeri* and *Methanothrix* (formerly *Methanosaeta*) *harundinacea*, the only methanogens definitively shown to participate in DIET (Rotaru et al., 2014a,b), do not possess outer-surface *c*-type cytochromes or e-pili. Their outer surface electrical contacts for DIET are unknown.

The basic physiology and biochemistry of *M. barkeri* are much better understood than for *Mt. harundinacea* (Thauer et al., 2008; Gonnerman et al., 2013; Welte and Deppenmeier, 2014; Boone and Mah, 2015; Kulkarni et al., 2018; Mand et al., 2018). This makes *M. barkeri* the organism of choice for initial DIET mechanistic studies. Another advantage is that methods are available for genetic manipulation of *M. barkeri* (Kohler and Metcalf, 2012), but not *Mt. harundinacea*. However, one caveat for the study of DIET is that *M. barkeri* mutants have been previously constructed in a strain adapted to grow in high salt concentrations to prevent cell aggregation (Kohler and Metcalf, 2012). *G. metallireducens*, the only known electron-donating partner for *M. barkeri*, has yet to be adapted to grow at such high salt conditions.

Thus, at least at present, alternative approaches to evaluating the physiology of *M. barkeri* during DIET are required. Comparing the transcriptome of cells grown via DIET versus cells grown via HIT clearly reflected differences in electron uptake mechanisms in studies in which *G. sulfurreducens* functioned as the electron-accepting partner (Shrestha et al., 2013). *G. sulfurreducens* was grown by DIET with *G. metallireducens* as the electron-donating partner, or by HIT in co-culture with *Pelobacter carbinolicus* a microorganism closely related to *G. metallireducens*, but which is incapable of DIET (Shrestha et al., 2013). The *G. sulfurreducens* transcriptome demonstrated that cells were poised for growth on $H_2$ when *G. sulfurreducens* was grown with *P. carbinolicus* and expressed genes for outer-surface proteins involved in direct uptake of electrons during DIET-based growth with *G. metallireducens* (Shrestha et al., 2013). *M. barkeri* can also be grown in co-culture with either *G. metallireducens* or *P. carbinolicus* (Rotaru et al., 2014a), providing an opportunity to compare *M. barkeri* gene expression patterns during growth via DIET and HIT.

Any model describing how the electron-accepting partner utilizes electrons derived from DIET must account for the uncoupling of the routes for interspecies electron and proton flux (**Figure 1**). e-Pili only transport electrons. Protons move between DIET partners by diffusion. This uncoupled transport of electrons and protons is in stark contrast to HIT in which $H_2$ simultaneously transports both electrons and protons as the $H_2$ diffuses between the two partners. When the $H_2$ is oxidized in the cytoplasm with electron transfer to an electron acceptor, protons are also released and are immediately available to balance the negative charge transferred to the electron acceptor. This maintains charge balance within the cell (**Figure 1**). In contrast, in DIET, e-pili and associated electron transport proteins deliver electrons to cytoplasmic electron acceptors. Protons have to be translocated into the cytoplasm for charge balance (**Figure 1**). This proton consumption also prevents acidification of the extracellular matrix of the DIET aggregates. Thus, proposed mechanisms for electron uptake during DIET need to include an explanation for how protons are translocated into the cytoplasm of the electron-accepting partner.

Here we report transcriptomic data from *M. barkeri* grown via DIET and HIT. The results suggest a mechanism for *M. barkeri* to utilize electrons and protons, derived from the electron-donating partner during DIET, to conserve energy to support growth from the reduction of carbon dioxide to methane.

# MATERIALS AND METHODS

## Co-culture Incubation and mRNA Extraction

Triplicate replicates of co-cultures of *G. metallireducens*/*M. barkeri* and *P. carbinolicus*/*M. barkeri* were grown under strict anaerobic conditions as previously described (Rotaru et al., 2014a). Cultures were harvested during the exponential phase of growth and mRNA was isolated as previously described (Shrestha et al., 2013).

## Illumina Sequencing and Assembly of Reads

Directional multiplex libraries were prepared with the ScriptSeq™ v2 RNA-Seq library preparation kit (Epicentre). Single end sequencing was performed with a Hi-Seq 2000 platform at the Deep Sequencing Core Facility at the University of Massachusetts Medical School in Worcester, MA, United States.

All raw data generated by Illumina sequencing were quality checked by visualization of base quality scores and nucleotide distributions with FASTQC[1]. Initial raw non-filtered forward and

[1]http://www.bioinformatics.babraham.ac.uk/projects/fastqc/

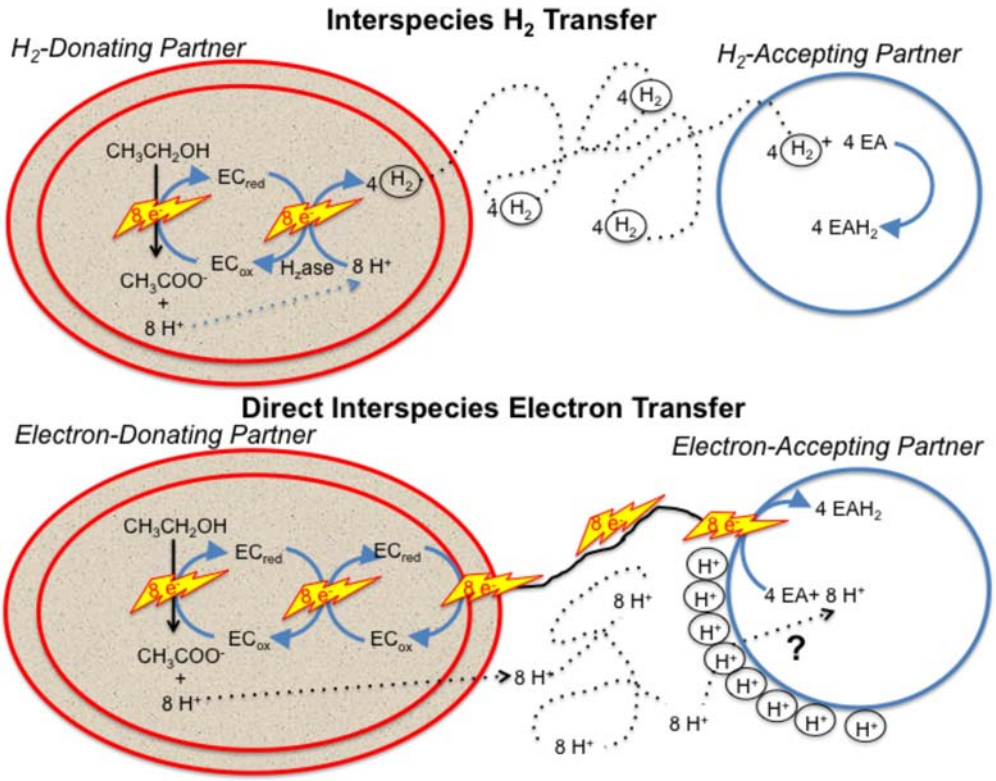


**FIGURE 1 |** Generalized model for electron and proton flux during hydrogen interspecies electron transfer (HIT) and direct interspecies electron transfer (DIET) with growth on ethanol as an example. $H_2$ diffusion shuttles both electrons and protons between cells and carries both electrons and protons into the cell when cytoplasmic electron acceptors are reduced. In contrast, electron and protons are transported by different mechanisms during DIET. Electron transfer is direct, through e-pili and other electrical contacts. Protons move by diffusion creating a positive proton pressure outside the cell. A mechanism for proton translocation into the cell is required for charge balance in the cytoplasm when cytoplasmic electron acceptors (EA) are reduced and to prevent acidification of the external space between cells. EC: electron carrier.

reverse sequencing libraries contained an average of 3892089 ± 134932 reads that were ∼100 basepairs long. Sequences from all of the libraries were trimmed and filtered with trimmomatic (Bolger et al., 2014) with the sliding window approach set to trim bases with quality scores lower than 3, strings of 3+N's, and reads with a mean quality score lower than 20. Bases were also cut from the start and end of reads that fell below a threshold quality of 3, and any reads smaller than 50 bp were eliminated from the library. These parameters yielded an average of 2732020 ± 217212 quality reads per RNA-Seq library. SortMeRNA (Kopylova et al., 2012) was then used to separate all ribosomal RNA (rRNA) reads from the libraries. Databases used by SortMeRNA to identify all rRNA sequences included Rfam 5.8S Eukarya, Rfam 5S Archaea/Bacteria, SILVA 16S Archaea, SILVA 16S Bacteria, SILVA 23S Bacteria, SILVA 18S Eukarya, and SILVA 28S Eukarya (Burge et al., 2013; Quast et al., 2013).

## Mapping of mRNA Reads

Trimmed and filtered mRNA reads from the triplicate samples for the two different co-culture conditions were mapped against the genome of *M. barkeri* strain MS DSM 800 downloaded from IMG/MER[2]. Mapped reads were normalized with the RPKM (reads assigned per kilobase of target per million mapped reads) method (Mortazavi et al., 2008; Klevebring et al., 2010) using ArrayStar software (DNAStar). Graphical analysis of reads from all three biological replicates for each condition demonstrated that the results were highly reproducible. Therefore, all reported values were obtained after merging and averaging replicates. Expression levels were considered significant only when the $\log_2$ RPKM value was higher than that of the median RPKM value.

Out of the 3,809 predicted protein-coding genes in the *M. barkeri* MS genome, 1,912 and 1,909 genes had expression levels that were higher than the median in DIET- and HIT-grown cells, respectively.

## Genome Data Analysis

Sequence data for all of the bacterial genomes was acquired from the U.S. Department of Energy Joint Genome Institute[3] or from GenBank at the National Center for Biotechnology Information (NCBI)[4]. Initial analyses were done with analysis tools available

[2]http://img.jgi.doe.gov
[3]http://www.jgi.doe.gov
[4]http://www.ncbi.nlm.nih.gov

on the Integrated Microbial Genomes (IMG) website (see text footnote 2). Some protein domains were identified with NCBI conserved domain search (Marchler-Bauer et al., 2015) and Pfam search (Finn et al., 2016) functions. Transmembrane helices were predicted with TMpred (Hofmann and Stoffel, 1993), TMHMM (Krogh et al., 2001), and HMMTOP (Tusnady and Simon, 2001) and signal peptides were identified with PSORTb v. 3.0.2 (Yu et al., 2010) and Signal P v. 4.1 (Petersen et al., 2011).

## Accession Number

Illumina sequence reads have been submitted to the NCBI database under project number PRJNA501858 and accession SAMN10346831-SAMN10346836.

# RESULTS AND DISCUSSION

As previously described (Rotaru et al., 2014a) co-cultures of *G. metallireducens* and *M. barkeri* that were well-adapted for growth via DIET required ca. 25 days to metabolize the 20 mM ethanol provided as substrate whereas *P. carbinolicus/M. barkeri* co-cultures required ca. 15 days. Both *G. metallireducens* and *P. carbinolicus* metabolized ethanol to acetate with either the production of $H_2$ (*P. carbinolicus*) or extracellular electron transfer (*G. metallireducens*). *M. barkeri* metabolized acetate in both co-cultures, but in the initial growth phases of the cultures acetate production was faster than consumption, resulting in an accumulation of acetate (Rotaru et al., 2014a).

## Transcriptome Reflects Faster Growth During HIT and Possible Greater Importance of Membrane and Outer-Surface Proteins During DIET

Transcript abundances for *M. barkeri* genes involved in amino acid biosynthesis, protein synthesis, and enzymes in the methane production pathways from both carbon dioxide and acetate were generally higher in the *P. carbinolicus/M. barkeri* co-cultures than in the *G. metallireducens/M. barkeri* co-cultures (**Figure 2** and **Supplementary Tables S1, S2**). This is consistent with the faster growth of the *P. carbinolicus/M. barkeri* co-cultures. The highest proportion of genes that were more highly expressed during DIET-based growth were genes for proteins predicted to be associated with the membrane or cell surface (**Figure 2**).

Genes for all three functional *M. barkeri* hydrogenases [Ech, Frh, and Vht (Mand et al., 2018)] were more abundant during HIT-based growth (**Table 1**). However, the results suggest that it will not be possible to use hydrogenase gene transcript levels to diagnose whether *M. barkeri* is participating in HIT or DIET in microbial communities. The increase in hydrogenase gene expression in HIT-grown cells was comparable to the general increase in expression of genes for other methanogenesis enzymes, such as Mcr (**Table 1** and **Supplementary Table S2**), suggesting that there was not a specific upregulation of hydrogenase genes in response to growth via HIT.

Considering that gene expression for many metabolic genes was generally lower in DIET-grown cells, any genes for which transcript abundance was higher during DIET, or even comparable to HIT-grown cells, are of considerable interest. In the following sections, genes with higher expression during growth on DIET are examined further. The results are placed in the context of a working model (**Figure 3**) for generating the reduced co-factors required for carbon dioxide reduction to methane ($F_{420}H_2$, reduced ferredoxin) while also providing a mechanism for CoM-S-S-CoB reduction and a chemiosmotic potential to provide energy to support DIET-based growth.

## Proton-Driven Reverse Electron Transport to Reduce $F_{420}$ With Fpo

Transcripts for genes for most of the subunits for the membrane-bound $F_{420}H_2$ dehydrogenase, Fpo, were higher in DIET-grown cells (**Table 2**). Considering that transcripts for most genes for methanogenesis were more abundant in HIT-grown cells, these

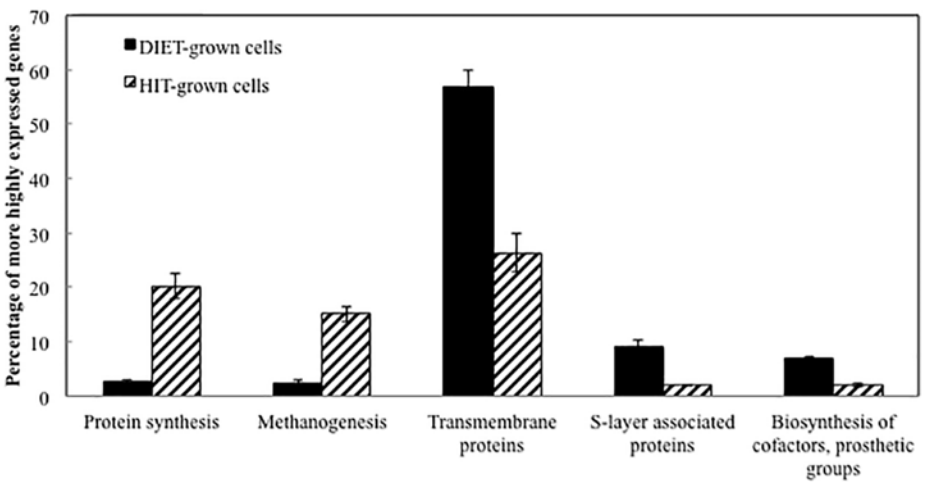


**FIGURE 2 |** Comparison of relative expression of genes for different major classes of proteins during growth via DIET and HIT.

**TABLE 1 |** Comparison of transcripts from genes coding for hydrogenase protein complexes (Ech, Frh, and Vht) and genes from the methyl coenzyme M reductase protein complex (Mcr) in *M. barkeri* cells growing via HIT in co-culture with *P. carbinolicus* or via DIET in co-culture with *G. metallireducens*.

| Locus ID | Annotation | Gene | Fold up-regulated in HIT | $log_2$ RPKM DIET | $log_2$ RPKM HIT |
|---|---|---|---|---|---|
| Ga0072459_113104 | Ech hydrogenase subunit F (ferredoxin) | *echF* | 6.9 | 7.8* | 10.2 |
| Ga0072459_113103 | Ech hydrogenase subunit E | *echE* | 3.4 | 9.2 | 11.0 |
| Ga0072459_113102 | Ech hydrogenase subunit D | *echD* | 8.7 | 7.9* | 11.0 |
| Ga0072459_113101 | Ech hydrogenase subunit C | *echC* | 3.5 | 8.8 | 10.6 |
| Ga0072459_113100 | Ech hydrogenase subunit B | *echB* | 3.4 | 8.9 | 10.6 |
| Ga0072459_113099 | Ech hydrogenase subunit A, proton antiporter | *echA* | 3.2 | 8.8 | 10.6 |
| Ga0072459_113332 | Coenzyme F420-reducing hydrogenase subunit beta | *frhB* | 2.3 | 8.5 | 9.7 |
| Ga0072459_113333 | Coenzyme F420-reducing hydrogenase subunit gamma | *frhG* | 2.5 | 8.1 | 9.5 |
| Ga0072459_113335 | Coenzyme F420-reducing hydrogenase subunit delta | *frhD* | 3.6 | 7.2* | 9.0 |
| Ga0072459_113336 | Coenzyme F420-reducing hydrogenase subunit alpha | *frhA* | 2.0 | 8.5 | 9.5 |
| Ga0072459_112833 | Methanophenazine hydrogenase maturation protease | *vhtD* | ND | 7.3* | 7.2* |
| Ga0072459_112832 | Methanophenazine-reducing hydrogenase, cytochrome B subunit | *vhtC* | 4.6 | 7.5* | 9.7 |
| Ga0072459_112831 | Methanophenazine-reducing hydrogenase large subunit | *vhtA* | 2.2 | 8.7 | 9.9 |
| Ga0072459_112830 | Methanophenazine-reducing hydrogenase small subunit | *vhtG* | 2.2 | 8.2 | 9.4 |
| Ga0072459_1188 | Methyl-coenzyme M reductase, alpha subunit | *mcrA* | 3.5 | 10.1 | 11.9 |
| Ga0072459_1187 | Methyl-coenzyme M reductase, gamma subunit | *mcrG* | 4.2 | 11.0 | 13.1 |
| Ga0072459_1186 | Methyl coenzyme M reductase, subunit C | *mcrC* | 6.0 | 10.2 | 12.8 |
| Ga0072459_1185 | Methyl coenzyme M reductase, subunit D | *mcrD* | 4.2 | 10.9 | 13.0 |
| Ga0072459_1184 | Methyl-coenzyme M reductase, beta subunit | *mcrB* | 4.4 | 10.2 | 12.3 |

*The $log_2$ RPKM median for HIT-grown M. barkeri cells was 7.5. The $log_2$ RPKM median for DIET-grown M. barkeri cells was 7.9. *Transcripts with values below the $log_2$ RPKM median. ND, no significant difference in transcription.*

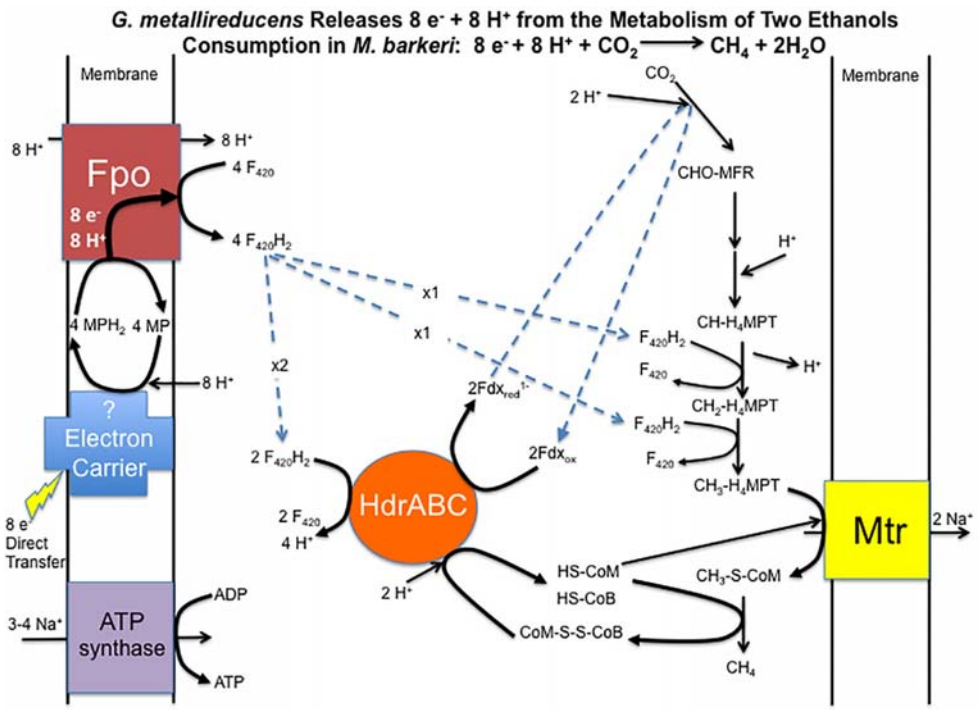


**FIGURE 3 |** Model for electron and proton flux for carbon dioxide reduction to methane in *Methanosarcina barkeri* during DIET-based growth. Each two moles of ethanol oxidized to acetate by *G. metallireducens* releases eight electrons and eight protons. Electrons delivered to methanophenazine in the cell membrane are transferred to Fpo. Proton translocation drives Fpo-catalyzed reduction of $F_{420}$ to $F_{420}H_2$. Half of the $F_{420}H_2$ produced serves as a reductant in the carbon dioxide reduction pathway. The remaining $F_{420}H_2$ is the electron donor for HdrABC, which reduces ferredoxin and CoM-S-S-CoB in an electron bifurcation reaction. The steps in carbon dioxide reduction, including the role of reduced ferredoxin, CoM-SH, and CoB-SH, as well as sodium pumping with Mtr, are as previously described (Thauer et al., 2008) for *M. barkeri.*

**TABLE 2 |** Comparison of transcripts from genes coding for subunits of Fpo dehydrogenase in *M. barkeri* cells growing via HIT in co-culture with *P. carbinolicus* or via DIET in co-culture with *G. metallireducens*.

| Locus ID | Annotation | Gene | Fold up-regulated in DIET | $log_2$ RPKM DIET | $log_2$ RPKM HIT |
|---|---|---|---|---|---|
| Ga0072459_111718 | $F_{420}H_2$ dehydrogenase subunit O | *fpoO* | 2.9 | 7.5* | 6.0* |
| Ga0072459_111719 | $F_{420}H_2$ dehydrogenase subunit N | *fpoN* | 2.4 | 8.2 | 6.9* |
| Ga0072459_111720 | $F_{420}H_2$ dehydrogenase subunit M | *fpoM* | 2.1 | 8.6 | 7.5* |
| Ga0072459_111721 | $F_{420}H_2$ dehydrogenase subunit L | *fpoL* | 1.5 | 8.5 | 7.9 |
| Ga0072459_111722 | $F_{420}H_2$ dehydrogenase subunit K | *fpoK* | 3.7 | 8.3 | 6.4* |
| Ga0072459_111723 | NADH dehydrogenase subunit J | *fpoJ* | 2.4 | 9.7 | 8.5 |
| Ga0072459_111724 | $F_{420}H_2$ dehydrogenase subunit J | *fpoJ* | 2.6 | 8.7 | 7.3* |
| Ga0072459_111725 | $F_{420}H_2$ dehydrogenase subunit I | *fpoI* | 1.7 | 7.6* | 6.9* |
| Ga0072459_111726 | $F_{420}H_2$ dehydrogenase subunit H | *fpoH* | 2.1 | 9.3 | 8.2 |
| Ga0072459_111727 | $F_{420}H_2$ dehydrogenase subunit D | *fpoD* | 1.7 | 8.3 | 7.6 |
| Ga0072459_111728 | $F_{420}H_2$ dehydrogenase subunit C | *fpoC* | 1.5 | 7.2* | 6.6* |
| Ga0072459_111729 | $F_{420}H_2$ dehydrogenase subunit B | *fpoB* | 2.1 | 8.0 | 6.9* |
| Ga0072459_111730 | $F_{420}H_2$ dehydrogenase subunit A | *fpoA* | 2.0 | 8.4 | 7.4* |
| Ga0072459_112975 | $F_{420}H_2$ dehydrogenase subunit F | *fpoF* | 1.0 | 9.0 | 9.1 |

*The $log_2$ RPKM median for HIT-grown M. barkeri cells was 7.5. The $log_2$ RPKM median for DIET-grown M. barkeri cells was 7.9. *Transcripts with values below the $log_2$ RPKM median.*

results suggest that Fpo plays a key role in electron transport for carbon dioxide reduction to methane during DIET. During methylotrophic methanogenesis Fpo oxidizes $F_{420}H_2$ with the reduction of methanophenazine in the membrane, coupled with vectorial proton translocation to the outside of the membrane (Welte and Deppenmeier, 2014; Kulkarni et al., 2018; Mand et al., 2018). However, under some conditions Fpo may catalyze the reverse reaction in which reduced methanophenazine serves as the electron donor for the reduction of $F_{420}$ (Mand et al., 2018). In this direction, proton translocation through Fpo into the cytoplasm is required in order to make the reaction thermodynamically favorable.

Therefore, it is proposed that electrons derived from DIET reduce methanophenazine in the oxidized state (MP) to $MPH_2$ and that $MPH_2$ is the electron donor for Fpo to reduce $F_{420}$ in the cytoplasm (**Figure 3**). A proton gradient to drive the reaction is available from the protons released into the extracellular matrix from *G. metallireducens* metabolism in direct proportion to electrons transported from *G. metallireducens* through e-pili. The proton flux through Fpo does not acidify the cytoplasm because an equivalent number of protons are consumed from the cytoplasm when MP is reduced to $MPH_2$ (**Figure 3**). The protons required to produce $MPH_2$ are transferred to $F_{420}$ during the Fpo-catalyzed reaction $MPH_2 + F_{420} \rightarrow MP + F_{420}H_2$. In this way electron transfer through methanophenazine to $F_{420}$ is achieved with charge balance.

## Possible Increased Methanophenazine Production to Support DIET

The proposed generation of $F_{420}H_2$ by Fpo with electrons derived from DIET requires an abundance of reduced methanophenazine (**Figure 3**). The pathway involved in biosynthesis of methanophenazine has not been identified, however, it is likely to resemble those of respiratory quinones because both have a polyprenyl side-chain connected to a redox-active moiety. In fact, studies have shown that a farnesylgeranyl pyrophosphate synthetase from the terpenoid backbone biosynthesis pathway is required for methanophenazine biosynthesis in *M. mazei* (Ogawa et al., 2010). Nine genes predicted to code for proteins involved in ubiquinone/menaquinone biosynthesis; six UbiE methyltransferase proteins, UbiA prenyltransferase, phenylacrylic acid decarboxylase (UbiD), and a ubiquinone biosynthesis protein (UbiB) were $\geq$2 fold more highly expressed in DIET-grown cells and another 11 putative ubiquinone biosynthesis genes were $\geq$1.5 fold up in DIET grown cells (**Table 3**). Given that *M. barkeri* does not contain ubiquinone or menaquinone, it seems likely that these genes code for enzymes involved in methanophenazine synthesis.

It has been calculated that the concentration of methanophenazine in membranes of *M. acetivorans* grown on methanol is sufficient to convert the membrane into an "electrically quantitized" conductive material (Duszenko and Buan, 2017). Methanophenazine concentrations in membranes of methanol-grown *M. barkeri* were too low for this effect (Duszenko and Buan, 2017). However, increased methanophenazine synthesis during growth via DIET might also yield an electrically quantitized membrane in *M. barkeri*, alleviating the need for redox-active proteins to aid in electron transport through the membrane during DIET.

## Generating Reduced Ferredoxin and Reducing CoM-S-S-CoB With HdrABC

In addition to $F_{420}H_2$, *M. barkeri* needs to generate reduced ferredoxin during DIET. It is required for the first step in carbon dioxide reduction to methane (Thauer et al., 2008). One of the few soluble protein complexes with higher gene transcript abundance during DIET is the heterodisulfide reductase HdrA1B1C1 (**Table 4**), suggesting that it is important for DIET. Transcript

**TABLE 3 |** Comparison of transcripts from genes coding for enzymes from the terpenoid backbone or terpenoid/quinone biosynthesis pathways in *M. barkeri* cells growing via DIET in co-culture with *G. metallireducens* or via HIT in co-culture with *P. carbinolicus*.

| Locus ID | Annotation | Fold up-regulated in DIET | $log_2$ RPKM DIET | $log_2$ RPKM HIT |
|---|---|---|---|---|
| Ga0072459_112001 | UbiE/COQ5 methyltransferase | 4.0 | 9.0 | 7.0* |
| Ga0072459_11404 | UbiE/COQ5 methyltransferase | 3.1 | 8.2 | 6.5* |
| Ga0072459_113351 | UbiE/COQ5 methyltransferase | 2.8 | 8.2 | 6.8* |
| Ga0072459_11983 | UbiE/COQ5 methyltransferase | 2.5 | 8.3 | 7.0* |
| Ga0072459_111147 | Ubiquinone biosynthesis protein | 2.3 | 8.9 | 7.7 |
| Ga0072459_11398 | UbiE/COQ5 methyltransferase | 2.3 | 7.9 | 6.7* |
| Ga0072459_11322 | UbiE/COQ5 methyltransferase | 2.1 | 8.7 | 7.6 |
| Ga0072459_111453 | UbiA prenyltransferase | 2.0 | 8.0 | 6.9* |
| Ga0072459_11572 | Phenylacrylic acid decarboxylase UbiD | 2.0 | 7.7* | 6.7* |
| Ga0072459_11988 | UbiE/COQ5 methyltransferase | 1.8 | 7.8* | 6.9* |
| Ga0072459_113640 | UbiE/COQ5 methyltransferase | 1.8 | 8.2 | 7.4* |
| Ga0072459_112914 | UbiA prenyltransferase | 1.7 | 8.5 | 7.8 |
| Ga0072459_111590 | UbiE/COQ5 methyltransferase | 1.7 | 7.8* | 7.0* |
| Ga0072459_111148 | UbiE/COQ5 methyltransferase | 1.7 | 7.5* | 6.8* |
| Ga0072459_112908 | Demethylmenaquinone methyltransferase | 1.7 | 7.3* | 6.6* |
| Ga0072459_113090 | UbiE/COQ5 methyltransferase | 1.6 | 7.1* | 6.4* |
| Ga0072459_112235 | UbiA prenyltransferase | 1.6 | 7.7* | 7.0* |
| Ga0072459_113530 | UbiE/COQ5 methyltransferase | 1.5 | 7.5* | 6.9* |
| Ga0072459_112514 | UbiE/COQ5 methyltransferase | 1.5 | 7.7* | 7.1* |
| Ga0072459_113346 | UbiE/COQ5 methyltransferase | 1.5 | 7.5* | 7.0* |
| Ga0072459_113347 | UbiE/COQ5 methyltransferase | 1.4 | 8.2 | 7.7 |
| Ga0072459_11898 | UbiA prenyltransferase | 1.4 | 8.2 | 7.7 |
| Ga0072459_11516 | Isopentenyl phosphate kinase | 1.3 | 8.8 | 8.4 |
| Ga0072459_11638 | Farnesylgeranyl pyrophosphate synthetase | 1.2 | 7.4* | 7.2* |
| Ga0072459_113679 | UbiA prenyltransferase | 1.2 | 8.4 | 8.2 |
| Ga0072459_11517 | Isopentenyl-diphosphate delta-isomerase | 1.0 | 8.5 | 8.5 |
| Ga0072459_11519 | Geranylgeranyl-diphosphate synthase | 0.7 | 8.1 | 8.6 |

*Negative values in the column "fold up-regulated in DIET" indicate that transcripts were more abundant in HIT-grown cells. The $log_2$ RPKM median for HIT-grown M. barkeri cells was 7.5. The $log_2$ RPKM median for DIET-grown M. barkeri cells was 7.9. *Transcripts with values below the $log_2$ RPKM median.*

**TABLE 4 |** Comparison of transcripts from genes coding for heterodisulfide reductase complexes HdrA1B1C1 and HdrA2B2C2 in *M. barkeri* cells growing via HIT in co-culture with *P. carbinolicus* or via DIET in co-culture with *G. metallireducens*.

| Locus ID | Annotation | Gene | Fold up-regulated in DIET | $log_2$ RPKM DIET | $log_2$ RPKM HIT |
|---|---|---|---|---|---|
| Ga0072459_11778 | Heterodisulfide reductase subunit A1 | *hdrA1* | 1.93 | 8.86 | 7.91 |
| Ga0072459_11777 | Heterodisulfide reductase subunit C1 | *hdrC1* | 2.04 | 9.32 | 8.29 |
| Ga0072459_11776 | Heterodisulfide reductase subunit B1 | *hdrB1* | 2.55 | 8.62 | 7.27* |
| Ga0072459_111651 | Heterodisulfide reductase subunit A2 | *hdrA2* | 1.27 | 8.75 | 8.40 |
| Ga0072459_113523 | Heterodisulfide reductase subunit B2 | *hdrB2* | 1.25 | 8.63 | 8.31 |
| Ga0072459_113524 | Heterodisulfide reductase subunit C2 | *hdrC2* | −2.05 | 6.80* | 7.84 |
| Ga0072459_113160 | Heterodisulfide reductase subunit E | *hdrE* | −2.63 | 9.08 | 10.47 |
| Ga0072459_113159 | Heterodisulfide reductase subunit D | *hdrD1* | −3.22 | 7.94* | 9.63 |
| Ga0072459_11492 | Heterodisulfide reductase subunit D2 | *hdrD2* | 2.05 | 7.80* | 6.75* |

*The $log_2$ RPKM median for HIT grown M. barkeri cells was 7.5. The $log_2$ RPKM median for DIET grown M. barkeri cells was 7.9. Negative values in the "Fold up in DIET" column indicate that genes were more highly transcribed in HIT-grown cells. *Transcripts with values below the $log_2$ RPKM median.*

abundance for the genes for subunits of the homologous HdrA2B2C2 was more comparable to that during growth on HIT, with the transcripts for the genes of the A2 and B2 slightly higher during DIET and lower transcripts for the C2 subunit. When the general pattern of higher gene transcript abundance for soluble proteins in HIT-grown cells is considered, these results suggest that HdrA2B2C2 might also be important in DIET.

*In vitro* purified HdrA2B2C2 from *M. acetivorans* oxidizes $F_{420}H_2$ with the reduction of ferredoxin and CoB-S-S-CoM through flavin-based electron bifurcation (Yan et al., 2017). The phenotypes for various *Methanosarcina* mutants have suggested

that HdrA1B1C1 can couple the oxidation of reduced ferredoxin with the reduction of both $F_{420}$ and CoB-S-S-CoM (Buan and Metcalf, 2010; Gonnerman et al., 2013). However, this reaction has not been verified biochemically (Yan and Ferry, 2018) and the direction of electron flow for the HdrA1B1C1 complex could be similar to that demonstrated for the HdrA2B2C2 complex, especially under conditions in which there is substantial production of reduced $F_{420}$ and limited routes for generating reduced ferredoxin. An electron bifurcation reaction in this direction would also be consistent with the electron bifurcation from flavin with the reduction of CoB-S-S-CoM and ferredoxin associated with the MvhADG/HdrABC complexes found in methanogens that specialize in growth with $H_2/CO_2$ (Kaster et al., 2011).

## The Completed Pathway for Energy Conservation During DIET

Therefore, it is proposed that half of the $F_{420}H_2$ generated with Fpo is the electron donor for HdrABC (one or both homologs) to produce reduced ferredoxin with the simultaneous reduction of CoM-S-S-CoB (**Figure 3**). In this way the coupled activity of Fpo- and HdrABC-catalyzed reactions deliver the eight moles of electrons derived from the oxidation of two moles of ethanol to each required step in the carbon dioxide reduction pathway (**Figure 3**).

As noted above, the Fpo-catalyzed reduction of $F_{420}$ is proton balanced. Protons are released from $F_{420}H_2$ oxidation by HdrABC, but an equivalent number of protons are consumed in other reactions in the carbon dioxide reduction pathway (**Figure 3**). Thus, the model also balances proton flux.

The proposed model generates a chemiosmotic gradient to produce ATP through the activity of the Mtr complex that is known to pump sodium across the membrane during methyl transfer in the carbon dioxide reduction pathway (Thauer et al., 2008). There are two possibilities for ATP generation from the sodium gradient. Genes for both the $A_1A_0$ ATP synthase and the $F_1F_0$ ATP synthase were expressed during DIET (**Supplementary Table S3**). The available evidence suggests that both can translocate sodium (Schlegel and Muller, 2013). Genes for several components of the $F_1F_0$ ATP synthase were more highly expressed during growth on DIET and others were expressed at levels comparable to HIT-grown cells (**Supplementary Table S3**). This suggests that the $F_1F_0$ ATP synthase may play a more important role during growth on DIET, but at present there is not enough information on $F_1F_0$ ATP function in *M. barkeri* to speculate why.

## Transcriptomics Suggests Potential Outer Surface Electrical Contacts

A number of genes predicted to encode redox active proteins expected to be associated with the *M. barkeri* membrane and/or cell surface were more highly expressed in cells grown via DIET (**Table 5**). However, it is premature to speculate on their possible role in mediating electron transfer into the cell in the absence of further biochemical characterization to determine whether important characteristics, such as redox potential and cellular localization, are appropriate for proposed roles.

For example, a gene putatively encoding a membrane-bound protein with a cupredoxin domain (Ga0072459_111371) was highly expressed specifically during DIET (**Table 5**). The cupredoxins rusticyanin and sulfocyanin play important roles in electron transfer into cells of *Acidithiobacillus* and *Sulfolobus* species during Fe(II) and $S^0$ oxidation (Komorowski and Schafer, 2001; Dennison, 2005) and thus might play a similar role in electron transport into *M. barkeri*. The mid-point potentials of known cupredoxins (150 to 680 mV) are more positive than that expected for an electron carrier involved in electron transport to methanophenazine [mid-point potential of −165 mV (Tietze et al., 2003)]. However, modifications in cupredoxin structure and environment may greatly influence their mid-point potential (Marshall et al., 2009) and thus a role in electron transport into the cell is conceivable.

In a similar manner, genes encoding proteins that putatively incorporate pyrroloquinoline quinone (PQQ) as a co-factor were highly expressed during growth via DIET (**Table 5**). Like rusticyanin and sulfocyanin, proteins with PQQ-binding domains are involved in electron transport into the cell during oxidation of Fe(II) or Mn(II) (Croal et al., 2007; Johnson and Tebo, 2008). The mid-point potential of proteins with PQQ domains (∼90–100 mV) is too positive to play a role in electron transfer to methanophenazine. However, genes for PQQ biosynthesis were not found in the *M. barkeri* genome. Thus, it is possible that these proteins with predicted PQQ domains may incorporate another co-factor. Methanophenazine is one possibility. Further analysis of these proteins and others with higher gene expression during DIET (**Table 5**) is warranted. The expression of genes for a number of soluble electron carriers/co-factors were higher in DIET-grown cells, further suggesting differences in electron flux during DIET (**Supplementary Table S4**), but more analysis will be required to evaluate their role/significance.

# IMPLICATIONS

The results suggest a pathway for electron and proton flux in *M. barkeri* during DIET that is significantly different than during HIT-based growth. The increased expression of genes for key components, including Fpo and HdrABC, and considerations of electron and proton transport during DIET, suggest an electron- and proton-balanced model in which the required electron donors are generated for each of the reductive steps of carbon dioxide reduction to methane while conserving energy to support growth (**Figure 3**). This model provides hypotheses that can be further evaluated experimentally with the appropriate *M. barkeri* mutants. However, as noted in the Introduction, this will require the discovery or development of an electron-donating strain capable of growing in the high salt medium that is used to generate *M. barkeri* mutants (Kohler and Metcalf, 2012). An alternative approach might be to adapt *M. barkeri* mutants to lower salt conditions, but this would require a time-consuming, labor-intensive adaption of each *M. barkeri* mutant strain with

**TABLE 5 |** Genes coding for putative transmembrane and/or surface associated electron transport proteins potentially involved in electron up-take during DIET.

| Locus ID | Annotation | Signal peptide | # Trans-membrane helices | Evidence of surface protein | Fold up-regulated in DIET | $log_2$ RPKM DIET | $log_2$ RPKM HIT | Redox protein category | Localization |
|---|---|---|---|---|---|---|---|---|---|
| Ga0072459_111371 | Cupredoxin domain protein | No | 1 | PS51257 | 7.3 | 10.4 | 7.5 | Cupredoxin | Membrane |
| Ga0072459_113267 | Cupredoxin | No | 1 | No | 2.9 | 7.9 | 6.4* | Cupredoxin | Potentially extracellular |
| Ga0072459_113594 | Cytochrome cd1-nitrite reductase-like, haem d1 domain | No | 0 | pfam08309 | 2.6 | 7.7* | 6.4* | Cytochrome b/d | Potentially extracellular |
| Ga0072459_112903 | Cytochrome bd-type quinol oxidase | No | 9 | No | 2.1 | 7.7* | 6.6* | Cytochrome b/d | Membrane |
| Ga0072459_11415 | Cytochrome b5-like heme/steroid binding domain | No | 1 | No | 2.0 | 7.8* | 6.8* | Cytochrome b/d | Membrane |
| Ga0072459_113465 | 4Fe-4S ferredoxin-type, iron-sulfur binding domain | No | 2 | No | 2.0 | 8.0 | 7.0* | Ferredoxin | Membrane |
| Ga0072459_11712 | PQQ domain protein | No | 0 | PS51257 | 4.3 | 9.2 | 7.1* | Quinonprotein | Potentially extracellular |
| Ga0072459_111886 | PQQ domain protein | No | 2 | No | 2.8 | 8.6 | 7.1* | Quinonprotein | Potentially extracellular |
| Ga0072459_113595 | PQQ domain protein | No | 1 | pfam08309 | 2.2 | 8.44 | 7.3* | Quinonprotein | Potentially extracellular |
| Ga0072459_111452 | Secreted thioredoxin protein | Yes | 0 | PS51257 | 2.7 | 8.9 | 7.5 | Thioredoxin | Extracellular |

*These genes were at least two fold more highly expressed in M. barkeri cells grown via DIET than M. barkeri cells grown via HIT. PS51527: prokaryotic lipoprotein attachment site; pfam08309: LVIVD repeat found in bacterial and archaeal surface proteins. Cell localization predictions were made with PSORTb v3.0.2 software. *Transcripts with values below the $log_2$ RPKM median (7.5 for HIT and 7.9 for DIET).*

the risk of additional mutations arising during the adaption process.

The DIET transcriptome did not conclusively identify electrical contacts for DIET beyond the cell membrane. One potential reason for this is that *M. barkeri* might constitutively express these contacts. It is difficult to envision how *Geobacter* or other electron-donating partners could make electrical contacts with the outer surface of *M. barkeri* unless those contacts were expressed in advance of the initial *Geobacter-M. barkeri* electrical interaction. *M. barkeri*'s low affinity for $H_2$ makes it a poor competitor for $H_2$ in many environments (Thauer et al., 2008). Constitutive production of outer surface electrical contacts could poise *M. barkeri* for DIET and provide a competitive advantage in utilizing this alternative source of electrons for carbon dioxide reduction.

Elucidating the role of *Methanosarcina* species in DIET in complex natural environments is complicated by the possibility that $H_2$ must also be considered as a potential electron donor for carbon dioxide reduction (Holmes et al., 2017). The differences in gene expression patterns between DIET- and HIT-grown cells suggest that metatranscriptional analysis is a route to better characterize the extent to which *Methanosarcina* are involved in DIET. It has been suggested that *M. barkeri* as well as other methanogens, can directly accept electrons from other extracellular sources such as electrodes, conductive carbon materials, and metals, but it has been difficult to rule out the possibility that $H_2$ might be an intermediary electron carrier (Cheng and Call, 2016; Blasco-Gomez et al., 2017; Lovley, 2017b,c). The finding that transcriptome patterns in cells directly accepting electrons from an external source differ substantially from cells utilizing $H_2$ as an electron donor suggests that the transcriptomic analysis approach described here could also help resolve this question.

## AUTHOR CONTRIBUTIONS

DH, A-ER, PS, and DL conceived the study. A-ER grew the co-cultures. PS extracted and processed the nucleic acids for sequences. DH re-annotated the genome as necessary and analyzed the transcriptome data. DH and DL wrote the initial version of the manuscript. All authors made important modifications and additions.

## FUNDING

This research was supported by the Army Research Office and was accomplished under Grant Number W911NF-17-1-0345. The views and conclusions contained in this document are those of the authors and should not be interpreted as representing the official policies, either expressed or implied, of the Army Research Office or the United States Government. During the writing of this manuscript A-ER was supported by two Danish Research Council Grants (Sapere Aude no. 418100203 and Innovationsfonden no. 410600017) and the Novo Nordisk Foundation.

## SUPPLEMENTARY MATERIAL

The Supplementary Material for this article can be found online at: https://www.frontiersin.org/articles/10.3389/fmicb.2018.03109/full#supplementary-material

## REFERENCES

Baek, G., Kim, J., Kim, J., and Lee, C. (2018). Role and potential of direct interspecies electron transfer in anaerobic digestion. *Energies* 11:107. doi: 10.3390/en11010107

Barua, S., and Dhar, B. R. (2017). Advances towards understanding and engineering direct interspecies electron transfer in anaerobic digestion. *Bioresour. Technol.* 244, 698–707. doi: 10.1016/j.biortech.2017.08.023

Blasco-Gomez, R., Batlle-Vilanova, P., Villano, M., Balaguer, M. D., Colprim, J., and Puig, S. (2017). On the edge of research and technological application: a critical review of electromethanogenesis. *Int. J. Mol. Sci.* 18:874. doi: 10.3390/ijms18040874

Bolger, A. M., Lohse, M., and Usadel, B. (2014). Trimmomatic: a flexible trimmer for Illumina sequence data. *Bioinformatics* 30, 2114–2120. doi: 10.1093/bioinformatics/btu170

Boone, D. R., and Mah, R. A. (2015). "Methanosarcina," in *Bergey's Manual of Systematics of Archaea and Bacteria*, ed. W. B. Whitman (Hoboken, NJ: John Wiley & Sons Ltd), 1–15.

Buan, N., and Metcalf, W. (2010). Methanogenesis by *Methanosarcina acetivorans* involves two structurally and functionally distinct classes of heterodisulfide reductase. *Mol. Microbiol.* 75, 843–853. doi: 10.1111/j.1365-2958.2009.06990.x

Burge, S. W., Daub, J., Eberhardt, R., Tate, J., Barquist, L., Nawrocki, E. P., et al. (2013). Rfam 11.0: 10 years of RNA families. *Nucleic Acids Res.* 41, D226–D232. doi: 10.1093/nar/gks1005

Cheng, Q., and Call, D. (2016). Hardwiring microbes via direct interspecies electron transfer: mechanisms and applications. *Environ. Sci. Process. Impacts* 18, 968–980. doi: 10.1039/c6em00219f

Croal, L. R., Jiao, Y. Q., and Newman, D. K. (2007). The fox operon from *Rhodobacter* strain SW2 promotes phototrophic fe(II) oxidation in *Rhodobacter capsulatus* SB1003. *J. Bacteriol.* 189, 1774–1782. doi: 10.1128/JB.01395-06

Dennison, C. (2005). Investigating the structure and function of cupredoxins. *Coord. Chem. Rev.* 249, 3025–3054. doi: 10.1002/pro.3310

Dubé, C.-D., and Guiot, S. R. (2015). Direct interspecies electron transfer in anaerobic digestion: a review. *Adv. Biochem. Eng.* 151, 101–115. doi: 10.1007/978-3-319-21993-6_4

Duszenko, N., and Buan, N. R. (2017). Physiological evidence for isopotential tunneling in the electron transport chain of methane-producing archaea. *Appl. Environ. Microbiol.* 83:e00950-17. doi: 10.1128/AEM.00950-17

Finn, R. D., Coggill, P., Eberhardt, R. Y., Eddy, S. R., Mistry, J., Mitchell, A. L., et al. (2016). The Pfam protein families database: towards a more sustainable future. *Nucleic Acids Res.* 44, D279–D285. doi: 10.1093/nar/gkv1344

Gonnerman, M. C., Benedict, M. N., Feist, A. M., Metcalf, W. W., and Price, N. D. (2013). Genomically and biochemically accurate metabolic reconstruction of *Methanosarcina barkeri* Fusaro, iMG746. *Biotechnol. J.* 8, 1070–1079. doi: 10.1002/biot.201200266

Hofmann, K., and Stoffel, W. (1993). TMbase - a database of membrane spanning proteins segments. *Biol. Chem. Hoppe Seyler* 374:166.

Holmes, D. E., Shrestha, P. M., Walker, D. J. F., Dang, Y., Nevin, K. P., Woodard, T. L., et al. (2017). Metatranscriptomic evidence for direct interspecies electron transfer between *Geobacter* and *Methanothrix* species in rice paddy soils. *Appl. Environ. Microbiol.* 83:e00223-17. doi: 10.1128/AEM.00223-17

Johnson, H. A., and Tebo, B. M. (2008). In vitro studies indicate a quinone is involved in bacterial Mn(II) oxidation. *Arch. Microbiol.* 189, 59–69. doi: 10.1007/s00203-007-0293-y

Kaster, A. K., Moll, J., Parey, K., and Thauer, R. K. (2011). Coupling of ferredoxin and heterodisulfide reduction via electron bifurcation in hydrogenotrophic methanogenic archaea. *Proc. Natl. Acad. Sci. U.S.A.* 108, 2981–2986. doi: 10.1073/pnas.1016761108

Klevebring, D., Bjursell, M., Emanuelsson, O., and Lundeberg, J. (2010). In-depth transcriptome analysis reveals novel TARs and prevalent antisense transcription in human cell lines. *Plos One* 5:e9762. doi: 10.1371/journal.pone.0009762

Kohler, P. R. A., and Metcalf, M. W. (2012). Genetic manipulation of *Methanosarcina* spp. *Front. Microbiol.* 3:259. doi: 10.3389/fmicb.2012.00259

Komorowski, L., and Schafer, G. (2001). Sulfocyanin and subunit II, two copper proteins with novel features, provide new insight into the archaeal SoxM oxidase supercomplex. *FEBS Lett.* 487, 351–355. doi: 10.1016/S0014-5793(00)02343-7

Kopylova, E., Noe, L., and Touzet, H. (2012). SortMeRNA: fast and accurate filtering of ribosomal RNAs in metatranscriptomic data. *Bioinformatics* 28, 3211–3217. doi: 10.1093/bioinformatics/bts611

Krogh, A., Larsson, B., Von Heijne, G., and Sonnhammer, E. L. (2001). Predicting transmembrane protein topology with a hidden Markov model: application to complete genomes. *J. Mol. Biol.* 305, 567–580. doi: 10.1006/jmbi.2000.4315

Kulkarni, G., Mand, T. D., and Metcalf, W. W. (2018). Energy conservation via hydrogen cycling in the methanogenic archaeon *Methanosarcina barkeri*. *mBio* 9:e01256-18. doi: 10.1128/mBio.01256-18

Lovley, D. R. (2017a). Electrically conductive pili: biological function and potential applications in electronics. *Curr. Opin. Electrochem.* 4, 190–198. doi: 10.1016/j.coelec.2017.08.015

Lovley, D. R. (2017b). Happy together: microbial communities that hook up to swap electrons. *ISME J.* 11, 327–336. doi: 10.1038/ismej.2016.136

Lovley, D. R. (2017c). Syntrophy goes electric: direct interspecies electron transfer. *Ann. Rev. Microbiol.* 71, 643–664. doi: 10.1146/annurev-micro-030117-020420

Mand, T. D., Kulkarni, G., and Metcalf, W. W. (2018). Genetic, biochemical, and molecular characterization of *Methanosarcina barkeri* mutants lacking three distinct classes of hydrogenase. *J. Bacteriol.* 200:e0342-18. doi: 10.1128/JB.00342-18

Marchler-Bauer, A., Derbyshire, M. K., Gonzales, N. R., Lu, S., Chitsaz, F., Geer, L. Y., et al. (2015). CDD: NCBI's conserved domain database. *Nucleic Acids Res.* 43, D222–D226. doi: 10.1093/nar/gku1221

Marshall, N. M., Garner, D. K., Wilson, T. D., Gao, Y. G., Robinson, H., Nilges, M. J., et al. (2009). Rationally tuning the reduction potential of a single cupredoxin beyond the natural range. *Nature* 462, 113–127. doi: 10.1038/nature08551

Morita, M., Malvankar, N. S., Franks, A. E., Summers, Z. M., Giloteaux, L., Rotaru, A. E., et al. (2011). Potential for direct interspecies electron transfer in methanogenic wastewater digester aggregates. *mBio* 2:e00159-11. doi: 10.1128/mBio.00159-11

Mortazavi, A., Williams, B. A., Mccue, K., Schaeffer, L., and Wold, B. (2008). Mapping and quantifying mammalian transcriptomes by RNA-Seq. *Nat. Methods* 5, 621–628. doi: 10.1038/nmeth.1226

Ogawa, T., Yoshimura, T., and Hemmi, H. (2010). Geranylfarnesyl diphosphate synthase from *Methanosarcina mazei*: different role, different evolution. *Biochem. Biophys. Res. Commun.* 393, 16–20. doi: 10.1016/j.bbrc.2010.01.063

Park, J. H., Kang, H. J., Park, K. H., and Park, H. D. (2018). Direct interspecies electron transfer via conductive materials: a perspective for anaerobic digestion applications. *Bioresour. Technol.* 254, 300–311. doi: 10.1016/j.biortech.2018.01.095

Petersen, T. N., Brunak, S., Von Heijne, G., and Nielsen, H. (2011). SignalP 4.0: discriminating signal peptides from transmembrane regions. *Nat. Methods* 8, 785–786. doi: 10.1038/nmeth.1701

Quast, C., Pruesse, E., Yilmaz, P., Gerken, J., Schweer, T., Yarza, P., et al. (2013). The SILVA ribosomal RNA gene database project: improved data processing and web-based tools. *Nucleic Acids Res.* 41, D590–D596. doi: 10.1093/nar/gks1219

Rotaru, A.-E., Shrestha, P. M., Liu, F., Nevin, K. P., and Lovley, D. R. (2014a). Direct interspecies electron transfer during syntrophic growth of *Geobacter metallireducens* and *Methanosarcina barkeri* on ethanol. *Appl. Environ. Microbiol.* 80, 4599–4605. doi: 10.3389/fmicb.2016.00236

Rotaru, A.-E., Shrestha, P. M., Liu, F., Shrestha, M., Shrestha, D., Embree, M., et al. (2014b). A new model for electron flow during anaerobic digestion: direct interspecies electron transfer to *Methanosaeta* for the reduction of carbon dioxide to methane. *Energy Environ. Sci.* 7, 408–415. doi: 10.1039/C3EE42189A

Schlegel, K., and Muller, V. (2013). Evolution of Na+ and H+ bioenergetics in methanogenic archaea. *Biochem. Soc. Trans.* 41, 421–426. doi: 10.1042/BST20120294

Shrestha, P. M., and Rotaru, A.-E. (2014). Plugging in or going wireless: strategies for interspecies electron transfer. *Front. Microbiol.* 5:237. doi: 10.3389/fmicb.2014.00237

Shrestha, P. M., Rotaru, A.-E., Summers, Z. M., Shrestha, M., Liu, F., and Lovley, D. R. (2013). Transcriptomic and genetic analysis of direct interspecies electron transfer. *Appl. Environ. Microbiol.* 79, 2397–2404. doi: 10.1128/AEM.03837-12

Summers, Z. M., Fogarty, H., Leang, C., Franks, A. E., Malvankar, N. S., and Lovley, D. R. (2010). Direct exchange of electrons within aggregates of an evolved syntrophic co-culture of anaerobic bacteria. *Science* 330, 1413–1415. doi: 10.1126/science.1196526

Thauer, R. K., Kaster, A.-K., Seedork, H., Buckel, W., and Hedderich, R. (2008). Methanogenic archaea: ecologically relevant differences in energy conservation. *Nat. Rev. Microbiol.* 8, 579–591. doi: 10.1038/nrmicro1931

Tietze, M., Beuchle, A., Lamla, I., Orth, N., Dehler, M., Greiner, G., et al. (2003). Redox potentials of methanophenazine and CoB-S-S-CoM, factors involved in electron transport in methanogenic archaea. *Chembiochem* 4, 333–335. doi: 10.1002/cbic.200390053

Tusnady, G. E., and Simon, I. (2001). The HMMTOP transmembrane topology prediction server. *Bioinformatics* 17, 849–850. doi: 10.1093/bioinformatics/17.9.849

Ueki, T., Nevin, K. P., Rotaru, A.-E., Wang, L.-Y., Ward, J. E., Woodard, T. L., et al. (2018). Geobacter strains expressing poorly conductive pili reveal constraints on direct interspecies electron transfer mechanisms. *mBio* 9:e01273-18. doi: 10.1128/mBio.01273-18

Welte, C., and Deppenmeier, U. (2014). Bioenergetics and anaerobic respiratory chains of aceticlastic methanogens. *Biochim. Biophys. Acta* 1837, 1130–1147. doi: 10.1016/j.bbabio.2013.12.002

Yan, Z., and Ferry, J. G. (2018). Electron bifurcation and confurcation in methanogenesis and reverse methanogenesis. *Front. Microbiol.* 9:1322. doi: 10.3389/fmicb.2018.01322

Yan, Z., Wang, M. Y., and Ferry, J. G. (2017). A ferredoxin-and F420H2-dependent, electron-bifurcating, heterodisulfide reductase with homologs in the domains bacteria and archaea. *mBio* 8:e02285-16. doi: 10.1128/mBio.02285-16

Yu, N. Y., Wagner, J. R., Laird, M. R., Melli, G., Rey, S., Lo, R., et al. (2010). PSORTb 3.0: improved protein subcellular localization prediction with refined localization subcategories and predictive capabilities for all prokaryotes. *Bioinformatics* 26, 1608–1615. doi: 10.1093/bioinformatics/btq249

**Conflict of Interest Statement:** The authors declare that the research was conducted in the absence of any commercial or financial relationships that could be construed as a potential conflict of interest.

frontiers in Microbiology

ORIGINAL RESEARCH
published: 28 September 2017
doi: 10.3389/fmicb.2017.01881

# Adaptation of Methanogenic Inocula to Anaerobic Digestion of Maize Silage

*Martyna Wojcieszak[1†], Adam Pyzik[2†], Krzysztof Poszytek[1], Pawel S. Krawczyk[2], Adam Sobczak[2,3], Leszek Lipinski[2], Otton Roubinek[4], Jacek Palige[4], Aleksandra Sklodowska[1] and Lukasz Drewniak[1]**

[1] Laboratory of Environmental Pollution Analysis, Faculty of Biology, University of Warsaw, Warsaw, Poland, [2] Institute of Biochemistry and Biophysics, Polish Academy of Sciences, Warsaw, Poland, [3] Institute of Genetics and Biotechnology, Faculty of Biology, University of Warsaw, Warsaw, Poland, [4] Institute of Nuclear Chemistry and Technology, Warsaw, Poland

A well-balanced microbial consortium is crucial for efficient biogas production. In turn, one of a major factor that influence on the structure of anaerobic digestion (AD) consortium is a source of microorganisms which are used as an inoculum. This study evaluated the influence of inoculum sources (with various origin) on adaptation of a biogas community and the efficiency of the biomethanization of maize silage. As initial inocula for AD of maize silage the samples from: (i) an agricultural biogas plant (ABP) which utilizes maize silage as a main substrate, (ii) cattle slurry (CS), which contain elevated levels of lignocelluloses materials, and (iii) raw sewage sludge (RSS) with low content of plant origin materials were used. The adaptation of methanogenic consortia was monitored during a series of passages, and the functionality of the adapted consortia was verified through start-up operation of AD in two-stage reactors. During the first stages of the adaptation phase, methanogenic consortia occurred very slowly, and only after several passages did the microbial community adapts to allow production of biogas with high methane content. The ABP consortium revealed highest biogas production in the adaptation and in the start-up process. The biodiversity dynamics monitored during adaptation and start-up process showed that community profile changed in a similar direction in three studied consortia. Native communities were very distinct to each other, while at the end of the Phase II of the start-up process microbial diversity profile was similar in all consortia. All adopted bacterial communities were dominated by representatives of *Porphyromonadaceae*, *Rikenellaceae*, *Ruminococcaceae,* and *Synergistaceae*. A shift from low acetate-preferring acetoclastic *Methanosaetaceae* (ABP and RSS) and/or hydrogenotrophic *Archaea*, e.g., *Methanomicrobiaceae* (CS) prevailing in the inoculum samples to larger populations of high acetate-preferring acetoclastic *Methanosarcinaceae* was observed by the end of the experiment. As a result, three independent, functional communities that syntrophically produced methane from acetate (primarily) and $H_2/CO_2$, methanol and methylamines were adapted. This study provides new insights into the specific process by which different inocula sampled from typical methanogenic environments that are commonly used to initiate industrial installations gradually adapted to allow biogas production from maize silage.

**Keywords: inoculum source, anaerobic digestion, maize silage, biodiversity dynamics, methanogenic consortia**

OPEN ACCESS

***Edited by:***
*Obulisamy Parthiba Karthikeyan, Hong Kong Baptist University, China*

***Reviewed by:***
*Feng Ju, Swiss Federal Institute of Aquatic Science and Technology, Switzerland*
*Raj Boopathy, Nicholls State University, United States*
*Surakasi Venkata Prasad, Prolog Biologicals Pvt Ltd., India*

***Correspondence:**
*Lukasz Drewniak*
*ldrewniak@biol.uw.edu.pl*

*† These authors have contributed equally to this work.*

***Specialty section:***
*This article was submitted to Microbiotechnology, Ecotoxicology and Bioremediation, a section of the journal Frontiers in Microbiology*

***Received:*** *21 June 2017*
***Accepted:*** *14 September 2017*
***Published:*** *28 September 2017*

***Citation:***
*Wojcieszak M, Pyzik A, Poszytek K, Krawczyk PS, Sobczak A, Lipinski L, Roubinek O, Palige J, Sklodowska A and Drewniak L (2017) Adaptation of Methanogenic Inocula to Anaerobic Digestion of Maize Silage. Front. Microbiol. 8:1881. doi: 10.3389/fmicb.2017.01881*

## INTRODUCTION

Since the 1990s, anaerobic digestion (AD) has emerged as one of the most effective and sustainable methods to limit the harmful effects of organic waste on the environment, reducing its disposal in landfills. Simultaneous to the reduction of organic content, AD processes generate a substantial amount of methane-rich biogas, which constitutes a promising fuel for renewable energy production. Biogas generation in AD allows complete recycling of various waste materials, including wastewater, industrial food waste, or animal manure, as well as energy crops, which are a valuable source of organic matter for biogas production. For example, maize is considered to have the highest yield potential due to its high content of dry matter (Oslaj et al., 2010; Tyagi and Lo, 2013).

Anaerobic digestion is a multistep process carried out by a number of specialized microorganisms which catalyze (i) the liquefaction and hydrolysis of insoluble organic compounds, (ii) the gasification of intermediates, and (iii) the mineralization and humification of organic matter. All of the stages of AD process: hydrolysis, acidogenesis, acetogenesis, and methanogenesis are strictly interrelated and the proper balance between growth and activities of particular group of microorganisms is crucial for high efficiency (Ali Shah et al., 2014). For example, activity of hydrolytic bacteria determines the rate and performance of other group of microorganisms involved in AD. Low rate of hydrolysis of lignocellulose results in the slowdown of the entire process of plant biomass degradation, thus leading to the reduction of the efficiency of biogas production (Sun and Cheng, 2002). It is also known that for stable and efficient biogas production a strict cooperation between syntrophic bacteria and methanogenic archaeon's is required. Excess of hydrogen produced by acetogenic bacteria can be toxic to them, therefore symbiosis with hydrogenotrophic archaea is required (Ali Shah et al., 2014). For this reason one of the key factors that directly influence on biogas yields is the selection and the use of the inoculum, which contain the appropriate groups of microorganism capable interacts with each other and able to adapt to various environmental conditions.

The most common practice in full-scale biogas plant systems, which allows selecting and using the most appropriate AD inoculum, is to obtain a starter microbial community from another, already running AD plant reactor. Alternatively, cow, poultry, or piggery dung is used as a source of methanogenic microorganisms (Dhamodharan et al., 2015). These biomass materials are rich in different groups of anaerobic microorganisms, and, during natural selection in new feedstock, the proper biogas-community is formed. However, stable and effective biogas production takes longer to achieve when starting up AD with such inoculum than when using inoculum from other well-performing biogas plants. Various batch experiments have shown that the use of inocula from different origins may vary the efficiency of the methanization process of the same specific substrate (e.g., corn stover, wastewater sludge, etc.) (Lopes et al., 2004; Xu et al., 2012). Furthermore, lab-scale inoculation experiments confirmed that the use of an adapted microbial consortium can accelerate start-up of the digestion process (Goncalves et al., 2011; Hidalgo and Martin-Marroquin, 2014). Goncalves et al. (2011) showed a five-fold faster start-up of an olive mill wastewater treatment reactor with an oleate-adapted consortium compared to a non-acclimated consortium. Our previous paper showed that adapted hydrolytic microbial consortia may improve the efficiency of maize silage degradation, which is demonstrated by increased glucose and volatile fatty acids (VFAs) production and increased biogas yield (Poszytek et al., 2017). The results of selection of hydrolytic consortia also showed that substrate input was the main driving force responsible for the changes in the community structure.

Along with the origin of the inoculum, an important parameter of the AD process is the reactor operation, which can determine the microbial structure in long-term process, allowing the adaptation of inoculum to changing conditions (De Vrieze et al., 2015; Wilkins et al., 2015; Han et al., 2016). Among the factors/parameters in the reactor environment that directly influence on the growth, performance, and the community structure are primarily: temperature variations (Ho et al., 2014), organic loading rate (OLR) (Kundu et al., 2014), increased VFAs and ammonia concentration (De Vrieze et al., 2015).

Despite studies conducted in recent years, our knowledge about the microbial structure and adaptation process of inoculum is still poor, and we are not yet able to draw concrete conclusions about how anaerobic microbiome behave against environmental and process disturbances, and which microorganisms are required for optimal performance of reactors. To achieve this goal, we should broaden our knowledge in this area by comparing the multiple studies monitoring methanogenic populations in biogas reactors enriched with different substrates, operating under different conditions, and, most importantly, considering the source of inoculum.

Based on the above considerations, the first objective of the present study is to evaluate the influence of inoculum sources from an agricultural biogas plant (ABP), cattle slurry (CS), and raw sewage sludge (RSS) on the adaptation of a biogas-producing microbial consortium and biogas production yields when maize silage is used as the sole substrate in a series of batch culture experiments. ABP community was selected as a reference inoculum, which has been adapted for anaerobic degradation of maize silage on an industrial scale bioreactor for several of months. CS represents community that use lignocelluloses materials as one of the main nutrient substrate. In turn, RSS community served as source of physiologically and phylogenetically diversified inoculum, for which plant materials are merely an admixture to the main pool of digested organic matter. The second goal of this work is to reveal the microbial community structure and the biogas production during start-up experiments in a quasi-continuous, two-phase process using previously adapted inocula. The microbial community structure in both experiments was

analyzed by sequencing of the bacterial and archaeal 16S rRNA gene amplicons.

# MATERIALS AND METHODS

## Inocula and Substrates

Inocula were taken from environments that are specialized in AD and methane production, including: (i) a fermenter tank of an ABP in Miedzyrzec Podlaski, (Poland), fed with maize silage and operated at mesophilic temperatures, (ii) RSS from the municipal sewage treatment plant "Czajka" in Warsaw (Poland), and (iii) CS from a farm in Mikanow (Poland). Methanogenic inocula (comprised of solid and liquids) were sampled in a hermetic canister or container, transported to the laboratory and stored for a maximum of 16 h at the following temperatures: (i) 37°C for ABP and RSS or (ii) in 23°C for CS sample prior to cultivation experiments. To analyze the microbial community structure, 50 mL of each sample was centrifuged (8000 × *g*, 4°C, 15 min) and the pellets were directly used for metagenomic DNA extraction.

In all performed experiments, the bioreactors were fed with maize silage provided by a farm located in Mikanow, Poland. A bulk amount of maize silage was transported from Mikanow to the laboratory at room temperature, portioned into plastic bags, and stored at 4°C. The physico-chemical characteristics of the methanogenic inocula and substrate are shown in **Table 1**.

## Laboratory Reactors Operation

Schematic visualization of laboratory scale experiments is shown in **Figure 1**. The preselection experiment was carried out in lab-scale bioreactors with a working volume of 800 mL, made of 1 L GL 45 glass bottles (Schott Duran, Germany) connected with Dreschel scrubbers and 1 L Tedlar gas bags (Sigma, Germany) as a biogas collector. The batch AD was conducted in triplicate. Batch cultivation was conducted until biogas productions in three successive passages were on the similar level and the methane content was above 60%. The similar biogas production with the high methane content was achieved in the second stage of adaptation (passages 8–12) (Supplementary Table S1).

The adapted consortia were then used in two-stage reactors to verify the procedure of scaling-up of the consortia volume and start-up enhancing properties for biogas production of the adopted microbial consortia. The remains of biomass from passages 8–12 were subsampled and further cultivated in batch reactors (in the same manner as for Stage II, **Figure 1**) in order to achieve sufficient amount of consortia required for inoculation of a two-stage biogas reactor used in the start-up experiment.

Two-stage bioreactor was constructed based on Polish Patent no. PL197595 (Krylowicz et al., 2001). The reactor was equipped with hydraulic agitation and operated in a quasi-continuous mode (**Table 2**).

Determination of the biodiversity of laboratory microbial consortia was performed on metagenomic DNA isolated from batch reactors (at the end of passage 4, 7, 12) and fermenter of the two-stage reactors (at the end of Phase II and Phase III).

## Analytical Methods

To control the AD process and characterize the initial inocula, the following parameters were determined: volume and composition of the biogas, VFAs, total solids (TS), volatile solids (VS), chemical oxygen demand (COD), total ammonia nitrogen (TAN), and pH. TS and VS analyses were performed according to standard methods described in the American Public Health Association [APHA] (1998) Standard Methods. VFAs, COD, and TAN were determined using Nanocolor®kits (Macherey-Nagel, Germany). The C and N elemental contents were quantified using a CHNS Elemental Analyzer EA1112 (Thermo Finnigan). Biogas production was monitored daily with a MilliGascounter MGC-1 (Ritter, Germany). Methane content was analyzed by Gas Chromatography Mass Spectrometry (GC-MS) (Agilent, United States) or with a gas analyzer GA5000 (Geotech, United Kingdom). The separation of biogas was performed using an Agilent 7890A Series Gas Chromatograph (GC) interfaced to an Agilent 5973c Network Mass Selective Detector (Agilent Technologies, United States). A gas sample was injected with split 1:500 (sample; carrier gas) by gastight injector to a HP-PLOT Q column (30 m × 0.32 mm I.D., 0.20 μm film thickness, Agilent Technologies, United States) using He as the carrier gas at 1 mL/min. The ion source was maintained at 250°C; the GC oven was programmed with a stable temperature 70°C (for 10 min). Mass spectrometry (MS) analysis was carried out in the electron-impact mode at an ionizing potential of 70 eV. Mass spectra were recorded from m/z 1 to 100 (0–10 min).

## DNA Extraction and 16S rRNA Gene Amplification

To analyze the microbial community structure at different stages of the experiment (inocula, adaptation, or start-up phase), 25–50 mL of each sample was centrifuged (8000 × *g*, 4°C, 15 min) and the pellet containing bacteria and plant debris was immediately transferred and stored on dry ice prior to DNA extraction. Metagenomic DNA was isolated according to the method described by Dziewit et al. (2015). Briefly, 1 g of centrifuged pellet (containing microbial cells) were disrupted with a 5-step bead-beating protocol, supplemented with freezing and thawing. Final DNA purification from protein, humic, and other substances was carried by CsCl density gradient ultracentrifugation. The concentration and quality of the purified metagenomic DNA was estimated using a NanoDrop 2000 instrument (NanoDrop Technologies) and gel electrophoresis.

The metagenomic DNA was used as a template for amplification of archaeal and bacterial hypervariable V3–V4 regions of the 16S rRNA gene with the following primers: S-D-Arch-0349-a-S-17/S-D-Arch-0786-a-A-20 (GYGCASCAGKCGMGAAW and GGACTACVSG GGTATCTAAT) and S-D-Bact-0341-b-S-17/S-D-Bact-0785-a-A-21 (CCTACGGGNGGCWGCAG and GACTACHV GGGTATCTAATCC), as described by Klindworth et al. (2013). The reaction mixture (50 μL) contained 100 ng template DNA and primers, and 0.02 U of Phusion High-Fidelity DNA Polymerase (Thermo Scientific).

**TABLE 1 |** Physico-chemical characteristics of the inoculum and maize silage.

| Parameters | Units | Maize silage | Agricultural biogas plant (ABP) | Cattle slurry (CS) | Raw sewage sludge (RSS) |
|---|---|---|---|---|---|
| pH | – | 3.77 | 7.35 | 7.45 | 6.00 |
| TS | % FM | 37.00 | 4.00 | 2.21 | 4.00 |
| VS | % TS | 96.00 | 70.93 | 45.60 | 64.81 |
| COD | g/L | 38.90 | 42.5 | 18.40 | 74.33 |
| VFAs | g/L | 1.05 | 7.44 | 11.30 | 11.93 |

*COD, chemical oxygen demand; TS, total solids; VFAs, volatile fatty acids; VS, volatile solid; FM, fresh matter.*

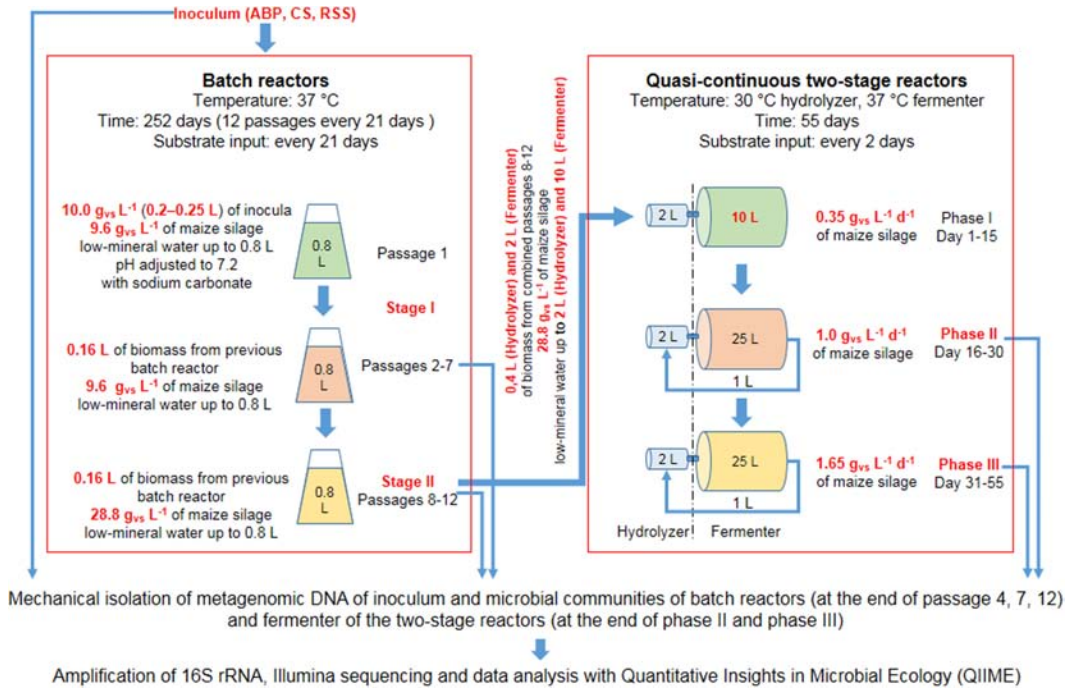


**FIGURE 1 |** Scheme of the laboratory reactors operation.

Archaeal and bacterial 16S rRNA fragments were PCR-amplified in a TProfessional Thermocycler (Biometra) with 25 and 20 cycles, respectively. PCR conditions were as follows: initial denaturation (5 min at 96°C), cycles consisting of denaturation (30 s at 96°C), annealing (50 s at 54°C for *Archaea* and 58°C for *Bacteria*), extension (25 s at 72°C), and a final extension step (5 min at 72°C). The PCR products were analyzed by horizontal gel electrophoresis (2% agarose with ethidium bromide in 1x TAE) and then purified with Agencourt AMPure XP beads (Beckman Coulter).

## Sequencing Library Preparation and Amplicon Sequencing

To prepare libraries, approximately 250 ng of amplified DNA (pooled from the PCR replicates) was used with the Illumina TruSeq DNA Sample Preparation Kit according to the manufacturer's protocol, except that the final library amplification step was omitted. Libraries were verified using the 2100 Bioanalyzer (Agilent) High-Sensitivity DNA Assay and KAPA Library Quantification Kits (Illumina).

Amplicon DNA sequencing was performed using the paired end Illumina MiSeq technology (MiSeq Illumina Kit V3) with a read length 2×300 bp. Computational analyses were performed in a similar manner as described in Nelson et al. (2012), using a local computing environment with the Quantitative Insights in Microbial Ecology (QIIME, v1.9.0) pipeline (Caporaso et al., 2010). Briefly, raw sequences were processed with the Cutadapt software enabling trimming of the nucleotides corresponding to the sequence of adapters and primers used for PCR amplification and library preparation. In a next step, sequences were merged and combined into a single fastq file, in order to ensure an even treatment and comparison QIIME analyses. This resulted in generation of 1.9 mln sequences with a mean length of 406 nucleotides (from 376 to 555 nt). Chimera detection was performed using usearch61 (Edgar et al., 2011) with subsequent filtering from sequences and *de novo* operational taxonomic unit (OTU) picking with uclust (Edgar, 2010) clustered at 97% similarity against the SILVA version 128 reference OTU alignment (Quast et al., 2013). A representative sequence for each OTU was selected and then the taxonomic assignment

**TABLE 2 |** Operational conditions of the two-stage reactors during the three experimental phases.

| Phase | Period (days) | HRT[a] (days) | OLR[b] ($g_{vs}$/L/day) |
|---|---|---|---|
| I | 1–15 | 12 | 0.35 |
| II | 16–30 | 28 | 1.00 |
| III | 31–55 | 28 | 1.65 |

[a]*Hydraulic retention time;* [b]*Organic loading rate.*

was made using the RDP Classifier v2.2 (Wang et al., 2007). Additional filtering for sequence errors was performed with the filter_otus_from_otu_table.py script by removing OTUs appearing in fewer than three samples and represented by less than 0.005% of the total sequences.

Taxonomic figures were prepared based on OTU tables specific for bacterial and archaeal amplicons, with a family level default. Sequences that were not assigned at the family level were named in accordance with the lowest taxonomy that can be assigned. A Principal Coordinates Analysis (PCoA) plot was constructed to visualize the dissimilarity of samples at different stages of the experiment.

Raw sequences obtained in this study were deposited in the SRA (NCBI) database under accession number PRJNA312575.

# RESULTS

## Reactors Performance

### Adaptation of the Microbial Consortia

The adaptation of specialized methanogenic microbial consortia from the three inocula that had a similar initial size (10 $g_{vs}$/L) was carried out on a fresh substrate sample (9.6 $g_{vs}$/L maize silage) until the methane content in each culture reached to ˜60% with similar level of biogas production (Supplementary Table S1). During the first three passages (9 weeks of cultivation), biogas production from maize silage was observed for all consortia, and the cumulative volume were 149.53 L/$kg_{vs}$, 142.33 L/$kg_{vs}$, and 121.7 L/$kg_{vs}$, for ABP, CS, and RSS, respectively. As expected in these early stages, the best biogas quality (49% of $CH_4$) was observed for ABP consortium (sampled from a stably running industrial biogas plant reactor fed with maize silage). Whereas, biogas from RSS and CS consortia contained only 15% and 19% of methane, respectively (data not shown).

During the passages 4–7 (week 10–21 of the experiment), the average methane content in the biogas increased. For the ABP community, improvement in biogas quality (only 4%) only reached 53%, but in the CS bioreactor the methane concentration nearly doubled, to 34%, and for RSS it even tripled, reaching 48%. The cumulative volume of biogas yield with ABP, RSS, and CS inocula reached 325.49 L/$kg_{vs}$, 264.14 L/$kg_{vs}$, and 281.20 L/$kg_{vs}$, respectively. The gradual increase in biogas yield and quality seen for all three consortia highlighted the ongoing process of community reorganization and adaptation for maize degradation. At this step of the AD process, physico-chemical parameters such as VFAs, COD, and TAN concentration were determined at the end of each passage (after 21 days of cultivation). At the end of each batch AD with different inoculum, the physico-chemical parameters were on the similar level, with the VFAs concentration ranging from 2.13 to 2.60 g/L, and with COD values between 5.5 and 7.2 g/L. Meanwhile, the TAN concentrations remained low (18.96–22.90 mg/L) in all reactors (**Table 3**).

In the second stage of the adaptation process (passages 8–12, weeks 22–36), the microbial consortia were fed with increased amounts of maize silage (up to 28.8 $g_{vs}$/L). Methane concentration in the produced biogas reached 59% (ABP), 65% (CS), and 68% (RSS) (**Table 3**), and the accumulated volume of biogas at the end of passage 12 was 499.42 L/$kg_{vs}$, 489.9 L/$kg_{vs}$, and 386.17 L/$kg_{vs}$, respectively. The TAN concentration was measured to be at low levels in all reactors, below 200 mg/L. Similar to the first step of adaptation, the VFAs and COD concentrations remained low and stable. VFAs concentrations ranged between 2.48 and 3.10 g/L, and the COD value was between 5.2 and 6.4 g/L (**Table 3**).

Agricultural biogas plant seems to be the best consortium for AD of maize silage (compared to CS and RSS inoculum). Only ABP consortium was able to biogas production above 300 L/$kg_{vs}$ with methane concentration above 50% in first stage of adaptation process. Moreover, in second stage of adaptation the ABP consortium revealed the higher biogas production than in reactors with inoculum CS and RSS.

### Start-up Operation of Anaerobic Digestion in a Two-Stage Reactor

The microbial communities adopted in one-stage, batch feed laboratory bioreactors were used in a subsequent phase of the experiment where we tested, if the adapted consortia would increase the rate of the start-up procedure of two-stage reactors where maize silage hydrolysis and methanization are separated. For this purpose, bioreactors were built with a hydrolyser of 2 L working volume separated from a fermenter of 25 L capacity. The reactors were inoculated with previously adapted methanogenic microbial consortia (ABP, CS, and RSS) coming from passages 8–12. The OLR increased gradually from Phase I to Phase III of start-up procedure 0.35–1.65 $g_{vs}$/L/day, respectively (**Table 2**). During this experiment, physical and chemical parameters like biogas production and methane content were monitored (**Figure 2** and **Table 4**).

During Phase I of the start-up procedure (1–15 days), the maize silage concentration was at the same level as that in the batch experiment (passage 1–7), 9.6 $g_{vs}$/L. Under these conditions, the biogas production in Phase I was unstable in each bioreactor. The average of daily biogas production in the first phase was 52.58 ± 17.24 L/$kg_{vs}$ for ABP, 21.11 ± 10.52 L/$kg_{vs}$ for CS, and 36.92 ± 27.91 L/$kg_{vs}$ for RSS. The daily biogas production in Phase II reached to more stable level than in Phase I and the average biogas production was 37.92 ± 11.95 L/$kg_{vs}$, 20.22 ± 3.65 L/$kg_{vs}$, and 17.85 ± 6.42 L/$kg_{vs}$, respectively. In the Phase III, further stabilization of the process was observed, as fluctuations between individual measurements points were ∼10%. The average daily biogas production during the last phase of operation was 27.12 ± 1.87 L/$kg_{vs}$ for ABP, 21.69 ± 6.10 L/$kg_{vs}$

**TABLE 3 |** Physico-chemical characteristics of the anaerobic digestion process.

| Parameters | Units | ABP | | CS | | RSS | |
|---|---|---|---|---|---|---|---|
| | | 4–7 | 8–12 | 4–7 | 8–12 | 4–7 | 8–12 |
| $CH_4$ content | % | 52.63 ± 11.23 | 58.98 ± 2.91 | 34.04 ± 10.71 | 65.40 ± 3.68 | 47.93 ± 19.81 | 68.00 ± 1.08 |
| Biogas production | $L/kg_{vs}$ | 325.49 ± 39.39 | 499.42 ± 9.66 | 281.20 ± 59.53 | 489.90 ± 10.90 | 264.14 ± 50.93 | 386.17 ± 23.82 |
| pH | – | 6.10 ± 0.50 | 6.88 ± 0.37 | 6.00 ± 0.56 | 6.95 ± 0.38 | 6.22 ± 0.58 | 7.19 ± 0.31 |
| COD | g/L | 5.50 ± 0.45 | 6.40 ± 0.83 | 7.07 ± 0.78 | 5.20 ± 1.05 | 7.20 ± 0.70 | 5.30 ± 0.80 |
| VFAs | g/L | 2.13 ± 0.35 | 3.10 ± 0.73 | 2.24 ± 0.18 | 2.58 ± 0.92 | 2.60 ± 0.44 | 2.48 ± 0.58 |
| TAN | mg/L | 22.90 ± 1.92 | 15.80 ± 3.73 | 21.00 ± 0.85 | 1.10 ± 0.20 | 18.96 ± 1.36 | 147.40 ± 17.45 |

*Average parameters of the results received from passage 4–7 or 8–12, measured on the 21st day after each passage. COD, chemical oxygen demand; TAN, total ammonia nitrogen; VFAs, volatile fatty acids.*

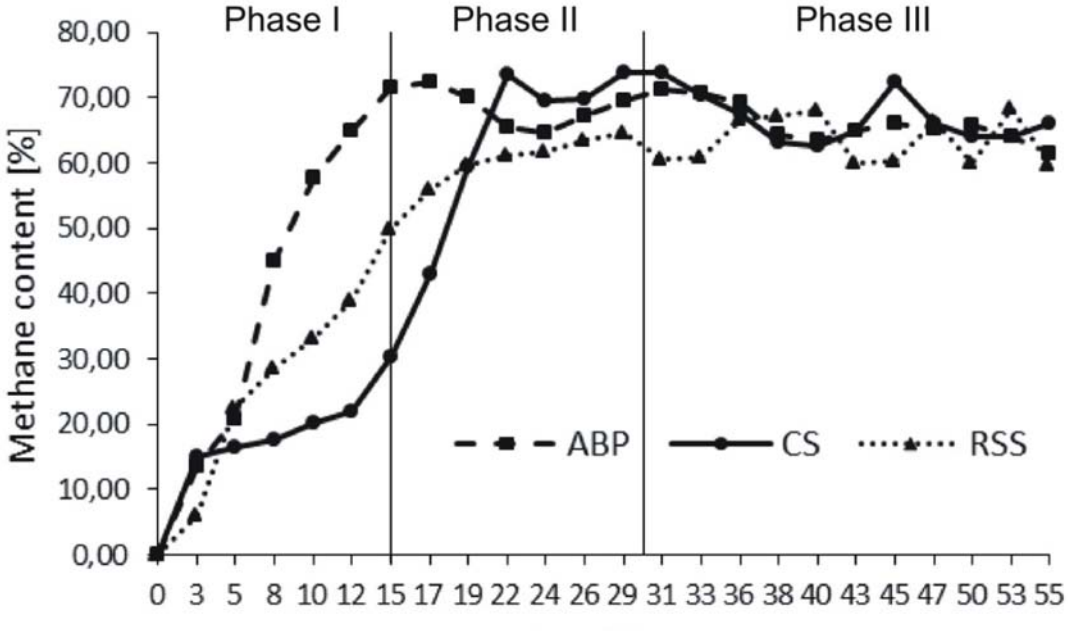


**FIGURE 2 |** Methane content in biogas produced during anaerobic digestion in two-stage reactors.

for CS, and 14.35 ± 1.97 $L/kg_{vs}$ for RSS (**Table 4**). The methane concentration analysis revealed that the ABP-adopted consortium needed only 15 days to start-up production of high methane content biogas (highest observed, 72%), while the CS and RSS bioreactors reached a similar level by day 20 ($CH_4$ content 74% and 61%, respectively). In Phase II of the start-up procedure (days 16–30), the observed maximum of methane content was 72% for ABP, 74% for CS, and 64% for RSS (**Figure 2**). What was most important, the average methane content during the entire Phase II of the start-up phase was 68% (ABP), 65% (CS), and 61% (RSS), which is considered to be good $CH_4$ levels desired by industrial biogas plants. During Phase III (days 31–55), the methane concentration was stable and exceeded 63% in all of the reactors (**Table 4**). The biogas quality evolution during each phase corresponds to a decline of daily biogas production during the start-up operation. The higher biogas production in Phase I was due to $CO_2$ overproduction in the start-up phase (data not shown). At the end of start-up operation of two-stage reactors, all methanogenic consortia were able to stable biogas production with high methane concentration (especially consortium ABP).

In this study, physico-chemical parameters were also monitored. During start-up phases pH value were 7.13–7.88 in all reactors. The TAN concentrations in all reactors were below 200 mg/L. In reactor ABP, CS, and RSS, the VFAs concentration were between 2.10 and 2.60, 4.48 and 3.42, and 4.32 and 1.64 g/L, respectively. Only in reactor RSS, the VFAs and COD concentration were significantly increasing during start-up process. The lower biogas production in reactor RSS in Phase III (14.34 $L/kg_{vs}$) (compared to reactor ABP – 27.12 $L/kg_{vs}$) corresponding with higher concentration of VFAs and COD. The higher VFAs and COD concentrations in reactor RSS showed that the microorganisms consortia in reactor RSS could not effectively convert the organics into biogas.

**TABLE 4 |** Physico-chemical characteristics of anaerobic digestion.

| Parameters | Units | ABP | | | CS | | | RSS | | |
|---|---|---|---|---|---|---|---|---|---|---|
| | | I | II | III | I | II | III | I | II | III |
| $CH_4$ content | % | 45.57 ± 23.86 | 68.21 ± 2.96 | 66.11 ± 3.08 | 20.29 ± 5.54 | 64.89 ± 11.99 | 66.88 ± 3.83 | 25.64 ± 14.95 | 61.11 ± 3.07 | 63.51 ± 3.75 |
| Daily biogas production | $L/kg_{vs}$ | 52.58 ± 17.24 | 37.92 ± 11.95 | 27.12 ± 1.87 | 21.11 ± 10.52 | 20.22 ± 3.65 | 21.69 ± 6.10 | 36.92 ± 27.91 | 17.85 ± 6.42 | 14.35 ± 1.97 |
| pH | – | 7.19 ± 0.52 | 7.47 ± 0.35 | 7.8 ± 0.07 | 7.13 ± 0.16 | 7.29 ± 0.05 | 7.88 ± 0.08 | 7.54 ± 0.15 | 7.85 ± 0.07 | 7.7 ± 0.16 |
| COD | g/L | 8.88 ± 2.16 | 3.70 ± 0.25 | 3.80 ± 0.36 | 8.75 ± 2.01 | 6.40 ± 0.44 | 6.90 ± 0.22 | 5.40 ± 2.02 | 7.04 ± 0.96 | 8.40 ± 0.70 |
| VFAs | g/L | 2.60 ± 0.25 | 2.07 ± 0.34 | 2.10 ± 0.83 | 4.48 ± 0.58 | 3.42 ± 0.38 | 3.52 ± 0.36 | 2.6 ± 0.30 | 1.64 ± 0.24 | 4.32 ± 0.11 |
| TAN | mg/L | 79.00 ± 15.17 | 100.30 ± 8.07 | 80.33 ± 7.51 | 112.00 ± 12.95 | 142.66 ± 6.43 | 113.00 ± 3.00 | 108.00 ± 25.14 | 41.66 ± 12.13 | 107.33 ± 3.06 |
| C:N | – | 21:01 | 15:01 | 10:01 | 33:01:00 | 20:01 | 14:01 | 39:01:00 | 20:01 | 15:01 |

*Average parameters of results achieved during each of the operation phases in the two-stage reactor. COD, chemical oxygen demand; TAN, total ammonia nitrogen; VFAs, volatile fatty acids.*

## Characterization of Microbial Communities

Microbial adaptation to methane fermentation form maize silage, was determined based on the analysis of 16S rRNA amplicons. The analysis of microbial dynamics of the selected methanogenic consortia was performed for three steps: (i) inoculum; (ii) adaptation to maize silage (passages 4, 7, 12); and (iii) start-up operation in a two-stage biogas reactor (Phase II and Phase III) (see Materials and Methods).

## Bacterial Diversity

Native communities used for the laboratory cultivation was very distinct to each other. Most of the sequences of ABP consortium were assigned to *Draconibacteriaceae* (24%), followed by families *Rikenellaceae* (12%), *Anaerolineaceae* (9%), and *Ruminococcaceae* (7%). In the case of CS inoculum, *Pseudomonadaceae* (21%) was found to be the most predominant family, followed by families *Carnobacteriaceae* (12%), *Porphyromonadaceae* (11%), *Campylobacteriaceae* (8%), *Moraxellaceae* (7%), Family XI (7%), and *Lachnospiraceae* (6%). Finally, the RSS sample consisted mainly of *Campylobacteraceae* (32%), *Aeromonadaceae* (15%), *Leptotrichiaceae* (9%), *Porphyromonadaceae* (9%), *Moraxellaceae* (9%), and *Bacteroidaceae* (5%) bacteria families (**Figure 3**).

After cultivation in laboratory reactors, at the end of passage 4, we observed significant increase of *Porphyromonadaceae* family in all of the studied samples, which accounted for 47% (ABP), 19% (CS), and 36% (RSS) of total microbial structure. Moreover, all three samples were abundant in sequences assigned to *Rikenellaceae* (9%, 7%, and 10%) and *Ruminococcaceae* (8%, 6%, and 10%) for the ABP, CS, RSS, respectively (**Figure 3**). In the case of laboratory consortia originated from CS and RSS, bacteria family which exceeded 5% of total community structure was also *Acidaminococcaceae* 9% (CS) and 7% (RSS). Furthermore, CS community was highly enriched in *Prevotellaceae* (18%) and *Bacteroidaceae* (8%) compared to ABP and RSS samples where they accounted for less than 2% of total microbial community. By the end of passage 7, in all three studied consortia, the dominant family became *Porphyromonadaceae* (21% 20%, 20%) and *Rikenellaceae* (24%, 23%, 18%) followed by *Desulfovibrionaceae* (6%, 12%, 13%), *Acidaminococcaceae* (5%, 5%, 7%) and *Bacteroidaceae* (5%, 10%, 4%), ABP, CS, and RSS, respectively (**Figure 3**). However, there were also significant differences in the abundance of families such as *Christensenellaceae* (3%, 2%, 10%), *Prevotellaceae* (1%, 8%, 0%), *Spirochaetaceae* (5%, 2%, 0%), *Synergistaceae* (3%, 6%, 9%), and *Ruminococcaceae* (7%, 2%, 5%) ABP, CS, and RSS, respectively. At the end of the selection process in batch reactors, namely passage 12, the most predominant family was *Bacteroidaceae* which accounted for 50% (ABP), 20% (CS), and 61% (RSS). Families *Porphyromonadaceae* and *Rikenellaceae*, which were dominant in previous passages, diminished at least two-fold to the level of 4% and 8% in ABP sample, 7% and 11% in CS sample, 4% and 1% in RSS sample, respectively. Moreover, there were several bacterial families which had high abundance at passage 12 in certain samples while in others they accounted for less than 2%. These families were *Petrotogaceae* in ABP (15%) and RSS (8%), *Acidaminococcaceae* in CS (12%) and RSS (8%), *Ruminococcaceae* in CS (7%) and RSS (6%), *Lachnospiraceae Erysipelotrichaceae*, *Prevotellaceae* in CS (14%, 6%, 5%, respectively), and *Xanthomonadaceae* in ABP (6%).

The microbial communities adopted in one-stage, batch feed laboratory bioreactors were used in a subsequent phase of the experiment where we tested if the adapted consortia would increase the rate of the start-up procedure of two-stage reactors where maize silage hydrolysis and methanization are separated. Biodiversity analysis at the end of Phase II of the start-up, showed that the microbial profile was similar in all three studied consortia (**Figure 4**) with predominance of *Porphyromonadaceae* (9%, 12%, 13%), *Rikenellaceae* (15%, 24%, 10%), *Ruminococcaceae* (9%, 13%, 12%), and *Synergistaceae* (5%, 5%, 11%) for ABP, CS, and RSS, respectively. Bacterial community of ABP sample had also high abundance of WCHB1-69 (8%) and *Puniceicoccaceae* (8%) while in the other two samples these two bacterial groups accounted for less than 1%. Furthermore, RSS consortium was enriched in bacteria from order W27 (8%), *Christensenellaceae* (7%), and *Lachnospiraceae* (5%). By the end of the experimental period (end of Phase III), CS community was very similar (1–2% difference) to that from Phase II, except for reduced abundance of *Rikenellaceae* in favor of ML635J-40 aquatic group bacteria (7%). In the case of ABP and RSS sample, at least three-fold increase of *Porphyromonadaceae* was observed, to the level of 24% and 44%, respectively. Additionally ABP consortium was enriched in

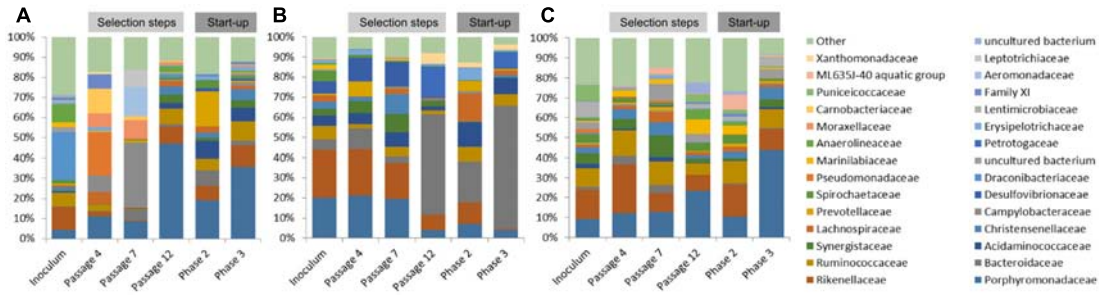


**FIGURE 3 |** Relative abundance of bacterial operational taxonomic units (OTUs). Only those bacterial families with an abundance >5% in at least one sample are shown. **(A)** ABP, agricultural biogas plant, **(B)** RSS, raw sewage sludge, **(C)** CS, cattle slurry.

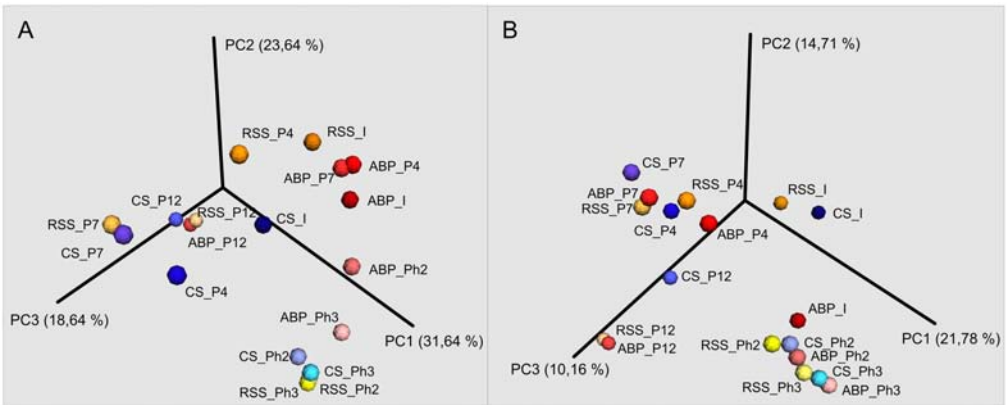


**FIGURE 4 |** Principal Coordinates Analysis (PCoA) of Bray–Curtis dissimilarity of archaeal **(A)** and bacterial **(B)** diversity of studied samples: ABP, agricultural biogas plant. CS, cattle slurry; RSS, raw sewage sludge, representing microbial community at different stage of the experiment; I, Inoculum; P, Passage; Ph, Phase.

bacteria from *Marinilabiaceae* (7%), *Anaerolineaceae* (5%), and order BS5 (5%).

## Archaea Diversity

In the case of communities originating from ABP and RSS, the dominant archaeal group was *Methanosaetaceae* which accounted for 31% (ABP) and 42% (RSS), whereas CS was clearly dominated by *Methanobacteriaceae* (46%) and representative of *Thermoplasmatales Incertae Sedis* (34%). In both the ABP and RSS samples, there were also a significant number of sequences that could be classified as *Thermoplasmatales Incertae Sedis* (11% and 8%, respectively). It is also worth mentioning that the ABP sample had a large proportion of *Methanosarcinaceae* (16%), *Methanomicrobiaceae* (16%), and ambiguous taxa of *Bathyarchaeota* (15%), RSS sample had abundant *Methanospirillaceae* (18%), *Methanoregulaceae* (11%), Terrestrial Miscellaneous Gp (TMEG) (8%) and *Methanobacteriaceae* (5%), while CS sample *Methanosarcinaceae* (8%), *Methanospirillaceae* (6%), and *Methanosaetaceae* (5%) (**Figure 5**).

After the cultivation process, at the passage 4, most of the sequences were assigned to *Methanobacteriaceae* (12%, 65%, 45%), *Methanosaetaceae* (55%, 2%, 27%), *Methanosarcinaceae* (9%, 20%, 2%), *Thermoplasmatales Incertae Sedis* (3%, 12%, 10%), ambiguous taxa of *Bathyarchaeota* (11%, 0%, 9%), and *Methanospirillaceae* (9%, 0%, 4%), ABP, CS, RSS, respectively. Archaeal dynamics was analyzed next at the seventh passage, for which we observed further increase of the abundance of *Methanobacteriaceae* to the level of 16% (ABP), 86% (CS), and 50% (RSS). In the case of ABP, predominant was *Methanosaetaceae* (41%), *Methanospirillaceae* (27%), and *Methanosarcinaceae* (9%) while in the CS and RSS sample, we detected high representation of *Thermoplasmatales Incertae Sedis* (10% and 46%, respectively). At the end of the adaptation process (passage 12), a drastic shift in the *Archaea* community occurred to make the *Thermoplasmatales Incertae Sedis* the most predominant in all bioreactors (ABP 92%; CS 96%; and RSS 70%). For the RSS sample, the second most abundant archeon was *Methanomicrobiaceae* (24%).

Microorganisms selected in batch culture were then used in two-stage biogas reactors. Biodiversity analysis at the end of Phase II of the start-up, showed that predominant methanogen became *Methanosarcinaceae* which constituted 29% (ABP), 58% (CS), and 80% (RSS) of the archaeal community (**Figure 5**). Other *Archaea* which was abundant in at least one sample were also ambiguous taxa of *Bathyarchaeota* (32%, 2%, 7%), *Methanobacteriaceae* (5%, 11%, 5%), *Methanomicrobiaceae* (10%, 10%, 3%), *Thermoplasmatales Incertae Sedis* (2%, 16%,

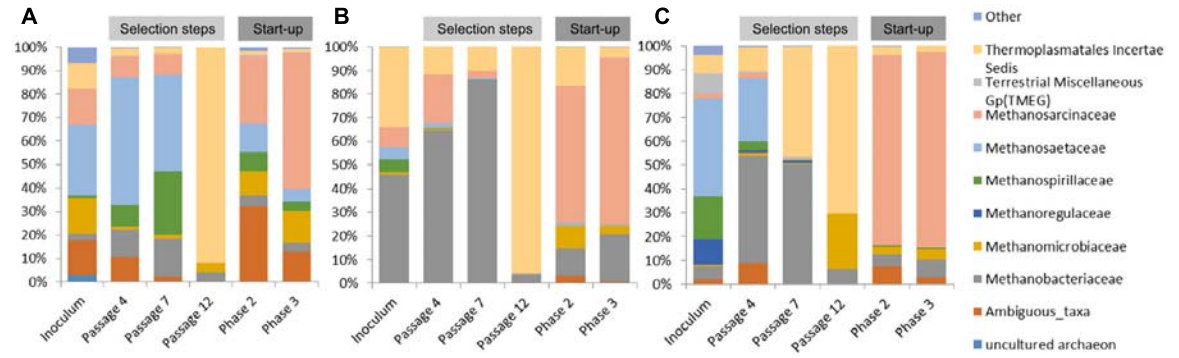


**FIGURE 5 |** Relative abundance of archaeal OTUs. Only those families with abundance >1% in at least one sample are shown. **(A)** ABP, agricultural biogas plant, **(B)** RSS, raw sewage sludge, **(C)** CS, cattle slurry.

4%), *Methanospirillaceae* (8%, 0%, 1%), *Methanosaetaceae* (12%, 1%, 0%), for ABP, CS, RSS, respectively. Following cultivation in laboratory reactors resulted in further increase of *Methanosarcinaceae* to the level of 58% (ABP), 70% (CS), and 82% (RSS) at the end of Phase III which was marked as the end of the experiment. At the same time, the richness of other archaeal families decreased, although abundance of some families increased for example *Methanobacteriaceae* to 20% (CS), 7% (RSS), and *Methanomicrobiaceae* to 13% (ABP).

## DISCUSSION

This study aimed to evaluate the influence of inoculum sources on the adaptation of a biogas-producing microbial consortium and biogas production yields from maize silage in a series of batch culture experiments and to reveal the influence of previously adapted inocula on the microbial community structure during start-up experiments in a quasi-continuous, two-phase process. Biogas production and phylogenetic sequencing analysis revealed that the three different source of inoculum were able to gradually adapt to biogas production form maize silage. Moreover, microbial community analysis broadens knowledge about microbial community shift during the initial stages of digestion of maize silage.

The biogas production results reveled that during the first stages of the adaptation phase, methanogenic consortia occurred very slowly, and only after several passages did the microbial community adapts to allow production of biogas with high methane content (**Table 3**). The biogas yield and methane level in second steps of adaption reached values close to the maximum reported in the literature for one-step anaerobic degradation of maize silage. For example, methanization of maize silage described by Oslaj et al. (2010) produced a biogas yield ranging from 515 to 620 L/kg$_{vs}$, and the methane content ranged from 55 to 58%. ABP consortium was firstly adapted to effective biogas production, because ABP inoculum was collected from industrial scale in which was used the same type of feedstock (maize silage).

During start-up AD, common physico-chemical parameters, biogas production and quality were monitored. The carbon to nitrogen (C/N) ratio is one of the important parameters influencing the digestion process. Many studies indicated that the optimal C/N ratios in methane fermentation were 20:1–30:1 (Puyuelo et al., 2011; Wang et al., 2014). TAN and VFAs also play a vital role in the performance and stability of AD. It is generally believed that TAN concentrations remain below 200 mg/L, thus they should not be considered as an inhibitor of the biogas production process (Rajagopal et al., 2013). VFAs can be accumulated during high organic loading, resulting in the decrease of pH and even the failure of AD (Wang et al., 2009; Zhang et al., 2014). The three reactors showed a similar increasing trend in methane production during the start-up phases (**Figure 2**). The reactor inoculated microbial consortium ABP already demonstrated after 15 days high quality biogas production (70% methane content), and the microbial communities CS and RSS adapted to produce biogas in the two-stage reactor after 20 days. During start-up phases of operation, two-stage reactors achieved the optimal parameters of C/N ratio in reactor ABP in Phase I and in reactors RSS and CS in Phase II (**Table 4**). The TAN concentration in all reactors was below 200 mg/L, therefore, it did not inhibit the process. In reactor ABP, VFAs concentration was stable between 2.07 and 2.6 g/L. In reactor RSS, VFAs accumulated to a concentration of 4.32 g/L, so they may have been the reason for the inhibition of biogas production in Phase III (**Table 4**).

Native communities used in this study differ from each other's, both in the terms of *Bacteria* and *Archaea* biodiversity. This difference had direct impact of methane production at early stages of laboratory cultivation (passages 1–3) for which different values of methane concentration (ABP 49%, CS 19%, and RSS 15%) and biogas production (ABP 149.53 L/kg$_{vs}$, CS 142.33 L/kg$_{vs}$, and RSS 121.7 L/kg$_{vs}$) were obtained. In the following passages 4–7, biogas yield doubled (ABP 325.49 L/kg$_{vs}$, RSS 264.14 L/kg$_{vs}$, and CS 281.20 L/kg$_{vs}$) and methane concentration increased to 53% (ABP), 34% (CS), and 48% (RSS). At this point of the adaptation process, we observed increase of abundance of fermentative microorganisms such as *Porphyromonadaceae*, *Rikenellaceae*, *Bacteroidaceae, Ruminococcaceae,* and *Prevotellaceae*, which could indicate enhanced degradation of maize silage and substrate release as

these microorganisms are described as VFAs and hydrogen producers (Kong et al., 2010; Mosoni et al., 2011; Ziganshin et al., 2011; Traversi et al., 2012; Stolze et al., 2015; Wegner and Liesack, 2016). Furthermore, at the passage 7, which marked the end of first stage of the adaptation process with 9.6 $g_{vs}$/L of maize silage, we observed a significant increase of *Synergistaceae* and *Desulfovibrionaceae* for which the cumulative abundance reached 9% (ABP), 18% (CS), and 22% (RSS). These microorganisms are known to syntrophically interact with methanogens, for example by hydrogen transfer and thus can improve *Archaea* performance through hydrogenotrophic pathway (Vartoukian et al., 2007; Walker et al., 2012; Bretschger et al., 2015). In fact, our two studied samples of CS and RSS, *Archaea* community was dominated by hydrogenotrophic *Methanobacteriaceae* which indicates that adaptation process is toward methanogens that utilize $H_2 + CO_2$. In comparison, adaptation of ABP sample occurs more toward acetate utilization as the most predominant archaeal family was *Methanosaetaceae* which is adapted to low concentration of acetate (Liu and Whitman, 2008). What is noteworthy, despite significant differences in the initial biodiversity of analyzed samples, the bacterial population in each bioreactor seems to be changed in similar manners, whereas shifts among *Archaea* at this stage of the adaptation proceeded differently in all three samples (**Figure 4**).

After switching bioreactors to higher maize silage concentration (28.8 $g_{vs}$/L), bacterial communities became dominated by *Bacteroidaceae* which suggests increased abilities to fermentative utilization of organic substrates (Chen et al., 2016). However, CS sample display higher versatility as the abundance of *Bacteroidaceae* was more even with other polysaccharide degraders, e.g., *Prevotellaceae, Lachnospiraceae*, *Rickenellaceae, Porphyromonadaceae*, and *Ruminococcaceae*. In turn, ABP and RSS sample were enriched in *Petrotogaceae*, which representatives are observed in anaerobic reactors where are involved in the fermentation of complex polysaccharides (Briones et al., 2007; Maus et al., 2016). What is more important is that, at passage 12 for all three studied communities, most of archaeal sequences (70–96%) were classified to group of *Thermoplasmatales Incertae Sedis*. This group was already abundant (46%) at passage 7 of RSS reactor. In all of the cases methane was still produced with good quality which indicates active methanogenesis, probably by utilization of methylated compounds (Borrel et al., 2012, 2014). However, further studies are needed to confirm this observation.

The microbial communities selected in adaptation process in one-stage, batch feed laboratory reactors were used for a start-up procedure of two-stage reactors. Bacterial structure of all three methanogenic consortia was again dominated by *Porphyromonadaceae*, *Rickenellaceae*, and *Ruminococcaceae* which shows their importance in the biogas system fed with maize silage. Moreover, analysis of *Archaea* biodiversity showed that *Methanosarcinaceae* outcompete other methanogens. This observation is in agreement with recent work of Goux et al. (2016). This indicates that *Methanosarcinaceae* it is better adapted to stable conditions of semi-continuous two-stage reactors as it is fast-growing and substrate-versatile methanogen which can utilize acetate, $H_2 + CO_2$ as well as methanol and methylamines for the methanogenesis (Liu and Whitman, 2008; De Vrieze et al., 2012). Interestingly, at Phase II, in the ABP sample approximately one third of archaeal sequences were classified to ambiguous taxa of *Bathyarchaeota* (formerly known as Miscellaneous Crenarchaeotic Group). Other studies suggests that these archeons may be involved in the degradation of complex organic matter and interaction with acetate-utilizing methanogens (Collins et al., 2005; Kubo et al., 2012). Our work also seems to confirm this suggestion as the ambiguous taxa of *Bathyarchaeota* and acetoclastic methanogens such as *Methanosaetaceae* and *Methanosarcinaceae* were abundant throughout cultivation of ABP community and the overall performance of biogas production was better than in other two studied consortia.

## CONCLUSION

The choice of the most suitable source of microorganisms to inoculate fermenters in biogas plants can have a tremendous influence on methane production and the efficacy of the entire installation. However, a common practice in the biogas industry is to inoculate fermenters with methanogenic samples without considering the given substrates, which in many cases can lead to insufficient methane production and can generate losses. This study provides new insights into the gradual adaptation of different inocula sampled from typical methanogenic environments that are commonly used to initiate industrial installations for biogas production from maize silage. The knowledge about adaption microbial community to biogas production from maize silage is important to understand microbial community shift during the initial stages of maize silage digestion. The adaptation process of methanogenic consortia during the first stages of the adaptation phases occurred very slowly, since only after several passages did the microbial community adapt to allow for the efficient production of biogas with high methane content. The start-up experiments showed that microbial communities that were previously adapted to a given substrate proved to be very effective inocula for new bioreactors, and could shorten the time until methane production began. The biogas production analysis revealed that ABP consortium was able to the highest biogas production in the adaptation and in the start-up process compared to consortia to CS and RSS. The high-throughput sequencing methods allowed us to follow changes in bacterial and archaeal biodiversity during the adaptation process. We observed a shift from acetoclastic methanogens (*Methanosaetaceae*, low-acetate preferring microorganisms) (ABP and RSS) and/or hydrogenotrophic *Archaea* (e.g., *Methanobacteriaceae*) (CS) that prevailed in the inoculum samples, to the dominance of high acetate-preferring acetoclastic methanogens (*Methanosarcinaceae*) at the end of experiment.

Based on available reference and our results, we concluded that archeons from *Thermoplasmatales Incertae Sedis* are

likely methanogens which utilizes methylated compounds while the ambiguous *Bathyarchaeota* could be involved in methanogenesis process by syntrophic interactions with acetate utilizing methanogens. However, this observations need to be further investigated in experiment where concentration of specific intermediate substrates are highly controlled. Ideally microbial dynamics should be quantitatively measured by qRT-PCR experiments.

## AUTHOR CONTRIBUTIONS

MW was involved in planning and executing adaptation and start-up experiments, DNA isolation, most of the chemical analyses, and in writing the manuscript. AP was involved in planning the metagenomics approach, isolating metagenomic DNA, deep sequencing, all bioinformatics analysis, and in writing the manuscript. KP participated in chemical analyses. PK participated in computational analysis. OR and JP constructed the two-stage bioreactors and participated in the start-up of the experiments. ASo and LL designed and supervised metagenomics and bioinformatics approaches, and helped draft the manuscript. ASk was involved in methodology and manuscript preparation, consultation, LD is the head of the project and directed microbial adaption, supervised biochemical analyses and was involved in consultation and article preparation. All authors read and approved the final manuscript.

## ACKNOWLEDGMENT

This study was funded by the Applied Research Program of the National Centre for Research and Development (grant number PBS1/A8/3/2012).

## SUPPLEMENTARY MATERIAL

The Supplementary Material for this article can be found online at: http://journal.frontiersin.org/article/10.3389/fmicb.2017.01881/full#supplementary-material

## REFERENCES

Ali Shah, F., Mahmood, Q., Maroof Shah, M., Pervez, A., and Ahmad Asad, S. (2014). Microbial ecology of anaerobic digesters: the key players of anaerobiosis. *Sci. World J.* 2014:183752. doi: 10.1155/2014/183752

American Public Health Association [APHA] (1998). *Standard Methods for the Examination of Water and Wastewater*, 18th Edn. Washington, DC: APHA.

Borrel, G., Harris, H. M., Tottey, W., Mihajlovski, A., Parisot, N., Peyretaillade, E., et al. (2012). Genome sequence of "*Candidatus Methanomethylophilus alvus*" Mx1201, a methanogenic archaeon from the human gut belonging to a seventh order of methanogens. *J. Bacteriol.* 194, 6944–6945. doi: 10.1128/JB.01867-12

Borrel, G., Parisot, N., Harris, H. M., Peyretaillade, E., Gaci, N., Tottey, W., et al. (2014). Comparative genomics highlights the unique biology of *Methanomassiliicoccales*, a *Thermoplasmatales*-related seventh order of methanogenic archaea that encodes pyrrolysine. *BMC Genomics* 15:679. doi: 10.1186/1471-2164-15-679

Bretschger, O., Carpenter, K., Phan, T., Suzuki, S., Ishii, S., Grossi-Soyster, E., et al. (2015). Functional and taxonomic dynamics of an electricity-consuming methane-producing microbial community. *Bioresour. Technol.* 195, 254–264. doi: 10.1016/j.biortech.2015.06.129

Briones, A. M., Daugherty, B. J., Angenent, L. T., Rausch, K. D., Tumbleson, M. E., and Raskin, L. (2007). Microbial diversity and dynamics in multi- and single-compartment anaerobic bioreactors processing sulfate-rich waste streams. *Environ. Microbiol.* 9, 93–106. doi: 10.1111/j.1462-2920.2006.01119.x

Caporaso, J. G., Kuczynski, J., Stombaugh, J., Bittinger, K., Bushman, F. D., Costello, E. K., et al. (2010). QIIME allows analysis of high-throughput community sequencing data. *Nat. Methods* 7, 335–336. doi: 10.1038/nmeth.f.303

Chen, S., Cheng, H., Wyckoff, K. N., and He, Q. (2016). Linkages of *Firmicutes* and *Bacteroidetes* populations to methanogenic process performance. *J. Ind. Microbiol. Biotechnol.* 43, 771–781. doi: 10.1007/s10295-016-1760-8

Collins, G., O'Connor, L., Mahony, T., Gieseke, A., deBeer, D., and O'Flaherty, V. (2005). Distribution, localization, and phylogeny of abundant populations of *Crenarchaeota* in anaerobic granular sludge. *Appl. Environ. Microbiol.* 71, 7523–7527. doi: 10.1128/AEM.71.11.7523-7527.2005

De Vrieze, J., Gildemyn, S., and Vilchez-Vargas, R. (2015). Inoculum selection is crucial to ensure operational stability in anaerobic digestion. *Appl. Microbiol. Biotechnol.* 99, 189–199. doi: 10.1007/s00253-014-6046-3

De Vrieze, J., Hennebel, T., Boon, N., and Verstraete, W. (2012). *Methanosarcina*: the rediscovered methanogen for heavy duty biomethanation. *Bioresour. Technol.* 112, 1–9. doi: 10.1016/j.biortech.2012.02.079

Dhamodharan, K., Kumar, V., and Kalamdhad, A. S. (2015). Effect of different livestock dungs as inoculum on food waste anaerobic digestion and its kinetics. *Bioresour. Technol.* 180, 237–241. doi: 10.1016/j.biortech.2014.12.066

Dziewit, L., Pyzik, A., Romaniuk, K., Sobczak, A., Szczesny, P., Lipinski, L., et al. (2015). Novel molecular markers for the detection of methanogens and phylogenetic analyses of methanogenic communities. *Front. Microbiol.* 6:694. doi: 10.3389/fmicb.2015.00694

Edgar, R. C. (2010). Search and clustering orders of magnitude faster than BLAST. *Bioinformatics* 26, 2460–2461. doi: 10.1093/bioinformatics/btq461

Edgar, R. C., Haas, B. J., Clemente, J. C., Quince, C., and Knight, R. (2011). UCHIME improves sensitivity and speed of chimera detection. *Bioinformatics* 27, 2194–2200. doi: 10.1093/bioinformatics/btr381

Goncalves, M. R., Costa, J. C., Marques, I. P., and Alves, M. M. (2011). Inoculum acclimation to oleate promotes the conversion of olive mill wastewater to methane. *Energy* 36, 2138–2141. doi: 10.1016/j.energy.2010.04.042

Goux, X., Calusinska, M., Fossépré, M., Benizri, E., and Delfosse, P. (2016). Start-up phase of an anaerobic full-scale farm reactor–Appearance of mesophilic anaerobic conditions and establishment of the methanogenic microbial community. *Bioresour. Technol.* 212, 217–226. doi: 10.1016/j.biortech.2016.04.040

Han, S., Liu, Y., Zhang, S., and Lou, G. (2016). Reactor performances and microbial communities of biogas reactors: effects of inoculum sources. *Appl. Microbiol. Biotechnol.* 100, 987–995. doi: 10.1007/s00253-015-7062-7

Hidalgo, D., and Martin-Marroquin, J. (2014). Effects of inoculum source and co-digestion strategies on anaerobic digestion of residues generated in the treatment of waste vegetable oils. *J. Environ. Manage.* 142, 17–22. doi: 10.1016/j.jenvman.2014.04.004

Ho, D. P., Jensen, P. D., and Batstone, D. J. (2014). Effects of temperature and hydraulic retention time on acetotrophic pathways and performance in high-rate sludge digestion. *Environ. Sci. Technol.* 48, 6468–6476. doi: 10.1021/es500074j

Klindworth, A., Pruesse, E., Schweer, T., Peplies, J., Quast, C., Horn, M., et al. (2013). Evaluation of general 16S ribosomal RNA gene PCR primers for classical and next-generation sequencing-based diversity studies. *Nucleic Acids Res.* 41:e1. doi: 10.1093/nar/gks808

Kong, Y., Teather, R., and Forster, R. (2010). Composition, spatial distribution, and diversity of the bacterial communities in the rumen of cows fed different forages. *FEMS Microbiol. Ecol.* 74, 612–622. doi: 10.1111/j.1574-6941.2010.00977.x

Krylowicz, A., Chrzanowski, K., and Usidus, J. (2001). Sposób i układ wytwarzania metanu i energii elektrycznej i cieplnej. Polish Patent No 19759. Warsaw: PL Patent and Trademark Office.

Kubo, K., Lloyd, K. G., Biddle, J. F., Amann, R., Teske, A., and Knittel, K. (2012). Archaea of the *Miscellaneous Crenarchaeotal* Group are abundant, diverse and widespread in marine sediments. *ISME J.* 6, 1949–1965. doi: 10.1038/ismej.2012.37

Kundu, K., Bergmann, I., Klocke, M., Sharma, S., and Sreekrishnan, T. R. (2014). Impact of abrupt temperature increase on the performance of an anaerobic hybrid bioreactor and its intrinsic microbial community. *Bioresour. Technol.* 168, 72–79. doi: 10.1016/j.biortech.2014.01.093

Liu, Y., and Whitman, W. B. (2008). Metabolic, phylogenetic, and ecological diversity of the methanogenic archaea. *Ann. N. Y. Acad. Sci.* 1125, 171–189. doi: 10.1196/annals

Lopes, W. S., Leite, V. D., and Prasad, S. (2004). Influence of inoculum on performance of anaerobic reactors for treating municipal solid waste. *Bioresour. Technol.* 94, 261–266. doi: 10.1016/j.biortech.2004.01.006

Maus, I., Koeck, D. E., Cibis, K. G., Hahnke, S., Kim, Y. S., Langer, T., et al. (2016). Unraveling the microbiome of a thermophilic biogas plant by metagenome and metatranscriptome analysis complemented by characterization of bacterial and archaeal isolates. *Biotechnol. Biofuels* 9:171. doi: 10.1186/s13068-016-0581-3

Mosoni, P., Martin, C., Forano, E., and Morgavi, D. P. (2011). Long-term defaunation increases the abundance of cellulolytic ruminococci and methanogens but does not affect the bacterial and methanogen diversity in the rumen of sheep. *J. Anim. Sci.* 89, 783–791. doi: 10.2527/jas.2010-2947

Nelson, M. C., Morrison, M., Schanbacher, F., and Yu, Z. (2012). Shifts in microbial community structure of granular and liquid biomass in response to changes to infeed and digester design in anaerobic digesters receiving food-processing wastes. *Bioresour. Technol.* 107, 135–143. doi: 10.1016/j.biortech.2011.12.070

Oslaj, M., Mursec, B., and Vindis, P. (2010). Biogas production from maize hybrids. *Biomass Bioenergy* 34, 1538–1545. doi: 10.1016/j.biombioe.2010.04.016

Poszytek, K., Pyzik, A., Sobczak, A., Lipinski, L., Sklodowska, A., and Drewniak, L. (2017). The effect of the source of microorganisms on adaptation of hydrolytic consortia dedicated to anaerobic digestion of maize silage. *Anaerobe* 46, 46–55. doi: 10.1016/j.anaerobe.2017.02.011

Puyuelo, B. S., Ponsa, T., and Sanchez, G. A. (2011). Determining C/N ratios for typical organic wastes using biodegradable fractions. *Chemosphere* 85, 653–659. doi: 10.1016/j.chemosphere.2011.07.014

Quast, C., Pruesse, E., Yilmaz, P., Gerken, J., Schweer, T., Yarza, P., et al. (2013). The SILVA ribosomal RNA gene database project: improved data processing and web-based tools. *Nucleic Acids Res.* 41, D590–D596. doi: 10.1093/nar/gks1219

Rajagopal, R., Massé, D. I., and Singh, G. (2013). A critical review on inhibition of anaerobic digestion process by excess ammonia. *Bioresour. Technol.* 143, 632–641. doi: 10.1016/j.biortech.2013.06.030

Stolze, Y., Zakrzewski, M., Maus, I., Eikmeyer, F., Jaenicke, S., Rottmann, N., et al. (2015). Comparative metagenomics of biogas-producing microbial communities from production-scale biogas plants operating under wet or dry fermentation conditions. *Biotechnol. Biofuels* 8:14. doi: 10.1186/s13068-014-0193-8

Sun, Y., and Cheng, J. Y. (2002). Hydrolysis of lignocellulosic materials for ethanol production: a review. *Bioresour. Technol.* 83, 1–11. doi: 10.1016/S0960-8524(01)00212-7

Traversi, D., Villa, S., Lorenzi, E., Degan, R., and Gilli, G. (2012). Application of a real-time qPCR method to measure the methanogen concentration during anaerobic digestion as an indicator of biogas production capacity. *J. Environ. Manage.* 111, 173–177. doi: 10.1016/j.jenvman.2012.07.021

Tyagi, V. K., and Lo, S. L. (2013). Sludge: a waste or renewable source for energy and resources recovery? *Renew. Sustain. Energy Rev.* 25, 708–728. doi: 10.1016/j.rser.2013.05.029

Vartoukian, S. R., Palmer, R. M., and Wade, W. G. (2007). The division "Synergistes". *Anaerobe* 13, 99–106. doi: 10.1016/j.anaerobe.2007.05.004

Walker, C. B., Redding-Johanson, A. M., Baidoo, E. E., Rajeev, L., He, Z., Hendrickson, E. L., et al. (2012). Functional responses of methanogenicarchaea to syntrophic growth. *ISME J.* 6, 2045–2055. doi: 10.1038/ismej.2012.60

Wang, Q., Garrity, G. M., Tiedje, J. M., and Cole, J. R. (2007). Naive Bayesian classifier for rapid assignment of rRNA sequences into the new bacterial taxonomy. *Appl. Environ. Microbiol.* 73, 5261–5267. doi: 10.1128/AEM.00062-07

Wang, X., Lu, X., Li, F., and Yang, G. (2014). Effects of temperature and carbon-nitrogen (C/N) ratio on the performance of anaerobic co-digestion of dairy manure, chicken manure and rice straw: focusing on ammonia inhibition. *PLOS ONE* 9:e97265. doi: 10.1371/journal.pone.0097265

Wang, Y., Zhang, Y., Wang, J., and Meng, L. (2009). Effects of volatile fatty acid concentrations on methane yield and methanogenic bacteria. *Biomass Bioenergy* 33, 848–853. doi: 10.1016/j.biombioe.2009.01.007

Wegner, C. E., and Liesack, W. (2016). Microbial community dynamics during the early stages of plant polymer breakdown in paddy soil. *Environ. Microbiol.* 18, 2825–2842. doi: 10.1111/1462-2920.12815

Wilkins, D., Rao, S., Lu, X., and Lee, P. K. H. (2015). Effects of sludge inoculum and organic feedstock on active microbial communities and methane yield during anaerobic digestion. *Front. Microbiol.* 6:114. doi: 10.3389/fmicb.2015.01114

Xu, F., Shi, J., Lv, W., Yu, Z., and Li, Y. (2012). Comparison of different liquid anaerobic digestion effluents as inocula and nitrogen sources for solid state anaerobic digestion of corn stover. *Waste Manag.* 33, 26–32. doi: 10.1016/j.wasman.2012.08.006

Zhang, W., Werner, J. J., Matthew, A. T., and Angenent, L. T. (2014). Substrates type drives variation in reactor microbiomes of anaerobic digesters. *Bioresour. Technol.* 151, 397–401. doi: 10.1016/j.biortech.2013.10.004

Ziganshin, A. M., Schmidt, T., Scholwin, F., Il'inskaya, O. N., Harms, H., and Kleinsteuber, S. (2011). Bacteria and archaea involved in anaerobic digestion of distillers grains with soluble. *Appl. Microbiol. Biotechnol.* 8, 2039–2052. doi: 10.1007/s00253-010-2981-9

**Conflict of Interest Statement:** The authors declare that the research was conducted in the absence of any commercial or financial relationships that could be construed as a potential conflict of interest.

frontiers in Microbiology

ORIGINAL RESEARCH
published: 24 August 2018
doi: 10.3389/fmicb.2018.01855

# A Prospective Study on the Fermentation Landscape of Gaseous Substrates to Biorenewables Using *Methanosarcina acetivorans* Metabolic Model

*Hadi Nazem-Bokaee and Costas D. Maranas**

*Department of Chemical Engineering, The Pennsylvania State University, University Park, PA, United States*

The abundance of methane in shale gas and of other gases such as carbon monoxide, hydrogen, and carbon dioxide as chemical process byproducts has motivated the use of gas fermentation for bioproduction. Recent advances in metabolic engineering and synthetic biology allow for engineering of microbes metabolizing a variety of chemicals including gaseous feeds into a number of biorenewables and transportation liquid fuels. New computational tools enable the systematic exploration of all feasible conversion alternatives. Here we computationally assessed all thermodynamically feasible ways of co-utilizing $CH_4$, CO, and $CO_2$ using ferric as terminal electron acceptor for the production of all key precursor metabolites. We identified the thermodynamically feasible co-utilization ratio ranges of $CH_4$, CO, and $CO_2$ toward production of the target metabolite(s) as a function of ferric uptake. A revised version of the iMAC868 genome-scale metabolic model of *Methanosarcina acetivorans* was chosen to assess co-utilization of $CH_4$, CO, and $CO_2$ and their conversion into selected target products using the optStoic pathway design tool. This revised version contains the latest information on electron flow mechanisms by the methanogen while supplied with methane as the sole carbon source. The interplay between different gas co-utilization ratios and the energetics of reverse methanogenesis were also analyzed using the same metabolic model.

**Keywords: gas fermentation, metabolic modeling, $CH_4$, CO, $CO_2$, *M. acetivorans***

OPEN ACCESS

***Edited by:***
*Deepak Kumaresan, Queen's University Belfast, United Kingdom*

***Reviewed by:***
*Deepak Pant, Flemish Institute for Technological Research, Belgium*
*Sandra R. R. Esteves, University of South Wales, United Kingdom*

****Correspondence:***
*Costas D. Maranas*
*costas@psu.edu*

***Specialty section:***
*This article was submitted to Microbiotechnology, Ecotoxicology and Bioremediation, a section of the journal Frontiers in Microbiology*

***Received:*** *28 March 2018*
***Accepted:*** *24 July 2018*
***Published:*** *24 August 2018*

***Citation:***
*Nazem-Bokaee H and Maranas CD (2018) A Prospective Study on the Fermentation Landscape of Gaseous Substrates to Biorenewables Using Methanosarcina acetivorans Metabolic Model. Front. Microbiol. 9:1855. doi: 10.3389/fmicb.2018.01855*

## INTRODUCTION

The global increase in oil production, fossil fuel combustion, biomass burning, and hydraulic fracturing of shale gas and climate change concerns has motivated the reduction of emissions from anthropogenic sources. Mitigation of gaseous emissions (such as methane, carbon dioxide, and carbon monoxide) from the environment and their microbial conversion into useful products provides a sustainable and transformative solution that avoids the "food vs. fuel" dilemma. Methane, the major constituent of natural gas, has the highest oxidation potential amongst carbon dioxide, carbon monoxide, and glucose to be converted into a wide range of products including liquid fuels such as ethanol and butanol. Carbon monoxide, often as synthesis gas with varying levels of carbon dioxide and hydrogen (Aasberg-Petersen et al., 2001), along with methane could yield a variable mixture of gases that can be tapped for microbial conversion.

Existing chemical gas-to-liquid (GTL) technologies (i.e., GTL process using the Fischer-Tropsch method) require high operating temperatures and pressures, involve high CapEx costs, yield generally low carbon conversion efficiency, and cannot directly convert methane into the desired bioproducts (Dry, 2002; Steynberg, 2004; Haynes and Gonzalez, 2014). The biological routes of methane utilization, have received renewed interest because of process simplicity (Lopez et al., 2013), selectivity toward targeted pathways (Haynes and Gonzalez, 2014; Mueller et al., 2015), and recent advancements in the characterization and genetic tools of methanotrophic microbes enabling direct transformation of methane into valuable chemicals and fuel molecules (Coleman et al., 2014; Fei et al., 2014; Strong et al., 2015; Henard et al., 2016). Much of the current industrial applications of methane utilization have been devoted to the use of aerobic methanotrophic bacteria (Fei et al., 2014). In contrast, the global methane cycle is primarily controlled by the syntrophy of microorganisms living in anoxic environments. Although biological methane conversion can occur in oxic habitats (Conrad, 2009; Knittel and Boetius, 2009), more than 80% of methane produced in the world's oceans is estimated to be converted anaerobically (Orphan et al., 2001). In addition, anaerobic routes for methane metabolism offer better carbon and energy efficiency compared with aerobic pathways (Mueller et al., 2015; Nazem-Bokaee et al., 2016). Difficulties in culturing anaerobic methanotrophs in the lab, arising from syntrophy requirements, have hampered their rapid characterization and application. Nonetheless, recent observation of methane utilization by anaerobic methanotrophic archaea (ANME) decoupled from their sulfate-reducing bacteria (SRB) partners in the presence of artificial electron acceptors (Scheller et al., 2016) revealed new avenues for direct anaerobic conversion of methane by ANMEs into useful chemicals. So far there is no microbe capable of AOM utilizing other gaseous substrates at industrial scale. Acetogens has been the workhouse for gas fermentation in industry for over two decades. Anaerobic conversion of carbon monoxide into valuable products such as ethanol, acetate, and 2,3-butanediol at industrial scale has been pursued using different strains of Clostridium (Simpson et al., 2010; Köpke et al., 2011a,b; Tran and Simpson, 2015; Daniell et al., 2016; Martin et al., 2016). A recent study on the co-utilization of carbon dioxide and carbon monoxide or hydrogen to produce acetate using *Moorella thermoacetica* (Hu et al., 2016) further demonstrates the need for systematic study of co-utilization of various $C_1$ gases in other potential microbial hosts.

In this work, we aim at developing a computational framework allowing for designing overall thermodynamically feasible conversions of mixes of gaseous molecules into selected metabolites and, then, investigating the metabolic capabilities of a selected microorganism in response to introducing new gas mixture combinations. Using optStoic (Chowdhury and Maranas, 2015) we exhaustively identified all thermodynamically feasible optimal conversion stoichiometries making use of a combination of $CH_4$, CO, and $CO_2$. Note that there exist many other computational tools for pathway design (Hadadi and Hatzimanikatis, 2015; Long et al., 2015; Nazem-Bokaee and Senger, 2015; Huang et al., 2017). Ten key branch point (precursor) metabolites (Noor et al., 2010) were selected owing to their essentiality for anabolic processes found in all forms of life as well as their crucial role as building blocks for producing many commodity and specialty chemicals listed as top value-added chemicals by the U.S. Department Of Energy (DOE). Maximum uptake of carbon coming from $CH_4$, CO, or $CO_2$ and their co-utilization ratios have been assessed as well as the indispensability of ferric ion as an electron acceptor. To analyze metabolic pathway usage at different co-utilization ratios of $CH_4$, CO, and $CO_2$ designed by optStoic algorithm, a revised version of the iMAC868 genome-scale metabolic model of the methanogenic archaeon *Methanosarcina acetivorans* (Nazem-Bokaee et al., 2016) was used allowing for full tracking of carbon and electron flow within the reversal of methanogenesis pathway. Recent studies identified the existence of an electron bifurcating multi-complex enzyme, cytosolic heterodisulfide reductase HdrABC, shedding light into pathways for utilizing methane by *M. acetivorans* in the presence of ferric to produce useful chemicals such as acetate (Yan et al., 2017; Nazem-Bokaee et al., 2018). It has been shown before that *M. acetivorans* is capable of growing with carbon monoxide (Rother and Metcalf, 2004; Lessner et al., 2006) and metabolizing carbon dioxide (in the form of bicarbonate) along with methane (Soo et al., 2016), thus, making the archaeon a suitable platform to study the conversion of varying mixtures of these gases into useful products. The computational framework put forth in this study could inform design of novel metabolic engineering strategies for the industrial production of bio-based chemicals and liquid fuels from mixed gaseous feeds.

# METHODS

## Computational Design of Overall Stoichiometries for Gas Co-utilization

To explore optimal overall stoichiometries for conversion of gaseous molecules (i.e., $CH_4$, CO, and $CO_2$) into target products, the optStoic procedure (Chowdhury and Maranas, 2015) was implemented in Python so that it can be freely accessible (**Supplementary Data Sheet 2**). The goal was to design overall stoichiometries informing thermodynamically feasible co-utilization of the gaseous molecules leading to the production of 10 C-mol of products listed in **Table 1** (equation 1).

$$(s_1)\ CH_4 + (s_2)\ CO_2 + (s_3)\ CO \xrightarrow{\text{in the presence of ferric}} \left(10\ C-mol\right)\ \text{target product} \quad (1)$$

In the postulated overall stoichiometry $s_1$, $s_2$, and $s_3$ are the optimal coefficients of methane, carbon dioxide, and carbon monoxide, respectively. Because the target products listed in **Table 1** contain varying number of carbons, fixing the stoichiometry of target product in Equation 1 enables a direct comparison of gaseous feed ratios on a per carbon mol basis. In the optStoic algorithm, water molecules and protons can be taken up or produced as needed so that Equation 1 remains elementally and charge balanced. Furthermore, phosphate, ammonia, and

**TABLE 1 |** The key branch point (precursor) metabolites essential for anabolic processes found in all forms of life considered as target products of gaseous fermentation in this study.

| Target product | Chemical formula | Degree of reduction |
|---|---|---|
| Pyruvate (**PYR**) | $C_3H_3O_3^-$ | 3 |
| Phosphoenolpyruvate (**PEP**) | $C_3H_3O_6P^{2-}$ | 2.66 |
| Glyceraldehyde-3-phosphate (**GAP**) | $C_3H_6O_6P^-$ | 3.66 |
| Oxaloacetate (**OXA**) | $C_4H_2O_5^{2-}$ | 2 |
| Erythrose-4-phosphate (**E4P**) | $C_4H_8O_7P^-$ | 3.75 |
| Ribose-5-phosphate (**R5P**) | $C_5H_{10}O_8P^-$ | 3.8 |
| 2-ketoglutarate (**2KG**) | $C_5H_4O_5^{2-}$ | 2.8 |
| Glucose-6-phosphate (**G6P**) | $C_6H_{12}O_9P^-$ | 3.83 |
| Acetyl CoA (**ACA**) | $C_{23}H_{35}O_{17}N_7P_3S^{3-}$ | 4.04 |
| Succinyl-CoA (**SCA**) | $C_{25}H_{36}O_{19}N_7P_3S^{4-}$ | 3.92 |

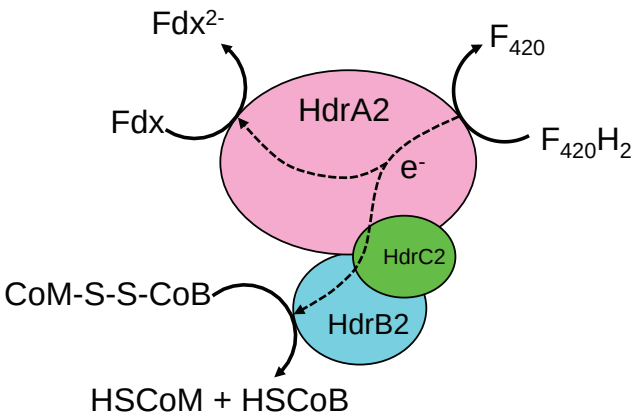


**FIGURE 1 |** Electron bifurcation mechanism by HdrA2B2C2 complex of *M. acetivorans* in the presence of external electron acceptor when grown with methane (see Yan et al., 2017 for more details). $F_{420}$: Cofactor $F_{420}$; $F_{420}H_2$: reduced form of cofactor $F_{420}$; Fdx: ferredoxin; $Fdx^{2-}$: reduced form of ferredoxin; HSCoM: coenzyme M; HSCoB: coenzyme B; CoM-S-S-CoB: heterodisulfide.

hydrogen sulfide were added to balance Equation 1 when a target product contains phosphorous, nitrogen, and sulfur, respectively. No carbon-containing compound other than methane, carbon dioxide, and carbon monoxide was allowed as an additional substrate. The choice of the products listed in **Table 1** is based on their essentiality in the metabolism of almost all forms of life (Noor et al., 2010) and their significance in being used as building blocks of many commodity and specialty chemicals as mentioned in the DOE list of top value-added chemicals. The performance criteria of the overall conversion shown in Equation 1 were to maximize $s_1$, $s_2$, or $s_3$ separately at a specified ferric uptake. To safeguard the thermodynamic feasibility of all conversions, the minimum overall standard $\Delta G$ was set to be less than zero. A previously assembled database of metabolites (Chowdhury and Maranas, 2015) was used to explore the optimal combination of reactants and products for any given overall stoichiometry. COBRApy (Ebrahim et al., 2013) with built-in cGLPK (http://www.gnu.org/software/glpk/) solver was used to solve the optimization problems written in Python 2.7.

## Modifications to the iMAC868 Metabolic Model of *M. acetivorans*

Since the development and release of the iMAC868 metabolic model (Nazem-Bokaee et al., 2016), there have been new experimental studies aimed at better understanding the electron flow mechanisms and biochemistry of *M. acetivorans* growing on methane (Yan et al., 2017, 2018; Nazem-Bokaee et al., 2018). This provided the impetus for updating the iMAC868 model of this methanogen to catalog these findings. It was recently shown that *M. acetivorans* expresses a multi-unit cytosolic heterodisulfide reductase complex, HdrA2B2C2, when grown with methane in the presence of ferric (Yan et al., 2017; Yan and Ferry, 2018) that can partition electrons (i.e., bifurcate electrons) coming from cofactor $F_{420}$ (reduced) between ferredoxin (with lower electrode potential) and heterodisulfide (with higher electrode potential) (**Figure 1**). Therefore, HdrA2B2C2 complex bypasses thermodynamic uphill for direct electron transfer from cofactor $F_{420}$ to ferredoxin during ferric-dependent methanotrophy by *M. acetivorans*. This important finding introduces a new metabolic capability of *M. acetivorans* and, therefore, was cataloged in the updated version of the iMAC868 metabolic model. The resulting coenzyme M and coenzyme B are re-used to regenerate heterodisulfide used for activation of methane. The reduced ferredoxin is used to drive the biosynthesis of acetyl-CoA by CO dehydrogenase, Cdh. Therefore, we replaced the previously used electron flow routes in our model with the new route representing the newly elucidated function of HdrA2B2C2 (see **Figure 1**). We found that the model accommodated the new electron bifurcation mechanism providing new insights about the key role of ferric in the distribution of electrons between major products of methanotrophy as well as on energy conservation mechanisms (Nazem-Bokaee et al., 2018). The model was assembled in a format compatible for flux balance analysis (Orth et al., 2010). FBA optimization problems were solved by GNU Linear Programming Kit (GLPK) (http://www.gnu.org/software/glpk/) solver in Matlab using COBRA toolbox (Schellenberger et al., 2011). Flux variability analysis (FVA) was performed to obtain range of fluxes under optimal growth conditions as described previously (Mahadevan and Schilling, 2003). Both FBA and FVA problems incorporated overall thermodynamic feasibility constraints (overall $\Delta G \leq 0$).

# RESULTS AND DISCUSSION

## Thermodynamically Feasible Gas Co-utilization Stoichiometries Designed by Optstoic

The thermodynamically feasible ranges of co-utilization of $CH_4$, CO, and $CO_2$ for the production of target chemicals listed in **Table 1** were predicted by optStoic to be dependent on the level of available ferric. **Figure 2** shows this dependency for three selected products with varying degrees of reduction. As the ferric level goes up (i.e., increasing the electron sink capacity), methane

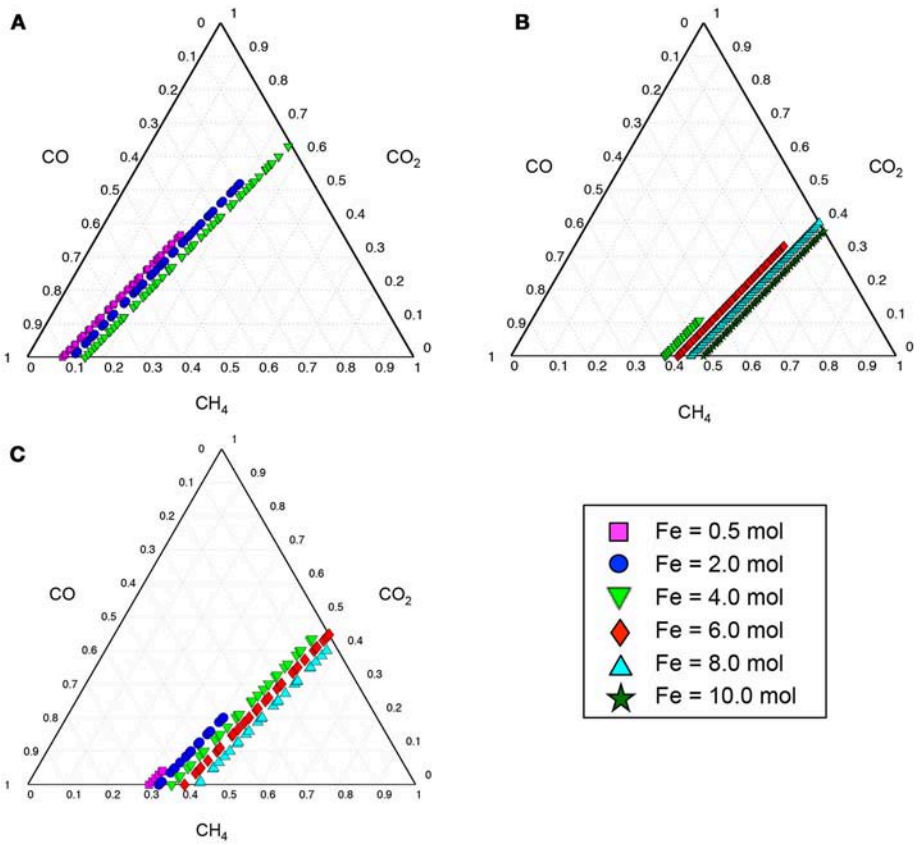


**FIGURE 2 |** Ternary diagrams showing the contribution of gaseous carbon sources (i.e., $CH_4$, CO, or $CO_2$) in the production of 10 C-mol oxaloacetate **(A)**, glyceraldehyde-3-phosphate **(B)**, or acetyl-CoA **(C)** as selected target products. Colorful symbols on the bottom right of the figure show the range of ferric ($Fe^{3+}$) uptake (in moles) at which the overall gases-to-product conversion shown in Equation 1 is thermodynamically feasible. Each symbol on the ternary plots represents a single independent thermodynamically feasible stoichiometric conversion of gases-to-product simulated by optStoic algorithm. In each simulation, the stoichiometries of the target product, ferric, and one of the gases are fixed and the objective is to maximize the stoichiometries of the other two gases. The moles of $CH_4$, CO, or $CO_2$ in the overall stoichiometry are normalized to be between zero and one in the ternary diagram.

usage increases in proportion. However, only some ratio ranges of the $CH_4$-CO-$CO_2$ triplet lead to thermodynamically feasible production of the target molecules (**Figure 2**). Here, increasing ferric levels provides opportunity for $CO_2$ utilization levels to go up by accepting electrons coming from methane. This increase, however, is at the expense of reduction in CO utilization levels to satisfy stoichiometric and thermodynamics feasibility of the overall conversion.

The minimum and maximum moles of ferric required to maintain any thermodynamically feasible gas co-utilization are given in **Table 2** for all target products listed in **Table 1**. For example, a minimum of 3.04 mol ferric was required to obtain any feasible conversion of gaseous substrates toward glyceraldehyde-3-phosphate (GAP) while no feasible overall stoichiometry was found with a methane carbon contribution <38%. The overall conversions given in **Table 2** also unmask the possibility of designing gas bi-utilization (where either $CH_4$ and CO or $CH_4$ and $CO_2$ can be co-utilized) at varying levels of ferric, which is further explained in the following sections.

The maximum amount of carbon that can be incorporated to target products from $CH_4$, CO, or $CO_2$, depends on the target molecule C/O ratio and reduction level. **Figure 3** displays how the choice of target molecule (those listed in **Table 1**) affects the maximum carbon contributed by the three gaseous feeds. For example, CO could be the top supplier of carbon for oxaloacetate (OXA), as expected, because OXA is highly oxidized. Note that **Figure 3** does not directly represent maximum co-utilization of ratios of gases; however, it demarcates the theoretical limits on utilizing any of the gases for the production of each target product. For example, under the defined criteria for optStoic, it would be thermodynamically infeasible to design an overall stoichiometry for pyruvate production in which carbon coming from methane co-utilized with other gases exceeded 50% (see also **Table 2** for all stoichiometric designs).

Nonetheless, methane contributes the most carbon at maximum ferric uptake levels. In addition, imposing a more negative requirement for the overall standard free energy of change results in less carbon contributed from $CO_2$ (since it has the lowest Gibbs free energy of formation among CO and

**TABLE 2 |** optStoic-predicted overall stoichiometric conversions (middle column) for which the stoichiometry of $CH_4$, $CO_2$, or CO were maximized independently.

| Optimization conditions | Overall stoichiometries | ΔG (kcal) |
|---|---|---|
| | Pyruvate (**PYR**) | |
| *max.* $s_{CH_4}$ | **4.999** $CH_4 + 5.000\ CO_2 + 0.0015\ H_2O + 6.66\ Fe^{3+} \rightarrow 3.333\ C_3H_3O_3^- + 9.993\ H^+ + 6.66\ Fe^{2+}$ | −87 |
| *max.* $s_{CO_2}$ | $4.603\ CH_4 + \mathbf{5.395}\ CO_2 + 3.5\ Fe^{3+} \rightarrow 3.33\ C_3H_3O_3^- + 0.791\ H_2O + 6.833\ H^+ + 3.5\ Fe^{2+}$ | −12 |
| *max.* $s_{CO}$ | $2.222\ CH_4 + \mathbf{7.777}\ CO + 2.222\ H_2O \rightarrow 3.333\ C_3H_3O_3^- + 3.333\ H^+$ | −40 |
| | Phosphoenolpyruvate (**PEP**) | |
| *max.* $s_{CH_4}$ | **5.416** $CH_4 + 4.583\ CO_2 + 3.333\ HPO_4^{2-} + 10\ Fe^{3+} \rightarrow 3.333\ C_3H_3O_6P^{2-} + 2.499\ H_2O + 10\ H^+ + 10\ Fe^{2+}$ | −128 |
| *max.* $s_{CO_2}$ | $4.791\ CH_4 + \mathbf{5.208}\ CO_2 + 3.333\ HPO_4^{2-} + 5\ Fe^{3+} \rightarrow 3.333\ C_3H_3O_6P^{2-} + 3.749\ H_2O + 5\ H^+ + 5\ Fe^{2+}$ | −16 |
| *max.* $s_{CO}$ | $2.245\ CH_4 + \mathbf{7.754}\ CO + 3.333\ HPO_4^{2-} + 0.14\ Fe^{3+} \rightarrow 3.333\ C_3H_3O_6P^{2-} + 1.087\ H_2O + 0.14\ H^+ + 0.14\ Fe^{2+}$ | −5 |
| | Glyceraldehyde 3-phosphate **(GAP)** | |
| *max.* $s_{CH_4}$ | **6.249** $CH_4 + 3.750\ CO_2 + 3.333\ HPO_4^{2-} + 10\ Fe^{3+} \rightarrow 3.333\ C_3H_6O_6P^- + 0.833\ H_2O + 6.667\ H^+ + 10\ Fe^{2+}$ | −82 |
| *max.* $s_{CO_2}$ | $5.874\ CH_4 + \mathbf{4.124}\ CO_2 + 3.333\ HPO_4^{2-} + 7\ Fe^{3+} \rightarrow 3.333\ C_3H_6O_6P^- + 1.583\ H_2O + 3.667\ H^+ + 7\ Fe^{2+}$ | −11 |
| *max.* $s_{CO}$ | $3.840\ CH_4 + \mathbf{6.159}\ CO + 0.506\ H_2O + 3.333\ HPO_4^{2-} + 0.293\ H^+ + 3.04\ Fe^{3+} \rightarrow 3.333\ C_3H_6O_6P^- + 3.04\ Fe^{2+}$ | −5 |
| | Oxaloacetate (**OXA**) | |
| *max.* $s_{CH_4}$ | **3.75** $CH_4 + 6.25\ CO_2 + 5\ Fe^{3+} \rightarrow 2.5\ C_4H_2O_5^{-2} + 10\ H^+ + 5\ Fe^{2+}$ | −53 |
| *max.* $s_{CO_2}$ | $3.50\ CH_4 + \mathbf{6.50}\ CO_2 + 3\ Fe^{3+} \rightarrow 2.5\ C_4H_2O_5^{-2} + 0.50\ H_2O + 8\ H^+ + 3\ Fe^{2+}$ | −6 |
| *max.* $s_{CO}$ | $0.83\ CH_4 + \mathbf{9.17}\ CO + 3.33\ H_2O \rightarrow 2.5\ C_4H_2O_5^{-2} + 5\ H^+$ | −65 |
| | Erythrose-4-phosphate (**E4P**) | |
| *max.* $s_{CH_4}$ | **6.25** $CH_4 + 3.75\ CO_2 + 2.50\ HPO_4^{2-} + 10\ Fe^{3+} \rightarrow 2.50\ C_4H_8O_7P^- + 7.50\ H^+ + 10\ Fe^{2+}$ | −86 |
| *max.* $s_{CO_2}$ | $5.875\ CH_4 + \mathbf{4.125}\ CO_2 + 2.50\ HPO_4^{2-} + 7\ Fe^{3+} \rightarrow 2.50\ C_4H_8O_7P^- + 0.75\ H_2O + 4.5\ H^+ + 7\ Fe^{2+}$ | −15 |
| *max.* $s_{CO}$ | $3.81\ CH_4 + \mathbf{6.19}\ CO + 1.31\ H_2O + 2.50\ HPO_4^{2-} + 2.85\ Fe^{3+} \rightarrow 2.50\ C_4H_8O_7P^- + 0.35\ H^+ + 2.85\ Fe^{2+}$ | −5 |
| | Ribose-5-phosphate (**R5P**) | |
| *max.* $s_{CH_4}$ | **6.25** $CH_4 + 3.75\ CO_2 + 0.5\ H_2O + 2\ HPO_4^{2-} + 10\ Fe^{3+} \rightarrow 2\ C_5H_{10}O_8P^- + 8\ H^+ + 10\ Fe^{2+}$ | −92 |
| *max.* $s_{CO_2}$ | $5.81\ CH_4 + \mathbf{4.19}\ CO_2 + 2\ HPO_4^{2-} + 6.5\ Fe^{3+} \rightarrow 2\ C_5H_{10}O_8P^- + 0.375\ H_2O + 4.5\ H^+ + 6.5\ Fe^{2+}$ | −10 |
| *max.* $s_{CO}$ | $3.76\ CH_4 + \mathbf{6.24}\ CO + 1.75\ H_2O + 2\ HPO_4^{2-} + 2.55\ Fe^{3+} \rightarrow 2\ C_5H_{10}O_8P^- + 0.55\ H^+ + 2.55\ Fe^{2+}$ | −5 |
| | 2-ketoglutarate (**2KG**) | |
| *max.* $s_{CH_4}$ | **4.75** $CH_4 + 5.25\ CO_2 + 6\ Fe^{3+} \rightarrow 2\ C_5H_4O_5^{2-} + 0.50\ H_2O + 10\ H^+ + 6\ Fe^{2+}$ | −85 |
| *max.* $s_{CO_2}$ | $4.38\ CH_4 + \mathbf{5.62}\ CO_2 + 3\ Fe^{3+} \rightarrow 2\ C_5H_4O_5^{2-} + 1.25\ H_2O + 7\ H^+ + 3\ Fe^{2+}$ | −14 |
| *max.* $s_{CO}$ | $2\ CH_4 + \mathbf{8}\ CO + 2\ H_2O \rightarrow 2\ C_5H_4O_5^{2-} + 4\ H^+$ | −57 |
| | Glucose-6-phosphate (**G6P**) and Fructose-6-phosphate (**F6P**) | |
| *max.* $s_{CH_4}$ | **6.248** $CH_4 + 3.748\ CO_2 + 1.666\ HPO_4^{2-} + 0.834\ H_2O + 10\ Fe^{3+} \rightarrow 1.666\ C_6H_{12}O_9P^- + 8.334\ H^+ + 10\ Fe^{2+}$ | −188 |
| *max.* $s_{CO_2}$ | $5.811\ CH_4 + \mathbf{4.185}\ CO_2 + 1.666\ HPO_4^{2-} + 6.5\ Fe^{3+} \rightarrow 1.666\ C_6H_{12}O_9P^- + 0.041\ H_2O + 4.834\ H^+ + 6.5\ Fe^{2+}$ | −11 |
| *max.* $s_{CO}$ | $3.744\ CH_4 + \mathbf{6.252}\ CO + 2.078\ H_2O + 1.666\ HPO_4^{2-} + 2.474\ Fe^{3+} \rightarrow 1.666\ C_6H_{12}O_9P^- + 0.808\ H^+ + 2.474\ Fe^{2+}$ | −5 |
| | Acetyl-CoA (**ACA**) | |
| *max.* $s_{CH_4}$ | **5.817** $CH_4 + 4.187\ CO_2 + 1.305\ HPO_4^{2-} + 3.045\ NH_3 + 0.435\ H_2S + 8.26\ Fe^{3+} \rightarrow 0.435\ C_{23}H_{35}O_{17}N_7P_3S^{3-} + 10\ H^+ + 6.2\ H_2O + 8.26\ Fe^{2+}$ | −99 |
| *max.* $s_{CO_2}$ | $5.410\ CH_4 + \mathbf{4.595}\ CO_2 + 1.305\ HPO_4^{2-} + 3.045\ NH_3 + 0.435\ H_2S + 5\ Fe^{3+} \rightarrow 0.435\ C_{23}H_{35}O_{17}N_7P_3S^{3-} + 7.015\ H_2O + 6.74\ H^+ + 5\ Fe^{2+}$ | −22 |
| *max.* $s_{CO}$ | $3.064\ CH_4 + \mathbf{6.941}\ CO + 1.305\ HPO_4^{2-} + 3.045\ NH_3 + 0.435\ H_2S + 0.117\ Fe^{3+} \rightarrow 0.435\ C_{23}H_{35}O_{17}N_7P_3S^{3-} + 4.765\ H_2O + 1.857\ H^+ + 0.117\ Fe^{2+}$ | −5 |
| | Succinyl-CoA (**ACA**) | |
| *max.* $s_{CH_4}$ | **5.7** $CH_4 + 4.3\ CO_2 + 1.2\ HPO_4^{2-} + 2.8\ NH_3 + 0.4\ H_2S + 8\ Fe^{3+} \rightarrow 0.4\ C_{25}H_{36}O_{19}N_7P_3S^{4-} + 10\ H^+ + 5.8\ H_2O + 8\ Fe^{2+}$ | −97 |
| *max.* $s_{CO_2}$ | $5.262\ CH_4 + \mathbf{4.738}\ CO_2 + 1.2\ HPO_4^{2-} + 2.8\ NH_3 + 0.4\ H_2S + 4.5\ Fe^{3+} \rightarrow 0.4\ C_{25}H_{36}O_{19}N_7P_3S^{4-} + 6.675\ H_2O + 6.5\ H^+ + 4.5\ Fe^{2+}$ | −15 |
| *max.* $s_{CO}$ | $2.933\ CH_4 + \mathbf{7.066}\ CO + 1.2\ HPO_4^{2-} + 2.8\ NH_3 + 0.4\ H_2S \rightarrow 0.4\ C_{25}H_{36}O_{19}N_7P_3S^{4-} + 4.266\ H_2O + 2\ H^+$ | −9 |

*Bold numbers are the maximum feasible stoichiometry of a gas molecule under the optimization conditions shown on the left column. The stoichiometry of the target product only was fixed to moles equivalent to 10 C-mol carbon. ΔG of formation of the overall conversions were also given (right column).*

$CH_4$) leading to a decline in maximum co-utilization ratios of $CO_2$-to-$CH_4$. Such information could be useful in designing and/or modifying bioconversions based on varying compositions of industrial gas waste streams (Subramani and Gangwal, 2008; Lackey et al., 2015).

In the following section we describe how overall stoichiometry designs generated by optStoic could be used to inform metabolic engineering strategies through using the updated iMAC868 metabolic model of *M. acetivorans* as a platform.

## Metabolic Capabilities of *M. acetivorans* During Gas Co-utilization

The ratio of industrial waste gases is often highly variable from stream to stream leading to difficulties in predicting desirable gas stream-to-target product conversions (Williams et al., 2007; Subramani and Gangwal, 2008). The optStoic designs could serve as a guide to estimate feasible conversions using the metabolic model of *M. activorans*. We selected oxaloacetate (OXA), glyceraldehyde 3-phosphate (GAP), and acetyl-CoA (ACA) (out of hundreds of unique overall stoichiometry designs) based on their distinct differences as shown in **Figures 2**, **3** (also

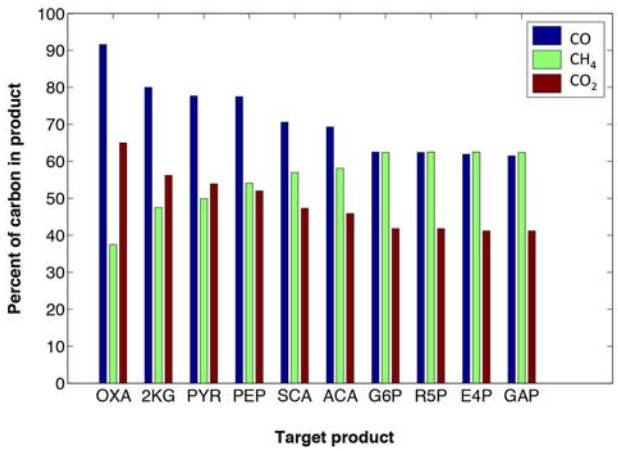


**FIGURE 3 |** optStoic-predicted maximum carbon (shown as percentage on the Y-axis) contribution from carbon monoxide (blue), methane (green), or carbon dioxide (red) for the production of different target products (For abbreviations see **Table 1**). These maxima are from different independent overall stoichiometry designs predicted by optStoic (see **Table 2** for all stoichiometries and performance criteria).

in **Table 1**) as well as their importance as building blocks of numerous valuable end products. We chose the stoichiometric ratios of $CH_4$, CO, and $CO_2$ at an arbitrary ferric level of 4 moles at which co-utilization of the three gases for the production of OXA, ACA, and GAP was predicted by optStoic to be thermodynamically feasible (**Table 3**). To implement these stoichiometric ratios in the context of the metabolic model of *M. acetivorans*, the lower and upper bounds of the reactions corresponding to the uptake of $CH_4$, CO, and $CO_2$ in the iMAC868 metabolic model were fixed to the stoichiometric ratios of $CH_4$, CO, and $CO_2$ shown in **Table 3**. Analysis of the flux distribution through the metabolic network confirmed the usage of the reversal of the methanogenesis pathway indicating the incorporation of the gaseous substrates into biomass and cofactor biosynthesis. The iMAC868 metabolic model also predicts the uptake of ammonia, hydrogen sulfide, and phosphate as essential sources of nitrogen, sulfur, and phosphorus, respectively, consistent with the overall optStoic design. Flux variability analysis results in predicting a maximum yield of 2.499 (mol per 10 C-mol of gases) for OXA. This is in agreement with a 2.5 stoichiometric value predicted by optStoic leading to the same ratio of $CH_4$, CO, and $CO_2$ co-utilization implying that metabolism remains unaffected even at maximum OXA production yield. The maximum yields of GAP and ACA predicted by the iMAC868 metabolic model are 2.944 and 0.388 (mol per 10 C-mol of gases), respectively, which is only 11.5, and 11% less than the optimal overall stoichiometries obtained by optStoic. This difference is due to the inclusion of many more cofactors and intermediate metabolites in the metabolic network compared to the consideration of one simple overall stoichiometry as that shown in Equation 1. Further analysis of the flux through the formation of biomass, as another product of the metabolic network, reveals a maximum biomass yield of 0.217 at a ferric level of 4.2 (mol per 10 C-mol of gases) when using the gas ratios optimized for ACA production predicted by optStoic (see **Table 3**). Therefore, the optStoic design could quickly inform potential gas co-utilization ratios at which a certain level of cellular growth can be achieved. It should be noted that there exist other possible gas co-utilization ratios that could end up obtaining similar biomass yields. For example, using the gas ratios optimized for GAP production (see **Table 3**) results in achieving a maximum biomass yield of 0.224 at a ferric level of 4.5 (mol per 10 C-mol of gases), which is only 3% higher than what could be achieved at a gas composition optimized for ACA production and is slightly richer in CO (see **Table 3**).

**TABLE 3 |** optStoic-designed stoichiometries (mol) of methane ($s_{CH_4}$), carbon monoxide ($s_{CO}$), and carbon dioxide ($s_{CO_2}$) resulted in the production of 10 C-mol of three selected target products used to constrain the *in silico* uptake of these gases by the iMAC868 metabolic model of *M. acetivorans*.

| Target Product | Gas Composition | | |
|---|---|---|---|
| | $s_{CH_4}$ | $s_{CO}$ | $s_{CO_2}$ |
| Glyceraldehyde-3-phosphate (GAP) | 4.333 | 4.666 | 1 |
| Oxaloacetate (OXA) | 1.833 | 7.166 | 1 |
| Acetyl-CoA (ACA) | 4.04 | 4.96 | 1 |

It has been postulated that *M. acetivorans* reduces ferric at multi-heme c-type cytochromes sites to which electrons are shuttled by membrane-bound methanophenazine (Yan et al., 2017). Depending on the composition of gaseous substrates being used (given in **Table 3**), the iMAC868 metabolic model predicts that at least 13% (up to 20%) of heterodisulfide has to be reduced through the membrane-bound heterodisulfide reductase (HdrDE) that reduces methanophenazine. The remaining heterodisulfide can be reduced via either the cytosolic HdrA2B2C2 or HdrDE. Reduced cofactor $F_{420}$, which donates electrons to ferredoxin and heterodisulfide at the HdrA2 site, can be regenerated through any of $F_{420}$ dehydrogenase (Fpo), $F_{420}$-dependent methylene-$H_4$MPT reductase (Mer), $F_{420}$-dependent methylene-$H_4$MPT dehydrogenase (Mtd), or $F_{420}$-dependent NADP reductase enzyme complexes according to the metabolic model predictions.

To further explore the metabolic capabilities of *M. acetivorans*, we decided to analyze the theoretical limits of ethanol and butanol co-production during $CH_4$ and CO co-utilization by the iMAC868 model. The biological co-production of alcohols has been reported in the literature where acetone/butanol/ethanol (ABE) fermentation process by clostridial strains has been studied the most and implemented industrially (Worden et al., 1991; Lee et al., 2008; Tracy et al., 2012; Carlson and Papoutsakis, 2017; Fernandez-Naveira et al., 2017). However, most traditional ABE process suffers from high feedstock costs (Green, 2011) and, thus, the use of cheap sources such as $C_1$ gas substrates suggests a promising alternate route (Dürre, 2017). Nonetheless, the current $C_1$ gas fermentation technology is mainly relied on making use of acetogens (De Tissera et al., 2017). Here, the motivation was to study the co-production of

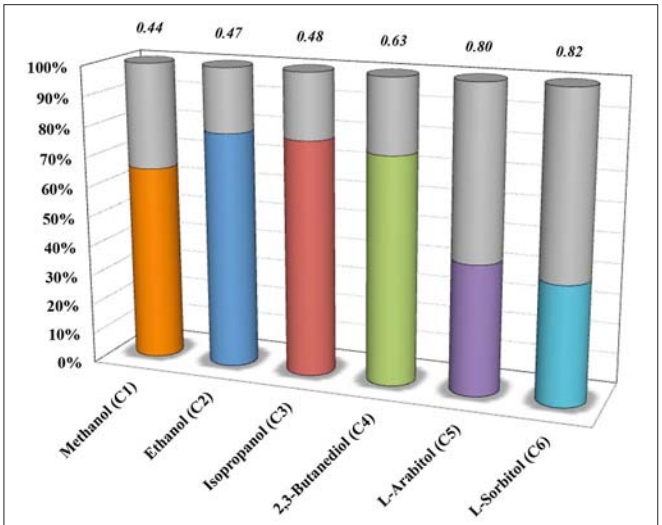


**FIGURE 4 |** optStoic-predicted co-production of selected alcohols (with their number of carbons given in parenthesis) along with butanol in the presence of ferric as electron acceptor. Y-axis indicates that under the design criteria of optStoic, where the only products of CO and $CH_4$ co-utilization are butanol and one of the shown alcohols, how much (in percent) of the total product could be each alcohol molecule (gray area of the bars show percent butanol of the total). Italic numbers on top of the bars show CO to $CH_4$ gas co-utilization ratios.

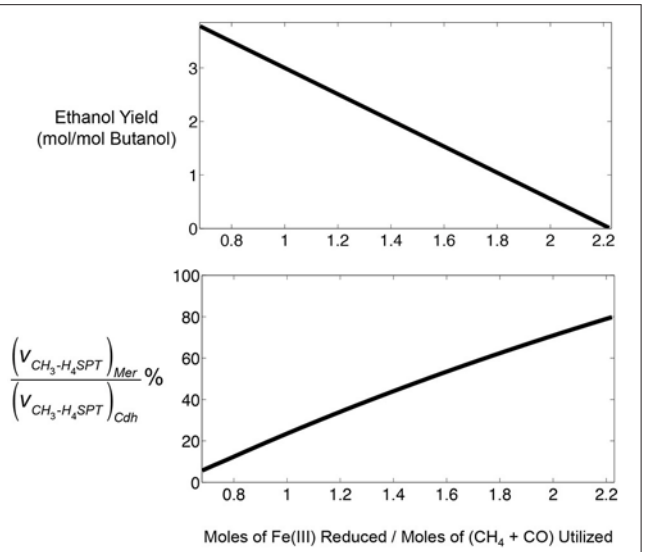


**FIGURE 5 |** Predictive capabilities of iMAC868 metabolic model of *M. acetivorans* during CO and $CH_4$ co-utilization in the presence of ferric for butanol and ethanol co-production. **Top panel**: prediction of ethanol and butanol co-production feasibility over a range of ferric reduction levels. **Bottom panel**: partitioning of methyl-tetrahydrosarcinapterin ($CH_3$-$H_4$SPT) flux (denoted as *v*) between $CO_2$ pathway (Mer) and acetyl-CoA biosynthesis pathway (Cdh) during reversal of the methanogenesis pathway by *M. acetivorans*.

alcohols from co-utilization of $C_1$ gaseous substrates in non-traditional hosts such as *M. acetivorans*. For that, first, optStoic was used to design overall conversions such that $CH_4$ and CO co-utilization (using one mole of ferric as basis) results in production of one mole butanol while maximizing the production of ethanol and several other alcohol molecules as co-products (**Figure 4**). optStoic was also applied to examine how conversion of $CH_4$ and CO to butanol would vary for different electron acceptors other than ferric. Almost all electron acceptors examined allowed for the same ratio of $CH_4$ and CO co-utilization except for thrithionate that enabled about three times higher co-utilization ratio (**Supplementary Figure S1** in Data Sheet 1). However, ethanol production as a co-product of butanol production when using trithionate/bisulfate as the electron acceptor pair was only 0.3% of that achievable by using ferric/ferrous as electron acceptor pair. Thus, the overall conversion design using ferric as electron acceptor was employed for analyzing metabolic capabilities of *M. acetivorans* for co-production of ethanol and butanol. The original version of the iMAC868 metabolic model comprises the biosynthetic pathways for ethanol and butanol production (Nazem-Bokaee et al., 2016).

By constraining the lower and upper bounds of the reaction corresponding to the exchange of butanol in the metabolic model to one, and fixing the bounds of reactions corresponding to the uptake of $CH_4$ and CO to the respective ratio given in **Figure 4** (i.e., 0.47), the model predicts that a maximum of 3.779 moles of ethanol per mole of butanol could be produced (**Figure 5**). The ethanol-to-butanol molar ratio predicted by optStoic at the same gas co-utilization ratio was 3.682, which is only 2.5% different from that predicted by the iMAC868 metabolic model.

Ethanol co-production with butanol was predicted by iMAC868 metabolic model to be feasible over a range of ferric reduction values from 0.68 up to 2.2 (**Figure 5**). However, ethanol co-production decreases as ferric reduction levels increases because the reducing power for generating acetyl-CoA, the precursor for both ethanol and butanol production, diminishes. The bottom panel of **Figure 5** shows that increasing ferric reduction capacity results in re-routing more methane (through Mer) toward the methyotrophic pathway. Thus, acetyl-CoA production via Cdh remains at stoichiometric limits necessary for satisfying fixed amount of butanol production. Nonetheless, the flux through Cdh could never become zero and at ferric levels of 2.2 mol/mol of gases at least 20% of the $CH_3$-$H_4$SPT has to be converted to acetyl-CoA to maintain cellular growth. This analysis demonstrate the usefulness of computational tools such as optStoic in guiding metabolic engineering design/analysis for a given bioconversion.

## SUMMARY AND CONCLUSION

In this work, we have demonstrated the utility of deploying computational tools such as optStoic along with "genome-scale" metabolic modeling to inform optimal metabolic engineering designs and strategies satisfying an overall desired bioconversion. The optStoic formulation allowed for the exploration of all overall conversions rooting from the co-utilization of low-value

$C_1$ gaseous feedstocks (i.e., $CH_4$, $CO_2$, and CO) ending up in the production of precursors used for making high-value biorenewables. We targeted ten key branch point metabolites that have been used extensively as building blocks for the production of many commodity and specialty chemicals such as acetate, terpenoids, and synthetic sugars among others. We showed that the proper choice of an electron acceptor (i.e., ferric) could bypass the thermodynamic barriers for electron flow in the gas-to-chemicals conversions. Furthermore, we showed that there exist well defined gas co-utilization ranges, which are feasible at varying levels of ferric, dependent on the choice of target product. Maximum ferric usage as well as maximum carbon contribution from each of the $CH_4$, $CO_2$, and CO was analyzed that could lead to new or improved gas co-utilization designs. Using optStoic designs as a guide, metabolic capacities of *M. acetivorans* as the model host was examined owing to its diverse substrate utilization abilities and the progress in its genetic engineering tools. Equipped with latest electron flow mechanisms during growth with methane, the iMAC868 metabolic model of *M. acetivorans* provided information on the partitioning of electrons within the methanogenesis reversal pathway as well as on distribution of carbons coming from co-utilization of mixtures of gases toward selected products. The combined use of optStoic and metabolic modeling presented in this work puts forth an efficient platform for quickly exploring *in silico* the feasibility and limits of various gaseous substrate utilization options.

## AUTHOR CONTRIBUTIONS

HN-B wrote computer scripts, performed the simulations and analyses, designed and generated the figures and tables, and wrote the manuscript. CM supervised and contributed to the design of the study, wrote the manuscript, and critically revised the manuscript. Both authors read and approved the final manuscript.

## FUNDING

This work was supported by funding from The Advanced Research Projects Agnecy-Energy (ARPA-E), US Department of Energy to CM, Drs. Thomas K. Wood, and James G. Ferry, Grant DE-AR0000431.

## SUPPLEMENTARY MATERIAL

The Supplementary Material for this article can be found online at: https://www.frontiersin.org/articles/10.3389/fmicb.2018.01855/full#supplementary-material

## REFERENCES

Aasberg-Petersen, K., Hansen, J. H. B., Christensen, T. S., Dybkjaer, I., Christensen, P. S., Nielsen, C. S., et al. (2001). Technologies for large-scale gas conversion. *Appl. Catal. Gen.* 221, 379–387. doi: 10.1016/S0926-860X(01)00811-0

Carlson, E. D., and Papoutsakis, E. T. (2017). Heterologous expression of the clostridium carboxidivorans CO dehydrogenase alone or together with the acetyl coenzyme a synthase enables both reduction of CO2 and oxidation of CO by clostridium acetobutylicum. *Appl. Environ. Microbiol.* 83:e00829-17. doi: 10.1128/AEM.00829-17

Chowdhury, A., and Maranas, C. D. (2015). Designing overall stoichiometric conversions and intervening metabolic reactions. *Sci. Rep.* 5:16009. doi: 10.1038/srep16009

Coleman, W. J., Vidanes, G. M., Cottarel, G., Muley, S., Kamimura, R., Javan, A. F., et al. (2014). *Biological Conversion of Multi-Carbon Compounds from Methane*. US Patent US20140273128 A1.

Conrad, R. (2009). The global methane cycle: recent advances in understanding the microbial processes involved. *Environ. Microbiol. Rep.* 1, 285–292. doi: 10.1111/j.1758-2229.2009.00038.x

Daniell, J., Nagaraju, S., Burton, F., Kopke, M., and Simpson, S. D. (2016). Low-carbon fuel and chemical production by anaerobic gas fermentation. *Adv. Biochem. Eng. Biotechnol.* 156, 293–321. doi: 10.1007/10_2015_5005

De Tissera, S., Kopke, M., Simpson, S. D., Humphreys, C., Minton, N. P., and Durre, P. (2017). Syngas biorefinery and syngas utilization. *Adv. Biochem. Eng. Biotechnol.* doi: 10.1007/10_2017_5. [Epub ahead of print].

Dry, M. E. (2002). The Fischer-Tropsch process: 1950-2000. *Catal Today* 71, 227–241. doi: 10.1016/S0920-5861(01)00453-9

Dürre, P. (2017). Gas fermentation - a biotechnological solution for today's challenges. *Microb. Biotechnol.* 10, 14–16. doi: 10.1111/1751-7915.12431

Ebrahim, A., Lerman, J. A., Palsson, B. O., and Hyduke, D. R. (2013). COBRApy: COnstraints-based reconstruction and analysis for python. *BMC Syst. Biol.* 7:74. doi: 10.1186/1752-0509-7-74

Fei, Q., Guarnieri, M. T., Tao, L., Laurens, L. M., Dowe, N., and Pienkos, P. T. (2014). Bioconversion of natural gas to liquid fuel: opportunities and challenges. *Biotechnol. Adv.* 32, 596–614. doi: 10.1016/j.biotechadv.2014.03.011

Fernandez-Naveira, A., Veiga, M. C., and Kennes, C. (2017). H-B-E (hexanol-butanol-ethanol) fermentation for the production of higher alcohols from syngas/waste gas. *J. Chem. Technol. Biotechnol.* 92, 712–731. doi: 10.1002/jctb.5194

Green, E. M. (2011). Fermentative production of butanol–the industrial perspective. *Curr. Opin. Biotechnol.* 22, 337–343. doi: 10.1016/j.copbio.2011.02.004

Hadadi, N., and Hatzimanikatis, V. (2015). Design of computational retrobiosynthesis tools for the design of de novo synthetic pathways. *Curr. Opin. Chem. Biol.* 28, 99–104. doi: 10.1016/j.cbpa.2015.06.025

Haynes, C. A., and Gonzalez, R. (2014). Rethinking biological activation of methane and conversion to liquid fuels. *Nat. Chem. Biol.* 10, 331–339. doi: 10.1038/nchembio.1509

Henard, C. A., Smith, H., Dowe, N., Kalyuzhnaya, M. G., Pienkos, P. T., and Guarnieri, M. T. (2016). Bioconversion of methane to lactate by an obligate methanotrophic bacterium. *Sci. Rep.* 6:21585. doi: 10.1038/srep21585

Hu, P., Chakraborty, S., Kumar, A., Woolston, B., Liu, H., Emerson, D., et al. (2016). Integrated bioprocess for conversion of gaseous substrates to liquids. *Proc. Natl. Acad. Sci. U.S.A.* 113, 3773–3778. doi: 10.1073/pnas.1516867113

Huang, Y., Zhong, C., Lin, H. X., and Wang, J. (2017). A method for finding metabolic pathways using atomic group tracking. *PLoS ONE* 12:e0168725. doi: 10.1371/journal.pone.0168725

Knittel, K., and Boetius, A. (2009). Anaerobic oxidation of methane: progress with an unknown process. *Annu. Rev. Microbiol.* 63, 311–334. doi: 10.1146/annurev.micro.61.080706.093130

Köpke, M., Mihalcea, C., Bromley, J. C., and Simpson, S. D. (2011a). Fermentative production of ethanol from carbon monoxide. *Curr. Opin. Biotechnol.* 22, 320–325. doi: 10.1016/j.copbio.2011.01.005

Köpke, M., Mihalcea, C., Liew, F., Tizard, J. H., Ali, M. S., Conolly, J. J., et al. (2011b). 2,3-butanediol production by acetogenic bacteria, an alternative route to chemical synthesis, using industrial waste gas. *Appl. Environ. Microbiol.* 77, 5467–5475. doi: 10.1128/AEM.00355-11

Lackey, J. C., Peppley, B., Champagne, P., and Maier, A. (2015). Composition and uses of anaerobic digestion derived biogas from wastewater

treatment facilities in North America. *Waste Manag. Res.* 33, 767–771. doi: 10.1177/0734242X15589781

Lee, S. Y., Park, J. H., Jang, S. H., Nielsen, L. K., Kim, J., and Jung, K. S. (2008). Fermentative butanol production by Clostridia. *Biotechnol. Bioeng.* 101, 209–228. doi: 10.1002/bit.22003

Lessner, D. J., Li, L., Li, Q., Rejtar, T., Andreev, V. P., Reichlen, M., et al. (2006). An unconventional pathway for reduction of CO2 to methane in CO-grown Methanosarcina acetivorans revealed by proteomics. *Proc. Natl. Acad. Sci. U.S.A.* 103, 17921–17926. doi: 10.1073/pnas.0608833103

Long, M. R., Ong, W. K., and Reed, J. L. (2015). Computational methods in metabolic engineering for strain design. *Curr. Opin. Biotechnol.* 34, 135–141. doi: 10.1016/j.copbio.2014.12.019

Lopez, J. C., Quijano, G., Souza, T. S., Estrada, J. M., Lebrero, R., and Munoz, R. (2013). Biotechnologies for greenhouse gases (CH(4), N(2)O, and CO(2)) abatement: state of the art and challenges. *Appl. Microbiol. Biotechnol.* 97, 2277–2303. doi: 10.1007/s00253-013-4734-z

Mahadevan, R., and Schilling, C. H. (2003). The effects of alternate optimal solutions in constraint-based genome-scale metabolic models. *Metab. Eng.* 5, 264–276. doi: 10.1016/j.ymben.2003.09.002

Martin, M. E., Richter, H., Saha, S., and Angenent, L. T. (2016). Traits of selected Clostridium strains for syngas fermentation to ethanol. *Biotechnol. Bioeng.* 113, 531–539. doi: 10.1002/bit.25827

Mueller, T. J., Grisewood, M. J., Nazem-Bokaee, H., Gopalakrishnan, S., Ferry, J. G., Wood, T. K., et al. (2015). Methane oxidation by anaerobic archaea for conversion to liquid fuels. *J. Ind. Microbiol. Biotechnol.* 42, 391–401. doi: 10.1007/s10295-014-1548-7

Nazem-Bokaee, H., Gopalakrishnan, S., Ferry, J. G., Wood, T. K., and Maranas, C. D. (2016). Assessing methanotrophy and carbon fixation for biofuel production by Methanosarcina acetivorans. *Microbial Cell Factories* 15, 1–13. doi: 10.1186/s12934-015-0404-4

Nazem-Bokaee, H., and Senger, R. S. (2015). ToMI-FBA: A genome-scale metabolic flux based algorithm to select optimum hosts and media formulations for expressing pathways of interest. *AIMS Bioeng.* 2, 335–374. doi: 10.3934/bioeng.2015.4.335

Nazem-Bokaee, H., Yan, Z., Maranas, C. D., and Ferry, J. G. (2018). "The biochemistry and physiology of respiratory-driven reversed methanogenesis," in *Methane Biocatalysis: Paving the Way to Sustainability*, eds M. G. Kalyuzhnaya and X. H. Xing, (Cham: Springer International Publishing), 183–197.

Noor, E., Eden, E., Milo, R., and Alon, U. (2010). Central carbon metabolism as a minimal biochemical walk between precursors for biomass and energy. *Mol. Cell* 39, 809–820. doi: 10.1016/j.molcel.2010.08.031

Orphan, V. J., House, C. H., Hinrichs, K. U., McKeegan, K. D., and DeLong, E. F. (2001). Methane-consuming archaea revealed by directly coupled isotopic and phylogenetic analysis. *Science* 293, 484–487. doi: 10.1126/science.1061338

Orth, J. D., Thiele, I., and Palsson, B. O. (2010). What is flux balance analysis? *Nat. Biotechnol.* 28, 245–248. doi: 10.1038/nbt.1614

Rother, M., and Metcalf, W. W. (2004). Anaerobic growth of Methanosarcina acetivorans C2A on carbon monoxide: an unusual way of life for a methanogenic archaeon. *Proc. Natl. Acad. Sci. U.S.A.* 101, 16929–16934. doi: 10.1073/pnas.0407486101

Schellenberger, J., Que, R., Fleming, R. M., Thiele, I., Orth, J. D., Feist, A. M., et al. (2011). Quantitative prediction of cellular metabolism with constraint-based models: the COBRA Toolbox v2.0. *Nat. Protoc.* 6, 1290–1307. doi: 10.1038/nprot.2011.308

Scheller, S., Yu, H., Chadwick, G. L., McGlynn, S. E., and Orphan, V. J. (2016). Artificial electron acceptors decouple archaeal methane oxidation from sulfate reduction. *Science* 351, 703–707. doi: 10.1126/science.aad7154

Simpson, S. D., Collet, C., Forster, R. L. S., Cockrem, M. C. M., Oakley, S. D., and Kopke, M. (2010). *Carbon Capture in Fermentation*. US Patent US20100323417 A1.

Soo, V. W., McAnulty, M. J., Tripathi, A., Zhu, F., Zhang, L., Hatzakis, E., et al. (2016). Reversing methanogenesis to capture methane for liquid biofuel precursors. *Microb. Cell Fact.* 15:11. doi: 10.1186/s12934-015-0397-z

Steynberg, A. P. (2004). Introduction to Fischer-Tropsch technology. *Fischer-Tropsch Technol.* 152, 1–63. doi: 10.1016/S0167-2991(04)80458-0

Strong, P. J., Xie, S., and Clarke, W. P. (2015). Methane as a resource: can the methanotrophs add value? *Environ. Sci. Technol.* 49, 4001–4018. doi: 10.1021/es504242n

Subramani, V., and Gangwal, S. K. (2008). A review of recent literature to search for an efficient catalytic process for the conversion of syngas to ethanol. *Energy Fuels* 22, 814–839. doi: 10.1021/ef700411x

Tracy, B. P., Jones, S. W., Fast, A. G., Indurthi, D. C., and Papoutsakis, E. T. (2012). Clostridia: the importance of their exceptional substrate and metabolite diversity for biofuel and biorefinery applications. *Curr. Opin. Biotechnol.* 23, 364–381. doi: 10.1016/j.copbio.2011.10.008

Tran, L. P., and Simpson, S. D. (2015). *Fermentation Process*. US Patent US20130065282 A1.

Williams, T. C., Shaddix, C. R., and Schefer, R. W. (2007). Effect of syngas composition and CO2-diluted oxygen on performance of a premixed swirl-stabilized combustor. *Combust. Sci. Technol.* 180, 64–88. doi: 10.1080/00102200701487061

Worden, R. M., Grethlein, A. J., Jain, M. K., and Datta, R. (1991). Production of butanol and ethanol from synthesis gas via fermentation. *Fuel* 70, 615–619. doi: 10.1016/0016-2361(91)90175-A

Yan, Z., and Ferry, J. G. (2018). Electron Bifurcation and Confurcation in Methanogenesis and Reverse Methanogenesis. *Front Microbiol.* 9:1322. doi: 10.3389/fmicb.2018.01322

Yan, Z., Joshi, P., Gorski, C. A., and Ferry, J. G. (2018). A biochemical framework for anaerobic oxidation of methane driven by Fe(III)-dependent respiration. *Nat. Commun.* 9:1642. doi: 10.1038/s41467-018-04097-9

Yan, Z., Wang, M., and Ferry, J. G. (2017). A Ferredoxin- and F420H2-dependent, electron-bifurcating, heterodisulfide reductase with homologs in the domains bacteria and archaea. *MBio* 8:e02285-16. doi: 10.1128/mBio.02285-16

**Conflict of Interest Statement:** The authors declare that the research was conducted in the absence of any commercial or financial relationships that could be construed as a potential conflict of interest.

frontiers in Microbiology

ORIGINAL RESEARCH
published: 10 October 2019
doi: 10.3389/fmicb.2019.02323

# Alteration of Methanogenic Archaeon by Ethanol Contribute to the Enhancement of Biogenic Methane Production of Lignite

*Xiuqing Yang[1]*, Qi Liang[1], Yanmei Chen[1] and Baoyu Wang[2,3]*

*[1] Key Laboratory of Chemical Biology and Molecular Engineering of the Ministry of Education, Institute of Biotechnology, Shanxi University, Taiyuan, China, [2] State Key Laboratory of Coal and CBM Co-Mining, Jincheng, China, [3] Yi'an Lanyan Coal and Coalbed Methane Simultaneous Extraction Technology Co., Ltd., Jincheng, China*

Bioconverting coal to methane is a green and environmental friendly method to reuse waste coal. In this study, heterologous bacteria were used for the gas-producing fermentation of lignite under laboratory conditions, simultaneously, different concentrations of ethanol added into the culture to investigate the effect of ethanol on gas production and microbial flora structure. Results show that when the ethanol concentration was 1%, the best methanogenesis was achieved at 44.86 mL/g, which was twice the gas production of 0% ethanol. Before and after gas fermentation, the composition and structure of the coal changed, the volatile matter and fixed carbon increased, and the ash decreased. The absorbance value at characteristic peaks of all functional groups decreased, new peaks were generated at 2,300/cm, and the peak value disappeared at 3,375/cm. Thus, microorganisms interacted with coal, consumed it, and produced new materials. The microbial flora changes during gas production were tracked in real time. 0.5 and 1% ethanol did not obviously change the bacterial communities but strongly influenced the archaeon communities, thereby changed the methane production pathway. In the absence of ethanol, *Methanosarcina* was continuously increasing with the extension of fermentation time, this pathway was the nutrient type of acetic acid. When ethanol was added, *Methanobacterium* gradually increased, the pathway was mainly hydrotropic type. In summary, adding ethanol can increase the coalbed methane production, change the structure and composition of coal, and facilitate the interaction of microbe with coal. Therefore, the methanogenic archaeon changes could help improve the methane-producing ability of lignite in the presence of ethanol.

**Keywords: coalbed methane (CBM), ethanol, enhanced biogenic methane, microbial community, physicochemical property**

OPEN ACCESS

***Edited by:***
*Bradley M. Tebo, Oregon Health & Science University, United States*

***Reviewed by:***
*Karen Budwill, Alberta Innovates, Canada*
*Surakasi Venkata Prasad, Prolog Biologicals Pvt. Ltd., India*

****Correspondence:***
*Xiuqing Yang*
*xiuqyang@sxu.edu.cn*

***Specialty section:***
*This article was submitted to Microbiological Chemistry and Geomicrobiology, a section of the journal Frontiers in Microbiology*

***Received:*** *21 December 2018*
***Accepted:*** *23 September 2019*
***Published:*** *10 October 2019*

***Citation:***
*Yang X, Liang Q, Chen Y and Wang B (2019) Alteration of Methanogenic Archaeon by Ethanol Contribute to the Enhancement of Biogenic Methane Production of Lignite. Front. Microbiol. 10:2323. doi: 10.3389/fmicb.2019.02323*

## INTRODUCTION

Coalbed methane (CBM) is an unconventional and self-preserving natural gas with methane as its main component. This gas has received considerable attention as a new type of clean energy. China's CBM reserves are next to Russia and Canada, ranking third worldwide. Although abundant, CBM has low extraction and utilization rates due to the long-term unreasonable mining in the early stage. These unfavorable factors limit the development of the CBM industry.

To fully utilize CBM resources, researchers have developed considerably numerous CBM technologies. The microbial stimulation of CBM technology has emerged among many because of its environmental protection and pollution free characteristics. Many methods can be used to increase CBM by using microorganisms. Adding nutrients such as main minerals, trace metals, and vitamins to the coal seam stimulates the microbial flora to metabolize coal for methane production (Ünal et al., 2012; Fallgren et al., 2013; Zhang et al., 2016b). Microbial activity can also be increased by adding new or additional microorganisms to enhance CBM production (Jones et al., 2008). In addition, microorganisms can further interact with coal by changing the fermentation environment, such as changing pH, temperature, and particle size of coal (Green et al., 2008; Gupta and Gupta, 2014).

As a non-toxic and inexpensive organic material, ethanol has attracted the attention of researchers. Bi et al. (2017) enhanced microbial activity by finding the best nutrient-based formula. The authors added surfactants (Tween-20 and SDS), organic solvents (ethanol, methanol, and isopropanol), and carbon sources (sodium formate and sodium acetate) to the culture medium to stimulate microbial activity; consequently, the three alcohols and sodium acetate were proven to be essential for maximizing the production of methane from coal (Bi et al., 2017). Ethanol has a statistically significant dose-dependent effect in increasing methane production. At 100 mM, ethanol increases methane yield by at least 24 times, but no further change was noted at 300 mM concentration (Zhang et al., 2016a). Similarly, Liu Y et al. discovered that when 5 or 10 mg of ethanol was added to 10 g of coal from Powder River Basin, the production of methane increased (Liu et al., 2013).

Since (Shimizu et al., 2007) first described the microbial community associated with CBM in Northern Japan, many studies on the microbial community of CBM have been reported. Ünal et al. (2012) found that the proper addition of trace elements could promote CBM production; the main methanogenic bacteria were *Methanobacterium subterraneum* and *Methanobacterium formicicum* after cultivation. Exogenous microorganisms could increase the production of CBM, and methane production correlates with the growth of *Methanosaeta concilii* (Jones et al., 2010). *Acetobacterium* spp., Bacteroidales, Firmicutes, *Methanolobus*, and *Methanosarcina* spp. were found in the coal seam water of Cook Bay, Alaska, United States (Dawson et al., 2012). Fuertez et al. (2018) found that *Methanofollis* and *Methanobacterium* were dominant in the optimized methane-producing bacteria solution. Although the microbial structure of CBM is extensively studied, the relationship between the increase in methane production and microbial flora, especially the reason why ethanol stimulates the increase in methane yield, is seldom reported.

This paper describes a process for biogas generation from coal. Small amounts of ethanol were added to a medium transforming coal to methane. This study aims to investigate the following: (1) the effect of adding ethanol on methane production, (2) the changes in the physical properties of coal during bioconversion, and (3) the bacterial and archaeon community changes before and after adding ethanol and the changes of gas production pathways.

# MATERIALS AND METHODS

## Coal and Microflora Samples

The lignite samples were collected from the Shengli coal mine located in Xilinhot City, Inner Mongolia. The coal briquettes were crushed and sieved to prepare coal powder with a particle size of 180–250 μm (60–80 mesh), vacuum-dried at 80°C for 24 h, and placed in a desiccator for use.

The coal formation water was collected from CBM production wells in the Sihe mine (Jincheng, China) of Qinshui Basin. Enrichment experiments in triplicate were performed for approximately 3 months. The enrichment culture was used as the inoculation source of this study. The specific method is the same as that of Yang et al. (2018).

## Experimental Setup and Operation

Twelve microcosms (500 mL bottle) were established. Each microcosm contained 20 g of coal, 250 mL of the medium and 50 mL of inoculum. The 12 bottles were divided into four groups, and three parallels in each group. The first, second, third and the fourth group, were added with ethanol at 0 (0%, V/V), 1.5 (0.5%, V/V), 3.0 (1.0%, V/V), and 6.0 mL (2.0%, V/V), respectively, and named them group A, group B, group C, and group D in turn.

In addition, a blank control group was created in which no coal was added, but added with ethanol at 3.0 mL (0%, V/V) and the other conditions were the same, and named it group coal-free, and three parallels in this group. All bottles were purged with nitrogen completely and then incubated at 30°C under static conditions. The medium contained the following (in g/L): yeast extract, 2.0 g; $KH_2PO_4$, 1.5 g; $K_2HPO_4$, 2.9 g; $MgCl_2$, 0.4 g; $NH_4Cl$, 1.8 g; cysteine, 3.0 g; resazurin, (0.2%) 2 mL; and trace element solution, 10 mL, pH = 7.0. The trace element solution formula is as follows: Nitrilotriacetic acid, 1.5 g; $CaCl_2$, 0.1 g; $MgSO_4{\cdot}7H_2O$, 3.0 g; $H_3BO_3$, 0.05 g; $FeSO_4$, 0.1 g; NaCl, 1.0 g; $COCl_2$, 0.1 g; $MnSO_4$, 0.5 g; $ZnSO_4$, 0.1 g; $NaMO_4$, 0.05 g; $AlK(SO_4)_2$, 0.01 g; $NiCl_2$, 0.1 g; and $CuSO_4$, 0.01 g. The samples were continuously cultured for approximately 3 months, and from the 28th day, samples were prepared for DNA extraction. On days 7, 14, 20, 28, 35, 42, 49, 60, 86, and 92, the concentration of $CH_4$ in the headspace was measured by gas chromatography (GC) in microcosms.

## Gas Composition Determination

Gas composition and content during gas fermentation were analyzed by the American Agilent GC-7890 gas chromatograph. Chromatographic parameters included the following: Agilent-Carbon PLOT column (60 m × 320 μm × 0.25 μm); the chromatographic inlet temperature was 150°C; the septum purge flow was 3 mL/min; the column oven temperature was 25°C, which was maintained for 7.5 min; the detector TCD temperature was 200°C, the injection volume was 0.5 mL, and the carrier gas was high-purity nitrogen.

## Ultimate, Proximate, and FTIR Analyses of the Coal Samples

Coal powder with a particle size of 180–250 μm was used for ultimate, proximate, and FTIR analyses after freeze drying. Ultimate and proximate analyses of the coal samples on a dry basis were completed by the Shanxi Institute of Coal Chemistry, Chinese Academy of Sciences. The proximate analysis was performed according to GB/T212-2001 (National Standards of China, 2001), whereas the ultimate analysis was performed according to GB/T476-2001 (National Standards of China, 2001).

An IR Prestige-21 IR Analyzer (Shimadzu, Japan) was used to monitor the alterations in chemical bonds in the coal, with the KBr pellet method used in the mid IR region (4000–400/cm). KBr pellets were made from 0.0250 g of coal samples and 2.000 g of KBr after accurate weighing and were mixed and powdered in an agate mortar at 80 kN. Interfering background bands in KBr were quantified with a pure KBr pellet and subsequently subtracted from the spectra of samples by using the Shimadzu IR solution software. Each spectrum resulted from the average of 10 scans recorded in the 4000–400/cm spectral range with a resolution of 4/cm. The measurement mode was an interferogram.

## DNA Extraction

The changes in the microbial community structure during coal bioconversion in different ethanol contents were analyzed. Microorganisms were sampled at the 0 day and 28th, 35th, 42nd, 49th, 60th, 86th, and 92nd day (named as 0, 28, 35, 42, 49, 60, 86, and 92, respectively) of processing in microcosms of group A, group B and group C. Total DNA was extracted from samples by using the Power Soil DNA Isolation Kit (MO BIO Laboratories, Carlsbad, CA, United States) according to the manufacturer's protocol. DNA quality and quantity were assessed by the ratios of 260 nm/280 nm and 260 nm/230 nm, respectively. The extracted genomic DNA was detected in 0.7% agarose gel to ensure size and integrity. DNA was stored at −80°C until further use.

## Amplification of 16S rRNA Genes

The extracted genomic DNA was used as a template for the PCR amplification of bacterial and archaeal 16S rRNA genes. The V3–V4 variable regions of the bacterial 16S rRNA genes were amplified by the primer pair forward primer 338F (5′-ACTCCTACGGGAGGCAGCA-3′) and reverse primer 806R (5′-GGACTACHVGGGTWTCTAAT-3′). The sequence of the archaeal V3-V4 region was amplified using the forward primer Arch349F (5′-GYGCASCAGKCGMGAAW-3′) and the reverse primer Arch806R (5′-GGACTACVSGGGTATCTAAT-3′). PCR amplification was performed in a total volume of 50 μL, which contained 10 μL of Buffer, 0.2 μL of Q5 high-fidelity DNA polymerase, 10 μL of high GC enhancer, 1 μL of dNTP, 10 μM of each primer, and 60 ng of genome DNA. Thermal cycling conditions were as follows: an initial denaturation at 95°C for 5 min, followed by 15 cycles at 95°C for 1 min, 50°C for 1 min, and 72°C for 1 min, with a final extension at 72°C for 7 min. The PCR products from the first-step PCR were purified through VAHTSTM DNA clean beads. A second-round PCR was then performed in a 40 μL reaction that contained 20 μL of 2 × Phusion HF Master Mix, 8 μL of $ddH_2O$, 10 μM of each primer, and 10 μL of PCR products from the first step. Thermal cycling conditions were as follows: an initial denaturation at 98°C for 30 s, followed by 10 cycles at 98°C for 10 s, 65°C for 30 s, and 72°C for 30 s, with a final extension at 72°C for 5 min. Finally, all PCR products were quantified by Quant-iT$^{TM}$ dsDNA HS reagent and then pooled together. The amplification systems and methods of bacteria and archaea were the same, except for the different primers. The qualities of the amplified PCR products were checked through electrophoresis in 1% agarose gel. High-throughput sequencing analysis of genes was performed on the purified, pooled PCR products using the Illumina Hiseq 2500 platform (2 × 250 paired ends) at Biomarker Technologies Corporation, Beijing, China.

## High-Throughput Sequencing and Analysis

After sequencing, FLASH v1.2.7 software was used to splice the reads of each sample, followed by Trimmomatic v0.33 software to filter the spliced raw tags to obtain high-quality tag data, and finally, UCHIME v4.2 Software to identify and remove chimeric sequences to obtain the final valid high-quality sequence. Further, UCLUST in QIIME (v. 1.8.0) software was used to cluster high-quality sequences at 97% similarity level, obtain OTU, and perform species annotation and abundance analysis. On the basis of the OTU number results, the bio-α diversity (including Chao1 value, ACE value, Shannon index, and Simpson index) and β-diversity of the sample were evaluated.

## Acquisition of Serial Number

The Illumina sequencing data were submitted to the Sequence Read Archive (SRA) of the National Center for Biotechnology Information (NCBI). The accession number is SRS3948544.

# RESULTS

## Effects of Different Concentration of Ethanol on Methane Production

The impact of different concentration of ethanol on the methane production is shown in **Figure 1**. As illustrated, the gas production process can be roughly divided into three stages: the first stage (0–40 days) of slow growth, the second stage (40–60 days) of rapid growth, and the third stage (60–90 days) of restrained growth. This observation is consistent with the conclusion drawn by Fuertez et al. (2018). In the first stage, the microflora needed to adapt to the new environment and their number was fewer, so less gas was produced (Take group C as an example, the cumulative methane production was 4.2 mg/g). In the second stage, gas production reached its peak (Take group C as an example, the cumulative methane production was 20.9 mg/g). The gas production of the experimental groups with added ethanol was significantly higher than that of the group A. In particular, the gas production of the group C was as high as 1332.06 μmol/g. Thus, adding ethanol obviously promoted the generation of biogas. On the third stage, the gas production

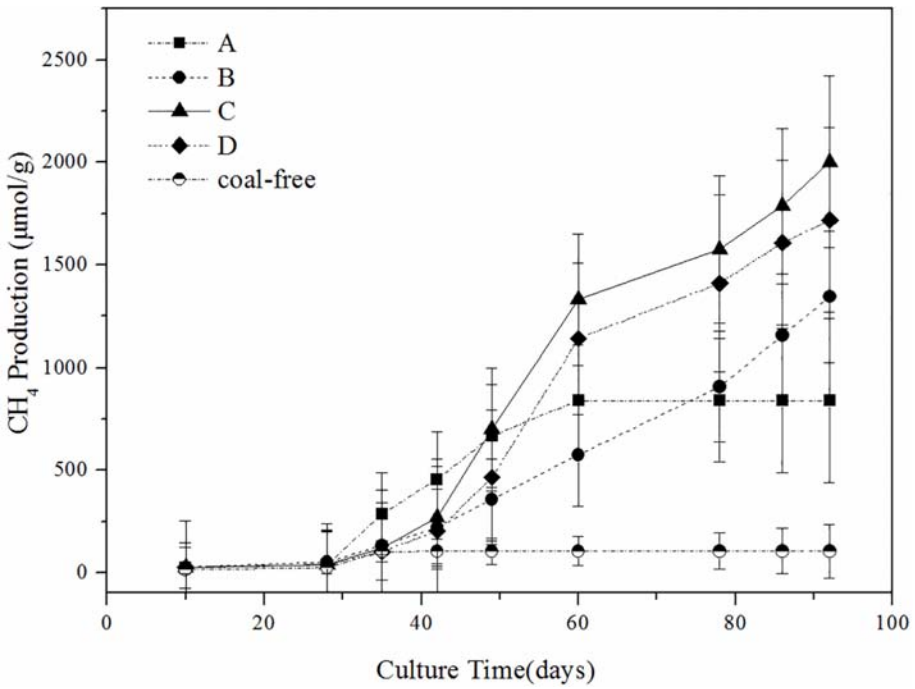


**FIGURE 1 |** Influence of different ethanol contents on methane production. A: no added ethanol, B: with added 0.5% ethanol, C: with added 1% ethanol, D: with added 2% ethanol, coal-free: no added coal. Error bars indicate the standard deviation of three parallel samples.

tended to increase slowly, possibly because many inhibitors were produced during the fermentation, thereby restricting the formation of methane (Ma et al., 2015). On the 92nd day of gas-producing fermentation, the cumulative methane production of ethanol content at 0, 0.5, 1, and 2% was 839.68, 1344.56, 2002.55, and 1718.64 μmol/g, respectively. So in terms of gas production, adding 1% ethanol was the best. The coal-free control group produced almost no methane, so it can confirmed that the methane produced in the experimental group comes from coal rather than added compounds in the microcosms.

## Proximate and Elemental Analysis

The coal samples were characterized by approximate and elemental analysis, as shown in **Table 1**. Raw coal samples contained approximately 13.22% water, 35.90% ash, 26.76% volatile substances, and 24.12% fixed carbon. Compared with raw coal samples, volatiles increased from 26.76 to 31.20%, even reached 33.75% in group C samples after gas fermentation, and the ash content fell from 35.90 to 25.14%. We speculated that the microbial community utilized coal as a substrate to generate some easily decomposed and oxidized organic matter, such as organic acids, aromatic hydrocarbons, alcohols, and carbohydrates. After the gas fermentation, the fixed carbon content increased to 28.31%, suggesting that microorganisms metabolized with coal as a carbon source and produced organic matter, which was then attached to coal particles. Oxygen content increased to 14.26%. Oxygen was the most abundant heteroatom, and the oxygen atoms in coal were connected by bonds such as ether, ester, carbonyl, and hydroxyl (Chen et al., 2017). The hydrogen, nitrogen, and sulfur contents did not remarkably change. In general, the proximate analysis and the element composition of coal before and after fermentation were significantly different, whereas the difference between the group C samples and the group A samples was obscure. Thus, the change of physical and chemical properties of coal was mainly affected by anaerobic fermentation.

**TABLE 1 |** Proximate and elemental composition of coal samples.

| Analysis of proximate and elemental | Coal (lignite) | | |
|---|---|---|---|
| | Raw coal | Group A | Group C |
| Moisture% | 13.22 | 15.35 | 14.66 |
| Ash% | 35.90 | 25.14 | 25.42 |
| Volatile matter% | 26.76 | 31.20 | 33.75 |
| Fixed carbon% | 24.12 | 28.31 | 26.17 |
| Carbon% | 35.81 | 40.05 | 40.23 |
| Hydrogen% | 2.73 | 2.82 | 2.83 |
| Nitrogen% | 0.50 | 0.88 | 0.80 |
| Sulfur% | 1.29 | 1.50 | 1.36 |
| Oxygen% | 10.55 | 14.26 | 14.70 |

## FTIR Characterization of the Coal Samples

Samples of raw coal, control (group A) and experimental groups (added ethanol-fermented samples) were selected for FTIR spectrum characterization, as shown in **Figure 2**. After

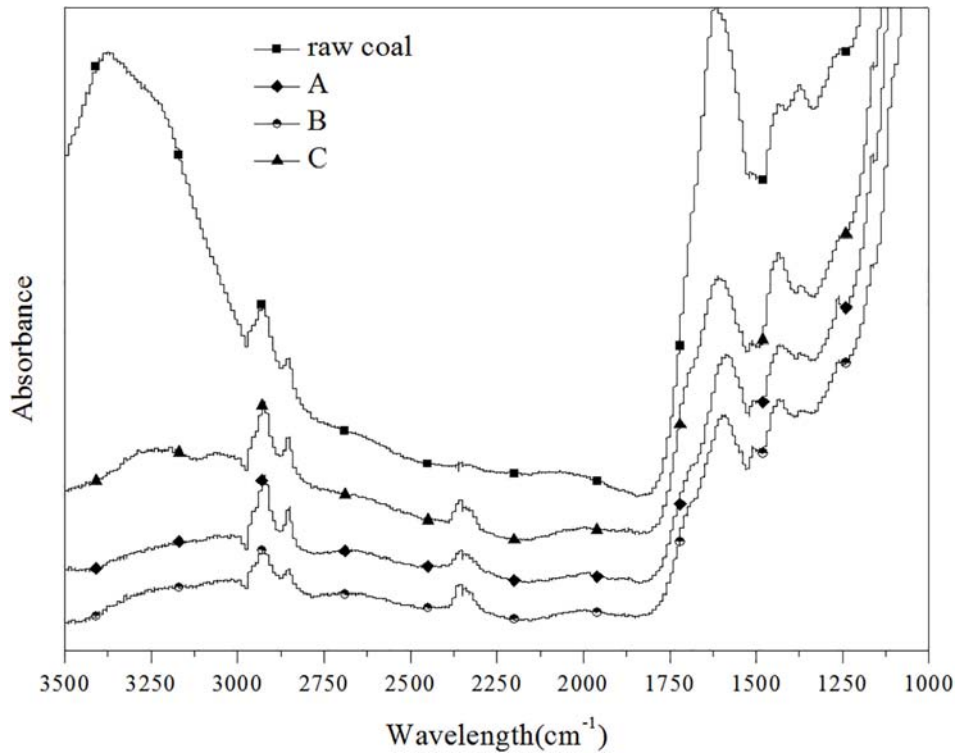


**FIGURE 2 |** FTIR spectra in the range of 3,500–1,000/cm for lignite coal sample (raw coal, A, B, C).

anaerobic fermentation, compared with raw coal, the structure of coal in the control (without ethanol) and experimental group changed significantly. However, there was no structural difference between the control group and the experimental group. The peak heights and peak areas of different coal samples were different, but the approximate peak shapes were the same, indicating that they contained similar functional groups. The structural composition of lignite can be described by alkyl-C, aromatic-C, carbonyl-C, and O-alkyl-C contents (Haq et al., 2018). The characteristic peaks in the IR spectrum were mainly divided into three categories: (1) Aromatic hydrocarbon: The peak at 2,919/cm was related to the stretching vibration of aromatic C-H bond; 1,600/cm was the characteristic absorption peak of the aromatic ring. (2) Aliphatic hydrocarbons: The peaks at 2,856 and 1,440/cm were respectively related to the symmetrical and asymmetric bending vibration of the alkane C-H bond. (3) Oxygen-containing functional group: The peak at 3,375/cm represented the stretching vibration of the O-H bond of fatty alcohol and phenol, and 1,230/cm represented the stretching vibration of phenol and ether C-O bond. As generally known, -O-$CH_3$ is the basic structural unit of coal (Strąpoć et al., 2011; Colosimo et al., 2016). After the biogas fermentation, the absorbance at all peaks decreased, indicating that the coal was consumed by the action of microorganisms, and the substances in the coal were utilized by the microorganisms. Two special peaks, that is, 3,375 and 2,300/cm, were considered. The peak at 3,375/cm clearly disappeared, suggesting that microorganisms can utilize aromatic hydrocarbons and long-chain fatty alcohols. A new peak appeared at 2,300/cm, which represented the asymmetric stretching vibration of the triple bond and the cumulative double bond, indicating that new small molecules, possibly an alkyne or an olefin, were produced during the gas fermentation process. The results suggested that the change in the structure of coal was mainly affected by anaerobic fermentation rather than by adding ethanol.

## High-Throughput Sequencing Analysis

High-throughput sequencing results showed that 2,522,076 high-quality sequences of 40 bacteria samples and 2,094,651 high-quality sequences of 40 archaea samples were obtained. The bacterial flora OTU was counted as 283, and the archaea flora OTU was counted as 22. All reads were deposited in the SRA of NCBI with the accession number SRS3948544.

## Characterization of Microbial Community Structure

For convenient data analysis, we presented the sequencing results after the randomly selected samples. The bacterial microbial community was mainly composed of Firmicutes, Proteobacteria, and Bacteroidetes at the phylum level during the gas-producing fermentation process (**Supplementary Figure S1**). As shown in **Figure 3**, from the community abundance analysis of bacterial genus, the main bacteria included *Proteus*, *Desulfovibrio*, *Macellibacteroides*, *Paraclostridium*, *Citrobacter*, *Enterococcus*, and *Tyzzerella*. With the extension of fermentation time, the

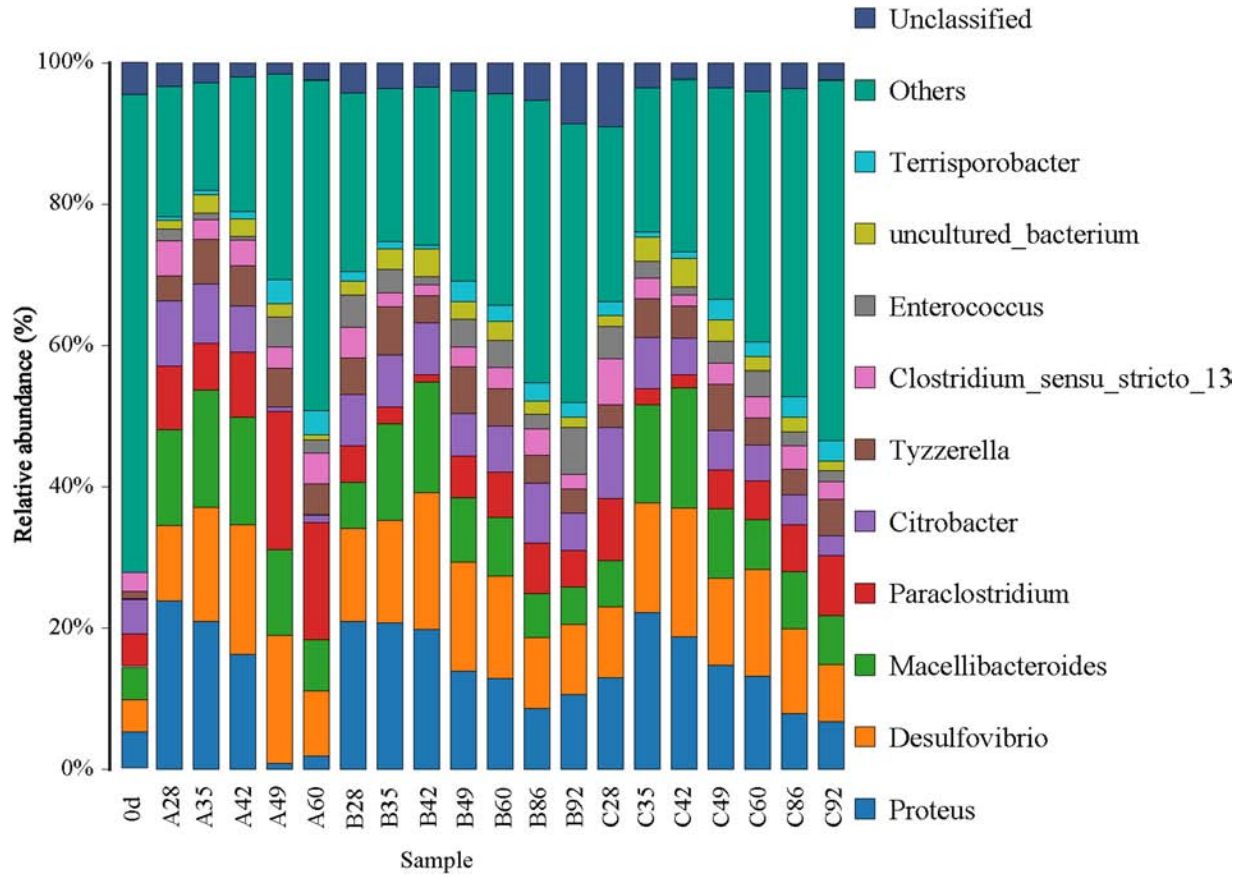


**FIGURE 3 |** Bar chart of the relative abundance of the top 10 bacteria of each group in genus level.

changes of species trend in the experimental groups A, B, and C were similar. It is suggested that ethanol had little effect on the structure of bacterial flora. **Figure 4** shows that the archaea flora is mainly composed of *Candidatus*-Methanoplasma, *Methanobacterium*, *Methanosarcina*, and a small amount of *Methanofollis*. In the early stage of fermentation, *Methanosarcina* occupied a certain proportion in the control group, but it could hardly found in the experimental group. With the extension of fermentation time, the difference of the flora between the control group and the experimental group was obvious. *Methanosarcina* was a continuously increasing microorganism in the control group, however, it was *Methanobacterium* in the experimental group.

*Candidatus*-Methanoplasma dominated the advantage in the sample A28, gaining the percentage of 81.75%. As the fermentation time was prolonged, its percentage gradually decreased. After 60 days of fermentation, its percentage decreased to 13.66% (A60). Its content was decreasing with the prolonged fermentation time in groups A, B, and C. In group A, the percentage of *Methanosarcina* in A28 was 4.33%, that of *Methanosarcina* in A49 was 7.16%, and that of *Methanosarcina* in A60 was 46.55%. When the fermentation time was prolonged, *Methanosarcina* gradually became dominant. In groups B and C, *Methanobacterium* gradually became the dominant bacteria, with 46.80% in B92, and 64.92% in C92. Clearly, compared with group A, the pathway of methane formation in groups B and C was changed, which was caused by the addition of ethanol.

## Effect of Ethanol on Microbial Flora

RDA/CCA is a sorting method based on correspondence analysis and is mainly used to reflect the relationship between flora or sample and environmental factors. RDA/CCA analysis and mapping use the R language vegan package. The results of RDA/CCA analysis of species diversity between samples at the genus level are as follows. The RDA/CCA diagram of bacteria is shown in **Figure 5**, and the RDA/CCA diagram of archaea is shown in **Figure 6**. The relationship between points and points in the figure is represented by distance, and the closer the distance was, the more similar the sample was. The relationship between ray and another ray is represented by an included angle, obtuse angle represents negative correlation, and acute angle represents positive correlation.

The angle between the two environmental factors in the two graphs is an acute angle, indicating the positive correlation of the two environmental factors, namely, the addition of ethanol and the fermentation time. In the two figures, the distance between group B and group C is short, and the distribution is concentrated. Therefore, the sample composition of the

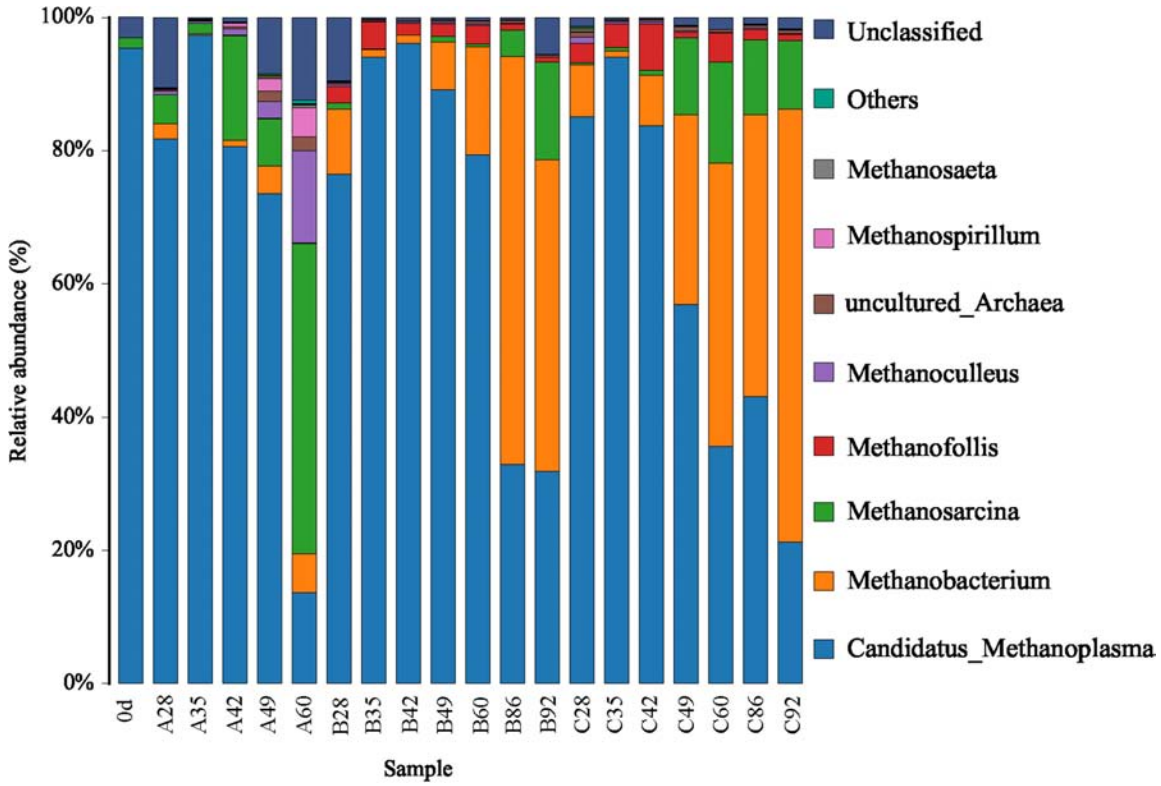


**FIGURE 4 |** Bar chart of the relative abundance of the top 10 archaea of each group in genus level.

added ethanol is similar according to bacterial and archaeal level analyses. As depicted in **Figure 5**, all of the bacterial microbial strains including *Citrobacter*, *Proteus*, *Desulfovibrio*, *Macellibacteroides*, *Enterococcus*, *Clostridium*, and *Tyzzerella*, and the environmental factor ethanol nearly presents an acute angle of rays, indicating a positive correlation between these bacteria and ethanol. Combined with the species distribution histogram of bacteria (**Figure 3**), the species composition of groups A, B, and C did not notably change, indicating that although the microbial flora positively correlated with ethanol, the effect was obscure.

From the RDA diagram of archaea (**Figure 6**), *Methanosarcina* was positively correlated with the fermentation time but negatively correlated with ethanol. This result is consistent with those shown in the distribution histogram of archaea (**Figure 4**). The *Methanosarcina* increased with the extension of fermentation time in group A, but not in groups B and C. A positive correlation existed between *Methanobacterium* and fermentation time, as well as ethanol. Combined with **Figure 4**, the effect of ethanol on *Methanobacterium* was far more powerful than that of the fermentation time.

## Correlation Analysis Between Gas Production and Microbial Flora

Cluster analysis of methanogenic flora with $CH_4$ yield, $CH_4$ content, and $CO_2$ content was performed. As shown in the **Figure 7**, two dominant types of microbial communities were clearly noted in the process of gas production, namely, *Methanobacterium* and *Methanosarcina*, which negatively correlated with *Candidatus*-Methanoplasma. Although the distribution histogram of archaea showed that *Candidatus*-Methanoplasma accounted for a large proportion of all samples (**Figure 4**), its presence did not help the production of methane gas. According to the above analysis, the addition of ethanol led to the differences in the structure of methanogenic community in the samples, and the *Methanobacterium* increased significantly. To further study *Candidatus*-Methanoplasma and *Methanobacterium* playing the role in the process of gas production, we made an intuitive analysis of the two bacterial populations, as shown in **Figure 8**. It showed the relationship between methane yield, ethanol content, and methanogenic community in all samples. The difference in bubble size was large in the figure, indicating that a large difference existed in methane production among the samples; the larger bubbles were clustered in the high position of *Methanobacterium* and in the low position of *Candidatus*-Methanoplasma, and their color belonged to the category of 1% ethanol content. Without the ethanol-added sample, bubbles were concentrated in the high position of *Candidatus*-Methanoplasma and in the low position of *Methanobacterium*, and they had smaller bubbles. With 0.5% ethanol-added sample, bubbles are gradually larger as the *methanobacterium* gradually increases. Results further indicated that the presence of *Candidatus*-Methanoplasma might

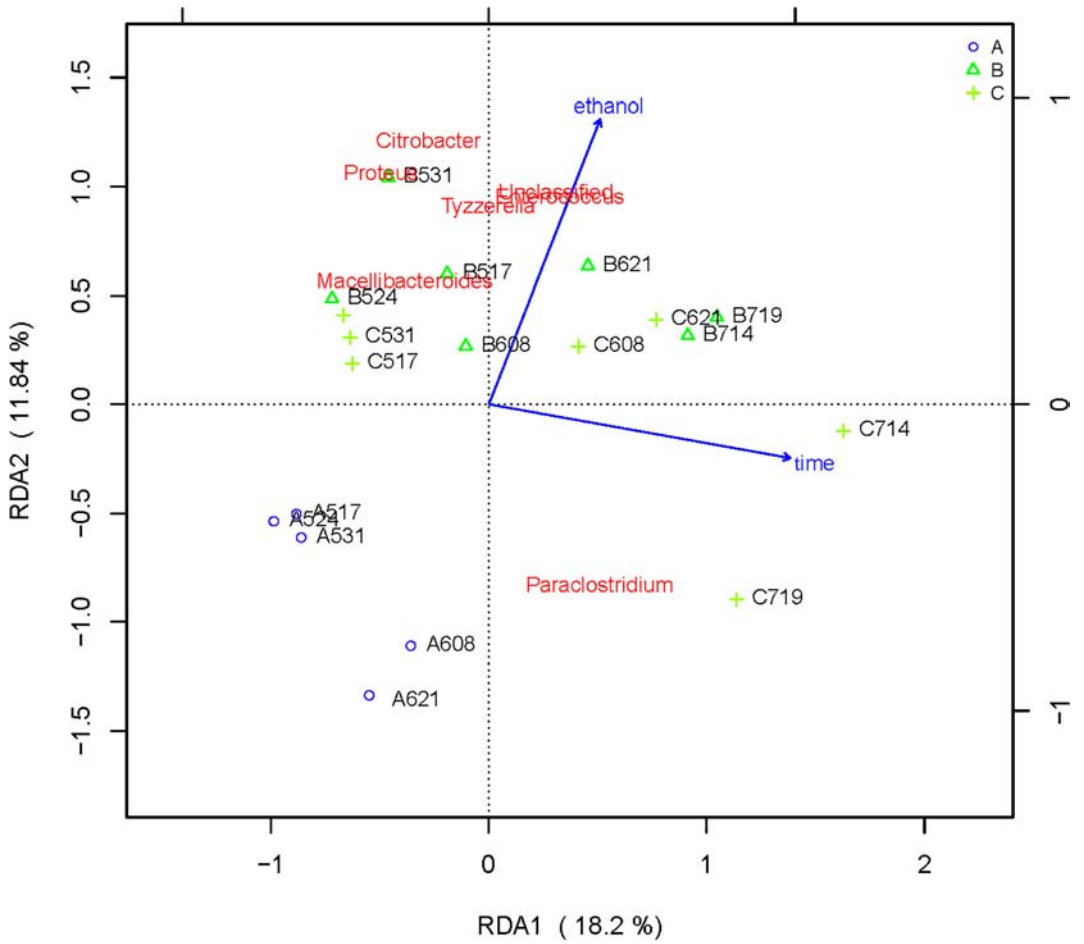


**FIGURE 5 |** Redundancy analysis shows the relationships between environmental variables and each sample at the bacterial flora level, Label: A no added ethanol, B with added 0.5% ethanol, C with added 1% ethanol. Red words represent microbial species, blue words represent environmental factors (ethanol and time).

not be conducive to the production of methane. Additionally, the presence of *Methanobacterium* was beneficial to the increase of gas production, and its positive effect was far greater than that of the negative effect of *Candidatus*-Methanoplasma.

## DISCUSSION

Microbial CBM production technology can produce new CBM and effectively alleviate energy stress. Scholars have performed many experimental studies on increasing CBM yield by optimizing gas production conditions from various aspects, such as culture temperature, pH of nutrient solution, coal granularity, solid–liquid ratio, and addition of different microelements, to achieve increased microbial CBM production (Ünal et al., 2012; Ghosh et al., 2014). As a kind of green, environment-friendly and cheap organic matter, ethanol is also used in CBM production. Some scholars stimulate microbial activity by adding ethanol, but other organic matters, such as methanol and isopropyl alcohol, are added at the same time (Bi et al., 2017). Such a case cannot be expressed qualitatively because of the increased production of CBM caused by the addition of ethanol, and possibly because of the interaction of ethanol with other substances. In this study, the composition of the medium was relatively single without adding other organics or surfactants, thereby allowing to better explore the role of ethanol. Most researchers are focused on the optimization of the conditions to increase CBM yield, but the changes in microbial flora structure during the optimization of gas production are poorly studied. In this current study, the changes of microbial flora were tracked in real time during the gas fermentation process. We found that the addition of ethanol led to significant changes in the methanogenic archaeon flora, thereby changing the gas production pathway.

This study once again confirmed the effect of ethanol on CBM production, and on the basis of previous studies, the mechanism of ethanol to increase methane production was more deeply studied. The results of biogenic gas experiment indicated that methane production in the experimental group was higher than that in the experimental group without ethanol. By comparison, the gas yield of 1% ethanol content was the highest, reaching up to 2002.55 μmol/g. The yield of methane was similar to that of Bi et al. (2017), and the yield increase

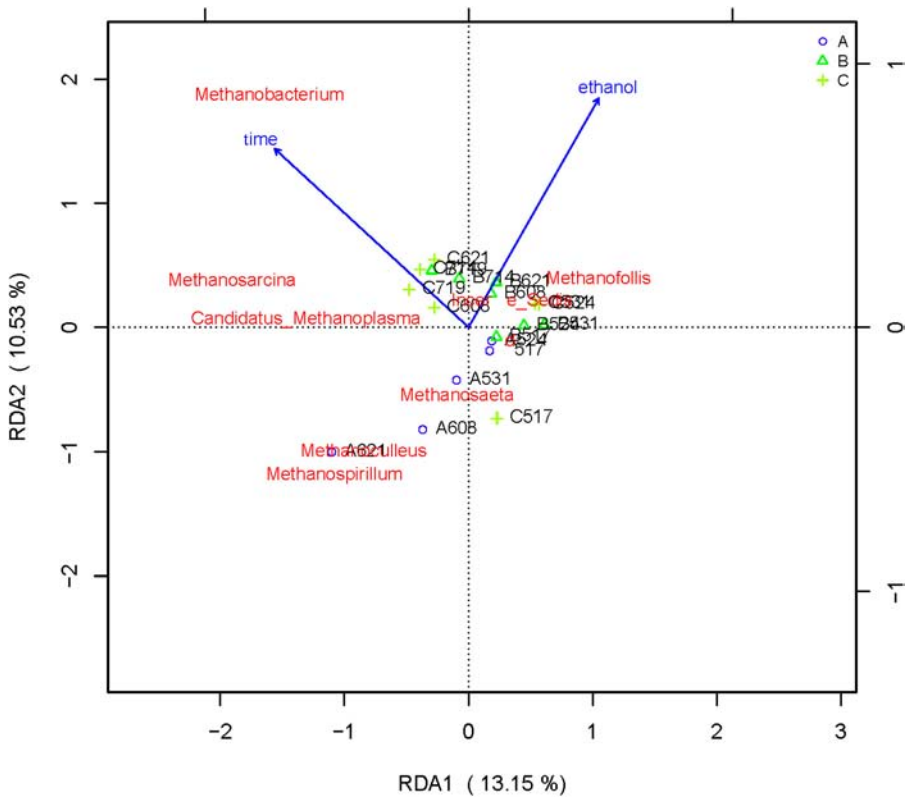


**FIGURE 6 |** Redundancy analysis shows the relationships between environmental variables and each sample at the archaea flora level, Label: A no added ethanol, B with added 0.5% ethanol, C with added 1% ethanol. Red words represent microbial species, blue words represent environmental factors (ethanol and time).

effect was also favorable. It was worth mentioning that methane production of the control was higher than that of the experiment groups B and C between days 30 and 50, it might be due to the microbial flora required a longer time to adapt to the environment with ethanol, which led to the phenomenon of the lag in producing methane in the experimental group in the early fermentation. In addition, from the change of $H_2$ content (**Supplementary Table S1**), it was hardly detected in the control group, while the presence of $H_2$ could be detected in the experimental group before 50 d. It is suggested that ethanol stimulated the production of $H_2$ in the initial stage. Since the 50th day *Methanobacterium* began to increase in the experimental group, which is a typical hydrotropic archaea that can use $H_2$ to produce methane. Due to the increase of quantity of *Methanobacterium*, it utilized $H_2$ accumulated in the earlier stage to produce more methane. Simultaneously, we also tracked the change in the number of flora in the whole gas generation stage through QPCR (**Supplementary Table S2**). The quantity of microflora increased with the extension of fermentation time. The quantity of flora in the experimental group with ethanol was more than that of control under the same fermentation time. It can be speculated that ethanol plays a role in stimulating microbial flora growth throughout the fermentation process. Although this study contained yeast extract and ethanol, it might provided a carbon source for bacterial growth. In the study of Zhang et al. (2019), it has been confirmed that the majority of methane was from the coal itself rather than the MS medium and added ethanol. The amount of ethanol added in the whole experiment had a limit, not the more the better. In Zhang et al. (2016a) experiment, he found that the best effect was achieved when the amount of ethanol was 100 mM, but the methane production was inhibited when the amount of ethanol was 300 mM.

In the analysis of physical and chemical properties of coal, the structure of coal changed greatly after fermentation, but it had no effect on the structure of coal after adding ethanol. In addition to stimulating microorganisms, ethanol played an important role as an organic solvent, which dissolved small biodegradable molecules in the coal matrix and enhanced their bioavailability (Takanohashi et al., 2000). It was only a physical change and would not lead to the changes in the coal structure. In this study, the microcosms contained 20 g coal, after fermentation for 90 daya, the average cumulated methane production of the experimental group with 1% ethanol was 897.2 mL, while that of the control group was 376.2 mL. Compared with the control group, although the methane production was more than double, the increased carbon content of methane only accounted for 1.86% of the total coal. It was conceivable that its impact on the overall structure of coal was negligible (**Supplementary Figure S2**).

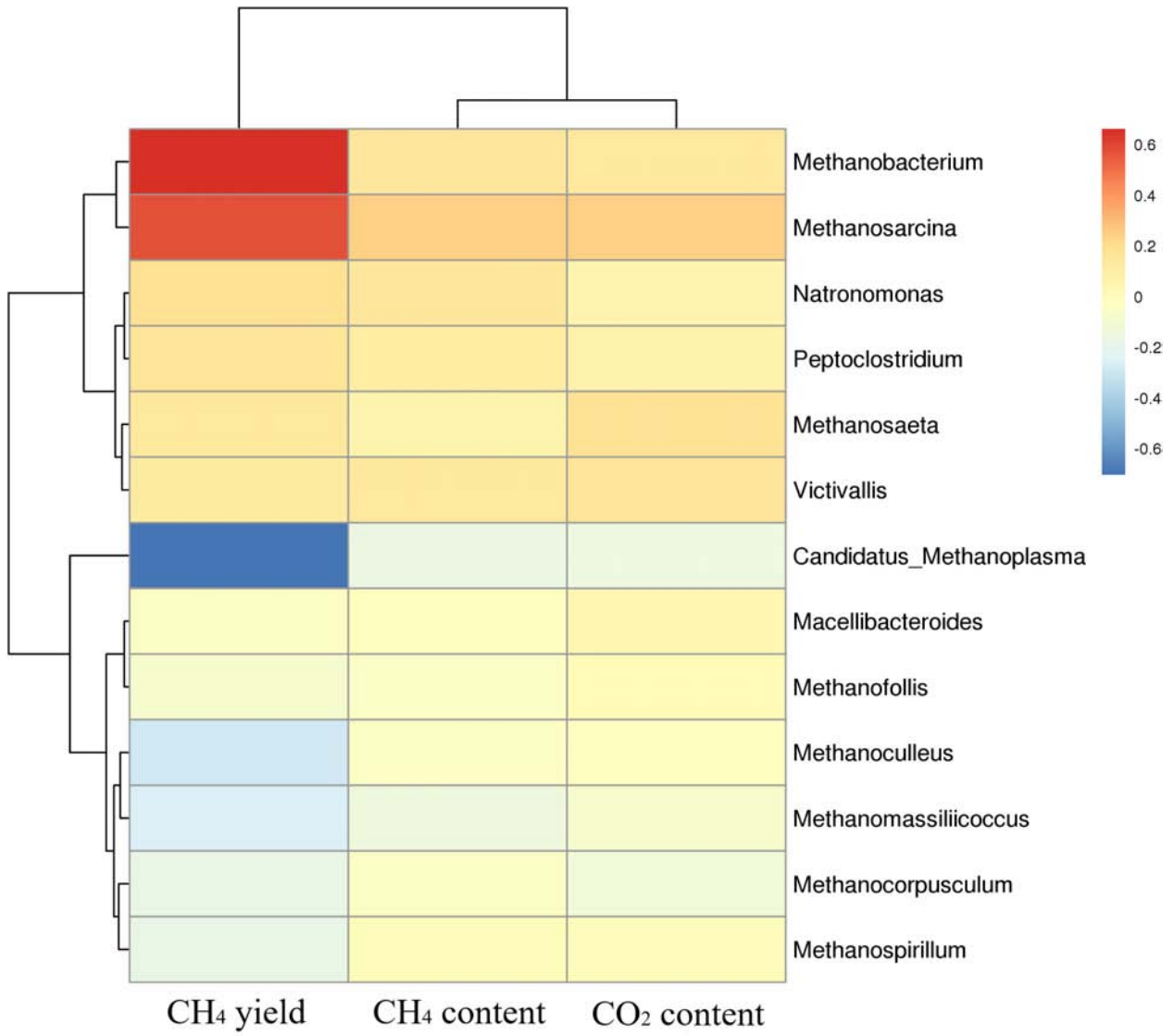


**FIGURE 7 |** Cluster analysis of methanogenic flora with $CH_4$ yield, $CH_4$ content, and $CO_2$ content. Red color represents slight difference among methanogenic flora, and blue color represents apparent differences.

According to the analysis results of bacteria, the participating bacteria mainly included Firmicutes, Proteobacteria, Bacteroidetes, and a small amount of Synergistetes in the whole process of gas production. They are very common in the study and cultivation of CBM (Fuertez et al., 2018). The Firmicutes microorganisms mainly participated in the generation of some mixed acids, alcohols, and neutral substances, it plays an important role in the degradation of coal and contributes to the degradation of coal into aromatic compounds, aliphatic compounds and alkanes (Colosimo et al., 2016). Proteobacteria are a kind of abundant bacteria. In general, Proteobacteria in CBM are mainly of β-, γ- and δ- mycetozoa for syntrophism type (Colosimo et al., 2016). The ability of the bacteria to degrade is variable, they can degrade benzene, aromatic, alcohols and other compounds, and use nitrate as the electron acceptor. The decrease of the peak value at 3,375/cm in the infrared spectrogram was probably related to the effect of Proteobacteria. The bacteria belonging to this phylum in the mixed flora of samples included *Paraclostridium*, *Tyzzerella*, and *Enterococcus*. Proteobacteria is a kind of bacteria with abundant species. In general, the deformation bacteria in biogenic CBM are mainly composed of syntrophic deformation bacteria such as β- and γ-δ- deformation bacteria. Bacteroidetes, which is common in sediments, is a large class of chemoautotrophic microorganisms. The bacteria involved in this phylum in all samples were *Macellibacteroides* and *Citrobacter*.

From the taxonomic level of the bacteria genus, the participating bacteria mainly included *Proteus*, *Desulfovibrio*,

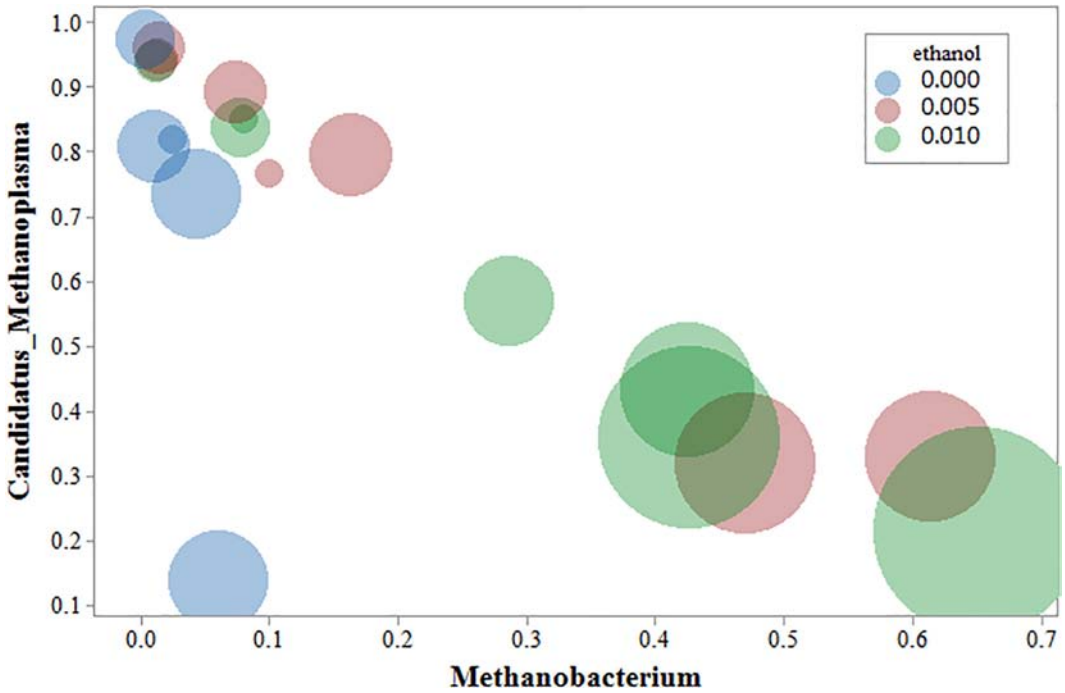


**FIGURE 8 |** Bubble chart of three variables: methanogens, ethanol content, and methane yield. The abscissa represents *Methanobacterium*; the ordinate represents *Candidatus*-Methanoplasma, the bubble size represents the amount of methane yield, blue represents the Group A sample, red represents the B sample, and green represents the C sample.

*Macellibacteroides*, *Paraclostridium* and *Citrobacter*, with a small amount of *Enterococcus* and *Tyzzerella*. As a strictly anaerobic bacterium, *Desulfovibrio* is a δ- mycetozoa and a sulfate-reducing bacterium that can only use sulfate for respiration (Colosimo et al., 2016). *Desulfovibrio* could also use acetic acid, $H_2$, it is possible to generate some unsaturated alkane compounds, thereby promoting the degradation of macromolecular coal. Members of *Desulfovibrio* have been identified in Ishikari Basin-Japan (Vick et al., 2018). In general, δ-proteobacteria can be found in oil fields, coal tar waste waters, coal beds, and formation waters (Jones et al., 2010). *Clostridium* is a kind of anaerobic bacterium that can produce spores with extensive catalytic and metabolic characteristics and degrades starch, chitin, xylose, and cellulose (Zhang et al., 2015). *Clostridium* BC1 and *Clostridium* scatologenes with heavy metal reduction and nitrogen fixation were found from coal (Küsel et al., 2000). *Clostridium* is dominant in stratigraphic water in Western Canada (Penner et al., 2010).

According to the archeal analysis, the archaea were mainly composed of Euryarchaeota at the phylum level and of *Candidatus*-Methanoplasma, *Methanobacterium*, *Methanosarcin*a, and a small amount of *Methanofollis* at the genus level. *Candidatus*-Methanoplasma belongs to Methanomassiliicoccales, which is currently the seventh type of methanogen (Lang et al., 2014). This type of bacteria is composed of obligate hydrogen-dependent methylotrophic bacteria. From the nutritional point of view, the methanogens are mixed nutrient type (Noel et al., 2016). Although the inoculum used in this study was the same as that used by Yang (Yang et al., 2018), *Candidatus*-Methanoplasma was not found in his study. This kind of bacteria has never been found in the study of the microbial flora of CBM. This species exists in the stomach of ruminants and in human feces (Noel et al., 2016). Herein, this kind of bacteria was unfavorable to the formation of methane from coal. The inoculation source used in this study was an enriched and domesticated culture medium. Therefore, we speculated that the bacteria were produced during enrichment and domestication.

Adding ethanol greatly affects the microbial community of archaea. Group A differed greatly from groups B and C. *Methanosarcina* and *Methanobacterium* belong to two completely different archaea. *Methanosarcina* has a wide range of available substrates, in addition to reducing $H_2/CO_2$, decomposing methyl compounds, and also decomposing acetic acid (Park and Liang, 2016). In the study of coal mining, the degradation of acetic acid pathway is the main one because acetate is more readily available than hydrogen (Beckmann et al., 2011). This finding suggests that *Methanosarcina* more likely followed the acetoclastic methanogenesis. Therefore, we speculated that with the extension of fermentation time, the group A was dominated by the methane production pathway of acetic acid type. By contrast, *Methanobacterium* is a typical hydrotrophic methanogen (Kimura et al., 2010). *Methanobacterium* was also discovered in the production of biogas from abandoned coal piles. The advantage of *Methanobacterium* is that similar to Firmicutes, they were consumed by during hydrogen production (Zheng et al., 2016).

Therefore, the ethanol-added experimental group was mainly concentrated on the hydrotrophic methane-producing pathways.

## CONCLUSION

Our study confirmed that the addition of ethanol to the coal-enriched culture could stimulate microorganisms to increase the production of coal-to-methane. Anaerobic fermentation had a great effect on the structure of coal, but the addition of ethanol mainly increased the bioavailability of coal and had little effect on the main structure of coal. The 16S rRNA gene sequencing data showed that ethanol had little effect on bacterial microflora, but changed the microflora structure of archaea significantly, changing the gas-producing pathway from acetoclastic to hydrogenotrophic. This study revealed the intrinsic mechanism of ethanol to increase CBM and provided assistance for future research. Ethanol is non-toxic, inexpensive, and can be used in large-scale operations either *in situ* or *ex situ*.

## AUTHOR CONTRIBUTIONS

XY designed the experimental plan, analyzed the results and read the final manuscript. QL made the experimental trials and wrote the manuscript. YC supported the technical part. BW provided some biological materials, participated to the experimental plan and read the final manuscript.

## FUNDING

This work was supported by the Natural Science and CBM Joint Foundation of Shanxi (2015012002) and the Key Scientific and Technological Project of Shanxi (MQ2014-03).

## ACKNOWLEDGMENTS

We are very grateful to the staff of Yi'an Lanyan Coal and Coalbed Methane Simultaneous Extraction Technology Co., Ltd., for facilitating the sample collection.

## SUPPLEMENTARY MATERIAL

The Supplementary Material for this article can be found online at: https://www.frontiersin.org/articles/10.3389/fmicb.2019.02323/full#supplementary-material

**FIGURE S1 |** Bar chart of the relative abundance of the top 10 bacteria of each group in phylum level.

**FIGURE S2 |** Figure of increasing the carbon content of methane as a percentage of total carbon content.

**TABLE S1 |** The content of $H_2$.

**TABLE S2 |** Quantitative results for bacteria and archaea (log x ± s).

## REFERENCES

Beckmann, S., Lueders, T., Kruger, M., Von Netzer, F., Engelen, B., and Cypionka, H. (2011). Acetogens and acetoclastic methanosarcinales govern methane formation in abandoned coal mines. *Appl. Environ. Microbiol.* 77, 3749–3756. doi: 10.1128/AEM.02818-10

Bi, Z., Zhang, J., Park, S., Harpalani, S., and Liang, Y. (2017). A formation water-based nutrient recipe for potentially increasing methane release from coal *in situ*. *Fuel* 209, 498–508. doi: 10.1016/j.fuel.2017.08.008

Chen, T., Zheng, H., Hamilton, S., Rodrigues, S., Golding, S. D., and Rudolph, V. (2017). Characterisation of bioavailability of Surat Basin Walloon coals for biogenic methane production using environmental microbial consortia. *Int. J. Coal Geol.* 179, 92–112. doi: 10.1016/j.coal.2017.05.017

Colosimo, F., Thomas, R., Lloyd, J. R., Taylor, K. G., Boothman, C., Smith, A. D., et al. (2016). Biogenic methane in shale gas and coal bed methane: a review of current knowledge and gaps. *Int. J. Coal Geol.* 165, 106–120. doi: 10.1016/j.coal.2016.08.011

Dawson, K. S., Dariusz, S. P., Brad, H., Ulrika, L., Matt, A., and Macalady, J. L. (2012). Quantitative fluorescence in situ hybridization analysis of microbial consortia from a biogenic gas field in Alaska's Cook Inlet basin. *Appl. Environ. Microbiol.* 78, 3599–3605. doi: 10.1128/AEM.07122-11

Fallgren, P. H., Zeng, C., Ren, Z., Lu, A., Ren, S., and Jin, S. (2013). Feasibility of microbial production of new natural gas from non-gas-producing lignite. *Int. J. Coal Geol.* 115, 79–84. doi: 10.1016/j.coal.2013.03.003

Fuertez, J., Cordoba, G., Mclennan, J. D., Adams, D. J., and Sparks, T. D. (2018). Potential application of developed methanogenic microbial consortia for coal biogasification. *Int. J. Coal Geol.* 188, 165–180. doi: 10.1016/j.coal.2018.02.013

Ghosh, S., Jha, P., and Vidyarthi, A. S. (2014). Unraveling the microbial interactions in coal organic fermentation for generation of methane — A classical to metagenomic approach. *Int. J. Coal Geol.* 125, 36–44. doi: 10.1016/j.coal.2014.02.005

Green, M. S., Flanegan, K. C., and Gilcrease, P. C. (2008). Characterization of a methanogenic consortium enriched from a coalbed methane well in the Powder River Basin, U.S.A. *Int. J. Coal Geol.* 76, 34–45. doi: 10.1016/j.coal.2008.05.001

Gupta, P., and Gupta, A. (2014). Biogas production from coal via anaerobic fermentation. *Fuel* 118, 238–242. doi: 10.1016/j.fuel.2013.10.075

Haq, S. R., Tamamura, S., Igarashi, T., and Kaneko, K. (2018). Characterization of organic substances in lignite before and after hydrogen peroxide treatment: implications for microbially enhanced coalbed methane. *Int. J. Coal Geol.* 185, 1–11. doi: 10.1016/j.coal.2017.11.009

Jones, E. J. P., Voytek, M. A., Corum, M. D., and Orem, W. H. (2010). Stimulation of methane generation from nonproductive coal by addition of nutrients or a microbial consortium. *Appl. Environ. Microbiol.* 76, 7013–7022. doi: 10.1128/AEM.00728-10

Jones, E. J. P., Voytek, M. A., Warwick, P. D., Corum, M. D., Cohn, A., Bunnell, J. E., et al. (2008). Bioassay for estimating the biogenic methane-generating potential of coal samples. *Int. J. Coal Geol.* 76, 138–150. doi: 10.1016/j.coal.2008.05.011

Kimura, H., Nashimoto, H., Shimizu, M., Hattori, S., Yamada, K., Koba, K., et al. (2010). Microbial methane production in deep aquifer associated with the accretionary prism in Southwest Japan. *ISME J.* 4, 531–541. doi: 10.1038/ismej.2009.132

Küsel, K., Dorsch, T., Acker, G., Stackebrandt, E., and Drake, H. L. (2000). Clostridium scatologenes strain SL1 isolated as an acetogenic bacterium from acidic sediments. *Int. J. Syst. Evol. Microbiol.* 50(Pt 2), 537–546. doi: 10.1099/00207713-50-2-537

Lang, K., Schuldes, J., Klingl, A., Poehlein, A., Daniel, R., and Brune, A. (2014). Comparative genome analysis of "*Candidatus* Methanoplasma termitum" indicates a new mode of energy metabolism in the seventh order of methanogens. *Appl. Environ. Microbiol.* 81, 1338–1352. doi: 10.1128/AEM.03389-14

Liu, Y., Urynowicz, M. A., and Bagley, D. M. (2013). Ethanol conversion to methane by a coal microbial community. *Int. J. Coal Geol.* 115, 85–91. doi: 10.1016/j.coal.2013.02.010

Ma, J., Zhao, Q. B., Laurens, L. L. M., Jarvis, E. E., Nagle, N. J., Chen, S., et al. (2015). Mechanism, kinetics and microbiology of inhibition caused by long-chain fatty acids in anaerobic digestion of algal biomass. *Biotechnol. Biofuels* 8:141. doi: 10.1186/s13068-015-0322-z

National Standards of China (2001). *National Standard of the People's Republic of China*. Beijing: China Standards Press.

Noel, S. J., Højberg, O., Urich, T., and Poulsen, M. (2016). Draft genome sequence of "*Candidatus* Methanomethylophilus" sp. 1r26, enriched from bovine rumen, a methanogenic archaeon belonging to the methanomassiliicoccales order. *Genome Announc.* 4, e1734–15. doi: 10.1128/genomeA.01734-15

Park, S. Y., and Liang, Y. (2016). Biogenic methane production from coal: a review on recent research and development on microbially enhanced coalbed methane (MECBM). *Fuel* 166, 258–267. doi: 10.1016/j.fuel.2015.10.121

Penner, T. J., Foght, J. M., and Budwill, K. (2010). Microbial diversity of western Canadian subsurface coal beds and methanogenic coal enrichment cultures. *Int. J. Coal Geol.* 82, 81–93. doi: 10.1016/j.coal.2010.02.002

Shimizu, S., Akiyama, M., Naganuma, T., Fujioka, M., Nako, M., and Ishijima, Y. (2007). Molecular characterization of microbial communities in deep coal seam groundwater of northern Japan. *Geobiology* 5, 423–433. doi: 10.1111/j.1472-4669.2007.00123.x

Strąpoć, D., Mastalerz, M., Dawson, K., Macalady, J., Callaghan, A. V., Wawrik, B., et al. (2011). Biogeochemistry of microbial coal-bed methane. *Annu. Rev. Earth Planet. Sci.* 39, 617–656. doi: 10.1146/annurev-earth-040610-133343

Takanohashi, T., Terao, Y., Yoshida, T., and Iino, M. (2000). Adsorption and diffusion of alcohol vapors by Argonne premium coals. *Energy Fuel* 14, 915–919. doi: 10.1021/ef000014q

Ünal, B., Perry, V. R., Sheth, M., Gomez-Alvarez, V., Chin, K. J., and Nüsslein, K. (2012). Trace elements affect methanogenic activity and diversity in enrichments from subsurface coal bed produced water. *Front. Microbiol.* 3:175. doi: 10.3389/fmicb.2012.00175

Vick, S. H. W., Greenfield, P., Tran-Dinh, N., Tetu, S. G., Midgley, D. J., and Paulsen, I. T. (2018). The Coal Seam Microbiome (CSMB) reference set, a lingua franca for the microbial coal-to-methane community. *Int. J. Coal Geol.* 186, 41–50. doi: 10.1016/j.coal.2017.12.003

Yang, X., Chen, Y., Wu, R., Nie, Z., Han, Z., Tan, K., et al. (2018). Potential of biogenic methane for pilot-scale fermentation ex situ with lump anthracite and the changes of methanogenic consortia. *J. Ind. Microbiol. Biotechnol.* 45, 229–237. doi: 10.1007/s10295-018-2023-7

Zhang, J., Catherine, Y., Xia, C., and Liang, Y. (2019). Evaluation of methane release from coals from the San Juan basin and Powder River basin. *Fuel* 244, 388–394. doi: 10.1016/j.fuel.2019.02.020

Zhang, J., Liang, Y., Pandey, R., and Harpalani, S. (2015). Characterizing microbial communities dedicated for conversion of coal to methane *in situ* and *ex situ*. *Int. J. Coal Geol.* 146, 145–154. doi: 10.1016/j.coal.2015.05.001

Zhang, J., Liang, Y., and Harpalani, S. (2016a). Optimization of methane production from bituminous coal through biogasification. *Appl. Energy* 183, 31–42. doi: 10.1016/j.apenergy.2016.08.153

Zhang, J., Park, S. Y., Liang, Y., and Harpalani, S. (2016b). Finding cost-effective nutrient solutions and evaluating environmental conditions for biogasifying bituminous coal to methane ex situ. *Appl. Energy* 165, 559–568. doi: 10.1016/j.apenergy.2015.12.067

Zheng, H., Chen, T., Rudolph, V., and Golding, S. D. (2016). Biogenic methane production from Bowen Basin coal waste materials. *Int. J. Coal Geol.* 169, 22–27. doi: 10.1016/j.coal.2016.09.006

**Conflict of Interest:** BW was employed by company Yi'an Lanyan Coal and Coalbed Methane Simultaneous Extraction Technology Co., Ltd.

The remaining authors declare that the research was conducted in the absence of any commercial or financial relationships that could be construed as a potential conflict of interest.

frontiers in Environmental Science

MINI REVIEW
published: 17 December 2018
doi: 10.3389/fenvs.2018.00151

# Recovery of Dissolved Methane From Anaerobic Membrane Bioreactor Using Degassing Membrane Contactors

*Perlie Velasco*[1,2]*, *Veeriah Jegatheesan*[1] *and Maazuza Othman*[1]

[1] School of Engineering, RMIT University, Melbourne, VIC, Australia, [2] Department of Civil Engineering, University of the Philippines, Los Baños, Philippines

At present, the recovery and utilization of methane from anaerobic wastewater treatment systems as a source of energy are well-researched and widely adopted for a more sustainable system approach. However, not all methane produced in an anaerobic treatment system is completely recovered; subsequently, dissolved methane present in the effluent can be released into the environment and contribute to greenhouse gas accumulation in the atmosphere and reduce the system's methane yield. Many studies have already investigated and discussed the factors affecting the production of dissolved methane, as well as the techniques for its recovery. Among the recovery techniques, the use of degassing membrane contactor is most preferred for wastewater treatment application. However, reported data in the literature is limited to certain types of wastewater characteristics and anaerobic systems. Studies on membrane-based recovery of dissolved methane from AnMBR effluents are reviewed in this paper. For the case of the degassing membrane contactor, porous, or micro-porous membranes provides higher dissolved methane recovery efficiency than non-porous. However, porous membranes are more susceptible to pore wetting problem. Among the different operating conditions of degassing membrane contactors, liquid velocity, or flow rate greatly affects the recovery, wherein higher velocity decreases the recovery efficiency of dissolved methane. Consequently, research priorities aimed at development of degassing membrane to accommodate higher liquid velocity and to reduce pore wetting. Moreover, energy analysis of the AnMBR with degassing membrane system should be analyzed for performance in full-scale applications.

**Keywords: methane, wastewater, anaerobic membrane bioreactor, dissolved methane, degassing membrane**

OPEN ACCESS

***Edited by:***
*Obulisamy Parthiba Karthikeyan, University of Michigan, United States*

***Reviewed by:***
*Gaurav Saxena, Babasaheb Bhimrao Ambedkar University, India*
*Suyun Xu, University of Shanghai for Science and Technology, China*

***Correspondence:**
*Perlie Velasco*
*s3686586@student.rmit.edu.au*

***Specialty section:***
*This article was submitted to Wastewater Management, a section of the journal Frontiers in Environmental Science*

***Received:*** *03 August 2018*
***Accepted:*** *29 November 2018*
***Published:*** *17 December 2018*

***Citation:***
*Velasco P, Jegatheesan V and Othman M (2018) Recovery of Dissolved Methane From Anaerobic Membrane Bioreactor Using Degassing Membrane Contactors. Front. Environ. Sci. 6:151. doi: 10.3389/fenvs.2018.00151*

## INTRODUCTION

Methane is a hydrocarbon compound resulting from the anaerobic degradation of organic materials. It is flammable and explosive gas, producing carbon dioxide and water vapor (Encyclopædia Britannica, 2018). The sources of global methane are a result of both natural and anthropogenic activities. The latter provides 60% of methane sources which are further classified as agriculture, energy, waste, and industrial sectors. The majority of methane produced from agriculture sector is released during the enteric fermentation in animal raising; methane from

the energy sector is mainly produced from the production and processing of oil; from the waste sector it is primarily generated from the solid waste and wastewater processing; and lastly, the industrial source of methane comes from chemicals and metal productions (Karakurt et al., 2012).

As part of the focus of this study, almost 9% of the methane released into the environment comes from the activities involved in wastewater systems—from its collection, treatment, and disposal (Karakurt et al., 2012; Hu et al., 2017; Short et al., 2017). Methane is released into the wastewater through the metabolism of methanogens in an anaerobic condition of wastewater treatment system (Crone et al., 2016). Water or wastewater treatment is an inevitable part of the human community to abate the negative impacts of its disposal on the environment and living beings. However, the high energy requirement for the collection and treatment of wastewater is a major concern. This emphasizes the need for processes which will allow recovery of methane and its utilization as a source of energy for the wastewater treatment plant to improve its energy efficiency (Rongwong et al., 2018). Theoretically, about 0.35 liters of methane is produced per grams of chemical oxygen demand (COD) removed from the wastewater (Tchobanoglous et al., 2003) and about one cubic meter of methane has an estimated energy potential of 9 kWh (Crone et al., 2016). As cited in the study of Molino et al. (2013), if methane produced from the wastewater treatment system is used as automotive fuel, around 97% of potential carbon dioxide emission can be reduced compared to the use of fossil fuel, provided that the methane content of biogas is at least 90% (Harasimowicz et al., 2007). A critical review study on nine pilot-scale AnMBR systems (treating domestic wastewater) estimated that five of these systems have positive energy balance, which proved the potential of AnMBR to be an energy producer (Shin and Bae, 2018). Aside from this energy impact, recovery and utilization of methane have an environmental impact, too. According to the Intergovernmental Panel on Climate Change in 2014, methane has 28 times global warming potential than carbon dioxide (IPCC, 2014). This establishes the need for the control on the release of methane into the environment.

However, not all methane produced in a wastewater treatment system is recovered, which in turn will be discharged with the effluent in the form of dissolved methane and released into the environment. Liu et al. (2014) provided correlations among the solubility of methane in water and the temperature and salinity of the water (**Figure 1**). From **Figure 1**, the theoretical dissolved methane present in municipal wastewater effluent (with an average influent soluble COD concentration of 200 mg/L and a COD removal efficiency of at least 90%) at 30°C is around 45% of the total methane produced (Liu et al., 2014). In support of this, Smith et al. (2013) found that the percentage

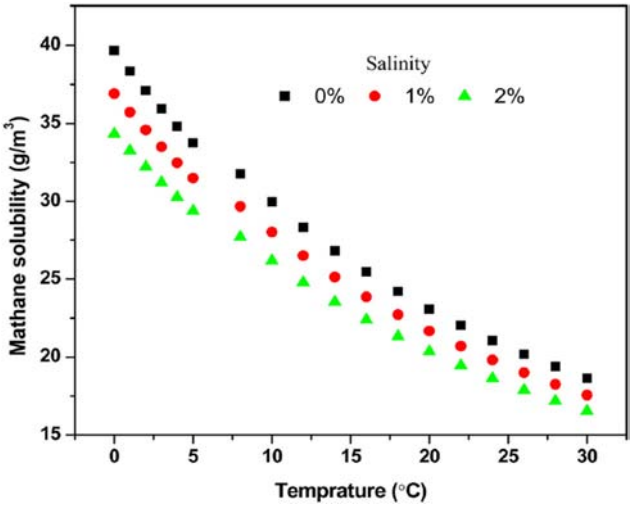


**FIGURE 1 |** Solubility of methane in water under different temperature and salinity (Adapted with permission from Dissolved Methane: A Hurdle for Anaerobic Treatment of Municipal Wastewater Liu et al., 2014. Copyright 2014 American Chemical Society).

of dissolved methane in the effluent is 40–50% at 15°C. This dissolved methane can be utilized as an additional energy source for the operation of wastewater treatment facilities. Rongwong et al. (2018) calculated that optimum net electricity energy of 0.178 MJ could be recovered from the dissolved methane per cubic meter of effluent from an AnMBR coupled with a degassing membrane. This is still around 85% of the total energy recovered from the dissolved methane.

## ANAEROBIC MEMBRANE BIOREACTOR (ANMBR): APPLICATIONS AND CHALLENGES IN WASTEWATER TREATMENT

Anaerobic membrane bioreactor (AnMBR) is a type of biological wastewater treatment system that operates in the absence of oxygen and utilizes membranes to provide solid-liquid separation (Lin et al., 2013). AnMBR is usually favored over other conventional aerobic and anaerobic treatment systems because it provides effluent with high quality, requires a smaller footprint, provides long solid retention time (SRT) while having low hydraulic retention time (HRT), and allows complete retention of biomass. Also, it has lesser start-up time and can be applied as either complete treatment or pre-treatment. However, the major challenge with AnMBR is to maintain the permeate flux which will tend to reduce over time due to the fouling of membrane. But with the addition of membrane fouling control, such as gas sparging and use of chemicals, the operating and maintenance expenditures will increase (Lin et al., 2013; Berkessa et al., 2018).

The configuration of AnMBR can either be an external crossflow AnMBR, where the membrane module is separated from the reactor, or submerged AnMBR (SAnMBR), where

**Abbreviations:** AnMBR, anaerobic membrane bioreactor; COD, chemical oxygen demand; EGSB, expanded granular sludge bed; HRT, hydraulic retention time; OLR, organic loading rate; PDMS, polydimethylsiloxane; PE, polyethylene; PP, polypropylene; PU, Polyurethane; PVDF, Polyvinylidene difluoride; SAF-MBR, staged anaerobic fluidized membrane bioreactor; SRT, solids retention time; SAnMBR, submerged anaerobic membrane bioreactor; UASB, upflow anaerobic sludge blanket.

the membrane is submerged in the reactor. Although external AnMBR provides more direct control of fouling and easier replacement of membrane module, studies confirm that SAnMBR has lower energy consumption, fewer cleaning procedures, and lower tangential velocities (Lin et al., 2013; Dvorák et al., 2015). Furthermore, membrane materials used in AnMBR is categorized as polymeric, metallic, and inorganic, and the membrane module configuration as flat sheet, hollow fiber, and tubular. Aside from the material and configuration of the membrane, its pore size also determines the treatment efficiency and the capability of AnMBR (Lin et al., 2013).

Based on the review by Lin et al. (2013), the applicability of AnMBR in wastewater treatment is described by the influent concentration, influent particulate characteristics, and extreme conditions, such as very high or very low temperature and pH. It was then concluded that AnMBR is applicable to treat all types of wastewater except those with high organic strength, low particulate concentration, and less extreme conditions. With this, new designs for AnMBR have emerged to improve the applicability of AnMBR to other environments, such as high strength and industrial wastewaters, with lesser problems with fouling (Liu et al., 2016; Hu et al., 2017; Berkessa et al., 2018).

## RECOVERY OF DISSOLVED METHANE FROM ANAEROBIC TREATMENT EFFLUENTS

One of the major challenges associated with the methane recovery from anaerobic processes is the high concentration of dissolved methane in the effluent (Liu et al., 2014). Many studies link this high concentration to the supersaturation index of dissolved methane which is defined as the ratio between the actual dissolved methane concentration and the theoretical concentration, based on Henry's Law (Crone et al., 2016). Supersaturation is caused by shock conditions and entrapped bubbles in the sludge (Smart Water Fund, 2013). Rongwong et al. (2018) reported that this supersaturation index varied in the different reactors, wherein upflow anaerobic sludge blanket has a higher supersaturation of methane (at most 6.9) than in AnMBR (at most 1.5). This low supersaturation index of AnMBR is due to the ability of the system to retain the biomass in the reactor (Crone et al., 2016).

Apart from the supersaturation, the release of methane gas in the headspace of the AnMBR would initially determine the concentration of the dissolved methane in the effluent. Guo et al. (2016) listed and analyzed the factors that affect the stability and transfer of methane in the headspace of AnMBR, namely temperature, pH, solid retention time (SRT), organic loading rate (OLR), and hydraulic retention time (HRT). For temperature, Henry's Law states that higher temperature lowers the solubility of gases. Thus, thermophilic conditions (50–60°C) are generally favorable for methane production since at psychrophilic temperatures (3–15°C), the dissolved methane in the effluent increases (Lin et al., 2013; Smith et al., 2015; Guo et al., 2016). However, the thermophilic condition is not widely utilized due to the additional energy requirement. The study emphasized the need for further research for optimal temperature condition and the effect of temperature shocks in biogas production. In the study of Gao et al. (2011), it is worthwhile to note that submerged AnMBR can tolerate temperature changes with little to no effect on the recovery of biogas. In the case of pH, methane production is higher within the optimal range of 6.0–8.0, which provides favorable pH condition for the growth of methanogenic bacteria (Huang et al., 2008; Ward et al., 2008; Weiland, 2010). Subsequently, a study by Gao et al. (2010) of submerged AnMBR for thermomechanical whitewater treatment with varying pH shocks found that it lowers the methane recovery, increases fouling, and lowers effluent quality. This lower methane recovery could be attributed to the increase in the supersaturation of methane due to shock condition. Lastly, longer SRT and HRT as well as higher OLR (since 0.35 liters of methane can be recovered for every gram of COD removed) provide higher methane production (Roh et al., 2006; Saddoud and Sayadi, 2007; Wijekoon et al., 2011; Guo et al., 2016). From the study of Yeo and Lee (2013), the production of methane gas is 45% higher for SRT of 40 days compared to that of 20 days. Also, they found out that supersaturation of dissolved methane occurred for 20 days and none for 40 days. However, lower HRT and higher OLR could induce fouling (Guo et al., 2016).

There are several techniques for the recovery of dissolved methane in the anaerobic wastewater treatment effluent. The most common techniques for these systems are aeration, gas stripping, and degassing membrane. The use of membranes provides the highest potential for dissolved methane recovery due to its ease of operation and high mass transfer area (Rongwong et al., 2018). Moreover, agitation provides the lowest methane recovery among the list, while sparging and degassing membrane produce the best methane recovery with medium to high capital and operating costs (Smart Water Fund, 2013).

The mechanism of the membrane to separate the gas from the liquid is from the concentration difference defined by Fick's Law and pressure drop across the membrane (Gabelman and Hwang, 1999; Crone et al., 2016). Moreover, the hydrophobicity of the membranes acts as a barrier between the gas and liquid phases (Wongchitphimon et al., 2017). The hollow fiber membrane is the most used configuration for the membrane due to its high gas-liquid separation efficiency, compactness, ease of scaling-up, and very high surface area as compared to flat sheet membranes. There is a wide range of commercially available hollow fiber membranes that varies from the type of hydrophobic polymer used, the porosity (non-porous, porous, microporous), and the inner and outer diameters, length, thickness, and the number of the fibers. However, membrane wetting, which is the penetration of liquid into the pores of the membrane, is the major issue in degassing due to the additional mass transfer resistance it poses (Wongchitphimon et al., 2017).

**Table 1** summarizes the different studies which used a degassing membrane contactor unit to improve the recovery of dissolved methane recovery from the effluent of the reactor. From these studies, use of a degassing unit improved the recovery of dissolved methane from the effluent of the reactors used to almost 99%. All of these studies concluded that low liquid velocity or

**TABLE 1 |** Literature on degassing membrane for improved dissolved methane recovery.

| References | Reactor (effluent source) | Degassing membrane specifications | Dissolved methane recovery efficiency (%) | Condition for higher dissolved methane recovery |
|---|---|---|---|---|
| Bandara et al., 2011 | UASB | Non-porous PE and porous PU (Mitsubishi Rayon Co.); contact area = 1.7 $m^2$ | 86 | Long retention time; High transmembrane pressure; Low temperature |
| Cookney et al., 2012 | EGSB | PDMS (Sterilin Ltd. UK); contact area = 0.139 $m^2$ | 72 | Low liquid velocity |
| Giménez et al., 2012 | SAnMBR | Hollow fiber ultrafiltration (PURON Koch, 0.05 micrometer) PVDF | 57 | Low influent soluble sulfate concentration |
| Luo et al., 2014 | UASB | Non-porous (PU) sandwiched between porous (PP) (Model 3504 Mitsubishi Rayon); with stirring | 86 | Carbon dioxide desorption |
| Cookney et al., 2016 | UASB and AnMBR | PDMS non-porous potted with PVC (area = 0.094 $m^2$) and PP micro-porous (area = 0.58 $m^2$) | 99 | PP (micro-porous) membrane; Low liquid velocity |
| Henares et al., 2016 | Expanded Granular Sludge Bed (EGSB) | Non-porous PDMS (area = 0.0159 $m^2$) and Micro-porous PP (area = 0.180 $m^2$) | 98 | Micro-porous PP; Low liquid flux; High transmembrane pressure; Flow at lumen side of membrane |

*SAnMBR, submerged anaerobic membrane bioreactor (AnMBR); UASB, upflow anaerobic sludge blanket; SAF-MBR, staged anaerobic fluidized membrane bioreactor; EGSB, expanded granular sludge bed; PE, Polyethylene; PU, Polyurethane; PP, Polypropylene; PDMS, Polydimethylsiloxane; PVDF, Polyvinylidene difluoride.*

flux, high transmembrane pressure, and porous/micro-porous membranes increase the recovery efficiency of dissolved methane from the effluent. At lower liquid flux, the membrane contact time increases the probability of methane to be diffused into the membrane (Cookney et al., 2012). In the study of Cookney et al. (2016), the recovery of dissolved methane decreased from 98.9 to 63.3% when the liquid velocity was increased from 0.0004 to 0.045 m/s. This decrease in the recovery efficiency is more pronounced for the case of non-porous membrane used, wherein the efficiency decreased from 92.6% (0.0004 m/s) to 10.8% (0.047 m/s). This shows that porous/micro-porous membrane is better than non-porous membrane in terms of dissolved methane recovery at high liquid flux.

A study by Cookney et al. (2016) found that the mass transfer resistance in porous membrane is 0.2% at high liquid velocity and 91% with non-porous membrane. However, in the study of Henares et al. (2016), the micro-porous membrane has lower recovery efficiency than non-porous membrane at higher liquid flux (for 90 L/h/$m^2$ at a vacuum pressure of 50 kPa). This is due to the pore wetting problem typically experienced with porous/micro-porous membranes at higher liquid flux (Henares et al., 2016). On the other hand, flow in lumen side of the hollow fiber membranes (flow is through the inside of the fiber) rather than its shell side (flow through the outside) is favorable for recovery of dissolved methane. This is because the lumen side provides higher mass transfer efficiency (Crone et al., 2016). Finally, these degassing units did not show any negative impact on the effluent quality.

## RESEARCH PRIORITIES

Several studies proved that AnMBR showed a more stable supersaturation index (1.0–1.5) than the upflow anaerobic sludge blanket reactor (1.34–6.9), as summarized in the review study of Crone et al. (2016). However, only a few studies have been carried out for AnMBR with the focus on the connection between the supersaturation and the dissolved methane recovery. As presented in the study of Cookney et al. (2016), although the supersaturation is almost 1.0, the percentage of dissolved methane in the effluent is 88%. In comparison to the other AnMBR study of Smith et al. (2013), the index is 1.5 while the percentage of dissolved methane in the effluent is at most 50%. This could be attributed to the operating condition of the reactor wherein biogas sparging or bubbling was employed and the organic loading rate was very high.

Aside from this, all of the studies presented in **Table 1** did not measure the actual dissolved methane concentration in the effluent; rather the concentration was computed based on temperature and partial pressure in the still headspace from Henry's Law. With the advancement of technology, now the actual methane concentration in the effluent can be measured for accurate quantification. At present, only two studies used a commercially available probe to measure the actual dissolved methane (Rongwong et al., 2017; Wongchitphimon et al., 2017). Other studies for AnMBR showed that the higher methane recovery is expected from hybrid system (two-stage/two-phased reactors) and with sparging (Roh et al., 2006; Saddoud and Sayadi, 2007; Huang et al., 2008; Lin et al., 2009; Gao et al., 2010; Xie et al., 2010, and Wijekoon et al., 2011). This is supported by the study of Shoener et al. (2016), wherein a cross-flow multi-tube and submerged hollow fiber with granular activated carbon (GAC) configurations were suggested. Moreover, as seen in **Table 1**, there are very limited studies on the use of degassing membrane contactor in recovering dissolved methane from the AnMBR effluent. Further studies should be aimed at the optimization of the different operating conditions of degassing membrane contactor, such as liquid flux and

transmembrane pressure, inclusion of carbon dioxide desorption, and development of new membrane that is durable and resistant to pore wetting (Rongwong et al., 2017; Wongchitphimon et al., 2017). Finally, energy analysis on the use of degassing membrane contactor is a must to justify its economic and environmental impact.

On the other hand, improvement of methane concentration in biogas recovered from wastewater should also be looked into for the better utilization of biogas. Huertas et al. (2011) stated that for energy management there should at least 70% methane, at most 10% carbon dioxide, and negligible hydrogen sulfide be present in the biogas. However, it should be noted that removal of carbon dioxide is only recommended if the recovered biogas is used as a vehicle fuel and as natural gas for the grid; removal of carbon dioxide is usually not required for boiler, kitchen stove, and combined heat and power (CHP) applications (Petersson and Wellinger, 2009). For the cases which require biogas upgrade, techniques such as absorption (at least 97% methane), adsorption (95–99% methane), membrane separation (at least 96% methane), and cryogenic separation (90–99% methane) can be employed (Chen et al., 2015). Among these techniques, the use of membranes showed the most benefits such as low energy consumption, good selectivity, ease of engineering (Chen et al., 2015).

## CONCLUSION

The use of the membranes in wastewater treatment is a well-established technology and currently used for the treatment of high strength or industrial wastewater. Moreover, the membrane can also be used as a technique to separate the dissolved methane from the effluent of an anaerobic treatment reactor. However, there are limited studies regarding the use of membranes for this kind of application, i.e., combining AnMBR and a degassing membrane contactor, with a focus on the recovery of dissolved methane. The studies reviewed showed that dissolved methane recovery using a degassing membrane contactor was higher under the following conditions: low liquid velocity or flux, higher transmembrane pressure, use of porous or micro-porous membrane, flow of liquid from the lumen side of the membrane, presence of carbon dioxide desorption, longer retention time, and low temperature. Moreover, the highest reported recovery of dissolved methane from an AnMBR effluent was around 99% obtained using a polypropylene micro-porous membrane with a liquid velocity of 0.0004 m/s. Therefore, further studies with an aim to optimize recovery and development of new membranes, while considering membrane fouling and pore wetting problem. Finally, this optimization should consider the economy of the system as well.

## AUTHOR CONTRIBUTIONS

PV synthesized the whole review paper, as part of her on-going doctorate study. This was then reviewed and edited by VJ and MO.

## FUNDING

This review is part of the on-going doctorate study of the first author under the grant from the Commission on Higher Education, Philippines, the University of the Philippines, and the RMIT University, Australia.

## ACKNOWLEDGMENTS

The authors would like to acknowledge RMIT University, Australia and the government of the Philippines for the academic and financial support.

## REFERENCES

Bandara, W. M., Satoh, H., Sasakawa, M., Nakahara, Y., Takahashi, M., and Okabe, S. (2011). Removal of residual dissolved methane gas in an upflow anaerobic sludge blanket reactor treating low-strength wastewater at low temperature with degassing membrane. *Water Res.* 45, 3533–3540. doi: 10.1016/j.watres.2011.04.030

Berkessa, Y. W., Yan, B., Li, T., Tan, M., She, Z., Jegatheesan, V., et al. (2018). Novel anaerobic membrane bioreactor (AnMBR) design for wastewater treatment at long HRT and high solid concentration. *Bioresour. Technol.* 250, 281–289. doi: 10.1016/j.biortech.2017.11.025

Chen, X. Y., duc Vinh, H., Ramirez, A. A., Rodrigue, D., and Kaliaguine, S. (2015). Membrane gas separation technologies for biogas upgrading. *RSC Adv.* 5, 24399–24448. doi: 10.1039/C5RA00666J

Cookney, J., Cartmell, E., Jefferson, B., and McAdam, E., J. (2012). Recovery of methane from anaerobic process effluent using poly-di-methyl-siloxane membrane contactors. *Water Sci. Technol.* 65, 604–610. doi: 10.2166/wst.2012.897

Cookney, J., McLeod, A., Mathioudakis, V., Ncube, P., Soares, A., Jefferson, B., et al. (2016). Dissolved methane recovery from anaerobic effluents using hollow fibre membrane contactors. *J. Memb. Sci.* 502, 141–150. doi: 10.1016/j.memsci.2015.12.037

Crone, B. C., Garland, J., L., Sorial, G., A., and Vane, L., M. (2016). Significance of dissolved methane in effluents of anaerobically treated low strength wastewater and potential for recovery as an energy product: a review. *Water Res.* 104, 520–531. doi: 10.1016/j.watres.2016.08.019

Dvorák, L., Gómez, M., Dolina, J., and Cernín, A. (2015). Anaerobic membrane bioreactors—a mini review with emphasis on industrial wastewater treatment: applications, limitations and perspectives. *Desalin. Water Treat.* 57, 19062–19076. doi: 10.1080/19443994.2015.1100879

Encyclopædia Britannica (2018). *Encyclopædia Britannica*. Available online at: https://www.britannica.com/science/methane (Accessed September 17, 2018).

Gabelman, A., and Hwang, S-T. (1999). Hollow fiber membrane contactors. *J. Memb. Sci.* 159, 61–106. doi: 10.1016/S0376-7388(99)00040-X

Gao, Jane, W., J., Lin, H., J., Leung, K., T., and Liao, B., Q. (2010). Influence of elevated pH shocks on the performance of a submerged anaerobic membrane bioreactor. *Proc. Biochem.* 45, 1279–1287. doi: 10.1016/j.procbio.2010.04.018

Gao, W. J., Leung, K., T., Qin, W., S., and Liao, B., Q. (2011). Effects of temperature and temperature shock on the performance and microbial community structure of a submerged anaerobic membrane bioreactor. *Bioresour. Technol.* 102, 8733–8740. doi: 10.1016/j.biortech.2011.07.095

Giménez, J. B., Marti, N., Ferrer, J., and Seco, A. (2012). Methane recovery efficiency in a submerged anaerobic membrane bioreactor (SAnMBR) treating sulphate-rich urban wastewater: evaluation of methane losses with the effluent. *Bioresour. Technol.* 118, 67–72. doi: 10.1016/j.biortech.2012.05.019

Guo, W., Ngo, H. H., Chen, C., Pandey, A., Tung, K-L., and Lee, D. J. (2016). "Anaerobic membrane bioreactors for future green bioprocesses," in *Green*

*Technologies for Sustainable Water Management* (Reston: ASCE Library), 867–901. doi: 10.1061/9780784414422.ch25

Harasimowicz, M., Orluk, P., Zakrzewska-Trznadel, G., and Chmielewski, A., G. (2007). Application of polyimide membranes for biogas purification and enrichment. *J. Hazard. Mater.* 144, 698–702. doi: 10.1016/j.jhazmat.2007.01.098

Henares, M., Izquierdo, M., Penya-Roja, J., M., and V. Martínez-Soria. (2016). Comparative study of degassing membrane modules for the removal of methane from Expanded Granular Sludge Bed anaerobic reactor effluent. *Sep. Purificat. Technol.* 170, 22–29. doi: 10.1016/j.seppur.2016.06.024

Hu, D., Su, H., Chen, Z., Cui, Y., Ran, C., Xu, J.,et al (2017). Performance evaluation and microbial community dynamics in a novel AnMBR for treating antibiotic solvent wastewater. *Bioresour. Technol.* 243, 218–227. doi: 10.1016/j.biortech.2017.06.095

Huang, Z., Ong, S., L., and Ng, H., Y. (2008). Feasibility of submerged anaerobic membrane bioreactor (SAMBR) for treatment of low-strength wastewater. *Water Sci. Technol.* 58, 1925–1931. doi: 10.2166/wst.2008.749

Huertas, J. I., Giraldo, N., and Izquierdo, S. (2011). "Removal of $H_2S$ and $CO_2$ from biogas by amine absorption," in *Mass Transfer in Chemical Engineering Processes* (London, UK: IntechOpen), 133–150. doi: 10.5772/20039

IPCC (2014). Climate Change 2014: Synthesis Report. *Contribution of Working Groups I, II and III to the Fifth Assessment Report of the Intergovernmental Panel on Climate Change*, eds R. K. Pachauri, M. R. Allen, V. R. Barros, J. Broome, W. Cramer, R. Christ, J. A. Church, L. Clarke, Q. Dahe and P. Dasgupta: IPCC.

Karakurt, I., Aydin, G., and Aydiner, K. (2012). Sources and mitigation of methane emissions by sectors: a critical review. *Renew. Energy* 39, 40–48. doi: 10.1016/j.renene.2011.09.006

Lin, H., Peng, W., Zhang, M., Chen, J., Hong, H., and Zhang, Y. (2013). A review on anaerobic membrane bioreactors: applications, membrane fouling and future perspectives. *Desalination* 314, 169–188. doi: 10.1016/j.desal.2013.01.019

Lin, H. J., Xie, K., Mahendran, B., Bagley, D., M., Leung, K., T., Liss, S., N., et al. (2009). Sludge properties and their effects on membrane fouling in submerged anaerobic membrane bioreactors (SAnMBRs). *Water Res.* 43, 3827–3837. doi: 10.1016/j.watres.2009.05.025

Liu, J., Jia, X., Gao, B., Bo, L., and Wang, L. (2016). Membrane fouling behavior in anaerobic baffled membrane bioreactor under static operating condition. *Bioresour. Technol.* 214, 582–588. doi: 10.1016/j.biortech.2016.05.016

Liu, Z. H., Yin, H., Dang, Z., and Liu, Y. (2014). Dissolved methane: a hurdle for anaerobic treatment of municipal wastewater. *Environ. Sci. Technol.* 48, 889–890. doi: 10.1021/es405553j

Luo, G., Wang, W., and Angelidaki, I. (2014). A new degassing membrane coupled upflow anaerobic sludge blanket (UASB) reactor to achieve *in-situ* biogas upgrading and recovery of dissolved $CH_4$ from the anaerobic effluent. *Appl. Energy* 132, 536–542. doi: 10.1016/j.apenergy.2014.07.059

Molino, A., Migliori, M., Ding, Y., Bikson, B., Giordano, G., and Braccio, G. (2013). Biogas upgrading via membrane process: modelling of pilot plant scale and the end uses for the grid injection. *Fuel* 107, 585–592. doi: 10.1016/j.fuel.2012.10.058

Petersson, A., and Wellinger, A. (2009). *Biogas Upgrading Technologies Developments and Innovations*. Technical Brochure, IEA Bioenergy 20, 1–19.

Roh, S., Chun, Y. N., Nah, J.-W., Shin, H.-J., and Kim, S.-I. (2006). Wastewater treatment by anaerobic digestion coupled with membrane processing. *J. Indust. Chem.* 12, 489–493.

Rongwong, W., Goh, K., and Bae, T-H. (2018). Energy analysis and optimization of hollow fiber membrane contactors for recovery of dissolve methane from anaerobic membrane bioreactor effluent. *J. Memb. Sci.* 554, 184–194. doi: 10.1016/j.memsci.2018.03.002

Rongwong, W., Wongchitphimon, S., Goh, K., Wang, R., and Bae, T-H. (2017). Transport properties of $CO_2$ and $CH_4$ in hollow fiber membrane contactor for the recovery of biogas from anaerobic membrane bioreactor effluent. *J. Memb. Sci.* 541, 62–72. doi: 10.1016/j.memsci.2017.06.090

Saddoud, A., and Sayadi, S. (2007). Application of acidogenic fixed-bed reactor prior to anaerobic membrane bioreactor for sustainable slaughterhouse wastewater treatment. *J. Hazard. Mater.* 149, 700–706. doi: 10.1016/j.jhazmat.2007.04.031

Shin, C., and Bae, J. (2018). Current status of the pilot-scale anaerobic membrane bioreactor treatments of domestic wastewaters: a critical review. *Bioresour. Technol.* 247, 1038–1046. doi: 10.1016/j.biortech.2017.09.002

Shoener, B. D., Zhong, C., Greiner, A. D., Khunjar, W. O., Hong, P-Y., and Guest, J. S. (2016). Design of anaerobic membrane bioreactors for the valorization of dilute organic carbon waste streams. *Energy Environ. Sci.* 9, 1102–1112. doi: 10.1039/C5EE03715H

Short, M. D., Daikeler, A., Wallis, K., Peirson, W., L., and Peters, G., M. (2017). Dissolved methane in the influent of three Australian wastewater treatment plants fed by gravity sewers. *Sci. Tot. Environ.* 599–600, 85–93. doi: 10.1016/j.scitotenv.2017.04.152

Smart Water Fund (2013). *Literature Review of Technology for the Recovery of Methane From Wastewater*.

Smith, A. L., Skerlos, S., J., and Raskin, L. (2013). Psychrophilic anaerobic membrane bioreactor treatment of domestic wastewater. *Water Res.* 47, 1655–1665. doi: 10.1016/j.watres.2012.12.028

Smith, A. L., Skerlos, S., J., and Raskin, L. (2015). Anaerobic membrane bioreactor treatment of domestic wastewater at psychrophilic temperatures ranging from 15°C to 3°C. *Environ. Sci. Water Res. Technol.* 1, 56–64. doi: 10.1039/C4EW00070F

Tchobanoglous, G., Burton, F. L., Stensel, D. H., Metcalf and Eddy, Inc., eds. (2003). *Wastewater Engineering: Treatment and Reuse, 4th Edn*, New York, NY: McGraw-Hill.

Ward, A. J., Hobbs, P., J., Holliman, P., J., and Jones, D., L. (2008). Optimisation of the anaerobic digestion of agricultural resources. *Bioresour. Technol.* 99, 7928–7940. doi: 10.1016/j.biortech.2008.02.044

Weiland, P. (2010). Biogas production: current state and perspectives. *Appl. Microbiol. Biotechnol.* 85, 849–860. doi: 10.1007/s00253-009-2246-7

Wijekoon, K. C., Visvanathan, C., and Abeynayaka, A. (2011). Effect of organic loading rate on VFA production, organic matter removal and microbial activity of a two-stage thermophilic anaerobic membrane bioreactor. *Bioresour. Technol.* 102, 5353–5360. doi: 10.1016/j.biortech.2010.12.081

Wongchitphimon, S., Rongwong, W., Chuah, C. Y., Wang, R., and Bae, T-H. (2017). Polymer-fluorinated silica composite hollow fiber membranes for the recovery of biogas dissolved in anaerobic effluent. *J. Memb. Sci.* 540, 146–154. doi: 10.1016/j.memsci.2017.06.050

Xie, K., Lin, H., J., Mahendran, B., Bagley, D., M., Leung, K., T., Liss, S., N., et al. (2010). Performance and fouling characteristics of a submerged anaerobic membrane bioreactor for kraft evaporator condensate treatment. *Environ. Technol.* 31, 511–521. doi: 10.1080/09593309035 27898

Yeo, H., and Lee, H. S. (2013). The effect of solids retention time on dissolved methane concentration in anaerobic membrane bioreactors. *Environ. Technol.* 34, 2105–2112. doi: 10.1080/09593330.2013.808675

**Conflict of Interest Statement:** The authors declare that the research was conducted in the absence of any commercial or financial relationships that could be construed as a potential conflict of interest.

# Advantages of publishing in Frontiers

**OPEN ACCESS**
Articles are free to read for greatest visibility and readership

**FAST PUBLICATION**
Around 90 days from submission to decision

**HIGH QUALITY PEER-REVIEW**
Rigorous, collaborative, and constructive peer-review

**TRANSPARENT PEER-REVIEW**
Editors and reviewers acknowledged by name on published articles

**Frontiers**
Avenue du Tribunal-Fédéral 34
1005 Lausanne | Switzerland

**Visit us:** www.frontiersin.org
**Contact us:** info@frontiersin.org | +41 21 510 17 00

**REPRODUCIBILITY OF RESEARCH**
Support open data and methods to enhance research reproducibility

**DIGITAL PUBLISHING**
Articles designed for optimal readership across devices

**FOLLOW US**
@frontiersin

**IMPACT METRICS**
Advanced article metrics track visibility across digital media

**EXTENSIVE PROMOTION**
Marketing and promotion of impactful research

**LOOP RESEARCH NETWORK**
Our network increases your article's readership